

Edited by
François Béguin and Elżbieta Frąckowiak

Supercapacitors

Related Titles

Stolten, D., Emonts, B. (eds.)

Fuel Cell Science and Engineering

Materials, Processes, Systems and Technology

2012

ISBN: 978-3-527-33012-6

Aifantis, K. E., Hackney, S. A., Kumar, R. V. (eds.)

High Energy Density Lithium Batteries

Materials, Engineering, Applications

2010

ISBN: 978-3-527-32407-1

Park, J.-K.

Principles and Applications of Lithium Secondary Batteries

2012

ISBN: 978-3-527-33151-2

Ozawa, K. (ed.)

Lithium Ion Rechargeable Batteries

Materials, Technology, and New Applications

2009

ISBN: 978-3-527-31983-1

Daniel, C., Besenhard, J. O. (eds.)

Handbook of Battery Materials 2nd completely revised and enlarged edition

2011

ISBN: 978-3-527-32695-2

O'Hayre, R., Colella, W., Cha, S.-W., Prinz, F. B.

Fuel Cell Fundamentals

ISBN: 978-0-470-25843-9

Zhang, J., Zhang, L., Liu, H., Sun, A., Liu, R-S. (eds.)

Electrochemical Technologies for Energy Storage and Conversion

2011

ISBN: 978-3-527-32869-7

Edited by François Béguin and Elżbieta Frąckowiak

Supercapacitors

Materials, Systems, and Applications



**WILEY-
VCH**

WILEY-VCH Verlag GmbH & Co. KGaA

The Editors

Prof. François Béguin

Poznan University of Technology
Faculty of Chemical Technology
u1. Piotrowo 3
Poznan, 60-965
Poland

Prof. Elzbieta Frąckowiak

Poznan University of Technology
Institute of Chemistry and Technical Electrochemistry
u1. Piotrowo 3
Poznan, 60-965
Poland

All books published by **Wiley-VCH** are carefully produced. Nevertheless, authors, editors, and publisher do not warrant the information contained in these books, including this book, to be free of errors. Readers are advised to keep in mind that statements, data, illustrations, procedural details or other items may inadvertently be inaccurate.

Library of Congress Card No.: applied for

British Library Cataloguing-in-Publication Data

A catalogue record for this book is available from the British Library.

Bibliographic information published by the Deutsche Nationalbibliothek

The Deutsche Nationalbibliothek lists this publication in the Deutsche Nationalbibliografie; detailed bibliographic data are available on the Internet at <<http://dnb.d-nb.de>>.

© 2013 Wiley-VCH Verlag GmbH & Co. KGaA, Boschstr. 12, 69469 Weinheim, Germany

All rights reserved (including those of translation into other languages). No part of this book may be reproduced in any form – by photoprinting, microfilm, or any other means – nor transmitted or translated into a machine language without written permission from the publishers. Registered names, trademarks, etc. used in this book, even when not specifically marked as such, are not to be considered unprotected by law.

Print ISBN: 978-3-527-32883-3
ePDF ISBN: 978-3-527-64669-2
ePub ISBN: 978-3-527-64668-5
mobi ISBN: 978-3-527-64667-8
oBook ISBN: 978-3-527-64666-1

Materials for sustainable energy and development (Print) ISSN: 2194-7813

Materials for sustainable energy and development (Internet) ISSN: 2194-7821

Typesetting Laserwords Private Limited, Chennai, India

Printing and Binding Markono Print Media Pte Ltd, Singapore

Cover Design Simone Benjamin, McLeese Lake, Canada

Printed in Singapore
Printed on acid-free paper

Editorial Board

Members of the Advisory Board of the “Materials for Sustainable Energy and Development” Series

Professor Huiming Cheng
Professor Calum Drummond
Professor Morinobu Endo
Professor Michael Grätzel
Professor Kevin Kendall
Professor Katsumi Kaneko
Professor Can Li
Professor Arthur Nozik
Professor Detlev Stöver
Professor Ferdi Schüth
Professor Ralph Yang

Contents

Series Editor Preface	XVII
Preface	XIX
About the Series Editor	XXI
About the Volume Editors	XXIII
List of Contributors	XXV

1	General Principles of Electrochemistry	1
	<i>Scott W. Donne</i>	
1.1	Equilibrium Electrochemistry	1
1.1.1	Spontaneous Chemical Reactions	1
1.1.2	The Gibbs Energy Minimum	1
1.1.3	Bridging the Gap between Chemical Equilibrium and Electrochemical Potential	3
1.1.4	The Relation between E and ΔG_r	3
1.1.5	The Nernst Equation	4
1.1.6	Cells at Equilibrium	5
1.1.7	Standard Potentials	5
1.1.8	Using the Nernst Equation – Eh–pH Diagrams	6
1.2	Ionics	6
1.2.1	Ions in Solution	6
1.2.1.1	Ion–Solvent Interactions	7
1.2.1.2	Thermodynamics	8
1.2.2	The Born or Simple Continuum Model	8
1.2.2.1	Testing the Born Equation	9
1.2.3	The Structure of Water	9
1.2.3.1	Water Structure near an Ion	11
1.2.3.2	The Ion–Dipole Model	11
1.2.3.3	Cavity Formation	12
1.2.3.4	Breaking up the Cluster	12
1.2.3.5	Ion–Dipole Interaction	12
1.2.3.6	The Born Energy	13
1.2.3.7	Orienting the Solvated Ion in the Cavity	13

1.2.3.8	The Leftover Water Molecules	14
1.2.3.9	Comparison with Experiment	14
1.2.3.10	The Ion–Quadrupole Model	14
1.2.3.11	The Induced Dipole Interaction	14
1.2.3.12	The Results	15
1.2.3.13	Enthalpy of Hydration of the Proton	15
1.2.4	The Solvation Number	16
1.2.4.1	Coordination Number	16
1.2.4.2	The Primary Solvation Number	16
1.2.5	Activity and Activity Coefficients	16
1.2.5.1	Fugacity (f')	16
1.2.5.2	Dilute Solutions of Nonelectrolytes	16
1.2.5.3	Activity (a)	17
1.2.5.4	Standard States	17
1.2.5.5	Infinite Dilution	18
1.2.5.6	Measurement of Solvent Activity	18
1.2.5.7	Measurement of Solute Activity	18
1.2.5.8	Electrolyte Activity	18
1.2.5.9	Mean Ion Quantities	19
1.2.5.10	Relation between f , γ , and γ	19
1.2.6	Ion–Ion Interactions	20
1.2.6.1	Introduction	20
1.2.6.2	Debye–Huckel Model for Calculating ψ_2	21
1.2.6.3	Poisson–Boltzmann Equation	22
1.2.6.4	Charge Density	22
1.2.6.5	Solving the Poisson–Boltzmann Equation	23
1.2.6.6	Calculation of $\Delta\mu_{i-1}$	24
1.2.6.7	Debye Length, K^{-1} or L_D	24
1.2.6.8	The Activity Coefficient	24
1.2.6.9	Comparison with Experiment	26
1.2.6.10	Approximations of the Debye–Huckel Limiting Law	26
1.2.6.11	The Distance of Closest Approach	27
1.2.6.12	Physical Interpretation of the Activity Coefficient	27
1.2.7	Concentrated Electrolyte Solutions	27
1.2.7.1	The Stokes–Robinson Treatment	27
1.2.7.2	The Ion-Hydration Correction	28
1.2.7.3	The Concentration Correction	28
1.2.7.4	The Stokes–Robinson Equation	29
1.2.7.5	Evaluation of the Stokes–Robinson Equation	29
1.2.8	Ion Pair Formation	29
1.2.8.1	Ion Pairs	29
1.2.8.2	The Fuoss Treatment	30
1.2.9	Ion Dynamics	32
1.2.9.1	Ionic Mobility and Transport Numbers	32
1.2.9.2	Diffusion	33

1.2.9.3	Fick's Second Law	33
1.2.9.4	Diffusion Statistics	35
1.3	Dynamic Electrochemistry	36
1.3.1	Review of Fundamentals	36
1.3.1.1	Potential	36
1.3.1.2	Potential inside a Good Conductor	37
1.3.1.3	Charge on a Good Conductor	37
1.3.1.4	Force between Charges	37
1.3.1.5	Potential due to an Assembly of Charges	37
1.3.1.6	Potential Difference between Two Phases in Contact ($\Delta\phi$)	38
1.3.1.7	The Electrochemical Potential ($\bar{\mu}$)	39
1.3.2	The Electrically Charged Interface or Double Layer	39
1.3.2.1	The Interface	39
1.3.2.2	Ideally Polarized Electrode	40
1.3.2.3	The Helmholtz Model	40
1.3.2.4	Gouy–Chapman or Diffuse Model	42
1.3.2.5	The Stern Model	43
1.3.2.6	The Bockris, Devanathan, and Muller Model	45
1.3.2.7	Calculation of the Capacitance	48
1.3.3	Charge Transfer at the Interface	49
1.3.3.1	Transition State Theory	49
1.3.3.2	Redox Charge-Transfer Reactions	50
1.3.3.3	The Act of Charge Transfer	53
1.3.3.4	The Butler–Volmer Equation	55
1.3.3.5	i in Terms of the Standard Rate Constant (k^0)	56
1.3.3.6	Relation between k^0 and I_0	56
1.3.4	Multistep Processes	57
1.3.4.1	The Multistep Butler–Volmer Equation	57
1.3.4.2	Rules for Mechanisms	58
1.3.4.3	Concentration Dependence of I_0	59
1.3.4.4	Charge-Transfer Resistance (R_{ct})	60
1.3.4.5	Whole Cell Voltages	60
1.3.5	Mass Transport Control	61
1.3.5.1	Diffusion and Migration	61
1.3.5.2	The Limiting Current Density (I_L)	62
1.3.5.3	Rotating Disk Electrode	64
	Further Reading	64
2	General Properties of Electrochemical Capacitors	69
	<i>Tony Pandolfo, Vanessa Ruiz, Seepalakottai Sivakkumar, and Jawahr Nerkar</i>	
2.1	Introduction	69
2.2	Capacitor Principles	70
2.3	Electrochemical Capacitors	71
2.3.1	Electric Double-Layer Capacitors	75

2.3.1.1	Double-Layer and Porous Materials Models	75
2.3.1.2	EDLC Construction	77
2.3.2	Pseudocapacitive Electrochemical Capacitors	86
2.3.2.1	Electronically Conducting Polymers	87
2.3.2.2	Transition Metal Oxides	93
2.3.2.3	Lithium-Ion Capacitors	98
2.4	Summary	100
	Acknowledgments	101
	References	101
3	Electrochemical Techniques	111
	<i>Pierre-Louis Taberna and Patrice Simon</i>	
3.1	Electrochemical Apparatus	111
3.2	Electrochemical Cell	111
3.3	Electrochemical Interface: Supercapacitors	114
3.4	Most Used Electrochemical Techniques	115
3.4.1	Transient Techniques	115
3.4.1.1	Cyclic Voltammetry	115
3.4.1.2	Galvanostatic Cycling	117
3.4.2	Stationary Technique	119
3.4.2.1	Electrochemical Impedance Spectroscopy	119
3.4.2.2	Supercapacitor Impedance	124
	References	129
4	Electrical Double-Layer Capacitors and Carbons for EDLCs	131
	<i>Patrice Simon, Pierre-Louis Taberna, and François Béguin</i>	
4.1	Introduction	131
4.2	The Electrical Double Layer	132
4.3	Types of Carbons Used for EDLCs	135
4.3.1	Activated Carbon Powders	135
4.3.2	Activated Carbon Fabrics	137
4.3.3	Carbon Nanotubes	138
4.3.4	Carbon Aerogels	138
4.4	Capacitance versus Pore Size	138
4.5	Evidence of Desolvation of Ions	141
4.6	Performance Limitation: Pore Accessibility or Saturation of Porosity	148
4.6.1	Limitation by Pore Accessibility	148
4.6.2	Limitation of Capacitor Performance by Porosity Saturation	150
4.7	Beyond the Double-Layer Capacitance in Microporous Carbons	153
4.7.1	Microporous Carbons in Neat Ionic Liquid Electrolyte	153
4.7.2	Extra Capacitance with Ionic Liquids in Solution	157
4.7.3	Ions Trapping in Pores	159
4.7.4	Intercalation/Insertion of Ions	161
4.8	Conclusions	162
	References	163

5	Modern Theories of Carbon-Based Electrochemical Capacitors	167
	<i>Jingsong Huang, Rui Qiao, Guang Feng, Bobby G. Sumpter, and Vincent Meunier</i>	
5.1	Introduction	167
5.1.1	Carbon-Based Electrochemical Capacitors	167
5.1.2	Elements of EDLCs	169
5.2	Classical Theories	172
5.2.1	Compact Layer at the Interface	172
5.2.2	Diffuse Layer in the Electrolyte	173
5.2.3	Space Charge Layer in the Electrodes	175
5.3	Recent Developments	176
5.3.1	Post-Helmholtz Models with Surface Curvature Effects	176
5.3.1.1	Models for Endohedral Capacitors	176
5.3.1.2	Models for Hierarchically Porous Carbon Materials	185
5.3.1.3	Models for Exohedral Capacitors	187
5.3.2	EDL Theories Beyond the GCS Model	189
5.3.3	Quantum Capacitance of Graphitic Carbons	191
5.3.4	Molecular Dynamics Simulations	192
5.3.4.1	EDLs in Aqueous Electrolytes	193
5.3.4.2	EDLs in Organic Electrolytes	196
5.3.4.3	EDLs in Room-Temperature ILs	197
5.4	Concluding Remarks	201
	Acknowledgments	202
	References	203
6	Electrode Materials with Pseudocapacitive Properties	207
	<i>Elżbieta Frąckowiak</i>	
6.1	Introduction	207
6.2	Conducting Polymers in Supercapacitor Application	208
6.3	Metal Oxide/Carbon Composites	212
6.4	Pseudocapacitive Effect of Heteroatoms Present in the Carbon Network	214
6.4.1	Oxygen-Enriched Carbons	215
6.4.2	Nitrogen-Enriched Carbons	216
6.5	Nanoporous Carbons with Electrosorbed Hydrogen	222
6.6	Electrolytic Solutions – a Source of Faradaic Reactions	226
6.7	Conclusions – Profits and Disadvantages of Pseudocapacitive Effects	231
	References	233
7	Li-Ion-Based Hybrid Supercapacitors in Organic Medium	239
	<i>Katsuhiko Naoi and Yuki Nagano</i>	
7.1	Introduction	239
7.2	Voltage Limitation of Conventional EDLCs	239
7.3	Hybrid Capacitor Systems	242

7.3.1	Lithium-Ion Capacitor (LIC)	243
7.3.2	Nanohybrid Capacitor (NHC)	247
7.4	Material Design for NHC	248
7.5	Conclusion	254
	Abbreviations	255
	References	255
8	Asymmetric and Hybrid Devices in Aqueous Electrolytes	257
	<i>Thierry Brousse, Daniel Bélanger, and Daniel Guay</i>	
8.1	Introduction	257
8.2	Aqueous Hybrid (Asymmetric) Devices	259
8.2.1	Principles, Requirements, and Limitations	259
8.2.2	Activated Carbon/PbO ₂ Devices	262
8.2.3	Activated Carbon/Ni(OH) ₂ Hybrid Devices	267
8.2.4	Aqueous-Based Hybrid Devices Based on Activated Carbon and Conducting Polymers	269
8.3	Aqueous Asymmetric Electrochemical Capacitors	272
8.3.1	Principles, Requirements, and Limitations	272
8.3.2	Activated Carbon/MnO ₂ Devices	274
8.3.3	Other MnO ₂ -Based Asymmetric or Hybrid Devices	278
8.3.4	Carbon/Carbon Aqueous Asymmetric Devices	279
8.3.5	Carbon/RuO ₂ Devices	280
8.4	Tantalum Oxide–Ruthenium Oxide Hybrid Capacitors	282
8.5	Perspectives	282
	References	283
9	EDLCs Based on Solvent-Free Ionic Liquids	289
	<i>Mariachiara Lazzari, Catia Arbizzani, Francesca Soavi, and Marina Mastragostino</i>	
9.1	Introduction	289
9.2	Carbon Electrode/Ionic Liquid Interface	291
9.3	Ionic Liquids	292
9.4	Carbon Electrodes	297
9.5	Supercapacitors	298
9.6	Concluding Remarks	302
	Ionic Liquid Codes	303
	Glossary	304
	References	305
10	Manufacturing of Industrial Supercapacitors	307
	<i>Philippe Azaïs</i>	
10.1	Introduction	307
10.2	Cell Components	309
10.2.1	Electrode Design and Its Components	309
10.2.1.1	Current Collector	309

10.2.1.2	Activated Carbons for Supercapacitors	312
10.2.1.3	Industrial Activated Carbons for Industrial Supercapacitors	317
10.2.1.4	Particle Size Distribution of Activated Carbons and Its Optimization	320
10.2.1.5	Binders	322
10.2.1.6	Conductive Additives	325
10.2.2	Electrolyte	326
10.2.2.1	Electrolyte Impact on Performance	327
10.2.2.2	Liquid-State Electrolyte and Remaining Problems	340
10.2.2.3	Ionic Liquid Electrolyte	341
10.2.2.4	Solid-State Electrolyte	343
10.2.3	Separator	343
10.2.3.1	Separator Requirements	343
10.2.3.2	Cellulosic Separators and Polymeric Separators	343
10.3	Cell Design	345
10.3.1	Small-Size Components	347
10.3.2	Large Cells	347
10.3.2.1	High-Power Cells	348
10.3.2.2	Energy Cells	350
10.3.2.3	Pouch Cell design	351
10.3.2.4	Debate on Cell Design: Prismatic versus Cylindrical Cells	351
10.3.2.5	Aqueous Medium Cells	351
10.4	Module Design	352
10.4.1	Large Modules Based on Hard-Type Cells	353
10.4.1.1	Metallic Connections Between Cells	354
10.4.1.2	Electric Terminal for Module	354
10.4.1.3	Insulator for Module	354
10.4.1.4	Cell Balancing and Other Information Detection	356
10.4.1.5	Module Enclosure	357
10.4.2	Large Modules Based on Pouch-Type Cells	357
10.4.3	Large Modules Working in Aqueous Electrolytes	359
10.4.4	Other Modules Based on Asymmetric Technologies	360
10.5	Conclusions and Perspectives	362
	References	363
11	Supercapacitor Module Sizing and Heat Management under Electric, Thermal, and Aging Constraints	373
	<i>Hamid Gualous and Roland Gallay</i>	
11.1	Introduction	373
11.2	Electrical Characterization	374
11.2.1	C and ESR Measurement	374
11.2.1.1	Capacitance and Series Resistance Characterization in the Time Domain	374
11.2.1.2	Capacitance and Series Resistance Characterization in the Frequency Domain	375

11.2.2	Supercapacitor Properties, Performances, and Characterization	376
11.2.2.1	Capacitance and ESR as a Function of the Voltage	376
11.2.2.2	Capacitance and ESR as a Function of the Temperature	378
11.2.2.3	Self-Discharge and Leakage Current	378
11.2.3	“Ragone Plot” Theory	381
11.2.3.1	Match Impedance	383
11.2.3.2	Power Available for the Load, Ragone Equation	384
11.2.4	Energetic Performance and Discharging at Constant Current	387
11.2.5	Energetic Performance and Discharging at Constant Power	389
11.2.6	Energetic Performance and Discharging at Constant Load	394
11.2.7	Efficiency	394
11.3	Thermal Modeling	395
11.3.1	Thermal Modeling of Supercapacitors	397
11.3.2	Conduction Heat Transfer	397
11.3.3	Thermal Boundary Conditions	399
11.3.4	Convection Heat Transfer Coefficient	401
11.3.5	Solution Procedure	402
11.3.6	BCAP0350 Experimental Results	404
11.4	Supercapacitor Lifetime	410
11.4.1	Failure Modes	411
11.4.2	Temperature and Voltage as an Aging Acceleration Factor	411
11.4.3	Physical Origin of Aging	413
11.4.4	Testing	415
11.4.5	DC Voltage Test	415
11.4.6	Voltage Cycling Test	417
11.5	Supercapacitor Module Sizing Methods	418
11.6	Applications	420
11.6.1	Power Management of Fuel Cell Vehicles	421
11.6.1.1	Problem Statement	421
11.6.1.2	Fuel Cell Modeling	421
11.6.1.3	Supercapacitors Modeling	422
11.6.2	The Power Management of a Fuel Cell Vehicle by Optimal Control	422
11.6.2.1	Optimal Control without Constraint	423
11.6.2.2	The Hamilton–Jacobi–Bellman Equation	423
11.6.3	Optimal Control with Inequality Constraints on the Fuel Cell Power and on the Fuel Cell Power Rate	427
11.6.3.1	Constraints on the Fuel Cell Power	427
11.6.3.2	Constraints on the Fuel Cell Power Rate	427
11.6.4	Power Management of Fuel Cell Vehicle by Optimal Control Associated to Sliding Mode Control	429
11.6.5	Conclusion	433
	References	434

12	Testing of Electrochemical Capacitors	437
	<i>Andrew Burke</i>	
12.1	Introduction	437
12.2	Summaries of DC Test Procedures	437
12.2.1	USABC Test Procedures	439
12.2.2	IEC Test Procedures	440
12.2.3	UC Davis Test Procedures	441
12.3	Application of the Test Procedures to Carbon/Carbon Devices	443
12.3.1	Capacitance	443
12.3.2	Resistance	443
12.3.3	Energy Density	448
12.3.4	Power Capability	449
12.3.5	Pulse Cycle Testing	453
12.4	Testing of Hybrid, Pseudocapacitive Devices	456
12.4.1	Capacitance	456
12.4.2	Resistance	456
12.4.3	Energy Density	459
12.4.4	Power Capability and Pulse Cycle Tests	460
12.5	Relationships between AC Impedance and DC Testing	460
12.6	Uncertainties in Ultracapacitor Data Interpretation	465
12.6.1	Charging Algorithm	466
12.6.2	Capacitance	466
12.6.3	Resistance	466
12.6.4	Energy Density	467
12.6.5	Power Capability	467
12.6.6	Round-Trip Efficiency	469
12.7	Summary	469
	References	469
13	Reliability of Electrochemical Capacitors	473
	<i>John R. Miller</i>	
13.1	Introduction	473
13.2	Reliability Basics	473
13.3	Cell Reliability	474
13.4	System Reliability	478
13.5	Assessment of Cell Reliability	481
13.5.1	Experimental Approach Example	484
13.6	Reliability of Practical Systems	491
13.6.1	Cell Voltage Nonuniformity	492
13.6.2	Cell Temperature Nonuniformity	494
13.7	Increasing System Reliability	499
13.7.1	Reduce Cell Stress	499
13.7.2	Burn-in of Cells	501
13.7.3	Use Fewer Cells in Series	501
13.7.4	Use “Long-Life” Cells	501

13.7.5	Implement Maintenance	502
13.7.6	Add Redundancy	502
13.8	System Design Example	503
13.8.1	Problem Statement	503
13.8.2	System Analysis	504
13.8.3	Cell Reliability	506
	References	507
14	Market and Applications of Electrochemical Capacitors	509
	<i>John R. Miller</i>	
14.1	Introduction: Principles and History	509
14.2	Commercial Designs: DC Power Applications	510
14.2.1	Bipolar Designs	510
14.2.2	Cell Designs	512
14.2.3	Asymmetric Designs	513
14.3	Energy Conservation and Energy Harvesting Applications	516
14.3.1	Motion and Energy	516
14.3.2	Hybridization: Energy Capture and Reuse	518
14.3.3	Energy Conservation and Efficiency	521
14.3.4	Engine Cranking	521
14.4	Technology Combination Applications	523
14.4.1	Battery/Capacitor Combination Applications	523
14.5	Electricity Grid Applications	523
14.5.1	Storage and the Utility Grid	523
14.6	Conclusions	524
	References	525
	Index	527

Series Editor Preface

The Wiley Series on New Materials for Sustainable Energy and Development

Sustainable energy and development is attracting increasing attention from the scientific research communities and industries alike, with an international race to develop technologies for clean fossil energy, hydrogen and renewable energy as well as water reuse and recycling. According to the REN21 (Renewables Global Status Report 2012 p. 17) total investment in renewable energy reached \$257 billion in 2011, up from \$211 billion in 2010. The top countries for investment in 2011 were China, Germany, the United States, Italy, and Brazil. In addressing the challenging issues of energy security, oil price rise, and climate change, innovative materials are essential enablers.

In this context, there is a need for an authoritative source of information, presented in a systematic manner, on the latest scientific breakthroughs and knowledge advancement in materials science and engineering as they pertain to energy and the environment. The aim of the *Wiley Series on New Materials for Sustainable Energy and Development* is to serve the community in this respect. This has been an ambitious publication project on materials science for energy applications. Each volume of the series will include high-quality contributions from top international researchers, and is expected to become the standard reference for many years to come.

This book series covers advances in materials science and innovation for renewable energy, clean use of fossil energy, and greenhouse gas mitigation and associated environmental technologies. Current volumes in the series are:

- Supercapacitors. Materials, Systems, and Applications
- Functional Nanostructured Materials and Membranes for Water Treatment
- Materials for High-Temperature Fuel Cells
- Materials for Low-Temperature Fuel Cells
- Advanced Thermoelectric Materials. Fundamentals and Applications
- Advanced Lithium-Ion Batteries. Recent Trends and Perspectives
- Photocatalysis and Water Purification. From Fundamentals to Recent Applications

In presenting this volume on Supercapacitors, I would like to thank the authors and editors of this important book, for their tremendous effort and hard work in completing the manuscript in a timely manner. The quality of the chapters reflects well the caliber of the contributing authors to this book, and will no doubt be recognized and valued by readers.

Finally, I would like to thank the editorial board members. I am grateful to their excellent advice and help in terms of examining coverage of topics and suggesting authors, and evaluating book proposals.

I would also like to thank the editors from the publisher Wiley-VCH with whom I have worked since 2008, Dr Esther Levy, Dr Gudrun Walter, and Dr Bente Flier for their professional assistance and strong support during this project.

I hope you will find this book interesting, informative and valuable as a reference in your work. We will endeavour to bring to you further volumes in this series or update you on the future book plans in this growing field.

Brisbane, Australia
31 July 2012

G.Q. Max Lu

Preface

Currently, our planet faces huge challenges related to energy. How to reduce CO₂ emissions and fossil fuel consumption? How to introduce renewable energies in the energy mix? Of course these are not new questions, but simply, until the end of the last century, no one cared about the scarcity of fossil fuels even if some warnings appeared during the successive oil crises.

The answer to the above questions is energy saving as well as energy management. It is exactly the role that can be played by electrochemical capacitors, so-called supercapacitors, because of their ability to store larger amounts of energy than the traditional dielectric capacitors. Such exceptional properties originate from the nanometric scale capacitors built from the polarized electrode material and a layer of attracted ions on its surface. The thickness of the electrode–electrolyte interface is directly controlled by the size of ions. Supercapacitors are able to harvest energy in very short periods (less than one minute) and to subsequently provide burst of energy when needed. They are now a reality in the market, where they are applied in automotive and stationary systems, and allow energy savings ranging from 10 to 40%. They can also play a role in the stabilization of current when intermittent renewable energies are introduced in the energetic mix.

Although supercapacitors are now commercially available, they still require improvements, especially for enhancing their energy density. It requires a fundamental understanding of their properties and exact operating principles, in addition to improving electrode materials, electrolytes past and integration in systems. All these topics led to a very strong motivation of academics and industry during the decade.

When Max Lu invited us to suggest a book in his series *Materials for Sustainable Energy and Development*, we immediately thought about Supercapacitors. Indeed, since the fantastic pioneer book *Electrochemical supercapacitors: Scientific Fundamentals and Technological Applications* published by B.E. Conway in 1999, no other comprehensive book was dealing extensively with the topic of supercapacitors, and until now the book is generally referred in almost all scientific publications concerning this subject. During the past 10 years new ideas appeared, such as a better description of what is really the double-layer in these systems and hybrid and asymmetric capacitors, requiring a comprehensive review.

Our book entitled *Supercapacitors: materials and systems* does not intend to substitute but be a complement to the Conway's book taking advantage of the developments which appeared in the past decade. It is dedicated to researchers and engineers involved with supercapacitor science, its developments, and implementation. The book is also intended for graduate and undergraduate students wanting to special in energy storage systems.

For these reasons, it has been written in collaboration with scientists world-wide renowned in supercapacitors science and also with contributors from the industry. The book includes 14 chapters: 3 being dedicated to general principles of electrochemistry, electrochemical characterization techniques and general properties of supercapacitors in order to allow reading the book without any prerequisite knowledge; 3 to fundamentals, general properties, and modelling of electrical double-layer capacitors, and pseudo-capacitors; 3 to new trends such as asymmetric and hybrid capacitors, and the use of ionic liquid electrolytes; 2 to manufacturing and modules sizing; 3 to testing, reliability, and applications of supercapacitors. Each chapter aims at giving the most detailed information using familiar terms.

We are very happy and proud that we could gather, in this book, the greatest names in supercapacitors science and technology. All are colleagues and friends who we met in international conferences or with whom we have had the pleasure to collaborate. They all kindly accepted to devote their time for contributing chapters; we sincerely and warmly thank them for their help. We also would like to thank our friend Max Lu for giving us this wonderful opportunity and also the Wiley staff for being patient. Finally, we would like to dedicate this book to our solve parents who would be very proud to see our small contribution in helping solve humanity problems.

Poznan
November 2012

François Bèguin and Elzbieta Frackowiak

About the Series Editor



Professor Max Lu

Editor, New Materials for Sustainable Energy and Development Series

Professor Lu's research expertise is in the areas of materials chemistry and nanotechnology. He is known for his work on nanoparticles and nanoporous materials for clean energy and environmental technologies. With over 500 journal publications in high-impact journals, including *Nature*, *Journal of the American Chemical Society*, *Angewandte Chemie*, and *Advanced Materials*, he is also coinventor of 20 international patents. Professor Lu is an Institute for Scientific Information (ISI) Highly Cited Author in Materials Science with over 17 500 citations (h-index of 63). He has received numerous prestigious awards nationally and internationally, including the Chinese Academy of Sciences International Cooperation Award (2011), the Orica Award, the RK Murphy Medal, the Le Fevre Prize, the ExxonMobil Award, the Chemeca Medal, the Top 100 Most Influential Engineers in Australia (2004, 2010, and 2012), and the Top 50 Most Influential Chinese in the World (2006). He won the Australian Research Council Federation Fellowship twice (2003 and 2008). He is an elected Fellow of the Australian Academy of Technological Sciences and Engineering (ATSE) and Fellow of Institution of Chemical Engineers (IChemE). He is editor and editorial board member of 12 major international journals including *Journal of Colloid and Interface Science* and *Carbon*.

Max Lu has been Deputy Vice-Chancellor and Vice-President (Research) since 2009. He previously held positions of acting Senior Deputy Vice-Chancellor (2012), acting Deputy Vice-Chancellor (Research), and Pro-Vice-Chancellor (Research

Linkages) from October 2008 to June 2009. He was also the Foundation Director of the ARC Centre of Excellence for Functional Nanomaterials from 2003 to 2009.

Professor Lu had formerly served on many government committees and advisory groups including the Prime Minister's Science, Engineering and Innovation Council (2004, 2005, and 2009) and the ARC College of Experts (2002–2004). He is the past Chairman of the IChemE Australia Board and former Director of the Board of ATSE. His other previous board memberships include Uniseed Pty Ltd., ARC Nanotechnology Network, and Queensland China Council. He is currently Board member of the Australian Synchrotron, National eResearch Collaboration Tools and Resources, and Research Data Storage Infrastructure. He also holds a ministerial appointment as member of the National Emerging Technologies Forum.

About the Volume Editors



Prof. François Béguin

*Poznan University of Technology,
Faculty of Chemical Technology,
Piotrowo 3, 60-965 Poznan, Poland
francois.beguin@put.poznan.pl
tel. ++48 61 665 3632
fax ++48 61 665 2571*

François Béguin is a professor at the Poznan University of Technology (Poland), where he was recently awarded the WELCOME stipend from the Foundation for Polish Science. His research activities are devoted to chemical and electrochemical applications of carbon materials, with special attention to the development of nanocarbons with controlled porosity and surface functionality for applications to energy conversion/storage and environment protection. The main topics investigated in his research group are lithium batteries, supercapacitors, electrochemical hydrogen storage, and reversible electrosorption of water contaminants. He published over 250 publications in high-ranking international journals, and his works are cited in 8300 papers, with Hirsch index 46. He is also involved in several books dealing with carbon materials and energy storage. He is a member of the International Advisory Board of the Carbon Conferences and has launched the international conferences on Carbon for Energy Storage and Environment Protection (CESEP). He is a member of the editorial board of the journal *Carbon*. He was Professor of materials science in the Orléans University (France) until 2012 and was Director of national programmes on Energy Storage (Stock-E), Hydrogen and Fuel Cells (H-PAC), and electricity management (PROGELEC) in the French Agency for Research (ANR).

**Prof. Elzbieta Frackowiak**

*Poznan University of Technology, Institute of
Chemistry and Technical Electrochemistry,*

Piotrowo 3, 60-965 Poznan, Poland

Elzbieta.Frackowiak@put.poznan.pl

tel. ++48 61 665 3632

fax ++48 61 665 2571

Elzbieta Frackowiak is a full professor at the Institute of Chemistry and Technical Electrochemistry at the Poznan University of Technology. Her main research topics are devoted to energy storage in electrochemical capacitors, Li-ion batteries, and hydrogen electrosorption. She is especially interested in the development of electrode materials (nanoporous carbons, template carbons, carbon nanotubes, graphene, etc.), composite electrodes from conducting polymers, and doped carbons and transition-metal oxides for supercapacitors, as well as in new concepts of supercapacitors based on the carbon/redox couples interface.

She serves as Chair of Division 3 “Electrochemical Energy Conversion and Storage” of the International Society of Electrochemistry (2009–2014). She is a member of International Advisory Boards – *Electrochimica Acta* from 2011 and *Energy & Environmental Science* from 2008. She was chair/cochair of a few international conferences (12th International Symposium on Intercalation Compounds (ISIC 12) Poznań, Poland, 1–5 June 2003; 2nd International Symposium on Enhanced Electrochemical Capacitors (ISEECap’11), Poznań, Poland, 12–16 June 2011; and the World CARBON conference in Krakow, 17–22 June 2012). She was the winner of the Foundation for Polish Science Prize, the so-called Polish Nobel (December 2011) and was also decorated with the Order of Polonia Restituta (December 2011) and the Order Sapientia Sat (October 2012).

She is the author of 150 publications, a few chapters, and tens of patent applications. The number of her citations is about 6000, with Hirsch index 36.

List of Contributors

Catia Arbizzani

Alma Mater Studiorum
Università di Bologna
Dipartimento di Scienza
dei Metalli
Elettrochimica e Tecniche
Chimiche
Via San Donato 15
40127 Bologna
Italy

Philippe Azais

Batscap Supercapacitor
Business Unit
Odet, Ergue-Gaberic
29556 Quimper Cedex 9
France

and

Commissariat à l'Energie
Atomique (CEA)
LITEN (Laboratoire d'Innovation
pour les Technologies des
Energies Nouvelles)
17 rue des Martyrs
38054 Grenoble Cedex 9
France

Daniel Bélanger

Université du Québec à Montréal
Département de Chimie
case postale 8888
succursale centre-ville
Montréal
Québec H3C 3P8
Canada

François Béguin

Poznan University of Technology
Faculty of Chemical Technology
u1. Piotrowo 3
60-965 Poznan
Poland

Thierry Brousse

Université de Nantes
Institut des Matériaux Jean
Rouxel (IMN)
CNRS/Université de Nantes
Polytech Nantes
BP50609
44306 Nantes Cedex 3
France

Andrew Burke

University of California-Davis
Institute of Transportation
Studies
One Shields Avenue
Davis, CA 95616
USA

Scott W. Donne

University of Newcastle
School of Environmental and Life
Sciences
Office C325, Chemistry
Callaghan
New South Wales 2308
Australia

Guang Feng

Clemson University
Department of Mechanical
Engineering
Clemson, SC 29634-0921
USA

Elżbieta Frąckowiak

Poznan University of Technology
Faculty of Chemical Technology
Institute of Chemistry and
Technical Electrochemistry
u1. Piotrowo 3
60-965 Poznan
Poland

Roland Gallay

Garmanage
Clos-Besson 6
CH-1726
Farvagny-le-Petit
Switzerland

Hamid Gualous

Université de Caen Basse
Normandie
Esplanade de la Paix
BP 5186
14032, Caen Cedex 5
France

Daniel Guay

INRS-Énergie
Matériaux et
Télécommunications
1650 Boulevard Lionel Boulet
case postale 1020
Varenes
Québec J3X 1 S2
Canada

Jingsong Huang

Center for Nanophase Materials
Sciences, and Computer Science
and Mathematics Division
Oak Ridge National Laboratory
Bethel Valley Road
Oak Ridge, TN 37831-6367
USA

Mariachiara Lazzari

Alma Mater Studiorum
Università di Bologna
Dipartimento di Scienza dei Metalli
Elettrochimica e Tecniche Chimiche
Via San Donato 15
40127 Bologna
Italy

Marina Mastragostino

Alma Mater Studiorum
Università di Bologna
Dipartimento di Scienza dei
Metalli
Elettrochimica e Tecniche
Chimiche
Via San Donato 15
40127 Bologna
Italy

Vincent Meunier

Center for Nanophase Materials
Sciences, and Computer Science
and Mathematics Division
Oak Ridge National Laboratory
Bethel Valley Road
Oak Ridge, TN 37831-6367
USA

John R. Miller

JME Inc
23500 Mercantile Road, Suite L
Beachwood, OH 44122
USA

and

Case Western Reserve University
Great Lakes Energy Institute
Electrical Engineering and
Computer Science
10900 Euclid Avenue
Cleveland, OH 44106
USA

Yuki Nagano

Tokyo University of Agriculture
and Technology
School of Engineering
Division of Applied Chemistry
2-24-16 Naka-cho
Koganei
Tokyo 184-8558
Japan

Katsuhiko Naoi

Tokyo University of Agriculture
and Technology
School of Engineering, Division
of Applied Chemistry
2-24-16 Naka-cho
Koganei
Tokyo 184-8558
Japan

Jawahr Nerkar

CSIRO Energy Technology
Normanby Rd
Clayton South
Victoria 3169
Australia

Tony Pandolfo

CSIRO Energy Technology
Normanby Rd
Clayton South
Victoria 3169
Australia

Rui Qiao

Clemson University
Department of Mechanical
Engineering
Clemson, SC 29634-0921
USA

Vanessa Ruiz

CSIRO Energy Technology
Normanby Rd
Clayton South
Victoria 3169
Australia

Seepalakottai Sivakkumar

CSIRO Energy Technology
Normanby Rd
Clayton South
Victoria 3169
Australia

Patrice Simon

Unversitè Toulouse III
Institut Carnot CIRIMAT - UMR
CNRS 5085
118 route de Narbonne
31062 Toulouse
France

Bobby G. Sumpter

Center for Nanophase Materials
Sciences, and Computer Science
and Mathematics Division
Oak Ridge National Laboratory
Bethel Valley Road
Oak Ridge, TN 37831-6367
USA

Francesca Soavi

Alma Mater Studiorum
Università di Bologna
Dipartimento di Scienza dei
Metalli
Elettrochimica e Tecniche
Chimiche
Via San Donato 15
40127 Bologna
Italy

Pierre-Louis Taberna

Unversitè Toulouse III
Institut Carnot CIRIMAT - UMR
CNRS 5085
118 route de Narbonne
31062 Toulouse
France

1 General Principles of Electrochemistry

Scott W. Donne

1.1 Equilibrium Electrochemistry

1.1.1 Spontaneous Chemical Reactions

Chemical reactions move toward a dynamic equilibrium in which both reactants and products are present but have no further tendency to undergo net change. In some cases, the concentration of products in the equilibrium mixture is so much greater than the concentration of the unchanged reactants that for all practical purposes the reaction is complete. However, in many important cases, the equilibrium mixture has significant concentrations of both reactants and products.

1.1.2 The Gibbs Energy Minimum

The equilibrium composition of a reaction mixture can be calculated from the Gibbs energy by identifying the composition that corresponds to a minimum in the Gibbs energy. To elaborate further, consider the simple chemical equilibrium:



Suppose now that an infinitesimal amount $d\xi$ of A turns into B, then the change in the amount of A present is $dn_A = -d\xi$ and the change in the amount of B present is $dn_B = +d\xi$. The quantity ξ is called the *extent of reaction*.

The reaction Gibbs energy (ΔG_r) is defined as

$$\Delta G_r = \left(\frac{\partial G}{\partial \xi} \right)_{P,T} = \mu_B - \mu_A \quad (1.2)$$

where μ represents the chemical potential or molar Gibbs energy for each species.

Because the chemical potentials vary with composition, the Gibbs energy will change as the reaction proceeds. Moreover, because the reaction runs in the direction of decreasing G , it means that the reaction $A \rightarrow B$ is spontaneous when

$\mu_A > \mu_B$, whereas the reverse reaction is spontaneous when $\mu_B > \mu_A$. When the derivative in Eq. (1.2) is zero, the reaction is spontaneous in neither direction, and so

$$\Delta G_r = 0 \quad (1.3)$$

which occurs when $\mu_A = \mu_B$. It follows that if the composition of the reaction mixture can be identified such that $\mu_A = \mu_B$, then we can identify the composition of the reaction mixture at equilibrium.

To generalize these concepts, consider the more generic chemical reaction:



When the reaction advances by $d\xi$, the amounts of reactants and products change by

$$dn_A = -ad\xi \quad dn_B = -bd\xi \quad dn_C = +cd\xi \quad dn_D = +dd\xi \quad (1.5)$$

and in general $dn_J = v_J d\xi$ where v_J is the stoichiometric number of J in the chemical equilibrium. The resulting infinitesimal change in the Gibbs energy at constant temperature and pressure is therefore

$$dG = \mu_C dn_C + \mu_D dn_D + \mu_A dn_A + \mu_B dn_B = (c\mu_C + d\mu_D - a\mu_A - b\mu_B) d\xi \quad (1.6)$$

The general form of this expression is

$$dG = \left(\sum_J v_J \mu_J \right) d\xi \quad (1.7)$$

It follows that

$$\Delta G_r = \left(\frac{\partial G}{\partial \xi} \right)_{P,T} = c\mu_C + d\mu_D - a\mu_A - b\mu_B \quad (1.8)$$

To progress further, we note that the chemical potential of a species J is related to its activity (a_J) by

$$\mu_J = \mu_J^0 + RT \ln(a_J) \quad (1.9)$$

Substituting an equivalent expression to Eq. (1.9) for each species into Eq. (1.8) gives rise to

$$\Delta G_r = c\mu_C^0 + d\mu_D^0 - a\mu_A^0 - b\mu_B^0 + RT \ln \left(\frac{a_C^c a_D^d}{a_A^a a_B^b} \right) = \Delta G_r^0 + RT \ln(Q) \quad (1.10)$$

where Q is the reaction quotient. Now, at equilibrium, where $\Delta G_r = 0$, the activities have their equilibrium values, and so

$$K = \left(\frac{a_C^c a_D^d}{a_A^a a_B^b} \right) \quad (1.11)$$

where K is the thermodynamic equilibrium constant. Furthermore, from Eq. (1.10)

$$\Delta G_r^0 = -RT \ln(K) \quad (1.12)$$

which is a very important thermodynamic relationship, for it enables us to predict the equilibrium constant of any reaction from tables of thermodynamic data, and hence to predict the equilibrium composition of the reaction mixture.

1.1.3

Bridging the Gap between Chemical Equilibrium and Electrochemical Potential

A cell in which the overall cell reaction has not reached chemical equilibrium can do electrical work as the reaction drives electrons through an external circuit. The work that a given transfer of electrons can accomplish depends on the potential difference between the two electrodes. This potential difference is called the *cell potential* (V). When the cell potential is large, a given number of electrons traveling between the electrodes can do a large amount of electrical work. When the cell potential is small, the same number of electrons can do only a small amount of work. A cell in which the overall reaction is at equilibrium can do no work, and then the cell potential is zero.

The maximum amount of electrical work ($w_{e,\max}$) that an electrochemical cell can do is given by the value of ΔG , and in particular that for a spontaneous process (in which both ΔG and w are negative) at constant temperature and pressure,

$$\Delta G = w_{e,\max} \quad (1.13)$$

Therefore, to make thermodynamic measurements on the cell by measuring the work it can do, we must ensure that it is operating reversibly. Only then is it producing maximum work and only then can Eq. (1.13) be used to relate that to work. Moreover, we have seen previously that the reaction Gibbs energy (ΔG_r) is actually a derivative evaluated at a specific composition of the reaction mixture. Therefore, to measure ΔG_r we must ensure that the cell is operating reversibly at a specific, constant composition. Both these conditions are achieved by measuring the cell potential when it is balanced by an exactly opposing source of potential so that the cell reaction occurs reversibly and that the composition is constant: in effect, the cell reaction is poised for change, but not actually changing. The resulting potential difference is called the *zero-current cell potential* or the *electromotive force* of the cell.

1.1.4

The Relation between E and ΔG_r

To establish this relationship, consider the change in G when the cell reaction advances by an infinitesimal amount $d\xi$ at some composition. At constant temperature and pressure, G changes by

$$dG = \sum_J \mu_J dn_J = \sum_J \nu_J \mu_J d\xi \quad (1.14)$$

The reaction Gibbs energy (ΔG_r) at the specific composition is

$$\Delta G_r = \left(\frac{\partial G}{\partial \xi} \right)_{P,T} = \sum_J \nu_J \mu_J \quad (1.15)$$

So we can write

$$dG = \Delta G_r d\xi \quad (1.16)$$

The maximum nonexpansion work that the reaction can do as it advances by $d\xi$ at constant temperature and pressure is therefore

$$dw_e = \Delta G_r d\xi \quad (1.17)$$

This work is infinitesimal, and the composition of the system is virtually constant when it occurs. Suppose the reaction advances by $d\xi$, then $\nu d\xi$ electrons must travel from the anode to the cathode. The total charge transported between the electrodes when this change occurs is $-\nu e N_A d\xi$ (because $\nu d\xi$ is the amount of electrons and the charge per mole of electrons is $-e N_A$). Hence, the total charge transported is $-\nu F d\xi$ because $e N_A = F$, where F is the Faraday's constant.

The work done when an infinitesimal change $-\nu F d\xi$ travels from the anode to the cathode is equal to the product of the charge and the potential difference E :

$$dw_e = -\nu F E d\xi \quad (1.18)$$

When Eqs. (1.17) and (1.18) are equated, the advancement $d\xi$ cancels, the result being

$$\Delta G_r = -\nu F E \quad (1.19)$$

This equation is the key connection between electrical measurements and thermodynamic properties. It follows that by knowing the reaction Gibbs energy at a specified composition, we can state the zero-current cell potential at that composition. Another way of explaining Eq. (1.19) is that it shows that the driving power of a cell is proportional to the slope of the Gibbs energy with respect to the extent of reaction. When a reaction is far from equilibrium (when the slope is steep), there is a strong tendency to drive electrons through an external circuit. When the slope is close to zero (when the cell reaction is close to equilibrium), the cell potential is small.

1.1.5

The Nernst Equation

From Eq. (1.10) we know how the reaction Gibbs energy is related to the composition of the reaction mixture. It follows then that by dividing both sides by $-\nu F$, that

$$E = -\frac{\Delta G_r^0}{\nu F} - \frac{RT}{\nu F} \ln(Q) \quad (1.20)$$

The first term on the right of Eq. (1.20) can be rewritten as

$$E^0 = -\frac{\Delta G_r^0}{\nu F} \quad (1.21)$$

and called the *standard cell potential*. The standard cell potential (E^0) is the standard reaction Gibbs energy expressed as a potential. It follows that

$$E = E^0 - \frac{RT}{\nu F} \ln(Q) \quad (1.22)$$

which is the Nernst equation. We see from this equation that the standard cell potential can be interpreted as the zero-current cell potential when all the reactants and products are in their standard states, for then all activities are unity, so $Q = 1$, and $\ln(Q) = 0$.

1.1.6

Cells at Equilibrium

Suppose the reaction has reached equilibrium; then $Q = K$, where K is the equilibrium constant of the cell reaction. However, a chemical reaction at equilibrium cannot do work, and hence it generates zero potential difference between the electrodes of a galvanic cell. Therefore, setting $E = 0$ V and $Q = K$ in the Nernst equation gives

$$\ln(K) = \frac{nFE^0}{RT} \quad (1.23)$$

This very important equation lets us predict equilibrium constants from measured standard cell potentials.

1.1.7

Standard Potentials

A galvanic cell is a combination of two electrodes, and each one can be considered as making a characteristic contribution to the overall cell potential. Although it is not possible to measure the contribution of a single electrode, we can define the potential of one of the electrodes as having zero potential and then assign values to others on that basis. The specially selected electrode is the standard hydrogen electrode (SHE):



for which $E^0 = 0$ V at all temperatures. The standard potential (E^0) of another couple is then assigned by constructing a cell in which it is the right-hand electrode and the SHE is the left-hand electrode.

An important feature of standard cell potentials is that they are unchanged if the chemical equation for the cell reaction of a half-reaction is multiplied by a numerical factor. A numerical factor increases the value of the standard Gibbs energy for the reaction, but it also increases the number of electrons transferred by the same factor, and from Eq. (1.21) the value of E^0 remains unchanged.

Table 1.1 Standard Gibbs energy data for the manganese and water system.

Compound	ΔG_f (kJ mol ⁻¹)	Compound	ΔG_f (kJ mol ⁻¹)
Mn	0	MnO ₂	-465
Mn ²⁺ (aq)	-228	MnO ₄ ⁻	-447
MnO	-363	H ₂ O	-237
Mn ₃ O ₄	-1283	O ₂ (g)	0
Mn ₂ O ₃	-881	H ₂ (g)	0
		H ⁺ (aq)	0

1.1.8

Using the Nernst Equation – Eh–pH Diagrams

One of the most important applications of the Nernst equation is its use in identifying domains of species stability within an Eh–pH diagram. As an example of this application, consider the manganese and water system, for which the appropriate standard Gibbs energy data is shown in Table 1.1. The relevant electrochemical half-reactions that the manganese and water system can undergo are shown in Table 1.2, together with their corresponding ΔG_r and E^0 values. This data can then be graphed, as shown in Figure 1.1, to produce the Eh–pH diagram. What such a diagram shows, for example, are the range of thermodynamically stable species present at a constant pH as the voltage is changed; for example, $\text{Mn} \rightarrow \text{MnO} \rightarrow \text{Mn}_3\text{O}_4 \rightarrow \text{Mn}_2\text{O}_3 \rightarrow \text{MnO}_2 \rightarrow \text{MnO}_4^-$ for an alkaline pH in Figure 1.1. Similarly, at a fixed potential, increasing the pH will also change the preferred phase; for example, $\text{Mn}^{2+} \rightarrow \text{Mn}_2\text{O}_3$. Interestingly, for the manganese and water system, MnO₂ is stable across the entire pH range. This is a rare example of an oxide compound covering the complete pH range. As a final point, it is important to remember that such a diagram represents the thermodynamically stable species at a certain Eh–pH combination. In no way does it account for the existence of metastable species, which may have very slow decomposition kinetics.

1.2

Ionics

1.2.1

Ions in Solution

The behavior of ions in solution plays a critical role in determining the properties of a particular electrode–electrolyte combination. By considering some simple models, we are able to explain the properties of electrolyte solutions and, in particular, the origin of their thermodynamic activity. Another part of this is the more kinetic properties of solutions such as diffusion and migration.

Table 1.2 Half-reactions for the manganese and water system, together with their corresponding ΔG_r and E^0 values.

Half-reaction	ΔG_r (kJ mol ⁻¹)	E^0 (V)
$\text{Mn}^{2+} + 2e^- \leftrightarrow \text{Mn}$	228	-1.181
$\text{MnO} + 2\text{H}^+ + 2e^- \leftrightarrow \text{Mn} + \text{H}_2\text{O}$	126	-0.653
$\text{Mn}_3\text{O}_4 + 2\text{H}^+ + 2e^- \leftrightarrow 3\text{MnO} + \text{H}_2\text{O}$	-43	0.223
$3\text{Mn}_2\text{O}_3 + 2\text{H}^+ + 2e^- \leftrightarrow 2\text{Mn}_3\text{O}_4 + \text{H}_2\text{O}$	-160	0.829
$2\text{MnO}_2 + 2\text{H}^+ + 2e^- \leftrightarrow \text{Mn}_2\text{O}_3 + \text{H}_2\text{O}$	-188	0.974
$\text{MnO}_4^- + 4\text{H}^+ + 3e^- \leftrightarrow \text{MnO}_2 + 2\text{H}_2\text{O}$	-492	1.700
$\text{Mn}_3\text{O}_4 + 8\text{H}^+ + 2e^- \leftrightarrow 3\text{Mn}^{2+} + 4\text{H}_2\text{O}$	-349	1.809
$\text{Mn}_2\text{O}_3 + 6\text{H}^+ + 2e^- \leftrightarrow 2\text{Mn}^{2+} + 3\text{H}_2\text{O}$	-286	1.482
$\text{MnO}_2 + 4\text{H}^+ + 2e^- \leftrightarrow \text{Mn}^{2+} + 2\text{H}_2\text{O}$	-237	1.228
$\text{O}_2 + 4\text{H}^+ + 4e^- \leftrightarrow 2\text{H}_2\text{O}$	-474	1.228
$2\text{H}^+ + 2e^- \leftrightarrow \text{H}_2$	0	0.000

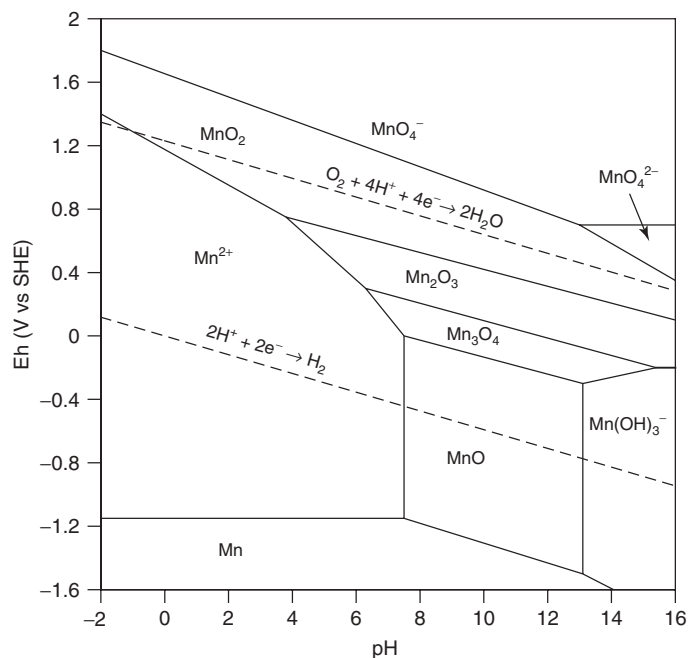


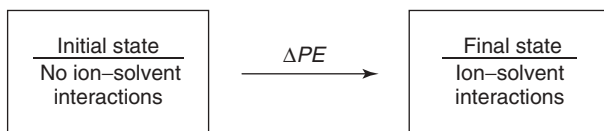
Figure 1.1 Eh-pH diagram for the Mn-O₂-H₂-H₂O system at 25 °C.

1.2.1.1 Ion-Solvent Interactions

A crystal of KCl dissolves readily in water. In the crystal, the K⁺ and Cl⁻ ions are held together mainly by coulombic forces. The dissolution of the crystal means that these forces must have been overcome by strong forces between the ions and the solvent. Thus, there must be a large energy of interaction between the ions and the solvent.

1.2.1.2 Thermodynamics

To calculate the energy of an ion–solvent interaction, consider a state in which there are no ion–solvent interactions and one in which there is.



Now, $-\Delta G$ is the maximum (i.e., reversible) useful work we can get from a system at constant temperature and pressure. Useful means excluding work against the atmosphere, $-P\Delta V$, which results from any expansion or contraction of the system. Thus, if our calculation neglects any change in the volume of the system and is at constant temperature and pressure, we have:

$$\Delta G_{i-s} = \Delta PE$$

- *Final state:* The ions dissolved in solution.
- *Initial state:* There must be no ion–solvent interactions, so let the ions and solvent be separated and let the ions be in a vacuum at very low pressure so there are no ion–ion interactions.

We can now calculate ΔG_{i-s} as the reversible work of transferring 1 mol of the ions from the vacuum to the solvent.

1.2.2

The Born or Simple Continuum Model

The Born model is the simplest for carrying out this calculation. It considers ions to be charged spheres and the solvent to be a continuous dielectric fluid, that is, uniform throughout (not composed of molecules and voids) and its only physical property is a dielectric constant. Thus, the interaction is electrostatic.

As G is a state function, we can calculate ΔG_{i-s} as

$$\Delta G_{i-s} = N_A (W_1 + W_2 + W_3) \quad \text{J mol}^{-1} \quad (1.25)$$

where W_1 is the reversible work to discharge an ion in a vacuum ($\epsilon = 1$) and W_2 the reversible work to put a discharged ion in the solvent. As the interaction is electrostatic, $W_2 = 0$, and W_3 is the reversible work to charge a discharged ion in a medium of dielectric constant (ϵ).

The reversible work to charge an ion from charge 0 to ze (z is the formal charge, and $e = 1.60 \times 10^{-19}$ C) is

$$W_3 = \frac{(ze)^2}{8\pi\epsilon\epsilon_0 r}$$

The reversible work to discharge an ion from ze to zero in a vacuum is the negative of this with $\varepsilon = 1$. Thus,

$$W_1 = -\frac{(ze)^2}{8\pi\varepsilon V_0 r}$$

Substituting into Eq. (1.25) gives the Born equation; that is,

$$\Delta G_{i-s} = -\frac{N_A(ze)^2}{8\pi\varepsilon_0 r} \left(1 - \frac{1}{\varepsilon}\right) \quad (1.26)$$

Further, since:

$$\begin{aligned} \Delta G &= \Delta H - T\Delta S \text{ (constant temperature)} \\ \Delta S_{i-s} &= -\frac{\partial \Delta G_{i-s}}{\partial T} = \frac{N_A(ze)^2}{8\pi\varepsilon_0 r} \left(\frac{1}{\varepsilon^2} \frac{d\varepsilon}{dT}\right) \\ \Delta H_{i-s} &= \Delta G_{i-s} + T\Delta S_{i-s} \\ \Delta H_{i-s} &= -\frac{N_A(ze)^2}{8\pi\varepsilon_0 r} \left(1 - \frac{1}{\varepsilon} - \frac{T}{\varepsilon^2} \frac{d\varepsilon}{dT}\right) \end{aligned} \quad (1.27)$$

Note that these equations refer to a single ionic species, for example, K^+ .

1.2.2.1 Testing the Born Equation

The enthalpy of a solution (heat liberated or absorbed at constant pressure) of a salt is

$$\Delta H_{\text{solution}} = \Delta H_{\text{lattice}} + \Delta H_{s-s}$$

where $\Delta H_{\text{lattice}}$ is the enthalpy to break up the crystal into individual ions and ΔH_{s-s} is the enthalpy of solvation of the positive and negative ions. Also,

$$\Delta H_{s-s} = \Delta H_{+s} + \Delta H_{-s}$$

Now the absolute enthalpy of hydration of the proton, ΔH_{p-s} is known (see later) to be $-1.09 \text{ MJ mol}^{-1}$. Thus, by measuring ΔH_{a-s} for an acid and measuring ΔH_{s-s} for a corresponding salt we can calculate ΔH_{+s} for the cation.

$$\begin{aligned} \Delta H_{p-s} - \Delta H_{+s} &= \Delta H_{a-s} - \Delta H_{s-s} \\ \Delta H_{-s} &= \Delta H_{s-s} - \Delta H_{+s} \end{aligned}$$

Values for the enthalpy of hydration for various ions are given in Table 1.3. The Born model values are not good but are by no means disastrous either. The glaring oversimplification of the Born model is that it does not consider the molecular nature of the solvent.

1.2.3

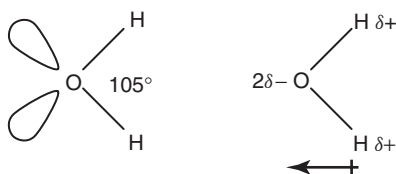
The Structure of Water

Water consists of two O-H σ bonds formed by the overlap of sp^3 hybrid orbitals of oxygen with the s orbitals of hydrogen. Oxygen has two lone pairs of electrons and

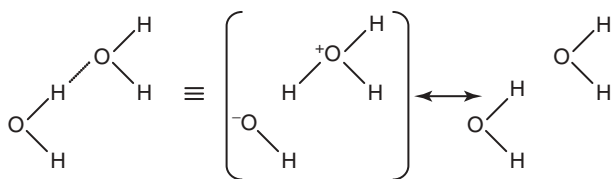
Table 1.3 Comparison between theoretical and experimental ion–water interactions at 25 °C.

Ion	ΔH_{i-H_2O} (kJ mol ⁻¹)	
	Theoretical	Experimental
Li ⁺	-66.4	-35.0
Na ⁺	-41.9	-28.4
K ⁺	-29.9	-23.6
Rb ⁺	-27.0	-22.4
Cs ⁺	-23.6	-21.0
F ⁻	-29.3	-23.6
Cl ⁻	-22.0	-15.5
Br ⁻	-20.4	-14.0
I ⁻	-18.5	-11.6

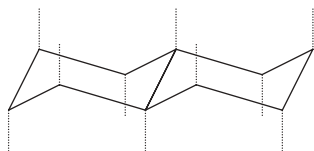
because of the repulsion between these lone pairs the angle between these O–H bonds is not quite the tetrahedral angle.



Water has a dipole moment, $\mu_w = 6.23 \times 10^{-30}$ C m. Because of the two lone pairs of electrons on O, each O can form two hydrogen bonds; that is,



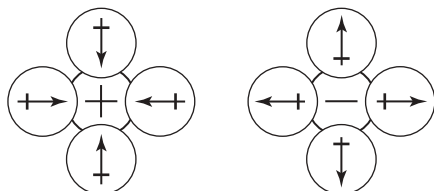
In ice, each water molecule is tetrahedrally coordinated to form a three-dimensional network of puckered hexagonal rings.



The structure of liquid water has been studied using many techniques (X-ray and neutron diffraction (D_2O) Raman, IR, and NMR). It is concluded that liquid water is best described as a somewhat broken down and slightly expanded form of ice. There is considerable short-range (4 or 5 molecular diameters) order. The nature of this order is similar to that of ice. Indeed, the heat of vaporization of water and ice are almost the same at the same temperature.

1.2.3.1 Water Structure near an Ion

The coulombic interaction between an ion and a dipole is always attractive and a certain number of water molecules are trapped and oriented in the ionic field. The ion has a sheath of coordinated water molecules.



Some way from the ion, the structure of the bulk water is undisturbed. Between the solvated ion and the bulk there is a narrow region where the structure of water is more or less broken down. As we have two regions where the structure of water is ordered differently, the intervening region must be at least partially disordered and is called the *structure-broken region*. The structure-broken region is responsible for electrolyte solutions having lower viscosities than pure water.

1.2.3.2 The Ion–Dipole Model

This model considers the dipolar nature of water molecules and liquid water to have a loose ice structure. The ion–solvent interaction now consists of the following:

- The interaction between the ion and n coordinated water molecules of its hydration sheath
- The energy of a hydrated ion in a dielectric medium
- The energy used to break the structure in the structure-broken region.

For simplicity, we will calculate only ΔH_{i-s} ; that is, the enthalpy change when ions are transferred from a vacuum into the solvent. The components of ΔH_{i-s} are as follows:

ΔH_{cf} Form a cavity in the water structure large enough to accommodate the ion with n coordinating water molecules. To do this, remove a cluster of $n + 1$ water molecules.

ΔH_{cb} Break up the cluster into $n + 1$ separate water molecules in the gas phase.

ΔH_{id} Form ion–dipole “bonds” between the ion and n of the water molecules.

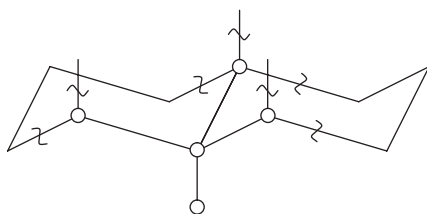
ΔH_{Bc} Transfer the solvated ion into the cavity. This is the Born enthalpy of salvation of the solvated ion.

ΔH_{cp} Position the solvated ion in the most stable orientation in the cavity, that is, the minimum energy orientation. ($\Delta H_{cf} - \Delta H_{cp}$ is the increase in the energy of the solvent due to structure breaking.)

ΔH_c Return the leftover water molecules from the gas phase to the solvent.

1.2.3.3 Cavity Formation

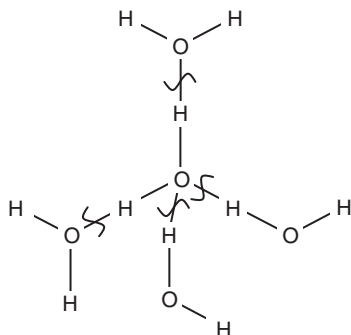
Consider only the case of $n = 4$. Remove a cluster of five water molecules.



This requires breaking 12 H-bonds. For water, a H-bond has ΔH_f^0 . Therefore,

$$\Delta H_{cf} = 250 \text{ kJ mol}^{-1} \text{ (i.e., per mole of ions)}$$

1.2.3.4 Breaking up the Cluster

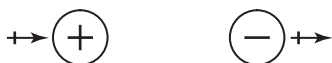


This requires the breaking of four H-bonds.

$$\Delta H_{cb} = 84 \text{ kJ mol}^{-1}$$

1.2.3.5 Ion–Dipole Interaction

Because the water dipoles orient in the field of the ion, the ion is always on the axis of the dipole and the force between them is attractive (negative).



$$F = -\bar{\epsilon} |ze|$$

The potential energy at the separation x is the reversible work of bringing the charge from ∞ to x . Therefore,

$$\begin{aligned} PE &= -\int_{\infty}^x 2\mu_w |ze| / 4\pi\epsilon\epsilon_0 x^3 dx \\ &= -2\mu_w |ze| / 4\pi\epsilon\epsilon_0 x^2 \end{aligned}$$

For the ion in contact with n water dipoles, each at separation $x = r_i + r_w$ and

$$\Delta G_{id} = -\frac{nN_A\mu_w |ze|}{4\pi\epsilon_0 (r_i + r_w)^2} \text{ J mol}^{-1}$$

Note that $\epsilon = 1$ because there is no medium between the ion and the dipole. As the temperature dependencies of μ_w , r_i , and r_w are all negligibly small,

$$\Delta S_{id} = -\frac{d\Delta G_3}{dT} \approx 0$$

and

$$\Delta H_{id} = -\frac{nN_A\mu_w |ze|}{4\pi\epsilon_0 (r_i + r_w)^2} \text{ J mol}^{-1}$$

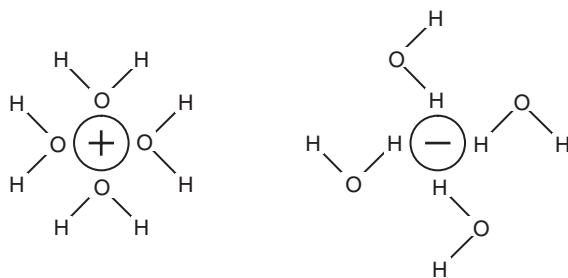
1.2.3.6 The Born Energy

This arises when we transfer the solvated ion, of radius $r_i + 2r_w$, into the cavity and is (Eq. (1.27)):

$$\Delta H_{Bc} = -\frac{N_A(ze)^2}{8\pi\epsilon_0 (r_i + 2r_w)} \left(1 - \frac{1}{\epsilon_w} - \frac{T}{\epsilon_w^2} \frac{d\epsilon_w}{dT} \right) \text{ J mol}^{-1}$$

1.2.3.7 Orienting the Solvated Ion in the Cavity

Energy is liberated when bonds are formed. Hence, the minimum energy orientation (the most stable) occurs when as many H-bonds as possible are made between the solvating waters and the water structure of the cavity. However, it is necessary that the dipoles solvating the ion are oriented so that unlike poles are in contact.



Models show that for cations it is possible to make 10 H-bonds but for anions only 8.

$$\Delta H_{cp} = -10 \times 21 = -210 \text{ kJ mol}^{-1} \text{ (cations)}$$

$$\Delta H_{\text{cp}} = -8 \times 21 = -167 \text{ kJ mol}^{-1} \text{ (anions)}$$

1.2.3.8 The Leftover Water Molecules

Returning this to the bulk liberates the heat of condensation of water.

$$\Delta H_{\text{c}} = -42 \text{ kJ mol}^{-1}$$

1.2.3.9 Comparison with Experiment

$$\Delta H_{\text{i-s}} = \sum_1^6 \Delta H'_{\text{s}}$$

$$\Delta H_{\text{i-s}} = 84 \times 10^3 + \Delta H_{\text{id}} + \Delta H_{\text{Bc}} \text{ J mol}^{-1} \text{ for cations}$$

$$\Delta H_{\text{i-s}} = 126 \times 10^3 + \Delta H_{\text{id}} + \Delta H_{\text{Bc}} \text{ J mol}^{-1} \text{ for anions}$$

The calculated values are in fair agreement with the experimental values and, overall, show a definite improvement over the simple continuum model values. Note that the ion–dipole interaction makes the largest contribution to the end result. This suggests that the ion–dipole interaction is the most profitable place to try to improve the calculation.

1.2.3.10 The Ion–Quadrupole Model

This model takes into account the quadrupole nature of water and the polarization of the water molecules by the ion.

Water has partial positive charges on each of the hydrogen atoms and partial negative charges on each of the lone pairs of oxygen. Thus, it is really a quadrupole and it is only an approximation to treat it as a dipole. This is accounted for by adding a quadrupole correction term to the dipole interaction term:



$$\Delta H_{\text{id}} \pm \Delta H_{\text{Q}} = \frac{nN_{\text{A}} |ze|}{4\pi\epsilon_0} \left(-\frac{\mu_{\text{w}}}{(r_{\text{i}} + r_{\text{w}})^2} \pm \frac{P_{\text{w}}}{2(r_{\text{i}} + r_{\text{w}})^3} \right)$$

where the positive sign applies to a cation and the negative sign to an anion. P_{w} is the quadrupole moment of water; $1.3 \times 10^{-39} \text{ C m}^2$.

1.2.3.11 The Induced Dipole Interaction

The force between the ion and the dipole it induces is

$$F = -\frac{2\alpha'(ze)^2}{4\pi\epsilon\epsilon_0 x^5}$$

The potential energy of interaction is obtained by integrating the negative of this force from ∞ to $x = r_{\text{i}} + r_{\text{w}}$ and is

$$PE = -\frac{\alpha'(ze)^2}{8\pi\epsilon_0 (r_{\text{i}} + r_{\text{w}})^4}$$

Table 1.4 Comparison between theoretical and experimental absolute heats of hydration for various individual ions at 25 °C.

Ion	ΔH_{i-H_2O} (kJ mol ⁻¹)	
	Theoretical	Experimental
Li ⁺	-36.6	-31.0
Na ⁺	-26.1	-24.5
K ⁺	-19.7	-19.9
Rb ⁺	-17.5	-18.5
Cs ⁺	-15.2	-17.1
F ⁻	-29.0	-27.6
Cl ⁻	-19.8	-19.5
Br ⁻	-17.7	-17.9
I ⁻	-15.1	-15.6

Thus,

$$\Delta H_{\text{ind}} = -\frac{nN_A \alpha' (ze)^2}{8\pi\epsilon_0 (r_i + r_w)^4}$$

1.2.3.12 The Results

The expressions for ΔH_{i-s} are for cations:

$$\Delta H_{i-s} = 84\,000 + \Delta H_{\text{id}} + \Delta H_{\text{Bc}} + \Delta H_{\text{ind}} + \Delta H_{\text{Q}} \text{ J mol}^{-1}$$

and anions:

$$\Delta H_{i-s} = 126\,000 + \Delta H_{\text{id}} + \Delta H_{\text{Bc}} + \Delta H_{\text{ind}} - \Delta H_{\text{Q}} \text{ J mol}^{-1}$$

Table 1.4 now shows very good agreement between theory and experiment for $n=4$. The worst result is for Li⁺, which is due to its very small size.

1.2.3.13 Enthalpy of Hydration of the Proton

Consider a salt MX in which the two ions have equal radii. Subtracting the enthalpy of hydration of the anion from that of the cation:

$$\begin{aligned} \Delta H_{+s} - \Delta H_{-s} &= -42\,000 + 2\Delta H_{\text{Q}} \\ \Delta H_{+s} - \Delta H_{-s} - 2\Delta H_{\text{p-s}} &= -2\Delta H_{\text{p-E}} - 42\,000 + 2\Delta H_{\text{Q}} \\ \Delta H_{+s} + \Delta H_{-s} - 2\Delta H_{-s} - 2\Delta H_{\text{p-E}} &= -2\Delta H_{\text{p-s}} - 42\,000 + 2\Delta H_{\text{Q}} \\ \Delta H_{\text{MX-s}} - 2\Delta H_{\text{HX-s}} &= -2\Delta H_{\text{p-s}} - 42\,000 + \frac{nN_A |ze| P_w}{4\pi\epsilon_0 (r_i + r_w)^3} \end{aligned}$$

Halliwell and Nyburg considered the series of salts KF, NH₄OH, RbOH, CsCl, and N(CH₃)₄I₃, in which the anions and cations have very nearly equal radii. A plot of the LHS against $(r_i + r_w)^{-3}$ yielded a straight line giving $\Delta H_{\text{p-s}}$ from the intercept as $-1.09 \text{ MJ mol}^{-1}$.

1.2.4

The Solvation Number

Unfortunately, there is no general agreement about the meaning of the often used terms *solvation number* and *hydration number*. We will use two other terms that appear to have accepted meanings.

1.2.4.1 **Coordination Number**

This is the number of solvent molecules that can be placed in contact with the ion. It is a geometric phenomenon that is important when considering the nonkinetic properties of ionic solutions.

1.2.4.2 **The Primary Solvation Number**

This is the average number of solvent molecules that are so strongly bound to the ion that they move with the ion when it moves (jumps). It is determined from kinetic measurements and is important in collision processes. It is larger for ions of high charge density and because it is an average it is often fractional, for example, for Na^+ it is 3 and for Cl^- it is 0.5.

1.2.5

Activity and Activity Coefficients1.2.5.1 **Fugacity (f')**

This is an idealized pressure or vapor pressure defined by

$$\mu = \bar{G} = RT \ln(f') + B(T) \quad (1.28)$$

where $B(T)$ is an unknown quantity. f' is defined this way because we cannot measure absolute values of μ , so to get absolute values of f' there must be an unknown in the equation.

Note that $f' = P$ when the gas behaves ideally. To illustrate, consider a change for n moles of gas from state i to state f we have from Eq. (1.28):

$$\begin{aligned} \Delta G &= n(\bar{G}_f - \bar{G}_i) \\ &= nRT \ln\left(\frac{f'_f}{f'_i}\right) \text{ Any gas} \end{aligned}$$

which compares to the well-known equation:

$$\Delta G = nRT \ln\left(\frac{P_f}{P_i}\right) \text{ Ideal gas}$$

1.2.5.2 **Dilute Solutions of Nonelectrolytes**

Henry's law (an empirical law) states that for very dilute solutions of nonelectrolytes:

$$f'_2 = k_N N_2 \quad (\text{Mole fraction scale})$$

where f'_2 is the fugacity of the solute, N_2 is the solute mole fraction, and k_N is the Henry's law constant (empirical). Note that 1 refers to solvent and 2 to solute. Also,

$$f'_2 = k_m m_2 \quad (\text{Molal scale})$$

$$f'_2 = k_M M_2 \quad (\text{Molar scale})$$

1.2.5.3 Activity (a)

Activity is defined as

$$a = \frac{f'}{f'^0} \quad (1.29)$$

where f'^0 is the fugacity in some chosen standard state. Thus,

$$\begin{aligned} \mu - \mu^0 &= RT \ln \left(\frac{f'}{f'^0} \right) \\ &= RT \ln(a) \end{aligned} \quad (1.30)$$

Note that for a given substance, x , in solutions 1 and 2, that:

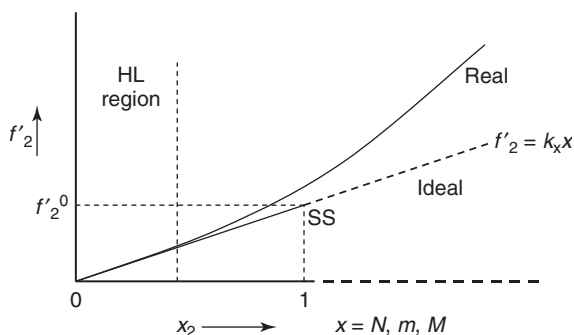
$$\frac{a_x(1)}{a_x(2)} = \frac{f'_x(1)}{f'_x(2)}$$

which is independent of the standard state chosen.

1.2.5.4 Standard States

We can actually choose any standard states we like but the most useful are

- Gases: The gas at $f' = 1$ atm.
- Solids and liquids: The pure substance at 1 atm external pressure.
- Solvents in a solution: The pure solvent at the same temperature and pressure as the solution.
- Solutes in a solution: The hypothetical solution of unit concentration that obeys Henry's law. As there are three concentration scales, there are three standard states giving three different values for " a " for the same solution.



The standard states are hypothetical because they do not, in general, correspond to real solutions.

1.2.5.5 Infinite Dilution

These standard states are preferred because at infinite dilution all activities become known. As the solution is made more dilute, the solvent approaches the pure solvent (the standard state); hence, $f' \rightarrow f'^0$ and $a \rightarrow 1$. Also, the solution obeys Henry's law and:

$$f'_2 = k_x x \quad \text{and} \quad f'^0_2 = k_x$$

$$a = \frac{f'_2}{f'^0_2} = x \quad (x = N, m, M)$$

The activity becomes equal to the concentration and the activity coefficient becomes unity.

1.2.5.6 Measurement of Solvent Activity

As $f' = P$ except at high pressures, it is usually sufficient to measure the vapor pressure above the solution and above the pure solvent at the same temperature.

$$a = \frac{P_{\text{solution}}}{P_{\text{solvent}}}$$

1.2.5.7 Measurement of Solute Activity

There are a great many methods but only one general method. It is based on the Gibbs–Duhem equation (for μ) and the measured values of a_1 .

$$n_1 d\mu_1 = -n_2 d\mu_2 \quad (\text{Gibbs – Duhem equation})$$

where n represents the number of moles. Now from Eq. (1.30):

$$\mu_1 - \mu_1^0 = RT \ln(a_1)$$

Hence,

$$d\mu_1 = RT d \ln(a_1)$$

Similarly,

$$d\mu_2 = RT d \ln(a_2)$$

Thus,

$$d \ln(a_2) = -\frac{n_1}{n_2} d \ln(a_1)$$

$$\ln(a_2) = -\int_0^{\ln(a_1)} \frac{n_1}{n_2} d \ln(a_1)$$

which can be integrated numerically.

1.2.5.8 Electrolyte Activity

The activity of the electrolyte as a whole is still defined by

$$a_2 = \frac{f'_2}{f'^0_2}$$

and can be measured as for nonelectrolytes. For individual ions, we define:

$$\begin{aligned}
 a_+ a_- &= a_2 \\
 a_+ &= f_+ N_+ & a_- &= f_- N_- \\
 a_+ &= \gamma_+ M_+ & a_- &= \gamma_- M_- \\
 a_+ &= \gamma_+ m_+ & a_- &= \gamma_- m_- \\
 f_+ f_- &= f_2 & \gamma_+ \gamma_- &= \gamma_2 & \gamma_+ \gamma_- &= \gamma_2
 \end{aligned}$$

where f , γ , and γ are the activity coefficients on the mole fraction and molar and molal scale.

1.2.5.9 Mean Ion Quantities

We cannot measure individual ion activities or activity coefficients. When we need them, we approximate them to the mean ion quantities defined by

$$\begin{aligned}
 a_{\pm} &= (a_+ a_-)^{1/2} = a_2^{1/2} \quad 1 : 1 \text{ electrolyte} \\
 f_{\pm} &= (f_+ f_-)^{1/2} = f_2^{1/2} \quad 1 : 1 \text{ electrolyte}
 \end{aligned}$$

Note that

$$\begin{aligned}
 a_2 &= a_{\pm}^2 \\
 &= (m\gamma_{\pm})^2 \quad 1 : 1 \text{ electrolyte} \\
 &= m^2 \gamma_2
 \end{aligned}$$

For a general electrolyte, $A_{\nu_+} B_{\nu_-}$ for which $\nu = \nu_+ + \nu_-$:

$$\begin{aligned}
 a_2 &= a_A^{\nu_+} a_B^{\nu_-} \\
 a_{\pm} &= a_2^{1/\nu} \\
 &= (a_A^{\nu_+} a_B^{\nu_-})^{1/\nu} \\
 f_{\pm} &= f_2^{1/\nu} \\
 &= (f_A^{\nu_+} f_B^{\nu_-})^{1/\nu} \tag{1.31}
 \end{aligned}$$

1.2.5.10 Relation between f , γ , and γ

Activity coefficients are usually tabulated as γ but we often need to convert these to f or γ . Consider 1 l of $A_{\nu_+} B_{\nu_-}$ solution of molarity M_2 and molality m_2 .

$$\text{Moles of positive ions} = M_2 \nu_+$$

$$\text{Moles of positive ions} = M_2 \nu_+$$

$$\text{Moles of ions} = M_2 \nu$$

$$\text{Moles of solvent} = \frac{1000\rho - M_2 W_2}{W_1}$$

ρ (g cm^{-3}) is the solution density and W_1 and W_2 the molar masses. Therefore,

$$\text{Mole fraction positive ions, } N_+ = \frac{W_1 M_2 \nu_+}{1000\rho - M_2 W_2 + M_2 W_1 \nu}$$

As $M_2 \rightarrow 0$, $\rho \rightarrow \rho_0$ (density of pure solvent), then

$$1000\rho_0 \gg M_2 W_2 + M_2 W_1 v$$

and

$$N_{+0} = \frac{W_1 M_2 v_+}{1000\rho_0}$$

As the ratio of activities is independent of the standard state chosen, and since all activity coefficients approach unity at infinite dilution, we have:

$$\frac{a_+}{a_{+0}} = \frac{f_+ N_+}{N_{+0}} = \frac{\gamma_+ M_+}{M_{+0}} = \frac{\gamma_+ m_+}{m_{+0}}$$

We can now work out the relation between any two activity coefficients. Consider f and γ :

$$\frac{f_+ N_+}{N_{+0}} = \frac{\gamma_+ M_+}{M_{+0}}$$

and substituting for N_+ and N_{+0} and rearranging yields:

$$f_+ = \gamma_+ \left(\frac{1000\rho - M_2 W_2 + M_2 W_1 v}{1000\rho_0} \right)$$

Similarly,

$$f_- = \gamma_- \left(\frac{1000\rho - M_2 W_2 + M_2 W_1 v}{1000\rho_0} \right)$$

and

$$f_{\pm} = \gamma_{\pm} \left(\frac{1000\rho - M_2 W_2 + M_2 W_1 v}{1000\rho_0} \right)$$

Further,

$$\gamma_{\pm} = \gamma_{\pm} \left(\frac{1000\rho - M_2 W_2 + M_2 W_1 v}{1000\rho_0 + m_2 W_1 v} \right)$$

and

$$f_{\pm} = \gamma_{\pm} (1 + 0.001 m_2 W_1 v)$$

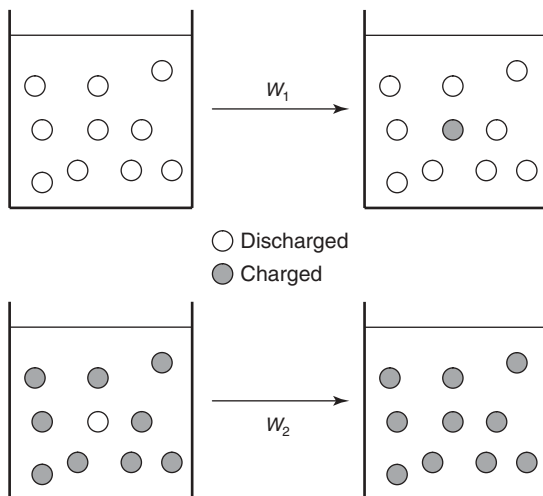
1.2.6

Ion–Ion Interactions

1.2.6.1 Introduction

We have seen that there are strong interactions between ions and solvent dipoles. As the latter have only a fraction of an ionic charge, we must expect that there will be even stronger interactions between the ions themselves.

We assume that we can discharge and recharge ions at will. Note that a discharged ion is not an atom because its radius must remain unchanged. We select one ion called the reference ion and calculate the reversible work for:



$W_2 - W_1$ is the change in potential energy of the reference ion due to ion-ion interactions. If we do not include $P\Delta V$ work in the work calculation, then:

$$\begin{aligned}
 N_A(W_2 - W_1) &= \text{Change in free energy of solution per mole of reference ions} \\
 &= \Delta \bar{G}_{\text{reference ion}} \\
 &= \Delta \mu_{i-1} \quad (1.32)
 \end{aligned}$$

Now,

$$W_1 = \int_0^{ze} \psi_1 dq \quad \text{and} \quad W_2 = \int_0^{ze} \psi_2 dq$$

ψ_1 is the potential at the surface of the ion when all the other ions are discharged and ψ_2 when they are charged. Equation (1.31) gives $W_1 = (ze)^2 / 8\pi\epsilon\epsilon_0 r_i$. The problem is to calculate ψ_2 .

1.2.6.2 Debye-Huckel Model for Calculating ψ_2

Debye and Huckel said that there are so many ions around the reference ion that it is a good approximation to consider these ions as a cloud of ions or a cloud of charge. As the solution as a whole must be neutral, the ion cloud must have a charge equal and opposite to that of the reference ion.

Total charge = -1



Here, we assume that the ions in the ion cloud are point charges and hence can come right up to the surface of the reference ion.

1.2.6.3 Poisson–Boltzmann Equation

Take the center of the reference ion as the origin. In spherical coordinates, Poisson's equation is

$$\frac{1}{r^2} \frac{d}{dr} \left(r^2 \frac{d\psi_r}{dr} \right) = -\frac{\rho_r}{\epsilon \epsilon_0}$$

or more conveniently

$$\frac{d^2(r\psi_r)}{dr^2} = -\frac{r\rho_r}{\epsilon \epsilon_0} \quad (1.33)$$

where r is the radial distance from the origin and ρ_r and ψ_r are the charge density (C m^{-3}) and potential at r .

1.2.6.4 Charge Density

Consider an element of volume δV at r :

$$\begin{aligned} \rho_r &= n_1 z_1 e + n_2 z_2 e + n_3 z_3 e + \dots + n_i z_i e \\ &= \sum n_i z_i e \end{aligned}$$

where n_1 is the number of ions of charge $z_1 e$ per unit volume in the ion cloud. We do not know these n values but we do know $n_1^0 \dots n_i^0$, which are the number per unit volume in the bulk. They are different because there is a potential in the ion cloud owing to the reference ion, which is absent in the bulk. Thus, the ions in the ion cloud have energy $z_i e \psi_r$ greater than those in the bulk, and so the Boltzmann equation yields:

$$n_i = n_i^0 \exp\left(-\frac{z_i e \psi_r}{kT}\right)$$

Thus,

$$\rho_r = \sum n_i z_i e = \sum n_i^0 z_i e \exp\left(-\frac{z_i e \psi_r}{kT}\right)$$

This equation can be linearized by recalling:

$$\exp\left(-\frac{z_i e \psi_r}{kT}\right) = 1 - \frac{z_i e \psi_r}{kT} \text{ when } \frac{z_i e \psi_r}{kT} \ll 1$$

Hence,

$$\rho_r = \sum n_i^0 z_i e - \sum n_i^0 \frac{z_i^2 e^2 \psi_r}{kT}$$

However, $\sum n_i^0 z_i e = 0$ as the bulk is electrically neutral. Thus

$$\rho_r = -\sum n_i^0 \frac{z_i^2 e^2 \psi_r}{kT}$$

This is mathematically invalid because $z_i e \psi_r / kT$ is not considerably less than 1. However, we must do it to end up with a linear relation between ρ_r and ψ_r , as demanded by the law of superposition of potential. This somewhat philosophical problem is the great unresolved difficulty with the Debye–Huckel theory.

1.2.6.5 Solving the Poisson–Boltzmann Equation

Substituting in Poisson's equation, Eq. (1.33) yields:

$$\begin{aligned} \frac{d^2(r\psi_r)}{dr^2} &= -\frac{r\rho_r}{\varepsilon\varepsilon_0} = \left(\frac{1}{\varepsilon\varepsilon_0 kT} \sum n_i^0 z_i^2 e^2\right)(r\psi_r) \\ &= K^2(r\psi_r) \quad (\text{Poisson–Boltzmann equation}) \end{aligned}$$

where K or L_D^{-1} is the Debye reciprocal length. The Poisson–Boltzmann equation is of the form:

$$\frac{d^2\gamma}{dx^2} = K^2\gamma$$

for which the general solution is

$$\psi_r = \frac{A'}{r} \exp(-Kr) + \frac{B'}{r} \exp(Kr)$$

where A' and B' are constants of integration requiring evaluation.

In the solution bulk, $r \rightarrow \infty$ and $\psi_r \rightarrow 0$. Thus, $B' = 0$. Further, the equation must hold in very dilute solution, that is, as $n_i^0 \rightarrow 0$ and hence as $K \rightarrow 0$.

$$\psi_r = \frac{A'}{r} \quad (\text{Infinite dilution})$$

But in an infinitely dilute solution there are no ion–ion interactions and the potential at r is due solely to the reference ion; that is,

$$\psi_r = \frac{q}{4\pi\varepsilon\varepsilon_0 r} \quad (\text{Infinite dilution})$$

Here, we use q for the charge on the reference ion as it is a variable when we charge it from 0 to ze . Hence,

$$A' = \frac{q}{4\pi\varepsilon\varepsilon_0}$$

and

$$\psi_2 = \frac{q}{4\pi\epsilon\epsilon_0 r} \exp(-Kr) \quad (1.34)$$

Now because r_i is small, $Kr_i \ll 1$ and the potential at the surface of the reference ion is given by

$$\psi_2 = \frac{q}{4\pi\epsilon\epsilon_0 r_i} (1 - Kr_i)$$

1.2.6.6 Calculation of $\Delta\mu_{i-1}$

From before:

$$\begin{aligned} W_2 &= \int_0^{ze} \psi_2 dq \\ &= \int_0^{ze} \frac{q}{4\pi\epsilon\epsilon_0 r_i} (1 - Kr_i) dq \\ &= \frac{(ze)^2}{8\pi\epsilon\epsilon_0 r_i} (1 - Kr_i) \end{aligned}$$

Now $W_1 = \frac{(ze)^2}{8\pi\epsilon\epsilon_0 r_i}$ and from Eq. (1.32)

$$\begin{aligned} \Delta\mu_{i-1} &= N_A(W_2 - W_1) \\ &= -\frac{N_A(ze)^2 K}{8\pi\epsilon\epsilon_0} \end{aligned} \quad (1.35)$$

1.2.6.7 Debye Length, K^{-1} or L_D

$$L_D = \left(\frac{1}{\epsilon\epsilon_0 kT} \sum n_i^0 z_i^2 e^2 \right)^{-1/2} \quad (1.36)$$

L_D is a distance characteristic of the solution, which increases as the solution becomes more dilute. Equation (6.3) shows that at distance d greater than L_D the influence of the reference ion falls off rapidly and the Debye length is called the *thickness of the ion cloud*.

1.2.6.8 The Activity Coefficient

For an ion in solution we have for the mole fractions scale:

$$\begin{aligned} \mu_i &= \mu_i^0 + RT \ln(N_i) + RT \ln(f_i) \quad (\text{real solution}) \\ \mu_i &= \mu_i^0 + RT \ln(N_i) \quad (\text{ideal solution}) \end{aligned}$$

Debye and Huckel hypothesized that the difference between real and ideal solutions is due to ion-ion interactions. Thus,

$$\Delta\mu_{i-1} = \mu_i(\text{real}) - \mu_i(\text{ideal}) = RT \ln(f_i)$$

and from Eq. (1.35)

$$RT \ln(f_i) = -\frac{N_A(ze)^2 K}{8\pi\epsilon\epsilon_0}$$

We now want to transform this equation into an explicit equation in f_{\pm} . From Eq. (1.31)

$$\begin{aligned}\ln(f_{\pm}) &= \frac{1}{\nu}(\nu_+ \ln(f_+) + \nu_- \ln(f_-)) \\ &= -\frac{N_A e^2 K}{8\pi\epsilon\epsilon_0 RT} \left(\frac{\nu_+ z_+^2 + \nu_- z_-^2}{\nu} \right)\end{aligned}$$

As the electrolyte is electrically neutral, $\nu_+ z_+ = -\nu_- z_-$ and the factor in brackets reduces to $-z_+ z_-$. Thus,

$$\ln(f_{\pm}) = -\frac{N_A (-z_+ z_-) e^2 K}{8\pi\epsilon\epsilon_0 RT} \quad (1.37)$$

Now, Eq. (1.36)

$$\begin{aligned}K &= \left(\frac{1}{\epsilon\epsilon_0 kT} \sum n_i^0 z_i^2 e^2 \right)^{1/2} \\ n_i^0 &= 1000 C_i N_A\end{aligned}$$

where C_i is concentration in mol l^{-1} . Thus,

$$\begin{aligned}\sum n_i^0 z_i^2 e^2 &= 1000 N_A e^2 \sum C_i z_i^2 \\ &= 2000 N_A e^2 I\end{aligned}$$

where the ionic strength, I , in molar units is defined by

$$I = \frac{1}{2} \sum C_i z_i^2$$

Thus,

$$\begin{aligned}K &= \left(\frac{2000 N_A e^2}{\epsilon\epsilon_0 kT} \right)^{1/2} I^{1/2} \\ &= 100 B I^{1/2}\end{aligned}$$

Substituting into Eq. (1.37) yields:

$$\ln(f_{\pm}) = -\frac{-100 B N_A e^2}{8\pi\epsilon\epsilon_0 RT} (-z_+ z_-) I^{1/2}$$

and the Debye–Huckel limiting law is written as

$$\ln(f_{\pm}) = -A (-z_+ z_-) I^{1/2}$$

where

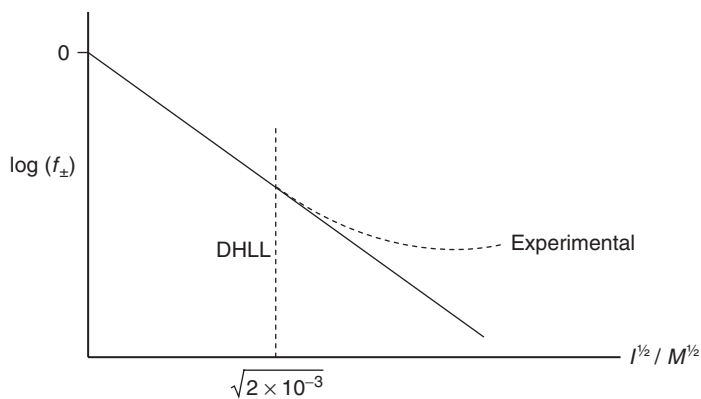
$$A = \frac{100 B N_A e^2}{2.303 \times 8\pi\epsilon\epsilon_0 RT}$$

Table 1.5 Radius of ion cloud at various concentrations of NaCl.

C_{NaCl} (M)	L_D (nm)
10^{-4}	30.0
10^{-3}	9.6
10^{-2}	3.0
10^{-1}	0.96

1.2.6.9 Comparison with Experiment

For concentrations less than 2 or 3 mM, the Debye–Huckel limiting law is a brilliant success. However, above ~ 5 mM significant discrepancies appear.



Note that the Debye–Huckel limiting law gives the mole fraction activity coefficient for concentration in M units. However, in the range of the Debye–Huckel limiting law there is no significant difference between f , γ , and γ or between m and M .

1.2.6.10 Approximations of the Debye–Huckel Limiting Law

Debye and Huckel reasoned that the limiting law breaks down at $I \sim 5$ mM because of the approximation of considering the ion in the ion cloud to be point charges. The diameter of an ion is typically 0.3 nm and it is valid to consider the ions in the ion cloud to be point charges only when the ion cloud is much larger than the ions. The approximation is clearly better at low concentrations, as shown in Table 1.5.

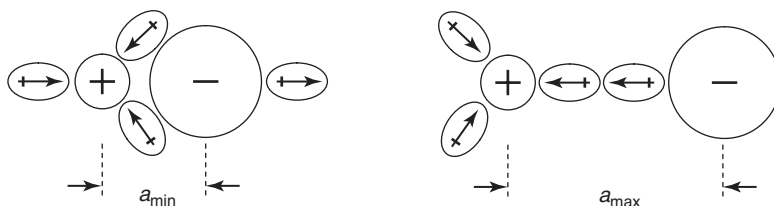
Debye and Huckel concluded that for ions of finite size the closest their centers could come together was the distance “ a ” called the *distance of closest approach*. Reworking the maths then leads to

$$\ln(f_{\pm}) = -\frac{A(-z_+z_-)I^{1/2}}{1 + 100aBI^{1/2}} \quad (\text{Debye - Huckel law}) \quad (1.38)$$

Here “ a ” is in m. It is only at concentrations greater than ~ 2 mM that the denominator varies significantly from 1. Thus, the Debye–Huckel law reduces to the limiting law at low concentrations. With the “right value” of “ a ” the Debye–Huckel law accurately predicts f_{\pm} up to 0.1 M.

1.2.6.11 The Distance of Closest Approach

This is also called the ion size parameter. The ions are closest when they collide and “ a ” is the distance between their centers on collision.



Cations are smaller than anions, and have a higher charge density and hold more water molecules in their charge density and hold more water molecules in their primary hydration sheath than do anions. “ a ” depends on the orientation during collision.

Currently, we are unable to calculate values of “ a .” In Robinson and Stokes’ book, there are extensive tables of “ a ” values that give the best fit of experimental f_{\pm} data to the Debye–Huckel law. The “right values” of “ a ” are empirical. However, it is heartening that these values fall between the two extremes illustrated here.

1.2.6.12 Physical Interpretation of the Activity Coefficient

The success of the Debye–Huckel law permits an unequivocal interpretation of the activity coefficient in solutions less than ~ 0.1 M. Because the Debye–Huckel law ignores all but the coulombic interaction between the ions, the deviations from ideal behavior must be due solely to the coulombic interactions between the ions.

1.2.7

Concentrated Electrolyte Solutions

1.2.7.1 The Stokes–Robinson Treatment

Stokes and Robinson hypothesized that there were two approximations made in the Debye–Huckel law that become untenable in concentrated solutions (>0.1 M).

- Because the Debye–Huckel law makes use of “ a ,” the distance of closest approach of hydrated ions, it really calculates f_{\pm} for hydrated ions and not for the actual ions. For example, it calculates f_{\pm} for Na^+ , $\text{Cl}^- + 3.5 \text{H}_2\text{O}$ and not just for Na^+ and Cl^- as required. Thus, it erroneously includes the ion- hydration free energy that needs to be subtracted out.
- In concentrated solutions, much of the water is bound up in the hydration sheaths of the ions and is not free to act as a solvent. For example, in 1 l of 5 M

LiCl (primary hydration number = 6) only 25.5 of the 55.5 mol of water are free solvent molecules. Thus, there is a concentration effect to be considered.

Stokes and Robinson formulated corrections to the Debye–Huckel law, and because we cannot add or subtract activity coefficients, these corrections must be formulated in terms of free energies. For n_2 moles of electrolyte, the contribution to the free energy due to nonideality is

$$n_2 \Delta \mu_{2-1} = n_2 RT \ln (f_2)$$

From Eq. (1.31)

$$\ln (f_2) = \frac{v \log (f_{\pm})}{2.303}$$

and Eq. (1.38)

$$\log (f_2) = -\frac{A(-z_+z_-) I^{1/2}}{1 + 100aBI^{1/2}}$$

we have

$$n_2 \Delta \mu_{2-1} = n_2 RT \ln (f_2) = -2.303 n_2 v RT \frac{A(-z_+z_-) I^{1/2}}{1 + 100aBI^{1/2}} \quad (1.39)$$

1.2.7.2 The Ion-Hydration Correction

Consider that the ions in the solution are switched off. As the main interaction between the ions and water molecules is electrostatic, removing this interaction causes the activity of water to revert to a value close to that of pure water; that is, 1. If a_w is the activity of water in the real solution, then the change in the free energy of the solution because of ion hydration is

$$RT \ln \left(\frac{a_w}{1} \right) \text{ J mol}^{-1} \text{ of hydrating water}$$

1.2.7.3 The Concentration Correction

The Debye–Huckel law calculates $\Delta \mu_{2-1}$ on the basis of the apparent concentration of the solution, whereas it should be done on the basis of the real concentration. Thus, we should add a term, ${}^r \Delta^a G$, to the free energy of the solution to account for the difference between the real and apparent concentrations. For $A_{v+} B_{v-}$, we write:

$$\begin{aligned} {}^r \Delta^a G &= RT \ln \left(\frac{a^r}{a^a} \right) \text{ J mol}^{-1} \\ &= RT \ln \left(\frac{N^r}{N^a} \right) \end{aligned}$$

where N is the mole fraction and activity coefficients have been neglected because no ion–ion interactions are being considered. The apparent mole fraction of cations is obtained by neglecting solvation and is

$$N_+^a = \frac{n_2 \nu_+}{n_w + n_2 \nu}$$

where n_w is the moles of water in the solution. However, the real mole fraction is

$$N_+^r = \frac{n_2\nu_+}{n_w + n_2\nu - n_2n_h}$$

For $n_2\nu_+$ moles of cations:

$${}^r\Delta^a G_+ = n_2\nu_+ RT \ln \left(\frac{n_w + n_2\nu}{n_w + n_2\nu - n_2n_h} \right)$$

Similarly, for anions:

$${}^r\Delta^a G_- = n_2\nu_- RT \ln \left(\frac{n_w + n_2\nu}{n_w + n_2\nu - n_2n_h} \right)$$

and for the electrolyte as a whole:

$${}^r\Delta^a G_2 = n_2\nu RT \ln \left(\frac{n_w + n_2\nu}{n_w + n_2\nu - n_2n_h} \right)$$

1.2.7.4 The Stokes–Robinson Equation

All our terms have been formulated as solution free energies for n_2 moles of electrolyte and can be summed directly into Eq. (1.39):

$$\begin{aligned} n_2\Delta\mu_{2-1} &= n_2 RT \ln(f_2) = -2.303n_2\nu RT \frac{A(-z_+z_-)I^{1/2}}{1 + 100aBI^{1/2}} - n_2n_h RT \ln(a_w) \\ &\quad + n_2\nu RT \ln \left(\frac{n_w + n_2\nu}{n_w + n_2\nu - n_2n_h} \right) \end{aligned}$$

Dividing through by $2.303 n_2\nu RT$ and rearrange to obtain the Stokes–Robinson equation:

$$\log(f_{\pm}) = -\frac{A(-z_+z_-)I^{1/2}}{1 + 100aBI^{1/2}} - \frac{n_h}{\nu} \ln(a_w) + \log \left(\frac{n_w + n_2\nu}{n_w + n_2\nu - n_2n_h} \right)$$

1.2.7.5 Evaluation of the Stokes–Robinson Equation

Comparison with experiments shows that it is very useful up to several molar. However, the quantities a , a_w , and n_h are all empirical (a_w depends on both the electrolyte and its concentration) and it is better to look up values of f_{\pm} than calculate them. The Stokes–Robinson treatment does, however, greatly contribute to our understanding of the contributions of ionic hydration to the nonideal behavior of concentrated electrolyte solutions.

1.2.8

Ion Pair Formation

1.2.8.1 Ion Pairs

Occasionally, ions of opposite charge get stuck in each other's coulombic field and for that time they constitute an ion pair. Ion pairs exist in a dynamic equilibrium

quantified by the association constant, K :

$$\begin{aligned}
 A^+ + B^- &\leftrightarrow A^+ B^- \\
 K &= \frac{[A^+ B^-]}{[A^+][B^-]} \\
 [A^+ B^-] &= K[A^+][B^-] = KM^2
 \end{aligned} \tag{1.40}$$

As ion pair formation increases with the square of the concentration, it is most pronounced at high concentrations.

1.2.8.2 The Fuoss Treatment

This supersedes the older Bjerrum treatment. Fuoss said an ion pair existed whenever two oppositely charged ions were within the distance “ a ” from each other.

A solution contains z positive and z negative ions and Z_{ip} ion pairs. The number of free positive and negative ions is

$$Z_f = Z - Z_{ip}$$

If the number of positive and negative ions is increased by δZ , most remain free and only a small proportion form ion pairs. Thus,

$$\begin{aligned}
 \delta Z_f &= \delta Z - \delta Z_{ip} \\
 &= \delta Z
 \end{aligned} \tag{1.41}$$

If an ion of opposite charge finds its way into the volume $(4/3)\pi a^3$ around each free ion, an ion pair is formed. If we neglect, for the moment, the forces between ions, the probability that a single ion introduced into the solution will form an ion pair is

$$P_{ip} = \frac{4\pi a^3 Z_f}{3V} \text{ (no ion - ion forces)}$$

where V is the solution volume. An ion in an ion pair has an energy, U (negative), different from that in the bulk. The Boltzmann factor, $\exp(-U/kT)$, gives the probability that a species will exist at an energy U greater than that of some reference state. Thus,

$$P_{ip} = \frac{4\pi a^3 Z_f}{3V} \exp\left(-\frac{U}{kT}\right) \text{ (ion - ion forces)}$$

The number of ion pairs formed by adding δZ positive and negative ions is

$$\delta Z_{ip} = 2 \frac{4\pi a^3 Z_f}{3V} \exp\left(-\frac{U}{kT}\right) \delta Z$$

Substituting δZ_f for δZ (Eq. (8.2)) and integrating between $Z_f = 0$ and Z_f yields the number of ion pairs.

$$Z_{ip} = \frac{4\pi a^3 Z_f^2}{3V} \exp\left(-\frac{U}{kT}\right) \tag{1.42}$$

To evaluate U , recall that the potential a distance “ a ” from a reference ion is Eq. (1.34):

$$\psi_r = \frac{ze}{4\pi\epsilon\epsilon_0 a} \exp(-Ka)$$

In a concentrated solution, Ka is not really small compared to unity and it is a slightly better approximation to write:

$$\exp(-Ka) = \frac{1}{1 + Ka}$$

$$\left(\begin{array}{l} \exp(-x) = 1 - x + \frac{x^2}{2!} - \frac{x^3}{3!} + \dots \\ \frac{1}{1+x} = 1 - x + x^2 - x^3 + \dots \end{array} \right)$$

thus,

$$\psi_r = \frac{ze}{4\pi\epsilon\epsilon_0 a} \left(\frac{1}{1 + Ka} \right)$$

and

$$U = \frac{z_+ z_- e^2}{4\pi\epsilon\epsilon_0 a} \left(\frac{1}{1 + Ka} \right)$$

Writing

$$\frac{U}{kT} = \frac{b}{1 + Ka}$$

where

$$b = \frac{z_+ z_- e^2}{4\pi\epsilon\epsilon_0 a kT}$$

we obtain by substitution into Eq. (1.42):

$$\begin{aligned} Z_{ip} &= \frac{Z_f^2}{V} \frac{4\pi a^3}{3} \exp\left(-\frac{b}{1 + Ka}\right) \\ \frac{Z_{ip}}{N_A V} &= \left(\frac{Z_f}{N_A V}\right)^2 \frac{4\pi a^3 N_A}{3} \exp\left(-\frac{b}{1 + Ka}\right) \\ [A^+ B^-] &= [A^+][B^-] \frac{4\pi a^3 N_A}{3} \exp\left(-\frac{b}{1 + Ka}\right) \end{aligned}$$

and comparing with Eq. (1.40) shows:

$$K = \frac{4\pi a^3 N_A}{3} \exp\left(-\frac{b}{1 + Ka}\right)$$

As “ a ” is in m, the units of K are $\text{m}^3 \text{mol}^{-1}$. In the more usual units of l mol^{-1} , K is:

$$K = \frac{4000\pi a^3 N_A}{3} \exp\left(-\frac{b}{1 + Ka}\right)$$

1.2.9

Ion Dynamics

Here, we consider only solutions that are sufficiently dilute for ion–ion interactions to be unimportant.

1.2.9.1 Ionic Mobility and Transport Numbers

Stokes' law gives the frictional retarding force, F , (e.g., wind resistance) experienced by a sphere of radius r moving through a medium of viscosity η at speed s .

$$F = 6\pi\eta rs \quad (\text{nondirectional}) \quad (1.43)$$

Surprisingly, it applies to microscopic as well as macroscopic bodies.

An ion in an electric field $\bar{\varepsilon}$ attains a steady drift speed when its accelerating and retarding forces are equal.

$$ze\bar{\varepsilon} = 6\pi\eta rs \quad (\text{N})$$

$$s = \frac{ze}{6\pi\eta r} \bar{\varepsilon} = u\bar{\varepsilon} \quad (1.44)$$

where u , the ionic mobility, is the drift speed in a unit field. The rate of movement of charge in the field $\bar{\varepsilon}$ is therefore:

$$zes = zeu\bar{\varepsilon} \quad (\text{Am})$$

or

$$zFs = zFu\bar{\varepsilon} \quad (\text{Am mol}^{-1})$$

and dividing by $\bar{\varepsilon}$ yields a quantity that depends only on the ion and is the molar conductivity of the ion, λ :

$$\frac{zFs}{\bar{\varepsilon}} = zFu = \lambda \quad (\text{Sm}^2\text{mol}^{-1})$$

For a $z : z$ electrolyte as a whole, the molar conductivity, Λ , is

$$\Lambda = \lambda_+ + \lambda_- = z(u_+ + u_-) F \quad (\text{Sm}^2\text{mol}^{-1})$$

Note: The conductivity (specific conductivity) K , is

$$K = \Lambda C \quad (\text{S m}^{-1})$$

which is related to the measured conductivity, $1/R$, by the cell constant C_C (m^{-1}):

$$K = C_C \frac{1}{R}$$

The transport number of an ion, t , is the fraction of the current carried by the ion, and for a $z : z$ electrolyte:

$$t_+ = \frac{u_+}{u_+ + u_-} \quad t_- = \frac{u_-}{u_+ + u_-}$$

1.2.9.2 Diffusion

This is a process that tends to make the composition of solutions uniform owing to the ceaseless random motion of the species. Species diffuse from regions of high μ to regions of low μ . Thus, the driving force for diffusion, F_D , is related to a decrease in μ and hence in activity. Recall that if a force does work on a body increasing its potential energy, then $dPE = Fdx$. Thus,

$$F_D = -\frac{d\mu}{dx} \quad (\text{N mol}^{-1})$$

Now,

$$\mu = \mu^0 + RT \ln(a) \approx \mu^0 + RT \ln(C)$$

hence,

$$\begin{aligned} F_D &= -RT \frac{d \ln(C)}{dx} = -\frac{RT}{C} \frac{dC}{dx} && (\text{N mol}^{-1}) \\ &= -\frac{kT}{C} \frac{dC}{dx} && (\text{N}) \end{aligned}$$

The ions or molecules attain a steady drift speed when the accelerating and retarding forces are equal (Eq. (9.1)) Then,

$$\begin{aligned} -\frac{kT}{C} \frac{dC}{dx} &= 6\pi\eta r s \\ s &= -\frac{kT}{6\pi\eta r C} \frac{dC}{dx} \end{aligned}$$

The flux, J , (moles passing through a plane of unit area in 1 s) is hence

$$\begin{aligned} J &= sC \\ &= -\frac{kT}{6\pi\eta r} \frac{dC}{dx} \quad (\text{Fick's first law}) \\ &= -D \frac{dC}{dx} \end{aligned} \tag{1.45}$$

where the diffusion coefficient, D , ($\text{m}^2 \text{s}^{-1}$) is

$$D = \frac{kT}{6\pi\eta r} \quad (\text{Stokes - Einstein equation})$$

and from the definition of u in Eq. (1.44):

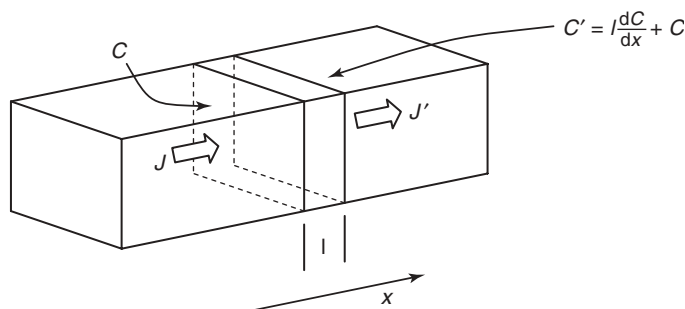
$$D = \frac{ukT}{ze} = \frac{uRT}{zF} \quad (\text{Einstein equation})$$

1.2.9.3 Fick's Second Law

Fick's first law applies to steady-state (time-independent) diffusion. We now consider time-dependent diffusion.

Consider a slab of solution of area A and thickness l , which is so small that the concentration gradient across it can be taken as linear. Ions diffuse into the slab from the left at rate AJ (mol s^{-1}) causing a concentration change given by:

$$\frac{dC}{dt} = \frac{AJ}{Al} = \frac{J}{l} \quad (\text{mol m}^{-3} \text{s}^{-1})$$



Ions diffusing from the slab to the right at rate AJ' , change the concentration according to:

$$\frac{dC}{dt} = -\frac{J'}{l} \left(\text{mol m}^{-3} \text{s}^{-1} \right)$$

The net rate of change of concentration is

$$\frac{dC}{dt} = -\frac{J - J'}{l} \quad (1.46)$$

And from Fick's first law in Eq. (1.45):

$$J = -D \frac{dC}{dx}$$

$$J' = -D \frac{dC'}{dx} = -D \left(\frac{dC}{dx} - l \frac{d^2 C}{dx^2} \right)$$

Substituting into Eq. (1.46) yields:

$$\frac{dC}{dt} = -D \frac{d^2 C}{dx^2} \quad (\text{Fick's second law})$$

For example, consider that n_0 moles of an ion (e.g., Cu^{2+}) are introduced into a solution in a tube by applying a short anodic current pulse (say, 10 A for 1 ms) to an electrode sealing one end of the tube. It can be shown that the $[\text{Cu}^{2+}]$ at a distance x from the electrode at time t after the pulse is

$$C(x, t) = \frac{n_0}{A(\pi Dt)^{1/2}} \exp\left(-\frac{x^2}{4Dt}\right)$$

It is easy to prove that this is a solution to Fick's second law. In a very thin slab of solution of thickness l :

$$n(x, t) = AlC(x, t)$$

and the fraction of the ions in the slab, $\theta(x, t)$ is

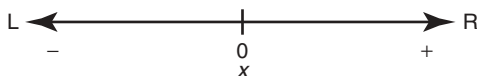
$$\theta(x, t) = \left(\frac{l^2}{\pi Dt} \right)^{1/2} \exp\left(-\frac{x^2}{4Dt}\right) \quad (1.47)$$

1.2.9.4 Diffusion Statistics

The buffeting that the ions or other solute species receive from solvent molecules causes them to move in a series of jumps. Let λ be the mean length of a jump and τ the mean time between jumps.

Of course, the ionic jumps occur in 3D but for simplicity we will consider only jumps in 1D (it has been shown that the end result is the same). Thus, we consider that ions are constrained to jump along a straight line either to the left or the right and the jump direction is chosen randomly.

In time t , the ions make N jumps; N_L to the left and N_R to the right.



$$N = \frac{t}{\tau} = N_L + N_R \quad (1.48)$$

$$N_R = N - N_L \quad N_L = N - N_R \quad (1.49)$$

The ion ends up a net distance x from the origin:

$$x = (N_R - N_L) \lambda$$

and substituting for N_R in Eq. (1.49) yields:

$$\frac{x}{\lambda} = N - 2N_L$$

and

$$N_L = \frac{N}{2} - \frac{x}{2\lambda} \quad (1.50)$$

Similarly,

$$N_R = \frac{N}{2} + \frac{x}{2\lambda} \quad (1.51)$$

Now the number of ways, W , of choosing m objects from a set of n objects is

$$\begin{aligned} W &= n(n-1)(n-2) \cdots (n-m+1) \\ &= \frac{n(n-1)(n-2) \cdots (n-m+1)(n-m)(n-m-1) \cdots 1}{(n-m)(n-m-1) \cdots 1} \\ &= \frac{n!}{(n-m)!} \end{aligned}$$

However, if the m objects chosen are all identical:

$$W = \frac{n!}{m!(n-m)!}$$

Thus, the number of ways we can take N_R steps to the right out of a total of N steps is

$$W = \frac{N!}{N_R!(N-N_R)!} = \frac{N!}{N_R!N_L!}$$

and substituting Eqs. (1.50) and (1.51) yields:

$$W = \frac{N!}{(N/2 + x/2\lambda)! (N/2 - x/2\lambda)!}$$

Now, the total number of different journeys of N steps is 2^N and the probability of being at x after N steps is $W/2^N$ or:

$$P_x = \frac{N!}{(N/2 + x/2\lambda)! (N/2 - x/2\lambda)!} 2^{-N}$$

$$\ln(P_x) = \ln(N!) - \ln[(N/2 + x/2\lambda)!] - \ln[(N/2 - x/2\lambda)!] - N \ln(2)$$

This can be simplified using Sterling's approximation:

$$\ln(M!) = (M + 1/2) \ln(M) - M + \frac{1}{2} \ln(2\pi)$$

$$\begin{aligned} \ln(P_x) &= \frac{1}{2} \ln\left(\frac{2}{\pi N}\right) - \frac{(N + 1 + x/\lambda)}{2} \ln\left(1 + \frac{x}{\lambda N}\right) \\ &\quad - \frac{(N + 1 - x/\lambda)}{2} \ln\left(1 - \frac{x}{\lambda N}\right) \end{aligned}$$

As $x/\lambda N \ll 1$ then $\ln(1 + x/\lambda N) = x/\lambda N$ and

$$\begin{aligned} \ln(P_x) &= \frac{1}{2} \ln\left(\frac{2}{\pi N}\right) - \frac{(N + 1 + x/\lambda)}{2} \frac{x}{\lambda N} + \frac{(N + 1 - x/\lambda)}{2} \frac{x}{\lambda N} \\ &= \frac{1}{2} \ln\left(\frac{2}{\pi N}\right) - \frac{x^2}{2\lambda^2 N} \end{aligned}$$

Substituting $N = t/\tau$ Eq. (1.48) time t as

$$P(x, t) = \left(\frac{2\tau}{\pi t}\right)^{1/2} \exp\left(-\frac{x^2 \tau}{2t\lambda^2}\right) \quad (1.52)$$

Comparing Eqs. (1.52) with (1.47), we see that if we take the thickness of the thin slab, l , as λ (which is the minimum value that has meaning in the statistical treatment), then the two equations are identical if

$$D = \frac{\lambda^2}{2\tau} \quad (\text{Einstein - Smoluwchowski equation})$$

This equation relates the macroscopic property of diffusion, D , to its microscopic properties λ and τ .

1.3

Dynamic Electrochemistry

1.3.1

Review of Fundamentals

1.3.1.1 Potential

The potential (ϕ) at a point is the potential energy of a unit positive charge at that point. The zero of the potential scale is the charge at rest at infinity called the *vacuum level*. Thus, by definition,

$$\text{Potential energy} = q\phi \text{ (J)}$$

where q is the charge in coulombs.

1.3.1.2 Potential inside a Good Conductor

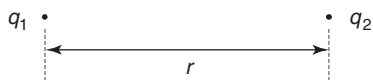
The potential inside a good conductor is everywhere the same; otherwise, charge would flow to equalize ϕ .

1.3.1.3 Charge on a Good Conductor

If a good conductor is charged (excess or deficiency of electrons), all that charge resides at the surface. If it did not, the charge would exist in the interior and produce a potential difference there contrary to the above point.

1.3.1.4 Force between Charges

For point charges, this is given by Coulomb's law; that is,



where ϵ is the dielectric constant (no units) and is the factor by which the medium reduces the force between charges. ϵ_0 is the permittivity of free space ($8.854 \times 10^{-12} \text{ C}^2 \text{ N}^{-1} \text{ m}^{-2}$ or $\text{C}^2 \text{ J}^{-1} \text{ m}^{-1}$).

Coulomb's law also applies to charged spheres if r is the distance between their centers. Thus, a charged sphere behaves as if all charge resides at its center.

1.3.1.5 Potential due to an Assembly of Charges

This is given by Poisson's equation which, for one dimension (x), is,

$$\frac{d^2\phi}{dx^2} = -\frac{1}{\epsilon\epsilon_0}\rho$$

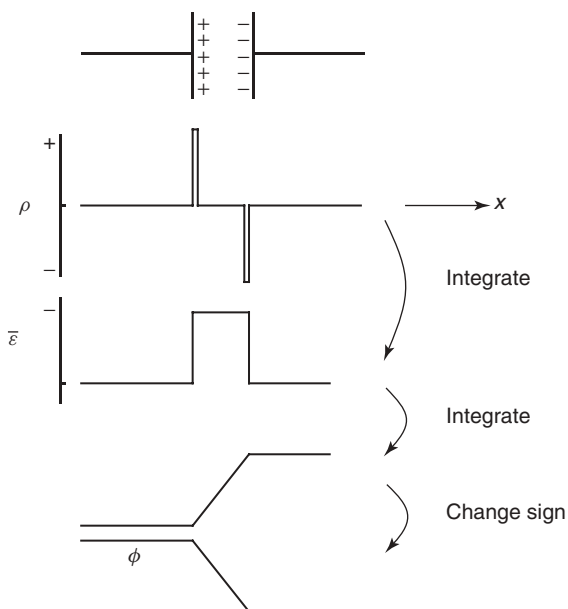
where ρ is the charge density (charge per unit volume, C m^{-3}) which is a function of x . The electric field ($\bar{\epsilon}$) is defined as

$$\begin{aligned}\bar{\epsilon} &= -\frac{d\phi}{dx} \\ &= \frac{1}{\epsilon\epsilon_0} \int \rho dx\end{aligned}$$

Hence,

$$\phi = -\int \bar{\epsilon} dx$$

Consider a parallel plate capacitor:



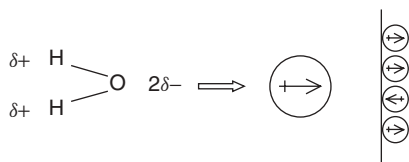
1.3.1.6 Potential Difference between Two Phases in Contact ($\Delta\phi$)

This is divided into two terms; that is,

$$\Delta\phi = \Delta\psi + \Delta\chi$$

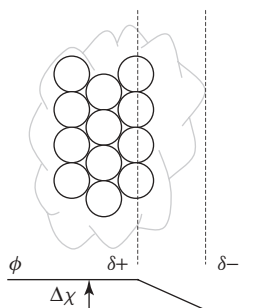
where $\Delta\phi$ is the Galvani, or inner potential difference, and is the total potential difference between the two phases; $\Delta\psi$ is the Volta, or outer potential difference, and is that part of $\Delta\phi$ due solely to charges in the interface; and $\Delta\chi$ is the surface potential difference, and is due to all but the charges on the phases. $\Delta\chi$ is mainly due to the following:

- The adsorption of water dipoles on the surface of the metal. Water is a dipole because the oxygen is electronegative and attracts electron density from the H–O σ bonds.



- Usually, more dipoles are oriented one way than the other, giving rise to a surface potential difference ($\Delta\chi$).

- A good model for a metal is that it is a matrix of ions embedded in a gas of electrons. The electron gas spills out a little way from the surface, resulting in a potential difference.



Note that:

- Almost always $\Delta\chi \ll \Delta\psi$ and then $\Delta\phi \approx \Delta\psi$.
- By convention, $\Delta = \text{metal} - \text{solution}$. Thus,

$$\Delta\phi = \phi_M - \phi_{\text{Solution}}$$

1.3.1.7 The Electrochemical Potential ($\bar{\mu}$)

This is the total potential energy of a charged chemical species in a phase; that is,

$$\begin{aligned}\bar{\mu} &= \text{Chemical potential energy} + \text{Electrical potential energy} \\ &= \mu + zF\phi\end{aligned}$$

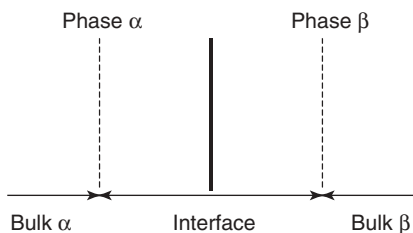
where μ is the chemical potential of the species, z its formal charge, and F is Faraday's constant.

1.3.2

The Electrically Charged Interface or Double Layer

1.3.2.1 The Interface

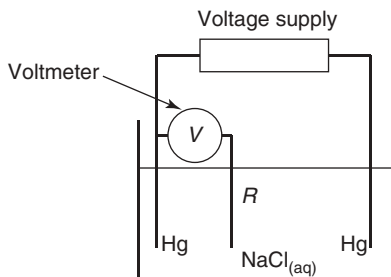
Consider two phases in contact; that is,



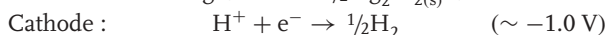
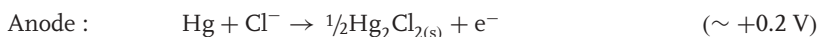
The interface is the region where the properties of each phase are influenced by the presence of the other phase.

1.3.2.2 Ideally Polarized Electrode

Consider

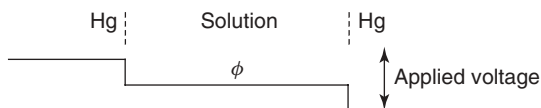


No significant current flows until the applied voltage is greater than 1.2 V; then,



An electrode is said to be ideally polarized when no charge-transfer reactions occur on it; for example, in the range -1.0 to $+0.2$ V for Hg in NaCl solution. Such electrodes are preferred for the study of the interface because of the absence of the complications of charge transfer.

The voltmeter measures the potential difference between one Hg electrode and the reference electrode (R). If we move the reference electrode back and forth between the two Hg electrodes we find that the voltmeter reading is unchanged. This means that all the applied voltage falls at the electrode/solution interfaces; that is,

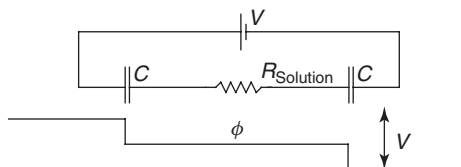


This would not be the case if current flowed. Current flowing through the resistance of the solution would produce an additional potential difference by Ohm's law; that is,

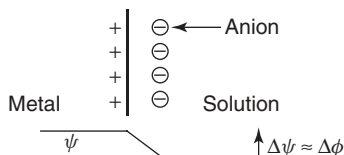
$$\Delta\phi = iR_{\text{Solution}}$$

1.3.2.3 The Helmholtz Model

Helmholtz noted that the above-mentioned form for ϕ would result if each electrode/solution interface behaved as a capacitor; that is,



He proposed that the interface behaves as a parallel plate capacitor. If $\Delta\phi = (\phi_M - \phi_{\text{Solution}})$ is positive, then the metal has a positive charge on its surface and Helmholtz said anions would be attracted from the solution to the interface where they would form a sheet of negative counter charge that balances the charge on the electrode.



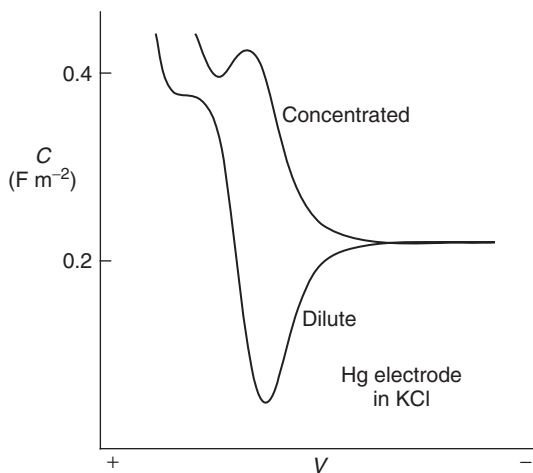
Note that:

- The opposite happens at the other electrode.
- ψ is that part of ϕ , which is due solely to charges.

The name “double layer” comes from the Helmholtz model, which depicts the interface as two layers of charge. We can test the model by comparing the experimental and predicted capacitances. For a parallel plate capacitor,

$$C = \frac{\epsilon\epsilon_0}{\delta_C}$$

where δ_C is the distance between the plates. We now know that good values are $\epsilon = 10$ and $\delta_C = 0.5 \text{ nm}$. Thus, $C = 0.2 \text{ F m}^{-2}$. However, experimentally,



In summary:

- The Helmholtz model does not predict the variation of capacitance with voltage found experimentally.

- However, the one value it does predict is remarkably typical of the range of experimental values.
- It is theoretically unsound because there seems no good reason why the counterions in a solution do not get attracted over to the electrode surface.

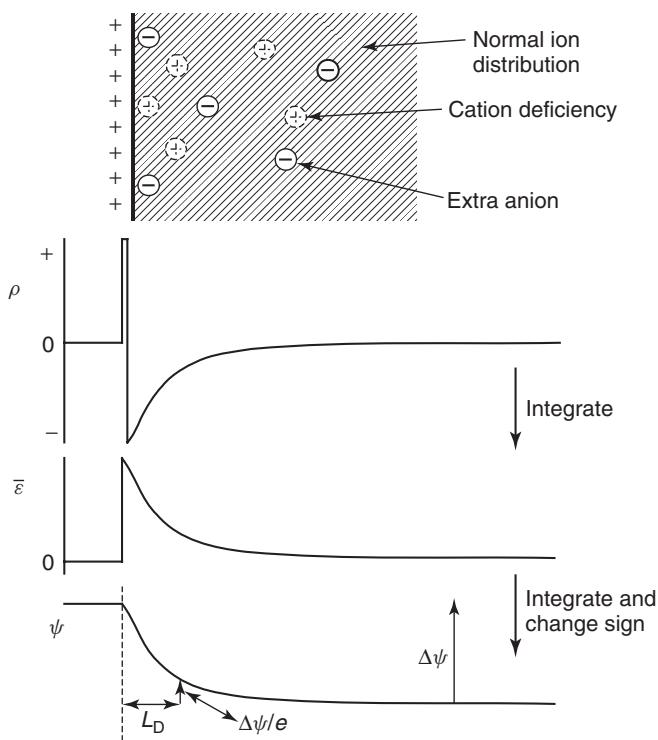
1.3.2.4 Gouy–Chapman or Diffuse Model

Gouy recognized that there were two effects.

- The charge on the electrode changes the distribution of ions by repelling like and attracting unlike ions. This reduces the internal energy (U), and consequently the enthalpy, making $\Delta H < 0$.
- The entropy (S) is maximum when the ions are distributed as randomly as possible. Repelling like and attracting unlike ions reduces S ; that is, $\Delta S < 0$.

The end result is the particular ionic distribution, which minimizes

$$\Delta G = \Delta H - T\Delta S$$



Chapman derived that for a $z : z$ electrolyte, the Debye length (L_D) is given by

$$L_D = \left(\frac{\epsilon \epsilon_0 kT}{2nz^2 e^2} \right)^{1/2}$$

where n is the number of cations or anions per m^3 .

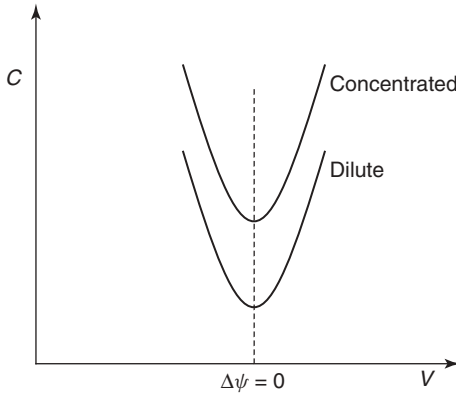
L_D is taken as a measure of the thickness of the diffuse layer. Note that L_D gets smaller as n and hence the concentration increases. By ~ 1 M, the counter charge has been compressed to a layer of thickness about the diameter of ions; that is, it is no longer diffuse, but has become a sheet of charge.

$$C = \left(\frac{2\epsilon \epsilon_0 n z^2 e^2}{kT} \right)^{1/2} \cosh \left(\frac{ze\Delta\psi}{2kT} \right) \quad (F \text{ m}^{-2})$$

Note that C increases with n , and hence concentration. Furthermore,

$$\cosh(x) = \frac{e^x + e^{-x}}{2}$$

is always positive and has a minimum value of 1 at $x = 0$. Thus, the capacitance is approximately parabolic around the potential at which $\Delta\psi = 0$. This occurs when the diffuse layer, and hence the metal, are uncharged.

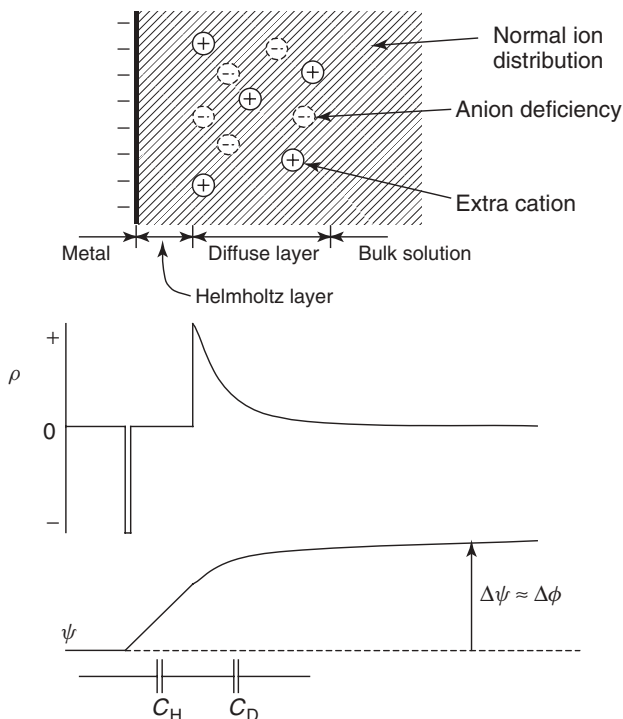


In summary:

- The predicted capacitance is a great disappointment.

1.3.2.5 The Stern Model

This is a combination of the Helmholtz model and the Gouy–Chapman model. As in the Gouy–Chapman model, there is a diffuse layer, but as in the Helmholtz model, the counter charge is not permitted to come right up to the electrode surface.



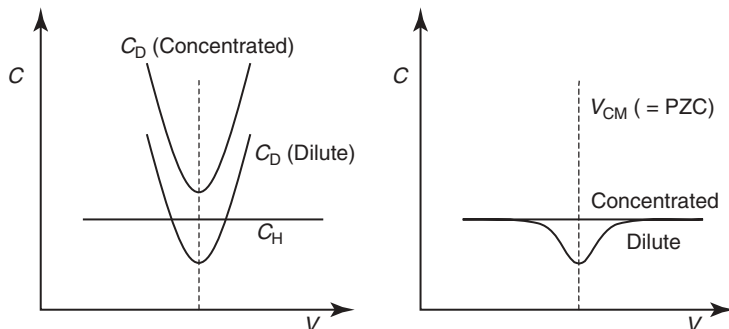
The capacitance of the interface is the Helmholtz layer capacitance in series with the diffuse layer capacitance; that is,

$$\frac{1}{C} = \frac{1}{C_H} + \frac{1}{C_D}$$

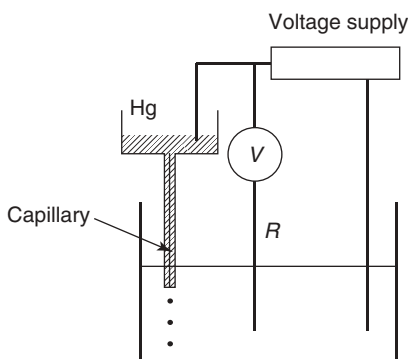
The capacitance is dominated by the smaller of C_H and C_D .

The minimum capacitance for dilute solutions occurs at the minimum of C_D , which corresponds to the diffuse layer being uncharged. In the Stern model (and the Gouy–Chapman model), that occurs when the metal is uncharged and the measured potential of the electrode is then called the *potential of zero charge* of the metal (PZC). According to the Stern model, the PZC corresponds to the potential of the capacitance minimum (V_{CM}) for dilute solutions. The PZC depends on the electrode and the solution; for example,

Electrode	Solution	PZC (V vs SHE)
Hg	0.1 m NaF	−0.200
Hg	0.1 m NaI	−0.470
Au	0.1 m KCl	+0.050
Pt	0.1 m KCl	+0.020



For solid metals, the PZC also depends a little on the history of the metal.
Apparatus for measuring the PZC on Hg:



The drop falls when the gravitational force exceeds the surface tension force. Surface tension is the force that minimizes the surface area of liquids (drops are spherical in a zero gravitational field). Like charges on a drop of liquid metal repel each other, thus tending to expand the surface and hence reduce the surface tension. At the PZC, the surface tension is maximum and hence so is the drop size. A fixed number of drops are collected at various values of V and weighed to find the PZC.

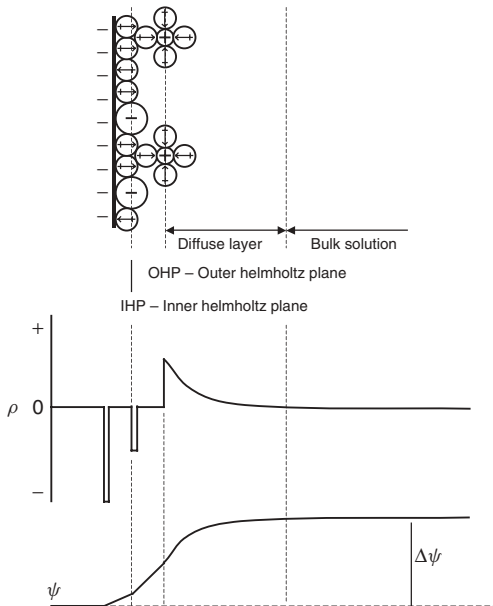
It is found that the PZC and V_{CM} agree for F^- but the PZC is always negative of V_{CM} for Cl^- , Br^- , and I^- . The cation makes no difference.

In summary:

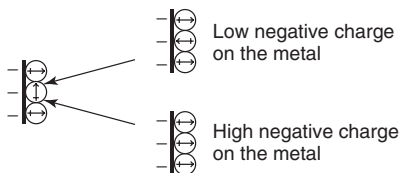
- The Stern model gives a much improved prediction of electrode capacitance.
- Its prediction that the PZC is the same as V_{CM} is wrong for all but F^- solutions.
- It suffers from the same theoretical problem as the Helmholtz model. Why does the counter charges not move over to the electrode surface?

1.3.2.6 The Bockris, Devanathan, and Muller Model

This is a development of the Stern model.

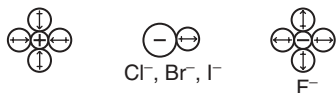


- Adsorbed water dipoles on the electrode. These can have only two orientations. Either the positive or the negative pole is against the metal and all other orientations are unstable (flip-flop water).

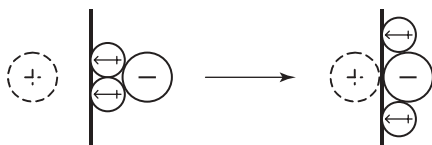


Electrode charge: Negative $\Rightarrow n(\oplus) > n(\ominus)$
 Positive $\Rightarrow n(\ominus) > n(\oplus)$
 Neutral $\Rightarrow n(\oplus) \approx n(\ominus)$

- The ions. In general, cations are small and have a high charge density. An average of four to six water dipoles are oriented and tightly held by the electric field of a cation. Anions (except F^-) are much larger and have a low charge density. They only weakly hold and average of up to one water dipole.



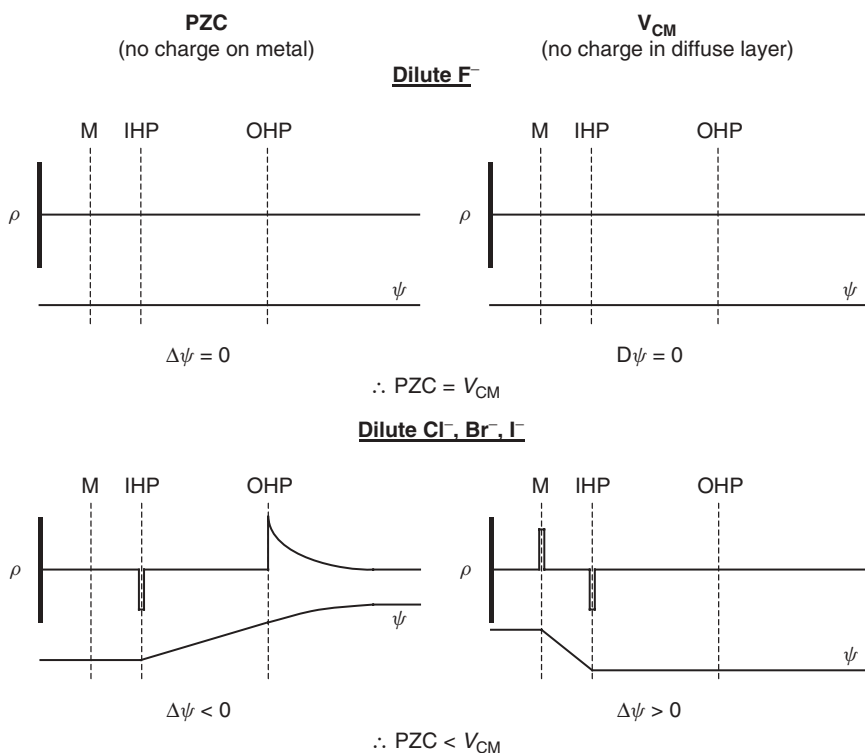
The hydration sheath around cations and F^- prevents them from coming close to the electrode. The closest they can approach is the outer Helmholtz plane. Anions can get closer, sufficiently close that the image force (IF) is strong enough to pull some of them on to the surface.



The IF is the force between a charge and its induced charge. It is always attractive; that is,

$$IF = -\frac{(ze)^2}{4\pi\epsilon\epsilon_0(2x)^2}$$

The IF falls off as $(2x)^2$ and is very strong only at close distances. IFs are so strong that anions (except F^-) contact adsorb (specifically adsorb) on the electrode even when it is negatively charged. Of course, the contact-adsorbed anions are expelled from the electrode if its potential is made sufficiently negative. The number of specifically adsorbed anions increases as the voltage is made more positive. The following figure shows that the model predicts that the PZC for Cl^- , Br^- , and I^- solutions are negative of their respective V_{CM} values, as found experimentally.



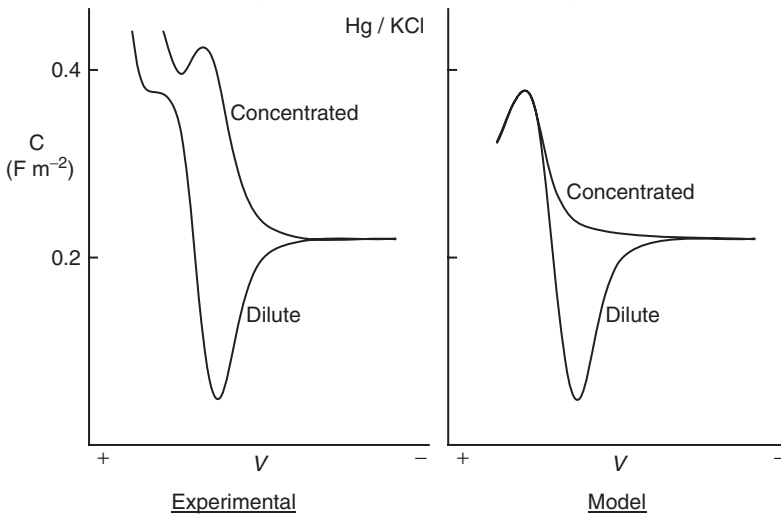
- Electrode capacitance. For F^- solutions, the capacitance is the same as that given by the Stern model.

$$\frac{1}{C} = \frac{1}{C_H} + \frac{1}{C_D}$$

and $C = C_H$ except in dilute solutions near V_{CM} . For solutions of specifically adsorbed anions, this model also predicts the hump in the capacitance at high positive potentials, which is experimentally observed. This is due to the increasing repulsion that contact-adsorbed ions exert on each other as the contact adsorption increases.

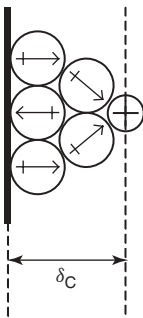
In summary:

- An improved prediction of the capacitance versus voltage curves results for large anions.
- The model explains the discrepancy between the PZC and V_{CM} values for large anions.
- The model is theoretically plausible and is the currently accepted model.



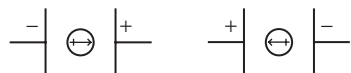
1.3.2.7 Calculation of the Capacitance

Recall that $C = 0.2 \text{ F m}^{-2}$ for $\epsilon = 10$ and $\delta_C = 0.5 \text{ nm}$. δ_C is determined geometrically thus:

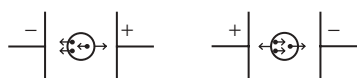


$r(\text{H}_2\text{O}) = 0.138 \text{ nm}$, $r(\text{cation}) < 0.1 \text{ nm}$; therefore, $\delta_c \approx 0.5 \text{ nm}$.

To measure ϵ , pure water is placed between the plates of a parallel plate capacitor and the capacitance determined. In the alternating electric field, each H_2O dipole changes orientation with the field; thus,



Measured at normal frequencies, $\epsilon = 78.3$. If the frequency of the electric field is increased, eventually it becomes so high that the water dipoles cannot turn fast enough to keep up. Then all that happens is that the nuclei and the electron cloud of each water molecule move a little in response to the field; that is,



Measured at very high frequencies, $\epsilon = 6$. Thus, $\epsilon = 6$ for water molecules that are not free to rotate. Between the electrode and the outer Helmholtz plane, only a small amount fraction of water dipoles are free to rotate (flip-flop water and cation hydration sheath water are too strongly bound) and it is estimated that ϵ has an average value of ~ 10 .

1.3.3

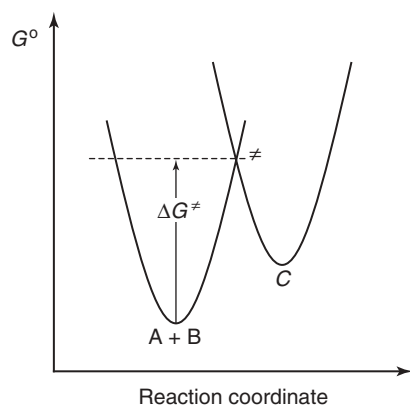
Charge Transfer at the Interface

1.3.3.1 Transition State Theory

Consider an ordinary chemical reaction, that is,



Its 2D reaction profile is



where \ddagger is the transition state. Progress of the reaction is described by the passage along the reaction coordinate. The rate (v) is given by

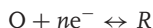
$$v = \lambda C_A C_B \exp\left(-\frac{\Delta G_C^\ddagger}{RT}\right)$$

where

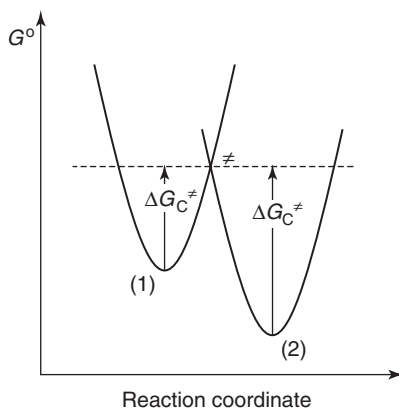
$$\lambda = \frac{k_B T}{h}$$

1.3.3.2 Redox Charge-Transfer Reactions

Consider,



Let this reaction occur at the PZC, then $\Delta\phi = 0$ assuming $\Delta\chi = 0$. Charged species only behave differently from ordinary chemical species in the presence of an electric field. Thus, at $\Delta\phi = 0$, this charge-transfer reaction behaves as an ordinary chemical reaction, that is,



where (1) is the potential energy of O as it vibrates about its equilibrium position in its solvent sheath, plus the potential energy of n electrons in the metal; and (2) is the potential energy of R vibrating in its solvent sheath.

The rate in the cathodic direction is

$$v_C = \lambda C_O C_{e^-(M)}^n \exp\left(-\frac{\Delta G_C^\ddagger}{RT}\right)$$

As $C_{e^-(M)}^n$ is a constant for a given metal,

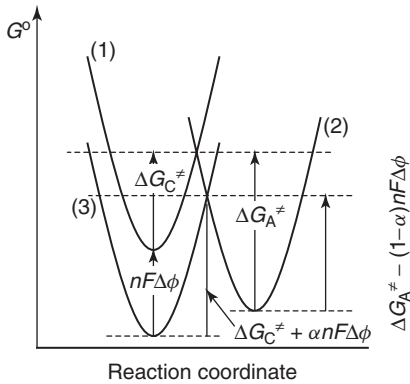
$$\begin{aligned} v_C &= \lambda' C_O \exp\left(-\frac{\Delta G_C^\ddagger}{RT}\right) \\ &= k_C' C_O \end{aligned}$$

where k_C' is a rate constant (m s^{-1}).

Similarly, the rate in the anodic direction is

$$\begin{aligned} v_A &= \lambda C_R \exp\left(-\frac{\Delta G_A^\ddagger}{RT}\right) \\ &= k'_A C_R \end{aligned}$$

Now, let us change the electrode potential so $\Delta\phi \neq 0$. As the bulk solution is the reference state for ϕ , then ϕ metal has changed while ϕ solution remains unchanged. Thus, only the potential energy of the n electrons has changed, and by the amount $-nF\Delta\phi$ J mol⁻¹.



Now, (3) is everywhere $nF\Delta\phi$ vertically below (1). As (2) cuts (1) and (3) at an angle to the vertical, then the cathodic free energy of activation is increased to only,

$$\Delta G_C^\ddagger + \alpha nF\Delta\phi \quad \text{where } 0 < \alpha < 1$$

Hence,

$$\begin{aligned} v_C &= \lambda' C_O \exp\left(-\frac{\Delta G_C^\ddagger + \alpha nF\Delta\phi}{RT}\right) \\ &= k'_C C_O \exp\left(-\frac{\alpha nF\Delta\phi}{RT}\right) \end{aligned}$$

Similarly, the anodic free energy of activation is reduced to

$$\Delta G_A^\ddagger - (1 - \alpha) nF\Delta\phi$$

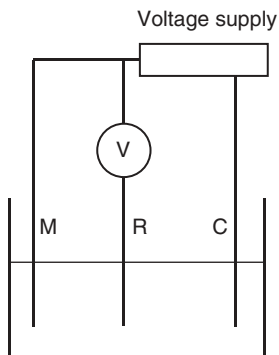
Hence,

$$v_A = k'_A C_R \exp\left(\frac{(1 - \alpha) nF\Delta\phi}{RT}\right)$$

Note:

- The fraction α is called the *transfer coefficient*.
- Changing $\Delta\phi$ changes the free energies of activation in the forward and reverse directions, causing the rates of both reactions to change.

We now need to relate these rates to the measured electrode potential (V). Consider,



The voltage supply changes the potential of the metal (M) by passing a current between the metal and the counter electrode (C). The reading on the voltmeter (V) is the measured potential of the metal versus the reference electrode (R).

$$\begin{aligned} V &= \phi_M - \phi_R \\ &= \phi_M - \phi_{\text{Solution}} - (\phi_R - \phi_{\text{Solution}}) \\ &= \Delta\phi - \Delta\phi_R \end{aligned}$$

At the PZC, $V = V_{\text{PZC}}$ and $\Delta\phi = 0$ (assuming $\Delta\chi = 0$). Thus,

$$V_{\text{PZC}} = -\Delta\phi_R$$

Hence,

$$\Delta\phi = V - V_{\text{PZC}}$$

As V_{PZC} is a constant for a given electrode/solution combination, then

$$v_C = k_C C_O \exp\left(-\frac{\alpha n F V}{RT}\right) \quad (1.53)$$

$$v_A = k_A C_R \exp\left(\frac{(1 - \alpha) n F V}{RT}\right) \quad (1.54)$$

Note that changing the voltage in the negative direction makes it easier for the electrode to expel electrons and more difficult to accept them. Hence, v_C increases and v_A decreases.

Now the overpotential (η) is a quantitative measure of the polarization and is defined by

$$\eta = V - E$$

where the reversible potential (E) is given by the Nernst equation; that is,

$$E = E^0 + \frac{RT}{nF} \ln\left(\frac{a_O}{a_R}\right)$$

If the solution composition is maintained constant, then E is a constant and Eqs. (1.53) and (1.54) become,

$$v_C = k_C^* C_O \exp\left(-\frac{\alpha n F \eta}{RT}\right)$$

$$v_A = k_A^* C_R \exp\left(\frac{(1 - \alpha) n F \eta}{RT}\right)$$

These rates in $\text{mol m}^{-2} \text{s}^{-1}$ can be changed to rates in current density (A m^{-2}) by multiplying by nF (C mol^{-1}), that is,

$$I_C = nFv_C \quad (\text{A m}^{-2})$$

$$I_A = nFv_A \quad (\text{A m}^{-2})$$

I_C and I_A are the partial cathodic and partial anodic current densities. The net current density (what we measure with an ammeter) we take as

$$I = I_A - I_C$$

$$> 0 \text{ (anodic processes)}$$

$$< 0 \text{ (cathodic processes)}$$

Therefore,

$$I = nF \left[k_A^* C_R \exp\left(\frac{(1 - \alpha) n F \eta}{RT}\right) - k_C^* C_O \exp\left(-\frac{\alpha n F \eta}{RT}\right) \right] \quad (1.55)$$

At the reversible potential ($\eta = 0$) there is no net oxidation or reduction, hence $I = 0$. Thus,

$$I_A = I_C = I_0$$

where

$$I_0 = nFk_A^* C_R = nFk_C^* C_O$$

is the exchange current density. We may now write

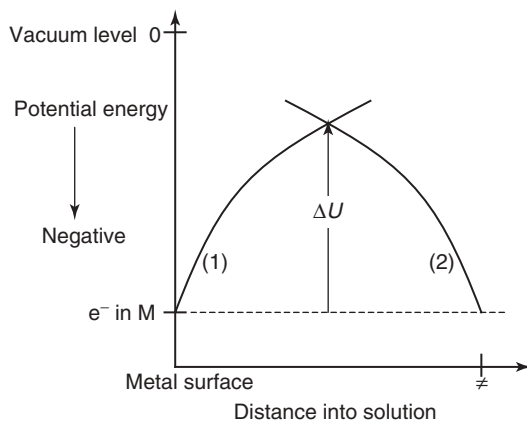
$$I = I_0 \left[\exp\left(\frac{(1 - \alpha) n F \eta}{RT}\right) - \exp\left(-\frac{\alpha n F \eta}{RT}\right) \right] \quad (1.56)$$

I_0 is the rate of the forward and back reactions in A m^{-2} at the reversible potential where they are equal. If I_0 is large, the charge-transfer reaction is facile and $|I|$ becomes large at small $|\eta|$.

1.3.3.3 The Act of Charge Transfer

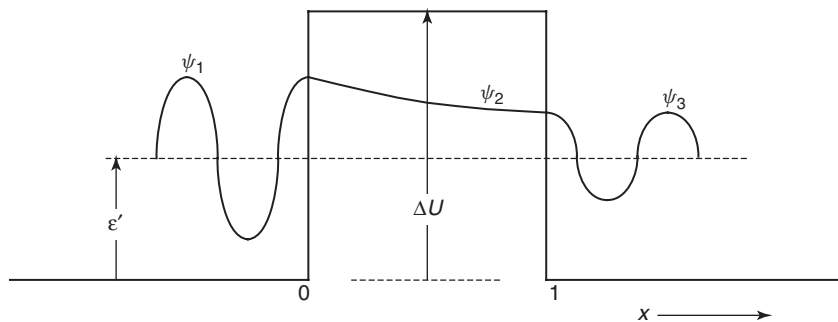
The electrons must transfer from the metal to O at the transition state because only at this point is the energy of ($\text{O} - ne^-$) equal to that of R. If the energies were not equal, the electron transfer would be accompanied by the emission or absorption of radiation. This does not occur.

Classically If we pull an electron out of a metal, work is done against the IF and the potential energy of the electron is increased. The potential energy of the electron is decreased when it is captured by an ion or molecule.



At (1) an electron is being removed from the metal, while at (2) an electron is being captured by O. There is an energy barrier of height ΔU between the metal and transition state and the probability of the electron going over the barrier can be calculated from the Boltzmann equation. It is found to be essentially zero at room temperature.

Quantum Mechanically Quantum particles can tunnel owing to their wavelike nature. Consider an electron of energy ε' incident on a potential energy barrier of height ΔU such that $\varepsilon' < \Delta U$.



In the front of the barrier, the wave function can be shown to be

$$\psi_1 = A_1 \exp(ikx) + B_1 \exp(-ikx)$$

where

$$k = \left(\frac{8\pi m \varepsilon'}{h^2} \right)^{1/2}$$

and m is the mass of an electron and the coefficients are complex. Now,

$$\exp(ikx) = \cos(kx) + i \sin(kx)$$

has a wave nature and $A_1 \exp(ikx)$ is a wave propagating in the forward direction, whereas $B_1 \exp(-ikx)$ propagates in the reverse direction. Thus, for $A_1 > B_1$, ψ_1 represents an electron wave incident on the barrier-only part of which is reflected back.

The wave function in the barrier,

$$\psi_2 = A_2 \exp\left(-\left(\frac{8\pi^2 M (\Delta U - \varepsilon')}{h^2}\right)^{1/2} x\right)$$

is decaying exponentially with x at a rate dependent on $(\Delta U - \varepsilon')$ and the amplitude of the wave function exiting the barrier (A_3) is small. On the other side of the barrier, the wave function is

$$\psi_3 = A_3 \exp(ikx)$$

This is again a forward propagating wave of amplitude smaller than that of ψ_1 .

Thus, an electron can penetrate a potential energy barrier, called *tunneling*, provided l is small ($l < \sim 1$ nm) and ΔU is not infinite. Tunneling is the means by which O is converted to R at the transition state, as it is considered to be no further from the metal than the outer Helmholtz plane; that is, ~ 0.5 nm.

The wave functions here refer to a single electron and thus only one electron can tunnel at a time. Hence, these equations (Eqs. (1.53–1.56)) are valid only for $n = 1$. This was not known when these equations were first derived and invalid versions ($n \neq 1$) of these equations still persist. If data obey these equations for $n \neq 1$, it is merely an empirical way of expressing the current density in terms of V or η . This can be quite useful.

1.3.3.4 The Butler–Volmer Equation

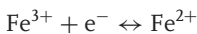
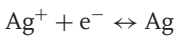
To make these equations strictly valid, replace n in the exponents by 1. Then Eq. (1.56) becomes

$$I = I_0 \left[\exp\left(\frac{(1 - \alpha) F \eta}{RT}\right) - \exp\left(-\frac{\alpha F \eta}{RT}\right) \right] \quad (1.57)$$

To avoid confusion with the older invalid equation, this is sometimes written with β , sometimes called the *symmetry factor*, replacing α , that is,

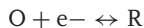
$$I = I_0 \left[\exp\left(\frac{(1 - \beta) F \eta}{RT}\right) - \exp\left(-\frac{\beta F \eta}{RT}\right) \right] \quad (1.58)$$

Each of these last two equations is the Butler–Volmer equation. It is found that α or β always has a value of ~ 0.5 . The Butler–Volmer equation applies to reactions involving a single charge transfer; for example,



1.3.3.5 I in Terms of the Standard Rate Constant (k^0)

Consider a reaction consisting of a single charge-transfer step, that is,



$$v_C = k_C C_O \exp\left(-\frac{\alpha FV}{RT}\right) \quad (1.53)$$

Let the measured potential (V) be made equal to the standard potential (E^0). Then,

$$\begin{aligned} v_C^0 &= k_C C_O \exp\left(-\frac{\alpha F E^0}{RT}\right) \\ &= k_C^0 C_O \end{aligned}$$

where,

$$k_C^0 = k_C \exp\left(-\frac{\alpha F E^0}{RT}\right)$$

Substituting into Eq. (1.53) yields,

$$v_C = k_C^0 C_O \exp\left(-\frac{\alpha F (V - E^0)}{RT}\right)$$

Similarly, in the reverse direction, Eq. (1.54) becomes

$$v_A = k_A^0 C_R \exp\left(\frac{(1 - \alpha) F (V - E^0)}{RT}\right)$$

If O and R are in their standard states, their concentrations are unity (neglecting activity coefficients) and $E = E^0$. If we also make $V = E$ then $v_A = v_C$ because it is at its reversible potential, and from the last two equations we see that

$$k_A^0 = k_C^0 = k^0$$

Hence,

$$I = nFk^0 \left[C_R \exp\left(\frac{(1 - \alpha) (V - E^0) F}{RT}\right) - C_O \exp\left(-\frac{\alpha (V - E^0) F}{RT}\right) \right] \quad (1.59)$$

1.3.3.6 Relation between k^0 and I_0

Considering I_a , we have from Eqs. (1.59) and (1.57),

$$I_a = nFk^0 C_R \exp\left(\frac{(1 - \alpha) (V - E^0) F}{RT}\right) \quad (1.60)$$

and

$$I_a = I_0 \exp\left(\frac{(1 - \alpha) \eta F}{RT}\right)$$

Substituting

$$\eta = V - E^0 - \frac{RT}{F} \ln \left(\frac{C_O}{C_R} \right)$$

yields,

$$\begin{aligned} I_a &= I_0 \exp \left(\frac{(1-\alpha)(V-E^0)F}{RT} \right) \exp \left(-(1-\alpha) \ln \left[\frac{C_O}{C_R} \right] \right) \\ &= I_0 \left(\frac{C_O}{C_R} \right)^{(\alpha-1)} \exp \left[\frac{(1-\alpha)(V-E^0)F}{RT} \right] \end{aligned} \quad (1.61)$$

From Eqs. (1.60) and (1.61),

$$nFk^0 C_R = I_0 \left(\frac{C_O}{C_R} \right)^{(\alpha-1)}$$

Taking $\alpha = 1/2$ gives:

$$I_0 = nFk^0 \left(\frac{C_O}{C_R} \right)^{1/2} \quad (1.62)$$

This same equation can be derived by considering I_c . Note that since k^0 is a constant, Eq. (1.62) gives the variation of I_0 with concentration for a single charge-transfer step.

1.3.4

Multistep Processes

1.3.4.1 The Multistep Butler–Volmer Equation

Many electrochemical reactions take place via a mechanism consisting of a number of steps, both chemical and charge transfer. Such reactions obey the multistep Butler–Volmer equation,

$$I = I_0 \left[\exp \left(\frac{\alpha_a \eta F}{RT} \right) - \exp \left(\frac{-\alpha_c \eta F}{RT} \right) \right] \quad (1.63)$$

where α_a and α_c are called the *anodic* and *cathodic* transfer coefficients, which, as we will see, depend on the mechanism, and do not necessarily equal $(1-\alpha)$ and α , respectively.

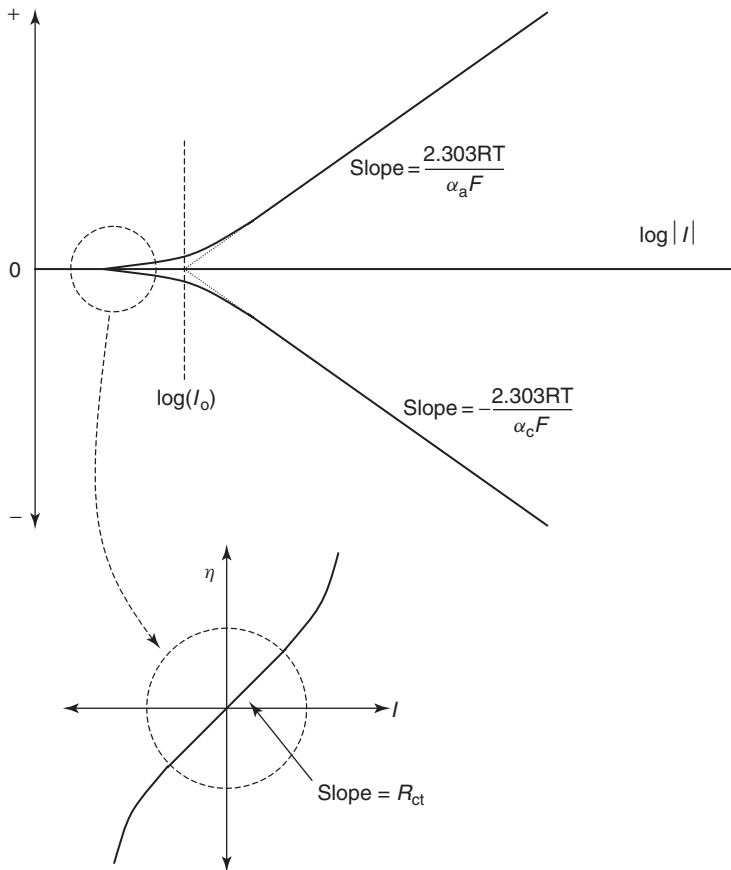
In Eq. (1.63) and other earlier equations, if $\eta > \sim 100$ mV then $I_a \gg I_c$ and I_c can be neglected; that is,

$$I = I_a = I_0 \left[\exp \left(\frac{\alpha_a \eta F}{RT} \right) \right] \quad (1.64)$$

Similarly, if $\eta < \sim -100$ mV, then I_a can be neglected, that is,

$$I = -I_c = -I_0 \left[\exp \left(\frac{-\alpha_c \eta F}{RT} \right) \right] \quad (1.65)$$

Equations (1.64) and (1.65) are called the *high field approximations*. I_0 , α_a , and α_c are determined from a plot of η versus $\log |I|$; that is,



Taking logs of Eq. (1.64) and rearranging gives,

$$\eta = \frac{RT}{\alpha_a F} \ln(I_a) - \frac{RT}{\alpha_a F} \ln(I_0)$$

$$\eta = b_a \ln(I_a) - a_a \quad (1.66)$$

Equation (1.66) is the old empirical Tafel equation. A similar equation can be written for the cathodic current density, that is,

$$\eta = b_c \ln(I_c) - a_c \quad (1.67)$$

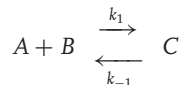
1.3.4.2 Rules for Mechanisms

We take the quasi-equilibrium approach, which is based on the tenets:

- There is only one step, the rate-determining step, which controls the rate of the reaction.

- All steps before the rate-determining step are in quasi-equilibrium.
- No step can have more than two chemical reactants.
- Only one electron can be transferred in a charge-transfer step.

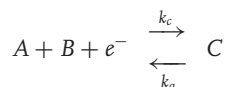
For an ordinary chemical step in a mechanism,



the law of mass action gives,

$$v_1 = k_1 C_A C_B \quad v_{-1} = k_{-1} C_C$$

For a charge-transfer step in a mechanism,



Equations (1.53) and (1.54) give

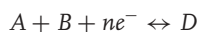
$$v_c = k_c C_A C_B \exp\left(-\frac{\alpha VF}{RT}\right)$$

$$v_a = k_a C_C \exp\left(-\frac{(1-\alpha) VF}{RT}\right)$$

Thus, the rate of a charge-transfer step is the same as that of a chemical step but with the appropriate exponent appended.

1.3.4.3 Concentration Dependence of I_0

Equation (1.62) gives this dependence for a simple charge-transfer reaction, but for a mechanism it can be more complicated. Consider,



and let it be “a” order in A and “b” order in B. Consider the cathodic direction,

$$I_c = nFk_c C_A^a C_B^b \exp\left(-\frac{\alpha_c VF}{RT}\right)$$

Thus,

$$I_0 = nFk_c C_A^a C_B^b \exp\left(-\frac{\alpha_c VF}{RT}\right)$$

Substituting,

$$E = E^0 + \frac{RT}{nF} \ln\left(\frac{C_A C_B}{C_D}\right)$$

yields

$$I_0 = nFk_c^* C_A^{(a-\alpha_c/n)} C_B^{(b-\alpha_c/n)} C_D^{(\alpha_c/n)}$$

Thus, if I_0 is known at one set of concentrations (C_A , C_B , and C_D) it can be calculated at any other.

1.3.4.4 Charge-Transfer Resistance (R_{ct})

Recalling that

$$\begin{aligned} e^x &= 1 + x + \frac{x^2}{2!} + \frac{x^3}{3!} + \dots \\ &= 1 + x \text{ for } x \rightarrow 0 \end{aligned}$$

The multistep Butler–Volmer equation (Eq. (1.63)) can be simplified for $\eta \rightarrow 0$; that is,

$$I = I_0 \left[\exp\left(\frac{\alpha_a \eta F}{RT}\right) - \exp\left(\frac{-\alpha_c \eta F}{RT}\right) \right] \quad (1.63)$$

$$I = I_0 \left(\frac{\alpha_a \eta F}{RT} + \frac{\alpha_c \eta F}{RT} \right)_{\eta \rightarrow 0}$$

$$\left(\frac{d\eta}{dI} \right)_{\eta \rightarrow 0} = \frac{RT}{(\alpha_a + \alpha_c) I_0 F} = R_{ct} \quad (\Omega \text{ m}^2) \quad (1.68)$$

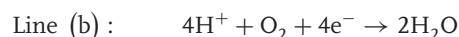
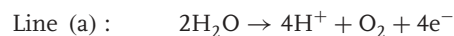
Thus, for small values of η ($|\eta| < \sim 10$ mV), the interface presents a pure resistance to charge transfer and R_{ct} yields $(\alpha_a + \alpha_c)$ if I_0 is known.

If we consider only single charge-transfer step reactions ($\alpha_a = 1 - \alpha$; $\alpha_c = \alpha$), then Eq. (1.68) simplifies to

$$\left(\frac{d\eta}{dI} \right)_{\eta \rightarrow 0} = \frac{RT}{I_0 F} = R_{ct} \quad (\text{single charge transfer})$$

1.3.4.5 Whole Cell Voltages

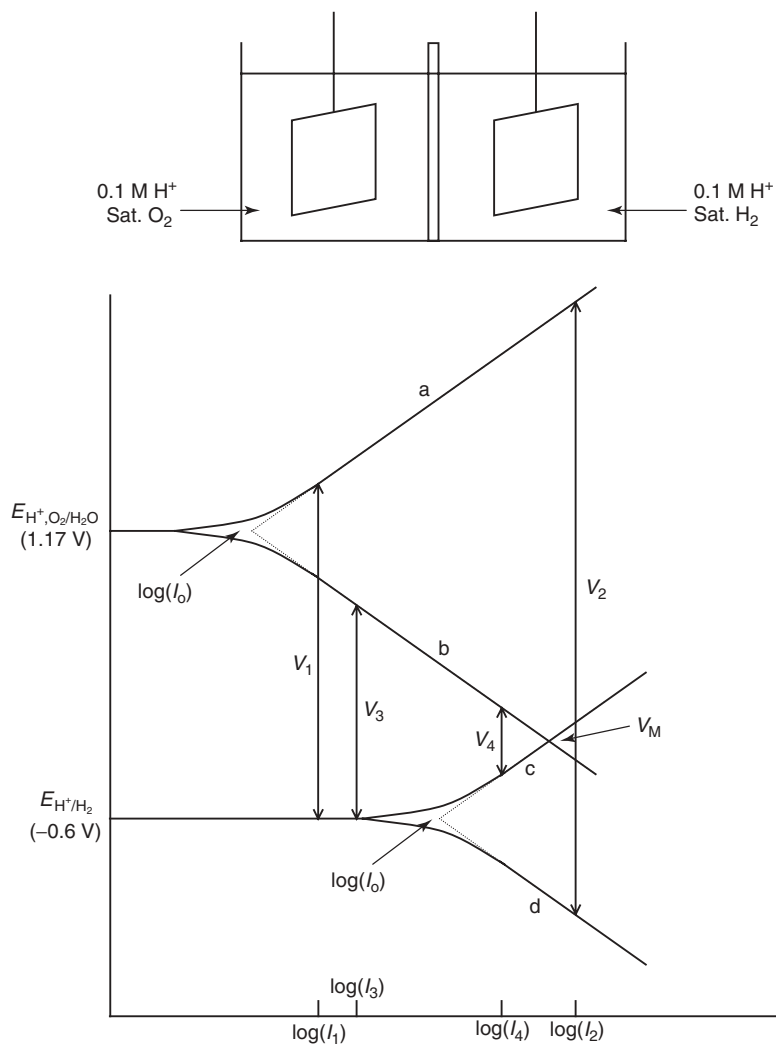
Consider the following figure in which the areas of the two electrodes are equal and it is assumed there is no iR drop in the solution or frit.



V_1 and V_2 are the applied voltages required to electrolyze the solution at I_1 and I_2 . $V_1 - 1.23$ and $V_2 - 1.23$ are the total cell overvoltages required.

V_3 and V_4 are the cell voltages developed by a fuel cell at I_3 and I_4 . $1.23 - V_3$ and $1.23 - V_4$ are the total overvoltage losses of the cell.

Good design minimizes the overvoltages and hence the power losses; for example, increase the area of the O_2 electrode as most of the overvoltage occurs at this electrode. Note that if the metal is placed in a solution saturated with both H_2 and O_2 it comes to a mixed potential (V_M) where the net current from (b) and (c) equals zero. Any metal in contact with any solution comes to a mixed potential at which the net of all the anodic and cathodic currents flowing equals zero.

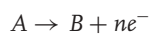


1.3.5

Mass Transport Control

1.3.5.1 Diffusion and Migration

If a solution has a nonuniform composition (i.e., not properly mixed) the composition will eventually become uniform owing to the random movement of molecules. This is diffusion and molecules diffuse from regions of high concentration (activity) to regions of low concentration. Consider,

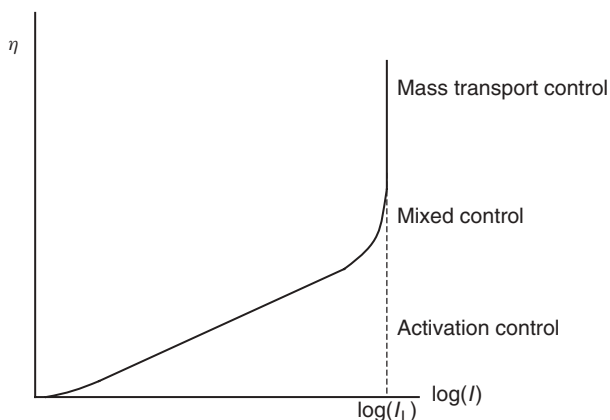


As A is consumed at the electrode, A diffuses from the bulk of the solution to the electrode. If A is an ion it will also migrate (migration is the movement of an ion in response to a potential difference). The passage of current through the solution produces an Ohm's law potential difference; that is,

$$\Delta\phi_{\text{soln}} = iR_{\text{soln}}$$

If η is increased, eventually the mass transport of A to the electrode by diffusion and migration cannot keep up with the consumption of A and C_A at the electrode surface drops significantly below C_A in the bulk solution. The current then depends on the mass transport of A to the electrode.

Note that the current reaches a maximum value (I_L), the limiting current density. Then the process has changed completely from activation controlled to mass transport controlled.



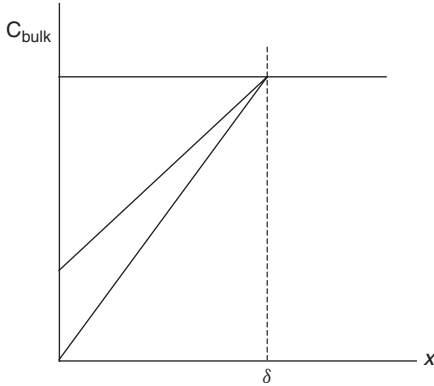
1.3.5.2 The Limiting Current Density (I_L)

Steady-state (time-independent) diffusion is described by Fick's first law; that is,

$$J_D = -D \frac{dC}{dx} \quad (\text{mol m}^{-2} \text{s}^{-1}) \quad (1.69)$$

where J_D is the diffusional flux of A; that is, the moles of A arriving at the electrode per unit area per second; dC/dx is the concentration gradient (mol m^{-4}); and D is the diffusion coefficient ($\text{m}^2 \text{s}^{-1}$). D has values of $\sim 10^{-8}$ for H^+ , 5×10^{-9} for OH^- , and 10^{-10} to 10^{-9} $\text{m}^2 \text{s}^{-1}$ for everything else.

The negative sign in Eq. (1.69) arises because diffusion occurs in the direction opposite to increasing concentration. In practice, dC/dx at the electrode is approximately linear; that is,



where δ is the diffusion layer thickness and has values of ~ 0.5 mm for quiescent solutions (natural convection only) to ~ 0.1 mm for stirred solutions. Hence, to a good approximation,

$$\frac{dC}{dx} = \frac{C_{el} - C_{bulk}}{\delta}$$

$$J_D = -D \frac{C_{el} - C_{bulk}}{\delta}$$

Now, the flux by migration (J_M) is

$$J_M = \pm \frac{tI}{|z|F} \quad (\text{mol m}^{-2} \text{ s}^{-1})$$

where t is the transport number of the ion in the particular solution, or in other words the fraction of the current carried by the ion in that solution. Take the positive sign when migration carries the ion toward the electrode (e.g., Fe^{2+} being reduced at the cathode) and the negative sign when migration takes the ion away from the electrode (e.g., Fe^{2+} being oxidized at the anode).

The total flux (J_T) is

$$\begin{aligned} J_T &= J_D + J_M \\ &= -D \frac{C_{el} - C_{bulk}}{\delta} \pm \frac{tI}{|z|F} \end{aligned}$$

Substituting

$$I = nFJ_T$$

gives

$$I = -\frac{nDF(C_{el} - C_{bulk})}{\delta \left[1 - \left(\pm \frac{nt}{|z|} \right) \right]}$$

Now, $t = 0$ for neutral molecules and $t \rightarrow 0$ if there is a large concentration of indifferent electrolyte (one that does not participate in the reaction) because almost

all the current is then carried by the indifferent electrolyte. Then, the process is diffusion controlled, and to a good approximation,

$$I = -\frac{nFD}{\delta} (C_{\text{el}} - C_{\text{bulk}}) \quad (1.70)$$

The maximum or limiting current density results when $C_{\text{el}} = 0$.

$$I = \frac{nFD}{\delta} C_{\text{bulk}} \quad (1.71)$$

Some electrochemical experiments require the current to be diffusion controlled; for example, polarography and cyclic voltammetry. To achieve this, make the concentration of the electroactive species small ($< \sim 5$ mM) and the concentration of the indifferent electrolyte much higher (~ 100 times).

Polarography and cyclic voltammetry are particularly suited to the study of reversible processes; that is, reactions for which I_0 is so large that I reaches I_L while η is still negligibly small. In polarography,



occurs with $\eta = 0$ and V is given by the Nernst equation.

$$V = E_{\text{Cd}^{2+}/\text{Cd}} = E_{\text{Cd}^{2+}/\text{Cd}}^0 + \frac{RT}{2F} \ln \left(\frac{a_{\text{Cd}^{2+}}}{a_{\text{Cd}(\text{Hg})}} \right)_{\text{el}}$$

Note that Eq. (1.70) gives the current only at a planar electrode and at the spherical Hg drop electrode,

$$I \propto -D^{1/2} (C_{\text{el}} - C_{\text{bulk}})$$

1.3.5.3 Rotating Disk Electrode

This electrode gives precise control over the diffusion layer thickness, δ . Solution of the hydrodynamic equations for solution flow across the disk electrode gives

$$\delta = \frac{1.61\nu^{1/6} D^{1/3}}{\omega^{1/2}} \quad (10 < \omega < 1000 \text{ s}^{-1})$$

where ν is the kinematic viscosity factor (viscosity/density, $\text{m}^2 \text{s}^{-1}$). Thus, for a charge-transfer reaction at a particular value of V , I is independent of ω if it is activation controlled, but dependent on $\omega^{1/2}$ if it is diffusion controlled.

Further Reading

- | | |
|--|---|
| Andersen, T.N. (1964) <i>Electrochim. Acta</i> , 9 , 347. | Atkins, P.W. (1998) <i>Physical Chemistry</i> , 6th edn, Oxford University Press, Oxford. |
| Argade, S.A. and Gileadi, E. (1967) The potential of zero charge, in <i>Electrosorption</i> (ed E. Gileadi), Plenum Press, New York. | Bernal, J.D. and Fowler, R.H. (1933) <i>J. Chem. Phys.</i> , 1 , 515. |
| Arrhenius, S. (1887) <i>Z. Phys. Chem.</i> , 1 , 631. | Bjerrum, N. (1906) <i>Kgl. Danske Videnskab. Selskab.</i> , 4 , 26. |
| Arvia, A.J., Marchiano, S.L., and Podesta, J.J. (1967) <i>Electrochim. Acta</i> , 12 , 259. | Bjerrum, N. (1920) <i>Z. Anorg. Allg. Chem.</i> , 109 , 175. |

- Bjerrum, N. (1926) *Kgl. Danske Videnskab. Selskab.*, 7, 9.
- Bockris, J.O'M. (1949) *Quart. Rev., (London)*, 3, 173.
- Bockris, J.O'M. (1954) Electrode kinetics, in *Modern Aspects of Electrochemistry*, Vol. I (ed J.O'M. Bockris), Butterworth's Publications, Ltd., London.
- Bockris, J. O'M., Devanathan, M. A. V., and K. Muller, *Proc. R. Soc. London, Ser. A*, 274, 55 (1963).
- Bockris J. O'M. and S. Srinivasan, *Electrode kinetics, Fuel Cells: Their Electrochemistry*, Chapter 2, McGraw-Hill Book Company, New York, 1969.
- Born, M. (1920) *Z. Phys.*, 1, 45.
- Brieter, M., Knorr, C.A., and Völkl, W. (1955) *Z. Elektrochem.*, 59, 681.
- Butler, J.A.V. (1924) *Trans. Faraday Soc.*, 19, 729.
- Butler, J.A.V. (1936) *Proc. R. Soc. London, Ser. A*, 157, 423.
- Carlsaw, H.S. and Jaeger, J.C. (1959) *Conduction of Heat in Solids*, Clarendon Press, Oxford.
- Chandrasekhar, S. (1943) *Rev. Mod. Phys.*, 15, 1.
- Chapman, D.L. (1913) *Philos. Mag.*, 25(6), 475.
- Choppin G. R. and Buijs K., *J. Chem. Phys.*, 39, 2035 and 2042 (1963).
- Conway B. E., Proton solvation and proton transfer processes in solution, in (ed. J. O'M. Bockris), *Modern Aspects of Electrochemistry*, Vol. 3, Butterworth's Publications, Inc., London, 1964.
- Conway, B.E. (1965) Electrochemical kinetic principles, in *Theory and Principles of Electrode Processes (Modern Concepts in Chemistry)* Chapter 6, The Ronald Press Co., New York.
- Conway B. E. and Bockris J. O'M., Ionic solvation in J. O'M. Bockris, (Ed.), *Modern Aspects of Electrochemistry*, Vol. 1, Butterworth's Publications, Inc., London, 1954.
- Conway, B.E. and Salomon, M. (1966) in *Chemical Physics of Ionic Solution* (eds B.E. Conway and R.G. Barradas), John Wiley & Sons, Inc., New York.
- Covington, A.K. and Jones, P. (1968) *Hydrogen Bonded Solvent Systems*, Taylor & Francis Ltd., London.
- Damjanovic, A. (1966) *Electrochim. Acta*, 11, 376.
- (a) Damjanovic, A. and Genshaw, M.A. (1967) *J. Electrochem. Soc.*, 114, 466.
- (b) Damjanovic, A., Genshaw, M.A., and Bockris, J.O'M. (1967) *J. Electroanal. Chem.*, 15, 173.
- Davies, C. W., *Ion Association*, Butterworth's Publications, Ltd., London, 1962.
- Debye, P. and Hückel, E. (1923) *Z. Physik*, 24, 185.
- Delahay, P. (1954) *New Instrumental Methods in Electrochemistry*, Interscience Publishers, Inc., New York.
- Delahay, P. (1956) Polarography and voltammetry, in *Instrumental Analysis* Chapter 4, The MacMillan Company, New York.
- Delahay, P. (1965) *Double Layer and Electrode Kinetics*, Interscience Publishers, Inc., New York.
- Delahay, P. (1961) in *Advances in Electrochemistry and Electrochemical Engineering*, Vol. 1 Chapter 5 (eds P. Delahay and C.W. Tobias), Interscience Publishers, Inc., New York.
- Denison, J.T. and Ramsey, J.B. (1955) *J. Am. Chem. Soc.*, 77, 2615.
- Despic, A. (1961) *Electrochim. Acta*, 4, 325.
- Dolin, P. and Erschler, B. (1940) *Acta Physicochim. USSR*, 13, 747.
- Einstein, A. (1926) *Investigations on the Theory of Brownian Movement*, Methuen and Co., Ltd., London.
- Eley, D.D. and Evans, M.G. (1938) *Trans. Faraday Soc.*, 34, 1093.
- Erdey-Gruz, T. and Volmer, M. (1930) *Z. Physik. Chem. (Leipzig)*, 150, 203.
- Eyring, H., Glasstone, S., and Laidler, K.J. (1939) *J. Chem. Phys.*, 7, 1053.
- Feynman, R.P. (1964) *Lectures on Physics*, Vol. 1, Addison-Wesley Publishing Company, Inc., Reading, MA.
- Feynman, R.P., Leighton, R.B., and Sands, M. (1964) *The Feynman Lectures on Physics*, Addison-Wesley Publishing Company, Inc., Reading, MA.
- Frank, H.S. (1958) *Proc. R. Soc. London, Ser. A*, 247, 481.
- Frank, H.S. (1966) in *Solvent Models and Interpretation of Ionization and Solvation Phenomena* (eds B.E. Conway and R.G. Barradas), John Wiley & Sons, Inc., New York.

- Frank, H.S. and Evans, M. (1945) *J. Chem. Phys.*, **13**, 507.
- Frank, H.S. and Quist, A.S. (1961) *J. Chem. Phys.*, **34**, 604.
- (a) Frank, H.S. and Wen, W.Y. (1957) *Discuss. Faraday Soc.*, **24**, 133. (b) Buckingham, A.D. (1957) *Discuss. Faraday Soc.*, **34**, 151.
- Friedman, J.L. (1962) *Ionic Solution Theory*, Interscience Publishers, Inc., New York.
- Frumkin, A.N. (1925) *Z. Physik. Chem. (Leipzig)*, **116**, 466.
- Frumkin, A.N. (1933) *Z. Physik. Chem.*, **A164**, 121.
- Frumkin, N. (1963) Hydrogen overvoltage and adsorption phenomena, in *Advances in Electrochemistry and Electrochemical Engineering*, Vol. III Chapter 5 (eds P. Delahay and C.W. Tobias), Interscience Publishers, Inc., New York.
- Frumkin, A.N. and Nekrasov, L.N. (1959) *Dokl. Akad. Nauk SSSR*, **126**, 115.
- Frumkin, N. and Shlygin, A.I. (1935) *Acta Physicochim. URSS*, **3**, 791.
- Fuoss, R.M. (1934a) *Z. Physik*, **35**, 559.
- Fuoss, R.M. (1934b) *Trans. Faraday Soc.*, **30**, 967.
- Fuoss, R.M. (1935) *Chem. Rev.*, **17**, 27.
- Fuoss, R.M. (1958) *J. Am. Chem. Soc.*, **80**, 5059.
- Fuoss, R.M. (1967) *Proc. Natl. Acad. Sci. U.S.A.*, **57**, 1550.
- Fuoss, R. M. and Accascina, F., *Electrolytic Conductance*, Interscience Publishers, Inc., New York, 1959.
- Fuoss, R. M. and Kraus, C. A., *J. Am. Chem. Soc.*, **55**, 476 and 1019 (1933).
- Fuoss, R. M. and L. Onsager, *Proc. Natl. Acad. Sci. U.S.A.*, **41**, 274 and 1010 (1955).
- Fuoss, R.M. and Onsager, L. (1957) *J. Phys. Chem.*, **61**, 668.
- Gerischer, H. (1962) in *Recent Advances in Electrochemistry*, Vol. I Chapter 2 (ed P. Delahay), Interscience Publishers, Inc, New York.
- Gibbs, W. (1924) Collected works, in *Longmans*, 2nd edn, Vol. I, Green and Co., Inc., New York.
- Gileadi, E. (1967) Adsorption in electrochemistry, in *Electrosorption* (ed E. Gileadi), Plenum Press, New York.
- Gilkinson, W.R. (1956) *J. Chem. Phys.*, **25**, 1199.
- Gilman, S. (1964) *J. Electroanal. Chem.*, **7**, 382.
- Giordano, M.C., Bazan, J.C., and Arvia, A.J. (1967) *Electrochim. Acta*, **12**, 723.
- Glasstone, S., Laidler, K.J., and Eyring, H. (1941) *The Theory of Rate Processes*, McGraw-Hill Book Company, New York.
- Glueckauf, E. (1955) *Trans. Faraday Soc.*, **51**, 1235.
- Glueckauf, E. (1964) *Trans. Faraday Soc.*, **60**, 572.
- Golden, S. and Guttman, C. (1965) *J. Chem. Phys.*, **43**, 1894.
- Gouy, G. (1910) *J. Phys.*, **9**, 457.
- Grahame, D.C. (1947) *Chem. Rev.*, **41**, 441.
- Green, M. (1959) Electrochemistry of the semiconductor-electrolyte interface, in *Modern Aspects of Electrochemistry*, Vol. II Chapter 5 (ed J.O'M. Bockris), Butterworth's Publications, Ltd., London.
- Guggenheim, E.A. and Adam, N.K. (1933) *Proc. R. Soc. London, Ser. A*, **139**, 218.
- Guoy, G. (1903) *J. Chim. Phys. (Paris)*, **29**(7), 145.
- Gurney, R.W. (1932) *Proc. R. Soc. London, Ser. A*, **134**, 137.
- Halliwel, H.F. and Nyburg, S.C. (1963) *Trans. Faraday Soc.*, **58**, 1126.
- Harned, H.S. and Owen, B.B. (1957) *The Physical Chemistry of Electrolytic Solution*, 3rd edn, Reinhold Publishing Corporation, New York.
- Harned, H.S. and Owen, B.B. (1958) *The Physical Chemistry of Electrolytic Solution*, 3rd edn, Reinhold Publishing Corporation, New York.
- von Helmholtz, H.L. (1879) *Wied. Ann.*, **7**, 337.
- Hinton, J.F. and Amis, E.S. (1967) *Chem. Rev.*, **67**, 367.
- Holmes, O.G. and McLure, D.S. (1957) *J. Chem. Phys.*, **26**, 1686.
- Horiuti, J. and Ikusima, M. (1939) *Proc. Imp. Acad. (Tokyo)*, **15**, 39.
- Horiuti, J. and Polanyi, M. (1935) *Acta Physicochim. USSR*, **2**, 205.
- Hunt, J.P. (1963) *Metal Ions in Aqueous Solution*, W. A. Benjamin, Inc., New York.
- Hurwitz, H.D. (1967) in *Electrosorption* (ed E. Gileadi), Plenum Press.
- Ilkovic, D. (1938) *J. Chim. Phys.*, **35**, 129.
- Ivanov, Y.B. and Levich, V.G. (1959) *Dokl. Akad. Nauk SSSR*, **126**, 1029.
- Ives, D.J.G. (1963) *Some Reflections on Water*, J. W. Ruddock & Sons Ltd, London.

- Jost, W. (1960) *Diffusion in Solids, Liquids, Gases*, Academic Press, Inc., New York.
- Kirkwood, J.G. (1950) *J. Chem. Phys.*, **18**, 380.
- Kolthoff, I.M. and Lingane, J.J. (1952) *Polarography*, Vol. I, Interscience Publishers, Inc., New York.
- Kortüm, G. (1965) *Treatise on Electrochemistry*, Elsevier, Amsterdam.
- Laidler, K.J. and Pegis, C. (1957) *Proc. R. Soc. London, Ser. A*, **241**, 80.
- Lange, E. and Mishchenko, K.P. (1930) *Z. Phys. Chem.*, **A149**, 1.
- Latimer, W.M., Pitzer, K.S., and Slansky, C.M. (1939) *J. Chem. Phys.*, **7**, 108.
- Lee Kavanau, J. (1964) *Water and Solute-Water Interactions*, Holden-Day Inc., San Francisco, CA.
- (a) Levich, V.G. (1942) *Acta Physicochim. URSS*, **17**, 257. (b) Levich, V.G. (1944) *Zh. Fiz. Khim.*, **18**, 335.
- Levich, V.G. (1962) Passage of current through electrolytic solutions, in *Physicochemical Hydrodynamics* Chapter 6, Prentice Hall, Inc., Englewood Cliffs, NJ.
- Levich, V.G. (1965) *Russ. Chem. Rev. (English Transl.)*, **34**, 792.
- Levich, Y. (1965) in *Recent Advances in Electrochemistry* (ed P. Delahay) Chapter 4, Interscience Publishers, Inc., New York.
- Levine, S. and Rozenthal, D.K. (1966) The interaction energy of an Ion pair in an aqueous medium, in *Chemical Physics of Ionic Solutions* (eds B.E. Conway and R.G. Barradas), John Wiley & Sons, Inc., New York.
- Lietzke, M.H., Stroughton, R.W., and Fuoss, R.M. (1968) *Proc. Natl. Acad. Sci. U.S.A.*, **59**, 39.
- Lippmann, G. (1875) *Ann. Chim. Phys. (Paris)*, **5**, 494.
- Losev, V.V., Molodov, A.I., and Gorodetzki, V.V. (1967) *Electrochim. Acta*, **12**, 475.
- Marchi, R.P. and Eyring, H. (1964) *J. Phys. Chem.*, **68**, 221.
- Marcus, R.A. (1965) *J. Chem. Phys.*, **43**, 679.
- Matthews, D.B. (1966) *Proc. R. Soc. London, Ser. A*, **292**, 479.
- D. B. Matthews and J. O'M. Bockris, Quantum mechanics of charge transfer at interfaces, in J. O'M. Bockris and B. E. Conway, (Eds.), *Modern Aspects of Electrochemistry*, Vol. VI, Chapter 1, Plenum Press, New York, 1969.
- Mehl, W. (1959) *Can. J. Chem.*, **37**, 190.
- Millen, W.A. and Watts, D.W. (1967) *J. Am. Chem. Soc.*, **89**, 6051.
- Milner, S.R. (1912) *Philos. Mag.*, **6**(23), 551.
- Mohilner, D. (1967) The electrical double layer, in *Electroanalytical Chemistry*, Vol. I Chapter 4 (ed A.J. Bard), Marcel Dekker, Inc.
- Monk, C.B. (1961) *Electrolytic Dissociation*, Academic Press, London.
- Nancollas, G.H. (1966) Thermodynamic and kinetic aspects of Ion association in solutions of electrolytes, in *Chemical Physics of Ionic Solutions* (eds B.E. Conway and R.G. Barradas), John Wiley & Sons, Inc., New York.
- G. Némethy and H. A. Scheraga, *J. Chem. Phys.*, **36**, 3882 and 3401 (1962).
- Nernst, W. (1904) *Z. Physik. Chem.*, **47**, 52.
- Orgel, L.E. (1952) *J. Chem. Soc.*, **1952**, 4756.
- Padova, J. (1964) *J. Chem. Phys.*, **40**, 391.
- Parsons, R. (1951) *Trans. Faraday Soc.*, **147**, 1332.
- Parsons, R., Equilibrium properties of electrified interphases, in J. O'M. Bockris and B. E. Conway, (Eds.), *Modern Aspects of Electrochemistry*, Vol. I, Butterworth's Publications, Ltd., London, 1954.
- Parsons, R. (1961) The structure of the electric double layer and its influence on the rates of electrode reaction, in *Advances in Electrochemistry and Electrochemical Engineering*, Vol. I (ed P. Delahay), Interscience Publications, Inc., New York.
- Passynsky, A. (1938) *Acta Physicochim. URSS*, **8**, 385.
- Pauling, L. (1960) *The Nature of the Chemical Bond*, 3rd edn, Cornell University Press, Ithaca, NY.
- Paunovic, M. (1967) *J. Electroanal. Chem.*, **14**, 447.
- Pearson, J.D. and Butler, J.A.V. (1938) *Trans. Faraday Soc.*, **34**, 1163.
- Perkins, R. S. and Andersen, T. N., Potential of zero charge of electrodes, in J. O'M. Bockris and B. E. Conway, (Eds.), *Modern Aspects of Electrochemistry*, Vol. V, Plenum Press, New York, 1969.
- Potter, E.C. (1952) *J. Chem. Phys.*, **20**, 614.
- Prue, J.E. (1966) Ion association and solvation, in *Chemical Physics of Ionic Solutions* (eds B.E. Conway and R.G. Barradas), John Wiley & Sons, Inc., New York.

- Pourbaix, M., Atlas of Electrochemical Equilibria in Aqueous Solutions, National Association of Corrosion Engineers, 1974.
- Riddiford, A.C. (1966) Rotating disk systems, in *Advances in Electrochemistry and Electrochemical Engineering*, Vol. IV Chapter 2 (eds P. Delahay and C.W. Tobias), Interscience Publishers, Inc., New York.
- Robinson, R.A. and Stokes, R.H. (1959) *Electrolyte Solutions*, 2nd edn, Butterworth's Publications, Ltd., London.
- Rosensteig, D.R. (1965) *Chem. Rev.*, **65**, 467.
- Ross, K. (1968) *Aust. J. Phys.*, **21**, 597.
- Samoilov, O.Y. (1965) *Structure of Aqueous Electrolyte Solutions and the Hydration of Ions*, Consultants Bureau, New York.
- Sand, H.J.S. (1900) *Philos. Mag.*, **1**, 45.
- Simonova, M.V. and Rotinyan, A.L. (1965) *Russ. Chem. Rev. (English Transl.)*, **34**, 318.
- Smoluchowski, M. (1908) *Ann. Phys. (Paris)*, **25**, 205.
- Stern, O. (1924) *Z. Elektrochem.*, **30**, 508.
- Stokes, R. H., *J. Am. Chem. Soc.*, **86**, 979, 982 and 2337 (1964).
- Stokes, R.H. and Robinson, R.A. (1948) *J. Am. Chem. Soc.*, **70**, 1870.
- Stokes, R.H. and Robinson, R.A. (1957) *Trans. Faraday Soc.*, **53**, 301.
- Swinkels, D.A.J. (1964) *J. Electrochem. Soc.*, **111**, 736.
- Tafel, J. (1905) *Z. Physik. Chem. (Leipzig)*, **50**, 641.
- Tikhomirova, V. I., Luk'yanycheva, V. I., and Bagotsky, V. S., *Sov. Electrochem.*, **3**, 673 (1967).
- Ulich, H. (1930) *Z. Elektrochem.*, **36**, 497.
- Ulich, H. (1934) *Z. Physik. Chem. (Leipzig)*, **168**, 141.
- Verwey, E. J. W., *Rec. Trav. Chim.*, **60**, 887 (1961); **61**, 127 (1942).
- (a)Vetter, K.J. (1950) *Z. Physik. Chem. (Leipzig)*, **194**, 284. (b)Vetter, K.J. (1951) *Z. Elektrochem.*, **55**, 121.
- Vetter, K.J. (1967a) *Electrochemical Kinetics 2, Theory of Overvoltage*, Academic Press, Inc., New York.
- Vetter, K.J. (1967b) Determination of the electrochemical reaction orders, in *Electrochemical Kinetics* Chapter 3c, Academic Press, Inc., New York.
- Will, F. G. and Knorr, C. A., *Z. Elektrochem.*, **64**, 258 and 270 (1960).
- Wroblowa, H. and Kovac, Z. (1965) *Trans. Faraday Soc.*, **61**, 1523.
- Yang, L. and Simnad, M. T., Measurement of diffusivity in liquid systems, in *Physicochemical Measurements at High Temperatures*, J. O'M. Bockris, J. L. White and J. W. Tomlinson, (Eds.), Butterworth's Publications, Ltd., London, 1959.
- Zana, R. and Yeager, E., *J. Phys. Chem.*, **71**, 521 and 4241 (1967).

2

General Properties of Electrochemical Capacitors

Tony Pandolfo, Vanessa Ruiz, Seepalakottai Sivakkumar, and Jawahr Nerkar

2.1

Introduction

The use of capacitors for electrical energy storage actually predates the invention of the battery. Alessandro Volta is attributed with the invention of the battery in 1800, where he first describes a battery as an assembly of plates of two different materials (such as copper and zinc) placed in an alternating stack and separated by paper soaked in brine or vinegar [1]. Accordingly, this device was referred to as *Volta's pile* and formed the basis of subsequent revolutionary research and discoveries on the chemical origin of electricity. Before the advent of *Volta's pile*, however, eighteenth century researchers relied on the use of Leyden jars as a source of electrical energy. Built in the mid-1700s at the University of Leyden in Holland, a Leyden jar is an early capacitor consisting of a glass jar coated inside and outside with a thin layer of silver foil [2, 3]. With the outer foil being grounded, the inner foil could be charged with an electrostatic generator, or a source of static electricity, and could produce a strong electrical discharge from a small and comparatively simple device.

Currently, there are a large variety of different types of capacitors available, largely classified by the specific dielectric used and/or its physical state (Figure 2.1). Each type has its own set of characteristics and applications ranging from small trimming capacitors for electronics, large power capacitors used in high-voltage power factor correction up to high-energy electrochemical capacitors (ECs) that can contain much greater capacitance (energy) than is achievable with regular capacitors for a given device size. Research into ECs has dramatically increased since the early 1990s and has been fueled by an emerging number of applications requiring their unique combination of properties that include high specific energy (for a capacitive device), reliability, long cycle life, high power (both charge and discharge), and high energy efficiency.

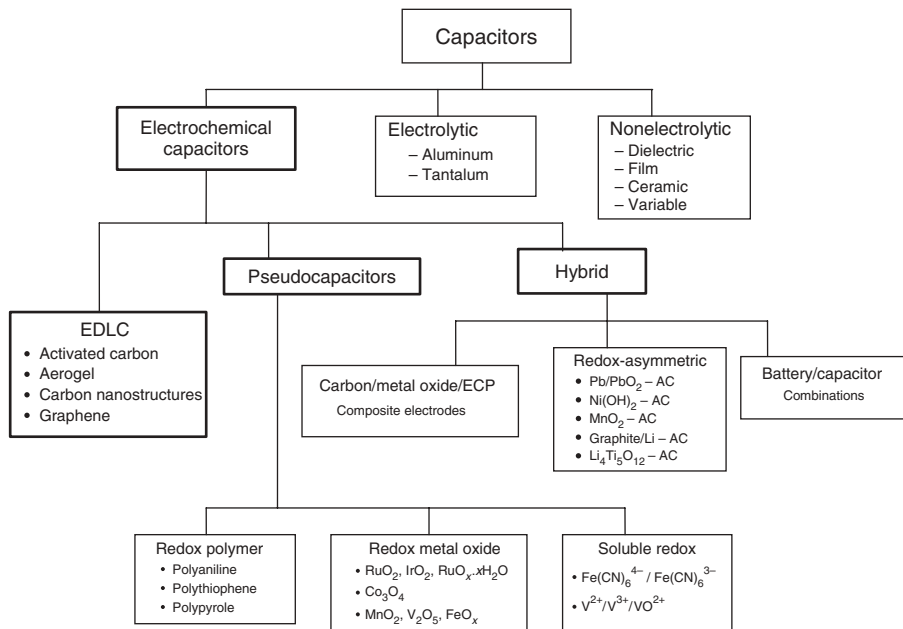


Figure 2.1 Classification of common types of capacitors.

2.2

Capacitor Principles

A capacitor is a passive component that stores energy in an electrostatic field rather than in chemical form. It consists of two parallel electrodes (plates) separated by a dielectric. The capacitor is charged by applying a potential difference (voltage) across the electrodes, which causes positive and negative charges to migrate toward the surface of electrodes of opposite polarity. When charged, a capacitor connected in a circuit will act as a voltage source for a short time. Its capacitance (C), which is measured in farads (F), is the ratio of electric charge on each electrode (Q) to the potential difference between them (V) so that:

$$C = \frac{Q}{V} \quad (2.1)$$

For a typical parallel plate capacitor, C is proportional to the area (A) of each electrode and the permittivity (ϵ) of the dielectric and inversely proportional to the distance (D) between the electrodes so that:

$$C = \frac{\epsilon_0 \epsilon_r A}{D} \quad (2.2)$$

where ϵ_0 is the permittivity of free space and ϵ_r is the dielectric constant (or relative permittivity) of the material between the plates. Therefore, the three main factors that determine the capacitance of a capacitor are

- plate area (common to the two electrodes)
- separation distance between the electrodes
- properties of the dielectric (insulator) used.

Two primary attributes of a capacitor are its energy and power density, both of which can be expressed as a quantity per unit weight (specific energy or power) or per unit volume. The energy E (J) stored in a capacitor is related to the charge Q (C), at each interface and the potential difference V (V), and therefore is directly proportional to its capacitance:

$$E = \frac{1}{2} \times CV^2 \quad (2.3)$$

Maximum energy is achieved when V is at a maximum, which is usually limited by the breakdown strength of the dielectric.

In general, power (P) is the rate of energy delivery per unit time. The resistance of the internal components of the capacitor (e.g., current collectors, electrode materials, dielectric/electrolyte, and separators) needs to be taken into account in order to determine P for a certain capacitor. The resistance of these components is usually measured in aggregate and collectively referred to as the equivalent series resistance (ESR) (Ω). The ESR, by introducing a voltage drop, determines the maximum voltage of the capacitor during discharge and therefore limits the maximum energy and power of a capacitor. The measurement of power for capacitors is often measured at matched impedance (i.e., the resistance of the load is assumed to be the same as the capacitor ESR) which corresponds to the maximum power P_{\max} , given by

$$P_{\max} = \frac{V^2}{4\text{ESR}} \quad (2.4)$$

However, even though the resistance of a good capacitor is typically much lower than that of the connected load, the actual delivered peak power, although still very high, is usually lower than P_{\max} .

2.3

Electrochemical Capacitors

ECs are a special kind of capacitors based on charging and discharging at the electrode–electrolyte interface of high surface area materials, such as porous carbons or some metal oxides [3]. They are governed by the same basic principles as conventional capacitors and are ideally suited to the rapid storage and release of energy. However, they incorporate electrodes with much higher effective surface areas (SA) and thinner dielectrics (which are defined by the thickness of the double layer), leading to an increase in both capacitance and energy; by a factor of 10 000 or so than those achievable by regular capacitors. Therefore, while conventional capacitors are often rated in the micro- and milli-farad ranges, ECs can be rated as high as tens, hundreds, and even thousands of farads per device. They still store electric charge in a highly reversible way, as does a regular capacitor, and

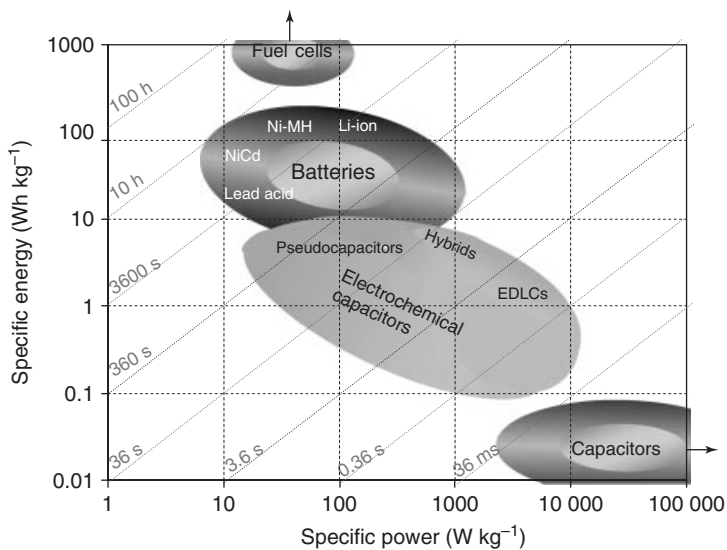


Figure 2.2 Specific energy and power capabilities of electrochemical energy storage/conversion devices.

by maintaining a low ESR, can be operated at high specific power (kW kg^{-1}); substantially higher than most batteries.

While ECs can also be regarded as functioning like rechargeable batteries in storing or delivering electric charge, their mechanism of charge storage differs from those typically operating in batteries (i.e., electrostatic/*non-faradic* vs chemical/*faradic*). Therefore, ECs should not be considered as battery replacements but rather as complementary energy storage devices occupying a niche position, in terms of specific power and energy. Through appropriate cell design, both the specific energy and specific power ranges for ECs can cover several orders of magnitude, which makes them extremely versatile as a stand-alone energy supply for certain applications, or in combination with batteries as a hybrid system. This unique combination of high power capability, coupled with good specific energy, allows ECs to occupy a functional position between batteries and conventional capacitors (Figure 2.2, Table 2.1). They can offer very fast charge and discharge rates relative to batteries of a comparable volume, but their specific energy is less than that of batteries. The highly reversible and rapid charge acceptance/delivery of ECs arises largely due to the fact that no slow chemical processes or phase changes take place between charge and discharge as they do in most *battery-type* energy storage devices. In addition to their high power density, ECs have several advantages over electrochemical batteries including very short charge times, longer cycle life (millions vs thousands for batteries), long shelf life, high efficiency (charge in \approx charge out) and can be fully charged or discharged without affecting performance or lifetime [3, 4]. An important difference between a capacitor and a battery is that there is always an intrinsic increase in voltage on charge (or decrease on discharge)

Table 2.1 Comparison of *typical* capacitor and battery characteristics.

Characteristics	Capacitor	Carbon EDLC	Battery
Examples	Al, Ta oxide, condenser	Activated carbon in H ₂ SO ₄ or TEABF ₄ /ACN	Lead acid, Ni-Cd, and Ni-MH
Storage mechanism	Electrostatic	Electrostatic	Chemical
E (Wh kg ⁻¹)	<0.1	1–10	~20–150
P (W kg ⁻¹)	≫10000	500–10 000	<1000
Discharge time (t_d)	10 ⁻⁶ –10 ⁻³ s	Seconds to minutes	0.3–3 h
Charging time (t_c)	10 ⁻⁶ –10 ⁻³ s	Seconds to minutes	1–5 h
Efficiency (t_d/t_c)	~1.0	0.85–0.99	0.7–0.85
Cycle life (cycles)	≫10 ⁶ (≫10 yr)	> 10 ⁶ (> 10 yr)	~1500 (~3 yr, less for high drain applications)
Limited by:	Design	Impurities	Chemical reversibility
	Materials	Side reactions	Mechanical stability
V_{\max}	High	<3 V	Low
Determined by:	Dielectric thickness	Electrode stability	Thermodynamics of phase reactions
	Strength	Electrolyte stability	
Charge stored	Between charged plates	Interface electrode/electrolyte	Entire electrode
Determined by:	Geometric area of the electrodes	Electrode microstructure	Active mass
	Dielectric	Active surface area	Thermodynamics
		Electrolyte	
Discharge profile	V/t : linear trend	V/t : linear trend	Discharge plateau
Self-discharge	Low	Moderate (μA mA)	Low

E , specific energy; P , specific power; V_{\max} , maximum cell voltage.

for a capacitor as a result of the increase (or decrease) in charge stored on the capacitor electrodes (Q/A). In contrast, a battery typically has a close to constant voltage during charge or discharge except when its state of charge approaches 100% charge (top of charge, TOC) or close to 0% (end of discharge, EOD) (Figure 2.3). Therefore, for applications requiring a constant output voltage, capacitors will require a DC–DC converter to regulate and stabilize their output. Both batteries and capacitors will require an inverter if alternating current is required.

A number of reviews have discussed both the science and technology of ECs for various configurations and electrode materials [3, 5–12]. Current research into ECs can be divided into three main areas, based primarily on their mode of energy storage and construction: (i) the electric double-layer capacitor (EDLC), (ii) the *redox* EC (also referred to as *pseudocapacitor*), and (iii) hybrid systems incorporating

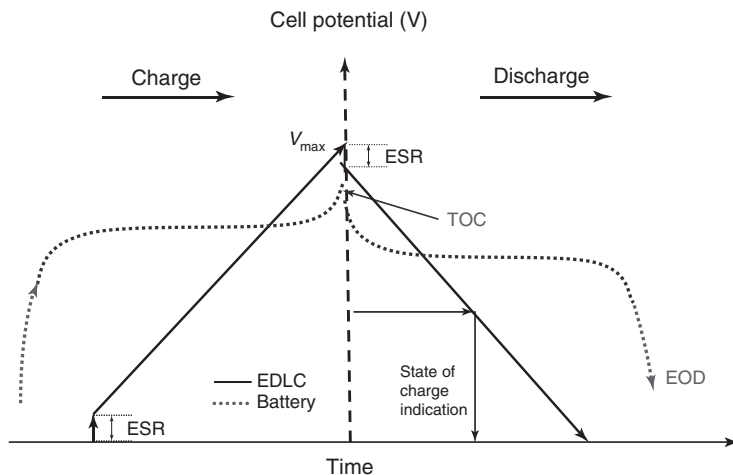


Figure 2.3 Comparison of charge and discharge behavior for an ideal capacitor and battery.

combinations of double layer and *pseudocapacitance* (Figure 2.1). Despite the wide array of possible materials and device architectures, the EDLC version is currently the most developed form of EC and dominates the market. Carbon, in its various forms, is currently the most extensively examined and widely utilized electrode material in commercial EDLCs.

ECs are also often referred to by a number of alternative names including double-layer capacitors, supercapacitors, ultracapacitors, power capacitors, gold capacitors, pseudocapacitors, and power cache, each supposedly used to indicate different types of capacitors that display high capacitance [13]. However, these names are often associated with a brand or company trade name and therefore do not always provide a useful indication of the type of capacitor or underlying storage mechanism. As the specific energy of ECs are many orders of magnitude higher than for conventional capacitors, the use of the terminology *super-* or *ultracapacitor*, in particular, is very popular and sometimes unwisely used to replace the broader, but more correct, electrochemical capacitor classification. Even then, there are also regional preferences as to whether supercapacitor or ultracapacitor is employed. NEC in Japan was the first to produce commercial EDLC-type devices, in the 1970s, under the name *supercapacitor*, whereas in the United States, Pinnacle Research Institute introduced a high-power EC in the 1980s under the name *PRI Ultracapacitor* [13–15]. This latter device was not an EDLC but rather a ruthenium/tantalum oxide device; a redox pseudocapacitor and yet *ultracapacitor* is routinely used nowadays to also describe EDLC type devices, particularly in the United States. As the EC market continues to grow and expand into a greater number of applications, the need for a uniform classification and taxonomy system will become essential.

2.3.1

Electric Double-Layer Capacitors

The concept of the double layer has been studied by chemists since the nineteenth century when von Helmholtz first developed and modeled the double-layer concept in his work on colloidal suspensions [16]. However, it was not until 1957 that the *practical use* of a double-layer capacitor, for the storage of electrical charge, was demonstrated and patented by H.I. Becker of General Electric [17]. This early patent utilized porous carbon electrodes in an aqueous electrolyte; however, it was not until 1966, in a patent granted to R.A. Rightmire [18] of the Standard Oil Company of Ohio (SOHIO) and a follow-up patent by SOHIO coworker D.L. Boos [19], that it was acknowledged that these devices actually store energy in the electrical double layer (non-faradically), at the *interphase* between the electrode and electrolyte solution. The first commercial double-layer supercapacitors originated from SOHIO [20] and consisted of carbon paste electrodes, formed by soaking porous carbon in an electrolyte separated by an ion-permeable separator [19]. SOHIO also utilized nonaqueous electrolytes in their early devices, but a lack of sales saw them transfer the license to NEC in 1971, who further developed and successfully marketed double-layer supercapacitors, primarily for memory backup applications [15]. Currently, a number of high-performance EDLC devices, based on porous carbons, are commercially available from a range of manufacturers and distributors around the world for an expanding range of applications [10, 14].

2.3.1.1 Double-Layer and Porous Materials Models

The Helmholtz double-layer model states that two oppositely charged layers are formed at an electrode–electrolyte interface and are separated by an atomic distance. This model was subsequently extended to the surface of metal electrodes in the late nineteenth and early twentieth centuries [21–25]. Stern [23] combined the early Helmholtz model with the more refined Gouy–Chapman model and recognized that two regions of ion distribution exist at the electrode–electrolyte interface: an inner region called the *compact layer* (or *Stern layer*) and a *diffuse layer* [9, 23]. In the compact layer, ions (usually solvated) are strongly adsorbed by the electrode while in the diffuse layer there is a continuous distribution of electrolyte ions (both anions and cations) in solution driven by thermal motion. Therefore, the capacitance at an electrode–electrolyte interface double layer (C_{dl}) can be regarded as consisting of two components, the compact double-layer capacitance (C_H) and the diffuse region capacitance (C_{diff}). C_H and C_{diff} are conjugate components of the overall double-layer capacitance (at a single electrode), C_{dl} , corresponding to the series relationship:

$$\frac{1}{C_{dl}} = \frac{1}{C_H} + \frac{1}{C_{diff}} \quad (2.5)$$

The factors that will ultimately determine the electric double-layer capacitance include the electrode material (conducting or semiconducting), electrode area, accessibility to the electrode surface, the electric field across the electrode, and

electrolyte/solvent properties (i.e., their interactions, size, electron-pair donicity, and dipole moments).

In EDLCs, the electrode material is usually highly porous, and therefore the double-layer behavior at the pore surface is more complex. In very fine pores, the dimensions of the double layer can be comparable with the effective pore width so that in the finest pores, the extension of the diffuse layer into the pore can result in an overlap of diffuse layers from opposite surfaces resulting in a redistribution of the diffuse layer ions [3]. This redistribution of the ionic concentration profile at the surface will be greater when the ionic content is low and may contribute to the enhanced double-layer capacitance observed for carbons containing very fine (<1 nm) porosity [8].

Recently, Huang *et al.* [26, 27] proposed an alternative approach for modeling the double layer at the surface of porous materials. Their heuristic model is based on density functional theory calculations and analysis of experimental data and takes into consideration the curvature of the pore walls, in the calculation of capacitance, by introducing appropriate curvature terms into Eq. (2.2). They observed that for significantly large pores (e.g., macropores, >50 nm), the capacitance can be adequately described by the traditional EDLC approach based on a parallel plate (discussed earlier) as the pore curvature is not significant and can be approximated as planar. However, they found that by taking into consideration the curvature of smaller pores into their model (i.e., mesopores, 2–50 nm and micropores, <2 nm), capacitance calculations displayed an improved correlation with electrode surface properties (pore size, surface area) and electrolyte properties (concentration, ion size, dielectric constant, etc.). By assuming that mesopores were cylindrical, the authors developed a model whereby the solvated counterions enter pores and approach the pore walls of the cylindrical pore to form an inner cylindrical arrangement of adsorbed ions to form an *electric double-cylinder capacitor* (EDCC). For micropores, however, the small pores do not allow the formation of a *double cylinder* as the pore width cannot readily accommodate more than one solvated counterion. Therefore, the solvated (or desolvated) ions line up to form a single line of counter ions, within the cylindrical micropore, which is described as an *electric wire-in-cylinder capacitor* (EWCC). This extension to the classical double-layer model has shown to be universally applicable to a diverse range of carbons and electrolytes and also supports the anomalous increase in capacitance for carbons with pores below 1 nm, reported by several authors [28–30], as well as the partial or complete desolvation of ions before their entry into fine micropores (for more details, see Chapter 7).

In addition to variations in double-layer properties, porous materials also introduce ion transportation restrictions through the complex network of pores. The high porosity of carbons that allow the high capacitance of EDLCs to be realized depends on fine porosity that may restrict electrolyte diffusion rates which in turn lead to a slower response time (relative to conventional capacitors). The movement of electrolyte ions within the pore network of EDLCs will experience varying degrees of mass transfer limitations associated with confined pores, the tortuous path through the carbon material, pore lengths, and ion sieving/exclusion effects at pore openings; particularly openings that approach,

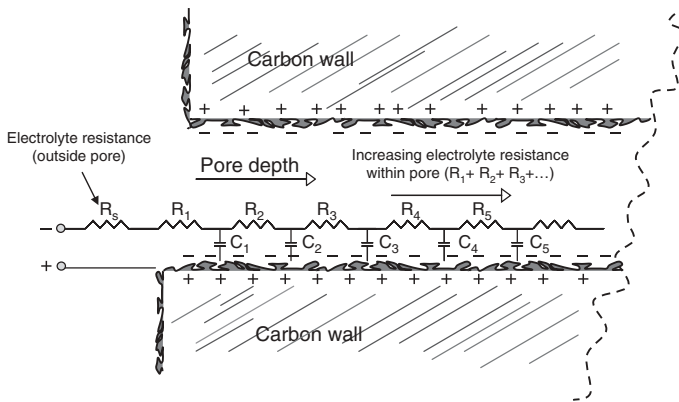


Figure 2.4 An idealized model of a cylindrical pore and distributed capacitance (RC networks) within a pore. The equivalent circuit model (*transmission line network*) highlights the increasing resistance of capacitive networks with increasing pore depth.

or are smaller than, the size of the solvated electrolyte molecules [30, 31]. Hence, not all the surface of the porous electrode will be accessed by the electrolyte in the same time frame and, therefore, upon discharge, the rate at which the capacitance can be delivered will also vary.

De Levie [32] developed a model to describe the distribution of capacitance in porous electrodes and it is summarized schematically in Figure 2.4. Figure 2.4 shows a small section of a single pore, which is assumed to be cylindrical, and the distribution of capacitance is represented as a simplified equivalent circuit consisting of parallel RC circuits (each a resistor and capacitor combination) sometimes also referred to as a *transmission line* model [3, 10, 32]. R_s , represents the bulk solution (electrolyte) resistance, and the electric double-layer capacitance, C_{dl} , is distributed across the pore wall surface. In series with each area of interfacial capacitance (C_{dl}) distributed down the pore wall, is an additional electrolyte resistance, R_x , associated with the movement of ions within the pores. As the electrolyte moves deeper into a pore (particularly narrow pores), it is increasingly influenced by interactions with the pore walls and pore geometry; which, in turn, influences the capacitive response of the material. Thus, the capacitance stored near the pore opening is accessed via a shorter and less resistive path than the capacitance deeper within the pore, which has additional electrolyte-resistive contributions ($R_{1+2+3+\dots}$). This distribution of charge creates a more complicated electrical response (particularly at high frequencies) with no single characteristic response time although typical EC response rates are still generally in the millisecond to seconds range, depending on design [10].

2.3.1.2 EDLC Construction

As previously described, EDLCs store energy in much the same way as a traditional capacitor, namely, by means of charge separation. The main difference is related to the higher capacitance values provided by EDLCs; achieved through the

utilization of high-surface-area porous materials (usually AC) in contrast to the two-dimensional planar plates typically found in conventional capacitors. EDLCs can store substantially more energy than a conventional capacitor (by several orders of magnitude) due to the following:

- 1) The increased amount of charge that can be stored on a highly extended electrode surface area (created by a large number of pores within a high-surface-area electrode material)
- 2) The small thickness of the so-called electrical double layer at the interphase between an electrode and the electrolyte.

EDLC construction is similar to a battery in that there are two electrodes immersed in an electrolyte, with an ion-permeable separator located between the electrodes to prevent electrical contact (Figure 2.5a). In the charged state, the electrolyte anions and cations move toward the positive and negative electrodes, respectively, giving rise to *two* double layers, one at each electrode–electrolyte interface. The separation of ions also results in a potential difference across the cell (Figure 2.5b). As each electrode–electrolyte interface represents a capacitor, the complete cell can be considered as two capacitors connected in series. For a symmetrical capacitor (i.e., identical electrodes) the cell capacitance (C_{cell}) will therefore be

$$\frac{1}{C_{\text{cell}}} = \frac{1}{C_+} + \frac{1}{C_-} \quad (2.6)$$

where, C_+ and C_- represent the capacitance of the positive and negative electrodes, respectively [3, 33]. Given the fact that in a symmetric device the capacitance for the positive electrode (C_+) equals that of the negative one (C_-), the capacitance of the complete cell becomes half of the capacitance of each individual electrode; that is,

$$C_{\text{cell}} = \frac{C_e}{2} \quad (2.7)$$

where $C_e = C_+ = C_-$.

Therefore, when reporting, or comparing capacitance values from different sources, it is important to specify if they are cell capacitance or electrode capacitance values. Literature values of specific capacitance often quote the capacitance of a single carbon electrode; usually derived from a *three-electrode* measurement that also incorporates a reference and counter electrode [34]. This value will be higher than the actual cell capacitance, which is also referred to as a *two-electrode* measurement. Moreover, it is necessary to compare relative *specific* capacitance values, either per unit mass or volume. The specific (gravimetric) capacitance of an electrode, C_e , is given by

$$C_e \text{ (F g}^{-1}\text{)} = \frac{2 \times C_{\text{cell}}}{m_e} \quad (2.8)$$

where m_e is the weight of active material (in grams) present in a single electrode. Conversely, by dividing C_e by 4, the gravimetric capacitance of the whole cell (on an active material basis) can be obtained. Capacitance may also be reported as

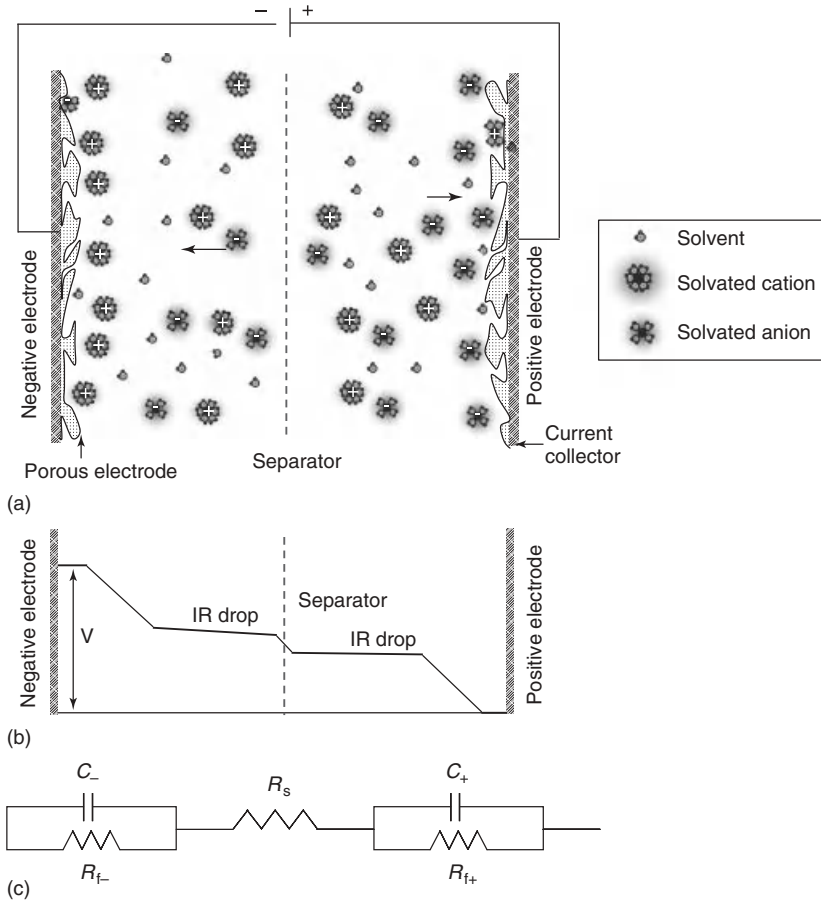


Figure 2.5 (a) Representation of an electrochemical double-layer supercapacitor (in its charged state), (b) typical potential profile across a charged electrochemical capacitor, and (c) equivalent circuit model for an electrochemical capacitor.

normalized capacitance (capacitance per unit area), defined as

$$C (\mu\text{F cm}^{-2}) = \frac{C_e (\text{F g}^{-1})}{SA (\text{m}^2 \text{g}^{-1})} 10^2 \quad (2.9)$$

where SA is the surface area of the active electrode material. In general, specific capacitance values for carbon are in the range of $10\text{--}30 \mu\text{F cm}^{-2}$ [3].

As many capacitor applications are constrained by volume rather than weight, it is sometimes more appropriate to express the data as volumetric capacitance (F cm^{-3}). This can be obtained by dividing the gravimetric capacitance by the density of the active material. While the volumetric and gravimetric capacitance of electrode materials are a useful guide to assess the quality of the active material, care must be taken in extrapolating these values to fully packaged cells as the weight (or volume) of other critical cell components (binder, additives, collectors,

electrolyte, separator, hermetic packaging, and connectors) needs to be taken into account. It is not usual for the active material to constitute only 20–30% of the final packaged device depending on the design, size, and intended application.

Analogous to De Levie's [32] approach to describe the distribution of capacitance in porous materials as parallel RC circuits, a simplified RC equivalent circuit is also often used to describe the basic operation of an EDLC. An RC circuit schematic representation of the double-layer capacitor described in Figure 2.5a,b is shown in Figure 2.5c. $C_{+/-}$ and $R_{f+/-}$ are the capacitance and faradic resistance for the positive and negative electrodes, respectively. R_f is considered to be responsible for the discharge of the cell. R_s is the ESR of the cell. A time constant, τ , is often determined to provide an indication of the time response of the device, which is calculated as the product of resistance (R) \times capacitance (C) [10].

The overall performance of an EDLC is influenced by two main factors, the choice of the active electrode material, which will define the capacitance of the device, and the electrolyte utilized, which will determine the operational voltage. These factors, and several additional sources, influence the internal resistance (ESR) of the device [33, 35] including the following:

- The intrinsic electronic resistance of the electrode material
- The interfacial resistance between the active electrode material and current collector
- The ionic (*diffusion*) resistance of ions moving in small pores
- The ionic resistance of ions moving through the separator
- Electrolyte ionic resistance.

A high internal resistance will limit the power capability of the capacitor, and ultimately, its application.

Similar to batteries, capacitors are often connected together in series and/or parallel combinations in order to reach a higher specific voltage and/or capacitance rating [36]. The number of cells required is determined by the system variables (which, in turn, are set by the application), such as allowable voltage change, current (or power), and duration time. As sustained overvoltage can cause cell failure, it is critical that when cells are attached in series, the voltage across each cell does not exceed the maximum rated voltage. This can easily occur if the individual ESR of the series-connected cells are not identical (a quality control issue) or if one or more cells begins to age, deteriorate, or even fail. Many electrochemical modules, which contain multiple cells, also incorporate a *cell balancing* system that utilizes a passive bypass component or an active bypass circuit to control the current and voltage across each cell [36].

The Electrolyte The types of electrolytes that can be used in EDLCs can be classified into three broad groups: (i) aqueous, (ii) salts dissolved in organic solvents, and (iii) ionic liquids (ILs). The advantages and disadvantages of each electrolyte system are summarized in Table 2.2. While early EDLCs were aqueous based, there has been a trend toward organic electrolytes in order to achieve higher operational voltages and therefore greater specific energy. Accordingly, another advantage of achieving

Table 2.2 Comparison of typical electrolyte properties.

Electrolyte	EW	K	η	Cost	Assembly environment	Toxicity	Ion size	Pseudo-capacitance
Aqueous	≤ 1	H	L	L	Air	L	HSO_4^- (aqueous) = 0.37 nm K^+ (aqueous) = 0.26 nm	Yes
Organic	2.5–2.7	L	M/H	M/H	Inert atmosphere	M/H	$\text{Et}_4\text{N}^+ \cdot 7\text{ACN}$ = 1.30 nm (solvated) (0.67 nm bare cation) $\text{BF}_4^- \cdot 9\text{ACN}$ = 1.16 nm (solvated) (0.48 nm bare anion)	No
ILs	3–6	VL	H	VH	Inert atmosphere	L	EMI^+ = 0.76 \times 0.43 nm TFSI^- = 0.8 \times 0.3 nm	No

EW (electrochemical window, V); κ (experimental ionic conductivity at 20 °C, mS cm^{-1}); η (viscosity at 20 °C, cP); L (low); M (moderate); H (high); VH (very high); VL (very low); ethylmethylimidazole (EMI^+); bis(trifluoromethanesulfonyl)imide (TFSI^-); and pseudocapacitance (pseudoC).

high cell voltages is that the number of cells required to obtain a high-voltage module (by connecting cells in series) is reduced. This will also partially offset the higher cost of organic cells, reduce the burden on voltage balancing circuits, and improve reliability.

Cell voltage is an important determinant of both the specific energy and power of ECs as their final operating voltage is dependent on electrolyte stability. Aqueous electrolytes, such as acids (e.g., H_2SO_4) and alkali (e.g., KOH) have the advantage of high ionic conductivity (up to $\sim 1 \text{ S cm}^{-1}$), low cost, and wide acceptance; however, they have a restricted voltage range with a relatively low decomposition voltage of $\sim 1.23 \text{ V}$ (determined by the electrochemical breakdown of water) [37]. Careful selection of current collectors (and packaging) is also required to avoid corrosion in alkali or acidic electrolytes. However, a major advantage of aqueous electrolytes is that the specific capacitance (F g^{-1}) of carbons in aqueous electrolytes tends to be significantly higher than that of the same electrode in nonaqueous solutions, a feature that is attributable to the higher dielectric constant of aqueous systems [38], together with the higher surface accessibility of smaller aqueous ions [9]. While the low operational voltage of aqueous systems poses a significant limitation if targeting high energy, they do offer alternative benefits particularly if targeting high-power or lower cost devices. Aqueous solutions (30% w/w) of sulfuric acid and potassium hydroxide have ionic conductivity values, 730 and 540 mS cm^{-1} , respectively; considerably higher than the conductivity of current organic or IL electrolytes. The higher conductivity of aqueous electrolytes will reduce the internal resistance of the device and maximize its specific power. Also, not only are aqueous electrolytes less costly but, since there is no need for thorough solvent drying or

assembly under inert atmospheres (as is generally the case for organic and IL electrolytes), their fixed manufacturing cost can also be considerably reduced.

Nonaqueous electrolytes of various types allow the use of cell operating voltages up to 2.7 V [37, 39]. As the specific energy of supercapacitors is proportional to the square of the operating voltage, high-voltage nonaqueous devices are attractive for high-energy applications, and electrolyte mixtures of solvents, containing dissolved quaternary alkyl ammonium salts, are routinely utilized in many commercial supercapacitors. However, since the electrical resistivity of nonaqueous electrolytes is at least an order of magnitude higher than that of aqueous electrolytes, the resulting capacitors generally have a higher internal resistance (ESR). The most common organic electrolyte for EDLCs is an alkyl ammonium salt dissolved in an aprotic solvent. A 1 M solution of tetra-ethylammonium tetrafluoroborate (TEABF₄) has an ionic conductivity of 60 mS cm⁻¹ when dissolved in acetonitrile (ACN) and around 11 mS cm⁻¹ when the less volatile propylene carbonate (PC) solvent is used.

While both aqueous- and organic-electrolyte-based EDLCs have found their way into the market, there are currently only limited reports of commercial EDLCs that contain IL electrolytes [40, 41]. ILs are a class of organic salts that are liquid at relatively low temperatures (<100 °C); some of these can be used as *solvent-free* electrolytes in EDLCs, thereby avoiding the flammability and volatility concerns often associated with organic solvent-based electrolytes. However, currently the ionic conductivity of room temperature ionic liquids (RTILs) is considerably lower than that of common organic EDLC electrolytes with the conductivity of the more promising low-viscosity ILs generally in the range between 0.1 and 15 mS cm⁻¹ at ambient temperatures [42]. RTILs containing imidazolium or pyrrolidinium cations with small anions such as tetrafluoroborate (BF₄⁻), dicyanamide (N(CN)₂⁻), (fluoromethanesulfonyl)imide (FSI⁻), or bis(trifluoromethanesulfonyl)imide (TFSI⁻) have been extensively investigated as electrolytes in EDLCs owing to their attractive combination of electrochemical stability, conductivity, and viscosity [43]. While their performance at ambient, or higher temperatures, is promising [44, 45], the viscosity of RTILs increases rapidly at sub-ambient temperatures, causing a dramatic reduction in ionic mobility and conductivity (conductivity is inversely linked to viscosity [46, 47]). The loss of electrolyte mobility at low temperatures results in a rapid increase in device ESR and loss of accessible capacitance. Another possible approach to reduce the viscosity of the ILs is the addition of solvents (e.g., butylene carbonate, diethyl carbonate, ACN [43], gamma-butyrolactone (GBL) [48], etc.), or addition of salts (LiBF₄ [49], LiTf [50], etc.); however, although the viscosity can be significantly reduced, it can also be accompanied by a decrease in the stable electrochemical window of the mixture [43].

An important consideration when selecting an electrolyte for porous materials is the size of the electrolyte ions as they need to be able to access the electrode porosity. For a given porous material, the smaller the ion size, the higher the accessible surface area available to the ions. Thus, as aqueous electrolytes often have a smaller ion size than nonaqueous electrolytes, they provide, in general, higher specific capacitance values (Tables 2.2 and 2.3). Studies proposed by several authors

Table 2.3 Properties of most common carbon materials used as electrodes in EDLCs.

Electrode material	SA ($\text{m}^2 \text{g}^{-1}$)	C (F g^{-1})		
		Aqueous	Organic	ILs
Activated carbons	1000–3000	200–400 [53, 54]	100–150 [55]	100–150 [30]
Templated carbons	500–2500	120–350	120–135	150
Carbon nanotubes (CNTs)	120–500	20–180	20–80	20–45 [56, 57]
Carbide-derived carbons	1000–1600	—	100–140 [28]	100–150
Carbon blacks	250–2000	<300 [58]	—	—
Aerogels/xerogels	400–1000	40–220 [59, 60]	<160	—

SA: surface area and C: gravimetric capacitance values.

confirm the accessibility of fine micropores, as small as 0.4–0.5 nm in diameter, to aqueous electrolytes [51, 52]. As ions in electrolyte solutions are stabilized by a solvation sheath, many early studies argued that micropores were difficult to access and that mesopores, (2–50 nm) were more useful in EDLCs. Currently, there seems to be general agreement that small pores including micropores (down to ~ 0.7 nm), are accessible to the majority of organic electrolytes as evidenced by the high capacitance of microporous carbons [9]. Interestingly, as the size of solvated electrolyte ions is often larger than 0.7 nm (Table 2.2) the possibility of desolvation, or partial desolvation, has been inferred from several studies [28, 29]. While mesopores are considered to be useful as transport or *feeder* pores to access the fine porosity of active materials, the higher surface-area-to-volume ratio of micropores makes them particularly effective for generating high surface area materials.

Electrode Materials EDLCs take advantage of the numerous and frequently cited properties of carbon materials that include good chemical stability, good electrical conductivity, availability, and low-moderate cost [61, 62]. Carbon materials have long been incorporated into the electrodes of energy storage devices primarily as electroconductive additives, supports for active materials, electron transfer catalysts, intercalation hosts, for current leads, heat transfer, porosity control, surface area, and capacitance [63]. The ultimate performance of carbon-based supercapacitors in EDLCs will be closely linked to the physical and chemical characteristics of the carbon electrodes. There are an enormous number of carbon materials produced from a variety of carbonization and activation procedures and materials ranging from conventional ACs to the more sophisticated carbon nanotubes (CNTs) that have been evaluated as electrode materials for EDLCs (Table 2.3).

Carbon materials, mainly in the form of ACs, are currently the most widely utilized active materials in commercial EDLCs. Very few, if any, materials can match AC for its unique combination of high conductivity and very high surface area. ACs are also attractive materials for EDLC preparation because of their stable supply, and the fabrication procedures are well established [64]. They can

be obtained from a wide variety of carbonaceous precursors (e.g., lignocellulosic materials, pitch, coal, and many other materials [64, 65]) and the development of surface area is relatively easy to achieve by means of chemical activation, physical activation, or a combination of both. Depending on the precursor and activation procedure used, Brunauer-Emmet-Teller (BET) surface areas varying from 500 to 3000 m² g⁻¹ can readily be obtained. These high surface areas arise from a complex network of interconnected pores consisting of micropores (<2 nm), mesopores (2–50 nm) and macropores (>50 nm). ACs generally tend to have a broad range of pore sizes; however, some porosity and pore size distribution control is possible (through precursor selection and activation method), so that the majority of pores develops in a particular pore size range. As smaller pores have a higher surface-area-to-volume ratio, microporous carbons (<2 nm) tend to have higher surface areas and are popular for EDLC applications, although some mesoporosity is also advantageous to ensure good pore accessibility.

In principle, the higher the surface area of the active material, the higher the specific capacitance value of the corresponding device. In reality, this relationship is not so straightforward and several studies have shown that capacitance values and surface area do not necessarily follow a linear trend, particularly for carbon materials with a varied or very fine porosity. Aspects such as pore size distribution, material precursor, electrolyte ion size, surface wettability, and pore accessibility also need to be considered when evaluating a potential electrode material [34]. While the correlation of capacitance with surface areas derived from gas adsorption data can be a useful guide, it is not always a reliable indicator of capacitance. This can be due to the following:

- 1) Inaccuracies in the determination of surface area [54]. For example, the widely utilized BET model for the surface area determination often gives an unrealistically large surface area value for microporous materials owing to the fact that nitrogen gas is condensed in micropores (rather than simply adsorbed onto a surface).
- 2) Different precursors provide ACs with different double-layer capacitance as explained by Shi *et al.* [34]. For example, the ratio between the concentration of basal and edge carbons in the graphite structure is important as it has been found that the capacitance of edge sites is greater than that for basal carbons [66–68].
- 3) Certain activation procedures, or precursors, lead to the formation of ACs rich in heteroatoms, usually in the form of oxygen or nitrogen [69, 70]. Heteroatoms are known to contribute additional capacitance (pseudocapacitance) owing to the presence of faradic charge-transfer reactions [3, 61, 62] (e.g., quinone/hydroquinone redox couple, reversible electrosorption of hydrogen, etc.). The presence of heteroatoms also influences other carbon properties such as wettability, point of zero charge, electrical conductivity, self-discharge characteristics, and long-term performance [71].
- 4) Inaccessibility of ions to small-diameter micropores, thereby not contributing to the double-layer formation [72]. On the basis of the experimental results,

several authors agreed that pores larger than 0.5 nm are electrochemically accessible to aqueous solutions [52, 54, 73–75]. Lin and coworkers [76] utilized a form of carbon aerogel to estimate that the optimum pore size in aqueous sulfuric acid was 0.8–2 nm. Simon and coworkers [8] reported a maximum of capacitance when the size of the pores is very close to that of the ion size.

- 5) Space constrictions for charge accommodation inside the pore walls [77]. For carbon materials whose pore wall thickness is <1 nm, the two adjacent space charge regions inside the solid begin to overlap, thereby causing a saturation of capacitance.

ACs can provide varying capacitance values depending on their surface area, pore size, chemical composition, and electrical conductivity (all a function of their precursor and activation treatment(s)). In general, capacitance values ranging from 100 to 400 F g^{-1} are reported in aqueous electrolytes and around $120\text{--}150 \text{ F g}^{-1}$ in organic or IL electrolytes. Among the highest capacitance values reported for carbon, Shi [54] obtained 412 F g^{-1} for activated Spectracorp carbon microbeads (in 30% w/w KOH) and Alonso *et al.* [53] obtained 400 F g^{-1} in H_2SO_4 (aqueous). ACs can also be prepared in the form of fabrics consisting of woven carbon fibers prepared from polymeric fiber precursors (e.g., rayon or polyacrylonitrile) [78]. They are a convenient form of carbon (for electrode fabrication) and highly microporous materials with high BET surface areas, in the range of $1000\text{--}2000 \text{ m}^2 \text{ g}^{-1}$, can be readily prepared. However, the cost of these materials is higher than powdered forms of carbon and their volumetric density is also typically low.

Several studies have prepared *templated* carbons, whereby carbons can be prepared with a very uniform and narrow pore size distribution [79]. Knox and coworkers [80] established the template technique in 1986, which subsequently enabled many porous carbon materials to be designed and synthesized with narrow and controlled porosity [81]. The process consists of the infiltration of a carbon precursor into the pores of a template (usually a porous alumina, silica, or zeolite) followed by the removal of the template, which leaves a carbonaceous porous structure as an inverse replica of the template with a very uniform pore size and morphology [82]. *Mesoporous templated* porous carbon materials have been a widely investigated material for the preparation of EDLCs [9, 83, 84] as the process allows the preparation of materials with a very narrow pore size distribution, in contrast to the rather broad pore size distribution of conventional ACs. Owing to the well-interconnected porous structure in templated carbons, ion diffusion is favorable and power performance improved. However, as the number and size of available template materials is limited, it may be difficult to produce a carbon with an optimized porosity. The majority of template materials produces predominately mesoporous carbons with only moderately high surface areas and capacitance values [26, 85], although highly microporous carbons, with BET surface areas of approximately $4000 \text{ m}^2 \text{ g}^{-1}$, have also been prepared from the nanochannels of zeolites [86, 87]. Although the templated approach is promising, the cost of templated carbons may be too high to make them a commercial alternative to other low-cost porous carbon materials.

Carbide derived carbons (CDCs) are also porous carbon materials with controllable microporosity obtained by the extraction of a metal from its carbide at high temperatures [88, 89]. Testing of CDC-based electrodes in an ethylmethimidazolium bis(trifluoromethanesulfonyl)imide electrolyte provided 150 F g^{-1} [31] and around $120\text{--}135 \text{ F g}^{-1}$ in 1.5 M TEABF_4 dissolved in ACN [55]. CNTs have also been evaluated as electrode materials for EDLCs. They are interesting as they have unique properties arising from their nanotubular structure and excellent electrical characteristics. However, the capacitance values that these materials provide are typically only in the range of 20 to 80 F g^{-1} [90]. In order to improve the performance of CNTs, additional activation or surface functionalization can be undertaken and capacitance values can be improved to ~ 80 to 130 F g^{-1} [91]. Similar to other fibrous carbons, CNTs can have low volumetric densities; however, several groups are investigating the preparation of closely aligned carbon CNTs, which can subsequently be densified [92–94] or even grown directly onto a collector with improved volumetric capacitance values [91]. Aerogels and xerogels, prepared from a sol–gel synthesis route, have also been extensively evaluated in EDLCs. They generally have a mesoporous structure with a quite controllable, ordered, and uniform porosity. However, as only moderately high surface areas are achievable (e.g., $400\text{--}1000 \text{ m}^2 \text{ g}^{-1}$); only moderate capacitance values are generally reported for these materials. Some studies have highlighted that further activation of carbon aerogels leads to the formation of additional microporosity and increased capacitance; up to 220 F g^{-1} [59].

2.3.2

Pseudocapacitive Electrochemical Capacitors

Pseudocapacitance: Some materials utilize fast and reversible redox reactions at their surface [3]. This represents a different kind of capacitance contribution to double-layer capacitance. This capacitance, which can be quite significant, is not electrostatic in origin (hence the “pseudo” prefix to differentiate it from electrostatic capacitance) and occurs when an electrochemical charge-transfer process takes place to an extent limited by a finite amount of active material or available surface [3].

The most commonly investigated classes of pseudocapacitive materials are the transition metal oxides (notably ruthenium oxide), and the family of conducting polymers, such as polyaniline (PANI), polypyrrole (PPy), or derivatives of polythiophene (PTh) [95–98]. The fact that charge storage is based on a redox process means that this type of supercapacitor is somewhat battery-like (faradic) in its behavior. Porous carbons that possess a significant proportion of heteroatoms (typically oxygen or nitrogen) and/or surface functionalities can also contain a pseudocapacitive component in their overall capacitance. That is, the double-layer capacitance derived from the extended carbon surface is supplemented by the pseudocapacitive contributions arising from the redox active functionalities, thereby substantially increasing the total capacitance of the material. Further details on the composition and performance of pseudocapacitive carbons are given in Chapter 6.

2.3.2.1 Electronically Conducting Polymers

Conductive polymers are defined as organic polymers that conduct electricity. In traditional polymers such as polyethylenes, the valence electrons are bound in sp^3 hybridized covalent bonds (σ bonding) that have low mobility. Conducting polymers have a conjugated π -system of alternating single and double bonds that is formed by the overlap of carbon p_z orbitals (leading to a contiguous backbone of sp^2 -hybridized carbon centers). An unpaired valence electron on each sp^2 center resides in a p_z orbital, which is orthogonal to the other three σ bonds, and forms a bonding π band and corresponding antibonding π^* band. In the presence of a suitable oxidant, an electron can be removed from this band to form a positive “hole” (electron deficiency), and the remaining electrons within this partially emptied band become more mobile, and hence conductive. In order to maintain electroneutrality, the polymer electrode must also take up ions in a process referred to as *polymer doping* (p-doping), which is an ion insertion process that raises the redox state and electronic conductivity of the polymer [99]. In principle, these same conjugated polymers can also be reduced, which adds an electron to an otherwise unfilled band (n-doping). In practice, most conductive polymers can be doped oxidatively to give p-type materials but the formation of n-doped polymers is less common [99, 100].

Electronically conducting polymers (ECPs) have been extensively studied as electrode materials for ECs and several reviews are available [101–106]. ECPs are attractive owing to their ability to store a significant amount of energy, low cost, ease of preparation, lightweight, and their flexible nature that allows considerable design flexibility. While double-layer capacitors store energy on the surface of the material, ECPs store charge throughout the entire (accessible) volume, via a fast doping/dedoping exchange of ions, and hence the amount of energy that can be stored with ECPs is generally higher than with EDLC-type materials. As ECP-based materials store charge by doping/dedoping (faradic), rather than adsorption/desorption (non-faradic), they are also prone to lower rates of self-discharge.

ECPs can be p-doped with anions when oxidized and n-doped with cations when reduced (Figure 2.6). Capacitors made solely from conducting polymers can be categorized into four types [106]: Type I (symmetric) uses the same p-dopable polymer for both electrodes; Type II (asymmetric) uses different p-dopable polymers on each electrode; Type III (symmetric) uses the same polymer as the p-doping (positive electrode) and n-doping (negative electrode) electrodes, and Type IV (asymmetric) uses different polymers as p-doping and n-doping electrodes. Therefore, Type I and III devices do not have any inherent polarity but the other two types are polar devices (fixed positive and negative electrodes) and will need to be connected appropriately.

When charging Type I devices, the positive electrode is fully oxidized and the negative electrode remains neutral, giving a potential difference (the cell voltage) of around 0.5–0.75 V [106]. When fully discharged, both electrodes are in the half-oxidized state and hence only 50% of the total polymer's p-doping capacity can be utilized. In Type II devices, the polymer with the more positive oxidation potential

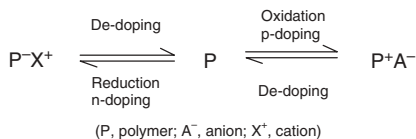


Figure 2.6 Doping and dedoping of counterions in ECPs.

is used as the positive electrode and the one with the less positive oxidation potential is used as the negative electrode. In the charged state, the positive electrode is fully oxidized, the negative electrode is completely neutral, and the cell voltage is typically higher – around 1.0–1.25 V. When fully discharged, the positive electrode is less than 50% oxidized and the negative electrode is more than 50% oxidized. Thus, approximately 75% of the polymer's p-doping capacity can be utilized (depending on the polymer combination employed). Owing to their relatively low voltages, Type I and II devices generally utilize aqueous-based electrolytes.

When Type III and IV ECP devices are fully charged, the positive electrode is fully oxidized (p-doped) and the negative electrode is fully reduced (n-doped) and the cell voltage is in the range of 1.3–3.5 V [106]. In the discharged state, both electrodes become neutral and this means that 100% of the polymer's p-doping and n-doping capacity can be utilized. Therefore, the amount of energy that can be stored in these types of devices generally follows the order: Type I < Type II < Type III ≤ Type IV. Note that the term fully oxidized, or doped, refers to the maximum achievable doping level of the polymer; which is an inherent characteristic of the polymer.

A brief literature summary of ECPs that have been evaluated as active electrode materials in ECs is presented in Table 2.4. The major classes of conducting polymers evaluated are PANI, PPy, PTh, and derivatives of PTh. Of these, only PTh-based materials were tested in Type III and IV devices mainly because of their ability to be n-doped. As the reduction (n-doping) potentials of PANI and PPy are more negative than the decomposition potential of the common organic solvents, such as ACN and PC, these polymers have been tested only as Type I and II devices. The main attributes and performance of selected ECPs are discussed subsequently.

Polyaniline (PANI) PANI is one of the more extensively studied ECPs for Type I devices owing to its ease of preparation (by both chemical and electrochemical methods) from aqueous electrolytes, high doping level (~0.5), good electrical conductivity ($0.1\text{--}5\text{ S cm}^{-1}$), high specific capacitance, and good environmental stability [99, 101]. PANI prepared by electrochemical methods usually displays higher specific capacitance values (as high as 1500 F g^{-1}) than materials prepared by chemical methods (typically around 200 F g^{-1}). This variation in capacitance is related to the polymer morphology, thickness of the electrode, and the presence (if any) of binder. PANI shows higher capacitance in aqueous acidic electrolytes as it requires protons to be charged (doped/exchange) and discharged; therefore, it shows improved electroactivity in protic solvents or protic ILs [165]. PANI prepared by electrochemical methods shows good cycle life in protic electrolytes, however,

Table 2.4 Reported performance of supercapacitor cells with ECP-based electrodes.

Polymer	Electrolyte	Positive–negative electrode configuration	V_{\max}	C ($F\ g^{-1}$)	E ($Wh\ kg^{-1}$)	P ($W\ kg^{-1}$)	Cycles	Capacity fade (%)	References
PANI	Aqueous	PANI-PANI	0.5–1.2	120–1530	9.6–239	59–16000	1 500	1–13	[107–119]
PANI	Nonaqueous	PANI-PANI	1.0	100–670	70–185	250–7500	9 000	9–60	[120–126]
PANI	Nonaqueous	PANI-PPy	1.0–1.2	14–25	1–4.9	150–1200	4 000	60	[120, 127]
PANI	Nonaqueous	PANI-AC	3.0	58	4.9	240–1200	1 000	60	[128]
PPy	Aqueous	PPy-PPy	0.7–2.0	40–588	12–250	—	10 000	9–40	[129–136]
PPy	Nonaqueous	PPy-PPy	1.0–2.4	20–355	10–25	2–1000	10 000	11–45	[137–142]
PTh	Nonaqueous	PTh-PTh	3.0	1.6–6.0	—	—	5 000	—	[143]
PTh	Nonaqueous	PTh-PMT	3.2	5.7	9.7	990	5 000	—	[143]
PMT	Nonaqueous	PMT-PMT	3.0	220	20	—	12 500	—	[144]
PMT	Nonaqueous	PMT-AC	3.0	28–39	10–40	500–4 344	10 000	40	[97, 145–147]
PMT	Ionic liquid	PMT-AC	1.9–3.65	19–225	~30	14 000	16 000	46	[148–151]
PMT	Nonaqueous	PMT-LTO	3.0	—	14	1 000	10 000	49	[152]
PEDOT	Aqueous	—	0.8–1.25	100–250	—	—	70 000	19	[153–156]
PEDOT	Nonaqueous	PEDOT-PEDOT	0.8–2.7	121	1–4	35–2 500	—	—	[157, 158]
PEDOT & PPrDOT	Ionic liquid	PEDOT-PPrDOT	0.5	130	—	—	50 000	2	[159]
PEDOT	Nonaqueous	PEDOT-AC	3.0	110	—	—	1 000	49	[160]
PFPT	Nonaqueous	PFPT-PFPT	3.0	17	39	35 000	—	—	[101, 161, 162]
PFPT	Nonaqueous	PFPT-AC	3.0	—	48	9 000	—	—	[163]
PFPT	Nonaqueous	PFPT-LTO	3.0	—	10–16	2 500	1500	14	[164]

PANI, polyaniline; PPy, polypyrrole; PTh, polythiophene; PMT, poly(3-methyl thiophene); PEDOT, poly(3,4-ethylenedioxythiophene); PPrDOT, poly(3,4-propylenedioxythiophene); PFPT, poly(4-fluorophenyl-3-thiophene); LTO, $Li_4Ti_5O_{12}$; and V_{\max} , maximum cell voltage or potential window.

limited data is available for PANI-based devices that have been cycled for more than 10 000 cycles. The repeated volume changes of the polymer electrode that accompanies the doping and dedoping of counterions during the charge/discharge process is reported to cause mechanical failure of the polymer during extended cycling. Another issue with PANI is that it is susceptible to oxidative degradation, even after slight overcharging, leading to poor performance. PANI can be modified to be more stable toward overoxidation by forming poly(*N*-methyl aniline) [166], where one proton in the NH_2 group is substituted by a methyl group. This stabilizes the positive charge created on the nitrogen during oxidation and improves the stability of polymer against electrochemical degradation.

Polyppyrrrole (PPy) PPy is considered to be one of the most promising electrode materials for both Type I and Type II (where it is used as cathode) devices. Unlike PANI, it shows good electroactivity in aprotic, aqueous, and nonaqueous electrolytes; however, its specific capacitance is generally lower than PANI (in the range of 100–500 F g^{-1} ; see Table 2.4). The reduced capacity of PPy is mainly attributed to the more dense morphology of the PPy, which leads to limited electrolyte access to the interior of the polymer, especially for thicker electrode coatings [167]. The best performing PPy electrodes are generally prepared as thin-film electrodes as increasing the material thickness (loading/density) leads to performance deterioration. Table 2.4 also indicates that PPy displays a higher specific capacitance in aqueous electrolytes than in nonaqueous electrolytes attributable to the higher ionic conductivity of the aqueous electrolytes. A PPy electrode material, prepared by galvanostatic pulse deposition, has been reported to produce an open morphology polymer, which displayed a specific capacitance of 400 F g^{-1} [129]. Subsequent galvanostatic cycling of the polymer (as a Type I device), however, displayed poor cycle life performance with 40% loss of capacitance after 4000 cycles. When PPy is used as a negative electrode in Type II devices, along with PANI as a positive electrode, a specific capacitance in the range of 14–25 F g^{-1} and the energy and power densities of around 4 Wh kg^{-1} and 150–1200 W kg^{-1} , respectively, are achieved [120, 127]. However, its cycle life is still limited.

Polythiophene (PTh) and Derivatives Unlike PANI and PPy, PTh is both p- and n-dopable (Type III). However, the n-doping process in PTh occurs at very negative potentials, close to the solvent decomposition potentials of common electrolytes. The polymer also exhibits poor conductivity and lower specific capacitance in the n-doped form, relative to its p-doped form [103, 145]. As a consequence, it has a high self-discharge rate and exhibits poor cycle life in devices. In order to overcome these limitations, several derivatives of PTh, with lower band gaps (i.e., n-doping occurs at less negative potentials), have been prepared [160, 168]. By substitution at the 3-position on the thiophene ring, with phenyl, ethyl, alkoxy, or other electron withdrawing groups, the stability of the PTh derivative is markedly improved [169]. Notable PTh derivatives include poly(3-methylthiophene) (PMT), poly(4-fluorophenyl-3-thiophene) (PFPT), and poly(3,4-ethylenedioxythiophene) (PEDOT), (Table 2.4).

A popular PTh derivative is PEDOT as the polymer has high conductivity in the p-doped state ($\sim 300\text{--}500\text{ S cm}^{-1}$), a wide potential window (1.2–1.5 V), high capacitance, good charge mobility (fast electrochemical kinetics), and good thermal and chemical stability (good cycle life) [160]. A device assembled with PEDOT as the positive electrode and poly(3,4-propylenedioxy thiophene) as the negative electrode (Type I), using an IL electrolyte, is reported to show good cyclability with 2% capacitance loss after 50 000 cycles [159]. However, owing to the high molecular weight of the monomer, and a low doping level of ~ 0.33 , PEDOT has a relatively modest specific capacitance of around 100 F g^{-1} [157].

ECP Composites In order to improve the performance of ECP-based electrodes in ECs, ECPs are often prepared as composites with carbons [107–110], CNTs [103, 170], or even metal oxides [171–173]. Composites with carbons are particularly effective in improving the specific capacitance and power capability of the electrode. The presence of carbon in the composite makes the electrode more electrically conducting, particularly while the polymer is in its less conductive neutral (undoped) state. In the case of ECP/CNT composite electrodes, there are reports that a charge-transfer complex between the ECP and CNT exists owing to the electron donating and accepting nature of ECP and CNT. The presence of CNT in the composite has been demonstrated to improve the cycle life of ECPs in supercapacitor devices [170]. The use of CNTs or other conductive carbonaceous additives with ECPs greatly improves the performance of ECPs by increased electrode conductivity, improved electrolyte percolation into the bulk active material, increased utilization of the ECP, and greater mechanical strength; and the carbon itself may also contribute additional double layer capacitance [174]. A detailed review on ECP/CNT composite electrodes for electrochemical applications is available [103].

ECP electrodes may also be prepared as composites with appropriate metal oxide materials. Combining PPy with iron oxide (Fe_2O_3) achieved a specific capacitance of around 400 F g^{-1} [171]. A PANI/Nafion composite has been used as a matrix for electrochemically depositing hydrous RuO_2 and the resultant composite electrode showed a specific capacitance of 325 F g^{-1} with 80% of this capacitance retained after 10 000 cycles at a scan rate of 500 mV s^{-1} , between -0.2 and 0.6 V [172]. From a systematic study, Sivakkumar *et al.* [173] have shown that the best way to improve the utilization of MnO_2 for capacitor applications is by preparing a ternary composite of CNT/polypyrrole/ MnO_2 . The MnO_2 in this ternary composite has been shown to have improved dispersion and enhanced electrochemical utilization when compared with binary composites such as CNT/ MnO_2 and polypyrrole/ MnO_2 . The ternary composite electrode delivered a specific capacitance of 281 F g^{-1} and retained 88% of the initial capacitance after 10 000 cycles.

ECP-Based Asymmetric Electrochemical Capacitors An ECP asymmetric EC is a device that utilizes a p-doping ECP positive electrode paired with an AC negative electrode. This configuration eliminates the difficulty in identifying a stable n-doping ECP electrode material as is the case with Type III supercapacitors. Several ECPs including PMT [97, 145–149], PFPT [163], PEDOT [160], PANI [128],

have been successfully evaluated as ECP–AC asymmetric hybrid devices that can operate at 3 V in nonaqueous electrolytes. Balancing the ratio of negative and positive electrode material (by capacity rather than weight) is an important parameter for optimal performance of asymmetric devices as the specific capacitance and the potential “swing” range of each electrode differs significantly. When the capacity of the AC electrode is limiting, the asymmetric device will show a close-to-linear charge/discharge curve, similar to that of a typical EDLC as most of the voltage swing will occur across the AC electrode. Conversely, when the capacity of the AC electrode is greater, a more battery-like charge/discharge curve is observed indicative of the redox behavior of the ECP.

Mastragostino *et al.* [97] have reported that a PMT/AC asymmetric device can deliver comparable performance to commercially available EDLCs, in terms of specific energy and power, although information on its cycle life is limited. Impedance analysis of their device also indicated that the PMT electrode exhibits lower ESR ($2 \Omega \text{ cm}^{-2}$) compared with the AC electrode ($12 \Omega \text{ cm}^{-2}$). Laforgue and coworkers [163] constructed PFPT/AC asymmetric laboratory test cells (4 cm^2 plate area) and galvanostatically cycled them between 1.2 and 3 V. The individual PFPT and AC electrodes exhibited specific capacitances of 245 and 130 F g^{-1} , respectively and, in combination, the cell delivered a maximum energy of 48 Wh kg^{-1} and power of 9 kW kg^{-1} (active material basis). Larger packaged prototypes in a PFPT/AC configuration were galvanostatically cycled at a current rate of 5 A between 1 and 3 V over 8000 cycles. These packaged prototypes achieved an initial maximum capacitance in the range of 2000–2600 F, which decreased by 50% after the initial 100 cycles and thereafter stabilized over the next 8000 cycles. PMT/AC asymmetric devices utilizing room-temperature IL electrolytes have also been evaluated [148–150]. A cell voltage of 3.65 V is achievable with these electrolytes and specific energy and power densities of up to 31 and 14 kW kg^{-1} (active material basis) have been reported [148, 149]. A 49% loss of initial capacitance, after 16 000 cycles was also observed.

While the specific capacitance of many p-doping ECPs is much higher than carbon-based EDLCs, their cycle life is currently limited (although still better than most reversible batteries). This is largely attributed to the mechanical failure of the polymer electrode, caused by the repetitive shrinkage/swelling, occurring as a result of the doping/de-doping of counter ions during charging and discharging. However, composite ECP materials and asymmetric devices that utilize p-dopable ECPs as the positive electrode and AC as the negative electrode show some promise. The cycle life of the asymmetric devices can also be improved when the positive ECP electrode voltage is controlled and operates in narrow potential window, during charge/discharge, by means of adjusting the electrode capacity ratios appropriately.

Further improvements to the intrinsic cycle life performance of the ECP are likely to be centered on improved composites with carbonaceous materials, especially with CNTs, the preparation of copolymers with facile open morphology and the use of IL electrolytes, both for the synthesis of ECPs and as electrolytes in the ECP-based devices. Despite opportunities for ongoing work, research interest in ECs based on conducting polymers is generally decreasing.

2.3.2.2 Transition Metal Oxides

Some metal oxides, notably RuO_2 , MnO_2 , PbO_2 , NiO_x , and Fe_3O_4 , undergo fast reversible redox reactions at their surface, displaying strong pseudocapacitive behavior. These oxides have been extensively studied as their capacitance usually greatly exceeds the double layer capacitance achievable with carbon materials. The development of pseudocapacitors has been driven by the desire to increase the specific energy of conventional EDLCs while retaining comparable the high power and long-term cyclability of EDLCs. However, as their charge storage mechanism is based on redox processes, similar to batteries, these materials can also suffer from poor long-term stability and cycle life. A significant amount of research on metal-oxide-based EC targets strategies to improve the long-term cyclability of these devices, which is often achieved through the formation of metal oxide composite materials or by utilizing asymmetric cell designs [175]. Composites of carbon with redox active materials, prepared by the insertion of electroactive particles of transition metal oxides into the carbon material [62], have been evaluated as electrode materials for ECs and show improved performance. Similarly, the construction of “asymmetric” devices whereby a faradic metal oxide electrode is matched to a non-faradic carbon electrode has been shown to be very promising [176]. Both these approaches can produce very high capacitance devices, as both double-layer and pseudocapacitance contributions are utilized, and the cyclability of the redox electrode can be improved by restricting its operating state of charge and voltage ranges.

An asymmetric EC contains two dissimilar electrodes and is a class of hybrid supercapacitor. The most common design typically consists of a “battery-type” electrode (e.g., a faradic or intercalating metal oxide) and an EDLC-type electrode (high surface area carbon) as shown schematically in Figure 2.7. The selection of the battery electrode is determined by the proximity of its potential to either the low or high limit of electrochemical window, as this can maximize the operational voltage and the energy density of the cell. As the voltage swing of the cell during charge/discharge occurs mainly across the carbon, the battery electrode experiences a relatively low depth of discharge and provides the conditions required for a high cycle life. The charge storage mechanisms in such devices is a combination of purely electrostatic adsorption–desorption at the non faradic (carbon) electrode and fast, reversible faradic (pseudocapacitive) reactions at the surface (and near surface) of the redox active electrode.

As with conventional capacitors, the capacitance of an asymmetric cell is also determined according to Eq. (2.6). In a symmetric device, the specific capacitance of the positive electrode is close to that of the negative electrode (i.e., $C_+ \approx C_- \approx C_e$) so that the capacitance of the complete cell becomes half the capacitance of each individual electrode; that is, $C_{\text{cell}} = C_e/2$. However, in an asymmetric device, the specific capacitance exhibited by the nonpolarizable faradic electrode (C_+) is usually much higher than the capacitance of the polarizable non-faradic (carbon) electrode (C_-), so the total capacitance of the asymmetric device becomes $C_{\text{cell}} \approx C_-$ (since $C_+ \gg C_-$). Thus, the total capacitance of the asymmetric device is almost doubled that exhibited by a symmetric EDLC with similar-sized carbon electrodes, thereby

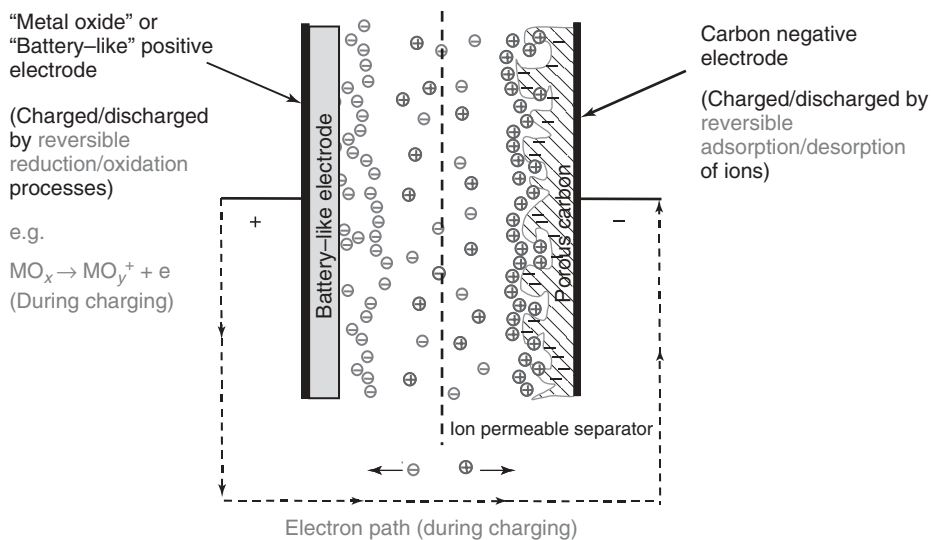


Figure 2.7 Schematic of a charged asymmetric electrochemical capacitor (e.g., PbO_2-AC).

also increasing the specific energy density of the device. Pell and Conway [175] have summarized, in some detail, the key parameters required in the design and optimization of asymmetric EC. Some of the main requirements to be considered are as follows:

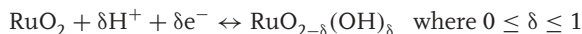
- 1) The faradic and non-faradic electrodes should be selected with a high charge/discharge rate capability.
- 2) The faradic and non-faradic electrodes should be selected such that their potentials are close to either the low or high end of the operating potential window, which will maximize the operational voltage and energy density of the asymmetric cell.
- 3) As the faradic electrodes exhibit much higher specific capacitance than the non-faradic electrode, this mismatch can be compensated for gravimetrically by balancing the active masses of the two electrodes, usually by using a thicker/dense non-faradic electrode.
- 4) The non-faradic electrode should have highest possible electronic conductivity, surface area, and porosity.

Various redox-active systems such as transition metal oxides, metal hydroxides, nitrides, and mixtures thereof, have been researched as potential electrode materials for asymmetric capacitors and/or pseudocapacitors. Selected materials and configurations are briefly discussed here.

Ruthenium Oxide (RuO_2) Ruthenium oxide has been extensively studied as an electrode material for ECs owing to its ideal capacitive behavior [95, 177–183] in terms of

- high theoretical pseudocapacitance ($>1300 \text{ F g}^{-1}$)
- high electrochemical reversibility
- long-term cyclability

The charge storage mechanism of RuO_2 in an aqueous electrolyte occurs via electrochemical protonation shown in the reaction:



over a voltage window of $\sim 1.2 \text{ V}$ [3, 184, 185].

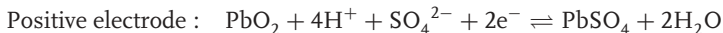
Hydrous forms of RuO_2 ($\text{RuO}_2 \cdot x\text{H}_2\text{O}$) have been reported to exhibit higher specific capacitance ($\sim 720 \text{ F g}^{-1}$) than the capacitance obtained for its crystalline counterpart ($\sim 350 \text{ F g}^{-1}$) in an acidic electrolyte [177]. McKeown *et al.* [185] proposed that the high capacitance values of $\text{RuO}_2 \cdot x\text{H}_2\text{O}$ can be ascribed to its high protonic and electronic conductivity, which facilitates the electrochemical redox reactions in RuO_2 . A symmetric pseudocapacitor constructed from hydrous RuO_2 using $1 \text{ M H}_2\text{SO}_4$ aqueous electrolyte exhibited a maximum specific capacitance of 734 F g^{-1} and delivered specific energies of 25 Wh kg^{-1} at a specific power of 92 W kg^{-1} and 12 Wh kg^{-1} at 21 kW kg^{-1} [183].

The high cost of ruthenium has limited the utilization of RuO_2 in commercial devices and several strategies have been pursued to reduce costs through the formation of mixed metal oxides of RuO_2 ($\text{Ru}_{1-x}\text{M}_x\text{O}_2$), or composites of RuO_2 with conducting polymers, carbon nanotubes, or high surface area carbon [179, 180, 186–194]. The formation of RuO_2 composites has been shown to enhance the electronic conductivity of the material and improves the utilization of RuO_2 [191–194]. A symmetric pseudocapacitor prepared from RuO_2 deposited onto PEDOT in an acidic electrolyte delivered a specific capacitance of 420 F g^{-1} (based on RuO_2 /PEDOT composite mass) and about 930 F g^{-1} (based on the active mass of RuO_2 only), which corresponds to an energy density of 27.5 Wh kg^{-1} over the potential range of $0\text{--}1.0 \text{ V}$ [190]. Wang and coworkers [195] also constructed an asymmetric capacitor comprising a composite of RuO_2 with TiO_2 nanotubes as the positive electrode and AC as the negative electrode in an alkaline KOH electrolyte. This asymmetric device achieved an energy density of 12.5 Wh kg^{-1} (unpacked) and power density of 150 W kg^{-1} over the potential range of $0\text{--}1.4 \text{ V}$. By depositing ruthenium oxide particles on amorphous carbon nanofibers, Barranco *et al.* [196] have prepared composite materials with exceptionally high capacitance values of 1000 F g^{-1} .

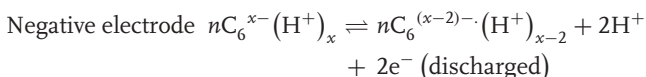
Lead Dioxide (PbO_2) The well-known lead dioxide (PbO_2)-based redox system used in lead-acid battery technology has also been investigated as a promising electrode material for pseudocapacitors or asymmetric ECs owing to its relatively low cost and high energy-storing capability [197, 198]. Kazaryan *et al.* [199] have undertaken mathematical modeling of the asymmetric PbO_2 /AC system and predict a maximum specific energy density of 24 Wh kg^{-1} .

The Russian firms, Eskin and ESMA, were one of the earliest groups to present an asymmetric capacitor technology consisting of a nonpolarizable positive electrode,

made of PbO_2 and lead sulfate (PbSO_4), and a polarizable AC as the negative electrode in aqueous H_2SO_4 electrolyte [200, 201]. During charge and discharge, the positive electrode undergoes the same common half reaction based on the double sulfate theory for lead-acid batteries – that is, lead dioxide reacts with acid and sulfate ions to form lead sulfate and water:



However, instead of having a lead counter electrode that reacts with sulfate to form lead sulfate, a high-surface-area AC electrode, which acts to adsorb and desorb protons (H^+ ions) in solution, is utilized:



The resulting device offers an energy density approaching lead-acid batteries, coupled with far longer cycle life and higher power.

Burke have also undertaken significant research on asymmetric PbO_2/AC devices. Laboratory prototypes developed and tested in their lab exhibited specific energy and power densities of 13.5 Wh kg^{-1} and 3.5 kW kg^{-1} , respectively, when cycled between 1.0 and 2.25 V [197]. These asymmetric prototypes showed an ESR as low as $0.12 \Omega \text{ cm}^2$ and an RC time constant of 0.36 s, which is comparable to that obtained for a symmetric carbon supercapacitor. Recently, Gao and coworkers [202] also fabricated a PbO_2/AC asymmetric capacitor in which electrodeposited thin films of PbO_2 on Ti/SnO_2 substrates were used as the positive electrode and high-surface-area AC as the negative electrode in H_2SO_4 . The asymmetric device, when galvanostatically cycled between 0.8 and 1.8 V, showed specific capacitances of 79.9 and 74.1 F g^{-1} at current densities of 0.75 mA cm^{-2} (1.2 C-rate) and 10 mA cm^{-2} (16 C-rate), respectively; which correspond to specific energies of 26.5 and 17.8 Wh kg^{-1} (active material basis), respectively. This asymmetric PbO_2/AC device retained 83% of its initial capacitance after 3000 charge/discharge cycles (at 4 C-rate).

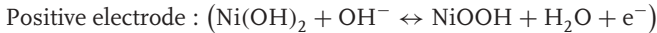
Axion Power International manufactures a *PbC Ultracapacitor*, which is described as a *multicelled asymmetrically supercapacitive lead-acid-carbon hybrid battery* [203]. These devices deliver 20.5 Wh kg^{-1} and can withstand more than 1600 deep discharge cycles (charge–discharge every 7 h to a 90% depth of discharge). In comparison, most lead-acid batteries designed for deep discharge applications can only survive 300–500 cycles under these operating conditions. Recently, Lam and coworkers have also developed a *hybrid lead acid battery* that combines an asymmetric supercapacitor (an “enhanced-power negative electrode”) and a lead-acid battery in a single unit [204]. The device, referred to as an *UltraBattery*, utilizes a conventional PbO_2 positive electrode with a negative lead electrode that also incorporates a significant amount of AC. The incorporation of the carbon improves the stability of the negative electrode and the overall performance of the device. The charge and discharge power of the UltraBattery is reported to be 50% higher and its cycle life at least three times longer than that of a conventional valve-regulated lead-acid battery [204].

Nickel Oxide (NiO) and Nickel Hydroxide (Ni(OH)₂) Among the reported transition metal oxides, porous nickel oxide has shown good electrochemical performance as an electrode material for pseudocapacitors [205–209]. In addition to some double-layer capacitance, additional pseudocapacitance of NiO arises from the surface faradic redox reaction between Ni²⁺ and Ni³⁺ given by



where z is the fraction of active Ni sites involved in the faradic redox reaction. Kim and coworkers claimed that NiO prepared by electrodeposition of Ni(OH)₂ films followed by heat treatment up to 300 °C exhibited higher specific capacitance, in the range of 200–278 F g⁻¹, than any other synthesis method [210, 211].

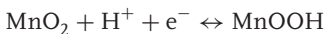
One of the earliest asymmetric ECs based on Ni(OH)₂ was reported by ESMA wherein a sintered Ni(OH)₂ was used as the positive and woven AC fibers, or powder, as the negative electrodes in an alkaline KOH electrolyte [212]. The reaction at the positive electrode is the well known Ni(OH)₂/NiOOH couple that also takes place in NiCd and NiMH batteries:



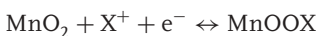
The Ni(OH)₂/NiOOH charge–discharge process is a solid-state, proton intercalation/deintercalation reaction, whereby both electrons and protons are exchanged and the processes are considered to be controlled by the bulk solid diffusion of protons [213–215].

Ganesh *et al.* [216] constructed a similar Ni/AC asymmetric supercapacitor, using 6 M KOH electrolyte, that delivered a specific energy of 35 Wh g⁻¹ at a power of 330 W kg⁻¹ between 0 and 1 V and an ESR in the range of 1–3 Ω. Recently, Liu and coworkers [208] reported a 3 V asymmetric capacitor comprising nickel-based mixed rare-earth metal oxide (NMRO; an alloy of Ni, La, Ce, Pr, and Nd) as the positive electrode and AC as the negative electrode in a room temperature IL electrolyte. The NMRO/AC asymmetric device achieved a high energy density of 50 Wh kg⁻¹ and with a power density of 458 W kg⁻¹ over 500 cycles. The enhanced energy density can be attributed to the wide electrochemical window (>3 V) of the 1-Butyl-3-methylimidazolium hexafluorophosphate (BMIM-PF₆) electrolyte.

Manganese Dioxide (MnO₂) Similar to PbO₂ and NiO, MnO₂ has been reported as an attractive, potential replacement for hydrous ruthenium oxide in electrochemical pseudocapacitors owing to its low cost and environmentally benign nature [217–224]. The pseudocapacitive charge storage mechanism in MnO₂ mainly occurs via the insertion and deinsertion of protons:



Many researchers [218, 223, 225] have proposed that MnO₂ also exhibits pseudocapacitance via surface adsorption of electrolyte cations (such as Li⁺, Na⁺, K⁺, etc.), depending on the electrolyte used, according to



Toupin and coworkers [223], have also postulated that the pseudocapacitive charge storage mechanism of MnO_2 is surface layer limited, possibly due to the difficulty of protonic or cationic diffusion in the bulk of the MnO_2 , resulting in only partial utilization of the active material. In order to maximize the specific capacitance of MnO_2 several treatments have been evaluated including the surface modification of MnO_2 , the preparation of binary oxides of manganese, and the preparation of hybrid nanoarchitected MnO_2 [223, 226–228]. While considerable performance variations exist, in neutral aqueous electrolytes coarse powdered MnO_2 generally shows a specific capacitance of around 150 F g^{-1} within an operating voltage window of $\sim 1 \text{ V}$.

Hong and coworkers [229] have constructed an asymmetric capacitor with $\alpha\text{-MnO}_2 \cdot n\text{H}_2\text{O}$ as the positive electrode paired with an AC negative electrode in a neutral aqueous KCl electrolyte. The device delivered an energy density of 28.8 Wh kg^{-1} , a power density of 0.5 kW kg^{-1} , and a 7% capacitance loss over 100 charge/discharge cycles. In an asymmetric configuration, MnO_2 -based devices can operate over a larger potential window of around 1.8–2.0 V in aqueous media (such as KCl and K_2SO_4) and therefore can achieve a higher energy density. Asymmetric supercapacitors, utilizing MnO_2 as the positive electrode and a conducting polymer, such as PEDOT, as the negative electrode, have also shown good performance with a specific energy of 13.5 Wh kg^{-1} and good power density [230]. The reported energy and power density for asymmetric MnO_2/AC devices are 10 Wh kg^{-1} and 3.6 kW kg^{-1} , respectively [231].

Both symmetric and asymmetric MnO_2 -based supercapacitors have shown a gradual capacity fade over the first 5000 cycles; possibly due to dissolution of the MnO_2 electrode material [232]. Yuan and coworkers [233] evaluated the electrochemical performance of a hybrid nanostructured manganese dioxide/AC supercapacitor in 1 M LiOH and 1 M KOH electrolytes. MnO_2/AC hybrid cells with 1 M LiOH electrolyte have shown a superior electrochemical performance compared to that obtained with 1 M KOH electrolyte, when charged/discharged over a voltage range of 0.5–1.5 V, presumably due to the co-intercalation of Li. The poor cycling performance of hybrid MnO_2/AC cell with 1 M KOH electrolyte was linked to the formation of inactive Mn_3O_4 during the discharge process.

2.3.2.3 Lithium-Ion Capacitors

Lithium Titanate (LTO) The use of lithium titanate, $\text{Li}_4\text{Ti}_5\text{O}_{12}$ (LTO) as an electrode material for asymmetric capacitors has been well demonstrated by Amatucci *et al.* [176]. LTO was first recognized by Ohzuku [234] as an excellent Li intercalating spinel anode material for Li-ion battery application owing to its zero-strain properties (i.e., negligible volume change on lithium intercalation/deintercalation). Nanostructured LTO has been reported to exhibit a specific capacity of $>150 \text{ mAh g}^{-1}$ with high rate capability and improved cyclability compared to coarse LTO. The asymmetric LTO/AC capacitor, created by Amatucci's team, is a nonaqueous device based on high-surface-area AC at the positive electrode and LTO as the negative electrode in 1 M LiPF_6 in EC:DMC (2 : 1 v/v) electrolyte solution. The device exhibits an unpackaged energy density of 25 Wh kg^{-1} and

packaged energy density of 10.4 Wh kg^{-1} and can maintain 90% of its initial capacity over 5000 cycles [235]. The electrochemical performance of larger LTO/AC prototypes were also evaluated using impedance spectroscopy (at 1000 and 0.1 Hz) at various operating voltages. The energy and power density values remained fairly stable up to 2.8 V, but were accompanied by a gradual decrease at 2.9 and 3.0 V. Unpackaged energy density values of 17 Wh kg^{-1} (constant current) and 11.8 Wh kg^{-1} (constant power) were also reported. A 500 F LTO/AC asymmetric device has also shown good performance over 10 000 cycles.

Lithium Manganese Oxide Spinel lithium manganese oxide (LiMn_2O_4) has been reported as a possible Li intercalating cathode material for Li-ion batteries [236]. Recently, Wang and coworkers [237] constructed an asymmetric capacitor comprising LiMn_2O_4 as the positive and AC as negative electrode in a 1 M Li_2SO_4 aqueous electrolyte. The charge storage mechanism of this asymmetric capacitor takes place through the faradic and nonfaradic reactions associated with the transfer of Li-ions between the two electrodes. The LiMn_2O_4 /AC asymmetric cell delivered a specific energy of 35 Wh kg^{-1} with a power density of 100 W kg^{-1} , losing only 5% of the initial capacity over 20 000 cycles [237, 238]. The self discharge of the AC/ LiMn_2O_4 device, however, was found to be high, especially at elevated temperatures where the AC electrode was observed to be a major contributor to the self-discharge. The rate of self-discharge was lower in polymer gel electrolytes than that observed in 1 M Li_2SO_4 solution because of the high viscosity of the polymer, which hinders the ion transport through gel electrolyte.

Li *et al.* [239] demonstrated a 5 V nonaqueous asymmetric EC with nickel-doped LiMn_2O_4 ($\text{LiNi}_x\text{Mn}_{2-x}\text{O}_4$) as the positive electrode coupled with AC as the negative electrode in 1 M LiPF_6 in an EC:DMC (1 : 2 V/v) electrolyte. Cycle life testing of the AC/ $\text{LiNi}_x\text{Mn}_{2-x}\text{O}_4$ cell indicated about 20% capacity loss after 1000 cycles when charged/discharged at 10 C-rate over a potential range between 0 and 2.8 V. The cell achieved a specific energy density of 55 Wh kg^{-1} (active material basis). Sun and coworkers [240] also fabricated an asymmetric capacitor wherein layered $\text{Li}[\text{Ni}_{1/3}\text{Co}_{1/3}\text{Mn}_{1/3}]\text{O}_2$ was employed as the positive electrode and AC as the negative electrode with 1 M LiBF_4 in PC electrolyte. Asymmetric cells of $\text{Li}[\text{Ni}_{1/3}\text{Co}_{1/3}\text{Mn}_{1/3}]\text{O}_2$ /AC cycled between 0.2 and 2.2 V at 15 C-rate (1.6 A g^{-1}) exhibited relatively high initial capacitances of $50\text{--}60 \text{ F g}^{-1}$; however, these asymmetric cells only retained 80% of their initial capacity after 500 charge/discharge cycles.

Dual Carbon Lithium-Ion Capacitors (LICs) The so-called dual carbon type of lithium-ion capacitors (LICs) utilize a high-surface-area AC material as the positive electrode and a lithium-ion intercalating carbon material (such as graphite or coke) as the negative electrode. They are capable of storing about five times more energy than conventional EDLCs while maintaining good power and long cycle life characteristics [176, 241–250]. During charge/discharge, lithium-ion intercalation/deintercalation occurs within the bulk of the negative electrode, whereas anion adsorption/desorption occurs on the surface of the AC positive electrode. As the latter process on the positive AC electrode is non-faradic, and

relatively fast in comparison with the lithium-ion exchange process at the negative electrode, the power capability of the LIC will generally be determined, or limited, by the rate capability of the negative electrode.

Yoshino *et al.* [243] utilized a composite electrode, prepared by heat treatment of an AC with pitch, as the negative electrode in their device. The lithium-ion intercalation/deintercalation of the negative electrode was shown to occur in a potential range similar to that of graphite but with improved kinetics. This cell operated in the potential window of 2.0–4.0 V and its power (2.2 kW l^{-1}) and energy density (20 Wh l^{-1}) has been claimed to be two to three times higher than EDLCs. This device also displayed an impressive cycle life maintaining the same discharge capacity for at least 100 000 cycles. Other non-graphitizable carbons [244], template-synthesized mesoporous carbons [245], and disordered carbons [246] have also been shown to perform well as a negative electrode in LICs. A disadvantage of semi-crystalline forms of graphite is that the lithium-ion intercalation/deintercalation process occurs over a wide voltage range (somewhat similar to the voltage changes associated with the charge/discharge of EDLC electrodes), which leads to a steep decrease in cell voltage (during discharge) and a corresponding decrease in energy density. In contrast, crystalline graphite has a rather *flat* lithium-ion exchange potential ($\sim 0.1 \text{ V vs Li}$) and a high theoretical capacity (372 mAh g^{-1} for LiC_6 stoichiometry). While graphite is relatively abundant and low cost, it does suffer from slow intercalation kinetics and its usage in LIC may limit the charge/discharge rates of the device [247, 251].

Several device configurations that utilize graphite as the positive electrode (involving anion intercalation/deintercalation) and AC as the negative electrode exist for charge storage applications [252, 253]. Recently, the use of lithium-ion predoped graphite as the negative electrode in LIC [249, 250] has been reported, which is achieved by using an additional internal sacrificial lithium metal electrode. The predoped graphite LIC also operates in the voltage window of 2.0–4.0 V, but with greater energy and power densities of 10 Wh kg^{-1} and 10 kW kg^{-1} , respectively, for the fully packaged device. This device has also been shown to have a stable discharge capacity over at least 3×10^5 cycles even when operated at relatively high rates ($\sim 10 \text{ C}$). The LIC using lithium-ion predoped graphite electrode appears to be promising and its advent into the market may be expected soon.

2.4

Summary

ECs, particularly EDLCs, are being evaluated as potential energy storage devices in an expanding number of applications. They are ideal for providing quick bursts of energy and can be configured in a variety of cell shapes/sizes and assembled into modules to meet the power, energy, and voltage requirements for many specific applications. Unlike batteries, which store charge chemically, EDLCs store charge electrostatically, at the electrode–electrolyte interface. This mode of energy storage is ideal for applications that require rapid charge/discharge capabilities, reliability, and very long life.

Considerable research is currently under way to increase the specific energy of ECs; by increasing their capacitance (C) or operating voltage (V), the stored energy (E) in a supercapacitor is given by $E = \frac{1}{2}CV^2$. Carbon, in its various forms, is currently the most extensively examined and widely utilized electrode material in EDLCs with a focus on achieving high surface area with low matrix resistivity and acceptable cost. Accordingly, there is great interest in the development of new and improved carbon-based materials for EDLCs. While carbon is one of the few accessible materials that can readily offer extremely high surface areas and good conductivities, considerable effort is still required to optimize these properties for use in EDLCs, without adversely affecting the overall performance of the material. In particular, surface area, pore size/distribution, density, and conductivity need to be carefully monitored as many of these properties can be mutually exclusive, that is, one can be improved only to the detriment of another. A suggested alternative to the use of AC, as the capacitive material in these devices, is carbon nanotubes with their highly accessible surface area and good specific capacitance, although the relatively high production costs and low volumetric densities associated with these materials require further improvement. The electrochemical capacity of carbon electrodes can also be enhanced by the formation of nanocomposites of porous carbon and redox-active materials such as electrically conducting polymers and certain transition metal oxides. These composite materials can combine the electric double-layer capacitance of carbon and the redox or (pseudo)capacitance of redox-active materials in a single electrode.

There has been an enormous growth in ECs since the early commercialization of EDLCs in the late 1970s and 1980s that initially targeted memory backup applications. Currently, there are literally dozens of companies that are actively manufacturing and distributing devices worldwide. Although the market is still currently dominated by EDLC-type devices, which service primarily the consumer electronic market, there is growing interest in asymmetric capacitors and pseudo-capacitors that have the potential to effectively bridge the critical performance gap between conventional EDLC and batteries. The use of innovative materials and improved designs of asymmetric capacitors has the potential to broaden the appeal of ECs in both existing and emerging energy storage markets such as electric vehicles, tramways, and high-drain portable power tools and electronics.

Acknowledgments

This work was funded through the CSIRO Energy Transformed Flagship. The helpful comments from Dr A.F. Hollenkamp are gratefully acknowledged.

References

1. Dell, R.M. and Rand, D.A.J. (2001) *Understanding Batteries*, Chapter 1, Royal Society of Chemistry, Cambridge.
2. Williams, H.S. (1904) *A History of Science*, Vol. II, Part VI, Harper & Brothers, New York.

- <http://www.worldwideschool.org/library/books/sci/history/AhistoryofScienceVolumeII/chap49.html>, (accessed, 2011).
3. Conway, B.E. (1999) *Electrochemical Supercapacitors. Scientific Fundamentals and Technological Applications*, Kluwer Academics/Plenum Publishers, New York.
 4. Miller, J. and Burke, A.F. (2008) *Electrochem. Soc. Interface*, **17** (Spring), 31–32.
 5. Sarangapani, S., Tilak, B.V., and Chen, C.P. (1996) *J. Electrochem. Soc.*, **143**, 3791–3799.
 6. Burke, A. (2000) *J. Power. Sources*, **91**, 37–50.
 7. Kötz, R. and Carlen, M. (2000) *Electrochim. Acta*, **45**, 2483–2498.
 8. Simon, P. and Gogotsi, Y. (2008) *Nat. Mater.*, **7**, 845–854.
 9. Zhang, L.L. and Zhao, X.S. (2009) *Chem. Soc. Rev.*, **38**, 2520–2531.
 10. Miller, J.R. (2009) in *Encyclopedia of Electrochemical Power Sources* (ed. J. Garche), Elsevier, pp. 587–599.
 11. Simon, P., Brodd, R., Abraham, K., Kim, K., Morita, M., Naoi, K., Park, S., Srinivasan, V., Sugimoto, W., and Zaghbi, K. (eds) (2008) *Electrochemical Capacitors and Hybrid Power Sources*, ECS Transaction, Vol. 16(1), The Electrochemical Society, Pennington, NJ, pp. 3–241.
 12. Halper, M.S. and Ellenbogen, J.C. (2006) Supercapacitors: A Brief Overview. Report No. MP-05 W0000272, MITRE, Virginia.
 13. Petreus, D., Moga, D., Galatus, R., and Munteanu, R.A. (2008) *Adv. Electr. Comput. Eng.*, **8**, 15–22.
 14. Miller, J. (2007) Batteries & Energy Storage Technology, Autum, pp. 61–78.
 15. Endo, M., Takeda, T., Kim, Y.J., Koshiba, K., and Ishii, K. (2001) *Carbon Sci.*, **1**, 117–128.
 16. von Helmholtz, H. (1853) *Ann. Phys. (Leipzig)*, **89**, 211–233.
 17. Becker, H.I. (1957) Low voltage electrolytic capacitor. US Patent 2,800,616, Jul. 23, 1957.
 18. Rightmire, R.A. (1966) Electrical energy storage apparatus. US Patent 3,288,641, Nov. 29, 1966.
 19. Boos, D.L. (1970) Electrolytic capacitor having carbon paste electrodes. US Patent 3,536,963, Oct. 27, 1970.
 20. Boos, D.L. and Argade, S.D. (1991) International Seminar on Double Layer Supercapacitors and Similar Energy Storage Devices, Florida Educational Seminars, 1, Deerfield Beach, FL.
 21. Gouy, G. (1910) *J. Phys.*, **9**, 457–468.
 22. Chapman, D.L. (1913) *Phil. Mag.*, **25**, 475–481.
 23. Stern, O. (1924) *Elektrochem.*, **30**, 508–516.
 24. Grahame, D.C. (1947) *Chem. Rev.*, **41**, 441–501.
 25. Brockis, J.O., Devanathan, M.A., and Muller, K. (1963) *Proc. R. Soc.*, **A274**, 55–79.
 26. Huang, J.S., Sumpter, B.G., and Meunier, V. (2008) *Chem. Eur. J.*, **14**, 6614–6626.
 27. Huang, J.S., Sumpter, B.G., and Meunier, V. (2008) *Angew. Chem.*, **45**, 520–524.
 28. Chmiola, J., Yushin, G., Gogotsi, Y., Portet, C., Simon, P., and Taberna, P.L. (2006) *Science*, **313**, 1760–1763.
 29. Raymundo-Piñero, E., Kierzek, K., Machnikowski, J., and Béguin, F. (2006) *Carbon*, **44**, 2498–2507.
 30. Largeot, C., Portet, C., Chmiola, J., Taberna, P.L., Gogotsi, Y., and Simon, P. (2008) *J. Am. Chem. Soc.*, **130**, 2730.
 31. Ania, C.O., Pernaik, J., Stefaniak, F., Raymundo-pinero, E., and Beguin, F. (2009) *Carbon*, **47**, 3158–3166.
 32. de Levie, R. (1963) *Electrochem. Acta*, **8**, 751–780.
 33. Andrieu, X. (2000) *Energy Storage Syst. Electron. New Trends Electrochem. Technol.*, **1**, 521–547.
 34. Qu, D.Y. and Shi, H. (1998) *J. Power. Sources*, **74**, 99–107.
 35. Burke, A.F. and Murphy, T.C. (1995) Materials for Electrochemical Energy Storage and Conversion – Batteries, Capacitors and Fuel Cells: MRS proceedings Symposium Held April 17–20, 1995, San Francisco, CA, Materials Research Society, Pittsburgh, PA, p. 375.
 36. Kim, Y. (2003) Power Electronics Technology (Oct.), pp. 34–39.

37. Bockris, J.M. and Reddy, A.K. (1970) *Modern Electrochemistry*, Chapter 1, Plenum, p. 720.
38. Conway, B.E. and Pell, W.G. (2003) *J. Solid State Electrochem.*, **7**, 637–644.
39. Rose, M.F., Johnson, C., Owens, T., and Stephens, B. (1994) *J. Power Sources*, **47**, 303–312.
40. Sato, T., Masuda, G., and Takagi, K. (2004) *Electrochim. Acta*, **49**, 3603–3611.
41. Tsuda, T. and Husser, C.L. (2007) *Electrochem. Soc. Interface.*, **16**, 42–49.
42. Galinski, M., Lewandowski, A., and Stepniak, I. (2006) *Electrochim. Acta*, **51**, 5567–5580.
43. McEwen, A.B., Ngo, H.L., LeCompte, K., and Goldman, J.L. (1999) *J. Electrochem. Soc.*, **146**, 1687–1695.
44. Frackowiak, E. (2007) *Phys. Chem. Chem. Phys.*, **9**, 1774–1785.
45. Balducci, A., Dugas, R., Taberna, P.L., Simon, P., Plée, D., Mastragostino, M., and Passerini, S. (2007) *J. Power Sources*, **165**, 922–927.
46. Fichett, B.D., Knepp, T.N., and Conboy, J.C. (2004) *J. Electrochem. Soc.*, **151**, E219–E225.
47. Every, H.A., Bishop, A.G., MacFarlane, D., Oradd, G., and Forsyth, M. (2004) *Phys. Chem. Chem. Phys.*, **6**, 1758–1765.
48. Zhy, Q., Song, Y., Zhu, X., and Wang, X. (2007) *J. Electroanal. Chem.*, **601**, 229–236.
49. Nakagawa, H., Izuchi, S., Kuwana, K., Nukuda, T., and Aihara, Y. (2003) *J. Electrochem. Soc.*, **150**, A695–A700.
50. Garcia, B., Lavallee, S., Perron, G., Michot, C., and Armand, M. (2004) *Electrochim. Acta*, **49**, 4583–4588.
51. Eliad, L., Salitra, G., Soffer, A., and Aurbach, D. (2001) *J. Phys. Chem. B*, **105**, 6880–6887.
52. Ruiz, V., Blanco, C., Santamaria, R., Juarez-Galan, J.M., Sepulveda-Escribano, A., and Rodriguez-Reinoso, F. (2008) *Microporous Mesoporous Mater.*, **110**, 431–435.
53. Alonso, A., Ruiz, V., Blanco, C., Santamaria, R., Granda, M., Menendez, R., and de Jager, S.G.E. (2006) *Carbon*, **44**, 441–446.
54. Shi, H. (1996) *Electrochim. Acta*, **41**, 1633–1639.
55. Portet, C., Yushin, G., and Gogotsi, Y. (2008) *J. Electrochem. Soc.*, **155**, A531–A536.
56. Barisci, J.N., Wallace, G.G., MacFarlane, D.R., and Baughman, R.H. (2004) *Electrochem. Commun.*, **6**, 22–27.
57. Zhang, H., Cao, G.P., Yang, Y.S., and Gu, Z.N. (2008) *Carbon*, **46**, 30–34.
58. Panic, V.V., Stevanovic, R.M., Jovanovic, V.M., and Dekanski, A.B. (2008) *J. Power Sources*, **181**, 186–192.
59. Hwang, S.-W. and Hyun, S.-H. (2004) *J. Non-Cryst. Solids*, **347**, 238–245.
60. Kim, S.J., Hwang, S.W., and Hyun, S.H. (2005) *J. Mater. Sci.*, **40**, 725–731.
61. Pandolfo, A.G. and Hollenkamp, A.F. (2006) *J. Power Sources*, **157**, 11–27.
62. Frackowiak, E. and Béguin, F. (2001) *Carbon*, **39**, 937–950.
63. Fialkov, A.S. (2000) *Russ. J. Electrochem.*, **36**, 389–413.
64. Taylor, R., Marsh, H., Heintz, E.A., and Rodríguez-Reinoso, F. (1997) *Introduction to Carbon Technologies*, Universidad de Alicante, Secretariado de Publicaciones, p. 167.
65. Marsh, H. and Rodríguez Reinoso, F. (2006) *Activated Carbon*, Elsevier Science & Technology.
66. Endo, M. and Kim, Y.-J. (2007) *Mol. Cryst. Liq. Cryst.*, **388**, 481–488.
67. Qu, D.Y. (2002) *J. Power Sources*, **109**, 403–411.
68. Kim, T., Lim, S., Kwon, K., Hong, S.-H., Qiao, W., Rhee, C.-K., Yoon, S.-H., and Mochida, I. (2006) *Langmuir*, **22**, 9086–9088.
69. Figueiredo, J.L., Pereira, M.F.R., Freitas, M.M.A., and Orfap, J.J.M. (1999) *Carbon*, **37**, 1379–1389.
70. Bansal, R.C., Donnet, J.B., and Stoeckli, F. (1988) *Active Carbon* Chapter 2, Marcel Dekker, New York.
71. Ruiz, V., Blanco, C., Granda, M., and Santamaria, R. (2008) *Electrochim. Acta*, **54**, 305–310.
72. Kierzek, K., Frackowiak, E., Lota, G., Gryglewicz, G., and Machnikowski, J. (2004) *Electrochim. Acta*, **49**, 515–523.
73. Soffer, A. and Folman, M. (1972) *J. Electroanal. Chem.*, **38**, 25–43.

74. Koresh, J. and Soffer, A. (1977) *J. Electroanal. Chem.*, **124**, 711–718.
75. Koresh, J. and Soffer, A. (1983) *J. Electroanal. Chem.*, **147**, 223–234.
76. Lin, C., Ritter, J.A., and Popov, B.N. (1999) *J. Electrochem. Soc.*, **146**, 3155–3160.
77. Barbieri, O., Hahn, M., Herzog, A., and Kotz, R. (2005) *Carbon*, **43**, 1303–1310.
78. Soon, S.H., Korai, Y., Mochida, I., Marsh, H., and Rodriguez-Reinoso, F. (2000) *Sciences of Carbon Materials*, Universidad de Alicante.
79. Sevilla, M., Alvarez, S., Centeno, T.A., Fuertes, A.B., and Stoeckli, F. (2007) *Electrochim. Acta*, **52**, 3207–3215.
80. Knox, J.H., Kaur, B., and Millward, G.R. (1986) *J. Chromatogr.*, **352**, 3–25.
81. Lee, J., Kim, J., and Hyeon, T. (2006) *Adv. Mater.*, **18**, 2073–2094.
82. Ryoo, R., Joo, S.H., and Jun, S. (1999) *J. Phys. Chem. B*, **103**, 7743–7746.
83. Vix-Guterl, C., Saadallah, S., Jurewicz, K., Frackowiak, E., Reda, M., Parmentier, J., Patarin, J., and Beguin, F. (2004) *Mat. Sci. Eng. B, Solid-State Mat. Adv. Technol.*, **108**, 148–155.
84. Zhou, H.S., Zhu, S.M., Hibino, M., and Honma, I. (2003) *J. Power. Sources*, **122**, 219–223.
85. Wang, D., Li, F., Liu, M., Lu, G.Q., and Cheng, H.M. (2008) *Angew. Chem. Int. Ed.*, **47**, 373–376.
86. Inagaki, I. (2009) *New Carbon Mater.*, **24**(3), 193–232.
87. Kyotani, T., Nagai, T., Inoue, S., and Tomita, A. (1997) *Chem. Mater.*, **9**(2), 609–615.
88. Dash, R., Chmiola, J., Yushin, G., Gogotsi, Y., Laudisio, G., Singer, J., Fischer, J., and Kucheyev, S. (2006) *Carbon*, **44**, 2489–2497.
89. Gogotsi, Y.G., Leon, I.D., and McNallan, M.J. (1997) *J. Mater. Chem.*, **7**, 1841–1848.
90. Talapatra, S. (2006) *Nat. Nanotechnol.*, **1**, 112–116.
91. Emmenegger, C., Mauron, P., Sudan, P., Wenger, P., Hermann, V., Gallay, R., and Zuttel, A. (2003) *J. Power. Sources*, **124**, 321–329.
92. Yu, C.J., Masarapu, C., Rong, J.P., Wei, B.Q., and Jiang, H.Q. (2009) *Adv. Mater.*, **21**, 4793–4797.
93. Futaba, D.N., Hata, K., Yamada, T., Hiraoka, T., Hayamizu, Y., Kakudate, Y., Tanaike, O., Hatori, H., Yumura, M., and Iijima, S. (2006) *Nat. Mater.*, **5**, 987–994.
94. <http://www.nanocarbon.jp/english/results/001.html>.
95. Zheng, J.P. (1999) *Electrochem. Solid-State Lett.*, **2**, 359–361.
96. Mastragostino, M., Soavi F., and Arbizzani, C. (2002) in *Advances in Lithium-Ion Batteries*, (eds W. van Schalkwijk and B. Scrosati), Kluwer Academic/Plenum Publishers, p. 481.
97. Mastragostino, M., Arbizzani, C., and Soavi, F. (2002) *Solid State Ionics*, **148**, 493–498.
98. Naoi, K., Oura, Y., and Tsujimoto, H. (1996) *Proc. Electrochem. Soc.*, **96**–25, 120.
99. Novak, P., Muller, K., Santhanam, K.S.V., and Haas, O. (1997) *Chem. Rev.*, **97**, 207–282.
100. Mozer, A.J. and Sariciftci, N.S. (2007) Conjugated polymer-based photovoltaic devices, in *Handbook of Conducting Polymers*, Chapter 10 (eds T.J. Skotheim and J.R. Reynolds), CRC Press, New York.
101. Rudge, A., Davey, J., Raistrick, I., Gottesfeld, S., and Ferraris, J.P. (1994) *J. Power. Sources*, **47**, 89–107.
102. Arbizzani, C., Mastragostino, M., and Meneghello, L. (1996) *Electrochim. Acta*, **41**, 21–26.
103. Peng, C., Zhang, S.W., Jewell, D., and Chen, G.Z. (2008) *Prog. Nat. Sci.*, **18**, 777–788.
104. Arbizzani, C., Mastragostino, M., and Scrosati, B. (1997) Conducting polymers for batteries, supercapacitors and optical devices, in *Handbook of Organic Conductive Molecules and Polymers*, Chapter 7 (ed. H.S. Nalwa), John Wiley & Sons, Inc., New York.
105. Osaka, T., Komaba, S., and Liu, X. (1999) Ionic conducting polymers for applications in batteries and capacitors, in *Nonaqueous Electrochemistry*,

- Chapter 7 (ed. E.D. Aurbach), Marcel Dekker Inc., New York.
106. Irvin, J. A., Irvin, D. J., Smith, J. D. S. Electroactive polymers for batteries and supercapacitors, in *Handbook of Conducting Polymers*, Chapter 9 (eds T. J., Skotheim and J. R., Reynolds), CRC Press, New York.
 107. Chen, W.C. and Wen, T.C. (2003) *J. Power. Sources*, **117**, 273–282.
 108. Lin, Y.R. and Teng, H.S. (2003) *Carbon*, **41**, 2865–2871.
 109. Hu, C.C., Li, W.Y., and Lin, J.Y. (2004) *J. Power. Sources*, **137**, 152–157.
 110. Zhou, Z.H., Cai, N.C., Zeng, Y., and Zhou, Y.H. (2006) *Chin. J. Chem.*, **24**, 13–16.
 111. Prasad, K.R. and Munichandraiah, N. (2002) *J. Power. Sources*, **112**, 443–451.
 112. Prasad, K.R. and Munichandraiah, N. (2002) *J. Electrochem. Soc.*, **149**, A1393–A1399.
 113. Zhou, H.H., Chen, H., Luo, S.L., Lu, G.W., Wei, W.Z., and Kuang, Y.F. (2005) *J. Solid State Electrochem.*, **9**, 574–580.
 114. Gupta, V. and Miura, N. (2005) *Electrochem. Solid-State Lett.*, **8**, A630–A632.
 115. Palaniappan, S. and Devi, S.L. (2008) *J. Appl. Polym. Sci.*, **107**, 1887–1892.
 116. Cuentas-Gallegos, A.K., Lira-Cantu, M., Casan-Pastor, N., and Gomez-Romero, P. (2005) *Adv. Funct. Mater.*, **15**, 1125–1133.
 117. Ko, J.M., Song, R., Yu, H.J., Yoon, J.W., Min, B.G., and Kim, D.W. (2004) *Electrochim. Acta*, **50**, 873–876.
 118. Mondal, S.K., Barai, K., and Munichandraiah, N. (2007) *Electrochim. Acta*, **52**, 3258–3264.
 119. Tamai, H., Hakoda, M., Shiono, T., and Yasuda, H. (2007) *J. Mater. Sci.*, **42**, 1293–1298.
 120. Fusalba, F., Guerec, P., Villers, D., and Belanger, D. (2001) *J. Electrochem. Soc.*, **148**, A1–A6.
 121. Prasad, K.R. and Munichandraiah, N. (2002) *Electrochem. Solid-State Lett.*, **5**, A271–A274.
 122. Ryu, K.S., Kim, K.M., Park, N.G., Park, Y.J., and Chang, S.H. (2002) *J. Power. Sources*, **103**, 305–309.
 123. Ryu, K.S., Kim, K.M., Park, Y.J., Park, N.G., Kang, M.G., and Chang, S.H. (2002) *Solid State Ionics*, **152**, 861–866.
 124. Ryu, K.S., Wu, X.L., Lee, Y.G., and Chang, S.H. (2003) *J. Appl. Polym. Sci.*, **89**, 1300–1304.
 125. Ryu, K.S., Hong, Y.S., Park, Y.J., Wua, X.G., Kim, K.M., Lee, Y.G., Chang, S.H., and Lee, S.J. (2004) *Solid State Ionics*, **175**, 759–763.
 126. Ryu, K.S., Jeong, S.K., Joo, J., and Kim, K.M. (2007) *J. Phys. Chem. B*, **111**, 731–739.
 127. Clemente, A., Paner, S., Spila, E., and Scrosati, B. (1998) *J. Appl. Electrochem.*, **28**, 1299–1304.
 128. Ryu, K.S., Lee, Y.G., Han, K.S., Park, Y.J., Kang, M.G., Park, N.G., and Chang, S.H. (2004) *Solid State Ionics*, **175**, 765–768.
 129. Sharma, R.K., Rasogi, A.C., and Desu, S.B. (2008) *Electrochem. Commun.*, **10**, 268–272.
 130. Hashmi, S.A., Latham, R.J., Linford, R.G., and Schlindwein, W.S. (1998) *Polym. Int.*, **47**, 28–33.
 131. Hu, C.C. and Lin, X.X. (2002) *J. Electrochem. Soc.*, **149**, A1049–A1057.
 132. Sung, J.H., Kim, S.J., and Lee, K.H. (2003) *J. Power. Sources*, **124**, 343–350.
 133. Fan, L.Z. and Maier, J. (2006) *Electrochem. Commun.*, **8**, 937–940.
 134. Wu, Q.F., He, K.X., Mi, H.Y., and Zhang, X.G. (2007) *Mater. Chem. Phys.*, **101**, 367–371.
 135. Park, J.H., Ko, J.M., Park, O.O., and Kim, D.W. (2002) *J. Power. Sources*, **105**, 20–25.
 136. Kim, J.H., Sharma, A.K., and Lee, Y.S. (2006) *Mater. Lett.*, **60**, 1697–1701.
 137. Panero, S., Clemente, A., and Spila, E. (1996) *Solid State Ionics*, **86**(8), 1285–1289.
 138. Noh, K.A., Kim, D.W., Jin, C.S., Shin, K.H., Kim, J.H., and Ko, J.M. (2003) *J. Power. Sources*, **124**, 593–595.
 139. Hashmi, S.A., Kumar, A., and Tripathi, S.K. (2005) *Eur. Polym. J.*, **41**, 1373–1379.
 140. Hussain, A.M.P., Saikia, D., Singh, F., Avasthi, D.K., and Kumar, A. (2005) *Nucl. Instrum. Methods Phys. Res., Sect. B*, **240**, 834–841.

141. Hussain, A.M.P. and Kumar, A. (2006) *J. Power. Sources*, **161**, 1486–1492.
142. Izadi-Najafabadi, A., Tan, D.T.H., and Madden, J.D. (2005) *Synth. Met.*, **152**, 129–132.
143. Mastragostino, M., Paraventi, R., and Zanelli, A. (2000) *J. Electrochem. Soc.*, **147**, 3167–3170.
144. Mastragostino, M., Arbizzani, C., Paraventi, R., and Zanelli, A. (2000) *J. Electrochem. Soc.*, **147**, 407–412.
145. Laforgue, A., Simon, P., Fauvarque, J.F., Mastragostino, M., Soavi, F., Sarrau, J.F., Lailler, P., Conte, M., Rossi, E., and Saguatti, S. (2003) *J. Electrochem. Soc.*, **150**, A645–A651.
146. Arbizzani, C., Mastragostino, M., and Soavi, F. (2001) *J. Power. Sources*, **100**, 164–170.
147. Di Fabio, A., Giorgi, A., Mastragostino, M., and Soavi, F. (2001) *J. Electrochem. Soc.*, **148**, A845–A850.
148. Balducci, A., Bardi, U., Caporali, S., Mastragostino, M., and Soavi, F. (2004) *Electrochem. Commun.*, **6**, 566–570.
149. Balducci, A., Henderson, W.A., Mastragostino, M., Passerini, S., Simon, P., and Soavi, F. (2005) *Electrochim. Acta*, **50**, 2233–2237.
150. Balducci, A., Soavi, F., and Mastragostino, M. (2006) *Appl. Phys. Mater. Sci. Process.*, **82**, 627–632.
151. Arbizzani, C., Beninati, S., Lazzari, M., Soavi, F., and Mastragostino, M. (2007) *J. Power. Sources*, **174**, 648–652.
152. Du Pasquier, A., Laforgue, A., and Simon, P. (2004) *J. Power. Sources*, **125**, 95–102.
153. White, A.M. and Slade, R.C.T. (2004) *Electrochim. Acta*, **49**, 861–865.
154. Li, W.K., Chen, J., Zhao, J.J., Zhang, J.R., and Zhu, J.J. (2005) *Mater. Lett.*, **59**, 800–803.
155. Patra, S. and Munichandraiah, N. (2007) *J. Appl. Polym. Sci.*, **106**, 1160–1171.
156. Liu, K., Hu, Z.L., Xue, R., Zhang, J.R., and Zhu, J.J. (2008) *J. Power. Sources*, **179**, 858–862.
157. Bhat, D.K. and Kumar, M.S. (2007) *J. Mater. Sci.*, **42**, 8158–8162.
158. Carlberg, J.C. and Inganas, O. (1997) *J. Electrochem. Soc.*, **144**, L61–L64.
159. Stenger-Smith, J.D., Webber, C.K., Anderson, N., Chafin, A.P., Zong, K.K., and Reynolds, J.R. (2002) *J. Electrochem. Soc.*, **149**, A973–A977.
160. Ryu, K.S., Lee, Y.G., Hong, Y.S., Park, Y.J., Wu, X.L., Kim, K.M., Kang, M.G., Park, N.G., and Chang, S.H. (2004) *Electrochim. Acta*, **50**, 843–847.
161. Rudge, A., Raistrick, I., Gottesfeld, S., and Ferraris, J.P. (1994) *Electrochim. Acta*, **39**, 273–287.
162. Laforgue, A., Simon, P., and Fauvarque, J.F. (2001) *Synth. Met.*, **123**, 311–319.
163. Laforgue, A., Simon, P., Fauvarque, J.F., Sarrau, J.F., and Lailler, P. (2001) *J. Electrochem. Soc.*, **148**, A1130–A1134.
164. Du Pasquier, A., Laforgue, A., Simon, P., Amatucci, G.G., and Fauvarque, J.F. (2002) *J. Electrochem. Soc.*, **149**, A302–A306.
165. Wu, M.Q., Snook, G.A., Gupta, V., Shaffer, M., Fray, D.J., and Chen, G.Z. (2005) *J. Mater. Chem.*, **15**, 2297–2303.
166. Sivakkumar, S.R. and Saraswathi, R. (2004) *J. Power. Sources*, **137**, 322–328.
167. Snook, G.A., Peng, C., Fray, D.J., and Chen, G.Z. (2007) *Electrochem. Commun.*, **9**, 83–88.
168. Villers, D., Jobin, D., Soucy, C., Cossement, D., Chahine, R., Breau, L., and Belanger, D. (2003) *J. Electrochem. Soc.*, **150**, A747–A752.
169. Arbizzani, C., Catellani, M., Mastragostino, M., and Mingazzini, C. (1995) *Electrochim. Acta*, **40**, 1871–1876.
170. Sivakkumar, S.R., Kim, W.J., Choi, J.A., MacFarlane, D.R., Forsyth, M., and Kim, D.W. (2007) *J. Power. Sources*, **171**, 1062–1068.
171. Mallouki, M., Tran-Van, F., Sarrazin, C., Simon, P., Daffos, B., De, A., Chevrot, C., and Fauvarque, J. (2007) *J. Solid State Electrochem.*, **11**, 398–406.
172. Song, R.Y., Park, J.H., Sivakkumar, S.R., Kim, S.H., Ko, J.M., Park, D.Y., Jo, S.M., and Kim, D.Y. (2007) *J. Power. Sources*, **166**, 297–301.
173. Sivakkumar, S.R., Ko, J.M., Kim, D.Y., Kim, B.C., and Wallace, G.G. (2007) *Electrochim. Acta*, **52**, 7377–7385.
174. Wilson, G. J., Looney, M. G., Pandolfo, A. G. *Synth. Met.*, **160**, 655–663.

175. Pell, W.G. and Conway, B.E. (2004) *J. Power. Sources*, **136**, 334–345.
176. Amatuucci, G.G., Badway, F., Du Pasquier, A., and Zheng, T. (2001) *J. Electrochem. Soc.*, **148**, A930–A939.
177. Zheng, J.P., Cygan, P.J., and Jow, T.R. (1995) *J. Electrochem. Soc.*, **142**, 2699–2703.
178. Zheng, J.P. and Jow, T.R. (1995) *J. Electrochem. Soc.*, **142**, L6–L8.
179. Kim, H. and Popov, B.N. (2002) *J. Power. Sources*, **104**, 52–61.
180. Hu, C.C., Chen, W.C., and Chang, K.H. (2004) *J. Electrochem. Soc.*, **151**, A281–A290.
181. Kim, I.H. and Kim, K.B. (2004) *J. Electrochem. Soc.*, **151**, E7–E13.
182. Kim, I.H. and Kim, K.B. (2006) *J. Electrochem. Soc.*, **153**, A383–A389.
183. Jang, J.H., Kato, A., Machida, K., and Naoi, K. (2006) *J. Electrochem. Soc.*, **153**, A321–A328.
184. Stefan, I.C., Mo, Y., Antonio, M.R., and Scherson, D.A. (2002) *J. Phys. Chem. B*, **106**, 12373–12375.
185. McKeown, D.A., Hagans, P.L., Carette, L.P.L., Russell, A.E., Swider, K.E., and Rolison, D.R. (1999) *J. Phys. Chem. B*, **103**, 4825–4832.
186. Cao, F. and Prakash, J. (2001) *J. Power. Sources*, **92**, 40–44.
187. Jeong, Y.U. and Manthiram, A. (2000) *Electrochem. Solid-State Lett.*, **3**, 205–208.
188. Jeong, Y.U. and Manthiram, A. (2001) *J. Electrochem. Soc.*, **148**, A189–A193.
189. Hu, C.C., Wang, C.C., and Chang, K.H. (2007) *Electrochim. Acta*, **52**, 2691–2700.
190. Hong, J.I., Yeo, I.H., and Paik, W.K. (2001) *J. Electrochem. Soc.*, **148**, A156–A163.
191. Hu, C.C., Chang, K.H., Lin, M.C., and Wu, Y.T. (2006) *Nano Lett.*, **6**, 2690–2695.
192. Deng, G.H., Xiao, X., Chen, J.H., Zeng, X.B., He, D.L., and Kuang, Y.F. (2005) *Carbon*, **43**, 1566–1569.
193. Park, J.H., Ko, J.M., and Park, O.O. (2003) *J. Electrochem. Soc.*, **150**, A864–A867.
194. Qin, X., Durbach, S., and Wu, G.T. (2004) *Carbon*, **42**, 451–453.
195. Wang, Y.G., Wang, Z.D., and Xia, Y.Y. (2005) *Electrochim. Acta*, **50**, 5641–5646.
196. Barranco, V., Pico, F., Ibañez, J., Lillo-Rodenas, M.A., Linares-Solano, A., Kimura, M., Oya, A., Rojas, R.M., Amarilla, J.M., and Rojo, J.M. (2009) *Electrochim. Acta*, **54**, 7452–7457.
197. Burke, A. (2007) *Electrochim. Acta*, **53**, 1083–1091.
198. Vol'fkovich, Y.M. and Serdyuk, T.M. (2002) *Russ. J. Electrochem.*, **38**, 935–958.
199. Kazaryan, S.A., Razumov, S.N., Litvinenko, S.V., Kharisov, G.G., and Kogan, V.I. (2006) *J. Electrochem. Soc.*, **153**, A1655–A1671.
200. Belyakov, I., Dashko, O.G., Kazarov, V.A., Kazaryan, S.A., Litvinenko, S.V., Kutyanin, V.I., Shmatko, P.A., Vasechkin, V.I., Volkovich, J.M., Schmatko, P.A., Kasarov, V.A., Volkovich, Y.U.M., Beljakov, A.I., Kazarjan, S.A., Kutjanin, V.I., Kutyanin, V.I., Schmatko, E.A., and Volkovich, J.M. (2001) Capacitor with dual electric layer. US Patent 6,195,252 B1, Feb. 2001.
201. Razoumov, S., Klementov, A., Litvinenko, S., and Beliakov, A. (2001) Asymmetric electrochemical capacitor and method of making. US Patent 6,222,723 B1.
202. Yu, N., Gao, L., Zhao, S., and Wang, Z. (2009) *Electrochim. Acta*, **54**, 3835–3841.
203. <http://www.greencarcongress.com/2008/02/axion-providing.html>.
204. Lam, L.T. and Louey, R. (2006) *J. Power. Sources*, **158**, 1140–1148.
205. Srinivasan, V. and Weidner, J.W. (1997) *J. Electrochem. Soc.*, **144**, L210–L213.
206. Srinivasan, V. and Weidner, J.W. (2000) *J. Electrochem. Soc.*, **147**, 880–885.
207. Liu, K.C. and Anderson, M.A. (1996) *J. Electrochem. Soc.*, **143**, 124–130.
208. Liu, H.T., He, P., Li, Z.Y., Liu, Y., and Li, J.H. (2006) *Electrochim. Acta*, **51**, 1925–1931.
209. Prasad, K.R. and Miura, N. (2004) *Appl. Phys. Lett.*, **85**, 4199–4201.
210. Nam, K.W. and Kim, K.B. (2002) *J. Electrochem. Soc.*, **149**, A346–A354.

211. Nam, K.W., Lee, E.S., Kim, J.H., Lee, Y.H., and Kim, K.B. (2005) *J. Electrochem. Soc.*, **152**, A2123–A2129.
212. Varakin, N., Stepanov, A.B, and Menukhov, V.V. (1999) Double layer capacitor. US Patent 5,986,876.
213. Acharya, R., Subbaiah, T., Anand, S., and Das, R.P. (2002) *J. Power. Sources*, **109**, 494–499.
214. Nelson, P.A. and Owen, J.R. (2003) *J. Electrochem. Soc.*, **150**, A1313–A1317.
215. Snook, G.A., Duffy, N.W., and Pandolfo, A.G. (2007) *J. Power. Sources*, **168**, 513–521.
216. Ganesh, V., Pitchumani, S., and Lakshminarayanan, V. (2006) *J. Power. Sources*, **158**, 1523–1532.
217. Lee, H.Y. and Goodenough, J.B. (1999) *J. Solid State Chem.*, **144**, 220–223.
218. Pang, S.C., Anderson, M.A., and Chapman, T.W. (2000) *J. Electrochem. Soc.*, **147**, 444–450.
219. Hu, C.C. and Tsou, T.W. (2002) *Electrochem. Commun.*, **4**, 105–109.
220. Hu, C.C. and Wang, C.C. (2003) *J. Electrochem. Soc.*, **150**, A1079–A1084.
221. Chang, J.K. and Tsai, W.T. (2003) *J. Electrochem. Soc.*, **150**, A1333–A1338.
222. Kim, H. and Popov, B.N. (2003) *J. Electrochem. Soc.*, **150**, D56–D62.
223. Toupin, M., Brousse, T., and Belanger, D. (2004) *Chem. Mater.*, **16**, 3184–3190.
224. Subramanian, V., Zhu, H.W., Vajtai, R., Ajayan, P.M., and Wei, B.Q. (2005) *J. Phys. Chem. B*, **109**, 20207–20214.
225. Owens, B.B., Passerini, S., and Smyrl, W.H. (1999) *Electrochim. Acta*, **45**, 215–224.
226. Chin, S.F., Pang, S.C., and Anderson, M.A. (2002) *J. Electrochem. Soc.*, **149**, A379–A384.
227. Devaraj, S. and Munichandraiah, N. (2005) *Electrochem. Solid-State Lett.*, **8**, A373–A377.
228. Khomenko, V., Raymundo-Pinero, E., and Beguin, F. (2006) *J. Power. Sources*, **153**, 183–190.
229. Hong, M.S., Lee, S.H., and Kim, S.W. (2002) *Electrochem. Solid-State Lett.*, **5**, A227–A230.
230. Khomenko, V., Raymundo-Pinero, E., Frackowiak, E., and Beguin, F. (2006) *Appl. Phys. Mater. Sci. Process.*, **82**, 567–573.
231. Brousse, T., Toupin, M., and Belanger, D. (2004) *J. Electrochem. Soc.*, **151**, A614–A622.
232. Cottineau, T., Toupin, M., Delahaye, T., Brousse, T., and Belanger, D. (2006) *Appl. Phys. Mater. Sci. Process.*, **82**, 599–606.
233. Yuan, A.B. and Zhang, Q.L. (2006) *Electrochem. Commun.*, **8**, 1173–1178.
234. Ohzuku, T., Ueda, A., and Yamamoto, N. (1995) *J. Electrochem. Soc.*, **142**, 1431–1435.
235. Du Pasquier, A., Plitz, I., Gural, J., Menocal, S., and Amatucci, G. (2003) *J. Power. Sources*, **113**, 62–71.
236. Whittingham, M.S. (2004) *Chem. Rev.*, **104**, 4271–4302.
237. Wang, Y.G. and Xia, Y.Y. (2006) *J. Electrochem. Soc.*, **153**, A450–A454.
238. Wang, Y.G., Luo, J.Y., Wang, C.X., and Xia, Y.Y. (2006) *J. Electrochem. Soc.*, **153**, A1425–A1431.
239. Li, H.Q., Cheng, L., and Xia, Y.Y. (2005) *Electrochem. Solid-State Lett.*, **8**, A433–A436.
240. Yoon, J.H., Bang, H.J., Prakash, J., and Sun, Y.K. (2008) *Mater. Chem. Phys.*, **110**, 222–227.
241. Du Pasquier, A., Plitz, I., Menocal, S., and Amatucci, G. (2003) *J. Power. Sources*, **115**, 171–178.
242. Dahn, J.R. and Seel, J.A. (2000) *J. Electrochem. Soc.*, **147**, 899–901.
243. Yoshino, A., Tsubata, T., Shimoyamada, M., Satake, H., Okano, Y., Mori, S., and Yata, S. (2004) *J. Electrochem. Soc.*, **151**, A2180–A2182.
244. Aida, T., Murayama, I., Yamada, K., and Morita, M. (2007) *J. Electrochem. Soc.*, **154**, A798–A804.
245. Woo, S.W., Dokko, K., Nakano, H., and Kanamura, K. (2007) *Electrochemistry*, **75**, 635–640.
246. Ogihara, N., Igarashi, Y., Kamakura, A., Naoi, K., Kusachi, Y., and Utsugi, K. (2006) *Electrochim. Acta*, **52**, 1713–1720.
247. Khomenko, V., Raymundo-Pinero, E., and Beguin, F. (2008) *J. Power. Sources*, **177**, 643–651.
248. Naoi, K. and Simon, P. (2008) *Electrochem. Soc. Interface*, **17**, 34–37.

249. Hatozaki, O. (2007) Proceedings of the 17th International Seminar on Double-Layer Capacitors and Hybrid Energy Storage Devices, Redox engineering. Deerfield Beach, FL, December 10–12, 2007, p. 156.
250. Hatozaki, O. (2008) Proceedings of the 18th International Seminar on Double-Layer Capacitors and Hybrid Energy Storage Devices, Redox engineering. Deerfield Beach, FL, December 8–10, 2008, p. 96.
251. Sivakkumar, S. R., Nerkar, J. Y., Pandolfo, A. G. *Electrochim. Acta*, **55**, 3330–3335.
252. Yoshio, M., Nakamura, H., and Wang, H.Y. (2006) *Electrochem. Solid-State Lett.*, **9**, A561–A563.
253. Yokoyama, Y., Shimosaka, N., Matsumoto, H., Yoshio, M., and Ishihara, T. (2008) *Electrochem. Solid-State Lett.*, **11**, A72–A75.

3

Electrochemical Techniques

Pierre-Louis Taberna and Patrice Simon

3.1

Electrochemical Apparatus

Recent electrochemical workstations are composed of three main components: a signal waveform generator (SWG), a potentiostat/galvanostat (PG), and a computer. Users define all the setup parameters on the computer, which transfers the different instructions to the SWG/PG block. The latter applies the required signal to the electrochemical cell and the measurement is performed (Figure 3.1).

Each electrochemical method is defined by its own waveform. There are transient techniques (cyclic voltammetry, chronopotentiometry, chronoamperometry, etc.) and stationary techniques (electrochemical impedance spectroscopy, rotating disk electrode, etc.)

To characterize an electrochemical cell, both two-electrode and three-electrode configurations can be performed. Figure 3.2a,b gives a schematic view of a cell connected to an electrochemical workstation. Basically, the current flows through the counter electrode (CE) and the working electrode (WE), and the voltage is measured (or controlled) between the reference electrode (RE) and the WE. For a two-electrode cell (Figure 3.2a), the voltage measured (or controlled) is the cell voltage since the CE and the RE are shorted; for a three-electrode cell (Figure 3.2b), a third electrode is added and it acts as the RE. The RE used for this purpose should exhibit an ideal nonpolarizable behavior, meaning that its voltage is constant over a large range of current densities. In this way, the WE voltage is accurately measured (or controlled).

Of course, many plugging combinations are possible, and the only limitation is the imagination of the experimenter. For instance, one can control the cell voltage while measuring the WE voltage or the opposite.

3.2

Electrochemical Cell

From an electrical point of view, an electrochemical cell can be basically represented by the following sketch (Figure 3.3):

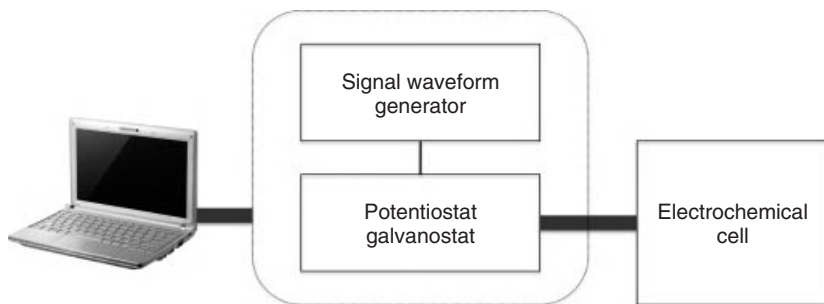


Figure 3.1 An electrochemical workstation: computer/signal waveform generator/potentiostat-galvanostat.

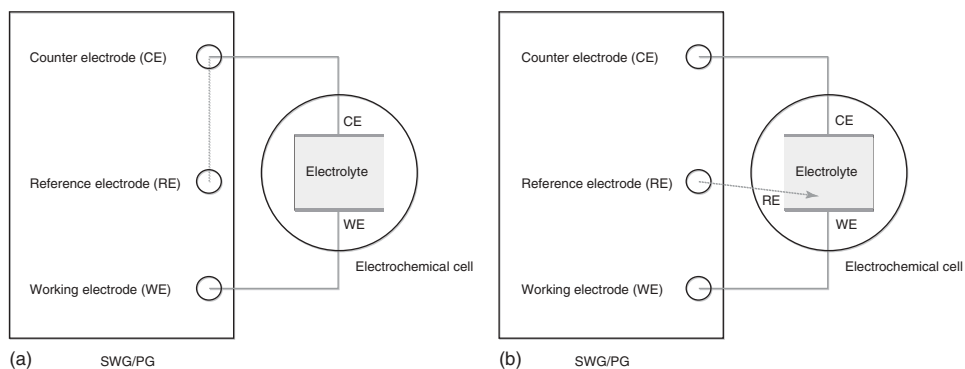


Figure 3.2 Electrochemical test configurations: (a) two-electrode cell, the counter and the reference electrodes are shorted and (b) three-electrode cell, the reference electrode is set close to the WE.

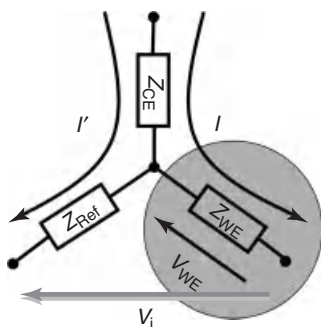


Figure 3.3 Equivalent electrical circuit of an electrochemical cell; each electrode is represented by its own impedance.

Z_{CE} is the counter electrode impedance, Z_{WE} the working electrode impedance, and Z_{Ref} the reference electrode impedance. i and i' are the current flowing through each electrical branch. Impedance is a sort of Ohm's law generalization (Eq. 3.1):

$$V(V) = Z(\Omega) I(A) \quad (3.1)$$

where V is the voltage drop, Z the impedance, and i the current.

When performing an electrochemical experiment, one has to control (or measure) the WE potential as accurately as possible. To tackle this, the first requirement is to down i' to zero. Manufacturers design their PG in this way and of late the input impedance is as high as $10^{15} \Omega$. A PG behaves like an operational amplifier in a potential follower configuration (Figure 3.4). The RE is plugged to one input of this amplifier, which is well known to have high input impedance. We have

$$V_O = G(V_+ - V_-)(V) \quad (3.2)$$

where V_O is the output voltage, G the amplifier gain, and V_+ and V_- the two input voltages. V_i (imposed voltage) = V_+ .

As for an ideal operational amplifier $G \rightarrow \infty$, we obtain:

$$V_i = Z_{WE} I(V) \quad (3.3)$$

Such an architecture allows following the voltage of the WE without any ohmic drop through the RE.

Thanks to this circuiting, the current only passes through the CE and the WE. Only the impedance of the WE has to be considered, and this is described here since the voltage is measured (or controlled) between the RE and the WE, as shown in Figure 3.5.

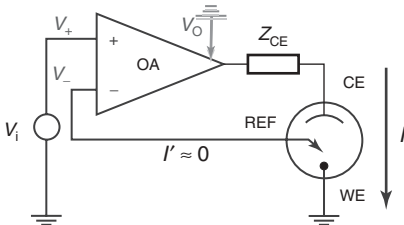


Figure 3.4 Schematic view of a PG. A PG can be reduced to an equivalent operational amplifier (OA) circuit.

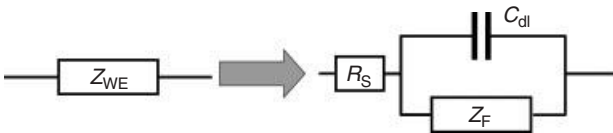


Figure 3.5 Impedance of the working electrode. R_S is the series resistance, Z_F the faradic impedance, and C_{dl} the double-layer capacitance.

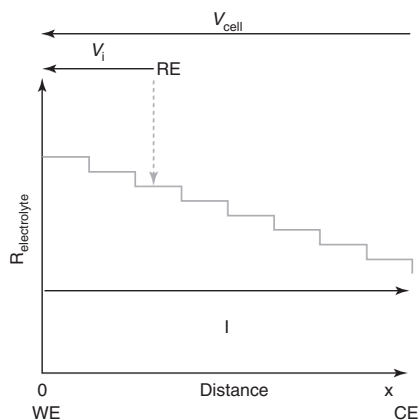


Figure 3.6 Voltage drop across an electrochemical cell. V_{WE} is the real working electrode voltage and V_i is the imposed (controlled) voltage.

As shown in this figure, the WE impedance is formed by a series resistance R_S , including mainly the bulk electrolyte resistance, $R_{\text{electrolyte}}$; C_{dl} and Z_F stand for the double-layer capacitance and the faradic processes, respectively, occurring at the electrode. The latter are the ones to be studied and $R_{\text{electrolyte}}$ has to be minimized as low as possible. Actually $V_i = V_{WE} + R_{\text{electrolyte}}i$, and $R_{\text{electrolyte}}$ is strongly dependant on the RE location in the electrochemical cell (Figure 3.6). It is not possible to eliminate this contribution and it is not required for consideration of stability, but attention must be paid to the cell design; the RE has to be set as close as possible to the WE and a Luggin capillary could be used for this purpose.

3.3 Electrochemical Interface: Supercapacitors

Two kinds of supercapacitors exist – the electrical double-layer capacitors and the pseudocapacitors. The former implies only electrostatic interactions, the latter surface faradic reactions [1].

The impedance of an electrical double-layer capacitor can be described as in the case of the equivalent circuit shown in Figure 3.7a. There are no faradic reactions involved and in a first order such an electrode can be reduced to a simple R – C series equivalent circuit, where C_{dl} can be simply written as follows:

$$C_{dl} = \epsilon_0 \epsilon_r \frac{S}{d} \text{ (F)} \quad (3.4)$$

with S the electrode surface area, d the charge separation corresponding to the outer Helmholtz plan [2], and ϵ_0 and ϵ_r the vacuum permittivity and the relative permittivity of the dielectric material, respectively. This equation shows why high-surface-area-activated carbons are used as electrical double-layer capacitor-active material.

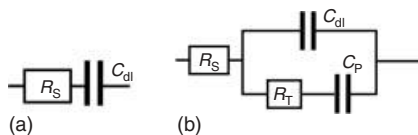


Figure 3.7 (a) Equivalent electrical circuit of an electrical double-layer capacitor and (b) equivalent electrical circuit of a pseudocapacitor.

In the pseudocapacitor case, the faradic impedance Z_F has to be taken into account, which can be expressed by a capacitance C_p in series with a charge-transfer resistance R_{CT} [2].

$$R_{CT} = \frac{RT}{\alpha n F i_0} \quad (\Omega) \quad (3.5)$$

$$C_p = \frac{zF}{RT} \frac{\theta(1-\theta)}{g\theta(1-\theta)-1} \quad (\text{F}) \quad (3.6)$$

where θ is the saturation coverage of the electrochemical sites and g is a repulsion factor that is negative when repulsive forces occur between each site and positive in the opposite case.

Of course, it is needless to say that for a real electrode, owing to its porous nature, a diffusion impedance and a geometric distribution have to be considered. This point is discussed further in this chapter.

3.4

Most Used Electrochemical Techniques

Two kinds of techniques are commonly used for characterizing either a supercapacitor electrode (three-electrode cells) or a supercapacitor device (two-electrode cells). There are transient techniques and stationary techniques.

3.4.1

Transient Techniques

Cyclic voltammetry and galvanostatic cycling are often used, and these techniques allow following the current variation or the voltage variation.

3.4.1.1 Cyclic Voltammetry

This is a widely used technique by electrochemists because of its versatility, but most of the time this technique is devoted to laboratory cells. Actually, large devices lead to very large volumes of current from several hundreds to thousands of amps; which could be technically difficult to handle. At the laboratory or material scale it is an accurate technique that enables:

- qualitative and pseudo-quantitative studies
- kinetic analysis by scanning a huge range of scan rates
- voltage window determination.

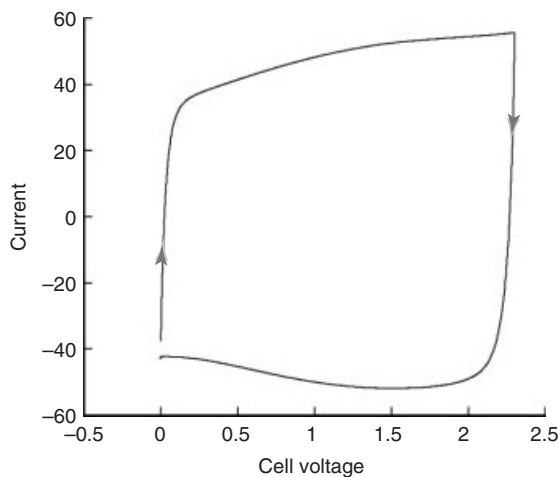


Figure 3.8 Cyclic voltammety of an activated-carbon-based supercapacitor. Measurement done at 25 °C and at $\nu = 20 \text{ mV s}^{-1}$ in a TEATBF-based electrolyte.

The principle of this technique is to apply a linear voltage ramp to an electrode (or a device) between two voltage limits and to measure the resulting current. The applied voltage is as follows:

$$V(t) = V_0 + \nu t \text{ for } V \leq V_1 \quad (3.7)$$

$$V(t) = V_0 - \nu t \text{ for } V \geq V_2$$

where ν is the scan rate (V s^{-1}) and V_1 and V_2 are the two voltage boundaries. Figure 3.8 shows the cyclic voltammety of an activated carbon two-electrode cell in acetonitrile-1.5 M tetraethylammonium tetrafluoroborate (TEATFB). A typical squared i - V curve is usually obtained for such supercapacitors.

Eq. (3.8) is commonly used to describe the electrochemical signature:

$$i = \nu C_{\text{dl}} [1 - \exp(-t/R_S C_{\text{dl}})] \text{ (A)} \quad (3.8)$$

where C_{dl} and R_S are the double-layer capacitance and the equivalent series resistance (often reduced to the bulk electrolyte resistance), respectively. From this curve it is possible to measure the voltage window of an electrode (or a supercapacitor), that is, a signal without including any irreversible faradic reactions; electrolyte degradation or electrode oxidation usually restricts the voltage window. Also, by applying Eq. (3.9), it is possible to plot Q versus V :

$$Q_i = \left| \int i dt \right|_{V_i} \text{ (C)} \quad (3.9)$$

where Q_i is the local capacity (C) obtained for $V = V_i$. To obtain the capacitance, it is usually calculated from the backward step of the cyclic voltammety, that is, while the supercapacitor (or the electrode) is discharged. The calculation is made for each V_i between V_1 and V_2 , which gives the following figure (Figure 3.9).

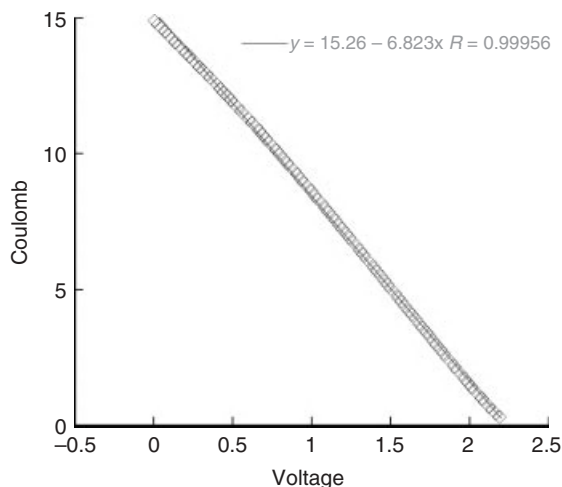


Figure 3.9 Capacity variation versus voltage upon discharge.

Since

$$Q = CV \text{ (C)} \quad (3.10)$$

the slope of this curve gives the capacitance C (F). The capacitance can be calculated in another way when $Q-V$ is not so linear. It is often the case when the material is pseudocapacitive. Figure 3.10 gives an example of two well-known electrochemical systems – MnO_2 (Figure 3.10a) and RuO_2 (Figure 3.10b). In such cases, the capacitance is more voltage dependant than activated-carbon-based electrodes; the accuracy of the linear regression is not as good as it should be. To overcome this issue, the expression (3.11) is applied:

$$C = \frac{\int_{V_1}^{V_2} i dt}{\int_{V_1}^{V_2} V dt} \text{ (F)} \quad (3.11)$$

where $[V_1; V_2]$ is the voltage window, C the capacitance, i the current, and V the voltage. The calculation is usually made on the backward scan (discharge).

Of course, cyclic voltammetry is useful to evaluate the cyclability of a supercapacitor (or an electrode), and the variation in capacitance on cycling would give a good idea of how things will go. But, usually, galvanostatic cycling is better when performing such experiments.

3.4.1.2 Galvanostatic Cycling

This technique is very different from cyclic voltammetry because the current is controlled and the voltage is measured. This is certainly the most widely used technique in the battery field because it can be extended from a laboratory scale to an industrial one. This method is also called *chronopotentiometry* and gives access to different parameters such as

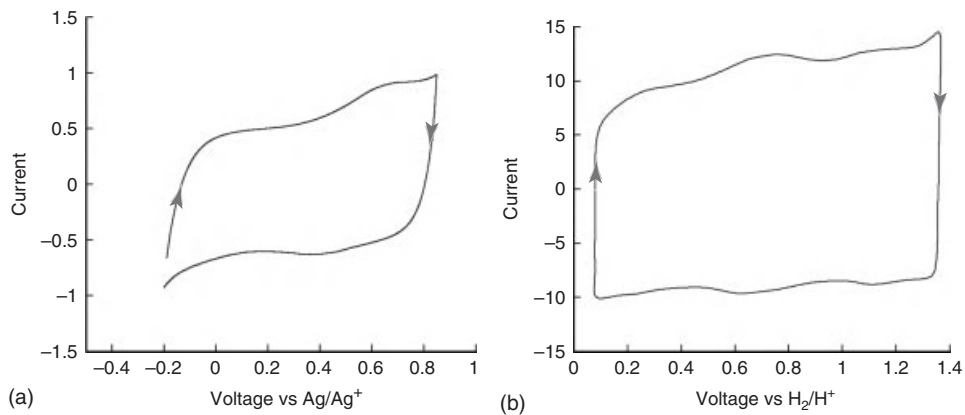


Figure 3.10 Cyclic voltammetry of (a) MnO_2 in aqueous K_2SO_4 electrolyte and (b) RuO_2 in aqueous H_2SO_4 electrolyte. Measurement done at 25°C and at $\nu = 20\text{ mV s}^{-1}$.

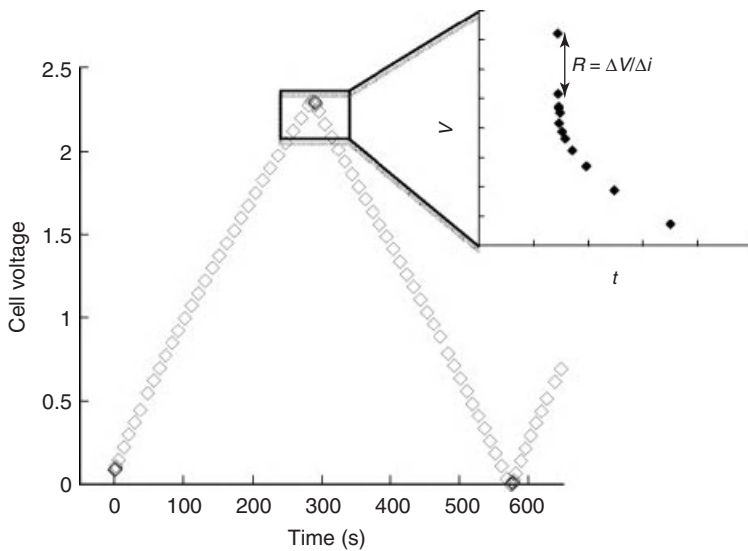


Figure 3.11 Galvanostatic curve: voltage variation versus time while applying a current through a supercapacitor cell. Inset: zoom-in of the current inversion region.

- capacitance
- resistance
- cyclability.

The voltage variation is described by Eq. (3.12):

$$V(t) = Ri + \frac{t}{C}i \quad (3.12)$$

The voltage variation of a supercapacitor is represented in Figure 3.11:

As can be seen from Eq. (3.13), the capacitance of a supercapacitor can be calculated from the slope of the curve; for a pseudocapacitor, when the $V-t$ curve profile is not as linear as it should be, the capacitance can be calculated by integrating the current over the discharge time or charge time:

$$C = I \frac{\partial t}{\partial V} \text{ (F)} \quad (3.13)$$

$$C = \frac{I \Delta t}{\Delta V} \text{ (F)} \quad (3.14)$$

where i is the set current, Δt is the discharge time (or charge time), and ΔV is the voltage window.

The series resistance is deduced from the voltage drop (V_{drop}) occurring over the current inversion (Δi); it is illustrated in the inset of Figure 3.11:

$$R = \frac{V_{\text{drop}}}{\Delta I} \text{ (\Omega)} \quad (3.15)$$

When the current is inverted or interrupted, the voltage drop is directly linked to the resistance of the cell. By repeating both capacitance and resistance measurements over cycling, it is then also possible to watch the cyclability of supercapacitors (electrical double-layer capacitors and pseudocapacitors).

3.4.2

Stationary Technique

3.4.2.1 Electrochemical Impedance Spectroscopy

This electrochemical method allows covering a large timescale (from microseconds to hours), meaning that electrochemical processes are parted depending on their own time constant. In addition, such measurements are made under steady-state conditions that allow acquisition times high enough to get accurate measurements. At last, in contrast to the previous techniques, small excitation signals are employed, permitting linearization of current–voltage characteristics. Actually, this last point means that this technique can be carried out by controlling either the current or the voltage, thus measuring either the voltage or the current. Here, the voltage control technique is focused on, but the same remarks or conclusions could be driven by controlling the current. Figure 3.12 presents the most widely used type of signal to perform electrochemical impedance spectroscopy. The voltage of the system is set as required (V_s) and a small-amplitude (a few millivolts or so) sinusoidal signal is overlaid and carried out at several frequencies (f , Hz). δv and δi are the amplitudes of the voltage and the current, respectively.

However, to get highly reliable measurements, it is to be ensured that stationary conditions are reached before launching the experiment, that is, $\partial i / \partial t \rightarrow 0$.

As the signal is small enough, a linear relation exists between the current and the voltage at each pulsation ($\omega = 2\pi f$):

$$V = Zi \text{ (V)} \quad (3.16)$$

where V is the voltage, i the current, and Z the impedance.

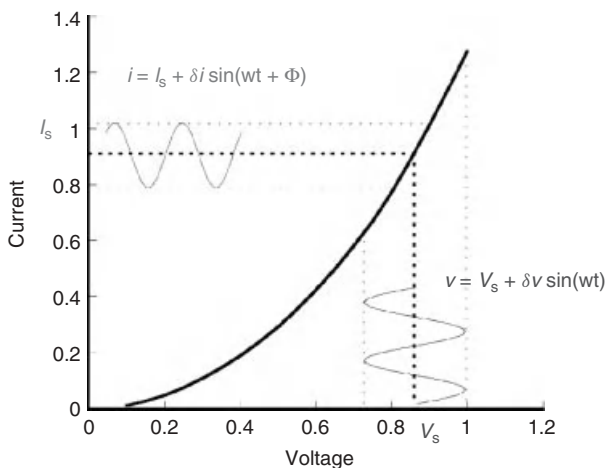


Figure 3.12 Stationary polarization curve (black bold line). A sinusoidal voltage is imposed over the steady voltage and the resulting current is measured. A measurement is made at different frequency ($f = \omega/2\pi$)

V and i can be also expressed using a complex notation, that is:

$$V(\omega) = \delta v \exp(j\omega t) \text{ (V)} \quad (3.17)$$

$$i(\omega) = \delta i \exp[j(\omega t + \Phi)] \text{ (A)} \quad (3.18)$$

Hence, the previous expression can be rewritten as follows:

$$Z(\omega) = \frac{\delta v}{\delta i} \exp(-j\Phi) \text{ (\Omega)} \quad (3.19)$$

where $Z(\omega)$ is also known to be the complex impedance and different definitions can now be given.

The impedance can also be represented as

$$Z(\omega) = Z_{\text{Re}} + jZ_{\text{Im}} \text{ (\Omega)} \quad (3.20)$$

with the impedance modulus as

$$|Z(\omega)| = \frac{\delta V}{\delta i} = \sqrt{Z_{\text{Re}}^2 + Z_{\text{Im}}^2} \text{ (\Omega)} \quad (3.21)$$

and the phase angle as

$$\Phi = \arctan(Z_{\text{Im}}/Z_{\text{Re}}) \text{ (}^\circ\text{)} \quad (3.22)$$

where Z_{Re} and Z_{Im} are the real and imaginary parts of $Z(\omega)$, respectively.

This technique is thus convenient for linearization of a complex electrochemical system. Such linearization enables the performance of the usual electrical analysis. It gives the opportunity to find an analogous electrical circuit behaving like the studied electrochemical cell (also called *equivalent circuit*). It helps predict the behavior of a system; moreover, with other physical analysis, it brings clues to the understanding of reaction kinetics. Of course, the user must handle modeling

tools with care since many equivalent circuits can fit experimental data and will not be related anymore to the electrochemistry of the system.

Before going further, the following table shows some impedances of simple ideal electrical components.

Component	$ Z $	Z_{Re}	Z_{Im}	Φ (rad)
Resistance	R	R	0	0
Capacitance	$\frac{1}{C\omega}$	0	$\frac{-1}{C\omega}$	$\frac{\pi}{2}$
Inductance	$L\omega$	0	$L\omega$	$\frac{-\pi}{2}$

The reader has to take care of the phase angle definition; indeed, it is easy to be confused since many electrochemical impedance spectrometer manufacturers assimilate the phase angle to the argument of the impedance. Actually, argument is the opposite of the phase angle, as is shown in Eq. (3.23):

$$Z(\omega) = |Z| \exp(-j\Phi) = |Z| \exp(j\theta) \quad (\Omega) \quad (3.23)$$

where Φ is the phase angle and θ the argument of the complex number.

Electrochemical systems are often more complex and can be modeled with a combination of components presented in the table. Most used components are usually resistances (R) and capacitances (C). The former are easily identified with electrochemical processes and kinetics, the latter more related to charge accumulation at different interfaces involved in an electrochemical cell.

Figure 3.13 represents the Randles equivalent electrical circuit. This is mostly used to describe simple electrochemical reactions as, for instance, copper electrodeposition.

While R_S is the series resistance mainly related to the bulk electrolyte resistance, C_{dl} is the double-layer capacitance related to a charge accumulation at the electrode/electrolyte interface and R_{CT} is the charge-transfer resistance linked to the exchanged current as defined in the Butler–Volmer equation (in Nernst-like systems, R_{CT} is close to zero). A last component is W , which is the diffusion impedance. This impedance is intended to define the polarization of an electrochemical system due to diffusion limitation. For an electrochemical reaction (Eq. (3.24)), the Warburg element can be expressed as



$$Z_W = \frac{\sigma(1-j)}{\omega^{1/2}} \quad (\Omega) \quad (3.25)$$

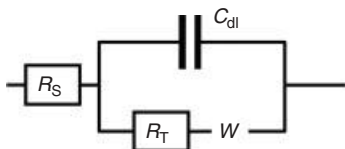


Figure 3.13 Randles' electrical equivalent circuit.

and

$$\sigma = \frac{RT}{n^2 F^2 S \sqrt{2}} \left(\frac{1}{D_{\text{Ox}}^{1/2} C_{\text{Ox}}} + \frac{1}{D_{\text{Red}}^{1/2} C_{\text{Red}}} \right) \left(\Omega \text{ rad}^{1/2} \text{ s}^{-1/2} \right) \quad (3.26)$$

where n is the number of the exchanged electron, R the gas constant, T the temperature in Kelvin, F the Faraday constant, S the footprint area, D_{Ox} and D_{Red} the diffusion coefficients of Ox and Red, respectively, and C_{Ox} and C_{Red} the bulk concentration of the electroactive species.

Electrochemists are used to plotting Nyquist plots and Bode plots, which are, respectively, Z_{Im} versus Z_{Re} and $|Z|$ - Φ versus frequency. Figure 3.14(a,b), B(a,b),

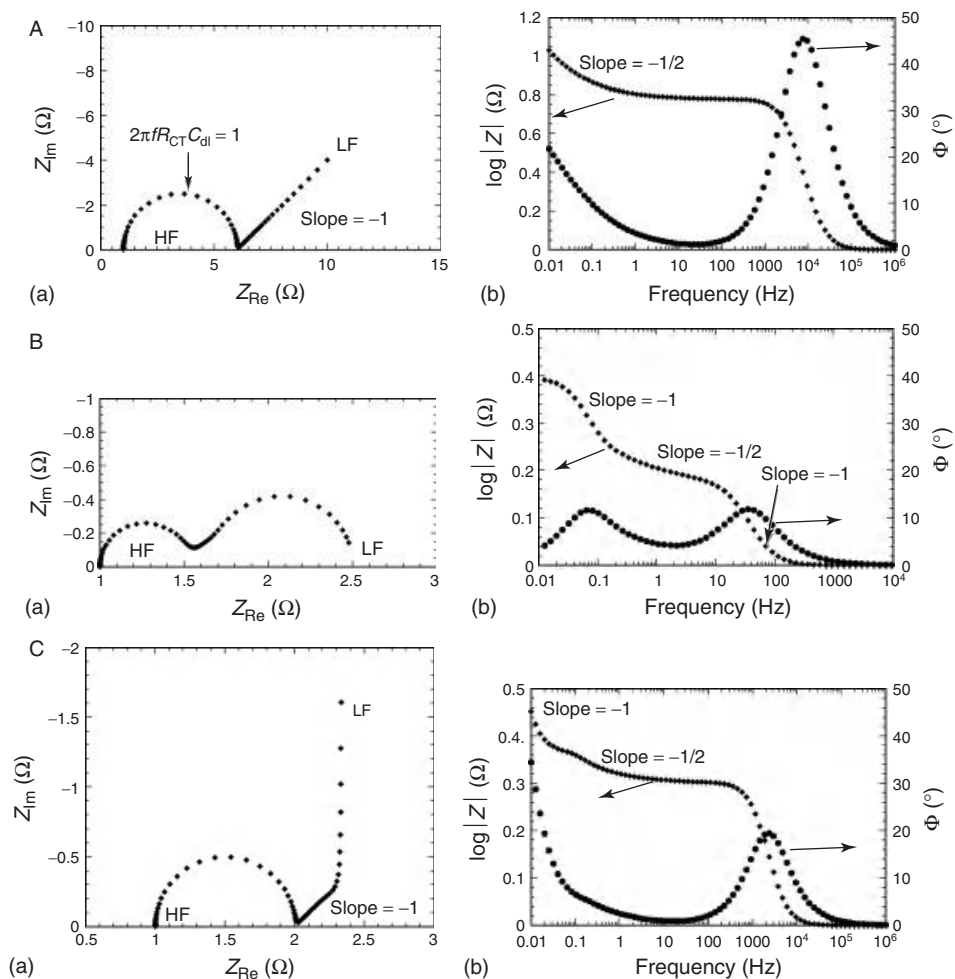


Figure 3.14 (A) (a) Nyquist plot and (b) Bode plots of Randles circuit. Under semi-infinite diffusion limitation. (B) (a) Nyquist plot and (b) Bode plots of Randles circuit. Under finite length diffusion limitation. (C) Nyquist plot and Bode plots of Randles circuit. Under restricted diffusion limitation.

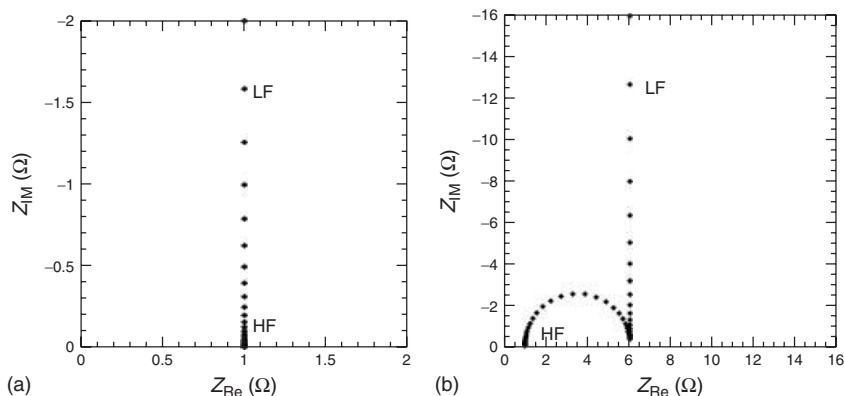


Figure 3.15 (a) Nyquist plot of an ideal electrical double-layer capacitor and (b) Nyquist plot of an ideal pseudocapacitor.

C(a,b) represents, respectively, the Nyquist and Bode plots of a Randles equivalent circuit. The left part of the Nyquist plot (low Z_{Re} values) is related to high frequencies (HFs) and the right part (high Z_{Re} values) is related to low frequencies (LFs). At HFs $R_{CT}-C_{dl}$ (Figure 3.13) is predominant and exhibits an HF loop in the Nyquist plot, a (-1) slope for the impedance modulus and a peak for the phase angle. At LF, the mass transport impedance is predominant, leading to a slope of (-1) in the Nyquist plot and a slope of $(-1/2)$ in the Bode impedance plot. Such diffusion impedance is observed for the semi-infinite condition, that is, when the diffusion layer thickness is continuously increasing from the electrode to the bulk of the electrolyte (but the diffusion layer is small enough compared to the electrode dimension).

Another particular diffusion condition can also be obtained when the diffusion layer has a finite length under specific hydrodynamic conditions as is the case, for example, for a rotating disk electrode. Figure 3.15 represents the Nyquist and Bode plots, respectively. At HF, R_{CT} is still observed but an LF loop related to finite length diffusion is observable. The transition between the two loops is particular and leads, in the Bode impedance plot, to a slope of $(-1/2)$. The resistance of the LF loop is directly linked to the thickness of the diffusion layer. This kind of plot is also encountered for spherical diffusion when the diffusion layer thickness is in the range (or larger) of the electrode dimension.

A last particular condition is when the diffusion layer is restricted as is the case for a thin electrochemical solution layered between the electrode and another nonreactive surface. As previously, the same HF behavior is obtained but the LF impedance is similar to that in a capacitor. A transition slope of (-1) is seen between the R_{CT} loop and the LF vertical line in the Nyquist plot ($(-1/2)$ slope at the Bode impedance plot), which means actually that $\sqrt{D/2\pi f} \gg l$ (l is the electrochemical solution thickness, D the diffusion coefficient, and f the frequency of the signal).

3.4.2.2 Supercapacitor Impedance

Supercapacitor electrodes are particular cases since most of the time the electrode impedance can be modeled by two simple sketches (Figure 3.7). Of course, this is a very basic description but it is sufficient to get the picture.

The first figure (Figure 3.15a) represents the behavior of an electrical double-layer capacitor, which can be easily described by a simple series resistance (R_S) and a capacitance (C_{dl}). The first term is mainly linked to the electrolyte resistance (contact resistances, but current collector resistance could be also included) and the second to the charge accumulation at the electrode/electrolyte interface. Many theories exist to describe such charge separation but the Helmholtz one is sufficient since electrolyte concentration is well above 0.1 mol l^{-1} ; thus, the diffusion layer (Gouy–Chapman layer) can be neglected [1, 2].

The second figure (Figure 3.15b) describes the behavior of a pseudocapacitor, which is basically described by an electrolyte resistance, a double-layer capacitance in parallel with a pseudocapacitive branch [1, 3]. This last branch is modeled by a charge-transfer resistance related to the involved faradic processes; the capacitance is linked to the charge accumulation at the electrolyte/electrode interface but this differs from the electric double-layer capacitor in that specific sites are related. Indeed, faradic reactions occur at favorable active sites, whereas it is not the case for purely capacitive charge accumulation. That means that kinetic rate constants exist (charge-transfer resistance) and mass transfer limitation could appear. The last point is not taken into account in our discussion but could be done with the addition of the relevant Warburg impedance to the pseudocapacitive branch.

Figure 3.15a represents the Nyquist plot of an ideal electrical double-layer capacitor (Figure 3.7a). As can be seen, a vertical line is obtained, meaning the capacitance is constant over the whole frequency window studied. An ideal pseudocapacitor behavior exhibits the electrochemical impedance response shown in Figure 3.15b (Figure 3.7b). A first HF loop related to the charge-transfer resistance and the double-layer capacitance is observed; the LF vertical line is linked to the charge storage on surface electrochemical reaction. This capacitance has been expressed in Eq. (3.6).

Actually, real electrode behavior is slightly more complex because of dispersion factors. These factors are mainly due to geometric aspects such as electrode porosity and electrode roughness but also active site activation energy dispersion, especially for pseudocapacitors. Such fractal electrodes induce frequency dispersions of the electrical parameters [4]. Resistances and capacitances are no more constant over the whole range of the studied frequencies. In the early 1960s, the porosity aspect was studied by de Levie by a unique pore model [5]. Of course, the recent models are more sophisticated and take into account a lot of parameters such as the shape of the pores [6]. But, so far, de Levie's model set the foundation for the influence of porosity on the electrochemical impedance signal.

Figure 3.16 shows an active material grain, in this case, activated carbon, that can be electrically modeled by a cylindrical pore structure.

A porous electrode can be simplified by a structure looking like the zoom-in of Figure 3.16. Actually, along the length of the pore, a transmission line model is

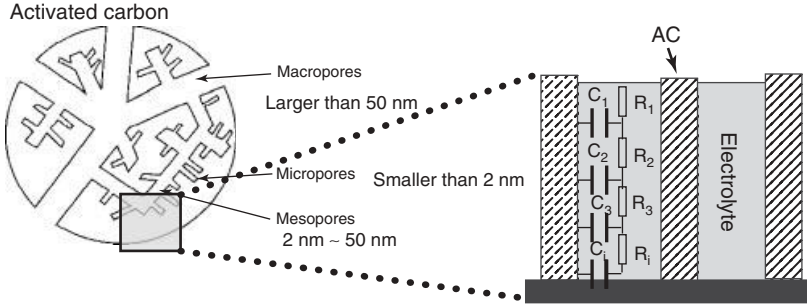


Figure 3.16 Schematic view of a porous electrode. Here, activated carbon is represented.

used to modelize the behavior of the electrochemical species mass transport. That means that the path toward each active site is not equivalent and is more or less time consuming depending on the tortuosity. To reflect on this aspect, de Levie [5] proposed a transmission line model exhibiting several RC constants. The following equation is the one proposed to describe the impedance of a porous electrode:

$$Z_p = \sqrt{R_p Z_E} \operatorname{coth} \left(\sqrt{R_p / Z_E} \right) (\Omega) \quad (3.27)$$

$$Z_{SC} = R_s + ZE (\Omega) \quad (3.28)$$

Z_p is the impedance due to the porosity of the electrode, R_p is the ionic resistance of the active material, and Z_E is the electrode/electrolyte interface impedance. For the particular case of the electrical double-layer capacitance, Z_E can be replaced by $1/jC_{dl}\omega$, which is achieved by removing the faradic resistance. Of course, the total impedance of an electrode is given by the expression (3.27) to which the series resistance is added (Eq. 3.28)). This last term is mainly governed by the bulk electrolyte resistance, but contact resistances, for example, could be considered as well.

Z_{SC} represents the total impedance of an electrode (or a device); this impedance is frequency dependant and Figure 3.17a gives an overview of the consequence on the electrode analysis.

While r_1 and r_2 are the radii of the pores, λ_1 and λ_2 are the penetration length of the electrical signal. Song *et al.* [7] demonstrated with this figure that the higher the frequency (f_1 and f_2) or/and the smaller the pore radius, the shallower the penetration of the AC signal. That means that at HF the external surface and the larger pores are only interacted with the electrochemical species. Thus, while decreasing the frequency, electrochemical species access more and more to the whole active electrode surface area.

Figure 3.17b shows the Nyquist plot obtained for an activated carbon electrode. If compared with Figure 3.15a, a sloppy region (slope = -1) is observable corresponding to the medium frequencies. This part is perfectly fitted by Eq. (3.27) and is linked to the “electrolyte penetration” into the depth of the porosity (actually this is the voltage propagation throughout the electrode). A transition frequency called *knee frequency* (Figure 3.17b) delimiting the sloppy region and the vertical

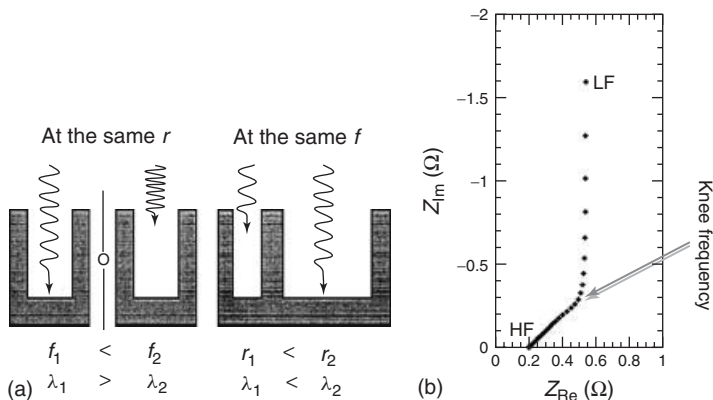


Figure 3.17 (a) Schematic view of AC signal penetration inside a porous electrode [7]. (b) Nyquist plot of an electrical double-layer capacitance.

one. The latter is reached when the whole surface is accessible; in other words, the frequency is small enough to allow the electrical signal going throughout the electrode. Thus, ions can cover the whole surface and the capacitance is no longer frequency dependant. Of course, the same analysis could be done for a pseudocapacitive electrode except that an HF charge-transfer loop has been added.

The de Levie analysis gives the picture of how a porous electrode behaves, but when more complex dispersions are considered, such as the shape of the pores, the mathematics becomes trickier to handle.

To render the electrical dispersions occurring in a real electrode, a more convenient mathematical tool is used, which is the constant phase element (CPE). The main drawback of such a tool is that it is a black box analysis but it is very easy to handle. It is expressed as

$$Z_{\text{CPE}} = \frac{1}{Y_0(j\omega)^\alpha} \quad (\Omega) \quad (3.29)$$

where Z_{CPE} is the equivalent impedance, Y_0 is the admittance modulus ($1/|Z|$); ω is the signal pulsation ($\omega = 2\pi f$); and α is the dispersion exponent. Three particular situations can be found depending on the value of α .

	$\alpha = 0$	$\alpha = 0.5$	$\alpha = 1$
Impedance	Resistor $R = \frac{1}{Y_0}$	Warburg $W = \frac{1}{Y_0(j\omega)^{0.5}}$	Capacitor $C = \frac{1}{j\omega Y_0}$

It can be seen from Figure 3.18 that CPE can be used to give an electrical description of the electrode and the two following figures give an idea of how an electrical double-layer capacitor or a pseudocapacitor varies with α .

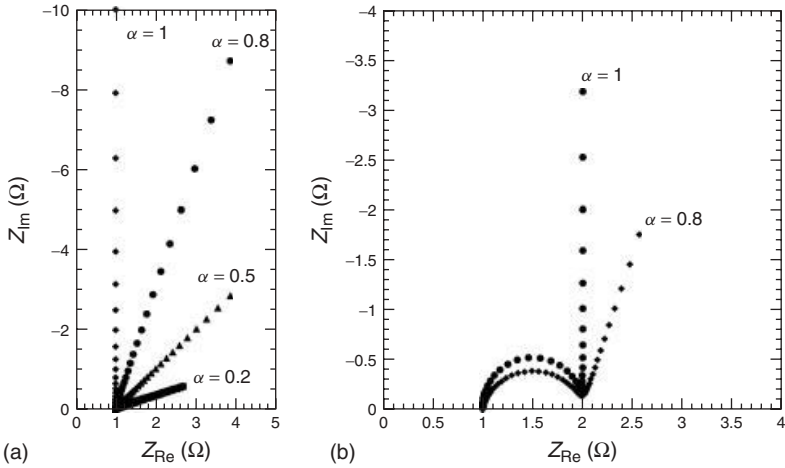


Figure 3.18 (a) Nyquist plot of a CPE for different values of α , (b) Nyquist plot of a pseudocapacitor including a CPE instead of C_{dl} .

As observed, when the frequency dispersion increased (low α), the Nyquist plots are shifted to higher resistances. Needless to say that for describing a real electrode, a linear combination of several CPE could be done:

$$Z = \frac{1}{Y_0(j\omega)^{\alpha_0}} + \frac{1}{Y_1(j\omega)^{\alpha_1}} + \frac{1}{Y_2(j\omega)^{\alpha_2}} \quad (\Omega) \quad (3.30)$$

For instance, Eq. (3.30) can be used to describe an activated carbon electrode (Figure 3.17) with $\alpha_0 = 0$, $\alpha_1 = 0.5$, and $\alpha_2 = 1$.

Electrochemical impedance spectroscopy is a powerful technique that allows measuring both the equivalent resistance and the capacitance at different frequencies. Also, the frequency analysis allows parting different processes occurring at the electrode. For example, combining galvanostatic cycling with such measurements gives information about resistances and capacitance evolution. An electrode degradation can be due to current collector corrosion, increased electrode resistance, increased contact resistance, electrochemical shuttles, and so on. It can be roughly said that at HF, contact resistances, current collector corrosion is mainly concerned; at medium frequencies, electrochemical species accessibility (Eq. (3.27)) throughout the electrode is involved; charge storage, diffusion limitations, and leak resistance (electrochemical shuttles, irreversible electrochemical processes) occur at LF. Thus, depending on the frequency region mainly implies that the impedance variation on cycling an accurate analysis can be done. Of course, an assumption made with the impedance technique has to be confirmed by using other analysis tools. Again, even if this technique is powerful it is really easy to be lost since the main drawback of impedance spectroscopy is that many equivalent circuits can be found to describe the same electrical behavior.

Figure 3.19 presents an impedance analysis of a supercapacitor electrode composed of an aluminum foil coated with an activated carbon film depending on

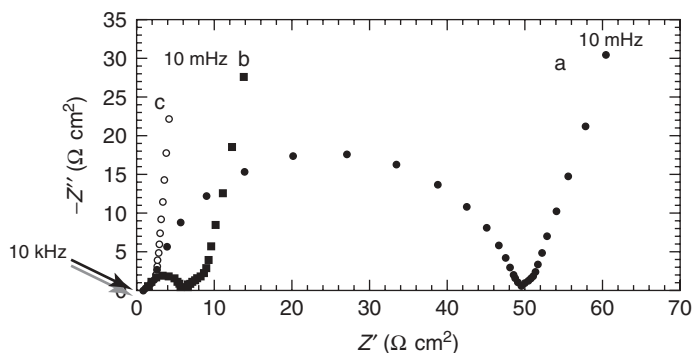


Figure 3.19 Influence of the electrode/current collector interface on the electrode impedance. (a) An aluminum current collector used as received and (b) an etched aluminum current collector, and (c) a treated aluminum current collector.

the current collector surface treatment. Actually, an important contribution to the impedance of such an electrode is the contact impedance between the current collector and the active material [8]. Portet *et al.* [9] showed that for a carbon–carbon electrical double-layer capacitor, surface treatment on an aluminum current collector was needed to improve the power ability. When current collectors are used as received, a large HF loop is observed owing to the thick aluminum oxide layer. By increasing the contact surface and decreasing the oxide layer thickness by acidic etching, the loop is reduced. The HF loop is removed and a decrease in the contact resistance is obtained by filling the etched aluminum foil using acetylene black. As can be seen, the HF loop is no longer observed and the total impedance of the electrode is drastically lowered [9].

Another way to analyze impedance data is to plot complex capacitance plots. The complex capacitance can be expressed as follows [10]:

$$C = C_{\text{Re}} - jC_{\text{Im}} \quad (\text{F}) \quad (3.31)$$

with

$$C_{\text{Re}} = \frac{-Z_{\text{Im}}}{\omega|Z|^2} \quad \text{and} \quad C_{\text{Im}} = \frac{Z_{\text{Re}}}{\omega|Z|^2} \quad (\text{F}) \quad (3.32)$$

Such expressions are very convenient to define accurately the knee frequency since a peak is observed on $C_{\text{Im}}-f$ plot and $C_{\text{Re}} = C_0/2$ for $f = f_{\text{knee}}$. C_0 is the LF capacitance that can also be measured by galvanostatic experiments. Figure 3.20 shows the capacitance plots of an activated-carbon-based electrical double-layer capacitor electrode depending on the type of electrolyte. It compares an acetonitrile (AN)-based electrolyte and a propylene carbonate (PC) electrolyte. The former solvent led to a more conductive electrolyte because of its lower viscosity and higher wettability.

As observed here, the lower the f_{knee} , the higher the dispersions. This frequency is very particular since it is the boundary between the full access of the electrode surface and the electrolyte penetration region. Also, it is the frequency of the

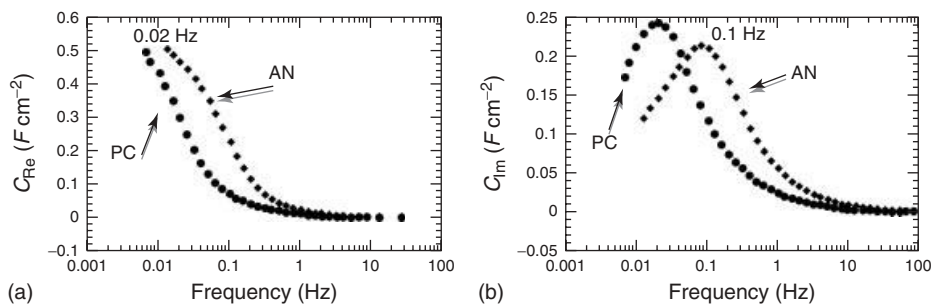


Figure 3.20 Evolution of the (a) real part and (b) imaginary part of the capacitance versus frequency for 4 cm² cells assembled with two electrodes containing 15 mg cm⁻² of PICAC-TIF SC activated carbon in AN and PC with 1.5 and 1.0 M NEt₄BF₄, respectively [10].

median charge storage efficiency and can be defined as a *merit factor*: at higher frequencies the charge storage efficiency is below 50% and at lower frequencies it is superior to 50%. Actually, this efficiency is the ratio of stored energy/loss energy. Such a representation is complementary to the other and gives directly the charge storage ability of an electrode. Actually, this f_{knee} also defines the bandwidth of the supercapacitor, which needs to be known when it is to be integrated in an electrical circuit. It is possible to see from Figure 3.20 that it is preferable to use an AN-based electrolyte if high-power applications are aimed at.

The goal of this chapter was to give the main keys to analyze electrical double-layer capacitors and pseudocapacitors. The electrochemical techniques exposed in this chapter are the most widely used to characterize supercapacitors and are sufficient to get relevant parameters. The combination of the three techniques allows understanding the electrochemical phenomena that occur. Some applications are shown all along this book.

References

- Conway, B.E. (1999) *Electrochemical Supercapacitors: Scientific Fundamentals and Technological Applications*, Kluwer Academic/Plenum Publishers.
- Bard, A.J. and Faulkner, L.R. (2000) *Electrochemical Methods: Fundamentals and Applications*, 2nd edn, John Wiley & Sons, Inc.
- Qu, D. (2002) Studies of the activated carbons used in double-layer supercapacitors. *J. Power. Sources*, **109**, 403–411.
- Sapoval, B., Gutfraind, R., Meakin, P., Keddad, M., and Takenouti, H. (1993) Equivalent-circuit, scaling, random-walk simulation, and an experimental study of self-similar fractal electrodes and interfaces. *Phys. Rev. E*, **48**, 3333.
- de Levie, R. (1963) On porous electrodes in electrolyte solutions: I. Capacitance effects. *Electrochim. Acta*, **8**, 751–780.
- Keiser, H., Beccu, K.D., and Gutjahr, M.A. (1976) Abschätzung der porenstruktur poröser elektroden aus impedanzmessungen. *Electrochim. Acta*, **21**, 539–543.
- Song, H.-K., Hwang, H.-Y., Lee, K.-H., and Dao, L.H. (2000) The effect of pore size distribution on the frequency dispersion of porous electrodes. *Electrochim. Acta*, **45**, 2241–2257.

8. Zheng, J.P. and Jiang, Z.N. (2006) Resistance distribution in electrochemical capacitors with spiral-wound structure. *J. Power. Sources*, **156**, 748–754.
9. Portet, C., Taberna, P.L., Simon, P., and Laberty-Robert, C. (2004) Modification of Al current collector surface by sol–gel deposit for carbon-carbon supercapacitor applications. *Electrochim. Acta*, **49**, 905–912.
10. Taberna, P.L., Simon, P., and Fauvarque, J.F. (2003) Electrochemical characteristics and impedance spectroscopy studies of carbon-carbon supercapacitors. *J. Electrochem. Soc.*, **150**, A292.

4

Electrical Double-Layer Capacitors and Carbons for EDLCs

Patrice Simon, Pierre-Louis Taberna, and François Béguin

4.1

Introduction

Accumulators, electrochemical capacitors (ECs) (or supercapacitors), and capacitors are the three main electrochemical systems that can be used to store energy. As described in the so-called Ragone plot shown in Figure 4.1, each of these systems offers different characteristics in terms of specific power and energy. From a general point of view, accumulators, and more precisely Li-ion batteries, can store high energy densities (up to 180 Wh kg^{-1} for commercial products) with low-power densities (up to about 2 kW kg^{-1}). Electrical double-layer capacitors (EDLCs) can deliver very high-power density (15 kW kg^{-1}) with lower stored energy (5 Wh kg^{-1}) than that of batteries.

EDLCs can be applied in the case of stationary and mobile systems requiring high-power pulses: car acceleration, tramways, cranes, forklifts, emergency systems, and so on. Moreover, owing to their low time constant, they can quickly harvest energy, for example, during deceleration or braking of vehicles.

Although EDLCs are able to provide high power with a long cycle life compared to accumulators, they suffer from a relatively low energy density. Therefore, the main ongoing research direction concerns the optimization of the existing electrode materials and the development of new materials.

Industrial EDLCs are essentially based on nanoporous carbon electrodes. The reasons for this choice lie in the high availability, low cost, chemical inertness, and good electrical conductivity of activated carbons (ACs), as well as a high versatility of texture and surface functionality. For these reasons, this chapter presents the capacitance properties of carbon-based electrodes, showing optimization strategies playing on the structure/nanotexture of the carbon and on the nature of the electrolyte.

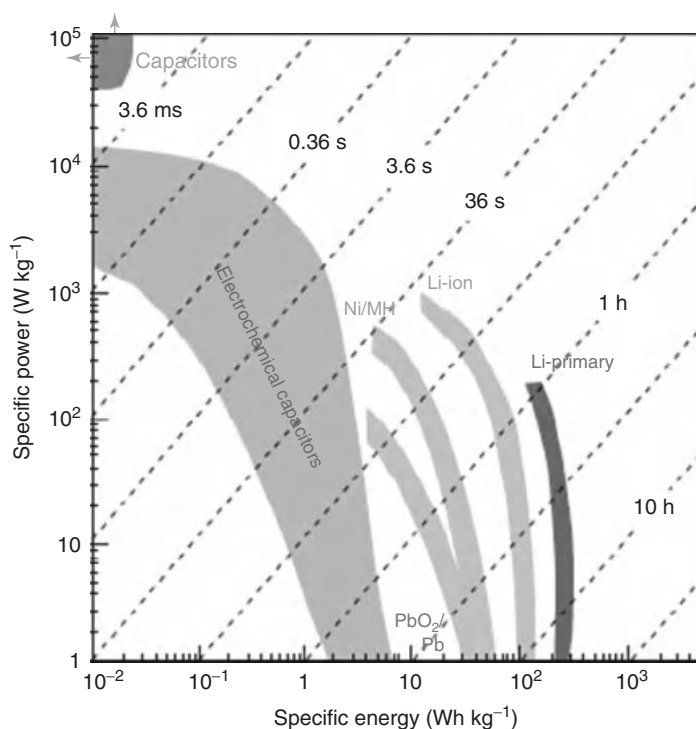


Figure 4.1 The Ragone plot for various electrochemical energy storage systems: accumulators, capacitors, and electrochemical capacitors. From Ref. [1].

4.2

The Electrical Double Layer

EDLCs are ECs storing the charge electrostatically by reversible adsorption of ions of the electrolyte onto electrochemically stable high specific surface area (SSA) carbonaceous active materials. Charge separation occurs on polarization at the electrode/electrolyte interface, producing what Helmholtz [2] described in 1853 as the double-layer capacitance C according to:

$$C = \frac{\epsilon_r \epsilon_0 A}{d} \quad \text{or} \quad C/A = \frac{\epsilon_r \epsilon_0}{d} \quad (4.1)$$

where ϵ_r is the relative dielectric constant of the electrolyte, ϵ_0 the dielectric constant of vacuum, d the effective thickness of the double layer (charge separation distance), and A is the surface area of the interface.

This capacitance model was later refined by Gouy and Chapman, and Stern and Geary [3] who suggested the presence of a diffuse layer in the electrolyte due to the accumulation of ions close to the electrode surface, as presented in Figure 4.2 for aqueous electrolytes. The double-layer capacitance is between 5 and 20 $\mu\text{F cm}^{-2}$ depending on the electrolyte used. Specific capacitance achieved with aqueous

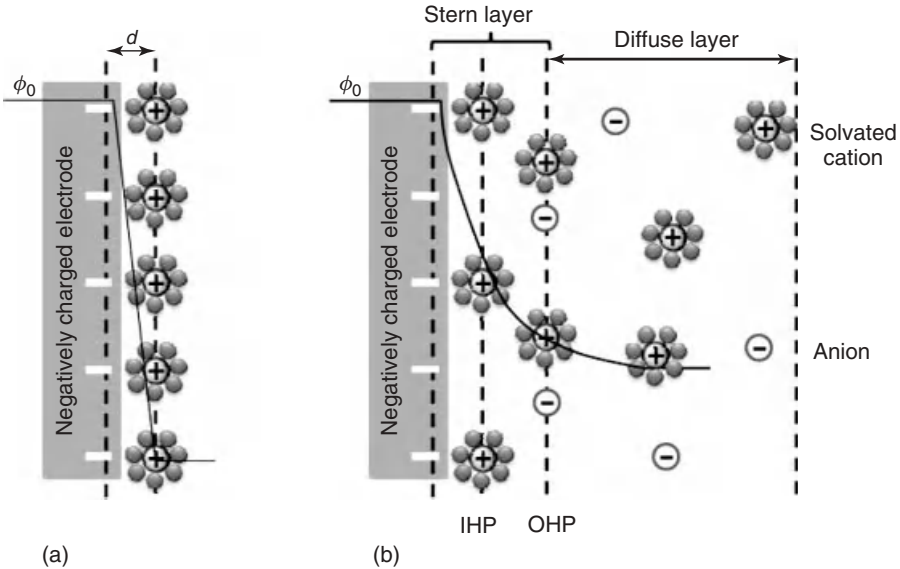


Figure 4.2 (a) Helmholtz and (b) Stern model of the electrical double layer formed at a negatively charged electrode/electrolyte interface in aqueous electrolyte. IHP refers to the distance of the closest approach of ions and OHP refers to that

of the nonspecifically adsorbed ions. The OHP is also the plane where the diffuse layer begins. d is the double-layer distance described by the Helmholtz model. ϕ_0 is the potential at the electrode surface [4].

alkaline or acid solutions is generally higher than in an organic electrolyte, but organic electrolytes are more widely used owing to a higher operation voltage (up to 2.7 V in symmetric systems). As the energy stored is proportional to voltage squared (Eq. (4.3)), a threefold increase in voltage, U , results in about 1 order of magnitude increase in energy, E , stored at the same specific capacitance.

To increase the charge stored, it is necessary to increase the surface area of the electrode/electrolyte interface; this is usually achieved by enhancing the carbon surface area using different precursors as well as different synthesis conditions. Surface area is generally increased by the development of porosity in the bulk of the carbon materials. Unfortunately, there is no simple linear relationship between the surface area and the capacitance [5]. Indeed, more than the total porous volume, the way this porosity is created – that is, control of the pore size as well as pore size distribution – greatly impacts on the carbon capacitance.

The main electrical characteristics of EDLCs are the energy and the power densities, and their electrostatic charge storage mechanism is responsible for the unique features shown in Figure 4.1.

The maximum power density is given by Eq. (4.2):

$$P = U^2 / (4R) \quad (4.2)$$

where U is the maximum cell voltage (V), R the series resistance (Ω), and P the maximum power (W).

Thanks to the electrostatic charge storage mechanism, the series resistance does not contain any charge-transfer resistance contribution associated with the electron exchange as is observed for redox reactions. Thus, the series resistance is lower than that of batteries at the cell level; that explains the higher power density of supercapacitors compared to that of batteries.

Cell voltage is mainly limited by electrolyte stability. When using aqueous-based electrolytes such as KOH or H_2SO_4 , the maximum cell voltage is about 0.9 V. Most of the commercial devices use an organic electrolyte, so that the operating voltage reaches 2.7 V. Conventional organic electrolytes are acetonitrile (CH_3CN , or ACN) or propylene carbonate (PC) containing $N(C_2H_5)_4^+BF_4^-$ salt.

The maximum energy density is given by Eq. (4.3):

$$E = \frac{1}{2} CU^2 \quad (4.3)$$

where U is the maximum voltage (V), C the capacitance (F), and E the energy (J).

Since the charge storage is achieved at the surface of the active material, at the difference of the batteries where the charge is stored in the bulk of the material (in the chemical bonds through electrochemical redox reactions), energy density of ECs is less than that of Li-ion cells. However, this storage mechanism also allows a very fast delivery of the stored charge. Thus, EC devices can deliver all the stored energy in a short time, about 5 s; this process is fully reversible and energy updates can be achieved within the same time period.

The *cyclability* of supercapacitors is not limited by the active materials' volume changes (and associated aging) between the charged and the discharged state as in batteries. Being an electrostatic charge storage mechanism, the efficiency (discharge time/charge time at the same current) is close to 100%, that is, higher than in batteries. Accordingly, supercapacitor cyclability is really outstanding, and more than 1 000 000 charge–discharge cycles up to the nominal voltage can be achieved with less than 20% decrease in capacitance and less than 100% increase in resistance (at room temperature).

The *low-temperature behavior* of supercapacitors is different from that of batteries. A key parameter to control for improving the low-temperature behavior is electrolyte conductivity, which decreases when the temperature is decreased. Li-ion batteries have to use carbonate-based electrolytes that are needed to build the solid electrolyte interphase (SEI) at the negative and positive electrodes. Such carbonate-based solvents (propylene carbonate (PC), ethylene carbonate (EC) dimethyl carbonate (DMC), etc.) exhibit limited ionic conductivity below $-15^\circ C$. Supercapacitors are not limited in the choice of solvents because no carbonate-based solvents are needed. Using ACN as the solvent guarantees an operation at temperatures down to $-40^\circ C$, although with degraded performances. The maximum operating temperature is in the same range as that of batteries, that is, $+70^\circ C$, limited by the electrolyte decomposition onto the high-surface-area-active carbon electrodes.

Typical performances of ECs are summarized in Table 4.1.

Table 4.1 Average performances of supercapacitors.

Specific energy (Wh kg ⁻¹)	2–5
Specific power (kW kg ⁻¹)	5–20
Charging time (s) ^a	1–5 s
Discharging time (s) ^a	1–5 s
Cyclability (cycles)	10 ⁶ and more
Calendar life	>10 years
Energetic efficiency (%)	>95
Operation temperature (°C)	–40 to +70 °C

^aTime for charging/discharging the usable total energy stored in the device.

4.3

Types of Carbons Used for EDLCs

Many different carbon forms can be used as active materials in EDLC electrodes and only a few examples that are thought to be the most representative are given subsequently. A recent and exhaustive review was published by Pandolfo and Hollenkamp and that paper [6] can be consulted for more detailed information.

4.3.1

Activated Carbon Powders

ACs are the most widely used active materials for EDLC applications because of their high SSA and relatively low cost. As in the case of batteries, the material cost is a limiting factor for EDLC applications, thus restricting the use of expensive synthesis processes and precursors. ACs are derived from carbon-rich organic precursors by heat treatment in an inert atmosphere (carbonization process), followed by physical or chemical activation to develop the surface area [7]. ACs can be obtained from natural – fruit shells such as coconut shells, wood, pitch, coke, and so on – or synthetic precursors such as selected polymers. The physical activation process consists in a partial, controlled gasification of the carbon precursor grains using CO₂ or steam, according to Eqs. (4.4) and (4.5):



Chemical (KOH, ZnCl₂, and H₃PO₄) routes can also be used. KOH activation is a complex process, involving several redox reactions with carbon, followed by potassium intercalation/insertion and expansion of the structure [8, 9]. In the particular case of H₃PO₄, carbonization and activation generally proceed simultaneously at temperatures lower than 600 °C [10].

On the nanotextural point of view, the activation process may lead to SSA as high as 3000 m² g⁻¹. In Figure 4.3a, the scanning electron micrograph (SEM) of an AC prepared from coconut shell shows macropores (>50 nm width) that are

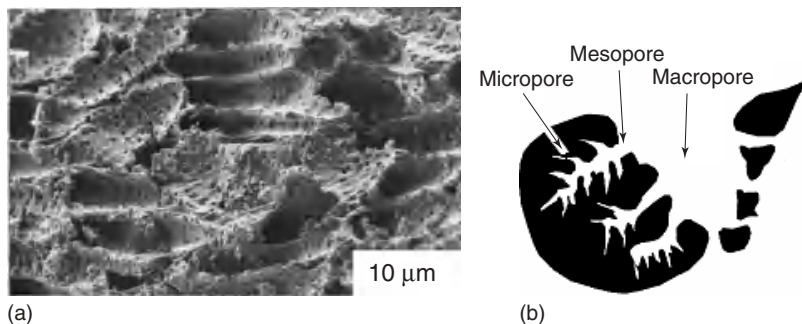


Figure 4.3 (a) Activated carbon produced from coconut shell and (b) relative disposition of the pores in an activated carbon. From Ref. [11].

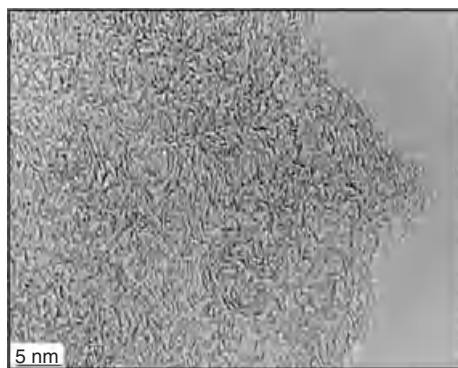


Figure 4.4 002 Lattice-fringe HRTEM image of an activated carbon.

originated from the cell structure of the precursor [11]. These macropores are not effective for adsorption of various molecules, but their presence before activation is preferable for creating mesopores (2–50 nm) and micropores (<2 nm) in the walls (small holes seen in Figure 4.3a). The pore texture of most ACs is illustrated in Figure 4.3b, where macropores and mesopores work as paths for oxidizing agents to create micropores during the activation process and also for adsorbate molecules/ions to reach the micropores during adsorption/electrosorption.

At the nanometric scale, several structural/nanotextural models have been proposed, but none of them gives a perfect description of the properties. The high-resolution transmission electron microscopy (HRTEM) 002 lattice-fringe image of an AC in Figure 4.4 shows short fringes, a few nanometers long, representing graphene-type layers, highly misoriented, some of them forming stacks of a few layers. The disorientation of the graphene-type units causes the porosity of the material. According to simulations [12, 13], the graphene layers are not perfectly planar, and curvatures might be produced by defects such as pentagons and heptagons in their structure.

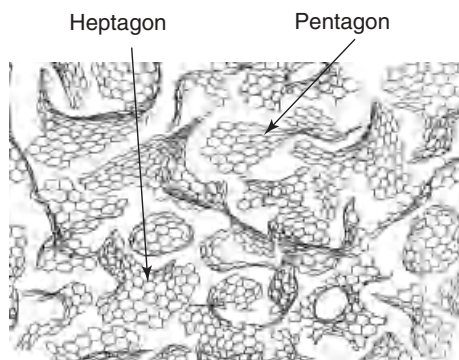


Figure 4.5 Schematic nanotextural and structural model of an AC showing fullerene-like elements [16].

On the basis of various observations, Harris *et al.* [14–16] proposed a model for the structure/nanotexture of non-graphitizable carbons that consists of discrete fragments of curved graphene sheets, in which pentagons and heptagons are dispersed randomly throughout networks of hexagons, as illustrated in Figure 4.5. Such a model is, of course, an imperfect representation of the arrangement of the graphene-type units; in particular, it does not show the three-dimensional connection of units together.

For making electrodes, AC powders are processed into active material films by mixing with conductive carbon black and an organic binder; films are coated onto metallic current collectors to obtain the electrodes. Most of the recent commercial devices use AC-based electrodes in organic electrolytes with a cell operating voltage up to 2.7 V. In such electrolytes, AC capacitance reaches about 100 F g^{-1} and 50 F cm^{-3} ; in aqueous electrolytes, it can be increased up to 200 F g^{-1} but the cell voltage is limited to less than 1 V [1, 17]. As detailed in Chapter 6, in protic electrolytes, the capacitance is enhanced by a pseudo-faradic contribution related to the surface functionality of carbons.

The pore size distribution in most AC materials is not optimum because very often it suffers from poor pore size control the activation process can achieve, thus limiting the possibility of fully exploiting the whole developed surface area to form the double layer.

4.3.2

Activated Carbon Fabrics

As compared to powders, AC fabrics or carbon nanofiber paper do not need any binder addition and can be directly used as active material films. Electrical conductivity is high ($200\text{--}1000 \text{ S cm}^{-1}$). AC fabrics [6] and paper [18] are obtained from polymeric fibers such as rayon and polyacrylonitrile. Once activated, the surface area is comparable to ACs, in the range of $1000\text{--}2000 \text{ m}^2 \text{ g}^{-1}$. However, the cost of these materials is highly restricting their use in EDLC to very specific applications.

4.3.3

Carbon Nanotubes

Similar to what has happened in the field of batteries, ECs have been identified as a potentially promising application for carbon nanotubes (CNTs). CNTs are produced from the catalytic decomposition of hydrocarbons. Depending on the synthesis parameters, single-wall carbon nanotubes (SWCNTs) as well as multiwalled carbon nanotubes (MWCNTs) can be prepared, combining both fully accessible external surface area and very high electrical conductivity. However, capacitance values achieved with purified CNT powders are not really impressive: from 20 up to 80 F g⁻¹ [19, 20]. This was mainly attributed to the poorly developed microporous volume of CNTs. In the case of MWCNTs, this volume can be increased by activation of the nanotubes [21], but the capacitance values still remain lower than for ACs. Surface functionalization by introducing pseudocapacitance contribution through oxidation treatments leads to significant improvement of the capacitive behavior in protic media [19]; however, the cycle life tends to be limited in this case. Currently, many efforts are focused on the development of dense, nano-ordered, aligned CNT forests perpendicular to the current collector that could help increase the capacitance by fine-tuning the inter-tube distance [22, 23]. Such CNT-based nanoarchitected electrodes appear to be very promising, mainly for microelectronics applications [20, 24].

4.3.4

Carbon Aerogels

Carbon aerogels are prepared from the sol–gel route, by the poly-condensation reaction of resorcinol and formaldehyde. A pyrolysis treatment in an inert atmosphere leads to the formation of a porous carbon aerogel with a controlled and uniform mesoporous texture (pore size between 2 and 50 nm), and a high electrical conductivity (several S cm⁻¹). SSAs are in the range of 400–900 m² g⁻¹, that is, lower than the AC ones. Thanks to this ordered and interconnected pore structure, power capabilities of carbon-aerogel-based electrodes are generally high [6]. However, specific gravimetric capacitance values in the range of 50–100 F g⁻¹, for organic and aqueous electrolytes, respectively, have been reported in the literature, thus limiting the usable energy density [25]. On the other hand, the very low density of these materials results in a poor volumetric capacitance and consequently to little interest for applications.

4.4

Capacitance versus Pore Size

The specific capacitance of carbons has generally a linear dependence on Brunauer-Emmet-Teller (BET) SSA for low values, but it rapidly tends to a plateau [5] when the SSA is higher than 1500–2000 m² g⁻¹. This kind of saturation phenomenon

is often interpreted by the fact that the BET model overestimates the values of the surface area [26, 27]. Therefore, some plots have been proposed versus the DFT (density functional theory) surface area, but saturation is still observed for the high surface area carbons, that is, for carbons with increasing activation degree. In order to explain this effect, Barbieri *et al.* [5] suggested that, owing to the decrease in average pore wall thickness in highly activated carbons, the electric field (and the corresponding charge density) no longer decays to zero within the pore walls.

A similar effect has been observed with a series of nanoporous carbons obtained by KOH activation of bituminous coal pyrolyzed at various temperatures [28], although these carbons were prepared from the same precursor using the same activation process and should be of comparable nanotexture. The authors remarked that the average pore size increases together with the SSA, that is, when the activation degree of carbon increases, and suggested that the interaction of ions with pore walls is weaker in larger pores, reducing the effect of porosity development on capacitance. The volumetric capacitance (gravimetric capacitance, in F g^{-1} , divided by the Dubinin–Raduskevich micropore volume, in $\text{cm}^3 \text{g}^{-1}$) of these carbons increases as the average micropore size, L_0 , decreases (Figure 4.6) [28]. Such a result fits well with the formula (4.1) expressing that capacitance increases when the distance d between pore walls and ions decreases. Contrary to the long-held axiom that pores of about twice the solvated ion size are needed to optimize the charge storage by minimizing the void volume [4], high capacitance could be obtained with microporous carbons, suggesting that even the small micropores (size less than 1 nm) contribute to the charge storage mechanism.

As a consequence, the way of developing the surface area greatly impacts the value of specific capacitance achieved. One of the key issues in designing nanotextured carbons for EDLC applications is therefore the understanding of the relationship between the electrolyte ion size and the carbon pore size. In other words, what is the best pore size to achieve the highest specific capacitance?

Considering the difficulty in perfectly controlling the pore size by the traditional activation processes, many studies have been focused over the past years on the design of tuned porous carbons for increasing the specific capacitance using different strategies. In this aim, the template synthesis route has appeared to be an efficient way to create controlled porosity in the mesoporous (2–10 nm) [29, 30] and microporous range [31]. Basically, the template process consists in filling the pores of an inorganic host matrix – the template – with a carbon precursor. After carbonization, the template is etched by acidic treatment and the obtained carbon has a pore size as a negative image of the template [32]. The specific capacitance values measured with mesoporous templated carbons, although slightly higher than standard ACs in some cases, did not show a real breakthrough: about 200 F g^{-1} in sulfuric acid and 110 F g^{-1} in organic electrolytes [29, 30, 33]. Moreover, the linear relationship shown in Figure 4.7 between gravimetric capacitance and the pore volume measured by CO_2 adsorption at 273 K (volume of pores smaller than 0.7–0.8 nm) indicates that the capacitance behavior of these carbons is essentially related to the subnanometric pores in the walls. The straight mesoporous channels

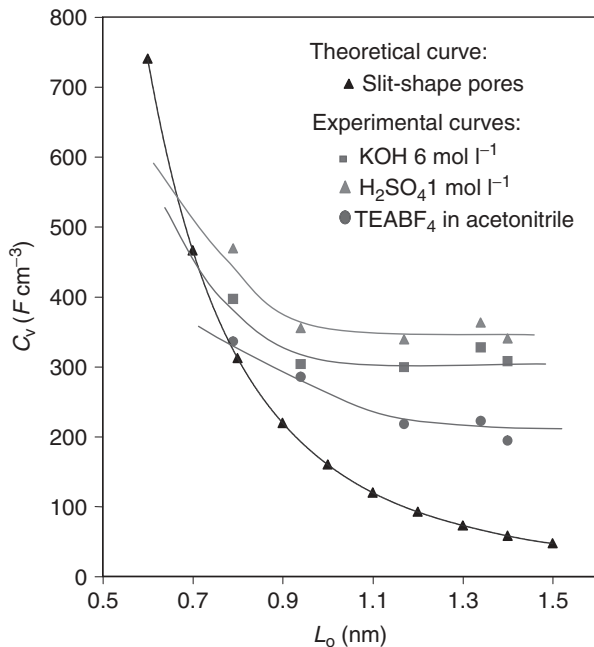


Figure 4.6 Theoretical volumetric capacitance (calculated for one ion occupying one pore of volume L_0^3) and experimental volumetric capacitance (gravimetric capacitance divided by Dubinin–Raduskevich micropore volume) in various electrolytes

(1 mol l⁻¹ H₂SO₄, 6 mol l⁻¹ KOH, and 1 mol l⁻¹ TEABF₄ in acetonitrile) versus average pore size L_0 for a series of bituminous-coal-derived carbons activated by KOH at 800 °C. From Ref. [28].

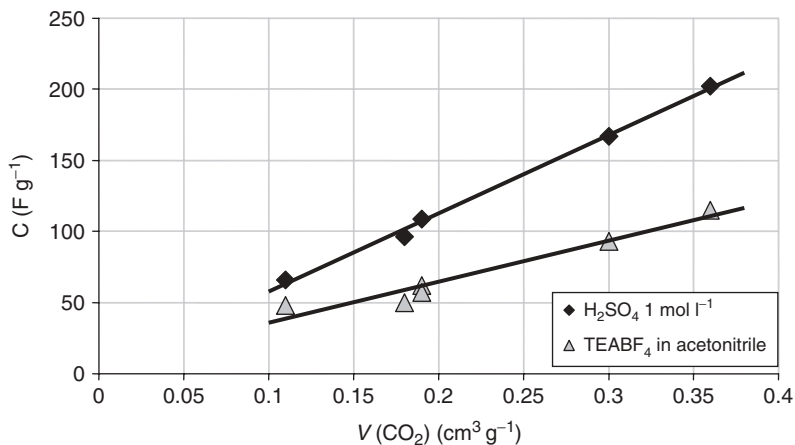


Figure 4.7 Capacitance in 1 mol l⁻¹ H₂SO₄ and 1 mol l⁻¹ TEABF₄ in acetonitrile versus ultramicropore volume for various templated carbons. From Ref. [30].

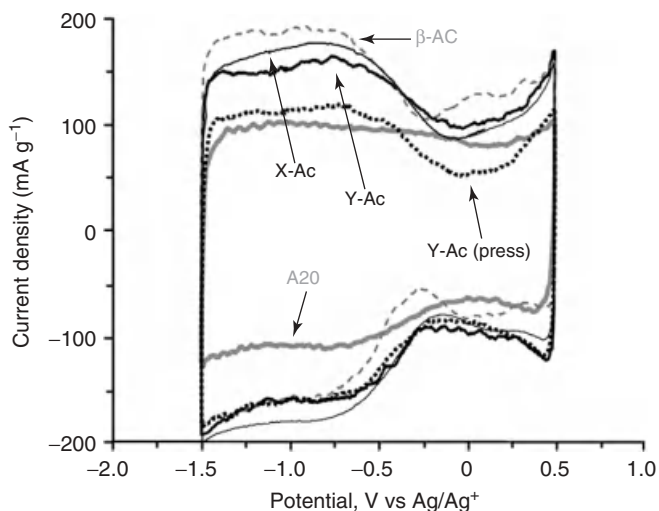


Figure 4.8 Three-electrode cyclic voltammograms of template microporous carbons. A20 is a typical microporous activated carbon taken as reference. From Ref. [35].

are only effective for a quick transportation of ions to the small micropores where they are stored [30].

The EDLC performances of ordered microporous carbons derived from zeolite templates were evaluated in $1 \text{ mol l}^{-1} \text{ Et}_4\text{NBF}_4$ in PC. The carbons were synthesized through acetylene chemical vapor deposition in zeolite Y (Y-Ac), zeolite X (X-Ac), and zeolite β (β -Ac) [31]. Another material named Y-Ac (press) was obtained after hot pressing of Y-Ac [34]. Despite their very thin pore walls (e.g., a single graphene, 0.34 nm), capacitance was found almost proportional to the SSA, even for the carbons with high SSA values ($>2000 \text{ m}^2 \text{ g}^{-1}$). By contrast with a reference microporous carbon, the cyclic voltammograms (CVs) of all template carbons in a three-electrode cell show a current drop around the zero charge potential at -0.2 V (Figure 4.8). This current minimum is attributed to the unique framework nature of the microporous template carbons made of a single graphene sheet [35] that may be semiconductive in nature [36]. Indeed, the voltammogram of SWNTs that contain semiconductive tubes showed a similar drop around 0 V in organic electrolyte, attributed to the poor electrical conductivity of the semiconductive tubes at this potential [22, 23].

4.5

Evidence of Desolvation of Ions

As already pointed out, the linear dependence of the capacitance of mesoporous template carbons with their ultramicropore ($<0.7\text{--}0.8 \text{ nm}$) volume clearly demonstrates that ions are essentially stored in small micropores [30]. On the other hand,

considering the diameters of solvated Et_4N^+ (1.30 nm) and BF_4^- (1.16 nm), and neat Et_4N^+ (0.68 nm) and BF_4^- (0.48 nm) [37], suggests that ions are at least partly desolvated when stored in ultramicropores.

Charge storage in pores smaller than the size of solvated electrolyte ions was fully evidenced by using carbide-derived carbons (CDCs) [38]. These materials are obtained from metal carbide chlorination at temperatures ranging from 400 to 1000 °C according to the following Eq. (4.6) [32]:



After preparation, the CDC samples are annealed at 600 °C under H_2 atmosphere to clean the surface and neutralize the reactive carbon dangling bonds. This method allows the synthesis of carbons with controlled pore range, since porosity is issued from the leaching out of metal atoms M. By playing with temperature and thermal treatment duration, narrow pore size distribution CDCs were prepared, with a mean value that is tunable with better than 0.05 nm accuracy. Table 4.2 lists the porous characteristics of these carbons. References [38–40] can be consulted for additional information.

The CDCs were used as model materials to study the ion adsorption in pores of average size between 0.6 and 1.0 nm. Figure 4.9 shows zone (I, II, III) the normalized capacitance (specific capacitance divided by BET SSA) versus the CDC pore size, obtained in an ACN-based electrolyte containing 1.5 mol l⁻¹ Et_4NBF_4 salt [38] in a two-electrode cell configuration. Each electrode contains an aluminum current collector foil coated on one side with the CDC material film with a loading of 15 mg cm⁻². The film composition is 95% CDC and 5% PTFE as binder and the separator is a TeflonTM sheet from Gore.

The normalized capacitance decreases with decreasing pore size until a critical value is reached, where it dramatically increases. Pores below 1 nm contribute greatly to the double-layer charge storage although they are smaller than the size of solvated ions. This capacitance increase for pore size <1 nm is explained by the distortion of the ion solvation shell, leading to a closer approach of the ions to the carbon surface, which by Eq. (4.1) leads to improved capacitance. Plotting the data obtained for bituminous coal (Ref. [28] and Figure 4.6) using the same scale

Table 4.2 Porosity characteristics of CDCs from Ar isotherms [41].

Chlorination temperature (°C)	BET SSA (m ² g ⁻¹)	Pore volume (cc g ⁻¹)	Average pore width (nm)	Maximum pore width ^a (nm)
500	1140	0.50	0.68	1.18
550	1202	0.51	0.72	1.29
600	1269	0.60	0.74	1.23
700	1401	0.66	0.76	1.41
800	1595	0.79	0.81	1.54
900	1625	0.8	1.0	2.5

^aEighty-five percentage of the pore volume is below this size.

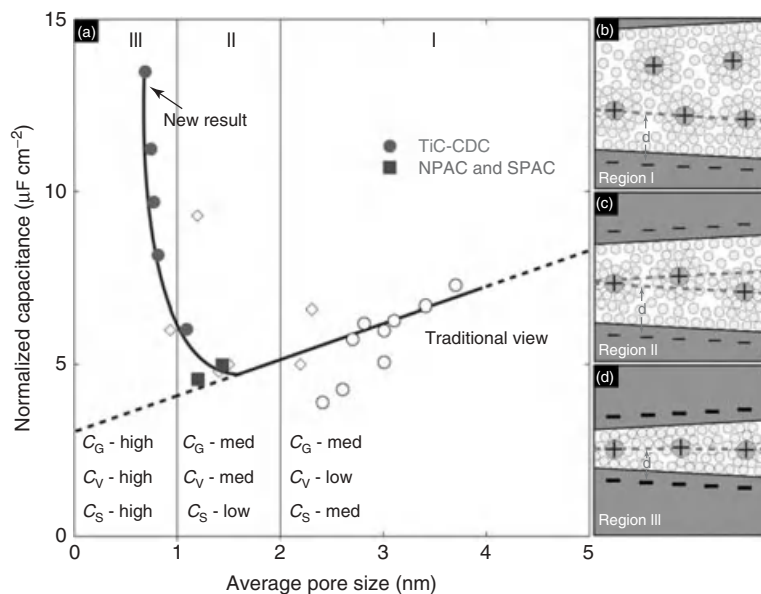


Figure 4.9 Normalized capacitance versus average pore size for TiC-CDC and other carbons from literature tested in the same electrolyte. NPAC and SPAC refer to natural porous activated carbon and synthetic porous activated carbon, respectively. From Ref. [38].

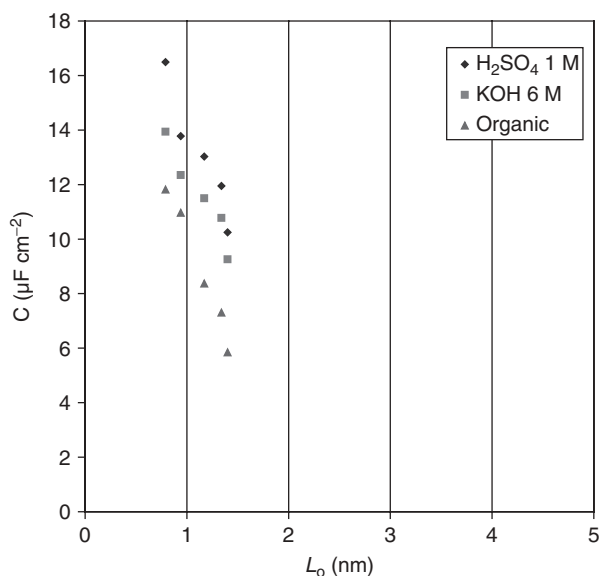


Figure 4.10 Normalized capacitance versus average pore size for bituminous-coal-derived nanoporous carbons in various electrolytes ($1 \text{ mol l}^{-1} \text{ H}_2\text{SO}_4$, $6 \text{ mol l}^{-1} \text{ KOH}$, and $1 \text{ mol l}^{-1} \text{ TEABF}_4$ in acetonitrile). Adapted from data of Ref. [28].

as in Figure 4.9 gives a comparable trend (Figure 4.10) demonstrating the high efficiency of subnanometric pores whatever the kind of precursor and/or process used for creating porosity.

Once it was unambiguously established that ions could access pores smaller than their solvated size, with a resulting normalized capacitance improvement, work has been focused on the study of the relationship between the ion size and the pore size to understand the ion confinement in these narrow pores. A first step consisted of using a three-electrode cell experimental setup (Chapter 3) to get the electrochemical signature of each electrode in ACN containing $1.5 \text{ mol l}^{-1} \text{ Et}_4\text{NBF}_4$. In such experiments, the cell voltage is controlled and a reference electrode is used to record the positive and negative electrode potentials.

A sketch of the cell stack is given in Figure 4.11; the working electrode and the counter electrode consist of an aluminum foil current collector coated with the CDC material film with a mass loading of 15 mg cm^{-2} . Two stainless steel clamps keep the electrode/separator/electrode stack under constant pressure.

Figure 4.12 shows the CVs at a voltage scan rate of 20 mV s^{-1} for two CDCs of different average pore size: 0.68 and 0.8 nm [42].

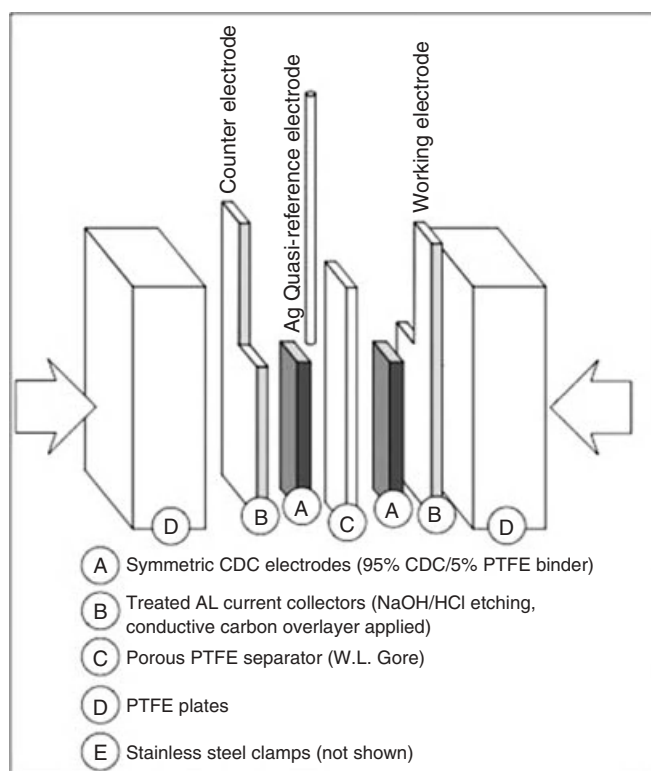


Figure 4.11 Sketch of the three-electrode cell used to run cyclic voltammograms (CVs) and galvanostatic cycling (GC) of microporous CDC carbons.

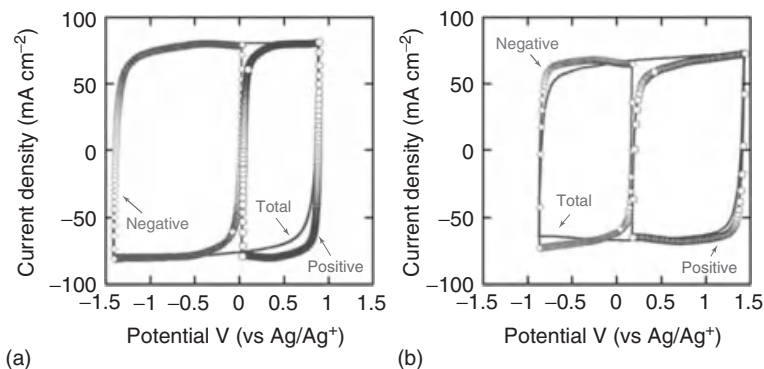


Figure 4.12 Three-electrode cell CVs of CDCs with average pore size 0.68 nm (a) and 0.8 nm (b) in ACN + 1 mol l⁻¹ Et₄NBF₄ electrolyte, showing the different capacitive behaviors for the cation and the anion. Voltage scan rate: 20 mV s⁻¹. From Ref. [42].

In Figure 4.12a, it can be seen that the potential range is larger for the negative electrode than for the positive one. Using Eq. (4.7) to calculate the capacitance:

$$C = \frac{I}{\left(\frac{dV}{dt}\right)} \quad (4.7)$$

it can be deduced that the positive electrode capacitance is larger than the negative one since the positive scan rate is smaller than the negative one.

Figure 4.13 shows an example of a positive and negative electrode capacitance measurement for the CDC with average pore size of 0.8 nm, using galvanostatic cycling (GC) in the three-electrode cell configuration. The voltage was set between 0 and 2.3 V, and the positive and negative electrode potential variations were recorded.

Figure 4.14 shows the capacitance values (calculated from the slopes of the galvanostatic discharge plots) versus the average pore size of the carbons for the cell, the positive and negative electrodes [42]. At the positive electrode, anion adsorption occurs while the cation is adsorbed at the negative electrode. The positive and negative electrode capacitance, as well as the cell capacitance, passes through a maximum at a different carbon pore size. The larger capacitance of the positive electrode (anion adsorption) can be explained by the difference in the ion size, the diameter of the bare Et₄N⁺ cation being larger than the BF₄⁻ anion (0.68 and 0.48 nm, respectively).

The average pore size value where the positive electrode capacitance is maximum (anion adsorption) is 0.7 nm. This value is between the bare anion diameter (0.48 nm) and the solvated ion diameter in ACN (1.16 nm). This confirms that the anions need to be partially desolvated to enter these micropores. The same can apply to the cation adsorption at the negative electrode, since the average pore size (0.76 nm) corresponding to the capacitance maximum is between the bare cation diameter (0.68 nm) and the solvated cation diameter (1.30 nm). Thus, it appears that there is an optimum pore size to maximize the capacitance for carbons in ACN + 1 mol l⁻¹ Et₄NBF₄ electrolyte; this optimum pore size depends on the ion size. The

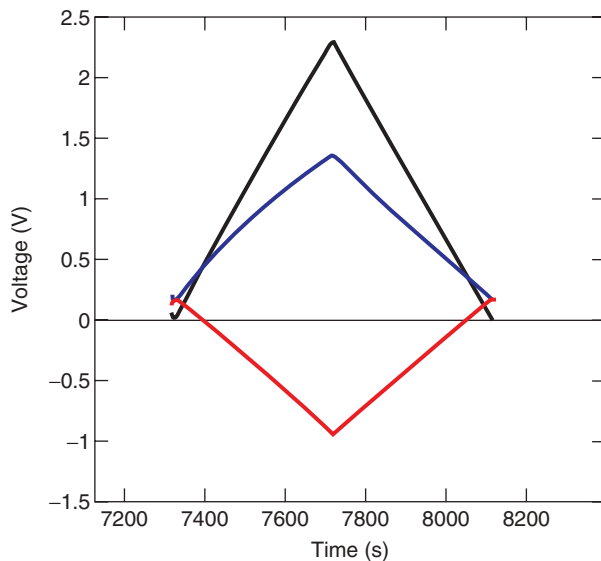


Figure 4.13 Galvanostatic cycling (20 mA cm^{-2}) of the cell (black) based on the 0.8 nm CDC in ACN + $1 \text{ mol l}^{-1} \text{ Et}_4\text{NBF}_4$ electrolyte. The positive (blue) and the negative (red) electrode potentials were recorded during the cell cycling.

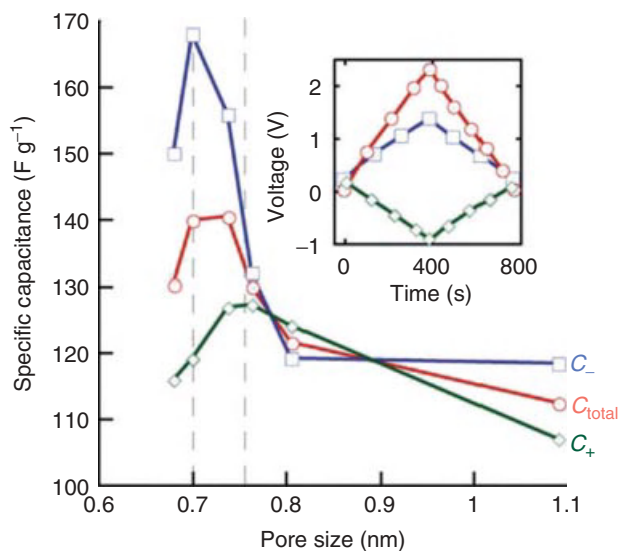


Figure 4.14 The specific capacitances calculated from a constant current discharge (inset, colors as for main plot) for the anion/positive electrode (C_-) and cation/negative electrode (C_+) show similar

behavior until a critical average pore size of $\sim 0.8 \text{ nm}$ is reached. At pore sizes below this value, the capacitance values of positive and negative electrodes diverge. From Ref. [42].

capacitance of the cell can be increased up to 140 F g^{-1} , which is more than the average capacitance of 100 F g^{-1} reported for ACs in the same electrolyte. There is definitely a significant interest in understanding the relationship between the ion size and the carbon pore size to optimize the capacitance of carbons in organic electrolytes, and, in this way, microporous carbons seem to have the capability to push away the limits.

In this sense, striking results have been obtained by Ania *et al.* [43] using a commercial AC cloth with narrow pore size distribution in $1 \text{ mol l}^{-1} \text{ Et}_4\text{NBF}_4$. Although the average QSDFT (Quenched Solid Density Functional Theory) pore size distribution of this carbon is centered at 0.58 nm , with 63% of the porosity below the computed cation size (0.68 nm for Et_4N^+), the carbon demonstrates a relatively high capacitance value of 92 F g^{-1} . Such an unexpected value confirms that the desolvated cationic species *in situ* squeeze in the pores under the effect of the electric field, showing slightly lower dimensions than their computed limiting size. It appears then that the approximation of computing the ionic dimensions based on their rigid and optimized minimum energy structure does not apply when the ions are forced to move driven by the imposed polarization of the electrodes. By computing several conformations, it has been shown that the limiting size in the case of the Et_4N^+ cation may apparently go down to values below the average pore size of the carbon as estimated by the maximum value in its pore size distribution [43].

The optimal match between the pore size and the dimensions of the distorted electrolyte gives rise to an enhanced capacitance because of multiple interactions of the ions with the pore walls of the carbon cloth. As shown in Figure 4.15, when

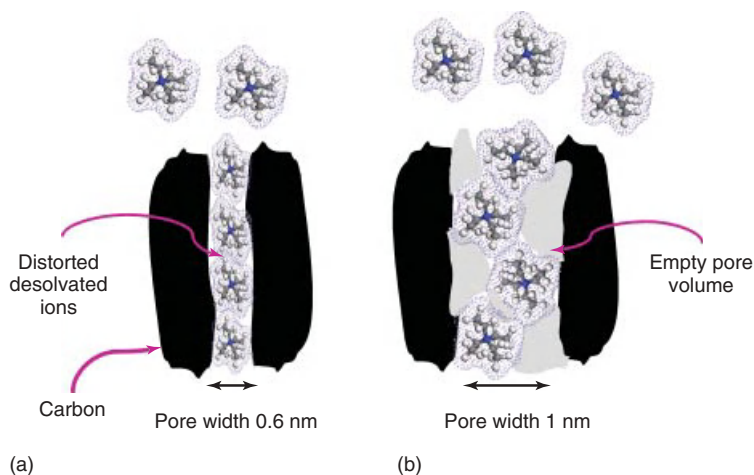


Figure 4.15 Illustration of the pore-ion interactions inside the pores of carbon electrodes; (a) pore width matching the dimensions of distorted electrolyte cations – carbon cloth in organic medium –

and (b) carbon with pore width much larger than the cation's limiting size (in this case the empty volume might be occupied by solvent molecules or even some anions). From Ref. [43].

distorted ions enter pores the size of which is smaller than the limiting size of the ionic species of the electrolyte, such a confinement state does not allow the formation of a traditional electrical double layer constituted by one layer of solvated ions adsorbed on each pore wall; the ions rather form a monolayer surrounded by the charged carbon surface. A model where ions form an electric wire-in-cylinder inside micropores of small sizes has recently been proposed by Huang *et al.* [44, 45] and is detailed in Chapter 5.

As ions are flexible species with a nonfixed diameter and since pores of the carbon are distributed around an average value, one should be always careful in interpreting the data obtained by comparing the respective dimensions and should not expect that it will be possible to obtain perfectly quantitative correlations.

4.6

Performance Limitation: Pore Accessibility or Saturation of Porosity

4.6.1

Limitation by Pore Accessibility

Galvanostatic or CV measurements using large cells do not permit getting any information about the extent of the solvation shell or the effective size of the ion seen by the carbon during the adsorption process. Such information can be obtained from dynamic measurements by using the cavity microelectrode (CME). Cachet-Vivier *et al.* [46] were the first to report an electrochemical study of powder materials by means of the CME. Such an electrode allows a small amount of powder (hundreds of micrograms, depending on the size of the cavity) to be characterized. As compared with conventional electrodes, the real electrochemical interface surface area is around a fraction of a square millimeter and the ohmic drop arising from the bulk of the electrolyte can be neglected, allowing the use of scan rates of a few volts per second to characterize the powder. Equally important, the time required to prepare and test an electrode is on the order of minutes instead of hours to days with a conventional electrode, enabling combinatorial electrochemistry studies [47].

A sketch of the CME is given in Figure 4.16. It consists of a Pt wire sealed in a glass rod. A microcavity of $\sim 10^{-6}$ cm³ (characteristic length of the electrode is about 100 μ m) was made by dissolving the Pt wire in aqua regia. The microcavity is filled with active material by pressing it on the carbon powder spread on a glass plate; cavity cleaning was achieved by soaking the electrode in alcohol in an ultrasonic bath after each experiment. The counter electrode is a rolled platinum foil of 1 cm²; a silver rod is used as a quasi-reference electrode.

CDC samples were used to pack the CME and they were electrochemically characterized in the ACN + 1 M NEt₄BF₄ electrolyte [41]. Figure 4.17 shows the three-electrode CVs for CDC samples with average pore size from 0.68 up to 1 nm. The CME not being a quantitative technique, all the CVs were normalized to the

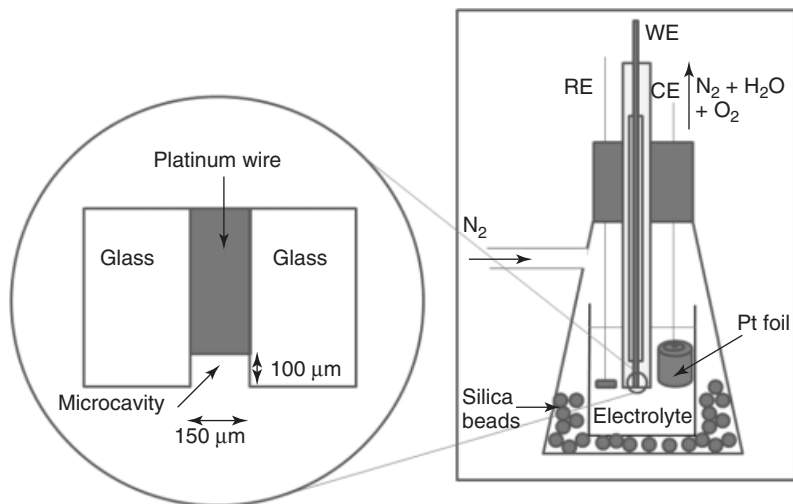


Figure 4.16 Three-electrode setup including the cavity microelectrode (CME) as working electrode (WE). Inset: detail of the CME; RE, reference electrode; CE, counter electrode. From Ref. [41].

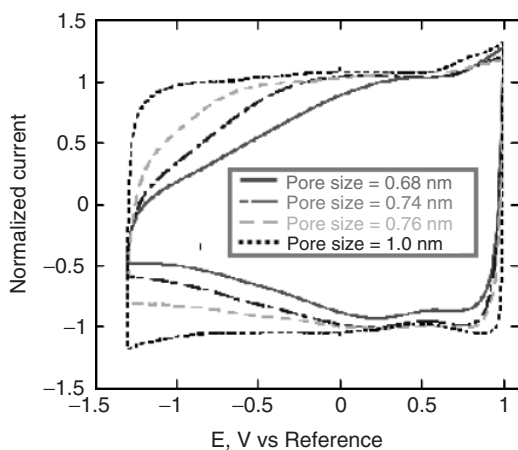


Figure 4.17 Normalized CVs of CDC samples in ACN+1.5 M NEt_4BF_4 electrolyte. Scan rate: 100 mV s^{-1} . From Ref. [41].

capacitive current for comparison purpose. The open-circuit potential (OCP) for all the samples was found to be close to 0.3 V versus Ag Ref.

In Figure 4.17, it can be seen that in the range 0.3–1 V versus Ag Ref, the shape of the CVs is purely capacitive with a rectangular shape. From this potential range corresponding to the anion adsorption, it can be deduced that the BF_4^- effective ion size seen by the carbons is less than – or close to – 0.68 nm. Keeping in mind the bare (0.48 nm) and solvated (1.16 nm) anion sizes, this result confirms the partial desolvation of the anion to access pores less than 1 nm.

The NEt_4^+ cation adsorption can be seen in the 0.3/–1.3 V versus Ag Ref potential window. For the large average pore size sample (1 nm), the shape of the CV exhibits the typical rectangular shape from a capacitive behavior. When the average pore size is decreased, the CVs are distorted and shift from the ideal capacitive behavior. It is assumed to be associated with a limitation in the pore accessibility because of a steric effect: when the pore size is decreased below a certain value, the cation cannot freely access the pore. This is more pronounced for the 0.68 nm pore size sample where the current continuously decreases with the applied voltage. The transition occurs between 1 and 0.76 nm average pore size and, accordingly, it can be deduced that the effective cation size seen by the carbon during the cation adsorption is larger than 0.76 nm and smaller than 1 nm, thus confirming that desolvation is needed for the NEt_4^+ cations to enter the micropores.

4.6.2

Limitation of Capacitor Performance by Porosity Saturation

From the foreword, it appears clearly that the capacitance is optimized when the average pore size of carbons is in the range 0.7–0.8 nm [30, 42]. NEt_4^+ cations are desolvated, and only the pores larger than the size of the bare NEt_4^+ cation are used; in such pores, there is obviously no size limitation for BF_4^- anion storage.

At this step, it is necessary to remember that the charge storage in a two-electrode cell is described by the formula (4.8) for two capacitors in series:

$$1/C = 1/C_+ + 1/C_- \quad (4.8)$$

where C is the cell capacitance and C_+ and C_- the respective capacitances of the positive and negative electrodes [48]. According to this formula, the overall capacitance C of the system is mostly influenced by the lowest value between C_+ and C_- . Because the tetraethylammonium cation is larger than the tetrafluoroborate, the cell capacitance is controlled by the capacitance of the negative electrode.

Although using carbons with pores in the optimal range – 0.7–0.8 nm – porosity may be saturated by NEt_4^+ cations before reaching the maximum possible voltage for the considered electrolyte, for example, 2.7–2.8 V for NEt_4BF_4 in ACN [49]. Figure 4.18b shows the CVs of two-electrode cells built from two carbons named PC ($S_{\text{DFT}} = 1434 \text{ m}^2 \text{ g}^{-1}$) and VC ($S_{\text{DFT}} = 2160 \text{ m}^2 \text{ g}^{-1}$) in ACN + 1.5 mol l^{-1} NEt_4BF_4 electrolyte. While VC shows a perfectly rectangular voltammogram in the whole voltage range, for PC the capacitive current dramatically decreases from around 1.5 V. According to the pore size distribution obtained from nitrogen adsorption on these carbons (Figure 4.18a), all pores of PC are narrower than 1 nm and consequently able to optimally interact with ions. However, if one considers the pores larger than the diameter of desolvated NEt_4^+ cations (0.68 nm), the corresponding DFT values are $198 \text{ m}^2 \text{ g}^{-1}$ and $964 \text{ m}^2 \text{ g}^{-1}$ for PC and VC, respectively, considering that one layer of ions lies in micropores ranging between 0.68 and 1.36 nm (surface area S_{a1}) and two layers in micropores larger than 1.36 nm (surface area S_{a2}). From these values, the maximum theoretical charge, Q_{max} ,

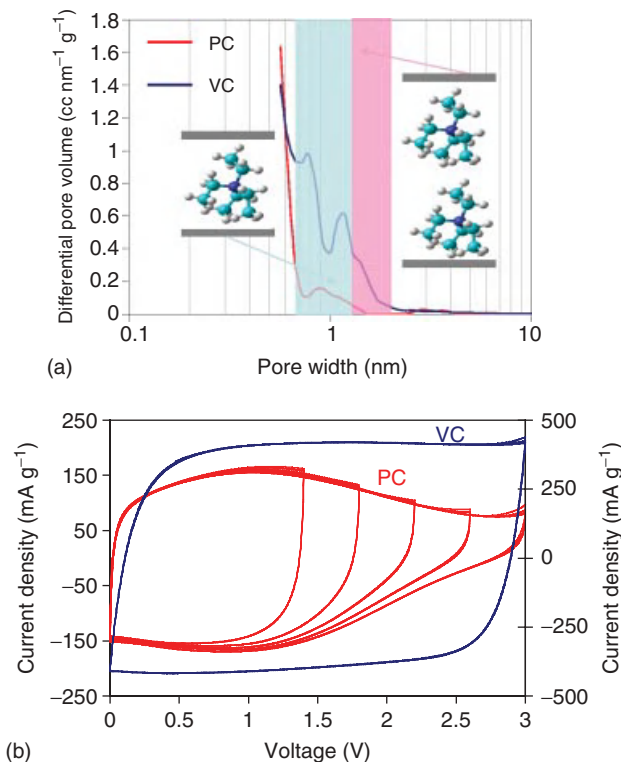


Figure 4.18 (a) Pore size distribution of carbons PC and vinylidene carbonate (VC); the blue region corresponds to pores accepting one Et_4N^+ layer and the pink one two layers, and (b) cyclic voltammograms for the EDLCs based on PC carbon (left-hand side Y-axis for current) and VC carbon (right-hand side Y-axis for current). Adapted from Ref. [49].

able to be accommodated in the pores has been calculated for both carbons, by considering the projected surface area of NEt_4^+ ions, and applying formula (4.9):

$$Q_{\max} = \frac{(S_{a1}/2 + S_{a2})}{S_{\text{ion}}} \times 1.6 \times 10^{-19} \quad (4.9)$$

Q_{\max} has been compared to the charge determined by the integration of the respective voltammograms, Q_{exp} , up to a voltage of 3 V. Values of porosity characteristics for PC and VC, together with the values of Q_{\max} and Q_{exp} are reported in Table 4.3. For PC, the theoretical and experimental values are almost identical, confirming that the narrowing of the voltammetry curve is due to porosity saturation by NEt_4^+ ions. The slightly higher value of Q_{exp} might be interpreted by some deformation of the ethyl chains by confinement in the pores [43], leading to a slightly smaller apparent diameter of NEt_4^+ . By contrast, in the case of VC, the theoretical value of charge is larger than the experimental one, demonstrating that for this carbon the porosity is not saturated, at least for the maximum voltage value reached in this experiment.

Table 4.3 Porosity characteristics of carbons PC and VC, maximum charge calculated by application of formula (4.9) and experimental charge obtained by integration of CVs.

Carbon	S_{DFT} ($\text{m}^2 \text{g}^{-1}$)	$S_{\text{DFT} > 0.68 \text{ nm}}$ ($\text{m}^2 \text{g}^{-1}$)	S_{a1} ($\text{m}^2 \text{g}^{-1}$)	S_{a2} ($\text{m}^2 \text{g}^{-1}$)	Q_{max} (C g^{-1})	Q_{exp} (C g^{-1})
PC	1434	189	105	83	61	77
VC	2160	929	768	161	246	225

Adapted from Ref. [49].

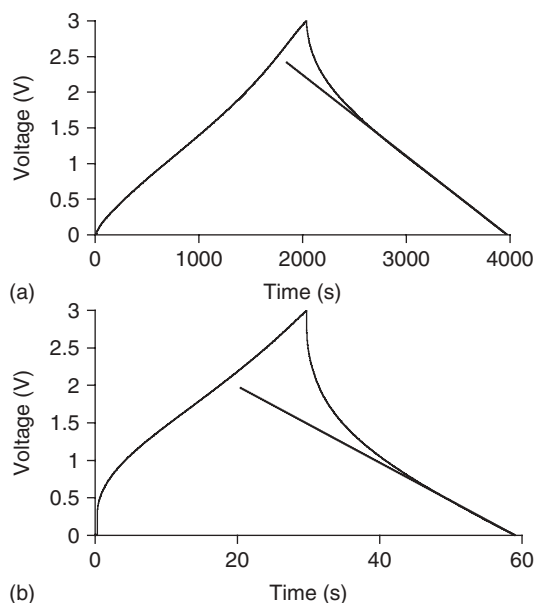


Figure 4.19 Galvanostatic charge–discharge curves for the EDLCs based on the nanoporous carbon PC ((a) current density 80 mA g^{-1} and (b) current density 960 mA g^{-1}). The straight part of the discharging line is extrapolated in order to discriminate the point of porosity saturation. This corresponds to a voltage of about 1–2 V, depending on the current density. From Ref. [49].

In the galvanostatic experiments, the porosity saturation is reflected for PC by the nonlinear shape of the “voltage–time” curve (Figure 4.19). This is not a resistivity-related effect because it is observed at a low current density of 80 mA g^{-1} (Figure 4.19a). At 960 mA g^{-1} , the drop of capacitive current at about 1.5–2 V (Figure 4.19b) shows the difficulty in storing more energy by further increasing voltage up to the electrolyte stability limits.

The carbon VC has been further applied with symmetrical tetraalkylammonium cations, NR_4^+ , of increasing chain length ($\text{R} = \text{C}_2\text{H}_5-$, C_3H_7- , C_4H_9- , $\text{C}_5\text{H}_{11}-$).

While tetraethyl cations show rectangular CVs with this carbon, the narrowing typical of saturation is clearly observed with the larger cations, the trend being a lower saturation voltage for the longest alkyl substituent [50]. The good correspondence between the maximum charge calculated on the basis of a distorted configuration of cations, Q_{max} , and the measured one, Q_{exp} , suggests that cations use a wider range of pore sizes than would be possible at their unconfined and undistorted geometries. Three-electrode cell experiments using other ACs with Bu_4NBF_4 and Et_4NBF_4 in PC confirmed that porosity saturation occurs at the negative electrode where the bulky tetraalkylammonium ions are electroadsorbed [51]. Monte Carlo simulations of a model ionic liquid (IL) in slitlike nanopores also show that the capacitance is almost constant for low voltages and vanishes above a certain threshold, that is, the energy density saturates at higher operating voltages [52].

In summary, the porous texture of carbons strongly influences their properties in ECs. With Et_4NBF_4 , the normalized capacitance is optimal in subnanometric pores, which also reveals that ions are partly desolvated in charged electrodes. However, if porosity is not sufficiently developed, saturation of pores by electrolyte ions limits the usable voltage and consequently the energy and power deliverable by a supercapacitor. Besides, taking into account that electrochemical intercalation is possible during charging [53, 54], the structural parameters of carbons might also play some role.

For enhancing capacitance, nanoporous carbons should exhibit high values of SSA ($\sim 2000 \text{ m}^2 \text{ g}^{-1}$) with a narrow pore size distribution between 0.7 and 1 nm. Therefore, innovative processes should be developed for reaching these objectives. In this context, cyclic low-temperature (200°C) oxidation of carbons by H_2O_2 , followed by thermal desorption of the surface functional groups at 900°C in an inert atmosphere, has been suggested to gradually adjust the pore size to that of ions [55]. Owing to the low burn-off of the overall process, the carbons form very dense coatings and are good candidates for improving the volumetric capacitance.

4.7

Beyond the Double-Layer Capacitance in Microporous Carbons

4.7.1

Microporous Carbons in Neat Ionic Liquid Electrolyte

Taking into account the size of the solvated Et_4N^+ and BF_4^- ions in ACN (1.30 and 1.16 nm, respectively [41]), the above-mentioned detailed data confirm that ions must be at least partially desolvated to enter the small pores. However, it is still unclear to what extent the remaining solvent molecules play a role in the capacitance increase observed for these microporous carbons. To address this issue, additional electrochemical experiments were conducted in solvent-free electrolytes: the room temperature ionic liquids (RTILs) [56, 57]. Accordingly, the size of ions in these electrolytes is well known and does not depend on the number of solvent molecules. The electrochemical behavior of the CDC materials has been studied in

an RTIL, namely the *ethyl-methyl-immidazolium-trifluoro-methane-sulfonylimide* (EMI-TFSI) IL [57, 58]. This electrolyte was selected for two main reasons: the ionic conductivity at 60 °C is high enough to allow electrochemical measurements at that temperature and the sizes of the EMI cation and TFSI anion are very similar: 0.76 and 0.79 nm, respectively, in their longest dimension. Three-electrode cells were assembled and tested in neat EMI-TFSI at 60 °C.

The change of gravimetric capacitance is plotted in Figure 4.20a for the cell, the positive as well as the negative electrode. Different from what was observed in Figure 4.14 for 1 mol l⁻¹ Et₄NBF₄ in ACN, in the present case of the EMI-TFSI electrolyte, there is no difference in the maximum observed for the positive and negative electrodes and each capacitance passes through a maximum at an average pore size of 0.72 nm. Figure 4.20b shows the change of normalized capacitance (capacitance divided by the SSA of CDC) versus the carbon pore size. The same behavior is observed and the maximum capacitance is reached for the same average pore size (0.72 nm). This result is interesting in that when both ions have the same size, the maximum capacitance appears at the same average pore size. But even more interesting, this average pore size is very close to the ion size, which is the same for both the cation and the anion (0.79 and 0.76 nm, respectively). This result means that the pore can accommodate only one ion within the pore thickness.

In addition, the capacitance reaches 150 F g⁻¹ for the 0.72 nm average pore size sample. For comparison, a commercial AC used for EDLC applications (YP17 from Kuraray) gave 95 F g⁻¹ under the same conditions. According to the data supplied by the manufacturer, this carbon has an SSA of 1709 m² g⁻¹, a pore volume of 0.877 cm³ g⁻¹ and >55% of pore volume corresponds to pores within the 1–1.265 nm range. Thus, it is a strong evidence of the interest in tailoring the carbon pore size to maximize the capacitance [58].

These results rule out the way charge storage was often described in EDLC materials, with ions adsorbed on both pore walls: carbon pore size is here in the

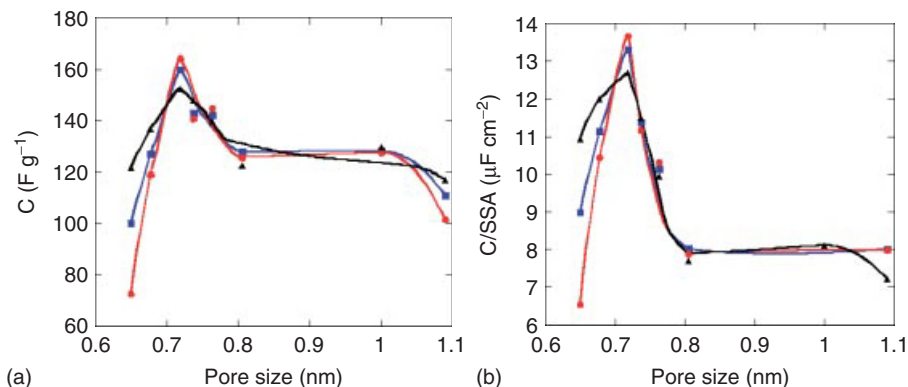


Figure 4.20 (a) Capacitance (F g⁻¹) versus average pore size for the cell (blue), positive (red) and negative (black) electrodes in neat EMI-TFSI electrolyte. From Ref. [58]. (b) Normalized capacitance (μF cm⁻²) versus average pore size for the cell (blue), positive (red) and negative (black) electrodes in neat EMI-TFSI electrolyte. From Ref. [58].

same range as the ion size and there is no space available for more than one layer of ions. Around 0.72 nm, the pore size is perfectly adapted to the ion size and ion adsorption is achieved in an efficient way. When the pore size is larger, the average distance between the pore wall and the center of the ion (d) is increased and then the capacitance for pores larger than around 0.72 nm decreases according to Eq. (4.1). For smaller pore size, the steric effect limits the ion accessibility and the capacitance is decreased.

This work suggests a general approach to selecting a porous electrode/electrolyte couple in order to maximize the capacitance. Accordingly, it seems that we have to reconsider the way the charge is stored in these subnanometer pores where no diffuse layer can be formed, moving from the traditional Helmholtz model with ions adsorbed on each pore wall, as presented in Figure 4.21a, to a situation where ions can be stacked along the pore axis (Figure 4.21b).

Shim and Kim [59] have studied the capacitive behavior of CNTs in the EMI-BF₄ IL electrolyte via molecular dynamics computer simulation and found interesting features. They modeled CNTs with different diameter (pore size) and confirmed that the distribution of ions inside the pores changes significantly with the pore size. For small pore size (<1 nm), only counter ions (of opposite charge with the surface charge of carbon) are adsorbed. Surprisingly, although these counter ions have the same charge, they lead to a charge density characterized by multiple layers with alternating signs owing to a preferential orientation inside the tubes (Figure 4.22). For pore sizes larger than 1.1 nm, counter ions as well as co-ions (of opposite charge) can enter the tube and that leads to the decrease in capacitance [59].

The specific capacitance of nanotubes normalized to the pore surface area (Figure 4.23) varies as in the electrochemical experiments on CDCs: it increases for pore size up to 0.95 nm, then decreases for larger pore size. The capacitance increase for small pore sizes is due to the nonmonotonic change of the CNT potential Φ_{CNT} , which can be decomposed into contributions from the surface charge ($\Phi\sigma_s$) and from the IL (Φ_{IL}) (4.10):

$$\Phi_{\text{CNT}} = \Phi\sigma_s + \Phi_{\text{IL}} \quad (4.10)$$

For pore sizes less than 1.1 nm, it was shown that Φ_{CNT} is dominated by Φ_{IL} , whereas it is mainly governed by $\Phi\sigma_s$ for larger pore sizes. In this pore range, according to molecular dynamics results, only counterions can enter the pores. Figure 4.24 shows the counterions aligned inside the carbon pores, denoted as the “exclusive solvation” phenomenon.

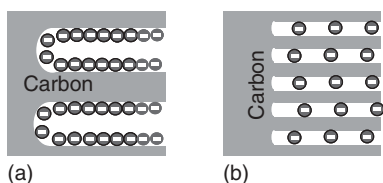


Figure 4.21 Electrical double-layer charge according to the (a) Helmholtz model and (b) in a subnanometer pore. In this example, the carbon surface is positively charged.

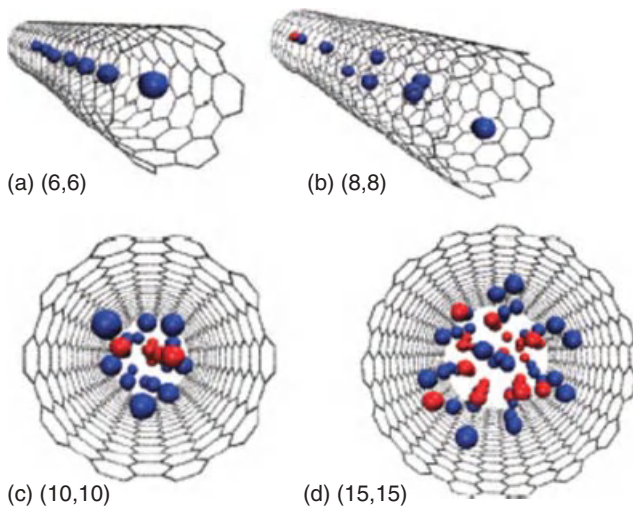


Figure 4.22 Snapshots of internal RTIL ions associated with the radial distributions inside a positively charged CNT electrode (the surface charge of CNTs is $+0.80\text{--}0.94\text{ e/nm}^2$). Red and blue dots represent the center-of-mass positions of EMI^+ and BF_4^- ions, respectively. The numbers in the legend denote the n values of the (n,n) armchair CNTs considered in the present study: 6×6 stands for a pore size of 0.81 nm , 8×8 for 1.08 nm , 10×10 for 1.35 nm , and 15×15 for 2.03 nm . From Ref. [59].

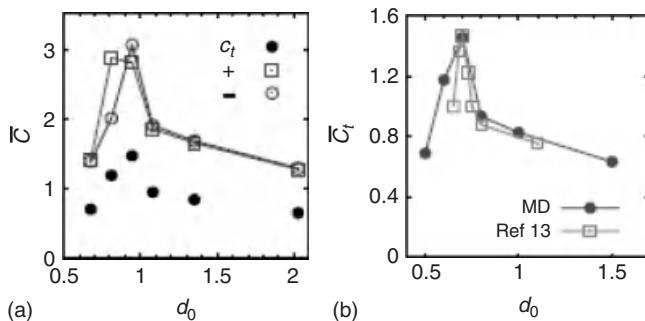


Figure 4.23 Specific capacitance of carbon nanotubes (CNTs) versus their diameter in EMI-BF_4 at 1 bar and 350 K. Units: specific capacitance ($\mu\text{F cm}^{-2}$) and d_0 (m). (a) The open squares and circles represent the positively and negatively charged electrodes, respectively, and the filled circles denote the total specific capacitance, and (b) comparison of the molecular dynamics (MD) predictions of the average specific capacitance with the experimental results. From Refs [58, 59].

Accordingly, because of their proximity to the carbon surface, the internal counterions make a major contribution to Φ_{IL} . This indicates that the alignment of the internal counterions inside the small carbon pores play a crucial role in increasing the capacitance.

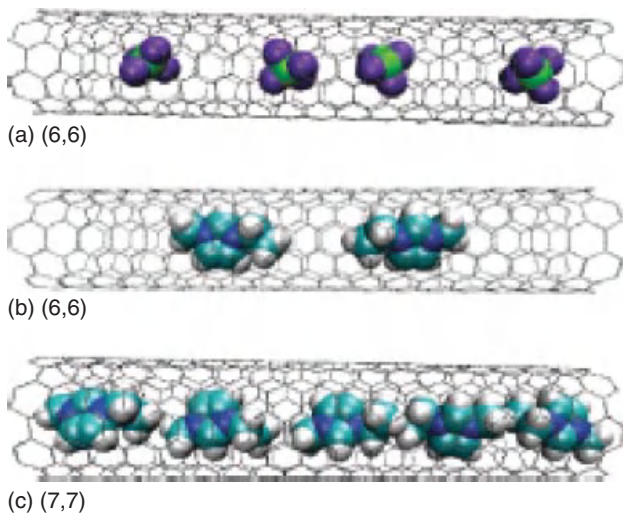


Figure 4.24 Snapshots of the internal RTIL ions inside the (a) positively and (b) negatively charged (6,6) nanotubes with a charge of $\sigma = +0.55 \text{ e/nm}^2$ (a) and $\sigma = -0.55 \text{ e/nm}^2$ (b); because of exclusive internal solvation, only cations (anions) are present inside the negative (positive) electrode. (c) Snapshot of internal RTIL ions of the (7,7) negatively charged electrode with a charge $\sigma = -0.47 \text{ e/nm}^2$. From Ref. [59].

4.7.2

Extra Capacitance with Ionic Liquids in Solution

ILs with 1-alkyl-3-methylimidazolium cations of different lengths of alkyl chain were used to study the effect of cation size on the capacitive response of carbons with tailored pore size distribution. While ion sieving appears in pure ILs, this effect is heavily mitigated for the same salts dissolved in ACN, most likely due to somewhat stronger geometrical flexibility of dissolved ions [60], as already suggested for Et_4NBF_4 [56]. Owing to this flexibility, cations can access smaller pores and the gravimetric capacitance values are higher than with pure ILs.

CDC samples of controlled average pore size were used to study the effective ion size of the EMI^+ and TFSI^- ions in ACN [58]. Figure 4.25 shows the CVs of the various samples obtained with the CME described in Figure 4.16, using 2 mol l^{-1} EMI-TFSI in ACN.

The EMI^+ cation adsorption occurs in the potential range below the open circuit voltage (OCV) (0.2 to -1.2 V vs Ref). Only the CV obtained for the 0.68 nm sample deviates from the ideal capacitive behavior; accordingly, it can be stated that the effective ion size of the EMI^+ cation is about 0.7 nm. This means that there is no real effect of solvation on the cation size when compared to the effective size found for the bare EMI^+ cation in neat EMI-TFSI electrolyte (Figure 4.20). For potentials higher than the open circuit potential (OCP), the slight distortion (shift from the ideal capacitive behavior) still observed for the 0.8 nm pore size sample tends to show that the effective size of the solvated TFSI^- anion in the ACN-based

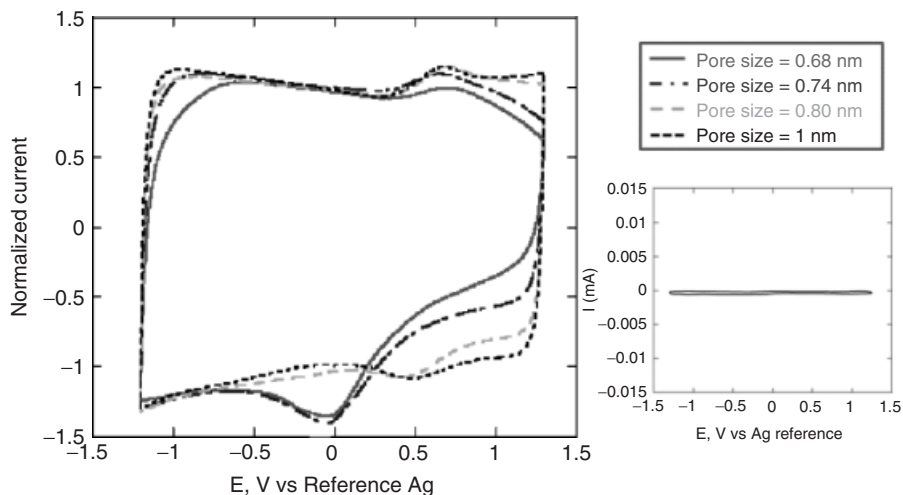


Figure 4.25 Normalized cyclic voltammograms of CDC samples using 2 mol l^{-1} EMI-TFSI in ACN; Ag reference electrode; scan rate of 100 mV s^{-1} . Right inset: CV of the Pt microelectrode alone. From Ref. [58].

electrolyte is larger than 0.8 nm , whereas the size of the bare ion size was estimated at about 0.7 nm in the neat EMI-TFSI electrolyte. Thus, the average effective size of the solvated EMI^+ ions in pores is somewhat lower than that of the TFSI^- ions, in spite the size of the bare ions being almost the same.

Below the OCP (0.2 V vs Ref) down to -1.2 V versus Ref where the EMI cation adsorption occurs, the shape of the CV for the 1 nm average pore size CDC sample is typical from an ideal capacitive behavior. However, when moving to the TFSI anion adsorption (above 0.2 V vs Ref), a set of reversible peaks appears at $0.5\text{--}0.7 \text{ V}$ vs Ref on the CVs, responsible for the capacitance increase. In a logarithmic plot of the peak current versus potential scan rate, the slope of 0.9 for both peaks is close to 1 , meaning that they can be attributed to a capacitive charge storage mechanism not limited by diffusion, according to Eq. (4.11):

$$I = CA\nu \quad (4.11)$$

where I is the current, C the capacitance (F m^{-2}), A the surface area (m^2), and ν the scan rate (V s^{-1}) [4]. Such a mechanism can be associated either with a double-layer process or a surface pseudocapacitive one. As surface pseudocapacitive redox reactions could be excluded, in particular a redox activity of the electrolyte is not observed on the CV of the Pt microelectrode alone (Figure 4.25, right side), the peaks are only linked with the adsorption of the TFSI ions inside the carbon pores.

In the specific configuration where the effective ion size is in the same range as the carbon pore size, as for the 1 nm pore size sample, the peak observed in the charge (positive scan) could be linked with the activation energy barrier to overcome and partially desolvate the ions and reorganize the solvent molecules inside the pores [61]. On the reverse scan, this process is reversible and an extra

capacitance is delivered, which is about 25–30% of the total capacitance at 10 mV s⁻¹. In this case, the associated reversible peaks would be linked with the additional activation energy created by this process, different from the case of a standard ion adsorption in larger pores.

4.7.3

Ions Trapping in Pores

In Figure 4.26 showing the CVs for the small pore size sample (0.68 nm), the plot in the first scan corresponds to a potential scan limited to the EMI adsorption potential range, where the rectangular shape is typical from a pure capacitive behavior involving EMI adsorption in the double layer. When the upper potential limit is increased to reach the TFSI anion adsorption range (above the OCV), the current dramatically drops down on the positive scan. On the reverse scan, a huge peak is observed at about 0.2 V versus Ref, before reaching back the EMI adsorption capacitive current. A logarithmic plot of peak current versus potential scan rate is presented in the inset of Figure 4.26. The slope of the plot is 0.65.

The change in the maximum current peak with the potential scan rate for a reversible diffusion-controlled reaction is given by the Randles–Sevcik equation [62] (Eq. (4.12)):

$$I_{\text{peak}} = 0.4463(nF)^{3/2}AC\left(\frac{D}{RT}\right)^{1/2} \times \nu^{1/2} \quad (4.12)$$

where I_{peak} is the maximum peak current, n the number of electrons involved, F the Faraday constant (A s), C the concentration of the diffusing species (mol cm⁻³), D the diffusion coefficient of the diffusing species (cm² s⁻¹), and ν the potential scan rate (V s⁻¹). This equation applies to any charge-transfer reaction under the

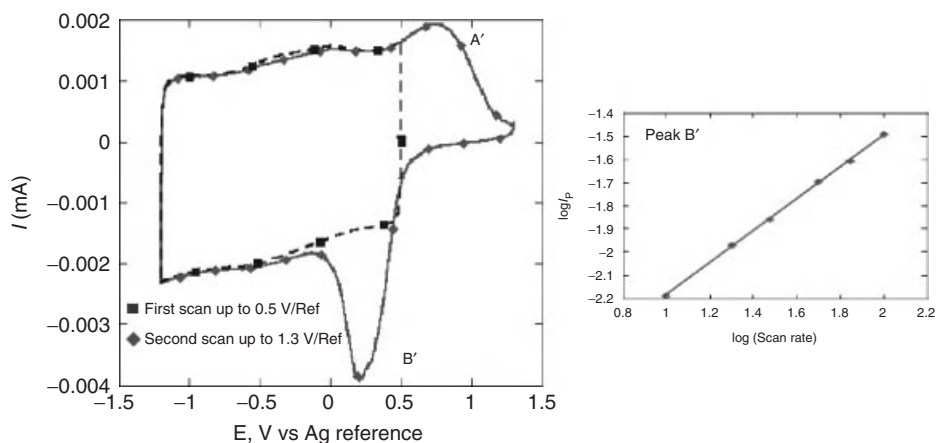


Figure 4.26 CV for the 0.68 nm average pore size sample in ACN + 2 mol l⁻¹ EMI-TFSI electrolyte, in the -1.2 V/Ref up to 0.5 V/Ref potential range (first scan) and the -1.2 V/Ref up to 1.3 V/Ref potential range (second scan). From Ref. [58].

diffusion control of the reactants to the electrode surface or the diffusion control of the products leaving the electrode surface. Accordingly, it can be used to describe a redox reaction as well as the ion transfer at an interface [58]. In the present case of the TFSI⁻ anion adsorption inside small pores of 0.68 nm, the slope of the I versus ν plot in a logarithmic scale was found to be 0.65. This value is close to 0.5, meaning that the reaction observed with the 0.68 nm average pore size sample seems to be under diffusion control. This small deviation from the theoretical 0.5 value can be explained by the nature of the electrode used in these experiments. By using porous carbon as working electrode, we are not in the ideal case of a smooth, planar electrode used in Eq. (4.12) and the geometric dispersion due to the porous network may explain the difference observed.

The current drop at a potential higher than 0.7 V/Ref on the positive scan demonstrates a limited accessibility of the TFSI⁻ anions to the small 0.68 nm pores. On the reverse scan, the huge cathodic peak occurring at 0.3 V/Ref is mainly associated with a diffusion-controlled process. During this reverse scan, the TFSI⁻ anions, which were forced to enter the small pores during the positive scan, are electrostatically forced to leave the carbon surface giving rise to the peak at ~ 0.3 V versus Ref.

A similar effect has been observed by Aurbach *et al.* [61]. as a consequence of cations trapping when using 1 mol l⁻¹ Et₄NBF₄ in propylene carbonate. A capacitor constituted of microporous carbon electrodes was charged up to 2.3 V, and maintained 1000 h at this voltage (floating) at 50 °C. After dismantling the capacitor, each electrode was then tested separately in a three-electrode cell configuration. The CV recorded in the operating range of the negative electrode shows a loss of capacitive current, C^- , while that of the positive electrode is the same before and after floating (Figure 4.27). By contrast, if the negative electrode is polarized up to 4.2 V versus Li, one notes during the first scan a very intense anodic peak, which is attributed to the desorption of Et₄N⁺ cations trapped in

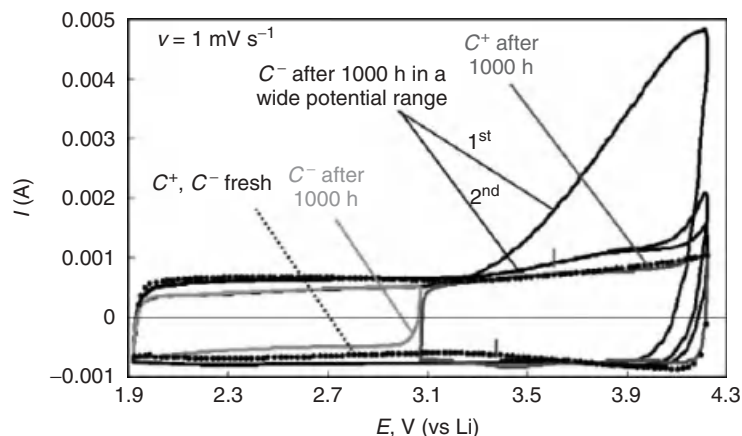


Figure 4.27 Voltammograms (1 mV s⁻¹) of each electrode of a symmetric cell before and after 1000 h floating at 50 °C. From Ref. [61].

the porosity during floating. The smaller capacitance of the negative electrode just after floating might be explained either by the adsorption of the Et_4N^+ ions in the narrow micropores or to their intercalation in disordered graphene clusters [63, 64]. The formation of decomposition products should also not be neglected [65, 66]

4.7.4

Intercalation/Insertion of Ions

Dilatometry measurements performed with a three-electrode configuration in $\text{Et}_4\text{NBF}_4/\text{ACN}$ have demonstrated size variations of the AC working electrode (Figure 4.28) [53]. The largest expansion is measured at negative polarization, with, for example, 0.6% for negative polarization of -1.35 V/ip (ip : zero charge potential) and less than 0.2% for positive polarization of 1.15 V/ip . During a potential scan from -2 to 2 V/ip , the expansion range is highly amplified, and reaches 3 and 2% for negative and positive polarizations, respectively. As Et_4N^+ cations are bigger than BF_4^- anions, Hahn *et al.* [53] suggested that the differences observed between the two electrodes are related to the insertion/intercalation of ions in the electrode material.

Later, the same authors also compared graphitic carbons and ACs [67]. Under negative polarization (2 V vs Li), the thickness of the AC electrode increases by

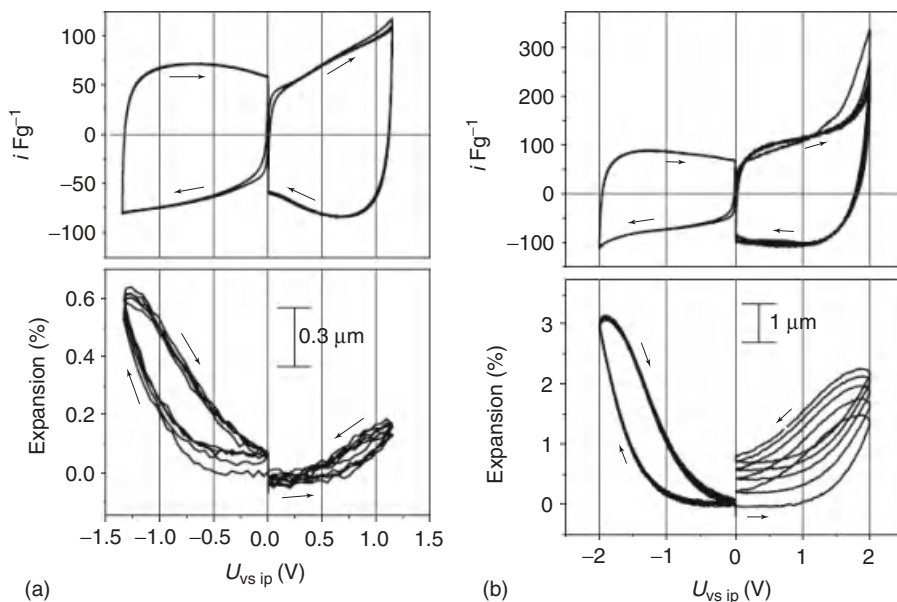


Figure 4.28 Voltammograms obtained in three-electrode configuration for different potential ranges (top) and simultaneous measurement of the expansion of each electrode (bottom). From Ref.

[53]. (a) Negative electrode from 0 to -1.35 V/ip , positive electrode from 0 to 1.15 V/ip . (b) Negative electrode from 0 to -2 V/ip , positive electrode from 0 to 2 V/ip .

about 1%, whereas it reaches around 10% for the graphitic carbons. At lower potentials (<2 V vs Li), the electrode rapidly swells and the coulombic efficiency drops. In the positive potential range (>3 V vs Li), the expansion is lower than 1% for ACs and it reaches 10% for the graphitic carbons. As the desolvated BF_4^- anions are smaller than the Et_4N^+ cations, the authors consider that the former do not intercalate into ACs. Consequently, the potential of the negative electrode is limited by cations intercalation, whereas the positive limit is associated with the oxidation of ACN. The intercalation of Et_4N^+ ions has been confirmed by *in situ* atomic force microscopic measurements on highly oriented pyrolytic graphite (HOPG) electrodes in $\text{Et}_4\text{NBF}_4/\text{PC}$ electrolyte [68]. These intercalation phenomena are probably closely related to the distortion of ions in small pores [56].

4.8

Conclusions

Desolvation, distorsion, intercalation, and ion trapping may play simultaneously during the charge of ECs in an organic electrolyte. The adsorption of ions inside the subnanometric pores should be reconsidered moving from the conventional Helmholtz model (Figure 4.29a) to a situation where counter ions (of opposite charge with the surface charge of the carbon) enter the pores partially desolvated and line up with no more than one ion within the pore thickness (Figure 4.29b). The extra capacitance observed in some cases at low scan rate could originate from additional effects related to intercalation.

The various effects related to the penetration of ions in the carbon structure, together with the particular utilization conditions of supercapacitors, may limit the operating voltage (through porosity saturation) or accelerate aging. Consequently, understanding the relationships between the electrochemical performance of supercapacitors and the structure of carbons may give additional information for optimizing these systems. For example, recent studies on SWCNT and ACs in organic electrolyte demonstrate clearly that the capacitance increase and resistance decrease under high polarization could be related to an electrochemical doping (shift of the Fermi level toward the valence band or the conduction band) of the graphene layers during charge, allowing the “butterfly” shape of voltamograms in the three-electrode cell to be partly explained [23, 69]. As the electrochemical doping strongly depends on the structure of the carbon, this feature adds to the difficulty in interpreting the repartition of ions in micropores on charging the capacitor.

Hence, from the fundamental point of view, there is a clear lack of understanding of the double-layer charging in the confined space of micropores, where there is no room for formation of the Helmholtz layer and diffuse layer expected at a solid–electrolyte interface. Computational modeling using molecular dynamics or *ab initio* methods would be, for instance, of great help in addressing the ion size in these subnanometer pores as well as solvent reorganization, one of the keys to designing the next generation of high-energy density EDLCs that can be used for longer discharge times, thus offering new application opportunities for

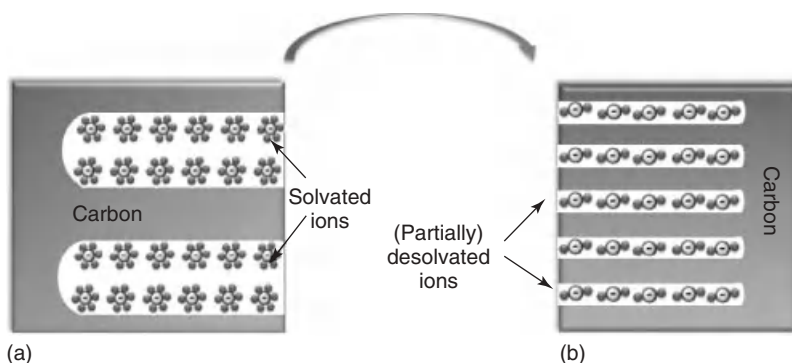


Figure 4.29 Electrical double-layer charge according to the (a) Helmholtz model and (b) in subnanometer pores. This example considers a carbon surface positively charged and the penetration of counter anions.

these devices. Magnetic resonance measurements on charged electrodes might also provide precious information on the solvation degree and on the displacements of ions in the pores [70].

References

- Simon, P. and Gogotsi, Y. (2008) *Nat. Mater.*, **7**, 845–854.
- Helmholtz, H.V. (1879) *Ann. Phys.*, **29**, 337.
- Stern, O. (1924) *Z. Elektrochem.*, **30**, 508–516.
- Conway, B.E. (1999) *Electrochemical Supercapacitors: Scientific Fundamentals and Technological Applications*, Kluwer.
- Barbieri, O., Hahn, M., Herzog, A., and Kotz, R. (2005) *Carbon*, **43**, 1303–1310.
- Pandolfo, A.G. and Hollenkamp, A.F. (2006) *J. Power. Sources*, **157**, 11–27.
- Marsh, H. and Rodríguez-Reinoso, F. (2006) *Activated Carbons*, Elsevier, London.
- Lillo-Ródenas, M.A., Juan-Juan, J., Cazorla-Amorós, D., and Linares-Solano, A. (2004) *Carbon*, **42**, 1371–1375.
- Raymundo-Piñero, E., Azais, P., Cacciaguerra, T., Cazorla-Amorós, D., Linares-Solano, A., and Béguin, F. (2005) *Carbon*, **43**, 786–795.
- Jagtoyen, M. and Derbyshire, F. (1998) *Carbon*, **36**, 1085–1097.
- Inagaki, M. (2010) in *Carbons for Electrochemical Energy Storage and Conversion Systems* (eds F. Béguin and E. Frackowiak), Taylor & Francis Group, Boca Raton, FL, pp. 37–76.
- Bandosz, T.J., Biggs, M.J., Gubbins, K.E., Hattori, Y., Pikunic, J., Thomson, K. (2003) in *Chemistry and Physics of Carbon*, Vol. 28, (ed. L.R. Radovic), Marcel Dekker, New York, pp. 137–199.
- Pikunic, J., Gubbins, K.E., Pellenq, R.J.M., Cohaut, N., Rannou, I., Guet, J.M., Clinard, C., and Rouzaud, J.N. (2002) *Appl. Surf. Sci.*, **196**, 98–104.
- Harris, P.J.F. and Tsang, S.C. (1997) *Philos. Mag. A*, **76**, 667–677.
- Harris, P.J.F. (1997) *Int. Mater. Rev.*, **42**, 206–218.
- Harris, P.J.F. (2005) *Crit. Rev. Solid State Mater. Sci.*, **30**, 235–253.
- Ruiz, V., Santamaría, R., Granda, M., and Blanco, C. (2009) *Electrochim. Acta*, **54**, 4481–4486.
- Ra, E.J., Raymundo-Piñero, E., Lee, Y.H., and Béguin, F. (2009) *Carbon*, **47**, 2984–2992.
- Frackowiak, E. and Béguin, F. (2002) *Carbon*, **40**, 1775–1787.
- Talapatra, S., Kar, S., Pal, S.K., Vajtai, R., Ci, L., Victor, P., Shaijumon, M.M., Kaur, S., Nalamasu, O., and Ajayan,

- P.M. (2006) *Nat. Nanotechnol.*, **1**, 112–116.
21. E. Frackowiak, S. Delpeux, K. Jurewicz, K. Szostak, D. Cazorla-Amoros, F. Béguin, *Chem. Phys. Lett.*, **361** (2002) 35–41.
 22. Futaba, D.N., Hata, K., Yamada, T., Hiraoka, T., Hayamizu, Y., Kakudate, Y., Tanaïke, O., Hatori, H., Yumura, M., and Iijima, S. (2006) *Nat. Mater.*, **5**, 987–994.
 23. Kimizuka, O., Tanaïke, O., Yamashita, J., Hiraoka, T., Futaba, D.N., Hata, K., Machida, K., Suematsu, S., Tamamitsu, K., Saeki, S., Yamada, Y., and Hatori, H. (2008) *Carbon*, **46**, 1999–2001.
 24. Pushparaj, V.L., Shaijumon, M.M., Kumar, A., Murugesan, S., Ci, L., Vajtai, R., Linhardt, R.J., Nalamasu, O., and Ajayan, P.M. (2007) *Proc. Natl. Acad. Sci. U.S.A.*, **104**, 13574–13577.
 25. Lee, Y.J., Jung, J.C., Yi, J., Baeck, S.-H., Yoon, J.R., and Song, I.K. (2010) *Curr. Appl. Phys.*, **10**, 682–686.
 26. Gregg, S.J. and Sing, K.S.W. (1982) *Adsorption, Surface Area and Porosity*, Academic Press, London, p. 103–104.
 27. Kaneko, K. and Ishii, C. (1992) *Colloids Surf.*, **67**, 203–212.
 28. Raymundo-Pinero, E., Kierzek, K., Machnikowski, J., and Béguin, F. (2006) *Carbon*, **44**, 2498–2507.
 29. Fuertes, A.B., Lota, G., Centeno, T.A., and Frackowiak, E. (2005) *Electrochim. Acta*, **50**, 2799–2805.
 30. Vix-Guterl, C., E.F., Jurewicz, K., Friebe, M., Parmentier, J., and Béguin, F. (2005) *Carbon*, **43**, 1293–1302.
 31. Hou, P.X., Yamazaki, T., Orikasa, H., and Kyotani, T. (2005) *Carbon*, **43**, 2624–2627.
 32. Kyotani, T. and Gogotsi, Y. (2010) in *Carbons for Electrochemical Energy Storage and Conversion Systems*, (eds F. Béguin and E. Frackowiak), Taylor & Francis Group, Boca Raton, FL, pp. 77–113.
 33. Fuertes, A.B. (2003) *J. Mater. Chem.*, **13**, 3085–3088.
 34. Hou, P.X., Orikasa, H., Itoi, H., Nishihara, H., and Kyotani, T. (2007) *Carbon*, **45**, 2011–2016.
 35. Nishihara, H., Yang, Q.H., Hou, P.X., Unno, M., Yamauchi, S., Saito, R., Paredes, J.I., Martinez-Alonso, A., Tascon, J.M.D., Sato, Y., Terauchi, M., and Kyotani, T. (2009) *Carbon*, **47**, 1220–1230.
 36. Geim, A.K. and Novoselov, K.S. (2007) *Nat. Mater.*, **6**, 183–191.
 37. Yang, C.M., Kim, Y.-J., Endo, M., Kanoh, H., Yudasaka, M., Iijima, S., and Kaneko, K. (2007) *J. Am. Chem. Soc.*, **129**, 20.
 38. Chmiola, J., Yushin, G., Gogotsi, Y., Portet, C., Simon, P., and Taberna, P.L. (2006) *Science*, **313**, 1760–1763.
 39. Dash, R., Chmiola, J., Yushin, G., Gogotsi, Y., Laudisio, G., Singer, J., Fischer, J., and Kucheyev, S. (2006) *Carbon*, **44**, 2489–2497.
 40. Laudisio, G., Dash, R., Singer, J.P., Yushin, G., Gogotsi, Y., and Fischer, J.E. (2006) *Langmuir*, **22**, 8945–8950.
 41. Lin, R., Taberna, P.L., Chmiola, J., Guay, D., Gogotsi, Y., and Simon, P. (2009) *J. Electrochem. Soc.*, **156**, A7–A12.
 42. Chmiola, J., Largeot, C., Taberna, P.L., Simon, P., and Gogotsi, Y. (2008) *Angew. Chem. Int. Ed.*, **47**, 3392–3395.
 43. Ania, C.O., Pernak, J., Stefaniak, F., Raymundo, E., and Béguin, F. (2009) *Carbon*, **47**, 3158–3166.
 44. Huang, J., Sumpter, B.G., and Meunier, V. (2008) *Angew. Chem.*, **120**, 530–534.
 45. Huang, J., Sumpter, B.G., and Meunier, V. (2008) *Chem.—Eur. J.*, **14**, 6614–6626.
 46. Cachet-Vivier, C., Vivier, V., Cha, C.S., Nedelec, J.Y., and Yu, L.T. (2001) *Electrochim. Acta*, **47**, 181–189.
 47. Portet, C., Chmiola, J., Gogotsi, Y., Park, S., and Lian, K. (2008) *Electrochim. Acta*, **53**, 7675–7680.
 48. Frackowiak, E. and Béguin, F. (2001) *Carbon*, **39**, 937–950.
 49. Mysyk, R., Raymundo-Piñero, E., and Béguin, F. (2009) *Electrochem. Commun.*, **11**, 554–556.
 50. Mysyk, R., Raymundo-Piñero, E., Pernak, J., and Béguin, F. (2009) *J. Phys. Chem. C*, **113**, 13443–13449.
 51. Sun, G., Song, W., Liu, X., Long, D., Qiao, W., and Ling, L. (2011) *Electrochim. Acta*, **56**, 9248–9256.
 52. Kondrat, S., Georgi, N., Fedorov, M.V., and Kornyshev, A.A. (2011) *Phys. Chem. Chem. Phys.*, **13**, 11359–11366.

53. Hahn, M., Barbieri, O., Campana, F.P., Kötz, R., and Gallay, R. (2006) *Appl. Phys. A*, **82**, 633–638.
54. Ruch, P.W., Hahn, M., Cericola, D., Menzel, A., Kötz, R., and Wokaun, A. (2010) *Carbon*, **48**, 1880–1888.
55. Mysyk, R., Gao, Q., Raymundo, E., and Béguin, F. (2012) *Carbon*, **50**, 3367–3374.
56. Ania, C.O., Pernak, J., Stefaniak, F., Raymundo, E., and Béguin, F. (2006) *Carbon*, **44**, 3126–3130.
57. Largeot, C., Portet, C., Chmiola, J., Taberna, P.L., Gogotsi, Y., and Simon, P. (2008) *J. Am. Chem. Soc.*, **130**, 2730–2731.
58. Lin, R., Huang, P., Ségalini, J., Largeot, C., Taberna, P.L., Chmiola, J., Gogotsi, Y., and Simon, P. (2009) *Electrochim. Acta*, **54**, 7025–7032.
59. Shim, Y. and Kim, H.J. (2010) *ACS Nano*, **4**, 2345–2355.
60. Mysyk, R., Ruiz, V., Raymundo, E., Santamaria, R., and Béguin, F. (2010) *Fuel Cells*, **10**, 834–839.
61. Aurbach, D., Levi, M.D., Salitra, G., Levy, N., Pollak, E., and Muthu, J. (2008) *J. Electrochem. Soc.*, **155**, A745–A753.
62. Girault, H. (2004) *Analytical and Physical Electrochemistry*, EPFL Press, pp. 379–380.
63. Hardwick, L.J. and Hahn, M. (2006) *Electrochim. Acta*, **52**, 675–680.
64. Hardwick, L.J. and Hahn, M. (2008) *J. Phys. Chem. Solids*, **69**, 1232–1237.
65. Azaïs, P., Duclaux, L., Florian, P., Massiot, D., Lillo-Rodenas, M.A., Linares-Solano, A., Peres, J.P., Jehoulet, C., and Béguin, F. (2007) *J. Power Sources*, **171**, 1046–1053.
66. Ruch, P.W., Cericola, D., Foelske, A., Kötz, R., and Wokaun, A. (2010) *Electrochim. Acta*, **55**, 4412–4420.
67. Hahn, M., Barbieri, O., Gallay, R., and Kötz, R. (2006) *Carbon*, **44**, 2523–2533.
68. Campana, F.P., Hahn, M., Foelske, A., Ruch, P., Kötz, R., and Siegenthaler, H. (2006) *Electrochem. Commun.*, **8**, 1363–1368.
69. Ruch, P.W., Kötz, R., and Wokaun, A. (2009) *Electrochim. Acta*, **54**, 4451–4458.
70. Deschamps, M., Gilbert, E., Azais, P., Raymundo-Pinero, E., Ammar, M.R., Simon, P., Massiot, D., and Béguin, F. (2012) *Nat. Mater.*, in press.

5

Modern Theories of Carbon-Based Electrochemical Capacitors

Jingsong Huang, Rui Qiao, Guang Feng, Bobby G. Sumpter, and Vincent Meunier

5.1

Introduction

5.1.1

Carbon-Based Electrochemical Capacitors

The growing demand for fossil fuels and their adverse impact on the environment continue to confront society with formidable energy and environmental challenges. New technologies for electrical energy conversion and storage are needed to harness sustainable and renewable energy sources and to develop electric vehicles with low or zero CO₂ emission [1]. Electrochemical capacitors, or supercapacitors, are a rising star on the horizon of energy storage devices, and have received a great deal of attention in recent years [2–7]. There are two classes of electrochemical capacitors depending on the interfacial chemistry and physics [8–11]: pseudocapacitors, which are based on various redox-active materials such as conducting polymers and transition metal oxides [12–14]; and electric double-layer capacitors (EDLCs), which can be made from various carbon materials with high surface area [15–18]. Pseudocapacitance relies on faradic reactions on the material surfaces. In comparison, the energy storage mechanism of EDLCs hinges on the electric double layer (EDL) established at the electrode/electrolyte interface. EDLCs are characterized by high-power density and exceptional cycle life, which make them ideal for the rapid storage and release of energy.

In this chapter, we are concerned with electrochemical capacitors based on carbon materials. The past two decades have witnessed extensive experimental studies of various carbon materials for EDLC applications. Typical examples include activated carbons, template carbons, carbide-derived carbons (CDCs), carbon onions, single-walled carbon nanotubes (SWCNTs) and multiwalled carbon nanotubes (MWCNTs), carbon nanofibers, and graphenes, among others (Figure 5.1) [10, 11, 15–25]. The existing studies are driven by two main motivations aimed at improving capacitance performances: to explore new materials and to probe the underlying fundamental energy storage principles. In spite of the significant experimental advances made in recent years, there is still an important gap in

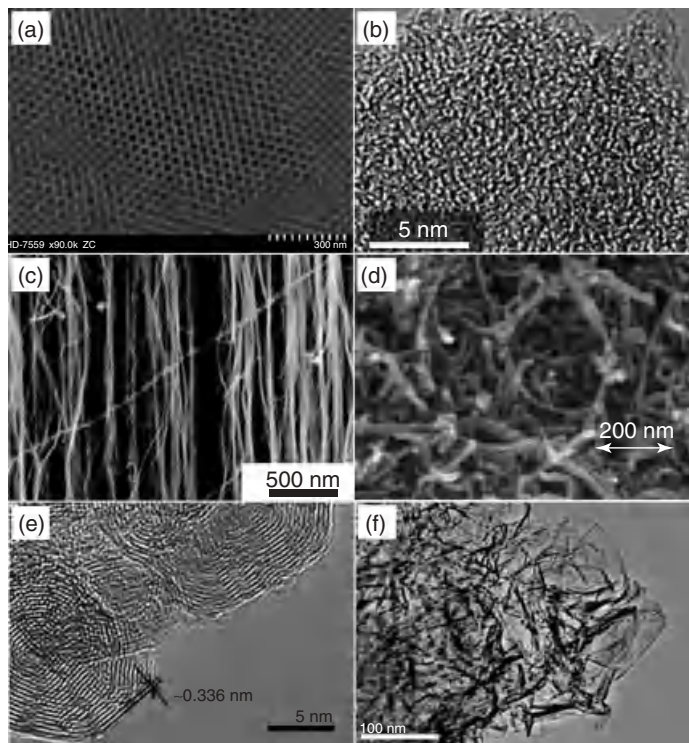


Figure 5.1 Representative carbon materials used for electrodes in EDLCs: (a) Template carbon. Reprinted with permission from Ref. [19]. (b) Silicon CDC. Reprinted with permission from Ref. [20]. (c) CNT arrays. Reprinted with permission from Ref. [22]. (d) Carbon nanofibers. Reprinted with permission from Ref. [23]. (e) Carbon onions. Reprinted with permission from Ref. [24]. (f) Chemically modified graphene (CMG) materials. Reprinted with permission from Ref. [25].

energy densities between EDLCs ($<10 \text{ Wh kg}^{-1}$) and batteries (on the order of 100 Wh kg^{-1}). However, EDLC research has a rather short history, indicating that capacitance performance can still be optimized from the current value. Supercapacitors will only compete with existing battery technology if the energy density can be increased while preserving high-power capability.

Aside from extensive experimental work, the amount of theoretical effort devoted to the fundamental understanding of EDLCs has also steadily increased [26–32]. Theoretical approaches range from the early Helmholtz model, to mean-field continuum models, and to modern molecular dynamics (MD) simulations. When coupled with experimental results, theoretical studies provide an important insight into the electrode/electrolyte interfacial behavior that is crucial for the understanding of the capacitance performance of EDLCs and subsequently for its optimization. In the following, we present an overview of the most common EDL models and how they provide a fundamental understanding of energy storage performance in supercapacitors.

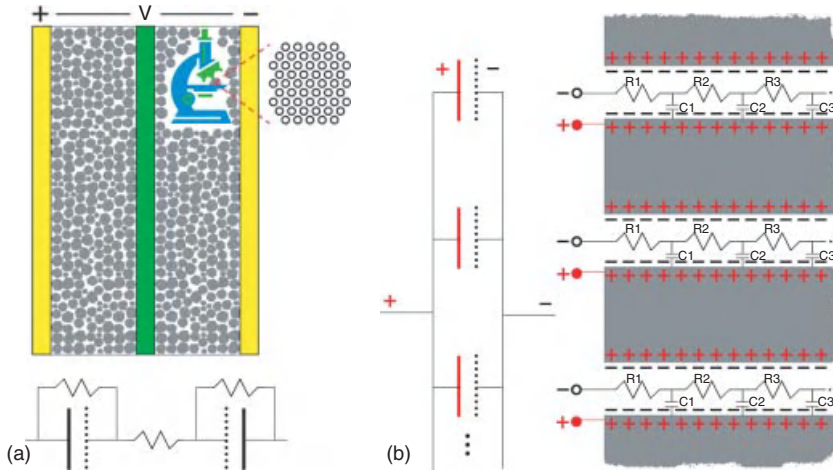


Figure 5.2 (a) Schematic representation of an EDLC cell using nanoporous carbon materials. Each carbon particle contains a large amount of pores at the nanoscopic level. In the equivalent circuit (bottom panel), the two electrode capacitors are connected in series where each electrode capacitor is denoted with a solid line segment for the electrode and a parallel dotted line segment for the electrolyte. The resistors account for the electrode and electrolyte resistances and

the energy lost by ions during charge and discharge [15]. (b) On each electrode (e.g., cathode), each pore in the carbon particle is represented by an equivalent circuit with capacitors connected in parallel and with series resistances R_n as a function of pore depth. The pore capacitors are connected in parallel where each pore capacitor is denoted with a solid line segment for the pore wall and a parallel dotted line segment for the counterions.

5.1.2

Elements of EDLCs

The device construction of EDLCs is similar to that of batteries (Figure 5.2a). The electrodes are made by laminating carbon-based active materials onto current collectors. Next, a porous membrane of paper, polymer, or glass fiber is sandwiched between the two electrodes. The cell is then immersed into an electrolyte. Different electrolytes can be utilized in EDLCs, with advantages and disadvantages [6, 16]. Aqueous H_2SO_4 or KOH electrolytes are common in EDLCs because of their higher electrical conductivity and higher dielectric constant. Organic electrolytes, such as tetraethylammonium tetrafluoroborate (TEA-BF_4) in acetonitrile (AN) or propylene carbonate (PC), are also widely used. Their use enables higher cell voltage up to 2.3 V compared to about 1 V for aqueous electrolytes. For aqueous and organic electrolytes, high electrolyte concentrations are often employed in order to increase the conductivity and to avoid electrolyte depletion problems so that the large surface area of carbon materials can be fully utilized. Ionic liquid (IL) electrolytes can also be used, allowing EDLCs to operate at voltages larger than 3 V. However, current generation ILs suffer from higher viscosities and lower conductivities than aqueous and organic electrolytes.

Carbon materials are chosen as the active electrode materials in EDLCs because of their high electrical conductivity, high specific surface area (SSA), tunable porosity, and relatively low production cost [8, 15, 16]. Compared to traditional semiconductors, which have conductivities $\leq 10^{-2} \text{ S cm}^{-1}$, carbon materials used for EDLCs typically have conductivities $\geq 1 \text{ S cm}^{-1}$. This large value is related to the high density of electronic states at the Fermi level [15]. In spite of their high conductivity, carbon materials differ from metals in terms of differential capacitance as a function of the charging state. For typical carbons, the galvanostatic method shows that the voltage increases linearly with applied potential; meanwhile, a cyclic voltammetry scan indicates that the current is nearly constant, giving a rectangle-shaped cyclic voltammogram (CV) [21, 33]. These results imply that the capacitance of a carbon-based EDLC is nearly independent of the charging state, while that of a metal such as mercury varies significantly with the potential [34]. However, some carbon materials exhibit butterfly-shaped CVs with a pronounced minimum of current near the potential of zero charge (PZC) [35, 36]. This behavior may be a manifestation of graphite's quantum capacitance and is discussed in detail later.

As the charge storage in EDLCs is an interfacial phenomenon, it is indispensable to examine the surface characteristics of the electrode materials. For instance, a close inspection of the topographic features of nanoporous carbon materials at the nanoscopic level reveals that while the grain size of carbon particles is on the order of micrometers, each carbon particle contains a large amount of pores with diameters on the order of nanometers (Figure 5.2a). The pore sizes are categorized into three regimes by IUPAC: micropores are less than 2 nm in diameter, mesopores are 2–50 nm in diameter, and macropores are larger than 50 nm [37]. The high SSAs of nanoporous carbons ($\sim 1500\text{--}2600 \text{ m}^2 \text{ g}^{-1}$) account not only for a major contribution of the internal pore surface but also for a relatively small contribution of the external surface area of the particles. As shown in Figure 5.2b, each pore can be represented by an equivalent circuit with parallel-connected capacitors and with series-connected resistances as a function of pore depth [38, 39]. For convenience, one may denote each pore-related capacitor by a solid line segment representing the capacitor plate formed by the pore wall and a parallel dotted line segment representing the capacitor plate formed by the counterions (Figure 5.2b). It is important to determine how the electrode capacitance is related to the pore capacitance, or in other words, to establish the relation between pore capacitors in an electrode. The figure illustrates that the pore capacitors are connected in parallel rather than in series because all the pore walls are connected to the same electrode, that is, they have the same potential. Therefore, for the electrode capacitance, one only needs to consider a single pore and computing the total effect is just a matter of summation of the surface areas for all the pores. Likewise, this relation holds true for EDLCs that are based on carbon onions, carbon nanotubes (CNTs), or carbon nanofibers. This consideration greatly simplifies the theoretical treatment of carbon-based EDLCs, as an understanding of each individual pore suffices to determine the capacitance of the whole electrode.

The relation between the capacitance of individual pores is different from that of a complete cell where the cathode and anode capacitors are connected in series

(Figure 5.2a). The definitions of cathode and anode are carried over from batteries, that is, the cathode is the positive terminal and the anode is the negative terminal. It follows that the total cell capacitance (C_{tot}) is given in terms of the electrode capacitances (C_+ and C_-) by the usual inverse relation:

$$\frac{1}{C_{\text{tot}}} = \frac{1}{C_+} + \frac{1}{C_-} \quad (5.1)$$

For a complete cell, the issue of symmetric versus asymmetric capacitors has to be considered carefully. In a symmetric capacitor, the two electrodes contribute equally to the capacitance. Often, a capacitor is said to be symmetric if the two electrodes are made of the same carbon materials [4]. However, we should point out that the presence of identical electrodes does not necessarily guarantee a symmetric cell since the cations forming the EDL at the anode may have a different ionic radius compared to that of the anions at the cathode. The variation in radii leads to EDLs of different thicknesses and in turn to an asymmetric capacitor. Even though the dielectric constants in the two EDLs may be close to one another, such a difference in ionic radii may lead to a different behavior in the voltage drops across the two EDLs. In spite of this, for simplicity, we will assume that the capacitors made of the same electrode materials on the cathode and anode are symmetric. With the assumption of symmetric capacitors, Eq. (5.1) becomes:

$$C_{\text{tot}} = \frac{1}{2}C_+ = \frac{1}{2}C_- \quad (5.2)$$

Note that a two-electrode measurement gives a value of C_{tot} , while a three-electrode measurement produces C_+ or C_- or their average value. Throughout this chapter, we choose to examine electrode capacitance instead of cell capacitance. The capacitance is conventionally reported in the literature as the gravimetric electrode capacitance, which is the capacitance of one electrode normalized by the mass of that electrode's active materials. It is important to note that for device property calculations, such as energy density, the gravimetric capacitance of the cell should be used. In fact, there is a factor of 4 between the gravimetric capacitances of an electrode and a cell due to the double weight and half capacitance of the complete cell.

EDLCs are classified into two categories depending on the way that the counterions interact with the carbon surface [28, 29]. The first category includes *endohedral* capacitors where counterions enter *inside* the pores to establish EDLs (Figure 5.3a). This category broadly applies to nanoporous carbons with negative surface curvature such as activated carbons, template carbons, and CDCs. The charge storage mechanism is slightly different depending on the pore size. The second category includes *exohedral* capacitors and applies to positively curved surfaces. Here, ions reside on the *outer* surface of carbon particles such as carbon onions, end-capped CNTs, and carbon nanofibers (Figure 5.3b). At the frontier between endohedral and exohedral capacitors, graphenes are relatively new carbon materials for EDLC electrode applications [25, 40]. Because of their zero curvature, they do not belong to either of the above-mentioned categories and are discussed separately.

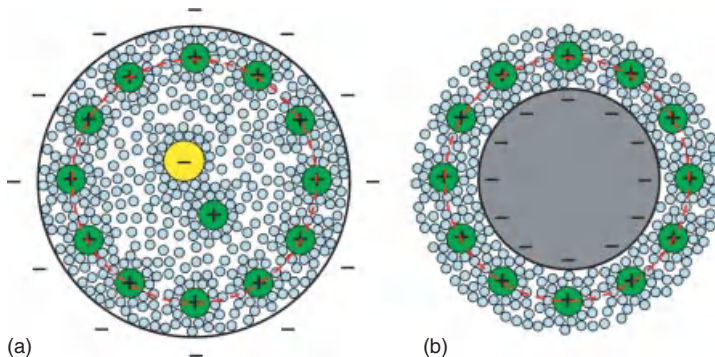


Figure 5.3 (a) An endohedral capacitor with counterions close to the inner wall of a negatively charged pore inside nanoporous carbons such as activated carbons, template carbons, or CDCs.

(b) An exohedral capacitor with counterions only residing on the outer surface of a negatively charged particle of carbon anions, end-capped CNTs, or carbon nanofibers.

5.2

Classical Theories

5.2.1

Compact Layer at the Interface

The simplest model for an EDL is the Helmholtz model [41]. Its original version assumes that the EDL at the electrolyte side consists of a compact layer of counterions, forming the so-called Helmholtz layer, which exactly counterbalances the surface layer of charges on the electrode (Figure 5.4a). This two-layer structure of charges resembles that of a conventional parallel-plate capacitor and explains the origin of the name EDL. At this level of approximation, the capacitance of the EDL is given by

$$C_H = \frac{\varepsilon_r \varepsilon_0 A}{d} \quad (5.3)$$

where ε_r is the dielectric constant inside the EDL, ε_0 the vacuum permittivity, A the electrode surface area, and d the distance between the surface charge layer and the counterion layer (or simply the thickness of the compact layer). The quantity ε_r is dimensionless, while the units of ε_0 is $C^2 N^{-1} m^{-2}$, which is equivalent to $F m^{-1}$.

The rich physics of the EDLs, treated with the dramatic simplification within the Helmholtz model, is effectively represented by the two free parameters of Eq. (5.3), that is, ε_r and d . The compact layer thickness d is affected by the way counterions are adsorbed on the electrode: if they are contact-adsorbed, that is, there is no solvent between the ion and the electrode, d is defined as the size of a bare ion; otherwise, d is defined primarily by the size of the solvated ion. The dielectric constant of the compact layer, ε_r , is not very well understood. Given that the solvent structure at the electrode/electrolyte interface differs significantly from that in the bulk and the magnitude of the electric field in the compact layer often reaches

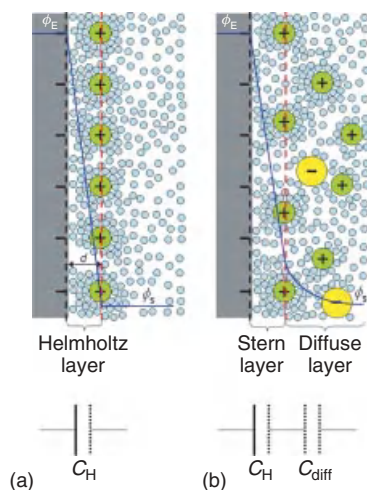


Figure 5.4 Electric double-layer models of planar surfaces: (a) Helmholtz model with a compact layer of counterions separated from the electrode surface by the double-layer thickness d . The Helmholtz layer fully screens the surface layer of charges on the electrode. (b) Gouy–Chapman–Stern model with a diffuse layer developed into the electrolyte owing to the thermal motions of electrolyte ions.

10^8 – 10^9 V m⁻¹, there is a consensus that the dielectric constant in the compact layer can differ dramatically from its bulk value. Both theoretical works [42–44] and experimental studies [45, 46] suggest that the dielectric constant of water near charged surfaces is in the range of 5–20, which is much smaller than the value of 78 for bulk water. The dielectric constants for organic electrolytes and ILs near electrified surfaces have not been studied extensively, but conceivably should also be lower than their bulk values. The original Helmholtz model was subsequently refined to account for the specific adsorption of large anions on the electrode and other effects. Specifically, the original compact layer has been further partitioned into an inner Helmholtz layer and an outer Helmholtz layer [34, 47].

5.2.2

Diffuse Layer in the Electrolyte

The assumption that the electrode surface charges are completely screened by the counterion charges in the Helmholtz layer is not always realistic. Owing to thermal motion, some counterions spread into a “diffuse layer” adjacent to the compact layer (Figure 5.4b). In other words, the EDL in reality consists of a Stern layer (i.e., Helmholtz or compact layer) and a diffuse layer connected in series (Figure 5.4b). This more sophisticated picture of the EDL is usually described using the Gouy–Chapman–Stern (GCS) model [48–50].

Within the framework of the GCS model, for monovalent electrolytes, the electric potential distribution in the diffuse layer is governed by the Poisson–Boltzmann

(PB) equation:

$$\nabla (\varepsilon_r \varepsilon_0 \nabla \phi) = 2e c_\infty \sinh(\phi / k_B T) \quad (5.4)$$

where ϕ is the electric potential, c_∞ the bulk electrolyte concentration, e the electron charge, k_B the Boltzmann constant, and T the absolute temperature. By solving the PB equation, the capacitance of the diffuse layer is obtained as

$$C_{\text{diff}} = \frac{\varepsilon_r \varepsilon_0 A}{\lambda_D} \cosh\left(\frac{e\phi_{\text{diff}}}{2k_B T}\right) \quad (5.5)$$

where ϕ_{diff} is the potential drop across the diffuse layer and λ_D is the characteristic Debye length which, for monovalent electrolytes, is defined as

$$\lambda_D = \left(\frac{\varepsilon_r \varepsilon_0 k_B T}{2e^2 c_\infty}\right)^{1/2} \quad (5.6)$$

The PB equation, Eq. (5.4), is a concise and elegant description of the diffuse layer and was one of the milestones in the development of the EDL theory. It should be credited to Gouy and Chapman, and for that reason, it is also termed the GC model. However, as a mean-field theory, the PB equation suffers from the following limitations [51]: (i) the solvent is treated as a structureless continuum and the dielectric constant of the solvent in the diffuse layer is often taken from that in the bulk electrolyte; (ii) electrostatic ion–ion interactions are accounted for, but the ion–ion correlations are neglected; and (iii) counterions are approximated as point charges without considering the finite size of ions. Because of these limitations, one should be cautious when the PB equation is used alone in the absence of the Stern layer. It is valid primarily in dilute electrolytes and at low potential drop ($<k_B T/e \approx 25$ mV at room temperature) across the diffuse layer. Near highly charged surfaces or in concentrated electrolytes, the PB equation used alone may predict an unphysically high ion concentration near electrodes polarized by voltages much greater than 25 mV. Another pitfall of using PB alone is that the EDL capacitance is significantly overestimated because the counterions may approach infinitely close to the electrode surface. When the GC model is used in concert with the Stern layer (the GCS model), these problems are partially avoided. Within the framework of the GCS model, the Stern layer holds the same physical meaning as the Helmholtz layer, and is the closest approach of counterions to the electrode surface. Its capacitance, C_H , is parameterized by the EDL's thickness and dielectric constant, as shown by Eq. (5.3).

For EDLCs, relatively high electrolyte concentrations are used, which give rise to a small Debye length according to Eq. (5.6), which in turn may lead to a rather large capacitance for the diffuse layer according to Eq. (5.5) ($>100 \mu\text{F cm}^{-2}$). In comparison, the compact layer has a much smaller capacitance (on the order of $10\text{--}20 \mu\text{F cm}^{-2}$). As shown in Figure 5.4b, the EDL is equivalent to two capacitors in series:

$$\frac{1}{C_{\text{dl}}} = \frac{1}{C_H} + \frac{1}{C_{\text{diff}}} \quad (5.7)$$

It follows that the diffuse layer contribution is negligible and the overall double-layer capacitance is dominated by the compact layer [52]. A simple way to understand this effect is that the effective thickness of the diffuse layer is reduced significantly by using high electrolyte concentrations and the double-layer structure on the electrolyte side is simplified to the Helmholtz or Stern layer (from Figure 5.4b to 5.4a).

The GCS model can be used to compute the EDL capacitance in any geometry if the compact layer and electrolyte properties can be explicitly determined. However, in the past, this model was mostly applied to EDLs near planar electrodes. This is not surprising since, until recently, pores and exohedral cylinders encountered in practical systems were so large that their surfaces could be considered as planar. A few studies on nonplanar surfaces were performed using this approach but did not include the compact layer [51]. In contrast, the work reported in Ref. [52] considers the compact layer explicitly and applies the PB equation to both slit and cylindrical pores to study the effects of diffuse layer and pore shapes in mesoporous carbon-based EDLCs.

5.2.3

Space Charge Layer in the Electrodes

The EDL model presented in Figure 5.4b is still too simple to accurately represent electrodes that are based on traditional semiconductors. In addition to the Helmholtz (or Stern) layer at the interface and the diffuse layer on the electrolyte side, a space charge layer on the electrode side can extend into the bulk of the electrode [2, 53]. It is not necessary to consider its effects in the case of metal electrodes since the Debye screening length is very small in metals. However, it cannot be neglected in semiconductors. The inclusion of a space charge layer on the electrode side leads to a situation where the electrode/electrolyte interface consists of three capacitors in series: a space charge layer (C_{SC}), a compact layer (C_H), and a diffuse layer (C_{diff}) [53, 54]. It follows that the overall double-layer capacitance can be expressed as a combination of three components in series:

$$\frac{1}{C_{dl}} = \frac{1}{C_{SC}} + \frac{1}{C_H} + \frac{1}{C_{diff}} \quad (5.8)$$

Note that this is not an electric triple-layer structure but still an EDL in a broad sense – one layer of charges on the electrode and another layer of counterions in the electrolyte.

The capacitance of the space charge layer is seldom considered in the literature for carbon-based capacitors, with the notable exception of the basal plane of graphite [55–57]. This is quite well justified in light of the good conductivity of most carbon materials [15]. High conductivities of carbons are associated with a high charge carrier concentration, which may lead to a small Debye screening length of charge carriers in carbons, similar to the effect of high electrolyte concentration. As a result, the C_{SC} is large and its inverse value is small, giving a negligible contribution to the overall capacitance. In other words, the high conductivities of carbon materials

justify a posteriori the use of the Helmholtz model for parallel-plate capacitors. However, in the case of the basal plane of graphite, the capacitance–potential curves exhibit a symmetrical V shape with a linear increase in capacitance on both sides. Such a behavior was rationalized by the space charge layer in graphite in the direction normal to the basal plane. The C_{SC} contribution is assumed to follow the same mathematical treatment as in the diffuse layer shown in Eqs. (5.5) and (5.6) [55]. This behavior is further discussed in Section 5.3.3.

5.3

Recent Developments

5.3.1

Post-Helmholtz Models with Surface Curvature Effects

5.3.1.1 Models for Endohedral Capacitors

The Helmholtz model has been extensively used to describe EDLCs for decades. However, it is essentially qualitative. Attempts to analyze experimental data in a quantitative manner are often found to be problematic. The fundamental problem is that while Eq. (5.3) predicts a linear C – A relationship, C – A is seldom observed to behave that way in real systems, for example, in nanoporous carbon materials. Generally, it is observed that higher capacitances are obtained for carbons with higher surface areas. While some experiments indicate a linear relationship between C and A [58–61], other experiments conclude that no such linear relationship exists [26, 61–63]. In addition, a number of experiments indicate that C is proportional to the micropore volume [64, 65]. This long-debated question on the C – A relationship suggests that a fundamental ingredient is missing in the classical model based on planar surfaces.

The large SSA of nanoporous carbons originates from the internal pore surfaces. This fact seems to be incompatible with the use of Eq. (5.3) for carbon-based EDLCs, since the simplification of the carbon/electrolyte interface to an EDLC fails to consider the close interactions between pore walls. More importantly, in the simple parallel-plate capacitor model, the curvature of each pore is neglected. Surface curvature effects are significant, as is well documented by the very strong local surface electric fields at the end of sharp tips. It is puzzling that until recently, the electric field enhancement factor encountered in the context of field emission or the physics of lightning rods was ignored in the description of EDLCs near curved surfaces.

Nanoporous materials can have various pore shapes, such as cylindrical, slit, and spherical types, depending on the synthesis approach [66, 67]. For instance, mesoporous carbon materials obtained by template methods usually have wormhole structures with circular cross sections (Figure 5.1a) [19, 64]. In such cases, cylindrical pores are generally the assumption for theoretical treatments for physical adsorption of gases [68, 69] and impedance spectroscopy [39, 70, 71]. If the mesopores are assumed to be cylindrical, as shown in Figure 5.5a, solvated counterions may enter the pores and approach the pore walls to form electric double-cylinder

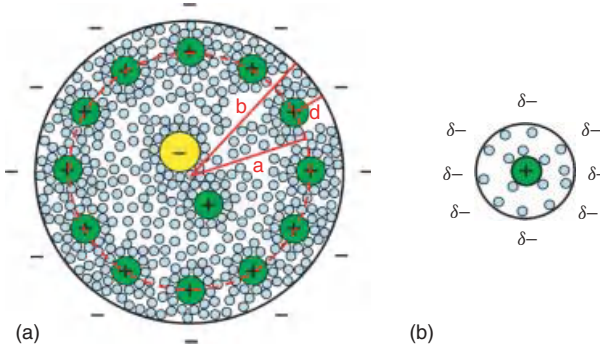


Figure 5.5 (a) A negatively charged mesopore with solvated cations approaching the pore wall to form an electric double-layer capacitor (EDCC) with radii b and a for the outer and inner cylinders, respectively, separated by a distance d . (b)

A negatively charged micropore of radius b with solvated cations of radius a_0 lining up along the pore axis to form an electric wire-in-cylinder-capacitor (EWCC). EWCC is also possible with desolvated ions (see text).

capacitors (EDCCs) [29, 30]. The corresponding capacitance is given by

$$C = \frac{2\pi\epsilon_r\epsilon_0 L}{\ln(b/a)} \quad (5.9)$$

where L is the pore length and b and a are the radii of the outer and inner cylinders, respectively. It is more convenient to analyze the experimental data using normalized capacitance with respect to the SSA:

$$\frac{C}{A} = \frac{\epsilon_r\epsilon_0}{b \ln[b/(b-d)]} \quad (5.10)$$

Equation (5.10) constitutes the starting point for a heuristic model based on two simplifying assumptions. First, in close similitude to the Helmholtz model, the counterions on the inner cylinder completely screen the charges on the pore walls. This simplification is valid for high concentrations, such as those used in practical EDLC devices [52]. Second, the space charge layer contribution to the overall double-layer capacitance can be neglected owing to the high conductivity of carbon materials. Therefore, the scenario of three capacitors in series indicated by Eq. (5.8) is essentially reduced to C_H only, with the important difference that surface curvature is now explicitly taken into account.

The EDCC model can be pushed to the limit of a subnanometer radius. This corresponds to the micropore regime. In this case, the confinement does not allow the formation of a double cylinder inside the pore. If the micropores are assumed to be cylindrical, as shown in Figure 5.5b, solvated (or desolvated) counterions may enter the pores and line up along the pore axis to form electric wire-in-cylinder-capacitors (EWCCs) [29, 30]. Although the molecular geometries of the counterions might be anisotropic, the pore walls experience an average effect owing to the room-temperature translation or rotation of the counterions along or with respect to the pore axis. The average geometry is identical to that of a thin inner cylinder.

Unlike the case of mesopores, the radius of the inner cylinder in micropores is not determined by the closest approach of counterions to the pore walls but rather by the effective size of the counterions, a_0 . This is an intrinsic property of the ion and is a measure of the extent of electron density around the ions. Introducing a_0 into Eq. (5.10), the equation for EWCC becomes:

$$\frac{C}{A} = \frac{\epsilon_r \epsilon_0}{b \ln(b/a_0)} \quad (5.11)$$

In a way, EWCCs can also be viewed as EDCCs, but the key quantity for EWCCs is no longer d but rather a_0 , that is, the effective size of the counterion. Note that both d and a_0 are approximately independent of pore sizes.

Equations (5.10) and (5.11) indicate that the capacitance becomes pore size dependent because of the surface curvature effects. This means that compared to the Helmholtz model, we no longer expect a linear C – A relationship. In order for the C – A relationship to be linear, the pore sizes must be fixed and only the surface areas and the capacitances must be allowed to change. This is illustrated in the case of the experimental gravimetric electrode capacitances of template carbons obtained in both aqueous and organic electrolytes from Ref. [64]. If all the capacitance data points are plotted as a function of the surface area, there is no obvious linear relationship (Figure 5.6a). However, if only the data points within a narrow pore size range of 2.9 ± 0.2 nm are included, a linear relationship emerges (Figure 5.6b). The fitting quality as indicated by the R^2 value for the organic electrolyte is better than that for the aqueous electrolyte, in which the EDLs are more susceptible to include pseudocapacitive contributions. Note also that the pore size effect does not exhaust all the factors that can distort the C – A linear relationship. One such factor

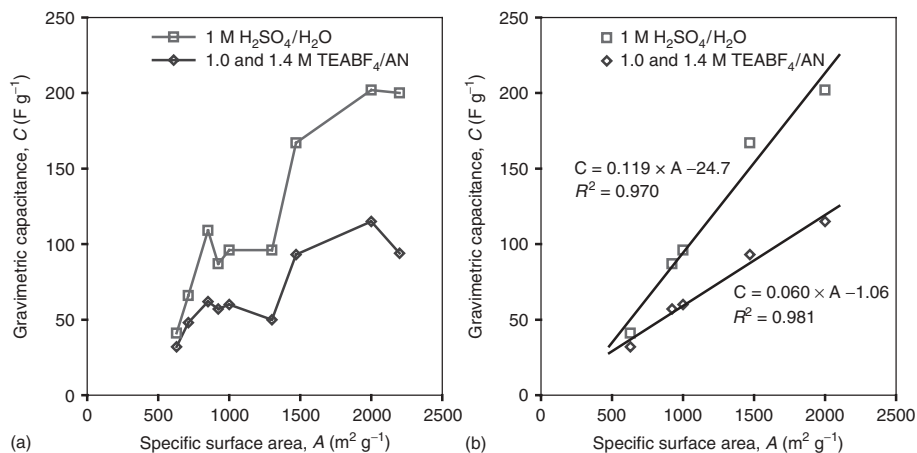


Figure 5.6 Correlations between gravimetric capacitances and SSAs of template carbons obtained in both aqueous and organic electrolytes from Ref. [64]: (a) no good linear relationship exists if all data points are

included and (b) a good linear relationship emerges if only the data points within a narrow pore size range of 2.9 ± 0.2 nm are included, as indicated by R^2 of the linear fits.

is the pore wall thickness that can affect the space charge accommodation within the pore wall and lead to a saturation or plateau of capacitance at high surface area on a plot of gravimetric capacitance versus SSA [35].

These curvature-based capacitance models have been demonstrated to be universal for nanoporous carbon EDLCs with diverse carbon materials in different pore regimes, including activated carbons, template carbons, and CDCs, and with diverse electrolytes, including organic electrolytes, aqueous H_2SO_4 and KOH electrolytes, and even an IL electrolyte (Table 5.1) [30, 72]. As an example, we first focus on the organic electrolyte of TEA-BF_4 in AN. Figure 5.7 shows the experimental data of CDCs [21] and template carbons [61, 64, 73] in 1.0, 1.4, and 1.5 M electrolyte concentrations. Unlike the analysis performed in Refs. [29, 30], the subdivision of experimental data of Ref. [64], according to their different concentrations of 1.0 and 1.4 M, is not performed. According to recent PB simulations of mesoporous carbon-based EDLCs in an electrolyte concentration range of 0.5 to 1.6 M, the dependence of capacitance on concentration is negligible [52]. Among the 13 data points in Figure 5.4 of Ref. [61], 9 data points have pore size available but only 5 of them have unimodal pore size distributions. Thus, only these five data points are included in the present analysis. The capacitance of nanoporous carbons is usually reduced at higher discharging current densities. However, the data in Figure 5.7 were obtained at small discharging current densities of 1 and 5 mA cm^{-2} or at a small voltammetric scan rate of 2 mV s^{-1} [21, 61, 64, 73] and therefore are close to their potential maximal values. Capacitances are normalized with respect to the SSA measured by the Brunauer-Emmet-Teller (BET) method [74]. The experimental data of microporous carbons (region I) and mesoporous carbons (region III) can be fit remarkably well by Eqs. (5.10) and (5.11), respectively.

In region III, the fit by Eq. (5.10) reproduces the experimental trend of slightly increasing area-normalized capacitance with increasing pore size. Recent PB simulations of double-layer capacitance of mesoporous carbons with slit-shaped and cylindrical pores concluded that such a trend only exists in cylindrical pores [52]. The actual overall pore shapes of most carbon mesopores are far from being cylindrical, even though some template carbons do show circular cross sections for the pores [19, 64]. However, the vast majority of pores can locally be approximated by cylinders. It is therefore reasonable to approximate the pores as cylinders rather than as slits. The dielectric constant obtained from the fit is $\epsilon_r = 9.73 \pm 1.29$, which is much smaller than the value of 36 for bulk AN at room temperature [84]. Incidentally, it has been found that the dielectric constant of an aqueous solution decreases in EDLs and confined spaces [2, 42, 44, 45]. The fitted value for $d = 9.43 \pm 0.69 \text{ \AA}$ is on the same order of magnitude as the calculated solvated ionic radii of $\text{TEA}^+ \cdot 7\text{AN}$ (6.5 \AA) and $\text{BF}_4^- \cdot 9\text{AN}$ (5.8 \AA) [85], and the Debye length of TEA-BF_4 in AN (6.6 \AA), estimated from impedance spectroscopy [86].

The extrapolation of the fitting curve into region IV shows that the curve approaches asymptotically the broken line calculated by Eq. (5.3) using the same parameters ϵ_r and d obtained in region III. This is not surprising since Eq. (5.10) for EDCs can be reduced to Eq. (5.3) for EDLCs using Taylor's expansion for large pores when $d \ll a$ [29]. The asymptotic behavior indicates that curvature plays a

Table 5.1 Fitting results for experimental data using Eqs. (5.10) and (5.11) for mesoporous and microporous carbons, respectively.

Pores	Carbons	Electrolytes	R^2	ϵ_r	d (Å)	a_0 (Å)	Ionic radii (Å)	
							r_+	r_-
Micro	CDC ^a	TEA- BF ₄ /AN (1.5 M)	0.985	2.23 (0.30) ^b	—	2.30 (0.14) ^b	3.4 ^c , 2.4 ^d	2.3 ^e
Meso	CDC ^a , template C ^f	(1.0, 1.4, and 1.5 M)	0.601	9.73 (1.29) ^b	9.43 (0.69) ^b	—	—	—
Micro	CDC ^g	EMIM- TFSI	0.944	1.12 (0.26) ^b	—	2.91 (0.16) ^b	2.15 ^{g,h} , 3.80 ^{g,i}	1.45 ^{g,h} , 3.85 ^{g,i}
Micro	CDC ^j , activated C ^k	H ₂ SO ₄ (1 M)	0.889	27.1 (18.7) ^b	—	0.05 (0.17) ^b	0.28 ^l	2.40, 2.58 ^m
Meso	Template C ⁿ	H ₂ SO ₄ (1 M)	0.328	17.4 (6.3) ^b	9.77 (1.92) ^b	—	—	—
Micro	Activated C ^k	KOH (6 M)	0.921	7.76 (3.06) ^b	—	1.64 (0.83) ^b	1.38 ^o	1.33 ^m
Meso	Activated C ^p	KOH (6 M)	0.618	13.4 (3.2) ^b	6.72 (1.03) ^b	—	—	—

^a Ref. [21].^b Numbers in parentheses are standard errors of fitting parameters.^c Refs. [75, 76].^d DFT calculations by the radial charge distribution of TEA⁺ that is confined inside a subnanometer pore with its C₂' axis in alignment with the pore axis Refs. [29, 30].^e Refs. [75–77].^f Refs. [61, 64, 73].^g Ref. [78].^h Along the short dimension.ⁱ Along the long dimension.^j Ref. [79].^k Ref. [80].^l Refs. [81, 82].^m Refs. [76, 77].ⁿ Ref. [64].^o Ref. [76].^p Ref. [83].

significant role for the capacitance of mesopores, but not for that of macropores, where the carbon/electrolyte interface can be adequately approximated by a parallel-plate capacitor. In fact, the normalized capacitance levels off more rapidly than the extrapolation of the fitting curve, as can be seen from the two data points in region IV. This may be ascribed to the fact that pore size is correlated with SSA and pore volume, which increase at the expense of pore wall thickness. The decrease in pore wall thickness can result in a constriction for space charge accommodation within the pore wall and in a concomitant reduction in capacitance [35]. The broken line represents the upper bound of normalized capacitance for large pores at the concentration of 1.0–1.5 M.

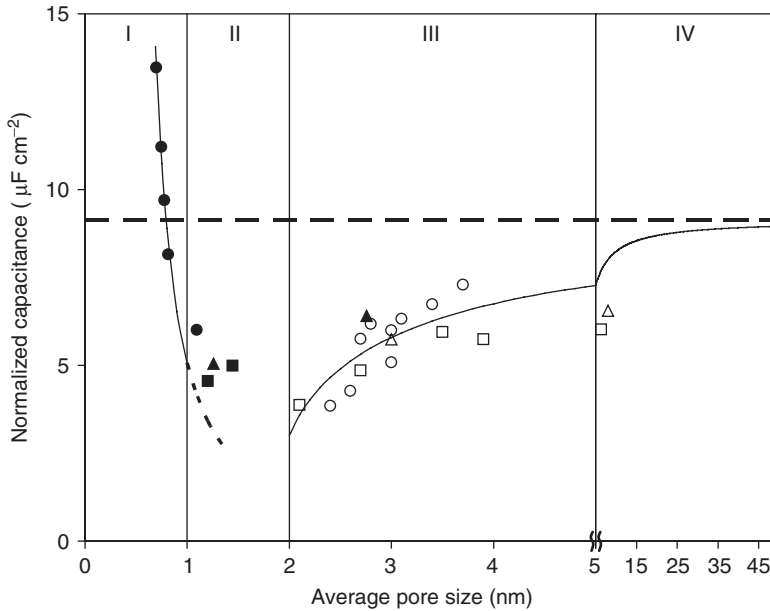


Figure 5.7 Experimental data of CDCs and template carbons in TEA-BF₄/AN electrolytes fit by Eq. (5.10) in region III and Eq. (5.11) in region I; the extrapolation of the curve in region III into region IV approaches the broken line calculated by Eq. (5.3) using the

same parameters as obtained from region III. ●, ■, and ▲: 1.5 M [21]; □: 1.0 M [61]; ○: 1.0 and 1.4 M [64]; and △: 1.0 M [73]; filled symbols are for CDCs and empty symbols for template carbons. Reprinted with permission from Ref. [72].

For the smaller pore size in region I, especially below 1 nm, the CDC materials exhibit an anomalous increase in area-normalized capacitance [21]. The highest normalized capacitance in microporous CDCs is found for the 0.7 nm pore and its value of $13.5 \mu\text{F cm}^{-2}$ is even higher than the upper bound of mesoporous carbons. This was originally considered as a puzzling result since it was believed that subnanometer pores were not accessible to electrolyte solution. This result contradicted the long-held assumption that pores smaller than the size of solvated electrolyte ions do not contribute to energy storage. Such anomalous behavior in subnanometer pores poses both a challenge of rationalization and an opportunity to improve the capacitance performance of microporous carbon supercapacitors [87]. By taking pore curvature into account using Eq. (5.11), the fit in region I reproduces remarkably well the anomalous increase in capacitance. This constitutes a stunning confirmation of the EWCC model. The fitted value of $\epsilon_r = 2.23 \pm 0.30$ is very close to the vacuum value of 1, which is reasonable because the space between counterions and pore walls is not an absolute vacuum but contains a finite electron density. It also suggests that the solvation shell of the counterions is almost completely removed, as suggested by Vix-Guterl *et al.* [64] and by Gogotsi and coworkers [21]. Desolvation of counterions is possible not only because the solvation free energies of TEA⁺ and BF₄⁻ are only -51.2 and $-45.1 \text{ kcal mol}^{-1}$, respectively, but also because the van

der Waals interactions between desolvated ions and the pore walls are strong [88]. The fitted value of $a_0 = 2.30 \pm 0.14 \text{ \AA}$ is in a very good agreement with the radius of about 2.3 \AA for BF_4^- documented in the literature [75–77] and with the ionic radius estimated from density functional theory (DFT) calculations of the radial charge distribution of BF_4^- [29, 30]. Literature reports an ionic radius of TEA^+ as about 3.4 \AA [75, 76], which does not agree with the a_0 value from the curve fitting. However, with its C_2' axis in alignment with the pore axis, TEA^+ has a smaller radius when confined inside a subnanometer pore, which is about 2.4 \AA , estimated from the DFT calculations of the radial charge distribution of TEA^+ [29, 30].

The EWCC model is also in quantitative agreement with the inter-ion distances probed from surface charge densities. Here, we focus on the leftmost data point in region I since it has the highest normalized capacitance of $13.5 \mu\text{F cm}^{-2}$ for the pore size of 0.7 nm . At the cell voltage of 2.3 V [21], the respective electrode voltage is 1.15 V , assuming a symmetric capacitor. According to $Q = CV$, the charge density $Q = 13.5 \mu\text{F cm}^{-2} \times 1.15 \text{ V} = 1.55 \times 10^{-21} \text{ C \AA}^{-2}$. With the electron charge of $1.602 \times 10^{-19} \text{ C e}^{-1}$, this corresponds to a point charge density of $0.0097 \text{ e \AA}^{-2}$. Alternatively, each point charge occupies an area of $1/0.0097 = 103 \text{ \AA}^2$. Within the EWCC model, ions line up in the cylinder with a pore diameter of 0.7 nm , and therefore the inter-ion distance is $103 \text{ \AA}^2 / 7\pi \text{ \AA} = 4.7 \text{ \AA}$. This value matches remarkably well with the ion size of BF_4^- and TEA^+ , showing that the 0.7 nm pores are packed with counterions at the cell voltage of 2.3 V . For this and other data points in region I, similar calculations can be performed using the capacitance values and voltage drops for the respective electrodes, which were obtained from CV measurements with a third quasi-reference silver electrode [33]. Results are tabulated in Table 5.2 for the CDCs with pore size from 0.700 to 0.806 nm , which is the pore size range that exhibits the anomalous increase in capacitance [30]. It is obvious that the inter-ion distance decreases with the pore size shrinking from 0.806 to 0.7 nm . In the 0.7 nm pore, the inter-ion distances are near the point of close packing, or, in other words, the charge storage almost reaches the surface saturation point [89, 90] at a cell voltage of 2.3 V .

Table 5.2 Inter-ion distances of TEA^+ and BF_4^- in subnanometer pores of CDCs calculated from charge densities on the basis of electrode capacitances and voltages in Ref. [33].

T ($^\circ\text{C}$)	Pore size (nm)	C_{tot} ($\mu\text{F cm}^{-2}$) ^a	BF_4^- results			TEA^+ results		
			C_- ($\mu\text{F cm}^{-2}$)	Voltage (V) ^a	Inter-ion distance (\AA)	C_+ ($\mu\text{F cm}^{-2}$)	Voltage (V) ^b	Inter-ion distance (\AA)
500	0.700	13.449	16.152	0.90	5.01	11.448	1.40	4.55
600	0.738	11.056	12.277	1.05	5.36	9.992	1.25	5.53
700	0.764	9.272	9.415	1.15	6.16	9.079	1.15	6.39
800	0.806	7.618	7.467	1.20	7.06	7.774	1.10	7.40

^aEstimated from the green branches of the $C-V$ curves (see Figures 5.2a and 5.2b of Ref. [33], for example).

^bEstimated from the red branches of the $C-V$ curves.

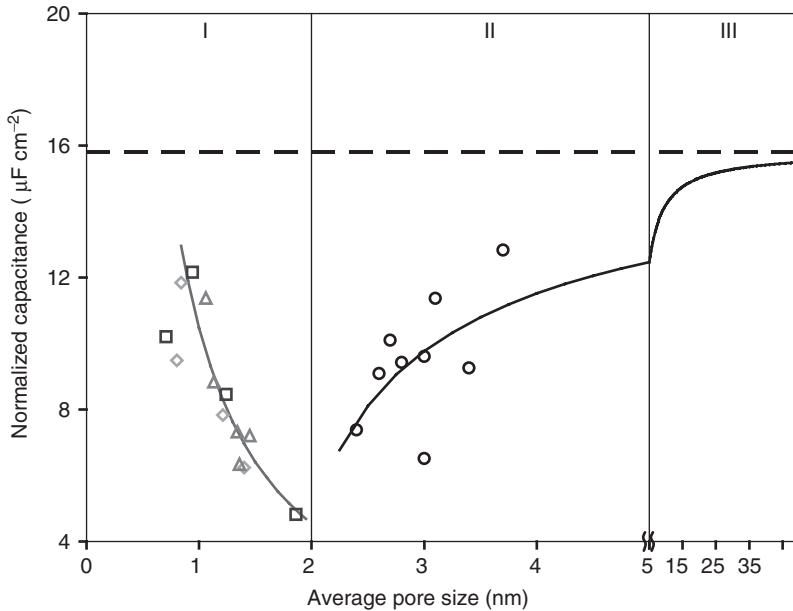


Figure 5.8 Experimental data for supercapacitors with diverse microporous and mesoporous carbon materials in a 1 M H_2SO_4 electrolyte fit by Eq. (5.11) and Eq. (5.10) in region I and II, respectively. The extrapolation of the curve in region II into region III approaches the broken line calculated

by Eq. (5.3) using the same parameters as obtained from region II. Note in region I, the two leftmost data points are excluded from the fit. ◇: ZrC-CDC, □: TiC-CDC, Δ: activated carbon material, and ○: template carbon material. Reprinted with permission from Ref. [30].

Capacitances of EDLCs show similar behavior in aqueous electrolytes, such as 1 M H_2SO_4 and 6 M KOH. Figure 5.8 presents the normalized capacitance in 1 M H_2SO_4 as a function of pore size for microporous CDCs and activated carbons in region I and mesoporous template carbons in region II. Similar to the case of organic electrolytes shown in Figure 5.7, the normalized capacitances of microporous and mesoporous carbons can be fit quite well using the EWCC and EDCC models, respectively. The fitting results are tabulated in Table 5.1. Owing to the difference in solvation free energies [88], a couple of notable differences are found between aqueous and organic electrolytes. The upper-bound normalized capacitance in 1 M H_2SO_4 is about $16 \mu\text{F cm}^{-2}$, a higher value than the largest one found in microporous carbons (about $12 \mu\text{F cm}^{-2}$, Figure 5.8). It is also noteworthy that for microporous carbons, the ϵ_r value of 27.1 ± 18.7 is much larger than the vacuum value of 1, indicating that the counterions may still be hydrated in micropores.

One important distinction between aqueous and organic electrolytes is the absence of a gap between microporous and mesoporous carbons. This gap is shown as region II in Figure 5.7. The origin of this gap region is intriguing and yet there is not a good model for it. Experimental data for organic electrolytes in region

II or for aqueous electrolytes that extend into pore sizes smaller than 1 nm are the key to answer this question, but such data are lacking in the literature. However, we found it enlightening to examine the experimental data for a series of activated carbons shown in Figure 5.9, albeit qualitatively. These data are borrowed from Figure 5.9 and Table 5.2 of Ref. [91]. For aqueous electrolytes of 1 M H_2SO_4 and 6 M KOH, starting from 1.4 nm pore size, the normalized capacitance increases with decreasing pore size, and then decreases slightly at 0.94 nm pore size, showing the same trend as in Figure 5.8. However, the capacitance increases sharply again at a pore size of 0.79 nm. On the basis of the quantitative analyses presented in Figure 5.8, it seems reasonable to extrapolate the curves into larger pore sizes (shown by the dashed curves). Likewise, for the organic electrolyte of 1 M TEA- BF_4/AN , it is also reasonable to extrapolate the curve into smaller pore sizes. Thus, these three capacitance curves in the entire pore size range exhibit a kink around 1 nm. As discussed before, the magnitude of the dielectric constant is an indication of the solvation or desolvation of counterions. On the basis of the ϵ_r values for both organic and aqueous electrolytes presented in Table 5.1, we conclude that the counterions experience a solvation/desolvation transition in the vicinity of 1 nm. For an organic electrolyte, the solvation/desolvation transition shows up at a larger pore size, in agreement with the larger ionic radii of organic counterions. The data in region II of Figure 5.7 are above the extrapolated dashed curve from region I, implying larger ϵ_r values. Pores in this region are still too small to accommodate

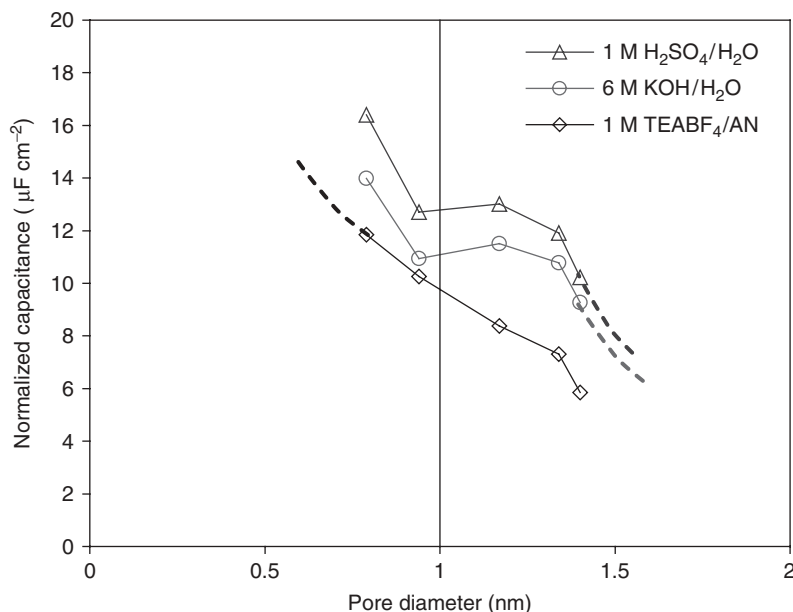


Figure 5.9 Normalized capacitance as a function of micropore size from Figure 5.9 and Table 5.2 of Ref. [91] for a series of activated carbons in aqueous and organic electrolytes showing the solvation/desolvation transition around 1 nm pore size as discussed in the text.

the inner cylinder of counterions, but solvated counterions can enter the pores to form EWCCs, leading to a higher ϵ_r value owing to the solvation shell.

The EWCC model was also successfully applied to the IL electrolyte of 1-ethyl-3-methylimidazolium bis(trifluoromethylsulfonyl)imide (EMIM-TFSI). With IL electrolytes, the counterions do not have any solvation shells because of the absence of solvent molecules. The bare ions allow one to discern the ion-sieving properties of porous carbon materials without the interference of solvent molecules [92]. The fitting results are $\epsilon_r = 1.12$ and $a_0 = 2.91 \text{ \AA}$ (Table 5.1). This ϵ_r value is very close to the vacuum value, confirming the absence of solvents in EMIM-TFSI. The a_0 value compares well with the ion sizes of EMIM⁺ and TFSI⁻. Both EMIM⁺ and TFSI⁻ ions can be approximated to have a rectangular shape with dimensions of 4.3×7.6 and $2.9 \times 7.9 \text{ \AA}^2$, respectively [78]. The ionic radii along the short and long dimensions are 2.15 and 3.80 \AA for EMIM⁺, respectively, and are 1.45 and 3.85 \AA for TFSI⁻, respectively. It appears that the a_0 value of 2.91 \AA from the fit is the average value of the ionic radii along the short and long dimensions, suggesting the quasi-free rotation of these ions inside the pores. This is likely related to the relatively high temperature of 60 °C at which the experiments were conducted.

5.3.1.2 Models for Hierarchically Porous Carbon Materials

The application of Eqs. (5.10) and (5.11) requires the analysis to be conducted for carbons with finely tuned pores or unimodal pore size distribution. Strictly speaking, among the materials discussed earlier, only CDCs have very narrow pore size distributions [21]. The relatively wider pore size distributions of other carbons may be responsible for the wide range of R^2 from 0.3 to 0.9. Figure 5.10 shows a cross section of a typical carbon particle [93]. There, the macropores serve as ion-buffering reservoirs; the mesopores facilitate ion transport and the micropores for optimal charge storage.

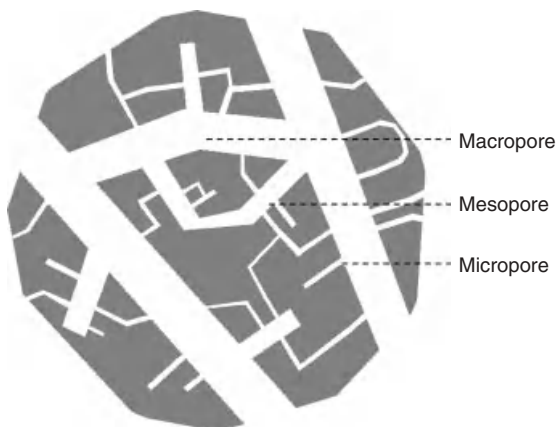


Figure 5.10 A cartoon of the cross section of a typical carbon particle showing macropores as ion-buffering reservoirs, mesopores facilitating ion transport, and micropores for optimal charge storage.

optimize charge storage [94]. Note that most micropores are shown to have two entrance (or exit) pathways. The theoretical work by Kaneko and coworkers [95] established that the 1 nm wide pores are packed with electrolyte ions even when the electrodes are not electrified. Thus, the micropores must have two entrances in order for the electrolytes already inside to exit through one of them and for the counterions to charge the pores through the other one, possibly under a nonuniform electric field along the pores. For such hierarchically porous carbon materials, the ideal approach would be to include the contributions to capacitance from macro-, meso-, and micropores [30]. This can be done using the following multimodal capacitance formula:

$$C = \frac{\varepsilon_{r,\text{macro}} \varepsilon_0 A_{\text{macro}}}{d} + \sum_j \frac{\varepsilon_{r,\text{meso}} \varepsilon_0 A_{j,\text{meso}}}{b_j \ln [b_j / (b_j - d)]} + \sum_i \frac{\varepsilon_{r,\text{micro}} \varepsilon_0 A_{i,\text{micro}}}{b_i \ln (b_i / a_0)} \quad (5.12)$$

where the three terms are obtained from Eqs. (5.3), (5.10), and (5.11) for macro-, meso-, and micropores. If different pore sizes are present in each pore regime, the summation over the pore sizes is necessary since the capacitance is pore size dependent, except for macropores.

In cases where macropores contribute only a small portion to the total SSA and the pore size distributions of micropores and mesopores are narrow, yielding bimodal pores, Eq. (5.12) reduces to

$$C = \frac{\varepsilon_{r,\text{micro}} \varepsilon_0 A_{\text{micro}}}{b_{\text{micro}} \ln (b_{\text{micro}} / a_0)} + \frac{\varepsilon_{r,\text{meso}} \varepsilon_0 A_{\text{meso}}}{b_{\text{meso}} \ln [b_{\text{meso}} / (b_{\text{meso}} - d)]} \quad (5.13)$$

or simply

$$C = C_{\text{micro}} A_{\text{micro}} + C_{\text{meso}} A_{\text{meso}} \quad (5.14)$$

If we are interested in normalized capacitance, we can divide both sides of Eq. (5.14) by A_{meso} , to yield:

$$\frac{C}{A_{\text{meso}}} = C_{\text{meso}} + C_{\text{micro}} \frac{A_{\text{micro}}}{A_{\text{meso}}} \quad (5.15)$$

Shi [26] employed Eq. (5.15) for carbons with bimodal pores, producing a linear relationship between C/A_{meso} and $A_{\text{micro}}/A_{\text{meso}}$. This method is widely used to obtain C_{meso} and C_{micro} from the intercept and the slope of the linear fit of experimental data. An alternative way to manipulate Eq. (5.14) is to divide it by A_{micro} , yielding:

$$\frac{C}{A_{\text{micro}}} = C_{\text{micro}} + C_{\text{meso}} \frac{A_{\text{meso}}}{A_{\text{micro}}} \quad (5.16)$$

The analysis of Rufford *et al.* [27] for a series of activated carbons in 1 M H_2SO_4 showed that Eq. (5.16) yields results as consistent as those obtained with Eq. (5.15). However, Gogotsi and coworkers [79] found that the use of Eq. (5.16) does not yield a linear relationship for CDCs in the same electrolyte. Other groups also found that the use of Eq. (5.15) leads to a negative C_{meso} , which has no physical meaning and simply points to its larger uncertainty [35, 96].

Noticing that the total normalized capacitance with respect to the mesoporous surface, C/A_{meso} , lacks physical meaning, Rufford *et al.* improved Shi's model by dividing Eq. (5.14) by the total surface area A_{tot} [27]:

$$\frac{C}{A_{\text{tot}}} = C_{\text{meso}} + (C_{\text{micro}} - C_{\text{meso}}) \frac{A_{\text{micro}}}{A_{\text{tot}}} \quad (5.17)$$

C/A_{tot} can be plotted as a function of $A_{\text{micro}}/A_{\text{tot}}$. C_{meso} is then obtained as the intercept of the linear fit, while C_{micro} is obtained from the sum of the intercept and the slope. This improved model has been applied to the experimental data of a series of activated carbons in 1 M H_2SO_4 , giving comparable results and uncertainty as the method proposed by Shi.

5.3.1.3 Models for Exohedral Capacitors

Zero-dimensional (0D) carbon onions, one-dimensional (1D) end-capped CNTs, and carbon nanofibers are nanoscale carbon materials that constitute the general category of exohedral EDLCs. Recently, several experiments were performed on carbon onions [24, 97], vertically aligned CNT arrays [98, 99], and carbon nanofibers [23], providing results that show superior rate capabilities of exohedral supercapacitors. General discussions in the literature on the pores of these carbon structures refer to the voids between carbon particles. An alternative description is that counterions can only reside on the outer surfaces of carbon particles, exploiting the positive surface curvature. These carbon particles can be approximated as being spherical or cylindrical, as shown in Figure 5.11 [28].

Solvated counterions approach the surface of an electrically charged carbon onion particle to form an exohedral electric double-sphere capacitor (xEDSC). For CNTs or carbon nanofibers, solvated counterions and the outer wall of the tube or fiber form an exohedral electric double-cylinder capacitor (xEDCC). Similar to the depiction of Figure 5.5a, the radius of the outer sphere or cylinder formed by counterions is b and the radius of the inner sphere/cylinder formed by the carbon surface is a , which characterizes the particle size. The difference between these two radii is the effective double-layer thickness d . The capacitance formulae of xEDSC

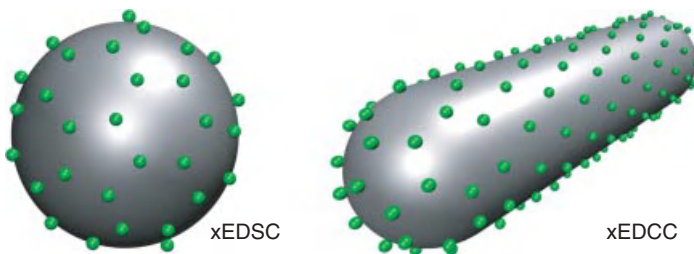


Figure 5.11 Steric views of a charged 0D carbon onion sphere and a 1D end-capped CNT with electrolyte counterions (solvent molecules not shown) approaching the outer surfaces to form an

exohedral electric double-sphere capacitor (xEDSC) and an exohedral electric double-cylinder capacitor (xEDCC), respectively. Reprinted with permission from Ref. [28].

and xEDCC can then be expressed as functions of a and d as follows [28]:

$$\frac{C}{A} = \frac{\varepsilon_r \varepsilon_0 (a + d)}{ad} \quad (5.18)$$

$$\frac{C}{A} = \frac{\varepsilon_r \varepsilon_0}{a \ln [(a + d)/a]} \quad (5.19)$$

The normalized capacitance, C/A , can be plotted as a function of carbon onion or tube/fiber radius a . The plot shows that C/A increases monotonically with decreasing diameter, in sharp contrast to the behavior of nanoporous carbon materials as shown in Figures 5.7 and 5.8 [28]. These different trends are ascribed to the positive curvature of exohedral capacitors versus the negative curvature of their endohedral counterparts. In addition, the capacitance of spheres increases at a faster rate than that of tubes/fibers, because a sphere has locally two positive principal Gaussian curvatures while a tube/fiber only has one (the other being zero, along the axis). The large diameter behavior of exohedral capacitors is similar to that of endohedral capacitors: the extrapolations of the C/A - a plots for both xEDSC and xEDCC into the large diameter range approach asymptotically the same EDLC line. This value is an upper bound for endohedral capacitors and a lower bound for exohedral capacitors.

Experimental electrochemical studies on the capacitance of 0D carbon onions with 1.5 M TEA-BF₄/AN showed a trend described earlier, according to the xEDSC model. As can be seen in Figure 5.12, the highest normalized capacitance value is for nanodiamond soot (diamond nanocrystals coated with fullerene-like carbon shells). The capacitance values of carbon onions decrease with increasing average particle size, which is correlated with increasing annealing temperature from 1200, 1500, 1800, to 2000 °C. The carbon black has primarily outer surfaces exposed to the electrolyte and does not have subnanometer pores on each particle. Its average particle size is about 40 nm and the normalized capacitance of 3 μF cm⁻² corroborates the predicted trend and also appears to be an asymptotic limit for the carbon onion data. The fit using Eq. (5.18) produced the following electrochemical parameters: $R^2 = 0.759$, $\varepsilon_r = 17.03 \pm 4.80$, and $d = 9.73 \pm 10.91$ nm. The values of R^2 and ε_r are acceptable but the d value seems to be too large compared to the dimension of organic ions and also has rather large standard errors. Nevertheless, the unique dependence of C/A as a function of a shown in the experimental data of carbon onions can be captured at least qualitatively by the xEDSC model.

Experimental gravimetric capacitance of 1D MWCNTs in 1.96 M TEA-BF₄/PC also exhibits a trend similar to that of the 0D carbon onions, which further supports the role of positive surface curvature. However, the lack of SSA for these CNT samples prevents the conversion of gravimetric capacitances into area-normalized values. It follows that the fit of the experimental data using Eq. (5.19) cannot be completed. Hulicova-Jurcakova *et al.* measured the gravimetric capacitance in 1 M H₂SO₄ of 1D carbon nanofibers synthesized by chemical vapor deposition. These structures are solid and nonporous. For the two samples, C1-700-25 and C1-500-25, the average fiber diameters can be estimated from the scanning electron microscopic (SEM) images shown in Figure 5.4 of Ref. [23] to be 20 and 40 nm,

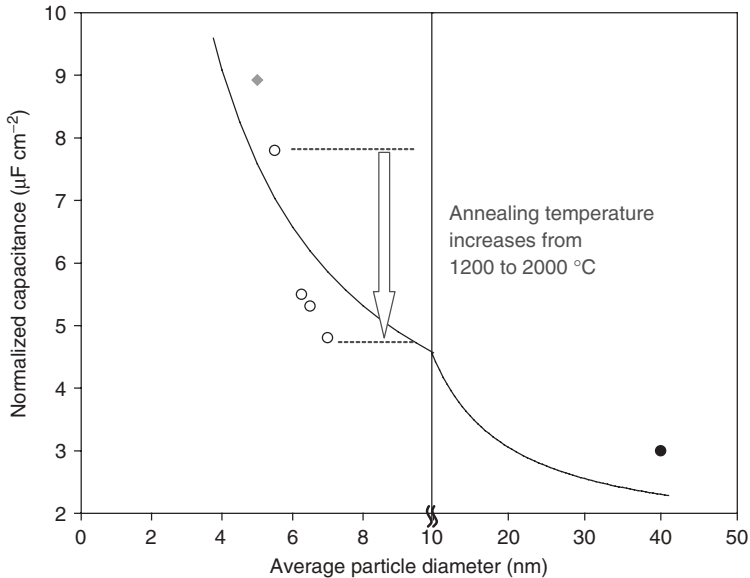


Figure 5.12 Normalized capacitance of nanodiamond soot (♦), carbon onions (○), and carbon black (●) as a function of average particle diameter (annealing temperature shown by the arrow) with an organic electrolyte of 1.5 M TEA-BF₄/AN. The fitting curve was obtained with Eq. (5.18), showing a trend that capacitance increases with decreasing particle diameter. Reprinted with permission from Ref. [28].

respectively. Figure 5.13 shows the normalized capacitance of these two samples as a function of current density. In the entire current density range, the 20 nm carbon nanofibers have higher normalized capacitance than the 40 nm ones, showing once again a trend compatible with the predictions made from Eq. (5.19).

Compared to the upper-bound capacitance of the endohedral capacitors about 10 and 16 $\mu\text{F cm}^{-2}$ in organic and aqueous electrodes as shown in Figures 5.7 and 5.8, respectively, the normalized capacitance values in Figures 5.12 and 5.13 are rather low, as a result of particle agglomeration during the electrode preparation process. This process reduces the particle surface areas measured for the powder samples. The caveats from these theoretical analyses are that both surface area and particle size should be measured in order to gain a deeper insight into the charge storage mechanism of these exohedral materials. In addition, the SSA should be measured after the electrodes are prepared so that the areas exposed to electrolytes can be used to normalize the capacitance.

5.3.2

EDL Theories Beyond the GCS Model

Numerous alternative mathematical models for EDLs have been developed. For instance, a number of modified PB equations have been derived to address the limitations of the classical PB equations. Some of the limitations are related to

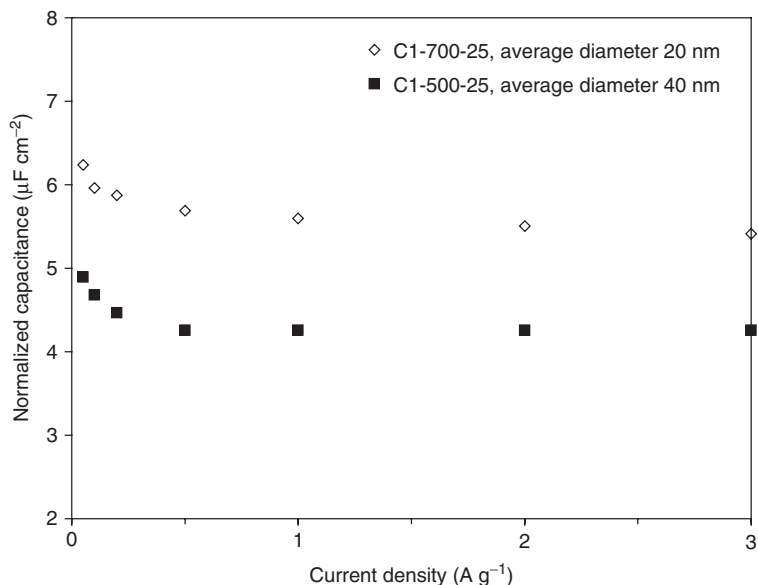


Figure 5.13 Normalized capacitance of 1D carbon nanofibers with diameters of 20 and 40 nm in 1 M H₂SO₄ as a function of current density showing that the thinner nanofiber has higher normalized capacitance than the thicker one.

the effects of finite ion size, fluctuating potentials, solvent effects, nonelectrostatic interactions, and dielectric saturation. They have been addressed in one form or another in a number of modified PB equations [100–106]. A detailed review of these models is beyond the scope of this chapter and we refer those interested to a recent comprehensive review [107]. Although these works have provided useful insights into the structure of EDLs and have rationalized some interesting experimental observations, quantitative prediction of EDL capacitance remains a significant challenge.

Essentially, all of the aforementioned modified PB equations are developed for electrolytes featuring solvents. For solvent-free electrolytes such as molten salts and room-temperature ILs, the existing models are generally inadequate and new theories are needed. For instance, since room-temperature ILs are promising electrolytes for supercapacitors, models for the EDLs in ILs are of particular interest. The first theoretical model for such EDLs was proposed by Kornyshev [108] and a qualitatively similar model was derived by Oldham [109]. In Kornyshev's model, the EDL consists of an inner compact layer and an outer diffuse layer. Using a mean-field theory approach, the differential capacitance of the diffuse layer in ILs featuring cations and anions of the same size was determined as

$$C_{\text{diff}} = \frac{\varepsilon_r \varepsilon_0 A}{\lambda_D} \times \frac{\cosh(u/2)}{1 + 2\gamma \sinh^2(u/2)} \times \sqrt{\frac{2\gamma \sinh^2(u/2)}{\ln[1 + 2\gamma \sinh^2(u/2)]}} \quad (5.20)$$

where

$$u = \frac{e\phi_{\text{diff}}}{k_{\text{B}}T} \quad (5.21)$$

$$\gamma = \frac{2c_0}{c_{\text{max}}} \quad (5.22)$$

λ_{D} is the Debye length based on the average bulk salt density \bar{c} , γ (< 1) is a lattice saturation parameter, ϕ_{diff} is the potential drop across the diffuse layer, and c_0 and c_{max} are the average bulk concentration of cation/anion and the maximal possible local concentration of ions, respectively. One of the key predictions of Eq. (5.20) is that the differential capacitance as a function of electrode potential (C - V) curves of the EDLs in ILs are bell-shaped or camel-like, in good agreement with some recent experimental data [110].

5.3.3

Quantum Capacitance of Graphitic Carbons

Single-layer and multilayer graphene materials constitute an entirely new class of carbon materials and have only recently been studied for EDLC applications [25, 40]. The SSA of a single graphene sheet is $1315 \text{ m}^2 \text{ g}^{-1}$ for each side of the sheet. This amounts to $2630 \text{ m}^2 \text{ g}^{-1}$ if both sides of the sheet are available for charge storage. Compared with endohedral or exohedral carbon materials, the advantage of high SSA is especially beneficial at high electrode voltage when one side of the sheet reaches surface saturation and the counterions can utilize the other side of the sheet to form a double layer.

Unlike most other carbon materials, the capacitance of graphene is strongly dependent on electrode potential. A recent experimental measurement on single-layer and bi-layer graphene materials showed that the differential capacitance exhibits a V shape as a function of electrode potential in the IL electrolyte of 1-butyl-3-methylimidazolium hexafluorophosphate (BMIM-PF₆) (blue curve in Figure 5.14) [111]. In typical electrode materials, the differential capacitance is independent of the electrode potential, yielding a rectangle-shaped C - V curve. By subtracting the contribution from the compact layer capacitance, it was found that such a V shape has a quantum mechanical origin (red curve in Figure 5.14) and results from the two-dimensional free-electron gas behavior in the basal plane of graphene. The low-energy electronic properties of graphene are characterized by the Dirac point, which is the point where quasi-linear electronic bands meet, at the Fermi energy [112]. The quantum capacitance has a nonzero minimum at the Dirac point and increases linearly on both sides of the minimum with a slope that depends on the impurity-induced carrier concentration. This behavior is similar to the previously observed symmetrical V shaped capacitance-potential curves on the basal plane of graphite [55–57]. Conventionally, such a behavior was rationalized by the space charge layer contribution C_{SC} in graphite, which is assumed to follow Eqs. (5.5) and (5.6). However, the space charge capacitance theory developed for semiconductors is not applicable to graphene for the following two reasons [111]: it cannot explain

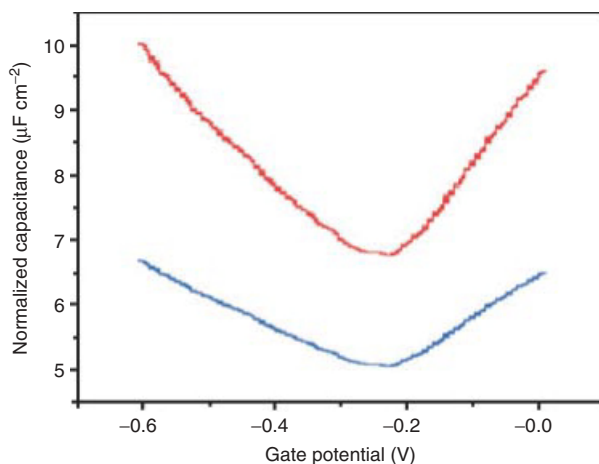


Figure 5.14 Normalized capacitance of a single-layer graphene as a function of gate potential with respect to a platinum quasi-reference electrode measured in the 1-butyl-3-methylimidazolium hexafluorophosphate (BMIM-PF₆). The blue and red curves are the total capacitance and quantum capacitance, respectively. Reprinted with permission from Ref. [111].

the shape of the capacitance curves and the Debye length of graphite is comparable to the lattice dimension owing to the high charge carrier concentrations in graphite.

The manifestation of quantum capacitance is likely to be responsible for the butterfly-shaped CV scans sometimes observed for typical carbon materials, showing a pronounced minimum of capacitance near the PZC value, although the slope of the capacitance–potential curves is usually much smaller than the $23 \mu\text{F cm}^{-2} \text{V}^{-1}$ predicted for an ideal graphene layer [111]. This behavior translates into a trapezoid-shaped CV for a two-electrode device, which is narrower at the zero voltage and becomes wider with increasing cell voltage (Figure 5.15) [36]. It is interesting to note that, similar to Figures 5.14 and 5.15, SWCNTs are also shown to exhibit a C – V curve with a parabolic shape that has its minimum near the PZC in 0.1 M tetrabutylammonium hexafluorophosphate in acetonitrile (TBA-PF₆/AN) [113], or a trapezoid-shaped CV for a two-electrode device with 1 M TEA-BF₄/PC electrolyte [114]. The fact that the quantum capacitance is often absent for most carbon materials, even including multilayer graphene [25, 40, 115–117], may be due to structural ordering during sample preparation at elevated temperatures to form graphitic carbons. This can be effectively monitored by examining the graphite band intensity relative to the disorder band intensity using Raman spectroscopy [21].

5.3.4

Molecular Dynamics Simulations

Although the theoretical models discussed earlier are useful for understanding EDLs, they have many limitations. For example, chemical details of ions and solvent molecules such as shapes and charge distributions are difficult to be

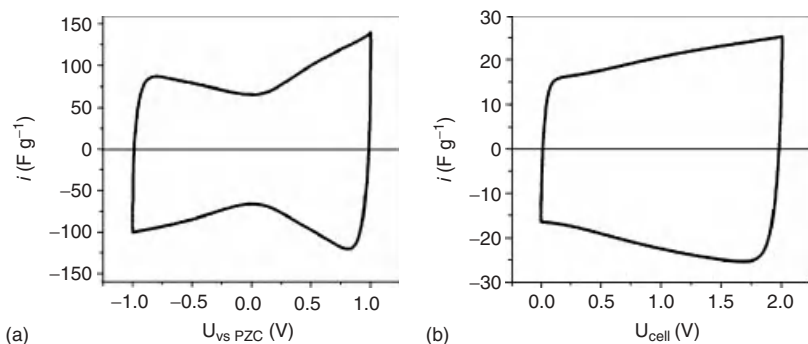


Figure 5.15 C–V curves of activated carbon materials measured in 1 M TEA-BF₄/AN at a scan rate of 10 mV s⁻¹ by (a) a three-electrode setup and (b) a two-electrode device. Reprinted with permission from Ref. [36].

accounted for in these models, and dramatic simplifications such as neglecting ion–ion correlation and dielectric constant variation in the EDL must often be made to render the models tractable. As the EDLs in supercapacitors constitute, for the most part, atomistic phenomena, many of these limitations can be addressed using MD modeling. We present below an overview of EDL modeling studies based on the type of electrolytes involved, that is, aqueous electrolytes, organic electrolytes, and room-temperature ILs.

5.3.4.1 EDLs in Aqueous Electrolytes

The EDLs near open electrodes or in wide pores, in which the EDLs of opposing surfaces do not interact, have been studied extensively using molecular simulations. Except in a few cases [118–122], the electrodes were modeled as surfaces with uniform charge densities. The EDL structures revealed from these studies are generally in good agreement with the predictions of the GCS model. In fact, except at positions within about 1 nm of electrified surfaces, the PB equation can accurately predict the ion distribution under moderate electrode charge densities and electrolyte concentrations [123]. At positions within 1 nm of the electrodes, many factors that are not accounted for in the classical PB equation, for example, ion hydration [118–120, 124, 125], interfacial water layering [126], finite ion size [127], and nonelectrostatic ion–electrode interactions [128], become important. Finite ion size and ion hydration are particularly relevant to supercapacitor applications because they can significantly affect the EDL capacitance. In particular, ion hydration can control the closest approach of an ion to the electrode and thereby the thickness of the Stern layer. This can be explained as follows: when an ion approaches very close to the electrode surface, part of its solvation shell must be removed because of geometrical confinement. If the energetic cost of this process is small, an ion can become contact-adsorbed on the electrode and its closest approach to the electrode will be defined by the radius of its bare ion. Otherwise, an ion’s closest approach to the electrode will be defined primarily by the radius of the hydrated ion. MD simulations determine that small ions such as Na⁺ and K⁺ ions cannot become

contact-adsorbed at moderate surface charge densities ($|\sigma| < 0.1 \text{ C m}^{-2}$) [118, 124], although they are contact-adsorbed at very high surface charge densities ($|\sigma| \geq 0.1 \text{ C m}^{-2}$) [129, 130]. However, larger ions such as Cl^- ions, whose hydration energies are smaller, can become notably contact-adsorbed on electrodes even on neutral electrodes. In addition to revealing the underlying physics not accounted for in the classical EDL theories, MD simulations also provide a detailed understanding of the ion packing inside the EDLs. For example, Cagle *et al.* [131] showed that Na^+ ions are contact-adsorbed on electrodes with a surface charge density of -0.26 C m^{-2} , and the closest separation between these ions is 0.92 nm. As such a separation is larger than, but comparable to, the hydrated diameter of Na^+ ions (0.72 nm), the packing of Na^+ ions is approaching, but still below, the steric limit defined by their hydrated diameters.

Much less work has been reported on the molecular modeling of EDLs in micropores filled with aqueous electrolytes. Yang and Garde [132] reported the selective partitioning of K^+ , Cs^+ , and Na^+ ions into negatively charged cylindrical micropores with a diameter of 6.7 Å. It was found that ions are excluded from neutral or nearly neutral pores and that the pore displays selectivity toward partitioning of larger cations K^+ and Cs^+ over that for the smaller Na^+ ions in pores with surface charge densities of -0.14 to -0.35 C m^{-2} . These results, along with observations of the partitioning kinetics, suggest the presence of a barrier for partitioning cations into the small pores. The trends in partitioning kinetics are consistent with the free energy of ion dehydration in bulk water, thus suggesting that the observed barriers are closely related to the partial dehydration of ions as they enter the nanopores. Feng *et al.* [133] studied the distribution of K^+ ions in electrified slit-shaped micropores with pore widths ranging from 9.36 Å to 14.7 Å (Figure 5.16). It was found that, in slit pores with widths larger than or equal to 14.7 Å, the K^+ ions form separate layers near each slit wall and the ion distribution is in qualitative agreement with the classical EDL theories. However, in pores with widths between 10 and 14.7 Å, fully hydrated K^+ ions accumulate primarily in the central plane of the slit pores (Figure 5.16a). Such an ion distribution differs qualitatively from the prediction of classical EDL theories, and is caused primarily by the ion hydration effects, that is, ions tend to accumulate at positions where they can maximize interactions with their hydration water molecules (Figure 5.16b). In 9.36 Å wide slits, the partially dehydrated K^+ ions also form separate layers near each slit wall. Interestingly, it was found that the electrostatic ion–ion repulsion plays a minor role in such a transition. Instead, the enthalpic effects associated with the interactions between the hydration water molecules of a K^+ ion with their surrounding water molecules were found to be responsible for this behavior [133]. Following the ion distribution shown in Figure 5.16, a sandwich capacitor model was proposed where a layer of counterions are located exactly midway between two slit-pore surfaces separated by a pore width of $2b$. The capacitance is given by

$$\frac{C}{A} = \frac{\epsilon_r \epsilon_0}{b - a_0} \quad (5.23)$$

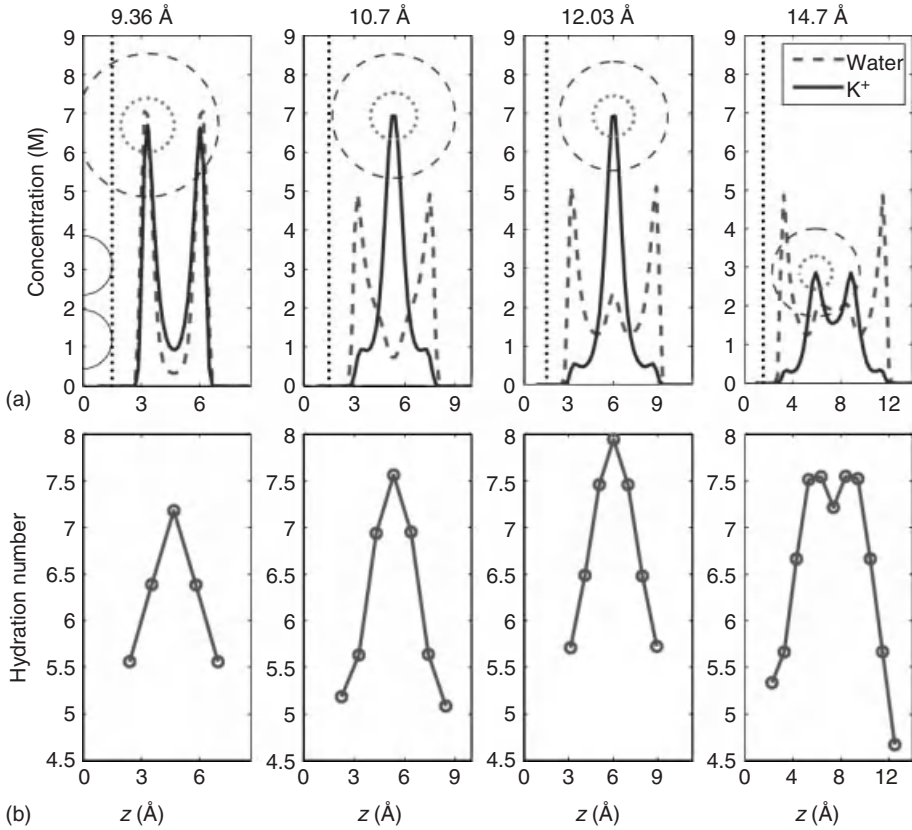


Figure 5.16 (a) Concentration profiles of water and K^+ ions inside slit pores with various widths. For clarity, the water concentration has been divided by a factor of 30. The concentric circles denote the size of bare and hydrated K^+ ions. The hemi-circles in the leftmost figure denote the van

der Waals radius of the wall atom and the dashed line denotes the effective boundary of the lower wall. (b) Hydration number of K^+ ions across slit pores with various widths. All slit walls have the same surface charge density of $\sigma = -0.055 \text{ C m}^{-2}$. Reprinted from Ref. [133] with permission.

This sandwich model can predict the anomalous enhancement of capacitance [133]. Fitting the experimental data of microporous CDCs in a pore size range of 10.6–14.5 Å in 6 M KOH electrolyte gave $R^2 = 0.926$, $\varepsilon_r = 3.33 \pm 0.57$, and $a_0 = 2.65 \pm 0.54 \text{ Å}$. Compared with the results in Table 5.1 using the EWCC model, the fitting quality as indicated by the R^2 value is similar, and the ε_r value also implies that the electrolyte ions are hydrated in the pore size range studied. However, the a_0 value is farther away from the literature value of K^+ ion radius (1.38 Å) than the EWCC fitting result (Table 5.1). This indicates that confinement effects (the use of a_0 explicitly) are key in a qualitative description of the capacitance behavior for small pores (i.e., sharp increase with decreasing width). However, curvature effects are indispensable for a quantitative description of the experimental capacitance

values, further implying that the microporous carbons studied in the experiment have a local pore geometry that is closer to a cylinder shape rather than a slit.

5.3.4.2 EDLs in Organic Electrolytes

Relatively little modeling work has been done for EDLs in organic electrolytes. Feng *et al.* [88] studied the EDLs adjacent to effectively open electrodes in 1.2 M TEA-BF₄/AN electrolyte. Their results show that the EDLs in organic electrolytes have several features not typically observed in aqueous electrolytes. First, TEA⁺ and BF₄⁻ ions are significantly contact-adsorbed on neutral electrodes, and alternating layers of cations/anions penetrate about 1.1 nm into the bulk electrolyte. Second, near the charged electrodes, a distinct counterion concentration peak forms. This peak is followed by a distinct co-ion concentration peak (Figure 5.17a). Such an ion distribution cannot be described by either the Helmholtz or the GCS model. This is because the number of counterions adsorbed on the electrode exceeds the number of electrons on the electrode, and the electrode is overscreened in parts of the EDL (Figure 5.17b). The contact adsorption originates from the fact that van der Waals

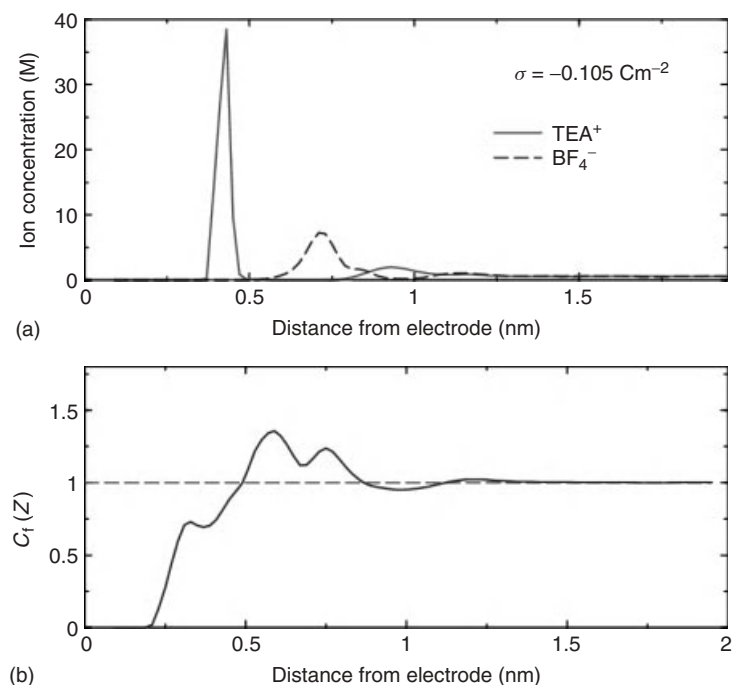


Figure 5.17 (a) Distribution of TEA⁺ and BF₄⁻ ions near an electrode with surface charge density of $\sigma = -0.105 \text{ C m}^{-2}$. (b) Distribution of the charge screening factor $C_f(Z) = -\int_0^Z \rho_e(s)/\sigma ds$ where $\rho_e(z)$ is the ion space charge density at position z

from the electrode. $C_f(z) = 1$ corresponds to a complete screening of the electrode charge at position z , and $C_f(z) > 1$ corresponds to an overscreening of the electrode charge. Reprinted with permission from Ref. [88].

interactions between organic ions and the electrode are strong and the partial desolvation of these ions occurs easily, as a result of the relatively small solvation energy of the bulky organic ions (the solvation free energies of TEA^+ and BF_4^- ions are -51.2 and -45.1 kcal mol $^{-1}$, respectively). The alternating layering of cations/anions near neutral/charged electrodes and the overscreening of electrode charges are both caused by the strong correlation between TEA^+ and BF_4^- ions, which form contact ion pairs in bulk solutions. The strong cation–anion correlation is mainly due to the relatively weak screening of electrostatic interactions by AN (the dielectric constant is 35.8 [134]).

Modeling work on EDLs in mesopores and micropores filled with organic electrolytes is also scant at present. Using synchrotron X-ray diffraction and reverse Monte Carlo simulations, Kaneko and colleagues studied the structure of PC confined in uncharged slit-shaped carbon micropores with a width of 1.0 nm in equilibrium with TEA- BF_4 electrolytes [95]. It was found that, in the absence of organic ions, PC molecules are randomly distributed inside the slit pore without long-range ordering. However, in the presence of TEA^+ and BF_4^- ions, PC molecules form a double-layer-like structure inside the slit to accommodate the ions. This suggests that solvent molecules can adjust their structure to allow the storage of organic ions inside the narrow slit in spite of the space restriction, which contributes to the high specific capacitance of carbon nanopores. In another related work, Pratt and colleagues [32] studied the capacitance of carbon nanotube forests (CNTFs) immersed in a TEA- BF_4 /PC electrolyte. The computed single electrode capacitance was about 80 F g $^{-1}$, in good agreement with experimental data [21]. Interestingly, it was found that as the effective pore size in the CNTF shrinks from 3.94 to 1.17 nm, the specific capacitance of the pore increases by about 10%. Although such a moderate increase is smaller than that observed in experiments [21], it reproduces the correct trend.

5.3.4.3 EDLs in Room-Temperature ILs

Most of the available modeling works on EDLs in ILs were performed in nanoslits featuring planar walls [135–142]. Given that an understanding of EDLs in ILs has only developed recently, most existing works focused on delineating the basic structure of the EDL and the dependence of its capacitance on electrode potential. From these studies, consensus is emerging on several aspects of the EDLs in ILs.

First, the EDL near open electrodes consists of a Helmholtz-like layer and a diffuse layer, and ions in the EDL exhibit strong orientational ordering. Such a structure, envisioned in earlier theoretical analysis of EDLs in ILs [108] and subsequently confirmed in MD simulations [138, 140], is more complicated than that inferred from earlier experimental studies [143]. Figure 5.18a,b shows the ion distributions near positively charged electrodes in contact with 1-butyl-3-methylimidazolium nitrate (BMIM- NO_3) [140]. At a surface charge density of $\sigma \geq 0.03$ C m $^{-2}$, a distinct layer of NO_3^- ions appears near the electrode. However, Figure 5.18c shows that the charge separation persists well beyond the first NO_3^- ion layer. Figure 5.18d,e shows that the BMIM^+ and NO_3^- ions in contact with the electrodes orient nearly parallel to the electrode. In addition, their orientation becomes more random as

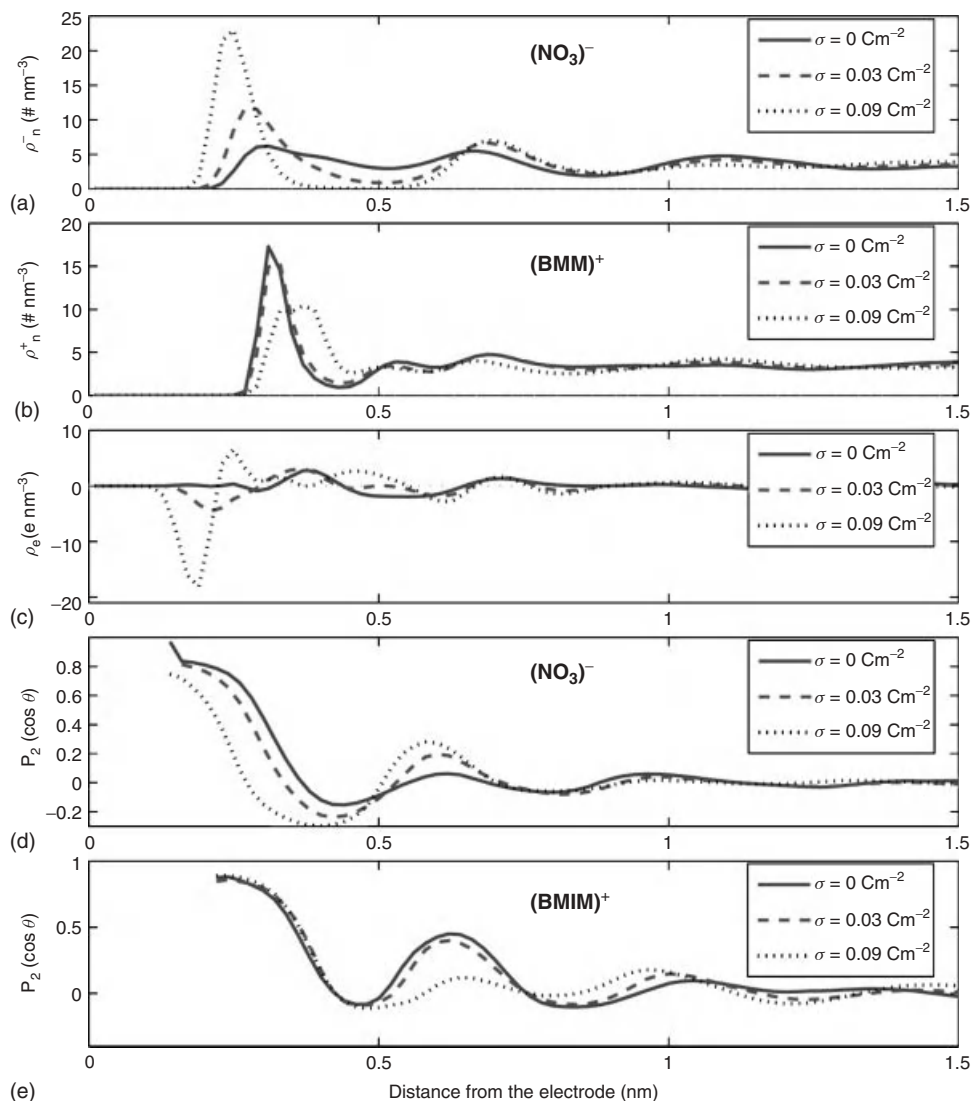


Figure 5.18 Number density of NO_3^- (a) and BMIM^+ (b) ions near neutral and positive electrodes. (c) Space charge density profiles near the electrodes. Orientation ordering parameter $P_2(\cos\theta) = \langle 3\cos^2\theta - 1 \rangle / 2$ of the NO_3^- (d) and BMIM^+ (e) ions

near electrodes. θ is the angle formed by the normal vector of the electrode surface and the normal vector of the imidazolium ring of the cation or the plane formed by the three oxygen atoms of the NO_3^- ion. Reprinted with permission from Ref. [140].

the distance from the electrode increases. Both the charge separation and ion orientation ordering penetrate about 1 nm into the bulk electrolyte, suggesting that the diffuse layer spans about 1 nm, in good agreement with other published works [135, 137, 141].

Second, adsorption of bulky cations on electrodes can be significant. This is evident in Figure 5.18b. Such adsorption persists even when the electrode becomes positively charged, and cannot be neglected at $\sigma = 0.09 \text{ C m}^{-2}$. The van der Waals attraction between the polyatomic ion and the electrode has been found to contribute to such persistent adsorption [140].

Third, the EDL structure change induced by the electrification of the electrode can be dominated by small co-ions. In dilute electrolyte solutions, as the electrode surface charge density increases, the EDL structure change is characterized by the significant accumulation of counterions near the electrode. However, Lynden-Bell and colleagues [137] studied dimethylimidazolium chloride (DMIM-Cl) confined between electrified walls and found that as the electrode surface charge density changes from 0 to -0.02 C m^{-2} , the concentration of bulky DMIM⁺ ions near the electrode changes slightly while smaller anions (Cl⁻) are repelled from the electrode toward the bulk ILs. Qiao and colleagues [140] also observed a similar phenomenon for EDLs in BMIM-NO₃. As capacitance is a macroscopic manifestation of the response of EDL structure to a charged electrode, these observations suggest that co-ions play an important role in determining the EDL capacitance.

Finally, overscreening is a universal phenomenon. Overscreening originates from the strong ion-ion correlation in ILs. Overscreening of electrode charge in IL was perhaps first envisioned by Kornyshev [108], and has subsequently been observed in molecular simulations [138]. As such a phenomenon cannot be predicted by mean-field theories, it highlights the need for developing more advanced theories for EDLs in ILs.

Given that research on EDLs in ILs is still at a very early stage, the current understanding of many important phenomena remains limited. In particular, the dependence of differential capacitance on electrode potential (i.e., $C-V$ correlation) is not fully understood. Experimentally, $C-V$ curves with various shapes, for example, concave, bell, or camel-like shapes, have all been reported [110, 143, 144]. However, the physical origins of these observations are still unclear. Fedorov and Kornyshev [138, 139] performed simulations of model ILs consisting of charged Lennard-Jones beads. Although the chemical details of ions were neglected to a large extent in these models, two key aspects of ILs, that is, solvent-free and strong ion-ion correlation were well captured. They found that the bell-shaped $C-V$ curves could be qualitatively reproduced in their simulations. In a more recent study (Figure 5.19) [142], they found that if one of the ions in the IL has neutral moieties, a double-hump camel shaped $C-V$ curve is obtained. These results suggest that the shape anisotropy and charge distribution on ions can play a subtle role in determining the EDL capacitance. Qiao and colleagues [140] investigated the EDLs in BMIM-NO₃ by modeling the size, shape, and charge delocalization of ions explicitly, and obtained an approximately concave $C-V$ curve (Figure 5.20). They attributed the observed $C-V$ curve shape to the significant adsorption of

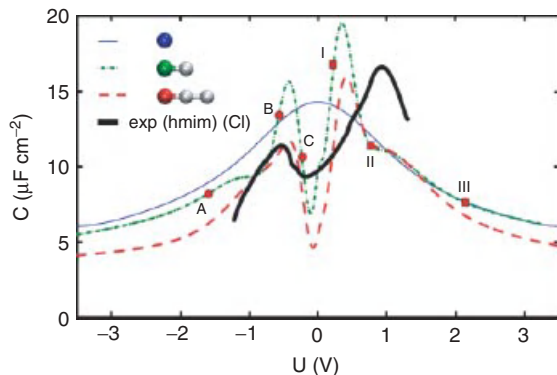


Figure 5.19 Differential capacitance of EDLs in three ILs. The dark solid curve is the experimental data for 1-hexyl-3-methylimidazolium chloride (HMIM-Cl) [110]. Anions are modeled as a single Lennard–Jones bead. Cations are modeled

as a single charged bead, a dumbbell with one charged bead and one neutral bead, a three-atom chain with one charged bead and two neutral beads. Reprinted with permission from Ref. [142].

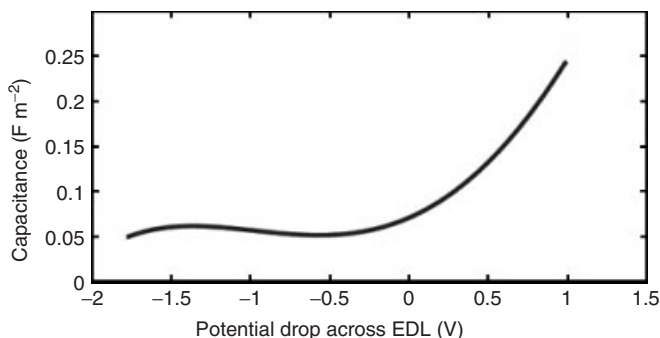


Figure 5.20 Differential capacitance of EDLs at the interfaces of BMIM-NO₃ and a planar electrode. Reprinted with permission from Ref. [140].

BMIM⁺ ions on electrodes, and the dominant contribution of a small anion to the response of EDL structure to a change in the electrode potential or charge [140]. The results shown in Figures 5.19 and 5.20 suggest that both the simplified model of ILs and the models with sophisticated chemical details capture some aspects of the EDLs observed in experiments. However, at present, the physical origins of the differences between these results are not yet well understood. It is possible that the potential window explored in Figure 5.20 is not large enough to observe the decrease in capacitance since it is known that the differential capacitance of an EDL decreases sharply when the packing of counterions reaches the steric limit, which can occur only at large electrode potentials. More research is needed to clarify the origins of these differences and to possibly reconcile these seemingly different results.

5.4 Concluding Remarks

Ever since the first patent issued in 1957 [145], EDLCs have prompted a great deal of interest. The research in this area has slowly become a global endeavor in the past couple of decades. The current state-of-the-art, as represented by a Ragone plot that characterizes energy and power densities of electrical energy storage devices, has EDLCs occupying the gap between batteries and conventional dielectric capacitors. They have much higher energy density compared to conventional dielectric capacitors, and they also feature much higher power density and longer cycle lifetime than batteries. The ideal goal is to achieve considerably higher energy densities while retaining high-power capabilities. To achieve this goal, various new electrolytes and novel carbon-based materials have been investigated for EDLCs. This has introduced complications to the fundamental understanding of the charge storage at the electrode/electrolyte interface. The intricate interfacial phenomena are imposing new challenges for fundamental science. However, these challenges also offer new opportunities to optimize capacitance performances of EDLCs. The hope of improving existing performance is further maintained by the much shorter history of EDLCs compared to that of batteries. New experimental tools, the availability of supercomputers, and theoretical developments are helping to achieve this goal.

Theoretical models range from the earliest Helmholtz model and mean-field continuum models, to the surface-curvature-based post-Helmholtz models, and to modern atomistic simulations. In this chapter, we have highlighted a number of studies that not only shed considerable light on experimental findings but also provide predictive capabilities that are needed to achieve the optimization of capacitance. Owing to the nonplanar surfaces of carbon materials at the nanoscale, the original Helmholtz EDLC model is gradually found to be outdated, in particular, for carbon materials. We have found that the surface-curvature-based EDCC and/or EWCC models provide a better description of the interface behavior of carbon materials. These post-Helmholtz models compare remarkably well with experimental data. In addition, MD simulations provide atomistic details such as ion solvation, ion-ion correlations, and van der Waals interactions between pore wall and ions or between solvent molecules.

Many real-world examples of the modern use of EDLCs for enhancing energy efficiency in heavy duty applications are already noted: the hybrid diesel/electric gantry cranes with fuel savings of 40% [3], the rideHybride gasoline/electric buses in Long Beach, California, that have replaced the earlier version of e-power buses (Figure 5.21a) [146], Siemens' hybrid energy storage systems for rail vehicles (Figure 5.21b) [147], emergency doors on an Airbus A380 [10], high-power energy sources for spaceflight applications [148], among others. By coupling theory and simulations with experiments, further improvements for the energy density problem that presently plagues the larger scale use of EDLCs for energy storage can be made possible. Thanks to the ever-increasing joint efforts from experimentalists and theoreticians, EDLCs will likely find their own market space instead of being dominated by only niche applications.



Figure 5.21 (a) A rideHybride gasoline/electric bus in Long Beach, California. The use of capacitors, located on the roof, improves the emissions and offers almost the same fuel efficiency as diesel fuel even for the less fuel efficient gasoline engine. Courtesy of Brynn Kernaghan and Juan Vigil of Long Beach Transit. (b) A tram without

using a pantograph serving between Almada and Seixal, the south of Lisbon, Portugal. It is equipped with Sitras[®] HES (hybrid energy storage system) based on Ni/MH batteries and EDLCs. Each vehicle saves up to 30% energy and reduces up to 80 t of CO₂ emission per year. Siemens press picture reprinted with permission from Siemens AG.

Acknowledgments

The authors at ORNL gratefully acknowledge the support from the Laboratory Directed Research and Development Program of ORNL, the Division of Materials Science and Engineering, Basic Energy Sciences, U.S. Department of Energy and the Center for Nanophase Materials Sciences (CNMS), sponsored by the Division of Scientific User Facilities, U. S. Department of Energy. The authors at Clemson acknowledge the support from the NSF under Grant No. CBET-0967175. RQ was partly supported by an appointment to the HERE program for faculty at ORNL administered by ORISE. We are indebted to Prof. Yury Gogotsi and Prof. Patrice Simon for providing the gravimetric capacitances, specific surface areas, and pore sizes, and $C-V$ curves for Ref. [33], which our analyses in Table 5.2 were based on. We thank Drs. Sheng Dai and Nancy Dudney, and Profs. Francois Béguin, Teresa A. Centeno, Elzbieta Frackowiak, Yushin Gleb, Yury Gogotsi, Miklos Kertesz, Patrice Simon, and George Zhao for helpful discussions.

References

1. US Department of Energy (2007) Workshop on Basic Research Needs for Electrical Energy Storage, Bethesda, Maryland, USA, April 2–4, 2007; Basic Research Needs for Electrical Energy Storage: Report of the Basic Energy Sciences Workshop on Electrical Energy Storage, <http://science.energy.gov/bes/news-and-resources/reports/basic-research-needs/>.
2. Conway, B.E. (1999) *Electrochemical Supercapacitors: Scientific Fundamentals and Technological Applications*, Kluwer Academic/Plenum, New York.
3. Miller, J.R. and Simon, P. (2008) *Science*, **321**, 651.
4. Winter, M. and Brodd, R.J. (2004) *Chem. Rev.*, **104**, 4245.
5. Burke, A. (2000) *J. Power. Sources*, **91**, 37.
6. Kötzt, R. and Carlen, M. (2000) *Electrochim. Acta*, **45**, 2483.
7. Sarangapani, S., Tilak, B.V., and Chen, C.-P. (1996) *J. Electrochem. Soc.*, **143**, 3791.
8. Béguin, F., Raymundo-Piñero, E., and Frackowiak, E. (2010) in *Carbons for Electrochemical Energy Storage and Conversion Systems* (eds F. Béguin and E. Frackowiak), CRC Press, Boca Raton, FL, pp. 329–375.
9. Mastragostino, M., Soavi, F., and Arbizzani, C. (2002) in *Advances in Lithium-Ion Batteries* (eds W. van Schalkwijk and B. Scrosati), Kluwer Academic/Plenum Publishers, New York, pp. 481–505.
10. Simon, P. and Gogotsi, Y. (2008) *Nat. Mater.*, **7**, 845.
11. Zhang, Y., Feng, H., Wu, X., Wang, L., Zhang, A., Xia, T., Dong, H., Li, X., and Zhang, L. (2009) *Int. J. Hydrogen Energy*, **34**, 4889.
12. Naoi, K. and Simon, P. (2008) *Electrochem. Soc. Interface*, **17**, 34.
13. Naoi, K. and Morita, M. (2008) *Electrochem. Soc. Interface*, **17**, 44.
14. Bélanger, D., Brousse, T., and Long, J.W. (2008) *Electrochem. Soc. Interface*, **17**, 49.
15. Pandolfo, A.G. and Hollenkamp, A.F. (2006) *J. Power. Sources*, **157**, 11.
16. Frackowiak, E. (2007) *Phys. Chem. Chem. Phys.*, **9**, 1774.
17. Obreja, V.V.N. (2008) *Physica E*, **40**, 2596.
18. Zhang, L.L. and Zhao, X.S. (2009) *Chem. Soc. Rev.*, **38**, 2520.
19. Liang, C., Hong, K., Guiochon, G.A., Mays, J.W., and Dai, S. (2004) *Angew. Chem. Int. Ed.*, **43**, 5785.
20. Korenblit, Y., Rose, M., Kockrick, E., Borchardt, L., Kvit, A., Kaskel, S., and Yushin, G. (2010) *ACS Nano*, **4**, 1337.
21. Chmiola, J., Yushin, G., Gogotsi, Y., Portet, C., Simon, P., and Taberna, P.L. (2006) *Science*, **313**, 1760.
22. Zhang, H., Cao, G., Wang, Z., Yang, Y., Shi, Z., and Gu, Z. (2008) *Nano Lett.*, **8**, 2664.
23. Hulicova-Jurcakova, D., Li, X., Zhu, Z.H., de Marco, R., and Lu, G.Q. (2008) *Energy Fuels*, **22**, 4139.
24. Portet, C., Yushin, G., and Gogotsi, Y. (2007) *Carbon*, **45**, 2511.
25. Stoller, M.D., Park, S., Zhu, Y., An, J., and Ruoff, R.S. (2008) *Nano Lett.*, **8**, 3498.
26. Shi, H. (1996) *Electrochim. Acta*, **41**, 1633.
27. Rufford, T.E., Hulicova-Jurcakova, D., Zhu, Z.H., and Lu, G.Q. (2009) *J. Phys. Chem. C*, **113**, 19335.
28. Huang, J., Sumpter, B.G., Meunier, V., Yushin, G., Portet, C., and Gogotsi, Y. (2010) *J. Mater. Res.*, **25**, 1525.
29. Huang, J., Sumpter, B.G., and Meunier, V. (2008) *Angew. Chem. Int. Ed.*, **47**, 520.
30. Huang, J., Sumpter, B.G., and Meunier, V. (2008) *Chem. Eur. J.*, **14**, 6614.
31. Shim, Y. and Kim, H.J. (2010) *ACS Nano*, **4**, 2345.
32. Yang, L., Fishbine, B.H., Migliori, A., and Pratt, L.R. (2009) *J. Am. Chem. Soc.*, **131**, 12373.
33. Chmiola, J., Largeot, C., Taberna, P.L., Simon, P., and Gogotsi, Y. (2008) *Angew. Chem. Int. Ed.*, **47**, 3392.
34. Grahame, D.C. (1947) *Chem. Rev.*, **41**, 441.
35. Barbieri, O., Hahn, M., Herzog, A., and Kötzt, R. (2005) *Carbon*, **43**, 1303.

36. Hahn, M., Baertschi, M., Barbieri, O., Sauter, J.-C., Kötz, R., and Gallay, R. (2004) *Electrochem. Solid-State Lett.*, **7**, A33.
37. Sing, K.S.W., Everett, D.H., Haul, R.A.W., Moscou, L., Pierotti, R.A., Rouquerol, J., and Siemieniowska, T. (1985) *Pure Appl. Chem.*, **57**, 603.
38. Miller, J.R. and Simon, P. (2008) *Electrochem. Soc. Interface*, **17**, 31.
39. de Levie, R. (1963) *Electrochim. Acta*, **8**, 751.
40. Zhu, Y., Stoller, M.D., Cai, W., Velamakanni, A., Piner, R.D., Chen, D., and Ruoff, R.S. (2010) *ACS Nano*, **4**, 1227.
41. von Helmholtz, H.L.F. (1853) *Ann. Phys. (Leipzig)*, **89**, 211.
42. Conway, B.E., Bockris, J.O.'M., and Ammar, I.A. (1951) *Trans. Faraday Soc.*, **47**, 756.
43. MacDonald, J.R. and Barlow, C.A. Jr., (1962) *J. Chem. Phys.*, **36**, 3062.
44. Dzubiella, J. and Hansen, J.-P. (2005) *J. Phys. Chem.*, **122**, 234706.
45. Palmer, L.S., Cunliffe, A., and Hough, J.M. (1952) *Nature*, **170**, 796.
46. Teschke, O. and de Souza, E.F. (1999) *Appl. Phys. Lett.*, **74**, 1755.
47. Bard, A.J. and Faulkner, L.R. (2001) *Electrochemical Methods: Fundamentals and Applications*, 2nd edn, John Wiley & Sons, Inc., New York.
48. Gouy, L.G. (1910) *J. Phys.*, **9**, 457.
49. Chapman, D.L. (1913) *Philos. Mag.*, **25**, 475.
50. Stern, O. (1924) *Z. Elektrochem.*, **30**, 508.
51. Lyklema, J. (1995) *Fundamentals of Interface and Colloid Science, Solid-Liquid Interfaces*, Vol. II, Academic Press, London, pp. 3.32–3.44.
52. Huang, J., Qiao, R., Sumpster, B.G., and Meunier, V. (2010) *J. Mater. Res.*, **25**, 1469.
53. Gerischer, H. (1990) *Electrochim. Acta*, **35**, 1677.
54. Qu, D.Y. (2002) *J. Power. Sources*, **109**, 403.
55. Randin, J.-P. and Yeager, E. (1971) *J. Electrochem. Soc.*, **118**, 711.
56. Randin, J.-P. and Yeager, E. (1972) *J. Electroanal. Chem.*, **36**, 257.
57. Randin, J.-P. and Yeager, E. (1975) *J. Electroanal. Chem.*, **58**, 313.
58. Lozano-Castelló, D., Cazorla-Amorós, D., Linares-Solano, A., Shiraiishi, S., Kurihara, H., and Oya, A. (2003) *Carbon*, **41**, 1765.
59. Lin, C., Ritter, J.A., and Popov, B.N. (1999) *J. Electrochem. Soc.*, **146**, 3639.
60. Morimoto, T., Hiratsuka, K., Sanada, Y., and Kurihara, K. (1996) *J. Power. Sources*, **60**, 239.
61. Sevilla, M., Álvarez, S., Centeno, T.A., Fuertes, A.B., and Stoeckli, F. (2007) *Electrochim. Acta*, **52**, 3207.
62. Qu, D. and Shi, H. (1998) *J. Power. Sources*, **74**, 99.
63. Endo, M., Kim, Y.J., Takeda, T., Maeda, T., Hayashi, T., Koshihara, K., Hara, H., and Dresselhaus, M.S. (2001) *J. Electrochem. Soc.*, **148**, A1135.
64. Vix-Guterl, C., Frackowiak, E., Jurewicz, K., Friebe, M., Parmentier, J., and Béguin, F. (2005) *Carbon*, **43**, 1293.
65. Frackowiak, E., Lota, G., Machnikowski, J., Vix-Guterl, C., and Béguin, F. (2006) *Electrochim. Acta*, **51**, 2209.
66. Lu, G.Q. and Zhao, X.S. (2004) in *Nanoporous Materials: Science and Engineering* (eds G.Q. Lu and X.S. Zhao), Imperial College Press, London, pp. 1–13.
67. Everett, D.H. and Powl, J.C. (1976) *J. Chem. Soc., Faraday Trans.*, **72**, 619.
68. Gregg, S.J. and Sing, K.S.W. (1967) *Adsorption, Surface Area and Porosity*, Chapter 3, Academic Press, New York.
69. Evans, R., Marconi, U.M.B., and Tarazona, P. (1986) *J. Chem. Soc., Faraday Trans. 2*, **82**, 1763.
70. Itagaki, M., Suzuki, S., Shitanda, I., Watanabe, K., and Nakazawa, H. (2007) *J. Power. Sources*, **164**, 415.
71. Jang, J.H. and Oh, S.M. (2004) *J. Electrochem. Soc.*, **151**, A571.
72. Huang, J., Sumpster, B.G., and Meunier, V. (2009) in *Mesoporous Materials: Properties, Preparations and Applications* (ed. L.T. Burness), Nova Science, New York, pp. 177–190.
73. Fuertes, A.B., Lota, G., Centeno, T.A., and Frackowiak, E. (2005) *Electrochim. Acta*, **50**, 2799.

74. Brunauer, S., Emmett, P.H., and Teller, E. (1938) *J. Am. Chem. Soc.*, **60**, 309.
75. Ue, M. (1994) *J. Electrochem. Soc.*, **141**, 3336.
76. Marcus, Y. (1994) *Biophys. Chem.*, **51**, 111.
77. Jenkins, H.D.B. and Thakur, K.P. (1979) *J. Chem. Educ.*, **56**, 576.
78. Largeot, C., Portet, C., Chmiola, J., Taberna, P.-L., Gogotsi, Y., and Simon, P. (2008) *J. Am. Chem. Soc.*, **130**, 2730.
79. Chmiola, J., Yushin, G., Dash, R., and Gogotsi, Y. (2006) *J. Power. Sources*, **158**, 765.
80. Lota, G., Centeno, T.A., Frackowiak, E., and Stoeckli, F. (2008) *Electrochim. Acta*, **53**, 2210.
81. Heyrovská, R. (2006) *Chem. Phys. Lett.*, **432**, 348.
82. Heyrovská, R. (2005) *Mol. Phys.*, **103**, 877.
83. Gryglewicz, G., Machnikowski, J., Lorenc-Grabowska, E., Lota, G., and Frackowiak, E. (2005) *Electrochim. Acta*, **50**, 1197.
84. Côté, J.-F., Brouillette, D., Desnoyers, J.E., Rouleau, J.-F., St-Arnaud, J.-M., and Perron, G. (1996) *J. Solution Chem.*, **25**, 1163.
85. Yang, C.-M., Kim, Y.-J., Endo, M., Kanoh, H., Yudasaka, M., Iijima, S., and Kaneko, K. (2007) *J. Am. Chem. Soc.*, **129**, 20.
86. Lust, E., Jänes, A., Pärn, T., and Nigu, P. (2004) *J. Solid State Electrochem.*, **8**, 224.
87. See the comments of Miller, J. in Service, R.F. (2006) *Science*, **313**, 902.
88. Feng, G., Huang, J., Sumpster, B.G., Meunier, V., and Qiao, R. (2010) *Phys. Chem. Chem. Phys.*, **12**, 5468.
89. Mysyk, R., Raymundo-Piñero, E., and Béguin, F. (2009) *Electrochem. Commun.*, **11**, 554.
90. Mysyk, R., Raymundo-Piñero, E., Pernak, J., and Béguin, F. (2009) *J. Phys. Chem. C*, **113**, 13443.
91. Raymundo-Piñero, E., Kierzek, K., Machnikowski, J., and Béguin, F. (2006) *Carbon*, **44**, 2498.
92. Salitra, G., Soffer, A., Eliad, L., Cohen, Y., and Aurbach, D. (2000) *J. Electrochem. Soc.*, **147**, 2486.
93. Simon, P. and Burke, A. (2008) *Electrochem. Soc. Interface*, **17**, 38.
94. Wang, D.W., Li, F., Liu, M., Lu, G.Q., and Cheng, H.M. (2008) *Angew. Chem. Int. Ed.*, **47**, 373.
95. Takana, A., Iiyama, T., Ohba, T., Ozeki, S., Urita, K., Fujimori, T., Kanoh, H., and Kaneko, K. (2010) *J. Am. Chem. Soc.*, **132**, 2112.
96. Jänes, A., Kurig, H., and Lust, E. (2007) *Carbon*, **45**, 1226.
97. Bushueva, E.G., Galkin, P.S., Okotrub, A.V., Bulusheva, L.G., Gavrilov, N.N., Kuznetsov, V.L., and Moiseev, S.I. (2008) *Phys. Status Solidi B*, **245**, 2296.
98. Honda, Y., Haramoto, T., Takeshige, M., Shiozaki, H., Kitamura, T., Yoshikawa, K., and Ishikawa, M. (2008) *J. Electrochem. Soc.*, **155**, A930.
99. Honda, Y., Takeshige, M., Shiozaki, H., Kitamura, T., Yoshikawa, K., Chakrabarti, S., Suekane, O., Pan, L.J., Nakayama, Y., Yamagata, M., and Ishikawa, M. (2008) *J. Power. Sources*, **185**, 1580.
100. Bikerman, J.J. (1942) *Philos. Mag.*, **33**, 384.
101. Borukhov, I., Andelman, D., and Orland, H. (1997) *Phys. Rev. Lett.*, **79**, 435.
102. Burak, Y. and Andelman, D. (2000) *Phys. Rev. E*, **62**, 5296.
103. Lue, L., Zoeller, N., and Blankschtein, D. (1999) *Langmuir*, **15**, 3726.
104. Das, T., Bratko, D., Bhuiyan, L.B., and Outhwaite, C.W. (1995) *J. Phys. Chem.*, **99**, 410.
105. Outhwaite, C.W. and Bhuiyan, L. (1982) *J. Chem. Soc., Faraday Trans.*, **78**, 775.
106. Woelki, S. and Kohler, H.H. (2000) *Chem. Phys.*, **261**, 421.
107. Bazant, M.Z., Kilic, M.S., Storey, B.D., and Ajdari, A. (2009) *Adv. Colloid Interface Sci.*, **152**, 48.
108. Kornyshev, A.A. (2007) *J. Phys. Chem. B*, **111**, 5545.
109. Oldham, K.B. (2008) *J. Electroanal. Chem.*, **613**, 131.
110. Lockett, V., Sedev, R., Ralston, J., Horne, M., and Rodopoulos, T.J. (2008) *J. Phys. Chem. C*, **112**, 7486.
111. Xia, J., Chen, F., Li, J., and Tao, N. (2009) *Nat. Nanotechnol.*, **4**, 505.

112. Wallace, P.R. (1947) *Phys. Rev.*, **71**, 622.
113. Barisci, J.N., Wallace, G.G., Chattopadhyay, D., Papadimitrakopoulos, F., and Baughman, R.H. (2003) *J. Electrochem. Soc.*, **150**, E409.
114. Futaba, D.N., Hata, K., Yamada, T., Hiraoka, T., Hayamizu, Y., Kakudate, T., Tanaike, O., Hatori, H., Yumura, M., and Iijima, S. (2006) *Nat. Mater.*, **5**, 987.
115. Wang, Y., Shi, Z., Huang, Y., Ma, Y., Wang, C., Chen, M., and Chen, Y. (2009) *J. Phys. Chem. C*, **113**, 13103.
116. Wang, D.-W., Li, F., Wu, Z.-S., Ren, W., and Cheng, H. (2009) *Electrochem. Commun.*, **11**, 1729.
117. Vivekchand, S.R.C., Rout, C.S., Subrahmanyam, K.S., Govindaraj, A., and Rao, C.N.R. (2008) *J. Chem. Sci.*, **120**, 9.
118. Spohr, E. (1998) *J. Electroanal. Chem.*, **450**, 327.
119. Spohr, E. (1999) *Electrochim. Acta*, **44**, 1697.
120. Spohr, E. (2002) *Solid State Ionics*, **150**, 1.
121. Schmickler, W. and Leiva, E. (1995) *Mol. Phys.*, **86**, 737.
122. Halley, J.W. (1996) *Electrochim. Acta*, **41**, 2229.
123. Qiao, R. and Aluru, N.R. (2003) *J. Chem. Phys.*, **118**, 4692.
124. Phipott, M.R., Glosli, J.N., and Zhu, S.B. (1995) *Surf. Sci.*, **335**, 422.
125. Dimitrov, D.I. and Raev, N.D. (2000) *J. Electroanal. Chem.*, **486**, 1.
126. Qiao, R. and Aluru, N.R. (2005) *Colloids Surf., A*, **267**, 103.
127. Crozier, P.S., Rowley, R.L., and Henderson, D. (2000) *J. Chem. Phys.*, **113**, 9202.
128. Freund, J.B. (2002) *J. Chem. Phys.*, **116**, 2194.
129. Qiao, R. and Aluru, N.R. (2004) *Phys. Rev. Lett.*, **92**, 198301.
130. Chen, Y.F., Ni, Z.H., Wang, G.M., Xu, D.Y., and Li, D.Y. (2008) *Nano Lett.*, **8**, 42.
131. Cagle, C., Feng, G., Qiao, R., Huang, J., Sumpster, B.G., and Meunier, V. (2010) *Microfluid. Nanofluid.*, **8**, 703.
132. Yang, L. and Garde, S. (2007) *J. Chem. Phys.*, **126**, 084706.
133. Feng, G., Qiao, R., Huang, J., Sumpster, B.G., and Meunier, V. (2010) *ACS Nano*, **4**, 2382.
134. Lide, D.R. and Haynes, W.M. (eds) (2009) *CRC Handbook of Chemistry and Physics*, 90th edn, CRC Press, Boca Raton, FL, pp. 6–148, Internet Version 2010.
135. Pinilla, C., Del Pópolo, M.G., Lynden-Bell, R.M., and Kohanoff, J. (2005) *J. Phys. Chem. B*, **109**, 17922.
136. Liu, L., Li, S., Cao, Z., Peng, Y., Li, G., Yan, T., and Gao, X.P. (2007) *J. Phys. Chem. C*, **111**, 12161.
137. Pinilla, C., Del Pópolo, M.G., Kohanoff, J., and Lynden-Bell, R.M. (2007) *J. Phys. Chem. B*, **111**, 4877.
138. Fedorov, M.V. and Kornyshev, A.A. (2008) *Electrochim. Acta*, **53**, 6835.
139. Fedorov, M.V. and Kornyshev, A.A. (2008) *J. Phys. Chem. B*, **112**, 11868.
140. Feng, G., Zhang, J.S., and Qiao, R. (2009) *J. Phys. Chem. C*, **113**, 4549.
141. Kislenco, S.A., Samoylov, I.S., and Amirov, R.H. (2009) *Phys. Chem. Chem. Phys.*, **11**, 5584.
142. Fedorov, M.V., Georgi, N., and Kornyshev, A.A. (2010) *Electrochem. Commun.*, **12**, 296.
143. Baldelli, S. (2008) *Acc. Chem. Res.*, **41**, 421.
144. Alam, M., Islam, M., Okajima, T., and Ohsaka, T. (2007) *Electrochem. Commun.*, **9**, 2370.
145. Becker, H.E. (1957) General electric. US Patent 2 800 616.
146. Huang, J., Sumpster, B.G., and Meunier, V. (2009) The 9th International Advanced Automotive Battery & EC Capacitor Conference & Symposia, Long Beach, California, USA, June 8–12, 2009.
147. Rechenberg, K. and Meinert, M. (2009) The 9th International Advanced Automotive Battery & EC Capacitor Conference & Symposia, Long Beach, California, USA, June 8–12, 2009.
148. Arepalli, S., Fireman, H., Huffman, C., Moloney, P., Nikolaev, P., Yowell, L., Higgins, C.D., Kim, K., Kohl, P.A., Turano, S.P., and Ready, W.J. (2005) *JOM J. Miner., Met. Mater. Soc.*, **57**, 26.

6

Electrode Materials with Pseudocapacitive Properties

Elzbieta Frackowiak

6.1

Introduction

The performance of electrical double-layer capacitors (EDLCs) is based on the electrostatic attraction of ions in the electrode/electrolyte interface. The most often used electrode materials for EDLCs are activated carbons (ACs) with developed surface area and porosity well matched with the size of the ions. The high conductivity, the chemical stability in aqueous and organic electrolytes, the low cost, and the different achievable forms of carbon are the main advantages for its practical application [1–5]. However, it is well known that independent of its origin, texture, and pore size, a carbon material is characterized by more or less constant surface capacitance about $10 \mu\text{F cm}^{-2}$ [5–7]. Consequently, a limited capacitance (100–200 F g^{-1} , depending on the electrolytic medium) is reached using a pure carbon material [5–22]. A great enhancement in capacitance values can be obtained if, apart from electrostatic forces, quick faradaic reactions take place. As the charge transferred during these faradaic processes is proportional to voltage, as in an EDLC, this effect is called *pseudocapacitance*. The pseudocapacitance classically comes into sight in such materials as conducting polymers [23–40], transition metal oxides [41–52], carbons enriched in heteroatoms (oxygen, nitrogen) [53–61], and nanoporous carbons with electrosorbed hydrogen [62–74]. Apart from electrode materials, it has been shown that pseudocapacitance could be originated from chemisorption and/or redox reactions of electrolyte species [75–79].

This chapter describes the electrode materials as well as the redox-active electrolytes with a pseudocapacitive character. Taking into account that, in faradaic processes, the diffusion is an important factor, the special role of texture of electrode materials used for capacitors is underlined. New trends in this topic are shown where the electrode is of hierarchical micro/mesoporous texture, very often with nanotubes and graphene as support for pseudocapacitive materials. Considering that the number of papers on pseudocapacitive phenomena grows enormously, this chapter is not an exhaustive presentation of all publications, but it shows the main trends through some examples.

6.2

Conducting Polymers in Supercapacitor Application

Electronically conducting polymers (ECPs) as polypyrrole (PPy), polyaniline (PANI), polythiophene (PTh), poly[3-methylthiophene] (PMTh), or poly[3,4-ethylenedioxythiophene] (PEDOT) can store and release charges through redox processes associated with the π -conjugated polymer chains [23–40]. When oxidation occurs (also referred to as *p-doping*), ions from the electrolyte are transferred to the polymer backbone and, on reduction (“undoping”), they are released back into the solution. Generally p-dopable polymers are more stable than n-dopable ones [36, 39]. The doping/undoping process takes place throughout the bulk of the electrodes, offering the opportunity to achieve high values of specific capacitance. As an example, Eq. (6.1) expresses the reversible doping of PPy:



However, the insertion/deinsertion of counterions during cycling causes volumetric changes of ECPs, with a progressive electrode degradation because of swelling, breaking, and shrinkage, being the origin of a conductivity loss. Therefore, it has been proposed to use a moderate amount of carbon materials, for example, carbon black, carbon fibers, carbon nanotubes (CNTs), or graphene as the resilient and surface-area-enhancing component for improving the mechanical properties of the electrodes [23, 30–32, 35, 80–89]. Moreover, the presence of carbon in the bulk of ECPs allows a good electronic conduction to be ensured in the electrode when the polymer is in its insulating state.

Carbon fibers can be easily applied as a support for ECPs. For example, a PPy/vapor-grown carbon fiber/AC composite has been produced with a 5–10 nm chemically polymerized PPy layer [28]. High values have been reported exceeding 500 F g^{-1} as measured using the voltammetry method.

A great deal of research has been devoted to nanotubes as a component of ECP composites. Generally, CNTs give an exceptional profit because of their mesoporous, well-conducting network, and high resiliency. CNTs, independently if multiwalled or single walled, serve as excellent support for ECPs because they can adapt well to the volumetric changes of the electrode material during long-term charge/discharge cycling.

Chemical and electrochemical polymerization of the suitable monomer can be considered in order to get ECP/CNT nanocomposites. Even if the electrochemical method gives more homogeneous deposits with better electrochemical activity, the chemical method is concurrent because of price and facile elaboration of porous composites. In addition, the porosity of the chemically elaborated composite is higher, in contrast to the compact electrochemically formed ECP/CNTs. Figure 6.1 shows the scanning electron microscopy (SEM) image of a chemically produced PANI/CNT composite with 80 wt% of PANI [30]. Films from pure PANI or other ECPs are dense, compact, and brittle, whereas the composite material is spongy and resilient, keeping the advantage of the nanotubes’ entangled network, which allows the electrolyte good access to the active polymer. There is no doubt that such

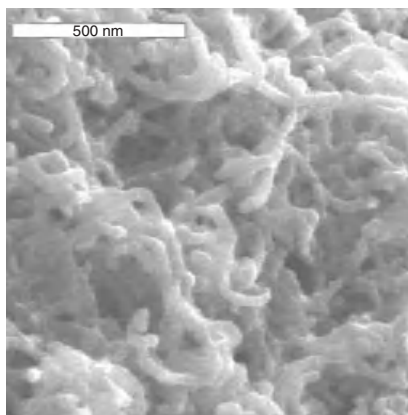


Figure 6.1 Scanning electron micrograph showing the morphology of a polyaniline/CNT composite material which contains 80 wt% of polyaniline [30].

a nanotexture of the composite is optimal for a fast ionic diffusion and migration in the polymer so that the electrode performance can be greatly improved. Obviously, the same useful effect is expected from application of graphenes possessing also a mesoporous and flexible character.

A positive effect of nanotubes and/or graphenes in ECP composites as capacitor electrodes was depicted by many authors [23, 27, 28, 30–35, 80–89]. Coating by a thin layer of conducting polymer has been realized on multiwalled carbon nanotubes (MWCNTs) [23, 27, 28, 30, 31, 33, 35, 81, 82], well-aligned MWCNTs [32, 83–85], single-wall carbon nanotubes (SWCNTs) [80], and graphenes [86–88]. A pretreatment of the nanotubular material before ECP deposition is crucial. When MWCNTs are oxidized, their surface is covered with oxygenated functionalities, which play the role of an anionic dopant for the electrodeposited PPy film [82]. These films are notably less brittle and more adhesive to the electrode than those formed using an aqueous electrolyte as a source of counterion.

The comparison of the redox performance of PPy films on aligned MWCNTs and on flat Ti and Pt surfaces shows a noticeable improvement in the case of the nanotubular composites owing to the high accessible surface area of the CNTs in the form of aligned arrays [85]. The great advantage of a nanotubular array as support for a pseudocapacitive material is schematically demonstrated in Figure 6.2.

Nanotubes play an important role in conduction paths; moreover, the regular mesopores in such arrays allow easy ion diffusion indispensable to the doping process. It is noteworthy to mention that aligned CNTs display one order higher conductivity than entangled ones [90, 91]. Apart from nanotubes, some other forms of carbon have been developed (onions, nanohorns, graphene, etc.), but owing to their exoticism, it seems that only graphene could be a perspective and concurrent material because of its moderately low cost and possibly superior conductivity depending on the preparation procedure. Graphene material has already been used for capacitor application alone or as hybrid material with nanotubes [86–88, 92–94], showing exceptional charge propagation.

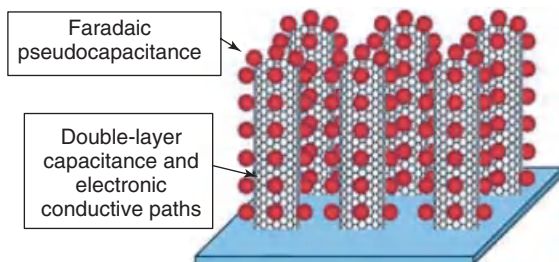


Figure 6.2 Scheme of microtexture and capacitance properties of a nanotube array coated by a pseudocapacitive material [85].

The testing of SWCNTs as support for ECP (PPy) demonstrated that SWCNT/PPy nanocomposites [80] in an alkaline electrolyte have very limited application because PPy degrades quickly in such a medium. Well-documented data in an acidic electrolyte have been presented for the MWCNT/PPy composite obtained electrochemically. The capacitance value reaches about 170 F g^{-1} with a good cyclic performance over 2000 cycles [35]. The high values of capacitance found with the MWCNT/ECP composites are due to the unique property of the entangled nanotubes, which supply a perfect three-dimensional volumetric charge distribution and a well-accessible electrode/electrolyte interface. Comparing the result of the two coating techniques, the nonhomogeneous PPy layer deposited chemically is more porous and less compact than electrochemically deposited; it contains some aggregates of small particles. The chemically deposited polymer displays a more developed surface area; the diffusion of ions proceeds easily, giving a better efficiency for charge storage [30].

The electrochemical behavior of ECP/CNT composites has been studied either in a two- or three-electrode cell. Various capacitance data can be found in the literature depending on the experimental techniques and conditions selected. Obviously, for practical supercapacitor application, only the two-electrode cell investigations give reliable data, whereas the three-electrode cell characteristics are useful to determine the electrochemical behavior of the electrode material. A high performance of the electrode material in the three-electrode system does not mean a superior operation of the real capacitor [95]. As a general rule, the thinner the layer of ECP the higher the capacitance values, but without practical use. The optimal choice of electrode thickness is crucial. Some detailed investigations clearly proved that the capacitance values for the composites with ECP, for example, PANI and PPy, strongly depend on the cell construction [30]. For chemically deposited ECP, extremely high values of specific capacitance can be found using a three-electrode cell – from 250 to 1100 F g^{-1} – depending on the selected potential range, whereas smaller values of 190 F g^{-1} for MWCNT/PPy and 360 F g^{-1} for MWCNT/PANI have been measured in a two-electrode cell. It highlights the fact that only two-electrode cells allow the performance of the materials to be well estimated for practical application in electrochemical capacitors.

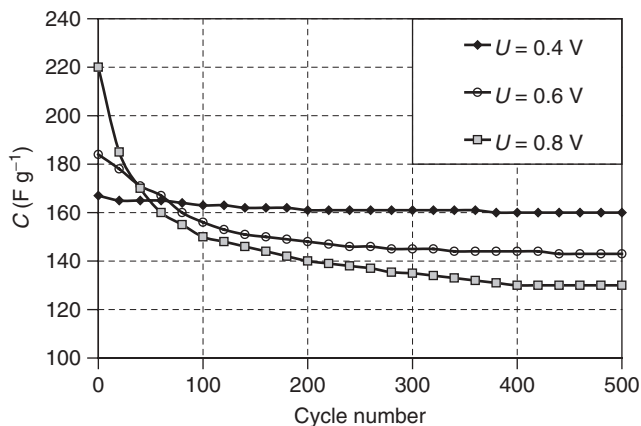


Figure 6.3 Specific capacitance (per mass of one electrode) versus the number of galvanostatic cycles for a symmetric two-electrode system based on a PPy/CNT composite (20 wt% of CNT) in $1 \text{ mol l}^{-1} \text{ H}_2\text{SO}_4$. Influence of the maximum cell voltage [30].

The applied voltage has been found to be the key factor influencing the specific capacitance of supercapacitors based on ECP/CNT nanocomposites [30]. Figure 6.3 shows the variation in specific capacitance by cycling a PPy/CNT-based symmetric capacitor. The cyclability of this capacitor is excellent when the maximum voltage is fixed at 0.4 V. On cycling up to 0.6 V, the capacitance loss is 20% of the initial value after 500 cycles, and it reaches almost 50% at 0.8 V. Hence, using the same ECP/CNT material for both electrodes provides a poor cycling stability of the supercapacitor if the maximum voltage exceeds some limit. Beyond this limit, one electrode reaches a potential at which the ECP is electrochemically unstable, being the reason for the capacity fade [30]. The impedance spectra of a supercapacitor based on PPy/CNT composite electrodes, before galvanostatic cycling and after 500 cycles at a maximum voltage of 0.8 V, show that the resistance drastically increases after cycling. Moreover, the semicircle at high frequency after cycling suggests the parallel existence of a charge-transfer resistance. Hence, irreversible redox transitions are at the origin of the high values of capacitance observed in Figure 6.3 at high voltage (0.8 V) during the first galvanostatic cycles [30]. Generally, the operating voltage of a symmetric capacitor based on ECP electrodes cannot exceed 0.6–0.8 V owing to oxygen evolution at the positive electrode and switching to an insulating state for the negative one [30].

Taking into account that ECP composites only operate reversibly in a narrow range of potential, their optimal application requires an asymmetric configuration, for example, selecting different types of ECPs for positive and negative electrodes or combining them with another electrode material (AC, metal oxide, etc.). Such a concept enables widening of the capacitor voltage, and, in turn, reaching higher energy and power density [43–45, 96–99].

It is noteworthy that the positive effect of MWCNTs in the composite can be more efficiently reached by a regular array of MWCNTs or SWCNTs in the form

of the so-called forest [90]. In this case, superior performance can be obtained owing to better conductivity and availability of the pores at the expense of cost for the final composite. It has been proved that the conductivity of a regular array of CNTs is significantly higher than for the entangled form. Lately, great interest has been devoted to graphene sheets as support for ECP composites. Taking into account the mesoporous character of all types of nanotubes as well as graphenes, a comparable positive effect has been obtained for both materials [86–88]. Simultaneous application of CNTs together with graphenes has been also exploited in the composites, with pseudocapacitive properties showing exceptional behavior [99–101]. Taking into account the economical aspect and the complex production of such composites, they could probably find only limited practical application.

6.3

Metal Oxide/Carbon Composites

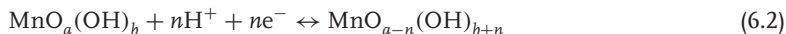
Transition metal oxides are considered attractive materials for supercapacitors. Among them, ruthenium oxide, RuO_2 , seems to be promising because of its high capacitance, good conductivity, excellent electrochemical reversibility, high rate capability, and long cyclability. However, the cost, lack of abundance, and toxic character necessitate seeking alternative materials. Hence, great attention has been devoted to manganese oxide, especially because of its environmentally friendly character [41–52].

Porous hydrous MnO_2 with pore sizes from 5 to 30 nm has been prepared by the organic–aqueous interfacial method [50]. Interestingly, the surface area and pore size distribution could be controlled by adjusting the reaction time and the concentration of surfactant in the aqueous phase. MnO_2 synthesized by this method pointed out a capacitance of 261 F g^{-1} with good cyclic performance but only at low charge/discharge rate, showing that pure manganese oxide cannot be applied for capacitor application.

Nearly pure manganese oxide ($\lambda\text{-MnO}_2$) has also been successfully obtained through lithium removal from the layered structure of spinel-type LiMn_2O_4 with aqueous acid [51]. After stirring the mixture for 3 h, most of the lithium ions are removed from the tetrahedral sites, but the preserved framework of spinel is confirmed by X-ray diffraction measurements. The final product has a very low specific surface area of $5 \text{ m}^2 \text{ g}^{-1}$. High values of capacitance (300 F g^{-1}), but only at moderate discharge current (100 mA g^{-1}), have been measured [51].

The mechanism of lithium removal from LiMn_2O_4 has been studied [102–104] and it was suggested by Feng *et al.* [104] that for the stoichiometric spinel mainly the redox reaction occurs. The charge of extracted lithium ions can be compensated by a change in valence state of the manganese ions. The dissolution of lithium oxide and a surface disproportionation reaction of two trivalent manganese ions take place. Mn^{3+} ions are soluble in the acid solution and Mn^{4+} remains in the lattice forming $\lambda\text{-MnO}_2$. The pseudocapacitance properties of amorphous manganese

oxide ($a\text{-MnO}_2 \cdot n\text{H}_2\text{O}$) are attributed to the redox exchange of protons and/or cations with the electrolyte as follows [42]



where $\text{MnO}_a(\text{OH})_b$ and $\text{MnO}_{a-n}(\text{OH})_{b+n}$ indicate interfacial $a\text{-MnO}_2 \cdot n\text{H}_2\text{O}$ in higher and lower oxidation states, respectively. However, owing to the high resistivity of $a\text{-MnO}_2 \cdot n\text{H}_2\text{O}$, a conducting additive, for example, CNTs, is required for the realization of supercapacitor electrodes. Therefore, $a\text{-MnO}_2$ has been precipitated on CNTs by adding $\text{Mn}(\text{OAc})_2 \cdot 4\text{H}_2\text{O}$ to a KMnO_4 solution that contained predetermined amounts of CNTs [49]. SEM observations confirmed a template role of nanotubes in this composite with an extremely good adhesion of the coating oxide layer. These textural characteristics are favorable at the same time for the easy access of ions to the bulk of the active material, an improvement in conductivity and a good resiliency of the composite electrodes. The values of specific capacitance and cell resistance obtained with symmetric two-electrode capacitors built with $a\text{-MnO}_2/\text{CNT}$ composite electrodes proved a drastic decrease in cell resistance from 2000 to $4 \Omega \text{ cm}^2$ and an increase in specific capacitance from 0.1 to 137 F g^{-1} after adding 15 wt% of nanotubes. It has been also proved experimentally that 15 wt% CNTs is an optimal amount in the composite. On the other hand, the application of CNTs supplied a better effect than the same amount of carbon black, usually used as percolating agent in electrodes.

A great deal of research has been devoted to maximally develop the specific surface area of oxides through a hierarchical structure of the composite, where the oxide component was deposited in various forms such as nanorods, nanoflowers, nanoflakes, and others [85, 105–112].

Manganese oxide, MnO_x , in the flower-like shape deposited on a carbon nanotube array (CNTA) is shown in Figure 6.4. Such a hierarchically porous structure electrodeposited on CNTA displays a specific surface area of $236 \text{ m}^2 \text{ g}^{-1}$. The high density of this composite ($1.5 \text{ cm}^3 \text{ g}^{-1}$) allows a high volumetric capacitance of 305 F cm^{-3} to be reached. Owing to the hierarchical morphology of the composite even at a high current load of 77 A g^{-1} , capacitance of 100 F g^{-1} has been observed.

These investigations show that only carbon/ MnO_2 composites with developed specific surface area and good dispersion of oxide can bring about a profitable solution. Another important issue is to use such composites in their stable potential range taking into account the thermodynamical data from the Pourbaix diagram. Generally, such composites are applied as positive electrodes in various asymmetric configurations with ACs, conducting polymers, or other oxides (see Chapter 8).

Apart from Ru- and Mn-based oxides, the profitable effects of CNTs as backbones for the nanocomposite electrodes have been shown with other pseudocapacitive oxides, for example, nickel, cobalt, vanadium, and iron oxides [84, 113].

In summary, transition metal oxides can supply attractive pseudocapacitive properties. However, the practical exploitation of this phenomenon is still a big challenge. The surface and bulk redox phenomena involve diffusion processes that

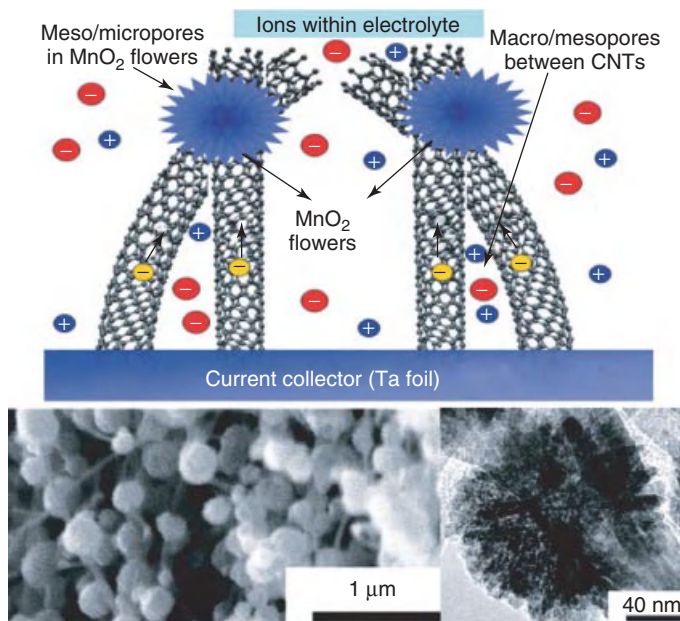


Figure 6.4 Schematic representing the microstructure of the MnO_x/CNTA composite and the way of energy storage in such a composite. The SEM images show a flower-like morphology of MnO_x deposited on the nanostructured carbon [112].

preclude the high rate performance of these materials. In addition, a limited conductivity of most oxides is at the origin of further problems, which can be overcome by using carbon, preferentially nanotubes. Some novel ternary composites based on two pseudocapacitive materials, that is, metal oxides and conducting polymers together with nanotubes, have also been developed [114–116]. The specific capacitance of such a ternary composite, for example, PEDOT/CNTs/ MnO_2 , can reach over 400 F g^{-1} with a good charge/discharge rate, satisfactory charge retention, and cycling stability. This combination gives a synergic effect and takes advantage of both pseudocapacitive materials being at the origin of a new generation of supercapacitor.

6.4

Pseudocapacitive Effect of Heteroatoms Present in the Carbon Network

A great enhancement in capacitance can also be reached by using different types of faradaic reactions originating from the presence of oxygen and nitrogen heteroatoms in the carbon network [53–61, 117–121]. Such pseudocapacitive effects additionally accompany the typical electrical double-layer charging, and they can be connected with quick faradaic reactions of suitable functional groups and also with a local modification of the electronic structure of the doped carbon. In this case,

the change of gap between the conduction and valence bands could manifest in a considerable increase in capacitive ions sorption due to an increase in free electrons [6, 74]. When using carbons enriched in heteroatoms, special attention should be paid to an optimal selection of the doped material depending on the electrode polarity. Some oxygenated functional groups, for example, quinone-hydroquinone redox pair, play a significant role in the electrode of positive polarity [117–119], preferably in an acidic medium, whereas quaternary nitrogen seems to be an optimal functionality for the negative electrode operating in an alkaline medium.

6.4.1

Oxygen-Enriched Carbons

An attractive possibility to enhance the capacitance properties is to introduce oxygenated functionalities in the carbon network [117–119]. Generally, there are two ways of obtaining a highly oxygenated carbon: (i) the selection of a suitable oxygen-rich precursor for carbonization or (ii) the carbon post treatment in a strongly oxidative atmosphere.

Very interesting materials were obtained by one-step carbonization of a seaweed biopolymer, for example, sodium alginate, without any further activation [117]. Although sodium alginate has a structure very close to the structure of cellulose, its thermal behavior is completely different. While the thermal decomposition of cellulose is completed at 400 °C, a noticeable weight loss associated with CO evolution is observed for sodium alginate between 700 and 900 °C. Taking into account this information, a carbon material has been prepared by pyrolysis of sodium alginate at 600 °C under argon flow. The resulting material is slightly microporous ($S_{\text{BET}} = 273 \text{ m}^2 \text{ g}^{-1}$) and it contains a high amount of oxygen (15 at%) retained in the carbon framework. From the deconvolution of the XPS C_{1s} peak, the oxygenated functionalities are phenol and ether groups (C-OR; 7.1 at%), keto and quinone groups (C=O; 3.5 at%), and carboxylic groups (COOR; 3.4 at%). Despite the low Brunauer-Emmet-Teller (BET) specific surface area of this carbon, the capacitance in $1 \text{ mol l}^{-1} \text{ H}_2\text{SO}_4$ medium reaches 200 F g^{-1} , that is, a value comparable to the best ACs available on the market. The contribution of pseudocapacitance is clearly confirmed by the presence of cathodic and anodic humps at around -0.1 and 0.0 V versus $\text{Hg}/\text{Hg}_2\text{SO}_4$, respectively, on the cyclic voltammograms in the three-electrode cell [117]. For ACs, peaks at such positions are traditionally assessed for electrochemical reactions of oxygenated surface functionalities such as the quinone/hydroquinone pair [122]. Pyrone-like structures (combinations of non-neighboring carbonyl and ether oxygen atoms at the edge of the graphene layers) can also effectively accept two protons and two electrons in the same electrochemical potential range as the quinone/hydroquinone pair [123]. Consequently, in the carbon obtained from sodium alginate, the high value of capacitance is related to the charge-transfer reactions on the quinone, phenol, and ether groups [117]. Moreover, this weakly porous material has a high density and a high electrical conductivity, which allow a volumetric capacitance higher than any AC to be exhibited, and the capacitors to be charged at high regime without

requiring any conductivity additive in the electrodes. Further research has been performed on the carbon from a pure seaweed precursor [118]. Special types of seaweeds, after carbonization, showed interesting capacitance properties. Some additional performance improvement was obtained by incorporating CNTs in the seaweeds before the thermal treatment [124].

6.4.2

Nitrogen-Enriched Carbons

Nitrogen is the next heteroatom considered as the main dopant in the carbon network. A part of N can be substituted to carbon (“lattice nitrogen”), and the other can be included in the form of functional groups (“chemical nitrogen”) at the periphery of polyaromatic structural units, as shown in Figure 6.5.

Nitrogen-enriched carbons can be obtained by ammoxidation of nanoporous carbons [121] or by carbonization of nitrogen-rich polymers followed by steam activation [53, 54]. However, since one of the reactions involved in these procedures occurs in oxidative conditions, oxygen is also incorporated together with nitrogen in the carbon network. Consequently, it is difficult to assess completely the measured values of capacitance to the unique contribution of the nitrogenated functionality. Nevertheless, a correlation has been found between capacitance and the nitrogen content for a unique series of nitrogen-enriched carbons prepared by carbonization of polyacrylonitrile (PAN) or pitch/PAN and pitch/polyvinylpyridine blends, followed by steam activation (Figure 6.6). These samples with comparable porous characteristics ($S_{\text{BET}} \approx 800 \text{ m}^2 \text{ g}^{-1}$) showed a capacitance in aqueous medium proportional to the N content, whereas it was almost constant in an organic electrolyte [7, 53]. Such dependence proves the important role of protons for pseudocapacitive effects.

The extrapolation of the curves to $\text{N}\% = 0$ in an aqueous electrolyte gives a capacitance of $75\text{--}100 \text{ F g}^{-1}$. Taking into account the average BET specific surface area of $800 \text{ m}^2 \text{ g}^{-1}$ for all materials, it gives a surface capacitance of $9.4\text{--}12.5 \mu\text{F cm}^{-2}$, in the range typically found when only the double layer is charged [5, 6]. The enhancement in capacitance with the nitrogen content in

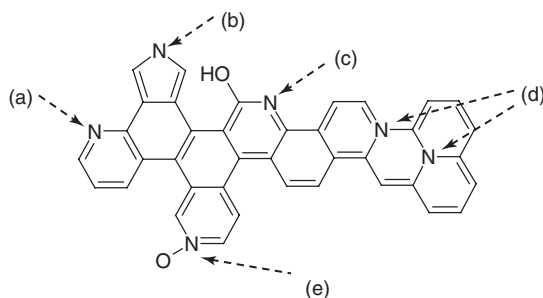


Figure 6.5 Nitrogenated functional groups in the carbon network (a) pyridinic (N-6); (b) pyrrolic; (c) pyridonic (N-5); (d) quaternary (N-Q); and (e) oxidized nitrogen (N-X).

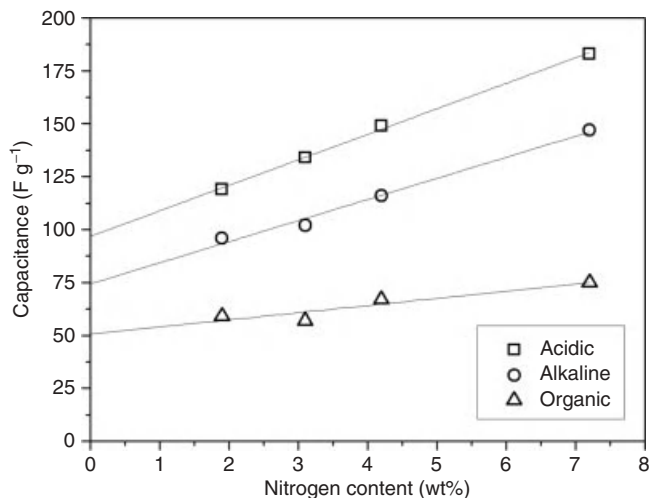


Figure 6.6 Capacitance values versus nitrogen content of N-enriched carbons in 1 mol l⁻¹ H₂SO₄, 6 mol l⁻¹ KOH, 1 mol l⁻¹ TEABF₄ in acetonitrile [53].

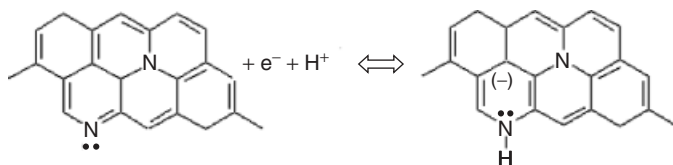


Figure 6.7 Scheme of a possible redox reaction with pyridinic nitrogen.

H₂SO₄ medium is interpreted by pseudo-faradaic reactions due to the nitrogenated functionality, such as those illustrated in Eqs. (6.3) and (6.4) [53, 61] and by the scheme in Figure 6.7:



where C* stands for the carbon network.

Self-standing C/C composite electrodes presenting pseudocapacitive properties and high electrical conductivity have been obtained by one-step pyrolysis of CNT/PAN blends at 700 °C [125]. It is important to underline that the composite electrodes have been prepared without the activation process. The specific surface area of PAN carbonized at 700 °C is negligible ($S_{\text{BET}} = 6 \text{ m}^2 \text{ g}^{-1}$), whereas the C/C pellets formed by pyrolysis of a CNT/PAN (30/70 wt%) blend at 700 °C have a more developed porosity ($S_{\text{BET}} = 157 \text{ m}^2 \text{ g}^{-1}$, $V_{\text{DR}} = 0.067 \text{ cm}^3 \text{ g}^{-1}$, $V_{\text{meso}} = 0.117 \text{ cm}^3 \text{ g}^{-1}$). The appearance of mesopores in the C/C composite is due to the templating effect of CNTs. It has been suggested that during the thermal decomposition of PAN, the layer that adheres to the nanotubes shrinks, leaving

pores that reflect directly the nanotexture of the pristine nanotubular framework [125]. The nitrogen content measured on this composite by XPS is 7.3 at%.

Two electrode cells built from such C/C composite pellets in $1 \text{ mol l}^{-1} \text{ H}_2\text{SO}_4$ show boxlike voltammograms up to high scan rates, for example, 100 mV s^{-1} , that indicate a quick dynamics of charge propagation with this kind of composite. The capacitance determined for the C/C composite obtained from the CNT/PAN (30/70 wt%) blend at 700°C is in the order of 100 F g^{-1} , whereas under the same conditions the capacitance value is 18 F g^{-1} for pristine CNTs and negligible for carbonized PAN. As the C/C composite has a BET specific surface area ($157 \text{ m}^2 \text{ g}^{-1}$) lower than the pristine nanotubes ($220 \text{ m}^2 \text{ g}^{-1}$), the main contribution to capacitance is due to pseudo-faradaic charge-transfer reactions. According to the XPS data, it may be assumed that pyridinic nitrogen, which is the dominant contribution, may play a prominent role in the pseudo-faradaic properties. The next noticeable fact, which is attributable to the presence of CNTs, is the low value of equivalent series resistance R_s measured by impedance spectroscopy, that is, below $0.7 \Omega \text{ cm}^2$. The capacitance dependence versus current load shown in Figure 6.8 confirms that the C/C composite can be charged/discharged in $1 \text{ mol l}^{-1} \text{ H}_2\text{SO}_4$ at an extremely high regime. The capacitance drop at low values of current is typical for a dominant charge-transfer process. The striking fact is that, after this drop, the capacitance remains quite stable, whereas typical pseudocapacitive materials without a CNT percolator usually demonstrate a continuous drop on the whole range of current load.

The remarkable capacitive behavior of this kind of composite is due to a synergy between CNTs and the nitrogenated functionality of carbonized PAN. Mesopores are created during the pyrolysis of PAN through a templating effect of the

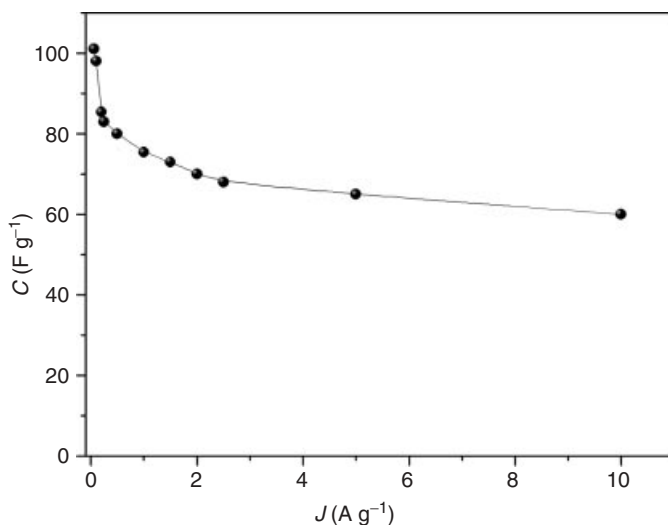


Figure 6.8 Capacitance versus current load for the C/C composite obtained by one-step pyrolysis of a CNT/PAN (30/70 wt%) blend at 700°C [125].

nanotube framework, and the presence of nanotubes as three-dimensional support enhances considerably the electrical conductivity of the composites, allowing high charge/discharge rates to be reached while involving a pseudocapacitive contribution. Obviously, such a good percolation effect could not be reached with the traditional carbon black generally used for the manufacture of electrodes.

The beneficial effect of nitrogen in composites with an incorporated nanotubular backbone has been also clearly demonstrated [61] using melamine as the nitrogen-rich (45 wt%) carbon precursor. The carbon composites have been obtained by polymerization of melamine with formaldehyde (without any catalyst) in the presence of a controlled amount of MWCNTs. The polymerized blend was carbonized at 750 °C for 1 h under nitrogen flow. The final carbonization products were named M + F (composite from melamine and formaldehyde without CNTs), Nt + M + F (composite with CNTs, melamine and formaldehyde), Nt + 2M + F (a similar composite with twofold melamine proportion in the blend), Nt + 3M + F (threefold melamine proportion). The results of elemental analysis showed that the nitrogen content in the final product varies from 7.4 to 21.7 wt%. The oxygen content was calculated by the difference and its amount is comparable in all the samples varying from 5.9 to 7.8 wt%.

The nitrogen adsorption/desorption isotherms (Figure 6.9) show that the carbon materials are typically mesoporous (apart from M + F, that is, without nanotubes), and the amount of micropores is very moderate. The BET specific surface area ranges from 329 to 403 m² g⁻¹, being the most developed for the Nt + 3M + F composite. The porosity characteristics of all the composites are illustrated in Table 6.1 and correlated with their capacitance properties.

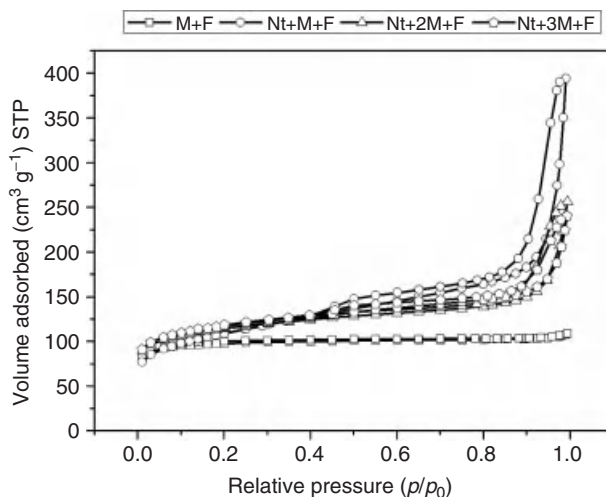


Figure 6.9 Nitrogen adsorption/desorption isotherms at 77 K for the nitrogenated composites [61].

Table 6.1 Physicochemical and electrochemical characteristics of the nitrogen-rich nanocomposites. C stands for the capacitance estimated at 5 A g⁻¹ current load, that is, 50 mA cm⁻². Two-electrode cell in 1 mol l⁻¹ H₂SO₄.

Sample	S _{BET} (m ² g ⁻¹)	V _{total} (cm ³ g ⁻¹)	V _{micro} (cm ³ g ⁻¹)	C (F g ⁻¹)	Nitrogen (wt%)
M + F	329	0.162	0.152	4	21.7
Nt + 3M + F	403	0.291	0.174	100	14.0
Nt + 2M + F	393	0.321	0.167	126	11.7
Nt + M + F	381	0.424	0.156	83	7.4

The voltammetry characteristics at a potential scan rate of 10 mV s⁻¹ for all the composites in 1 mol l⁻¹ H₂SO₄ illustrate a mirrorlike behavior typical for an ideal capacitor. Only the M + F composite without nanotubes presents definitively worse characteristics, most probably because of a higher resistance. The best value of capacitance determined from the galvanostatic discharge is observed for the Nt + 2M + F composite (126 F g⁻¹ at 5 A g⁻¹ current load). Surely, the nitrogen presence has a profitable effect on the capacitance values by modifying the electronic properties as well as wettability. However, an excess of nitrogen (presumably over 15%) definitively aggravates the conducting properties, and, in turn, the capacitance characteristics and supercapacitor cyclability. Pyridinic and quaternary groups seem to play the most important role in the electrochemical behavior; however, their participation in capacitance is different depending not only on the electrode polarity but also on the type of electrolyte.

Figure 6.10 shows that the ability for charge accumulation diminishes with the increase in current load, but the Nt + 2M + F sample is still able to supply a capacitance of 60 F g⁻¹ at an extremely high current density of 50 A g⁻¹. The high charge propagation of this composite should be explained by an exceptional electronic transport in CNTs, which are still preserved after the carbonization process.

Apart from the acidic electrolyte, attention has been also devoted to 6 mol l⁻¹ KOH, 1 mol l⁻¹ Na₂SO₄, and the organic electrolyte – 1 mol l⁻¹ tetraethylammonium tetrafluoroborate (TEABF₄) in acetonitrile (ACN). Figure 6.11 shows the voltammetry characteristics of the Nt + M + F composite at 10 mV s⁻¹ in these electrolytic solutions. The best performance (101 F g⁻¹) is observed in an acidic solution, slightly exceeding the alkaline one (92 F g⁻¹). As expected, in an organic solution and in neutral aqueous Na₂SO₄, the capacitance values are relatively low because of the absence of pseudo-faradaic reactions in these media; only the EDL capacitance contributes. The low specific surface area of the electrode material (393 m² g⁻¹) explains the low values of capacitance (35 and 26 F g⁻¹ in organic and neutral aqueous media, respectively).

The trials have been undertaken to correlate the N content in carbons with the electron density states from molecular quantum calculation. The energy

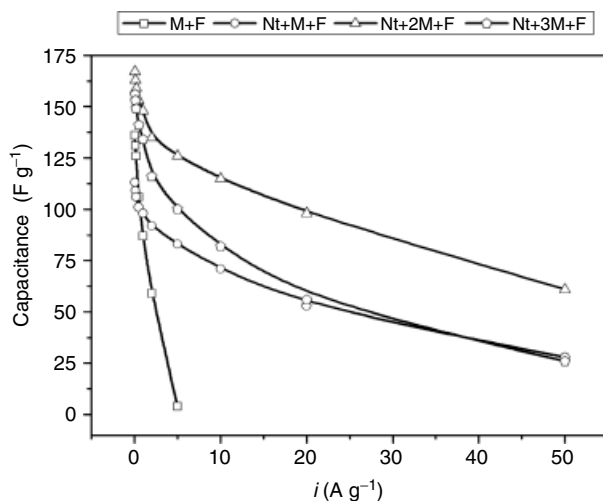


Figure 6.10 Capacitance versus current load for all the composites investigated in acidic electrolytic solution. Two-electrode cell [74].

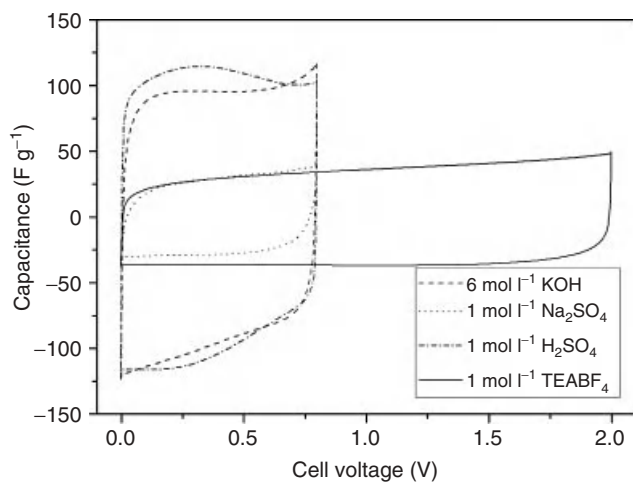


Figure 6.11 Voltammetry characteristics at 10 mV s^{-1} for the Nt + M + F nitrogen-enriched composite using various aqueous electrolytic solutions and organic medium [74].

gap between conduction and valence bands affected by nitrogen content was qualitatively correlated with the conductivity and capacitance properties of the composite [74].

Some authors have focused on differently prepared nitrogenated carbons using N-rich precursors. With melamine polymerized in mica [58] followed by ammonia treatment [60], the highest capacitance values (280 F ml^{-1}) have been obtained in KOH medium, whereas values of 152 F ml^{-1} were measured in sulfuric acid. A very high capacitance (340 F g^{-1}) has been reached using templated carbons from

acrylonitrile pyrolysis in NaY zeolite [120]. This high value results from the synergy between the highly developed surface area of the material and the pseudo-faradaic reactions related to the presence of the nitrogenated functionalities. Another approach is based on the nitrogen plasma treatment of graphene; the authors reported high capacitance values on the order of 280 F g^{-1} (four times higher than that for the pristine graphene) [57].

6.5

Nanoporous Carbons with Electrosorbed Hydrogen

Pseudocapacitance properties can also be observed with nanoporous carbons through the reversible electrosorption of hydrogen in aqueous medium. In that case, during the negative polarization of an electrode, water is reduced and nascent hydrogen is sorbed in the material; the sorbed hydrogen is desorbed by anodic oxidation [62–74].

The results proved that the hydrogen sorption/desorption process in a carbon electrode can proceed at high current loads, leading to an interesting application for the negative electrode of electrochemical capacitors. It is noteworthy that the pure double-layer charging takes place in a short timescale of micro- to milliseconds, while hydrogen pseudocapacitance would need a slightly longer time because of the diffusion limitation typical of faradaic reactions.

Electrosorption of hydrogen can be performed on ACs in the form of cloth or powder. The most important parameters of the carbon material for H storage are ultramicroporosity, mesopore fraction, surface functionality, conductivity, number of defects, and so on. The investigations performed on carbons with a controlled hierarchical micro/mesoporosity [65, 67, 68, 71, 72] have shown that hydrogen capacity can be definitely increased.

Figure 6.12 presents voltammetry curves that have been obtained with a micro-porous activated carbon cloth (ACC) electrode in $6 \text{ mol l}^{-1} \text{ KOH}$ [126]. The various loops have been recorded with a stepwise shift of negative potential cutoff. For electrode potentials higher than the thermodynamic value corresponding to water decomposition (theoretically -0.924 V versus Hg/HgO, in $6 \text{ mol l}^{-1} \text{ KOH}$), the boxlike shape of the curves confirms the reversible charging of the electrical double layer. The increase in negative current, which is observed from the third loop, that is, when the potential cutoff is lower than the equilibrium potential, is proof that the faradaic water decomposition starts to gradually take place according to Eq. (6.5):



The nascent hydrogen formed in Eq. (6.5) is partly fixed on the nanopore's surface as in Eq. (6.6):



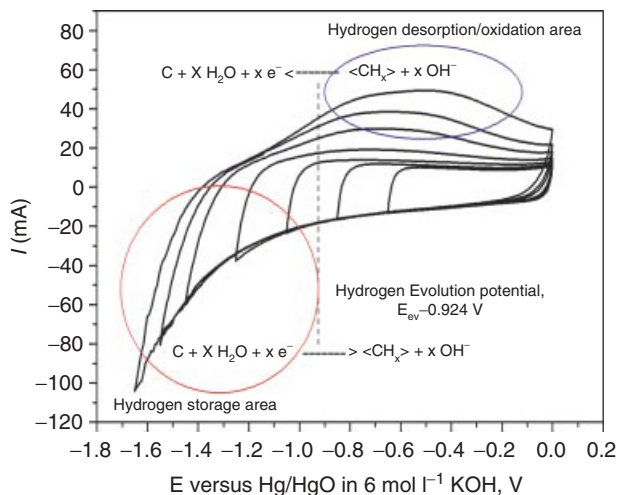


Figure 6.12 Voltammetry cycling of a carbon electrode (AC) in $6 \text{ mol l}^{-1} \text{ KOH}$ at 5 mV s^{-1} scan rate with a gradual shift to negative values of potential [126].

whereas another part may recombine to form H_2 molecules. Equation (6.7) summarizes the overall process:



where $\langle \text{C} \rangle$ and $\langle \text{CH}_x \rangle$ stand for the nanotextured carbon substrate and for hydrogen inserted into this substrate, respectively. As a consequence, during the anodic scan, the positive current recorded above the equilibrium potential increases, being related with the electrooxidation of hydrogen trapped in AC. During the oxidation step, Eq. (6.7) runs in the opposite direction.

When the negative potential cutoff decreases, the positive current due to hydrogen oxidation increases and the corresponding hump shifts toward more positive potential values (Figure 6.12). The high overpotential required for hydrogen oxidation reveals either strong hydrogen trapping in the carbon material or important diffusion limitations.

Taking into account that the electrochemical hydrogen trapping takes place essentially in ultramicropores (i.e., pores smaller than $0.7\text{--}0.8 \text{ nm}$) [62–66], and that tortuous voids may slow down the desorption process from these pores, one easily understands the improved tendency to reversibility at low scan rate.

A careful analysis of the voltammetry curves at various scan rates supplies information on the reversibility but also assumption of weak $\langle \text{C} \rangle \text{H}$ bonding. Weak chemical bonding of hydrogen has been confirmed by thermoprogrammed desorption (TPD) analyses on AC samples obtained after a galvanostatic charge during 15 min or 12 h at -500 mA g^{-1} in $6 \text{ mol l}^{-1} \text{ KOH}$. In order to avoid a discarded hydrogen desorption, the samples were not rinsed with water after the electrochemical charging. As a consequence, they both present a peak above 400°C ,

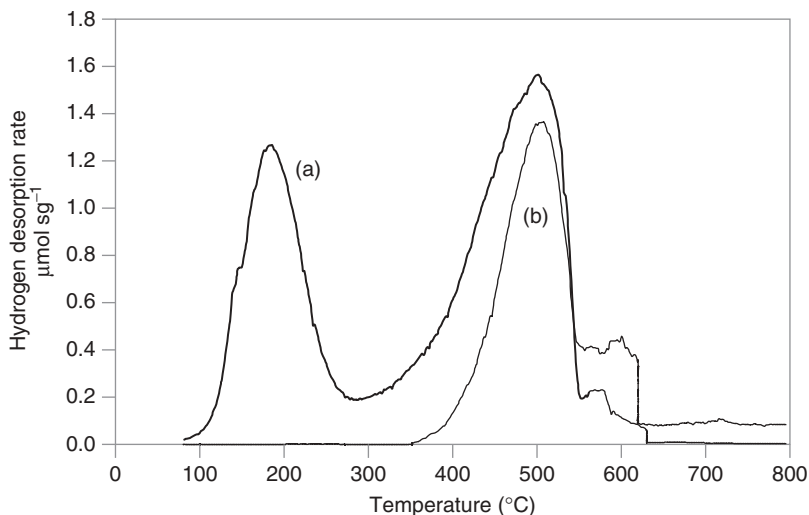


Figure 6.13 TPD analysis of hydrogen evolved from a microporous activated carbon cloth (ACC) charged at -500 mA g^{-1} in 6 mol l^{-1} KOH during (a) 12 h and (b) 15 min. Adapted from Ref. [66].

which is due to the reaction of excess KOH with carbon, according to Eq. (6.8):



It is the only peak observed for the sample charged 15 min at -500 mA g^{-1} . Within this limited time, the Nernst potential for water reduction is not reached, and only the electrical double layer is charged. By contrast, when charging is prolonged during 12 h, an additional peak appears in the TPD curve around 200°C (Figure 6.13). This peak location confirms the weak chemical bonding of hydrogen with the carbon surface. Hence, it is likely that the major fraction of nascent hydrogen produced during water electroreduction reacts with the active sites of carbon – being energetically trapped – instead of being purely physisorbed on the surface.

As a consequence of the chemical type of hydrogen bonding with the carbon surface, it was shown that the electrochemical properties depend on temperature. The voltammetry curves (Figure 6.14) on the ACC recorded at different temperatures from 20 to 60°C show that the amplitude of the reduction and oxidation peak increases with temperature (i.e., the amount of reversibly sorbed hydrogen increases), while the polarization between the two peaks decreases.

Similar information is given by the galvanostatic charge/discharge curves (Figure 6.15). As the cell temperature increases, the value of the potential reached during the charging step is less negative because of a reduced polarization by enhancement of the ionic conductivity of the solution. When temperature is raised to 60°C , one can see a better defined discharge plateau and a shift of oxidation potential from about -0.5 to -0.7 V versus NHE (see the shift of the derivative curve maximum – inset in Figure 6.15). This shift indicates that the temperature increase

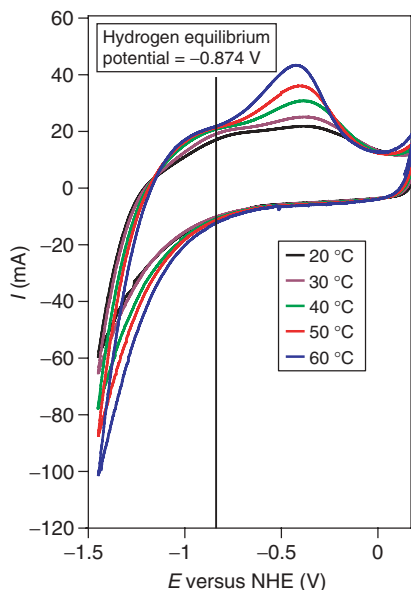


Figure 6.14 Cyclic voltammetry on a nanoporous carbon cloth (ACC) at different temperatures in 6 mol l^{-1} KOH. Adapted from Ref. [66].

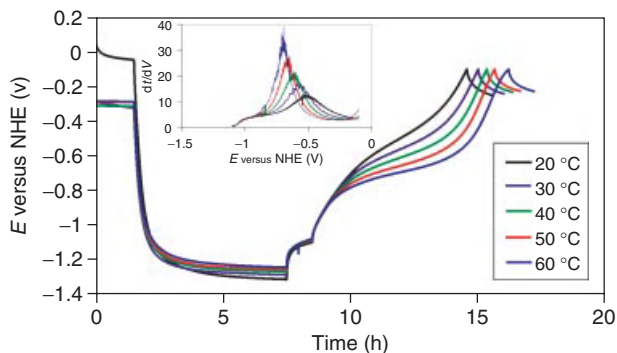


Figure 6.15 Effect of temperature on the galvanostatic charge/discharge characteristics of a microporous activated carbon cloth (ACC) in 6 mol l^{-1} KOH. Charging current -150 mA g^{-1} ; discharging current

$+50 \text{ mA g}^{-1}$. Inset: derivative of the galvanostatic oxidation curves showing a shift of maximum from -0.5 to -0.7 V versus NHE as temperature increases from 20 to $60 \text{ }^\circ\text{C}$. From Ref. [66].

reduces the kinetic barrier and facilitates the hydrogen extraction (oxidation) from the micropores. However, the most interesting observation from the curves is a noticeable increase in the amount of reversibly stored hydrogen, confirming that hydrogen electro-sorption in nanoporous carbons is activated by temperature [66].

As hydrogen is stabilized in the carbon substrate by weak chemical bonds, the self-discharge is not important [66, 68]. On the other hand, the voltage (and

consequently the energy density) of a cell using AC as the negative electrode in aqueous solution will be enhanced by operating at higher values of temperature. Therefore, hydrogen electrosorption on nanoporous carbon electrodes in aqueous medium is very interesting for the construction of asymmetric capacitors, which associate a negative carbon electrode storing hydrogen and a positive electrode in the form of a carbon or a composite based on MnO_2 or a conducting polymer [43–45]. Such electrochemical capacitors in the aqueous medium can operate with a good cycle life at voltage values as high as 1.6 V (Chapter 8). Recently, it has been demonstrated that even better performance (1.6–2.0 V) can be reached with symmetrical AC/AC capacitors using alkali sulfates as electrolyte [127–129]. Taking into account the high conductivity of the positive carbon electrode compared to any MnO_2 -based composite, this new concept represents a great advantage for high-power applications.

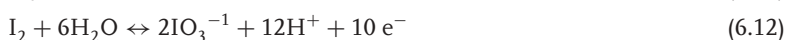
6.6

Electrolytic Solutions – a Source of Faradaic Reactions

The enhancement of capacitance by pseudocapacitive properties can be also realized by the application of redox-active electrolytes instead of using the electrode material as a source of redox reactions. In this case, the electrolyte is the main source of capacitance because of various oxidation states of the electrolytic species, for example, iodine, bromine, and hydroxyquinones [75–79, 130]. Taking into account that the faradaic reactions proceed at the electrode/electrolyte interface, the carbon must be suitably selected.

An exceptional electrochemical behavior of the carbon/iodide interface has been demonstrated and successfully used in supercapacitor application [75, 76]. This efficient charge storage is based on the specific sorption of iodide ions as well as the stable reversible redox reactions connected with various possible oxidation states of iodine from -1 to $+5$. The iodide ions play a useful dual role, that is, electrolytic solution with a good ionic conductivity as well as a source of faradaic reactions, that is, pseudocapacitive effects. It is important to note that the domain of iodide ions in the Pourbaix diagram is moderately stable in the range of water stability with a possibility of various oxidation states depending on potential and pH.

The 1 mol l^{-1} KI solution used in the experiments is neutral, with a pH close to 7. In such a case, the following reactions, especially from Eqs. (6.9) to (6.11), could be considered as a source of pseudo-faradaic effects.



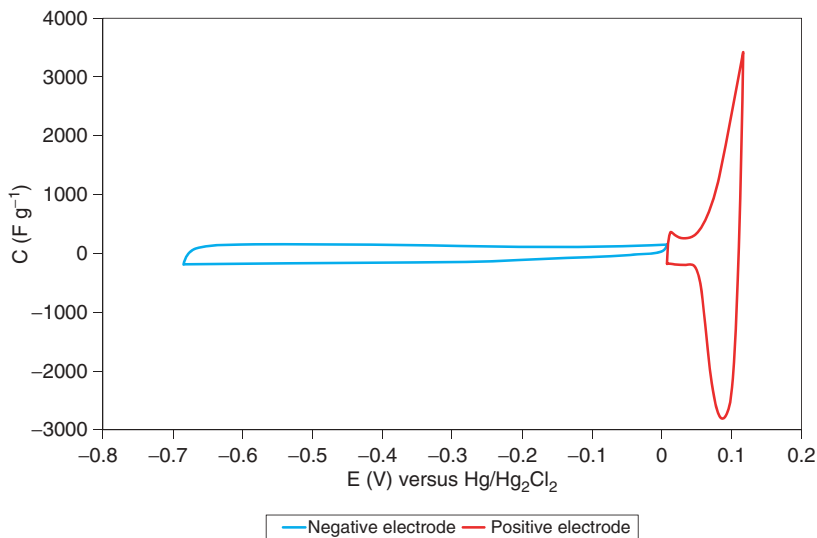


Figure 6.16 Voltammetry curve at 5 mV s^{-1} scan rate for an activated carbon AC1 in 1 mol l^{-1} KI solution. Potentials of both electrodes are measured separately versus the saturated calomel electrode [75].

Iodine, even though it exists as a solid and/or volatile element, easily dissolves in iodide solution forming the I_3^- complex. The potential range measured experimentally in the capacitor by voltammetry and galvanostatic techniques (Figures 6.16 and 6.17) matches well with the thermodynamic values of the reactions presented earlier [75]. From both characteristics, it is seen that this striking effect of iodide ions is observed for the positive electrode operating in a narrow range of potential and giving extremely high capacitance values exceeding 1840 F g^{-1} (estimated from the integrated area of the voltammetry curve). As opposed to typical pseudocapacitive effects from electrode materials, for example, oxides, which are often characterized by some diffusion limitations and observed only at moderate regimes, this two-electrode system can be loaded up to 50 A g^{-1} supplying still 125 F g^{-1} . For the first time, such an innovative electrochemical concept could be successfully used for supercapacitor performance.

Obviously, a long cyclic durability is a crucial problem for supercapacitor application. Extraordinary capacitance values of the carbon/iodide interface have been proved during long-term cycling at a high current density of 1000 mA g^{-1} . Amazingly, the cyclability is greatly affected by the type of metallic collector used for cycling tests. In the case of gold collectors, a moderate decrease in capacitance (less than 20%) after 10 000 cycles was observed, whereas in the case of stainless steel, some anomalous increase occurs from 235 F g^{-1} during the first cycles up to 300 F g^{-1} after 10 000 cycles. As the stainless steel current collectors are not corroded, this capacitance increase cannot be explained by a development of the surface area of the electrode/electrolyte interface. In fact, a mutual shift of the

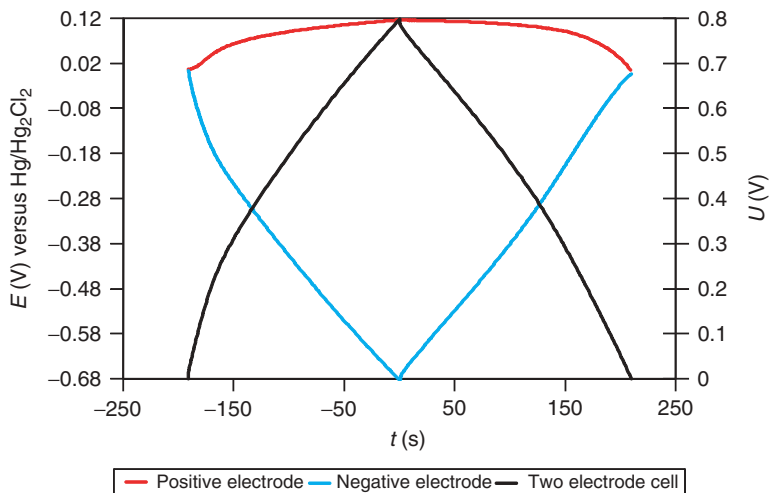


Figure 6.17 Galvanostatic charge/discharge of a capacitor built from an activated carbon AC1 in 1 mol l^{-1} KI solution. Current load of 500 mA g^{-1} . The voltage of the two-electrode cell (black) as well as the potential of the positive (red) and negative (blue) electrodes versus SCE are shown separately [75].

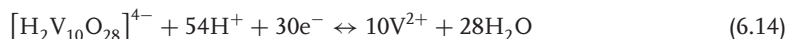
operating potentials has been proved experimentally for both electrodes (through additional potential measurements after cycling) and might explain this profitable effect. The negative electrode with lower capacitance values operates in a more narrow range, while the operating potential range of the positive electrode, with extremely high capacitance values, is extended to the negative direction. This anomalous phenomenon needs some further clarification; for instance, a gradual oxidation of the carbon material by iodine during long-term cycling could be also considered.

The application of this novel carbon/iodide electrochemical system is original and represents a significant breakthrough in supercapacitor development. This bifunctional iodide electrolyte, which ensures ionic conductivity and supplies pseudocapacitive effects, has great advantages because it is inert, neutral, and environmentally friendly. It gives an additional benefit concerning the choice of the current collectors. Different metallic foils can be considered for this target but obviously stainless steel is the most suitable candidate. However, it is necessary to stress that this system is not yet fully optimized. Indeed, even though striking values – 10 times exceeding typical capacitance values – are observed for the positive electrode, unfortunately the total capacitance of the electrochemical capacitor is the outcome of the two electrodes, determined by the electrode revealing the lowest capacitance, i.e., the negative one.

Apart from iodides, interesting properties have been obtained when bromides are applied as electrolyte [77], serving also as a source for pseudocapacitive phenomena. However, it is worth pointing out that among all halides, the iodide ions are the most environmentally friendly. In addition, because of its rich variety of oxidation

states, iodine is probably the unique halide able to demonstrate the most exceptional performance.

In order to circumvent the disadvantage of low capacitance of the negative electrode in the halide-based systems, a new concept using two different electrolytes acting as conjugated redox couples has been developed [130]. Basically, the halide electrolyte is kept for the positive electrode and another redox pair operates on the negative side. Owing to the excellent redox activity of vanadium-based aqueous electrolytes, these species were selected as tentative candidates for pseudocapacitance source at the negative electrode. The wide variety of electrochemical reactions with several transferred electrons are presented in the following equations.



In the literature, a high activity of vanadium-based species is reported mainly in acidic solutions, which severely restrict their commercialization because of the prohibitive price of corrosion-resistant current collectors (such as gold or platinum). For this reason, neutral (pH 7) aqueous electrolytes were applied; according to the pragmatic rule, “supercapacitor will see the growth only when their cost falls.” Drawing on the experience of pure iodide-based electrolyte and considerable redox activity of vanadium-based systems, 1 mol l⁻¹ potassium iodide (KI) has been applied as electrolyte for the positive electrode and 1 mol l⁻¹ vanadyl sulfate (VOSO₄) solution for the negative one (Figures 6.18–6.20). Both electrolytes act

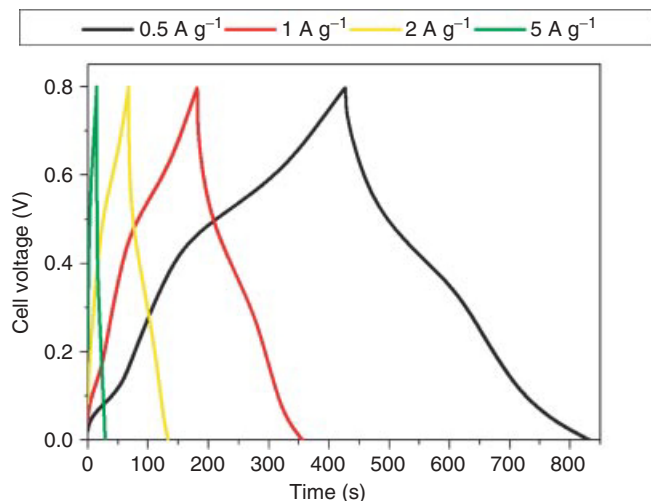


Figure 6.18 Various constant current charging/discharging curves for a capacitor operating in iodide/vanadium conjugated redox couples as electrolyte solutions [130].

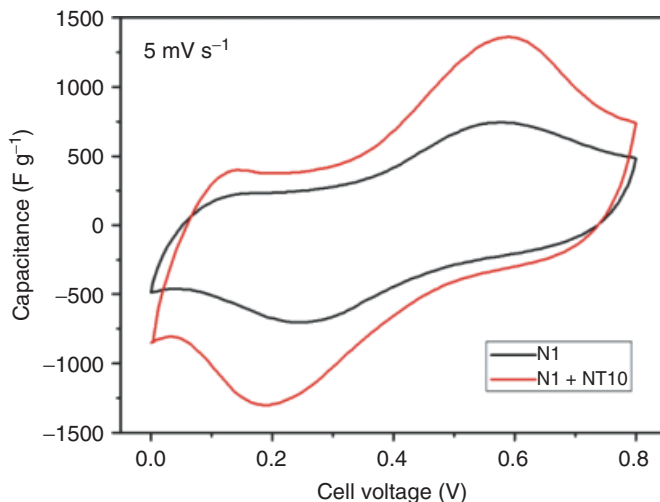


Figure 6.19 Beneficial effect of nanotubes on the cyclic voltammety performance of cells constituted of two redox couples KI/VOSO₄ aqueous solutions (1 mol l⁻¹). 5 mV s⁻¹ scan rate [131].

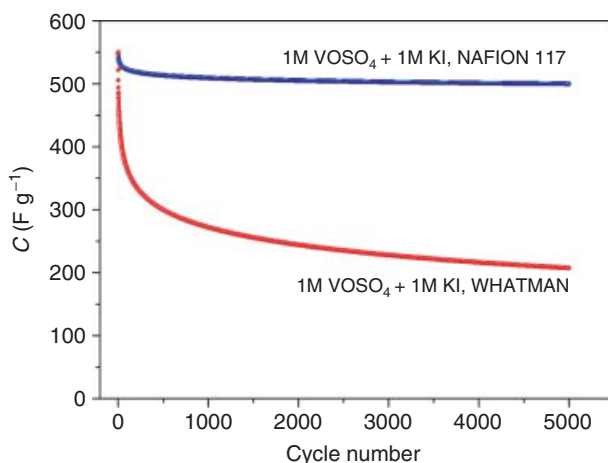


Figure 6.20 Influence of the separating membrane on the cyclability of supercapacitors based on the two redox couples – 1 M KI and 1 M VOSO₄ – at a current load of 1 A/g and 1 V maximum operating voltage [131].

as conjugated redox couples with AC electrodes of BET specific surface area about 2520 m² g⁻¹. In some cases, because of their exceptional mesoporosity and conductivity, nanotubes (10 wt%, NT10) have been added to the AC to improve the electrodes performance (Figure 6.19). The two electrodes of the capacitor are soaked in the appropriate electrolytes and separated by a glass fiber paper and a Nafion[®] 117 membrane, to avoid mixing of the electroactive electrolytic species.

Comparable results were obtained by three different electrochemical techniques such as constant current charging/discharging (Figure 6.18), cyclic voltammetry (Figure 6.19) and electrochemical impedance spectroscopy (EIS). The irregular shape of the galvanostatic charge/discharge dependence and well-defined humps on the voltammetry curves, especially at slow scan rates, are the best proof of pseudocapacitive phenomena. The useful effect of nanotubes (10%) for enhancing capacitance is well visible on the voltammetry characteristics in Figure 6.19; it underlines the crucial importance of mesopores in the development of the interface between the redox species for both polarities of the system.

The difference in cycling performance depending on the kind of separator (Whatman paper or Nafion® 117 membrane) is shown in Figure 6.20. Superior capacitance values as well as cycling stability is observed in the case of the proton exchange membrane, which allows only the ionic transport of protons but protects from a mutual mixing of both redox couple solutions (Figure 6.20).

In summary, great pseudocapacitance values (from 300 to 1000 F g⁻¹ depending on the current load) are obtained using ACs with two different electrolytic solutions separated by a Nafion® membrane. The selected redox-active electrolytes, that is, 1 mol l⁻¹ potassium iodide (KI) and 1 mol l⁻¹ vanadyl sulfate (VOSO₄) aqueous solutions, allow reaching a high energy density of the system, about 20 Wh kg⁻¹, with a maximum power density of 2 kW kg⁻¹ (calculated on the basis of the total mass of both electrodes).

A few papers describe also the profitable effect of hydroquinone dissolved in the electrolytic solution, being the source of pseudocapacitance effects [78, 79]. The application of such a redox-active couple presents a new attractive trend in capacitor development to increase the energy of this device.

6.7

Conclusions – Profits and Disadvantages of Pseudocapacitive Effects

Nanostructured carbons with a developed surface area are fundamental materials for enlarging the electrode/electrolyte interface in supercapacitors. However, the capacitance of electrodes can be noticeably enhanced by an additional contribution related to quick faradaic reactions, referred to as *pseudocapacitance*. Pseudocapacitive materials such as conducting polymers (ECPs), transition metal oxides, nitrogenated or oxygenated functionalities incorporated in the carbon framework, and electrosorbed hydrogen have been briefly described in this chapter. Apart from pseudocapacitive electrode materials, another source of pseudocapacitance originated from aqueous electrolytic solutions (based on halides, dihydroxybenzenes, vanadium species) has also been presented.

It has been demonstrated that the electrochemical performance of conducting polymers and/or transition metal oxides can be improved by the realization of composites with a carbon material, preferably in the nanostructured form, for example, MWCNTs, SWCNTs, or graphenes, acting as a perfect support for such pseudocapacitive materials. Owing to the synergy between the high electronic

conductivity of the graphitic type layers and the fast diffusion of ions to the bulk of the active material through mesopores, the electrical series resistance of the capacitor drastically diminishes. In the case of conducting polymer (ECP) composites, the potential range in which the polymer operates in the doped state is essentially quite narrow; hence, for an extension of the operating voltage range, an asymmetric configuration with two different ECPs is more profitable than a symmetric one.

Taking into account the mechanism involving the surface as well as the bulk of metal oxides, the diffusion of protons accompanying the charge transfer must be ensured by the presence of mesopores. However, even if high capacitance values can be reached from thin oxide layers, a significant aggravation of performance is observed for thicker layers used in practice. Taking into account that, apart from ruthenium oxide, other oxides present a low conductivity, well-distributed carbon in the composite is indispensable. In both composites, that is, ECPs and oxides, using highly resilient nanotubes as an electrode component allows the capacitors to be charged/discharged over a large number of cycles without mechanical degradation of the active phase, especially when the suitable combination of materials and range of operating voltage are selected.

The next group of pseudocapacitive materials are carbons enriched in heteroatoms (nitrogen, oxygen) able to give faradaic reactions through particular functionalities such as the quinone/hydroquinone pair. The exceptional conducting and mechanical properties of MWCNTs again play a useful role. The advantageous effect of nitrogen functionalities (pyridinic, quaternary groups) is connected both with faradaic reactions and a significant modification of the electronic density of states. In addition, a suitable amount of nitrogen without any conductivity aggravation is not only able to enhance the capacitance but also to improve the wettability of electrodes in aqueous medium. An exceptionally good dynamics of charge propagation was obtained for a composite from melamine precursor with optimal N content, but only in the acidic and alkaline medium. Neutral and organic solutions are not adapted as electrolyte for nitrogenated carbons because of the lack of protons.

Interesting materials, with a dominant contribution of pseudocapacitance based on oxygenated functionalities, can be obtained by one-step carbonization of a seaweed biopolymer, for example, sodium alginate. Although only slightly developed, the porosity of these materials is sufficient for a good access of ions to the functionality being at the origin of the pseudo-faradaic charge-transfer reactions. As a consequence of its limited porosity, the carbon from alginate has a volumetric capacitance that is at least twice higher than the usual nanoporous carbons proposed for supercapacitors.

In summary, composites where nanotubes are homogeneously dispersed in an active phase with pseudocapacitive properties, for example, carbons doped by heteroatoms, ECPs and oxides represent an interesting breakthrough for developing a new generation of supercapacitors.

Reversible hydrogen sorption is another possibility for introducing an additional pseudocapacitive contribution during charging/discharging a nanoporous carbon electrode in aqueous medium. Hydrogen storage based on a weak chemical bonding

during charging, that is, negative polarization, and its oxidation during the positive polarization step is an additional interesting source of capacitance for the negative electrode of a supercapacitor and allows the operating voltage to be extended.

It is necessary to underline that an asymmetric construction of a capacitor using two different pseudocapacitive electrodes is generally more effective than a symmetric one. In the case of pseudo-faradaic charge-transfer processes, the potential of each electrode must be controlled in order to avoid irreversible reactions. This is the reason symmetric capacitors based on pseudocapacitive materials cannot operate with a high voltage. High voltage values were reached in aqueous medium using an asymmetric configuration, with two different materials working in their optimal potential range for each electrode, for example, a nanoporous carbon at the negative electrode and conducting polymers or oxides at the positive electrode. Therefore, developing asymmetric supercapacitors with two different materials for the negative and positive electrodes should supply high-energy and high-power devices owing to the great extension of the operating voltage. For the development of low-cost and environment-friendly systems, this is certainly a research direction that should be extensively investigated in the future.

A novel concept of a supercapacitor with a redox-active electrolyte has been presented. Iodine, vanadium, and hydroxyquinone electroactive species have been considered separately or as two coupled redox pairs. Especially, in the case of two redox couples, the separation of both electrolytes is fundamental.

In conclusion, this chapter demonstrates that pseudocapacitive materials can drastically enhance the energy of supercapacitors. For that, a wide variety of composites has been revealed. It has been proved that the presence of small mesopores is a key factor in preserving a quick diffusion of redox species. However, keeping in mind that industrial systems require the highest volumetric energy, the amount of mesopores must be adjusted as low as possible in order to keep electrodes with the highest density. Finally, since protons are mainly required for an efficient exploitation of pseudocapacitance, the aqueous medium should be more carefully considered by the industry for capacitor construction. It is the most environment-friendly medium and, because of its good electrical conductivity, it is also the most appropriate for high-power devices.

References

1. Marsch, H. and Rodriguez-Reinoso, F. (2006) *Activated Carbons*, Elsevier, Amsterdam.
2. Inagaki, M. (2000) *New Carbons; Control of Structure and Functions*, Elsevier, Amsterdam.
3. Bansal, R.C., Donnet, J., and Stoeckli, F. (1988) *Active Carbon*, Marcel Dekker, New York.
4. Boehm, H.P. (1994) *Carbon*, **32**, 759.
5. Frackowiak, E. and Béguin, F. (2001) *Carbon*, **39**, 937–950.
6. Conway, B.E. (1999) *Electrochemical Supercapacitors—Scientific Fundamentals and Technological Applications*, Kluwer Academic/Plenum Publishers, New York.
7. Frackowiak, E. and Béguin, F. (2006) in *Recent Advances in Supercapacitors* (ed V. Gupta),

- Transworld Research Network, Kerala, pp. 79–114.
8. Kötz, R. and Carlen, M. (2000) *Electrochim. Acta*, **45**, 2483–2498.
 9. Balducci, A., Bardi, U., Caporali, S., Mastragostino, M., and Soavi, F. (2004) *Electrochem. Commun.*, **6**, 566.
 10. Frackowiak, E., Lota, G., and Pernak, J. (2005) *Appl. Phys. Lett.*, **86**, 30517.
 11. Shi, H. (1996) *Electrochim. Acta*, **41**, 1633.
 12. Qu, D. and Shi, H. (1998) *J. Power Sources*, **74**, 99.
 13. Gambly, J., Taberna, P.L., Simon, P., Fauvarque, J.F., and Chesneau, M. (2001) *J. Power Sources*, **101**, 109.
 14. Shiraishi, S., Kurihara, H., Tsubota, H., Oya, A., Soneda, Y., and Yamada, Y. (2001) *Electrochem. Solid-State Lett.*, **4**, A5.
 15. Lozano-Castelló, D., Cazorla-Amorós, D., Linares-Solano, A., Shiraishi, S., Kurihara, H., and Oya, A. (2003) *Carbon*, **41**, 1765.
 16. Guo, Y., Qi, J., Jiang, Y., Yang, S., Wang, Z., and Xu, H. (2003) *Mater. Chem. Phys.*, **80**, 704.
 17. Kierzek, K., Frackowiak, E., Lota, G., Gryglewicz, G., and Machnikowski, J. (2004) *Electrochim. Acta*, **49**, 515–523.
 18. Raymundo-Piñero, E., Kierzek, K., Machnikowski, J., and Béguin, F. (2006) *Carbon*, **44**, 2498.
 19. Salitra, G., Soffer, A., Eliad, L., Cohen, Y., and Aurbach, D. (2000) *J. Electrochem. Soc.*, **147**, 2486.
 20. Eliad, L., Salitra, G., Soffer, A., and Aurbach, D. (2001) *J. Phys. Chem.*, **B105**, 6880.
 21. Eliad, L., Salitra, G., Soffer, A., and Aurbach, D. (2002) *J. Phys. Chem. B*, **106**, 10128.
 22. Lota, G., Centeno, T.A., Frackowiak, E., and Stoeckli, F. (2008) *Electrochim. Acta*, **53**, 2210–2216.
 23. Peng, C., Zhang, S., Jewel, D., and Chen, G.Z. (2008) *Progr. Nat. Sci.*, **18**, 777–788.
 24. Laforge, A., Simon, P., Fauvarque, J.F., Sarrau, J.F., and Lailier, P. (2001) *J. Electrochem. Soc.*, **148**, A1130–A1134.
 25. Li, H., Wang, J., Chu, Q., Wang, Z., Zhang, F., and Wang, S. (2009) *J. Power Sources*, **190**, 578–586.
 26. Gupta, V. and Miura, N. (2006) *Mater. Lett.*, **190**, 1466–1469.
 27. Sivakkumar, S.R., Kim, W.J., Choi, J.A., Mac Farlane, D.R., Forsyth, M., and Kim, D.W. (2007) *J. Power Sources*, **171**, 1062–1068.
 28. Kim, J.H., Lee, Y.S., Sharma, A.K., and Liu, C.G. (2006) *Electrochim. Acta*, **52**, 1727–1732.
 29. Muthulakshimi, B., Kalpana, D., Pitchumani, S., and Renganathan, N.G. (2006) *J. Power Sources*, **158**, 1533–1537.
 30. Khomeenko, V., Frackowiak, E., and Béguin, F. (2005) *Electrochim. Acta*, **50**, 2499–2506.
 31. Peng, C., Jin, J., and Chen, G.Z. (2007) *Electrochim. Acta*, **53**, 525–537.
 32. Zhang, H., Cao, G., Wang, W., Yuan, K., Xu, B., Zhang, W., Cheng, J., and Yang, Y. (2009) *Electrochim. Acta*, **54**, 1153–1159.
 33. Fang, Y., Liu, J., Yu, D.J., Wicksted, J.P., Kalkan, K., Topal, C.O., Flanders, B.N., Wu, J., and Li, J. (2010) *J. Power Sources*, **195**, 674–679.
 34. Laforge, A., Simon, P., Sarrazin, C., and Fauvarque, J.F. (1999) *J. Power Sources*, **80**, 142.
 35. Jurewicz, K., Delpoux, S., Bertagna, V., Béguin, F., and Frackowiak, E. (2001) *Chem. Phys. Lett.*, **347**, 36–40.
 36. Arbizzani, C., Mastragostino, M., and Soavi, F. (2001) *J. Power Sources*, **100**, 164.
 37. Mastragostino, M., Arbizzani, C., and Soavi, F. (2002) *Solid State Ionics*, **148**, 493.
 38. Campomanes, R.S., Bittencourt, E., and Campos, J.S.C. (1999) *Synth. Met.*, **102**, 1230.
 39. Ryu, K.S., Wu, X., Lee, Y.G., and Chang, S.H. (2003) *J. Appl. Polym. Sci.*, **89**, 1300–1304.
 40. Sandler, J., Shaffer, M.S.P., Prasse, T., Bauhofer, W., Schulte, K., and Windle, A.H. (1999) *Polymer*, **40**, 5967.
 41. Naoi, K. and Simon, P. (2008) *Electrochem. Soc. Interface*, **17**, 34–37.
 42. Hong, M.S., Lee, S.H., and Kim, S.W. (2002) *Electrochem. Solid-State Lett.*, **5**, A227.

43. Brousse, T., Toupin, M., and Bélanger, D. (2004) *J. Electrochem. Soc.*, **151**, A614.
44. Khomenko, V., Raymundo-Piñero, E., and Béguin, F. (2005) *J. Power. Sources*, **153**, 183.
45. Khomenko, V., Raymundo-Piñero, E., Frackowiak, E., and Béguin, F. (2006) *Appl. Phys. A*, **82**, 567–573.
46. Miller, J.M., Dunn, B., Tran, T.D., and Pekala, R.W. (1999) *Langmuir*, **15**, 799.
47. Toupin, M., Brousse, T., and Bélanger, D. (2002) *Chem. Mater.*, **14**, 3946.
48. Wu, N.L. (2002) *Mater. Chem. Phys.*, **75**, 6.
49. Raymundo-Piñero, E., Khomenko, V., Frackowiak, E., and Béguin, F. (2005) *J. Electrochem. Soc.*, **152**, A229.
50. Yang, X.H., Wang, Y.G., Xiong, X.M., and Xia, Y.Y. (2007) *Electrochim. Acta*, **53**, 752–757.
51. Malak, A., Fic, K., Lota, G., Vix-Guterl, C., and Frackowiak, E. (2010) *J. Solid State Electrochem.*, **14**, 811–816.
52. Nam, K.W., Lee, C.W., Yang, X.Q., Cho, B.W., Yoon, W.S., and Kim, K.B. (2009) *J. Power. Sources*, **188**, 323–331.
53. Frackowiak, E., Lota, G., Machnikowski, J., Vix-Guterl, C., and Béguin, F. (2006) *Electrochim. Acta*, **51**, 2209–2214.
54. Lota, G., Grzyb, B., Machnikowska, H., Machnikowski, J., and Frackowiak, E. (2005) *Chem. Phys. Lett.*, **404**, 53–58.
55. Lee, Y.H., Lee, Y.F., Chang, K.H., and Hu, C.C. (2011) *Electrochem. Commun.*, **13**, 50–53.
56. Qin, C., Lu, X., Yin, G., Jin, Z., Tan, Q., and Bai, X. (2011) *Mater. Chem. Phys.*, **126**, 453–458.
57. Jeong, H.M., Lee, J.W., Shin, W.H., Choi, Y.J., Shin, H.J., Kang, J.K., and Choi, J.W. (2011) *Nano Lett.*, **11**, 2472–2477.
58. Hulicova, D., Yamashita, J., Soneda, Y., Hatori, H., and Kodama, M. (2005) *Chem. Mater.*, **17**, 1241–1247.
59. Hulicowa, D., Kodama, M., and Hatori, H. (2006) *Chem. Mater.*, **18**, 2318–2326.
60. Hulicova-Jurcakova, D., Kodama, M., Shiraishi, S., Hatori, H., Zhu, Z.H., and Lu, G.Q. (2009) *Adv. Funct. Mater.*, **19**, 1800–1809.
61. Lota, G., Lota, K., and Frackowiak, E. (2007) *Electrochem. Commun.*, **9**, 1828–1832.
62. Jurewicz, K., Frackowiak, E., and Béguin, F. (2001) *Electrochem. Solid-State Lett.*, **4**, A27–A29.
63. Jurewicz, K., Frackowiak, E., and Béguin, F. (2002) *Fuel Process. Technol.*, **77–78**, 213–219.
64. Jurewicz, K., Frackowiak, E., and Béguin, F. (2004) *Appl. Phys. A*, **78**, 981–987.
65. Vix-Guterl, C., Frackowiak, E., Jurewicz, K., Friebe, M., Parmentier, J., and Béguin, F. (2005) *Carbon*, **43**, 1293–1302.
66. Béguin, F., Friebe, M., Jurewicz, K., Vix-Guterl, C., Dentzer, J., and Frackowiak, E. (2006) *Carbon*, **44**, 2392–2398.
67. Qu, D. (2008) *J. Power. Sources*, **179**, 310.
68. Béguin, F., Kierzek, K., Friebe, M., Jankowska, A., Machnikowski, J., Jurewicz, K., and Frackowiak, E. (2006) *Electrochim. Acta*, **51**, 2161–2167.
69. Bleda-Martinez, M.J., Pérez, J.M., Linares-Solano, A., Morallón, E., and Cazorla-Amorós, D. (2008) *Carbon*, **46**, 1053.
70. Fang, B., Zhou, H., and Honma, I. (2006) *J. Phys. Chem. B*, **110**, 4875.
71. Fang, B., Kim, J.H., Kim, M., and Yu, J.S. (2008) *Langmuir*, **24**, 12068.
72. Babel, K. and Jurewicz, K. (2008) *Carbon*, **46**, 1948.
73. Conway, B.E. and Tilak, B.V. (2002) *Electrochim. Acta*, **47**, 3571.
74. Lota, G., Fic, K., and Frackowiak, E. (2011) *Energy Environ. Sci.*, **4**, 1592–1605.
75. Lota, G. and Frackowiak, E. (2009) *Electrochem. Commun.*, **11**, 87–90.
76. Lota, G., Fic, K., and Frackowiak, E. (2011) *Electrochem. Commun.*, **12**, 38–41.
77. Yamazaki, S., Ito, T., Yamagata, M., and Ishikawa, M. *Electrochim. Acta*, <http://dx.doi.org/10.1016/j.electacta.2012.01.031>, article in press.
78. Roldan, S., Blanco, C., Granda, M., Menendez, R., and Santamaria, R. (2011) *Angew. Chem.*, **123**, 1737–1739.

79. Roldan, S., Granda, M., Menendez, R., Santamaria, R., and Blanco, C. (2011) *J. Phys. Chem.*, **115**, 17606–17611.
80. An, K.H., Jeon, K.K., Heo, J.K., Lim, S.C., Bae, D.J., and Lee, Y.H. (2002) *J. Electrochem. Soc.*, **149**, A1058–A1062.
81. Lota, K., Khomeenko, V., and Frackowiak, E. (2004) *J. Phys. Chem. Solids*, **65**, 295–301.
82. Chen, G.Z., Shaffer, M.S.P., Coleby, D., Dixon, G., Zhou, W., Fray, D.J., and Windle, A.H. (2000) *Adv. Mater.*, **12**, 522.
83. Hughes, M., Schaffer, M.S.P., Renouf, A.C., Singh, C., Chen, G.Z., Fray, D.J., and Windle, A.H. (2002) *Adv. Mater.*, **14**, 382–385.
84. Obreja, V.V.N. (2008) *Physica E*, **40**, 2596–2605.
85. Zhang, W.D., Xu, B., and Jiang, L.C. (2010) *J. Mater. Chem.*, **20**, 6383–6391.
86. Hong, W., Xu, Y., Lu, G., Li, C., and Shi, G. (2008) *Electrochem. Commun.*, **10**, 1555.
87. Wu, Q., Xu, Y., Yao, Z., Liu, A., and Shi, G. (2010) *ACS Nano*, **4**, 1963.
88. Wang, H.L., Hao, Q.L., Yang, X.J., Lu, L.D., and Wang, X. (2009) *Electrochem. Commun.*, **11**, 1158.
89. Frackowiak, E. (2004) in *Encyclopedia of Nanoscience and Nanotechnology* (eds J.A. Schwarz *et al.*), Marcel Dekker, New York, p. 537.
90. Futaba, D.N., Hata, K., Yamada, T., Hiraoka, T., Hayamizu, Y., Kakudate, Y., Tanaike, O., Hatori, H., Yumura, M., and Iijima, S. (2006) *Nat. Mater.*, **5**, 987.
91. Zhang, H., Cao, G., Jang, Y., and Gu, Z. (2008) *J. Electrochem. Soc.*, **155**, K19–K22.
92. Zhu, Y., Murali, S., Cai, W., Li, X., Suk, J.W., Potts, J.R., and Ruoff, R.S. (2010) *Adv. Mater.*, **22**, 3906–3924.
93. Miller, J.R., Outlaw, R.A., and Holloway, B.C. (2010) *Science*, **329**, 1637–1639.
94. Stoller, M.D., Park, S., Zhu, Y., An, J., and Ruoff, R.S. (2008) *Nano Lett.*, **8**, 3498.
95. Stoller, M.D. and Ruoff, R.S. (2010) *Energy Environ. Sci.*, **3**, 1294–1301.
96. Zheng, J.P. (2003) *J. Electrochem. Soc.*, **150**, A484.
97. Ganesh, V., Pitchumani, S., and Lakshminarayanan, V. (2006) *J. Power. Sources*, **158**, 1523.
98. Nohara, S., Asahina, T., Wada, H., Furukawa, N., Inoue, H., Sugoh, N., Iwasaki, H., and Iwakura, C. (2006) *J. Power. Sources*, **157**, 605.
99. Frackowiak, E. (2007) *Phys. Chem. Chem. Phys.*, **9**, 1774–1785.
100. Byon, H.R., Lee, S.W., Chen, S., Hammond, P.T., and Shao-Horn, Y. (2011) *Carbon*, **49**, 457.
101. Yu, D. and Dai, L. (2010) *J. Phys. Chem. Lett.*, **1**, 467–470.
102. Ma, S.B., Nam, K.W., Yoon, W.S., Yang, X.Q., Ahn, K.Y., Oh, K.H., and Kim, K.B. (2007) *Electrochem. Commun.*, **9**, 2807–2811.
103. Ammundsen, B., Aitchison, P.B., Burns, G.R., Jones, D.J., and Rozière, J. (1997) *Solid State Ionics*, **97**, 269–276.
104. Feng, Q., Miyai, Y., Kanoh, H., and Ooi, K. (1992) *Langmuir*, **8**, 1861–1867.
105. Kang, Y.J., Kim, B., Chung, H., and Kim, W. (2010) *Synth. Met.*, **60**, 2510.
106. Kawaoka, H., Hibino, M., Zhou, H., and Honma, I. (2005) *Solid State Ionics*, **176**, 621.
107. Jin, X., Zhou, W., Zhang, S., and Chen, G.Z. (2007) *Small*, **3**, 1513.
108. Zhang, H., Cao, G., Wang, Z., Yang, Y., Shi, Z., and Gu, Z. (2008) *Nano Lett.*, **8**, 2664–2668.
109. Zheng, H., Kang, W., Fengming, Z., Tang, F., Rufford, T.E., Wang, L., and Ma, C. (2010) *Solid State Ionics*, **181**, 1690.
110. Reddy, A.L.M., Shaijumon, M.M., Gowda, S.R., and Ajajan, P.M. (2010) *J. Phys. Chem. C*, **114**, 658.
111. Bordjiba, T. and Bélanger, D. (2010) *Electrochim. Acta*, **55**, 3428.
112. Zhang, H., Cao, G., and Yang, Y. (2009) *Energy Environ. Sci.*, **2**, 932.
113. Pan, H., Li, J., and Feng, Y.P. (2010) *Nanoscale Res. Lett.*, **5**, 654–668.
114. Sivakkumar, S.R., Ko, J.M., Kim, D.Y., Kim, B.C., and Wallace, G.G. (2007) *Electrochim. Acta*, **52**, 7377.
115. Li, Q., Liu, J., Zou, J., Chunder, A., Chen, Y., and Zhai, L. (2011) *J. Power. Sources*, **196**, 565.
116. Hou, Y., Cheng, Y., Hobson, T., and Liu, J. (2010) *Nano Lett.*, **10**, 2727.

117. Raymundo-Piñero, E., Leroux, F., and Béguin, F. (2006) *Adv. Mater.*, **18**, 1877–1882.
118. Raymundo-Piñero, E., Cadek, M., and Béguin, F. (2009) *Adv. Funct. Mater.*, **19**, 1–8.
119. Frackowiak, E., Méténier, K., Bertagna, V., and Béguin, F. (2000) *Appl. Phys. Lett.*, **77**, 2421.
120. Ania, C.O., Khomenko, V., Raymundo-Piñero, E., Parra, J.B., and Béguin, F. (2007) *Adv. Funct. Mater.*, **17**, 1828–1836.
121. Jurewicz, K., Babel, K., Ziolkowski, A., and Wachowska, H. (2003) *Electrochim. Acta*, **48**, 1491–1498.
122. Biniak, S., Swiatkowski, A., and Makula, M. (2001) in *Chemistry and Physics of Carbon*, Vol. 27 Chapter 3 (ed L.R. Radovic), Marcel Dekker, New York.
123. Montes-Moran, M.A., Suarez, D., Menendez, J.A., and Fuente, E. (2004) *Carbon*, **42**, 1219–1224.
124. Raymundo-Piñero, E., Cadek, M., Wachtler, M., and Béguin, F. (2011) *ChemSusChem*, **4**, 943–949.
125. Béguin, F., Szostak, K., Lota, G., and Frackowiak, E. (2005) *Adv. Mater.*, **17**, 2380.
126. Lota, G., Fic, K., Jurewicz, K., and Frackowiak, E. (2011) *Cent. Eur. J. Chem.*, **9**, 20–24.
127. Demarconnay, L., Raymundo-Piñero, E., and Béguin, F. (2010) *Electrochem. Commun.*, **12**, 1275–1278.
128. Fic, K., Lota, G., Meller, M., and Frackowiak, E. (2012) *Energy Environ. Sci.*, **5**, 5842–5850.
129. Bichat, M.P., Raymundo-Piñero, E., and Béguin, F. (2010) *Carbon*, **48**, 4351–4361.
130. Frackowiak, E., Fic, K., Meller, M., and Lota, G. (2012) *ChemSusChem*, **5**, 1181–1185.
131. Fic, K. (2012) ‘Electrode/electrolyte interface in electrochemical energy conversion and storage systems’ PhD thesis. Poznan University of Technology.

7

Li-Ion-Based Hybrid Supercapacitors in Organic Medium

Katsuhiko Naoi and Yuki Nagano

7.1

Introduction

Environment protection and sustainable energy development have recently become a growing industry, in which energy storage devices are such important components that they play crucial roles. Energy storage devices include batteries, for example, lithium-ion batteries, nickel-metal hydride batteries, and lead-acid batteries, which have high energy densities. The batteries are under vigorous study for further increasing their energy density so that they can power electric vehicles. On the other hand, electric double-layer capacitors (EDLCs), which are high-power energy storage devices capable of effectively utilizing energy, have been also studied and are practically used in tracks, buses, elevators, and in heavy-duty construction and railway usage such as forklifts, yard cranes, and bullet trains [1].

However, since EDLCs generally have low energy densities, their uses are limited and they cannot fully meet the various performance demands of the recent markets as shown in Figure 7.1. Particularly in the field of automobiles, new energy devices are strongly desired to have hybrid characteristics between lithium-ion batteries and EDLCs, and, thereby, can be suitably employed in idle reduction systems. Accordingly, it is expected for them to form a large market [2]. In order to satisfy the performance demands, it is often suggested that the energy density of EDLCs be enhanced to 20–30 Wh l⁻¹, which is approximately twice or more that of the present EDLCs, namely 5–10 Wh l⁻¹. To realize this high energy density, hybrid capacitor systems comprising nonaqueous redox materials are being dynamically researched and developed in recent years [3–11]. This chapter deals with the recent contributions to get this high energy density by focusing on two major hybridized cell configurations in organic media.

7.2

Voltage Limitation of Conventional EDLCs

As described, increasing the energy density is one of the most crucial matters. For conventional EDLC systems, designed with two symmetrical activated carbon

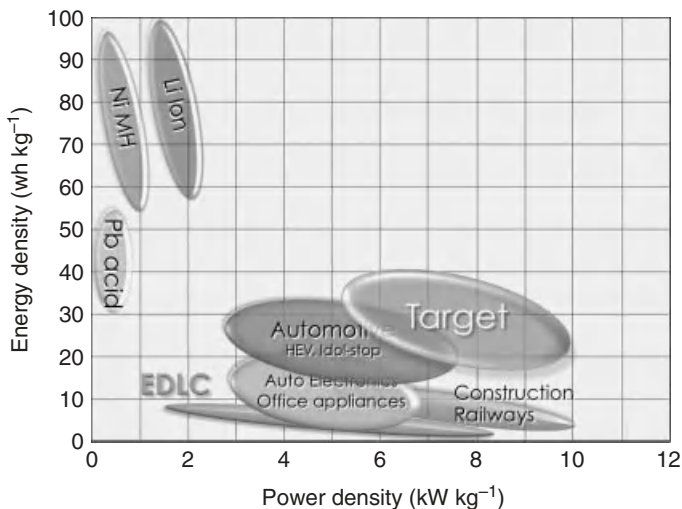
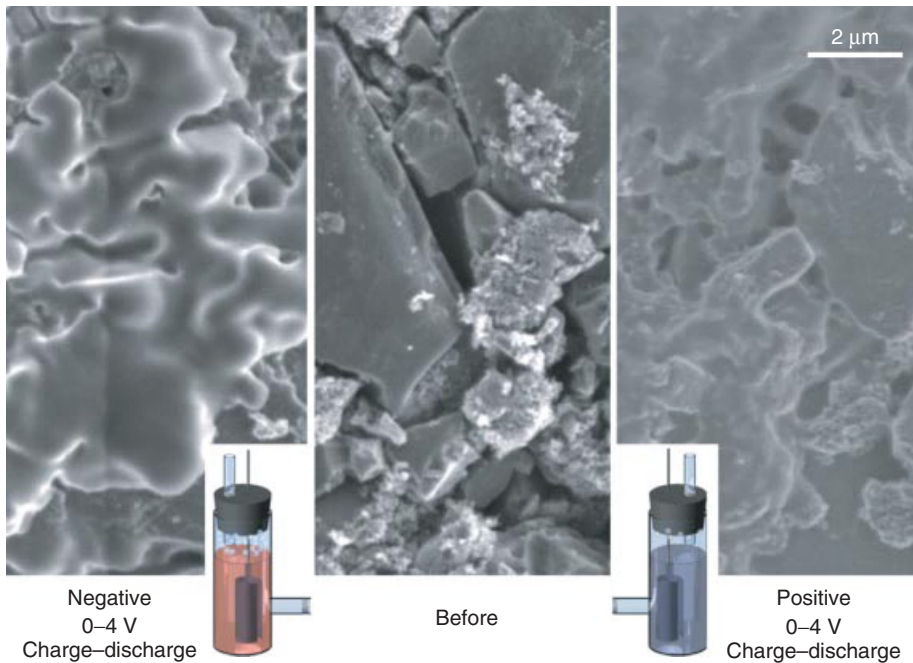
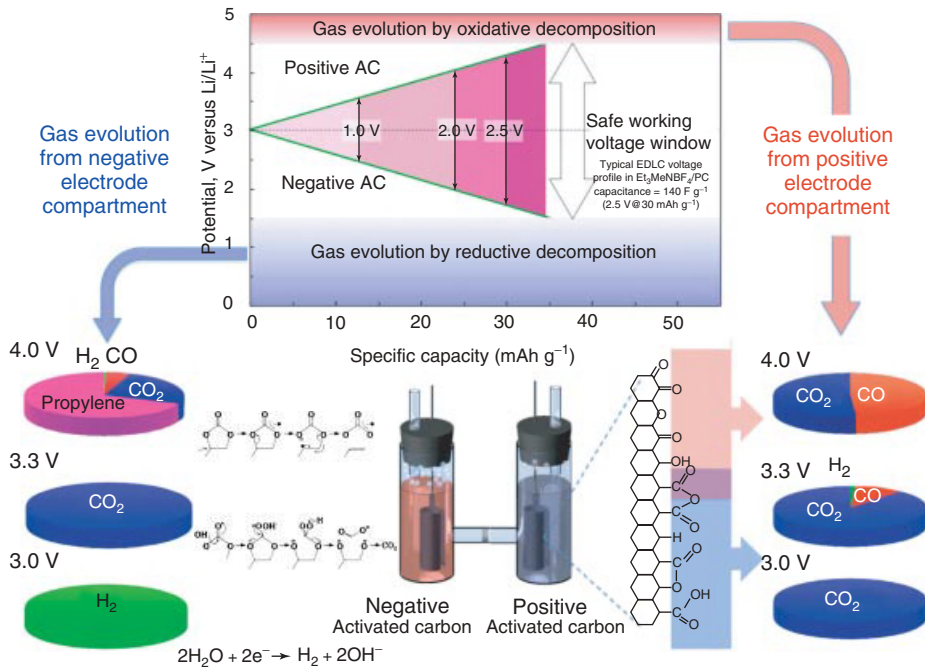


Figure 7.1 Ragone plots for representative energy storage devices of batteries (lead-acid, nickel-metal hydride, and Li-ion) and EDLCs. The energy-power requirements are indicated for important applications (automotive, office appliances, railways, etc.) and the target areas of enhanced electrochemical supercapacitors for the next generation.

(AC) electrodes, increasing the voltage is the most effective in increasing energy density because of its square dependence on voltage. Thus, it is essential to develop higher electrochemical durability at the electrode/electrolyte interface. Currently, the maximum voltage of a normal EDLC is, however, limited to 2.5–2.7 V. Exceeding this voltage limitation will cause serious damage to an EDLC cell and considerable side reactions such as gas evolution and surface film formation on the electrode surfaces.

The gas evolution was practically analyzed by using an H-type cell (Figure 7.2) capable of separately collecting gases from the positive and negative compartments. The gaseous products were separately collected after applying constant voltages of 3.0, 3.3, and 4.0 V at 60 °C for 50 h. In the positive compartment, mainly two components, CO₂ and CO, were detected resulting from the electrochemical oxidation of propylene carbonate (PC) and surface functional groups of carbon. The easily oxidizable functional groups such as carboxyl can be oxidized at 3.0 V and released as CO₂ gas, while phenol and ketone produce CO gas at a higher voltage

Figure 7.2 Limitation in polarizing conventional EDLCs, suggesting the safe working voltage window (2.5–2.7 V) free from various gases evolution at the positive and negative activated carbon electrodes. The evolved gases were collected after floating tests (at 60 °C for 50 h) and characterized by gas chromatography, and are shown as a function of applied voltages of 3.0, 3.3, and 4.0 V. The SEM images show the surface aspect of the positive and negative electrodes after charging–discharging in the voltage range of 0–4.0 V [31].



than 3.3 V. The gasification of such functional groups automatically detaches the adsorbed water clusters and release free water (from initially 11 up to 300 ppm) into the electrolyte, as mostly observed in the positive compartment. In the negative compartment, on the other hand, the evolved gaseous products are quite different. Hydrogen (H_2) is observed together with OH^- at 3.0 V, both resulting from water electrochemical reduction. At 3.3 V, the OH^- -catalyzed PC hydrolysis occurs in the negative compartment consuming water (11 down to 1 ppm) after a 50 h floating test. Other gases such as propylene, CO_2 , ethylene, and CO are detected at higher voltages of 4.0 V, indicating that a direct electrochemical reduction of PC occurs [12].

According to these reactions, applying a voltage over 2.7 V causes a significant decrease in capacitance and an increase in damage to the AC electrodes. As shown in the lower part of Figure 7.2, with an increase in polarization voltage to 4.0 V, a considerable surface film formation is observed, the latter being normally more pronounced at the negative electrode surface. In fact, after 30 days at 2.7 V, the cell lost 13% of its initial capacitance and its internal resistance increased. At 2.9 V, the capacitance loss became more significant ($\Delta C = -28\%$) for the same duration. The threshold cell overvoltage between 2.5 and over 2.7 V certainly triggers a consecutive and fatal degradation. The undesired faradic process (failure modes) that leads to a capacitance fade is the most critical metrics that determines the life of the current EDLCs [2]. This withstand voltage limitation (2.5–2.7 V) is certainly a big barrier for further enhancement in energy density.

7.3 Hybrid Capacitor Systems

There is presently a major effort to increase the energy density of supercapacitors up to a target value in the vicinity of 20–30 Wh kg^{-1} [1]. Many studies have been undertaken to meet the following important issues (Figure 7.3) in order to increase the energy density of EDLC devices. There are mainly three approaches, by (i) changing the electrode material (by higher capacitance carbons or redox materials), (ii) changing the electrolyte (by durable new electrolyte or ionic liquids), and (iii) developing hybrid capacitors. Various hybrid capacitor systems are possible by coupling redox-active materials (e.g., graphite [3, 4], metal oxides [10–12], conducting polymers [13, 14], and an AC). This approach can overcome the energy density limitation of the conventional EDLCs because it employs a hybrid system of battery-like (faradic) and capacitor-like (non-faradic) electrodes, producing higher working voltage, and capacitance. With these systems, one can certainly achieve twice or triple enhancements in energy density compared to the conventional EDLCs (Figure 7.4).

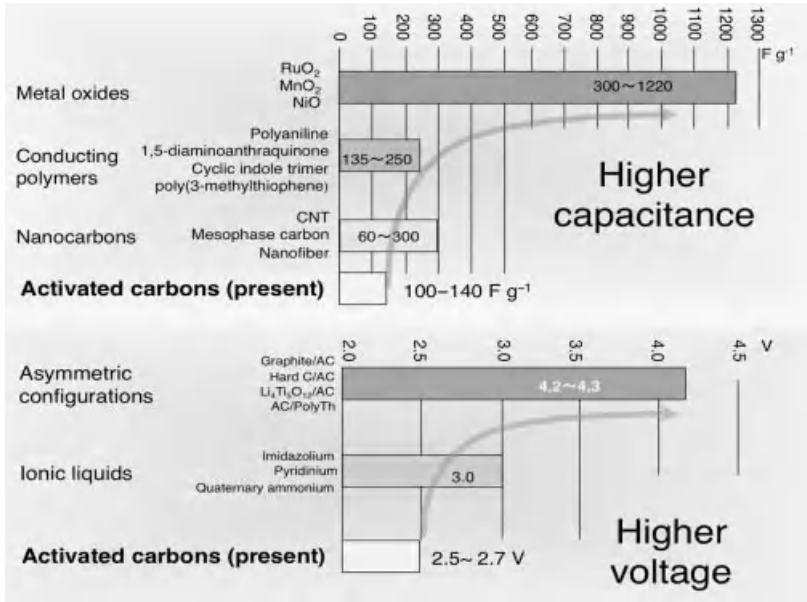


Figure 7.3 Major approaches to get enhanced energy density of supercapacitors: higher capacitance by replacing activated carbons with various pseudocapacitive materials, higher voltage by having hybrid cell configurations and durable electrolytes.

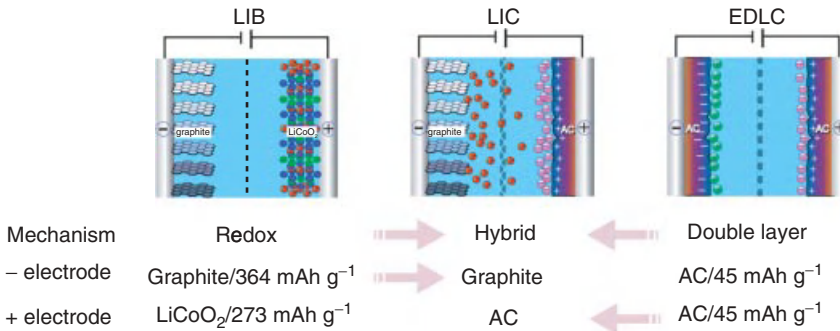


Figure 7.4 Cell configurations and mechanisms for Li-ion battery (LIB), LIC, and EDLC.

7.3.1

Lithium-Ion Capacitor (LIC)

Among high-energy hybrid capacitors comprising nonaqueous redox materials, a hybrid system called the *lithium-ion capacitor* (abbreviated as LIC) has particularly attracted attention [3–5]. As shown in Figure 7.5, the LIC is a hybrid capacitor in which the positive and negative electrodes are made of AC and of graphite predoped

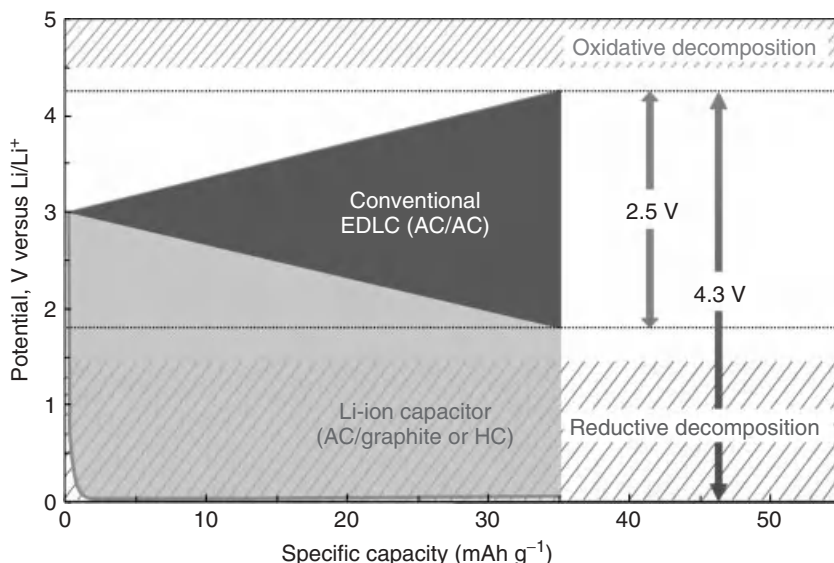


Figure 7.5 Comparison of the voltage profiles for a conventional electric double-layer capacitor (EDLC) utilizing activated carbon for both positive and negative electrodes, and a hybrid nonaqueous lithium-ion capacitor (LIC) where the negative electrode is replaced by prelithiated graphite.

with lithium ions, respectively. Hence, the LIC is a hybrid of a Li-ion battery (LIB) negative electrode and EDLC positive electrode. Li^+ intercalation–deintercalation occurs in the graphite electrode with shallower state of charge (SOC; less than 50%) compared with the LIB system, while adsorption–desorption of anions, most typically BF_4^- or PF_6^- , occurs on the AC electrode, as in the EDLC. The overall process is not a “rocking-chair”-type reaction as LIB, but a cation- and anion-consuming reaction.

Figure 7.5 represents the voltage profiles of the conventional EDLC system and LIC, whereby one can have a good scenario attaining higher voltage and higher energy density.

As the graphite-negative electrode undergoes the reaction at a potential a little over 0 V versus Li/Li^+ , the LIC has a high working voltage of 3.8 to 4.0 V. This high working voltage enables the lithium-ion capacitor to realize both a high-power density of approximately 5 kW kg^{-1} and an energy density of approximately $20\text{--}30 \text{ Wh kg}^{-1}$. The LIC thus exhibits favorable performance, and is regarded as a promising candidate of the next generation of electrochemical supercapacitors. Hence, some Japanese companies (JM Energy, FDK, etc.) have already started commercializing LIC and its modules [4].

The limited charging rate, especially at low temperatures, would be the possible drawback of the LIC because it exhibits some metal deposition, as observed in Figure 7.6. Generally speaking, instead of achieving energy density improvement, the high working voltage causes an electrolyte decomposition problem, especially

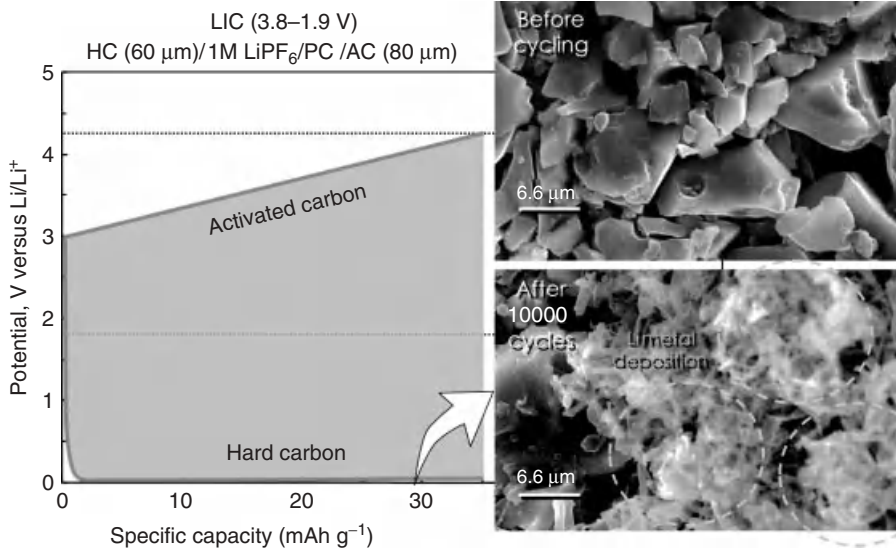


Figure 7.6 Low-temperature performance of LIC (activated carbon/hard carbon – HC) system. SEM micrographs for the surface of negative HC electrode before and after cycling (at 25 °C) 10 000 times at -10°C .

at the negative graphite electrode [14]. This is an issue that is specifically important for an electrochemical capacitor as a “power device” because it leads to a high impedance electrode/electrolyte interface and thus eventually to a deteriorated power performance for longer cycling.

However, the LIC system has an advantage at high voltage (4 V) and high-temperature performance (60°C). As both the positive (AC) and negative (graphite or hard carbon) electrode materials are already commercially available, it is easy to start assembling LIC cells. The only issue is the process of Li^+ predoping to the negative electrode. Figure 7.7 describes an original Li^+ predoping developed for laminated electrodes and first patented by Fuji Heavy Industry [15]. The Li^+ predoping is a thermodynamically “downhill” process that starts automatically from the adjacent Li metal plate when an electrolyte is introduced into an LIC cell. Also, Li^+ ions pass through holes on the current collector (mostly Cu) to efficiently dope all the bipolar-stacked cells. However, Li^+ predoping for larger capacity cells takes a longer time to complete. Effective Li^+ predoping methods have eagerly been researched and this may not be a major problem for reliability under mass production. Béguin *et al.* [5] suggested a unique method called *formation cycles* for preconditioning graphite electrode, enabling deeper Li^+ predoping. The method involves a sequential application of voltage pulses (4.0 V) followed by open-circuit relaxation periods. With this method, the potential of the graphite electrode is lowered and the Li^+ is perfectly injected without requiring an auxiliary lithium metal electrode, making the system potentially safer.

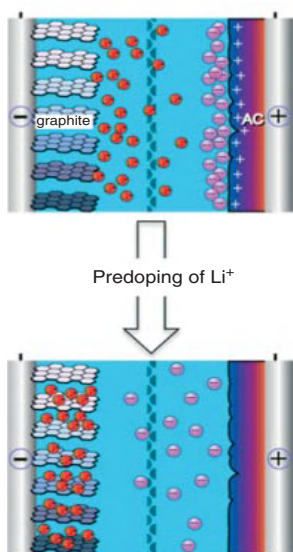


Figure 7.7 Li⁺ predoping for LIC systems patented by Fuji Heavy industry [15].

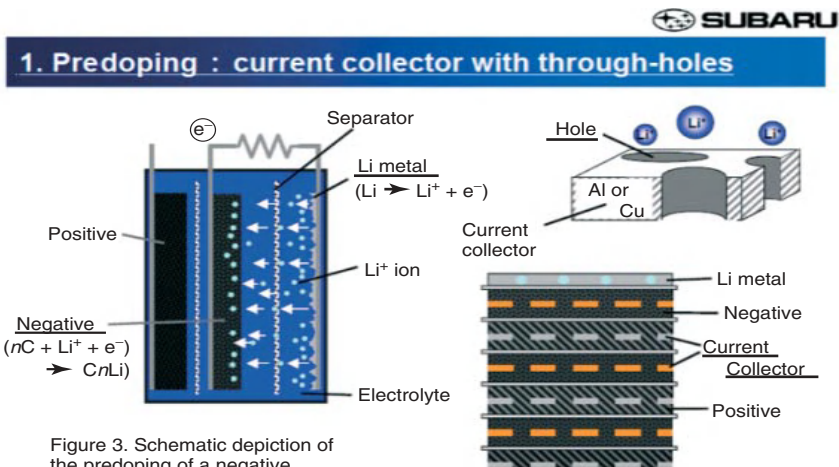


Figure 3. Schematic depiction of the predoping of a negative electrode using Li metal. Pre doping automatically starts when electrolyte solution is introduced to a cell.

Figure 4. Schematic depiction of pre doping for a laminated electrodes cell. Li ions pass through the holes on current collectors to dope all anodes.

7.3.2

Nanohybrid Capacitor (NHC)

Very recently, Naoi's group developed a hybrid capacitor system that certainly achieves a high energy density, high stability, and high safety. This is called *nanohybrid capacitor* (abbreviated as NHC) using a super-high-rate nanostructured lithium titanate ($\text{Li}_4\text{Ti}_5\text{O}_{12}$)/carbon composite negative electrode. The authors have kept their eyes on lithium titanate ($\text{Li}_4\text{Ti}_5\text{O}_{12}$) as a stable and safe redox material capable of increasing the energy density of hybrid capacitors without sacrificing interfacial characteristics. $\text{Li}_4\text{Ti}_5\text{O}_{12}$ operates at a potential (1.55 V vs. Li/Li^+) out of the range where the electrolyte solution may be decomposed, and hence play key roles for providing capacitor systems as stable and safe as EDLCs (Figure 7.8).

Amatucci *et al.* [16] first introduced the $\text{Li}_4\text{Ti}_5\text{O}_{12}/\text{AC}$ hybrid as a safer energy storage system. However, conventional $\text{Li}_4\text{Ti}_5\text{O}_{12}$ has the greatest problem of low-power characteristics that stem from inherent poor Li^+ diffusion coefficient ($<10^{-6} \text{ cm}^2 \text{ s}^{-1}$) [17] and poor electronic conductivity ($<10^{-13} \text{ S cm}^{-1}$) [18]. Such slow output characteristics were not fully developed for the application in electrochemical capacitors at that time. For the purpose of solving the problem of poor output performance, the $\text{Li}_4\text{Ti}_5\text{O}_{12}$ may be ground from a few $10 \mu\text{m}$ down to less than 10 nm particles and may be combined with an electroconductive material to prepare a composite [33, 34].

$\text{Li}_4\text{Ti}_5\text{O}_{12}$ as a redox material for hybrid capacitors, described in Figure 7.9, has the following essential advantages in energy density, stability, and safety:

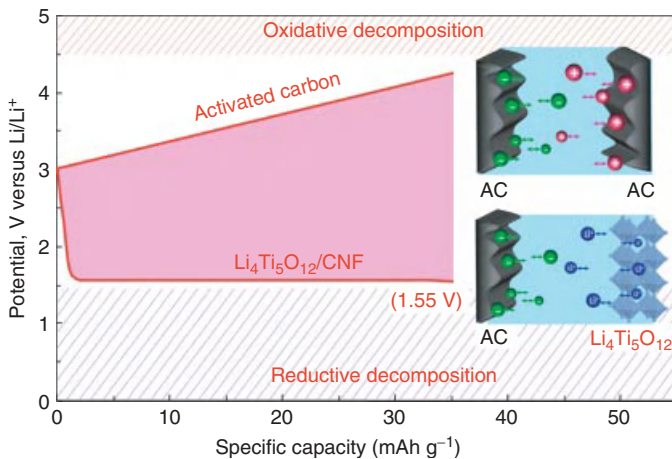


Figure 7.8 Configuration of a “nanohybrid capacitor” consisting of an ultrafast $\text{Li}_4\text{Ti}_5\text{O}_{12}$ (LTO)/CNF nanocomposite negative electrode combined with an activated carbon (AC) positive electrode. This is a hybrid system of a highly accelerated faradic Li-intercalating LTO electrode and a non-faradic AC electrode employing anion (typically BF_4^-) adsorption-desorption process.

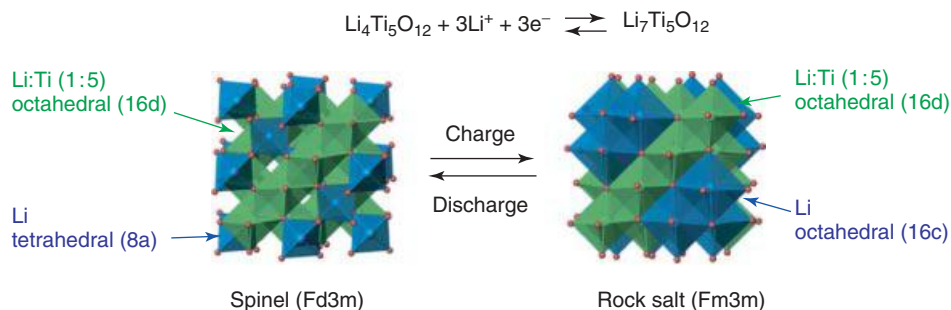


Figure 7.9 Electrochemical and structural changes for $\text{Li}_4\text{Ti}_5\text{O}_{12}$ during the charge–discharge process.

- 1) It exhibits a high coulombic efficiency close to 100% during charge–discharge cycling [32].
- 2) It has a theoretical capacity (175 mAh g^{-1}) four times higher than AC.
- 3) It undergoes charging and discharging at a constant potential of 1.55 V versus Li/Li^+ , where the electrolyte solution is free from any degradation (little SEI formation and little gas evolution) [19–21].
- 4) It exhibits very small volumetric changes (0.2%) (zero-strain insertion).
- 5) It is an inexpensive raw material.

As summarized in Figure 7.10, a capacitor cell comprising $\text{Li}_4\text{Ti}_5\text{O}_{12}$ does not require predoping by lithium ions. There is a large selection of electrolytes for NHC because of its narrower voltage window (2.7–3.0 V) compared with the LIC system (4.0–4.3 V). Acetonitrile (AN), ionic liquids and linear carbonates (dimethyl carbonate (DMC) or DEC) can be utilized for NHC. The selection of electrolyte is very important for getting even better power performances. In fact, an AN-based NHC exhibited nine times higher power density compared with the conventional PC-based EDLCs. The reason is uncertain at present but may be due to better accessibility of AN (compared with viscous PC) to the microporous $\text{Li}_4\text{Ti}_5\text{O}_{12}$ nanocomposite. The low-temperature performance is excellent down to -40°C for NHC because of the nature of $\text{Li}_4\text{Ti}_5\text{O}_{12}$. The internal resistance of NHC can be minimized to values comparable to EDLCs in a wide range of temperatures.

7.4

Material Design for NHC

Composites of nanosized $\text{Li}_4\text{Ti}_5\text{O}_{12}$ particles and carbon nanofibers (CNFs) ($\text{Li}_4\text{Ti}_5\text{O}_{12}/\text{CNF}$) were synthesized by means of a new method referred to as *ultracentrifuging force (UC) method* [22, 23]. Specifically, the composite comprises nanocrystalline $\text{Li}_4\text{Ti}_5\text{O}_{12}$ particles hyperdispersed on CNFs [24] having high electronic conductivity ($25 \Omega^{-1} \text{ cm}^{-1}$) (Figure 7.11). The authors utilized the composite as a negative electrode active material, and thereby succeeded in producing a novel

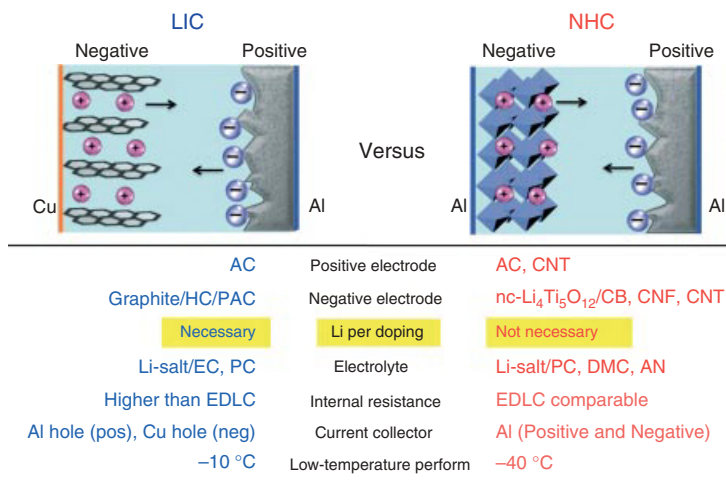


Figure 7.10 Comparison of LIC and NHC characteristics.

hybrid capacitor (nanohybrid capacitor) realizing both high power and high energy density.

The nc-Li₄Ti₅O₁₂ negative electrode was developed to have a unique nanostructure that can operate at unusually high current densities. Nanocrystalline Li₄Ti₅O₁₂ attached onto carbon nanofibers was prepared by a unique technique, UC treatment, inducing a mechanochemical sol-gel reaction under UC at 75 000 G [25], followed by an instantaneous heat treatment under vacuum for very short duration. The UC treatment is a buildup synthetic scheme that involves starting materials and the following four steps (Figure 7.11) namely, carbon matrix (CNF), Ti, and Li sources are premixed, (1) starting ultracentrifuging which initiates unbundling of the carbon matrix for maximum dispersion of reactant species, (2) sol-gel reaction takes place and produces the Li₄Ti₅O₁₂ precursor *in situ* on carbon, and (3) terminating UC induces rebundling and restructuring of the carbon matrix to form a “nano-nano composite,” highly dispersed with nanoscale Li₄Ti₅O₁₂ precursors. This process simultaneously produces a mesoporous network that acts as an electrolyte reservoir due to a pillar effect of trapped LTO precursors. (4) Post-heat treatment effectively completes the crystallization process, producing LTO spinel structures without crystal growth [10, 23].

XRD analysis was performed to confirm the formation of nc-Li₄Ti₅O₁₂ and to detect the presence of CNF in the nc-Li₄Ti₅O₁₂/CNF composites. Figure 7.12a shows the XRD patterns of the prepared nc-Li₄Ti₅O₁₂/CNF composite and pristine CNF. The composite has several sharp diffraction peaks at $2\theta = 18, 35, 42, 57,$ and 63° . These peaks correspond to (111), (311), (400), (511), and (440) planes of a face-centered cubic spinel structure with $Fd\bar{3}m$ space group [26, 27], respectively, indicative of the formation of crystalline Li₄Ti₅O₁₂ after annealing at 900 °C under vacuum. A broad peak at around $2\theta = 24.5^\circ$ is observed, which corresponds to the (002) plane of the pristine CNF [28]. This means that the CNFs exist in the annealed

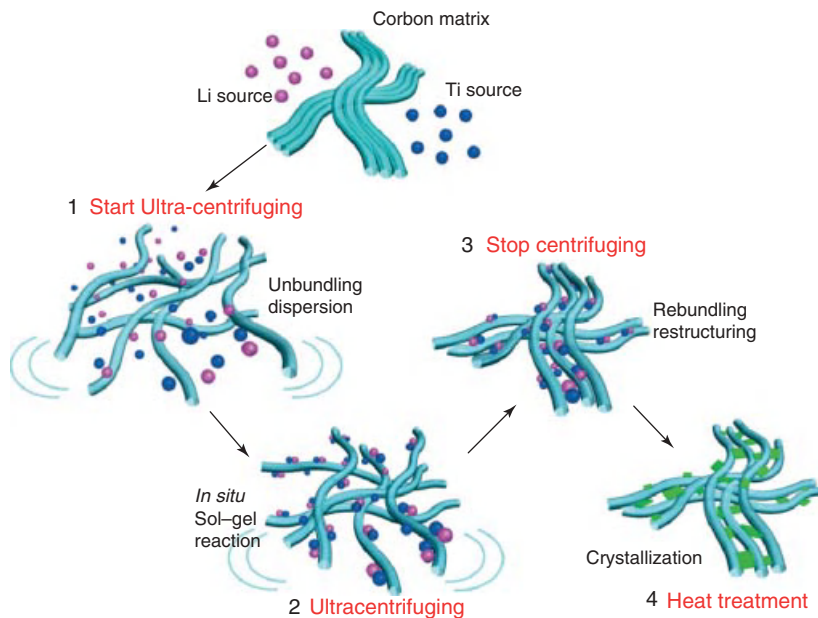


Figure 7.11 Concept of “ultra-centrifuging (UC) treatment.” The UC treatment involves a simple one-step rapid generation scheme yielding a series of optimized “nano-nano composites,” capable of storing and delivering energy at the highest sustained capacity with remarkable C rates.

composite and preserve their graphene layered structure. The fact that there are no other peaks observed corresponding to some possible impurities such as TiO_2 , Li_2CO_3 , and Li_2TiO_3 [29, 30, 35] suggests that there are only two species, crystalline $\text{Li}_4\text{Ti}_5\text{O}_{12}$ and CNF.

Thermogravimetric (TG) measurement on the nc- $\text{Li}_4\text{Ti}_5\text{O}_{12}$ /CNF composite was performed under air to estimate the weight ratio of CNF. The obtained TG curve is shown in Figure 7.12b. The weight loss at 400–600 °C corresponds to the oxidation of CNF, and exactly 50 wt% of the nc- $\text{Li}_4\text{Ti}_5\text{O}_{12}$ remains. This value is consistent with the $\text{Li}_4\text{Ti}_5\text{O}_{12}$ to CNF weight ratio calculated on the basis of dosed Ti alkoxide weight before the UC method. This fact implies that the sol–gel reaction under UC treatment stoichiometrically proceeds, and the optimized (very short duration) annealing does not cause oxidative decomposition of the CNF. Such a stoichiometric preparation process (UC method and instantaneous annealing) is one of the important factors for cost-effectiveness of capacitor production.

The nanostructure and crystallinity of nc- $\text{Li}_4\text{Ti}_5\text{O}_{12}$ and CNF in the composite were observed by HR-TEM (Figure 7.13 & 7.14). The image indicates that the edge or defect graphene sites of CNF accommodate and graft nc- $\text{Li}_4\text{Ti}_5\text{O}_{12}$ particles. The clear facet of $\text{Li}_4\text{Ti}_5\text{O}_{12}$ reflects the high crystallinity that is consistent with the sharp XRD lines (Figure 7.12a) despite such a nanosize. Such a high crystallinity results in a reversible, smooth Li^+ insertion performance, and about 100% of coulombic

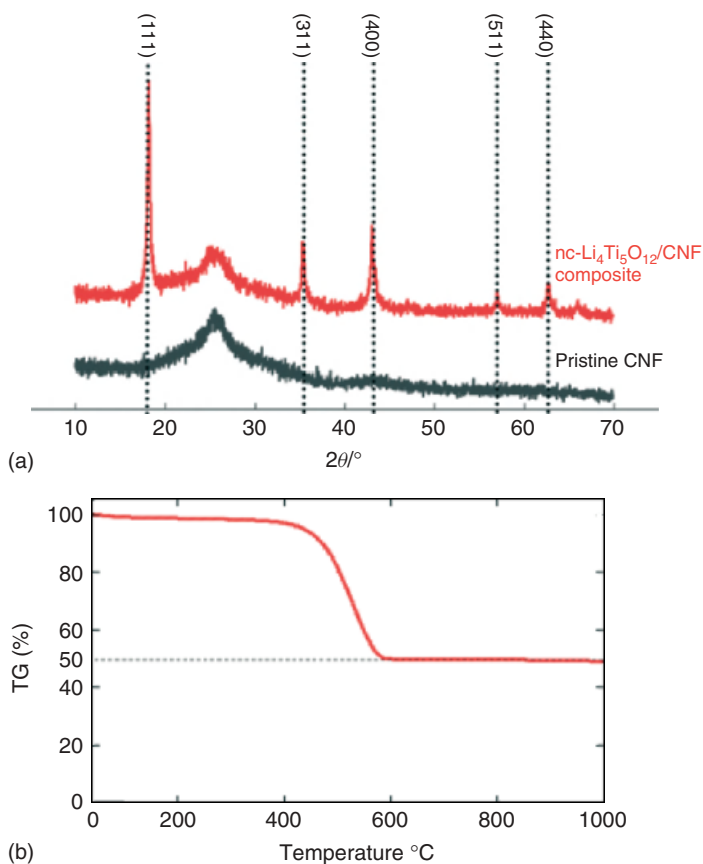


Figure 7.12 (a) XRD patterns of the nc-Li₄Ti₅O₁₂/CNF composite and pristine CNF. (b) TG curve of the nc-Li₄Ti₅O₁₂/CNF composite at 1 °C min⁻¹ under air. The residual weight ratio corresponds to the nc-Li₄Ti₅O₁₂ content in the composite.

efficiency. Also, the HR-TEM images of CNF show clear graphene layers indicative of crystalline structure (Figure 7.13). Thus, this composite is considered to be the junction material of two crystalline species, Li₄Ti₅O₁₂ and CNF (Figure 7.13a). Of particular interest is that the lattice matching of the nc-Li₄Ti₅O₁₂ particles and CNFs is perfect and they are firmly attached (Figure 7.13b). This could bring about an establishment of good electronic paths between the two species.

Another HR-TEM image (Figure 7.14) indicates the multiple attachments of the nc-Li₄Ti₅O₁₂ particles on the inner and outer walls of the CNF graphene substrate. This may indicate that the crystallization would be so efficient on CNF and, more importantly, can enhance both the energy density and the specific gravity of the nc-Li₄Ti₅O₁₂.

Figure 7.15a shows the galvanostatic charge–discharge characteristics of the half-cell Li/(nc-Li₄Ti₅O₁₂/CNF) at 1 C. The plateau at about 1.5 V versus Li/Li⁺

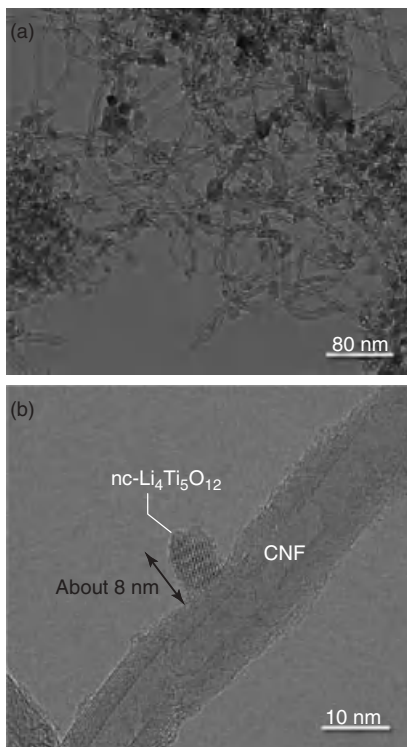


Figure 7.13 Nanostructure of the nc-Li₄Ti₅O₁₂ and CNF. (a) A bird's eye view of a HR-TEM image of the nc-Li₄Ti₅O₁₂/CNF composite. (b) A worm's eye view focusing on the junction of an nc-Li₄Ti₅O₁₂ particle on the CNF surface.

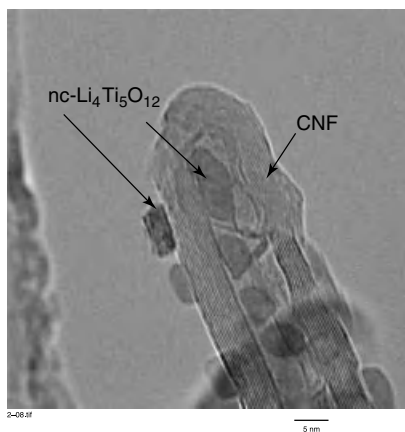


Figure 7.14 HR-TEM image of multiple nc-Li₄Ti₅O₁₂ attachments inside and outside the CNF wall.

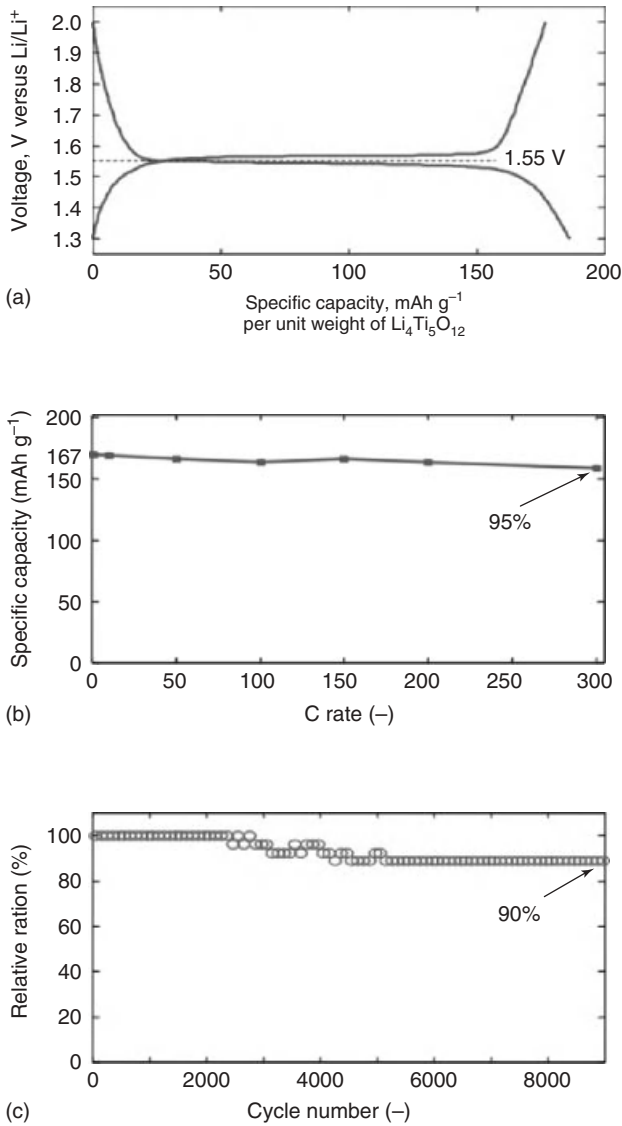


Figure 7.15 Electrochemical properties of the nc-Li₄Ti₅O₁₂/CNF composite in 1M LiBF₄/EC+DEC(1 : 1). (a) Charge–discharge at 1 C. (b) Rate capability in the range from 1 to 300 C. (c) Cycleability at 20 C.

corresponds to the Li^+ intercalation–deintercalation process in crystalline $\text{Li}_4\text{Ti}_5\text{O}_{12}$ [22,24, 27], indicating that the capacity of the composite is determined by the redox capacity of nc- $\text{Li}_4\text{Ti}_5\text{O}_{12}$. The capacity obtained after subtracting the double-layer capacity of the CNF (8 mAh g^{-1}), was 167 mAh g^{-1} per $\text{Li}_4\text{Ti}_5\text{O}_{12}$, which is 95% of the theoretical capacity. This result indicates that almost all of the nc- $\text{Li}_4\text{Ti}_5\text{O}_{12}$ particles in the composite are electrochemically active, meaning that ionic and electric paths are fully established in the composite.

The rate capability of the composite is shown in Figure 7.15b. Even at a high rate of 300 C, the composite shows a reversible capacity of 158 mAh g^{-1} per $\text{Li}_4\text{Ti}_5\text{O}_{12}$ which corresponds to 95% of the capacity obtained at 1 C. Such an excellent rate capability indicates that the optimized nanostructure of the nc- $\text{Li}_4\text{Ti}_5\text{O}_{12}$ /CNF composites as observed in HR-TEM images well overcomes the inherent problems of the $\text{Li}_4\text{Ti}_5\text{O}_{12}$ material, such as poor Li^+ diffusivity and poor electronic conductivity. Probably, this is because the nanocrystallized $\text{Li}_4\text{Ti}_5\text{O}_{12}$ and $\text{Li}_4\text{Ti}_5\text{O}_{12}$ /CNF junctions lead to facile ionic diffusion and electronic conduction, respectively. The cyclability of the composite is shown in Figure 7.15c. Even after 9000 cycles, 90% of the initial capacity is maintained, showing that the composite is electrochemically stable. The result strongly suggests that the aggregation and detachment of the nc- $\text{Li}_4\text{Ti}_5\text{O}_{12}$ particles hardly happen during operation at high charge–discharge rate for a prolonged cycling.

Figure 7.16 shows Ragone plots obtained from charge–discharge measurements for the hybrid ((nc- $\text{Li}_4\text{Ti}_5\text{O}_{12}$ /CNF)/ LiBF_4 -PC/AC) cell. The charge–discharge was performed between 1.5 and 3.0 V at various current densities ranging from 0.2 to 30 mA cm^{-2} (0.18 – 26.8 A g^{-1}). For comparison, a conventional EDLC system (AC/TEABF₄-PC/AC) was also assembled and measured between 0 and 2.5 V. In the low-power density range of 0.1 – 1 kW l^{-1} , the hybrid capacitor shows an energy density of 28 – 30 Wh l^{-1} , which is a value comparable to that of the Li-ion capacitors [3]. Even at a high power of 6 kW l^{-1} , the energy density of the hybrid capacitor remains at 15 Wh l^{-1} , which is double that of the conventional EDLC system (AC/AC). Accordingly, this configuration of the capacitor system is anticipated as an energy device utilizable for both high-energy and high-power applications.

7.5

Conclusion

Practical research and development are now vigorously conducted to improve the energy density of the existing electrochemical capacitors. Soon, we will witness high-energy density capacitors of the next generation. Hybrid capacitors attract much attention owing to their higher withstanding voltage and increase in energy density. In fact, the appearance of LIC and NHCs is certainly regarded as the beginning of an “age of tripled energy density.” If the cost is reduced enough to meet the market’s demand, they will surely grow in business.

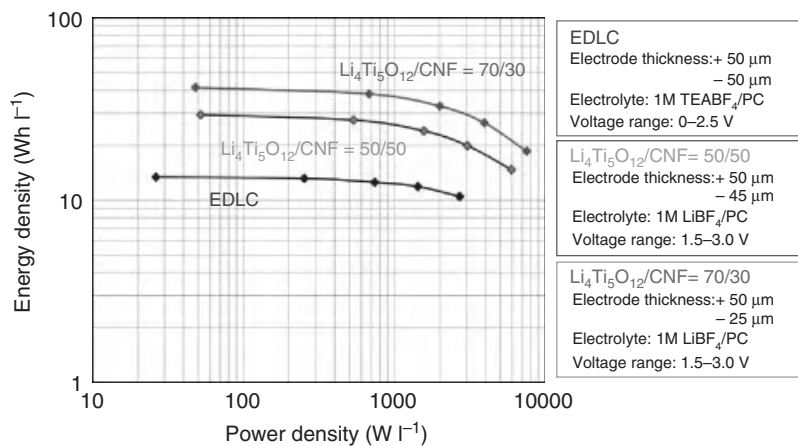


Figure 7.16 Ragone plots of nanohybrid capacitors ((nc-Li₄Ti₅O₁₂/CNF)/AC) with two different Li₄Ti₅O₁₂ loadings (50 and 70%) and conventional EDLC (AC/AC) all in 1 M LiBF₄/PC.

Abbreviations

AC	activated carbon
CNT	carbon nanotube
HC	hard carbon
PAC	polyacene
CB	carbon black
CNF	carbon nano fiber
EC	ethylene carbonate
PC	propylene carbonate
DMC	dimethyl carbonate
AN	acetonitrile
Al	aluminum
Cu	copper
pos	positive electrode
neg	negative electrode
SEI	solid electrolyte interface
DEC	diethylcarbonate
LTO	Li ₄ Ti ₅ O ₁₂
XRD	x-ray diffraction

References

- Burke, A. (2007) *Electrochim. Acta*, **53**, 1083.
- Simon, P. and Gogotsi, Y. (2008) *Nat. Mater.*, **7**, 845.
- Yoshino, A., Tsubata, T., Shimoyamada, M., Satake, H., Okano, Y., Mori, S., and Yata, S. (2004) *J. Electrochem. Soc.*, **151**, A2180.

4. Hato, Y. (2007) *Jidosha Gijutsu*, **61**, 62.
5. Khomenko, V., Raymundo-Piñero, E., and Béguin, F. (2008) *J. Power Sources*, **177**, 643.
6. Azais, P., Duclaux, L., Florian, P., Massiot, D., Lillo-Rodenas, M.-A., Linares-Solano, A., Peres, J.-P., Jehoulet, C., and Béguin, F. (2007) *J. Power Sources*, **171**, 1046.
7. Burke, A. (2000) *J. Power Sources*, **91**, 37.
8. Pandolfo, A.G. and Hollenkamp, A.F. (2006) *J. Power Sources*, **157**, 11.
9. Köetz, R. and Carlen, M. (2000) *Electrochim. Acta*, **45**, 2483.
10. Plitz, I., DuPasquier, A., Badway, F., Gural, J., Pereira, N., Gmitter, A., and Amatucci, G.G. (2006) *Appl. Phys. A*, **82**, 615.
11. Duffy, N.W., Baldsing, W., and Pandolfo, A.G. (2008) *Electrochim. Acta*, **54**, 535.
12. Kazaryan, S.A., Kharisov, G.G., Litvinenko, S.V., and Kogan, V.I. (2007) *J. Electrochem. Soc.*, **154**, A751.
13. Laforgue, A., Simon, P., Fauvarque, J.F., Mastragostino, M., Soavi, F., Sarrau, J.F., Lailler, P., Conte, M., Rossi, E., and Saguatti, S. (2003) *J. Electrochem. Soc.*, **150**, A645.
14. Machida, K., Suematsu, S., Ishimoto, S., and Tamamitsu, K. (2008) *J. Electrochem. Soc.*, **155**, A970.
15. Tasaki, S., Ando, N., Nagai, M., Shirakami, A., Matsui, K., and Hato, (2006) Lithium ion capacitor. WO 2006/112067.
16. Amatucci, G.G., Badway, F., Pasquier, A.D., and Zheng, T. (2001) *J. Electrochem. Soc.*, **148**, A930.
17. Takai, S., Kamata, M., Fujine, S., Yoneda, K., Kanda, K., and Esaka, T. (1999) *Solid State Ionics*, **123**, 165.
18. Chen, C.H., Vaughey, J.T., Jansen, A.N., Dees, D.W., Kahaian, A.J., Goacher, T., and Thackeray, M.M. (2001) *J. Electrochem. Soc.*, **148**, A102.
19. Naoi, K. and Simon, P. (2008) *Interface*, **17**, 34.
20. Yoshida, M. (2008) *Nikkei Electron.*, **991**, 77.
21. Shu, J. (2008) *Electrochem. Solid-State Lett.*, **11**, A238.
22. Naoi, K. (2010) *Fuel Cells*, **10**, 825.
23. Huang, S., Wen, Z., Zhu, X., and Gu, Z. (2004) *Electrochem. Commun.*, **6**, 1093.
24. Naoi, K., Ishimoto, S., Isobe, Y., and Aoyagi, S. (2010) *J. Power Sources*, **195**, 6250.
25. Naoi, K., Ishimoto, S., Ogihara, N., Nakagawa, Y., and Hatta, S. (2009) *J. Electrochem. Soc.*, **156**, A52.
26. Ohzuku, T., Ueda, A., and Yamamoto, N. (1995) *J. Electrochem. Soc.*, **142**, 1431.
27. Thackeray, M.M. (1995) *J. Electrochem. Soc.*, **142**, 2558.
28. Zhou, J.H., Sui, Z.J., Li, P., Chen, D., Dai, Y.C., and Yuan, W.K. (2006) *Carbon*, **44**, 3255.
29. Shen, C.M., Zhang, X.G., Zhou, Y.K., and Li, H.L. (2002) *Mater. Chem. Phys.*, **78**, 437.
30. Hao, Y., Lai, Q., Xu, Z., Liu, X., and Ji, X. (2005) *Solid State Ionics*, **176**, 1201.
31. Ishimoto, S., Asakawa, Y., Shinya, M., and Naoi, K. (2009) *J. Electrochem. Soc.*, **156**, A563.
32. Kim, J. and Cho, J. (2007) *Electrochem. Solid-State Lett.*, **10**, A81.
33. Yu, H., Zhang, X., Jalbout, A.F., Yan, X., Pan, X., Xie, H., and Wang, R. (2008) *Electrochim. Acta*, **53**, 4200.
34. Huang, J. and Jiang, Z. (2008) *Electrochim. Acta*, **53**, 7756.
35. Bai, Y., Wang, F., Wu, F., Wu, C., and Bao, L.Y. (2008) *Electrochim. Acta*, **54**, 322.

8

Asymmetric and Hybrid Devices in Aqueous Electrolytes

Thierry Brousse, Daniel Bélanger, and Daniel Guay

8.1

Introduction

Carbon-based symmetrical electrochemical double-layer capacitors (EDLCs) demonstrate higher energy density and power capability in organic-based electrolytes compared to aqueous-based electrolytes owing to their high operating voltage (2.5–2.7 V). Indeed, despite a lower capacitance of carbon-based electrodes in organic electrolytes (C), the maximum energy density (E_{\max}) is expressed as

$$E_{\max} = \frac{1}{2} C U_{\max}^2 \quad (8.1)$$

and is proportional to the square of the maximum operating voltage (U_{\max}), which is limited to the water electrochemical stability window that cannot theoretically exceed 1.23 V. Thus, even if the capacitance of a symmetrical carbon-based device in an aqueous electrolyte is twice that of an EDLC in an organic electrolyte ($C_{\text{aq}} = 2C_{\text{org}}$), the maximum operating voltage of an organic-based device is more than twice that of an aqueous-based capacitor ($U_{\text{org}} = 2U_{\text{aq}}$) resulting in:

$$E_{\text{org}} = \frac{1}{2} C_{\text{org}} U_{\text{org}}^2 = \frac{1}{2} \left(\frac{1}{2} C_{\text{aq}} \right) (2U_{\text{aq}})^2 = 2E_{\text{aq}} \quad (8.2)$$

Obviously, this simple calculation does not take into account additional factors such as electrolyte concentration, ionic conductivity, packaging, and so on, but some more detailed theoretical calculation [1] points out the superiority of symmetrical carbon-based EDLC in an organic electrolyte (5.7 vs 1.7 Wh kg⁻¹ for symmetrical carbon-based devices in aqueous electrolytes). Practically, the superiority of organic-based carbon/carbon devices has been demonstrated and most commercial-based devices use organic electrolytes.

However, aqueous-based devices possess a number of advantages that can be emphasized in a commercial system, such as their high ionic conductivity, which can be useful to achieve high power density [2, 3]. In addition, the electrothermal safety of aqueous-based devices will be greater in all cases than for organic-based electrolytes [4], which is one of the major points now addressed by electrochemical capacitor (EC) manufacturers as high currents and fast cycling rates are usually required, thus possibly leading to thermal rather than chemical runaway of the

devices. Even device manufacturing will cause less technical stress (no special atmosphere required for manufacturing the devices, no organic solvents, etc.) and concomitantly will help reduce manufacturing costs when aqueous electrolytes are preferred to organic-based media.

According to Eqs. (8.1) and (8.2), an obvious way to increase the energy density of an aqueous-based device is to overcome the theoretical electrochemical stability window of water and/or to enhance cell capacitance. This last solution has been shown to be efficient when pseudocapacitive RuO_2 symmetrical devices are designed [5]. However, the operating cell voltage is still limited to ≈ 1.2 V.

Not all aqueous-based electrochemical devices are limited to 1.2 V operating voltage. Several battery-type systems exceed this value by play exploiting the gas (oxygen/hydrogen) evolution overpotential, which strongly depends on the chemical nature of the electrodes. The best example is the lead-acid battery that exhibits an operating voltage above 2 V in concentrated H_2SO_4 acid [6]. The same trend is observed for nickel-zinc secondary batteries for which the operating voltage is close to 1.65 V. This has given rise to a series of devices using a negative carbon-based capacitive electrode and a positive faradic one, such as PbO_2 or $\text{Ni}(\text{OH})_2$ electrode [7–9]. These devices exhibit an operating cell voltage of 2.25 and 1.65 V for the PbO_2 or $\text{Ni}(\text{OH})_2$ positive electrode, respectively. As they are operated in concentrated H_2SO_4 or KOH aqueous electrolytes, they get the beneficial effects of high ionic conductivity, thermal stability, and ease of manufacturing. The second main effect of replacing a capacitive positive electrode by a faradic one is the drastic increase in cell overall capacitance owing to the very high capacity of the positive faradic electrode compared to a carbon capacitive electrode: 1041 C g^{-1} for $\text{Ni}(\text{OH})_2$ or 807 C g^{-1} for PbO_2 vs 280 C g^{-1} for an activated carbon (AC) electrode ($\approx 280 \text{ F g}^{-1}$) operated on a 1 V potential range. However, the use of a faradic electrode instead of a capacitive one has several drawbacks such as poor cycling ability compared to the carbon-based electrode, structural and microstructural changes on cycling, limited power capability, and so on, but different solutions have been proposed to overcome these drawbacks.

As previously mentioned, another approach to increase the energy density of aqueous-based ECs is the use of pseudocapacitive electrodes such as RuO_2 or, more recently, MnO_2 [10]. Despite an increase in cell capacitance, the cell voltage limitation in oxide-based symmetrical devices is still a problem to increase the energy density. As for carbon- PbO_2 or carbon- $\text{Ni}(\text{OH})_2$ cells, the use of two different electrodes can widen the cell voltage. This has been recently proposed for MnO_2 -based ECs, where the negative electrode of a symmetrical $\text{MnO}_2/\text{MnO}_2$ device was replaced by AC [11–13], conducting polymer [14], or iron oxides [15] in a mild aqueous electrolyte, thus enabling the electrode to reach a more negative potential with an increased cell voltage as a result [10]. As MnO_2 is a pseudocapacitive electrode with a capacitance value close to that of AC in a mild aqueous electrolyte, the AC/ MnO_2 asymmetric device looks like a symmetric one. Consequently, the energy density increase is based on the widening of the cell voltage compared to a symmetrical $\text{MnO}_2/\text{MnO}_2$ EC. Increasing the cell voltage from ≈ 1 to 2 V for AC/ MnO_2 asymmetric EC leads to a four times increase in

the energy density. The figures are similar to those reported for AC/Ni(OH)₂ or AC/PbO₂ but with the great advantage of maintaining long-term cycling ability on the MnO₂ positive electrode, and subsequently on the AC/MnO₂ device, owing to its pseudocapacitive behavior.

Finally, it is also possible to couple a pseudocapacitive oxide (RuO₂) in H₂SO₄ electrolyte with a porous tantalum oxide positive electrode from an electrolytic capacitor [16]. The resulting device takes advantage of the high-voltage operation of the Ta₂O₅ anode while keeping the negative RuO₂ electrode in its electrochemical stability window. The device exhibits performances closer to those of standard electrolytic capacitors rather than regular ECs, mainly because the cell capacitance is strongly limited by the “dielectric” electrode (Ta₂O₅ anode).

From the designs described above, a question arises about the vocabulary related to these devices. Zheng and Conway [3, 7] explained that they should be called *asymmetric* devices as they are usually assembled with a capacitive carbon electrode coupled with a faradic (PbO₂ or Ni(OH)₂) electrode. However, what should be the right denomination for a capacitive carbon electrode coupled with a pseudocapacitive electrode such as MnO₂? A suggestion can be to term as either *asymmetric* (different materials as positive and negative electrodes) or *hybrid* (battery-type electrode coupled with EDLC-type electrode) a device that is a combination of a faradic electrode together with a capacitive one, and as *asymmetric* a device using only capacitive or pseudocapacitive compounds. Subsequently and in the following section, the AC/Ni(OH)₂ or AC/PbO₂ system will be called *hybrid* or *asymmetric device* and AC/MnO₂ will be called *asymmetric EC*.

The principles ruling the fabrication of these three types of asymmetric aqueous-based ECs are detailed in the following sections, together with representative examples of the different designs and major trends for future hybrid systems.

8.2 Aqueous Hybrid (Asymmetric) Devices

Hybrid devices were proposed by the end of the 1990s. They were an answer to the energy density limitation of symmetrical AC ECs. Combining the advantages of long-term cycling, the fast and reversible AC negative electrode, and those of a high-capacity positive faradic electrode in a highly conductive ionic aqueous electrolyte, they were supposed to fulfill the requirements of high energy, high power density devices.

8.2.1 Principles, Requirements, and Limitations

When a symmetrical AC EC is used in aqueous electrolytes (e.g., KOH or H₂SO₄) [17], it presents limited cell voltage operation owing to gas evolution reactions and carbon oxidation. Subsequently, the maximum operating cell voltage is 1.23 V, but practically this value hardly exceeds 1 V (Figure 8.1). Concomitantly, each carbon

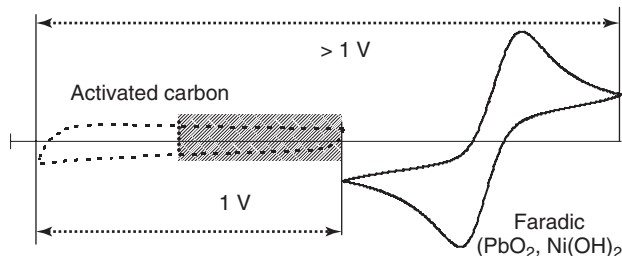


Figure 8.1 Schematic drawing of the cyclic voltammograms of a hybrid device electrode in aqueous electrolyte (KOH, H_2SO_4 , etc.) operating with a negative activated carbon electrode and a positive faradic electrode ($\text{Ni}(\text{OH})_2$, PbO_2). The gain in operating cell voltage is depicted.

electrode has to work in a limited electrochemical window of ≈ 0.5 V (Figure 8.1, dashed area), which means that the resulting capacitance (F g^{-1}) of the carbon symmetrical device is only one fourth that of a single carbon electrode measured in a three-electrode cell configuration [7].

By adding a faradic positive electrode (Figure 8.1), which operates in a complementary electrochemical window thanks to the high oxygen evolution reaction overpotential, the cell voltage is increased above 1 V. In addition, the carbon electrode can now be operated in its full electrochemical window, while the faradic electrode has almost an infinite capacity (C g^{-1}) compared to the capacitive one (Figures 8.1 and 8.2). This results in an overall capacitance that is much higher than that of carbon symmetrical ECs (Figure 8.2). The full calculations of the expected capacitance of such hybrids can be found in Zheng and Conway's papers [3, 7]. The influence of the electrolyte concentration must be taken into account when calculating the optimized weight balance between positive/negative/electrolyte amounts. A maximum energy density of 50 Wh kg^{-1} is calculated for a carbon/ $\text{Ni}(\text{OH})_2$ hybrid device based on 1.65 V working voltage in 6.25 M KOH and 1/3.30/1.97 positive/negative/electrolyte weight ratio, while the same calculation for a symmetrical AC EC in 5.26 M H_2SO_4 leads to 7.2 Wh kg^{-1} [3]. Conway indicates a similar energy density for the carbon/ $\text{Ni}(\text{OH})_2$ hybrid device ($55\text{--}65 \text{ Wh kg}^{-1}$), which can be raised up to $63\text{--}67 \text{ Wh kg}^{-1}$ for the carbon/ PbO_2 hybrid device in H_2SO_4 electrolyte [7]. Not only the energy density but also the power density is supposed to increase compared to that in the symmetrical carbon device (Figure 8.2). However, this last calculation precludes the limits of the hybrid device.

Indeed, all the calculations are usually based on a full use of the faradic electrode capacity, which is difficult to achieve for different reasons, and on a kinetic response of the faradic electrode that is as fast as that of the carbon electrode, which practically will hardly be achieved. Requirements for the faradic electrode in a hybrid device are listed in Conway's paper [7]. To summarize and generalize to other hybrid cells, two main requirements can be specified:

- 1) The capacity (Ah) of the hybrid cell must be limited by the carbon capacitive electrode so that the faradic-type battery electrode can be operated down to a

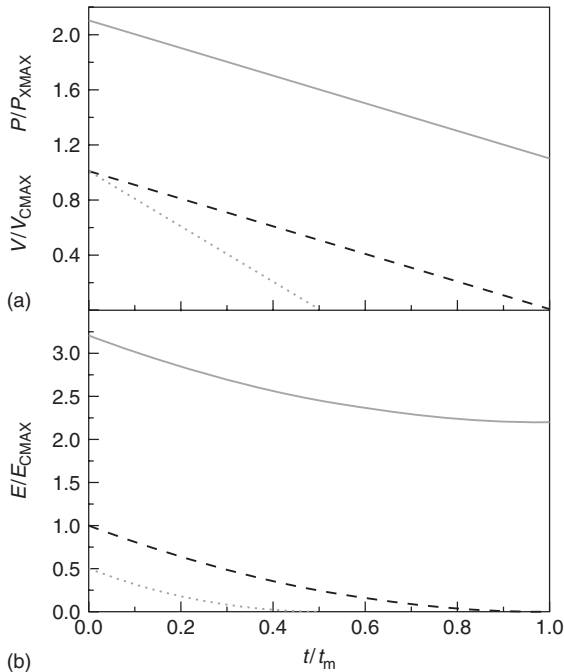


Figure 8.2 Energy, E ; power, P ; and voltage, V for each of a single capacitor electrode (— — —), a symmetric two-electrode capacitor ($\cdot \cdot \cdot$), and an asymmetric capacitor device (—) plotted as $E/E_{C_{MAX}}$, $P/P_{C_{MAX}}$ and $V/V_{C_{MAX}}$ as a function of the reduced time, t/t_m ; where $E_{C_{MAX}}$, $P_{C_{MAX}}$, and $V_{C_{MAX}}$ are the maximum voltage, energy, and power of a single capacitive electrode and t_m is the time to fully discharge the capacitive electrode. From Ref. [7].

reasonable state of charge (SOC). Usually, this SOC cannot exceed 10–50% in order to assure electrode cycle life. Indeed, a large SOC leads to capacity fade of the electrode as in a “standard” secondary battery and only a few hundred (or few thousand) charge/discharge cycles can usually be achieved. A way to extend the cycling ability of the faradic electrode is to limit the SOC. In this case, only a limited amount of the electrode material is affected by the electrochemical cycling, leading to limited structural/microstructural changes. The limited SOC also provides a “reserve” amount of faradic material, which will be activated as some faradic material is consumed and becomes inactive owing to mechanical/chemical modification of the electrode. Subsequently, long-term cycling ability can be achieved with a hybrid device but at the expense of energy density as a larger amount than what is necessary to balance the negative electrode is needed.

- 2) The charge/discharge rate must be adapted to that of the faradic electrode, which is the limiting one for power capability of the hybrid device. Thus, the time constant of the hybrid device is usually 1 or 2 orders of magnitude greater than for symmetric carbon device (≈ 100 – 1000 s instead of 1–10 s).

This suggests that nanostructured faradic electrode material might be used instead of standard microsized compounds in order to promote ionic diffusion in the solid. However, since the surface of the positive and negative electrodes has to be the same for designing the hybrid device, the faradic electrode will be much thinner than the carbon one, thus intrinsically enabling faster charging/discharging rates than a standard battery electrode.

The major hybrid devices proposed up to now are described in the following sections.

8.2.2

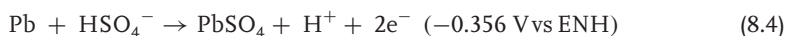
Activated Carbon/PbO₂ Devices

The two half reactions that are occurring in lead-acid batteries during charge and discharge are described by the well-known double sulfate theory [6]:

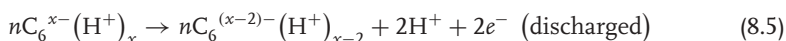
Positive electrode



Negative electrode



One of the earliest asymmetric capacitor device was based on a faradically rechargeable Pb/PbO₂ battery-type electrode with a non-faradically carbon-based rechargeable supercapacitor electrode. In an asymmetric AC/PbO₂ device, the positive electrode and the electrolyte are the same as in a conventional Pb/PbO₂ battery but the negative electrode is replaced by a highly reversible double-layer carbon-based electrode whose charge and discharge mechanism is best described by the following equation



Following the convention used by Conway [7], the net overall capacity density, C_T , of an asymmetric capacitor is given by the following equation

$$\frac{1}{C_T} = \frac{1}{C_p} + \frac{1}{C_n} \quad (8.6)$$

where C_p and C_n are the electrode capacities of the positive and negative electrodes, respectively. Thus, the net capacity density is mainly determined by the smaller of the two capacitances. As the PbO₂ faradic electrode has effectively infinite capacitance compared to carbon electrode, this means that C_T will be equal to the capacitance of the negative electrode and that the full charge capacity of that component electrode is then utilizable.

The reduction of PbO₂ to PbSO₄ involves two electrons and the equivalent weight of lead dioxide is 119 g. The equivalent weight of carbon will depend on several factors, including the specific surface area and the specific double-layer capacitance but an effective equivalent weight of 200 g was reported. The mass of

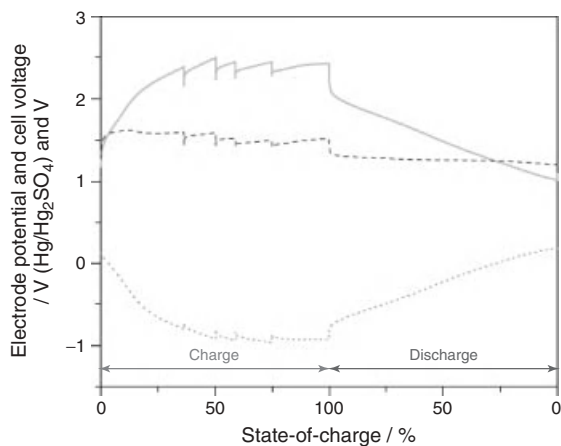


Figure 8.3 Cell voltage (—), anode (· · ·), and cathode (— —) potential with respect to a stable reference electrode as a function of time for recharge and discharge of an asymmetric activated carbon/ PbO_2 device. Taken from Ref. [7].

both electrodes must therefore be adjusted if charge balance is to be achieved in the combined two-electrode system.

In the fully charged state, H^+ are adsorbed at the surface of the negative electrode and are moving to the positive electrode during discharge where they are neutralized to form water. The result is reduced acid concentration swings from the charged to discharged state, which reduces grid corrosion on the positive electrode and leads to longer life of the positive electrode.

The benefit of using a PbO_2 faradic electrode as the positive element in an asymmetric capacitor is particularly evident from an inspection of Figure 8.3, where it is seen that the electrode potential (measured against a stable reference electrode) of the PbO_2 positive electrode varies by less than 100 mV during the successive charge and discharge cycle. This translates into an operating voltage of the asymmetric combination of electrodes that has higher discharge and remains longer than for the symmetric capacitor (Figure 8.2)

The reproducibility of the forms of the cathode/anode half-cycle was maintained over 10 000 cycles and the coulombic and energy efficiencies were better than 90 and 63%, respectively. The coulombic efficiency is similar to that of lead-acid battery but the energy efficiency is somewhat lower.

One of the first asymmetric AC/ PbO_2 devices in the literature was reported in 1998 at a specialized meeting [18] and was discussed in Ref. [19]. The ratio between the active masses of both electrodes was selected so as to ensure the capacitor's operation is limited by the negative electrode and the basic parameters of the device are given in Table 8.1.

However, only a few papers in the literature demonstrate the assembly of the carbon/ PbO_2 hybrid device [7, 20–22], but some companies are proposing products based on this technology. Axion Power International Inc. [23] is proposing a hybrid device known as the *PbC*[®] battery that uses the standard lead-acid battery positive

Table 8.1 Basic parameters of the hybrid electrochemical supercapacitor developed in Russia.

Parameter	Value
Specific capacitance of carbon electrode ($F\ g^{-1}$)	600
Specific energy density ($Wh\ kg^{-1}$)	20–25
Specific volume energy density ($Wh\ dm^{-3}$)	60–75
Maximum discharge voltage (V)	2.0
Minimum discharge voltage (V)	0.5
Internal resistance ($m\Omega$)	3–5
Cycle life (cycles)	10 000
Charge time (min)	20–30
Working temperature ($^{\circ}C$)	–40 to +60

Taken from Ref. [19].

electrode and a high surface area ($1500\ m^2\ g^{-1}$) carbon-based supercapacitor negative electrode. Axion's PbC battery is a sealed unit and requires virtually no maintenance, resulting in low operating costs. It can also be recycled in existing lead-acid battery recycling facilities. Also, manufacturability of PbC batteries is facilitated as it can be done in existing lead-acid battery facilities, thus eliminating large capital investment to build new advanced battery facilities. The rapid charge/discharge capabilities and high power output of PbC battery fit the requirements for hybrid-electric vehicle (HEV) applications. It is believed that the PbC technology can fill the gap between advanced battery technologies and advanced supercapacitors in the energy/power/cost profile. The company is currently working to develop higher power starting batteries with better cold temperature performance, higher energy and longer life deep-cycle batteries.

Apart from the problem related to the cycling ability, which is often solved by adding an excess of PbO_2 at the positive electrode, resulting in a “reserve” of active material, the power capability has been addressed by different groups [21, 24]. The trend is to use a nanostructured lead dioxide electrode, usually thin film, nanowires, etc.) in order to maximize the surface in contact with the electrolyte. Thus, PbO_2 thin films were electrodeposited on the Ti/SnO_2 substrates from the $Pb(NO_3)_2$ solution by the pulse current technique and used as positive electrode in a hybrid device in front of a negative AC electrode in 5.3 M H_2SO_4 solution. The resulting device showed high-power and fair cycle performances (≈ 4000 charge/discharge cycles with 10% energy loss). In the voltage range of 0.8–1.8 V, the PbO_2/AC hybrid system delivered a specific energy density of $\approx 30\ Wh\ kg^{-1}$ at a power density of $1\ kW\ kg^{-1}$ based on the total weight of both active electrode materials [21] (Figure 8.4).

PbO_2 nanowires have shown improved energy density and power capability compared to thin films, but the benefit of the nanostructure is lost after few cycles owing to microstructural changes occurring on sulfatation [24] (Figure 8.5).

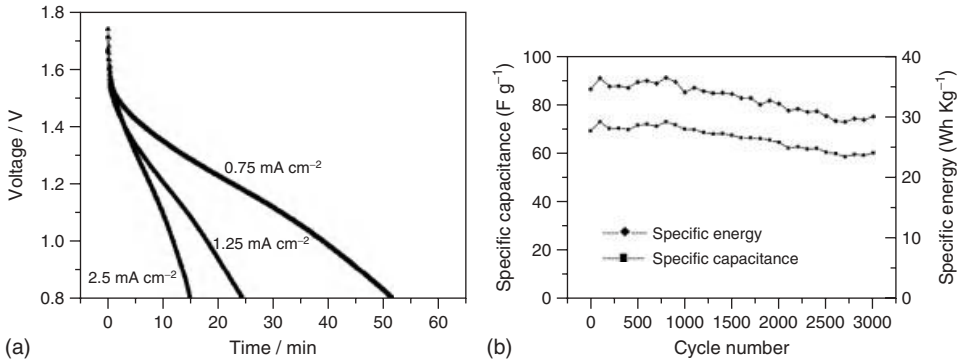


Figure 8.4 (a) Discharge behavior of PbO_2/AC hybrid capacitor at various discharge current densities in H_2SO_4 solution. (b) Cycle performance of active materials of both electrodes at a charge/discharge current of 2.5 mA cm^{-2} (4 C rate) in H_2SO_4 solution. From Ref. [21].

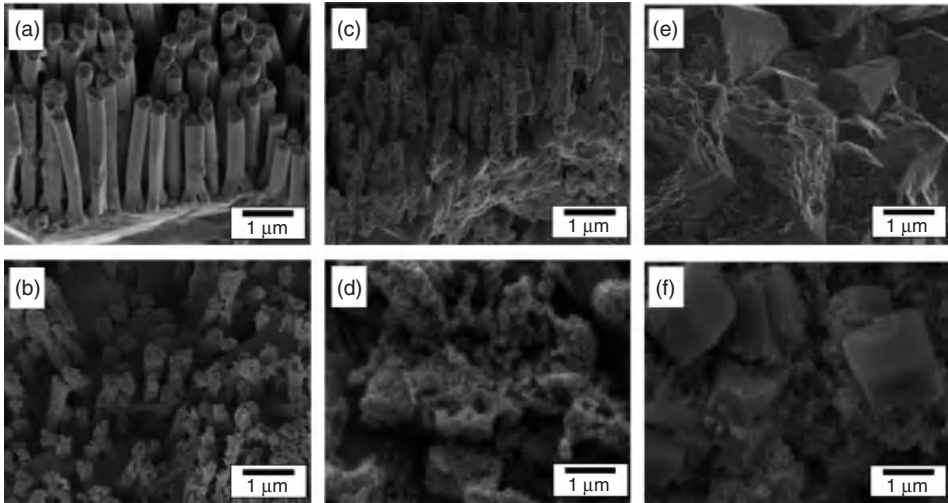


Figure 8.5 SEM micrographs of PbO_2 (a–d) nanowires and (e) and (f) thin film after cycling in 1 M H_2SO_4 : (a) and (e) as-deposited and (b) 3 cycles, (c) 5 cycles, and (d) and (f) 10 cycles. The deposition charge was 40 C for the PbO_2 nanowires and thin film. All samples were examined in the charged state. Taken from Ref. [24].

An analysis was performed to find a common mathematical expression to describe how the reactivity of PbO_2 thin films and nanowires vary with the deposition charge and how it evolves with cycling [24]. This was done by assuming that the reactivity r is given by the following expression

$$r = a(Q_{\text{dep}})^b = \frac{Q_{\text{red}}}{Q_{\text{dep}}} \quad (8.7)$$

where Q_{dep} is the deposition charge, and a and b are two independent parameters. For $b = 0$, the reactivity is constant and independent of the deposition charge. Hence, Eq. (8.7) translates into

$$Q_{\text{red}} = a Q_{\text{dep}} \quad (8.8)$$

This would be the case for nanowires growing perpendicular to the surface of the substrate, assuming that the electrolyte has access to the whole surface of the nanowire. Assuming that the thickness of the reacting layer at the surface of the nanowire is constant, increasing the length of the nanowires would yield a constant r value. This is obviously the best-case scenario because the charge that can be extracted from PbO_2 , which is given by $r \times Q_{\text{dep}}$, would increase linearly with the amount of material deposited. In contrast, for $b = -1$, Eq. (8.7) shows that the reactivity decreases with Q_{dep} . Indeed, $b = -1$ corresponds to the case where Q_{red} is fixed and independent of the deposition charge

$$Q_{\text{red}} = a \quad (8.9)$$

This would be the case of a dense thin film growing in a direction perpendicular to the substrate surface and whose reactivity is limited to a fixed layer thickness at the outermost surface close to the film/electrolyte interface. Assuming that the thickness of the reacting layer is fixed, increasing the thickness of the deposited layer decreases the reactivity of the layer.

As expected from the previous theoretical calculations, the b value of PbO_2 nanowires is closer to 0, while that of PbO_2 thin films is closer to -1 . However, after 10 charge/discharge cycles, the a and b parameters for thin films and nanowires reached the same values and the initial effect of the nanostructured electrode is completely lost. Thus, the use of H_2SO_4 as electrolyte is detrimental to power capability and long-term cycling despite its high ionic conductivity.

Alternative electrolytes such as methanesulfonic acid already used in redox flowcell [25] can be used in carbon/ PbO_2 devices, leading to improved cycling ability [26].

Another strategy for improving the energy density of the carbon/ PbO_2 hybrid device is to lower its weight. Indeed, the total weight of the hybrid carbon/ PbO_2 device is mainly controlled by the weight of the positive electrode and especially the current collector, which is still based on metallic lead. A substantial gain in weight can be made by using a carbon-based substrate on which a thick Pb or Pb-Sn film is deposited. Compared to bulk lead-tin grids, the layered current collector can reach 1/10 in weight with good cycling performance in 5 M H_2SO_4 [27].

A related concept was developed by Lam and Louey [28] (from CSIRO Energy Technologies) by adding a carbon-based supercapacitive negative electrode to the faradic sponge Pb negative electrode (Figure 8.6) to yield what is termed an *ultrabattery*. With this design, it is hoped that the carbon-based supercapacitive negative electrode will enhance the power and lifespan of the lead-acid battery by acting as a buffer during charging and discharging. To achieve this, hydrogen evolution from the combined Pb and C negative electrode should be minimized since it can lead to a permanent loss of water (the same phenomenon could occur

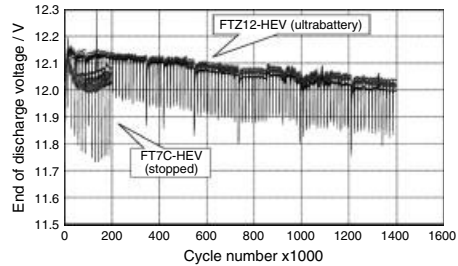
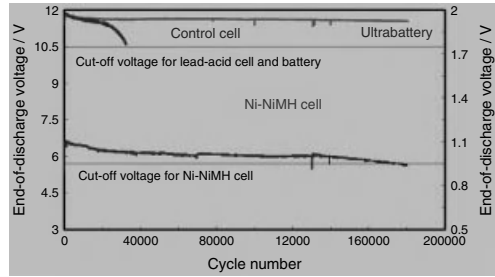
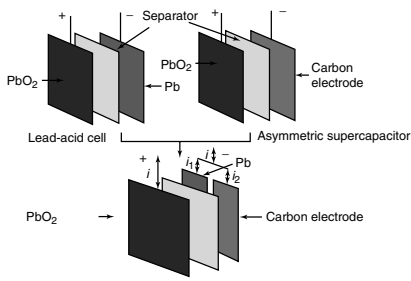


Figure 8.6 Schematic view of the UltraBattery and UltraBattery cycling versus NiMH under the EUCAR power-assist profile, the UltraBattery in place and changes in the discharge voltages

of individual conventional VRLA batteries and VR UltraBatteries in the respective 144-V strings during testing under the simulated, medium-HEV duty. From Refs. [30, 31].

in valve-regulated lead-acid battery, VRLA) [29]. To achieve this, an additive is used to reduce the hydrogen evolution current of the carbon-based electrode to the level typical of the lead-acid negative plate. The ultrabattery with a capacity of 30 Ah has been demonstrated, with more than 100 000 cycles. A cost analysis was performed showing significant advantages compared to competing energy-storage technologies. Again, these ultrabatteries can be produced and recycled in existing lead-acid battery factories and recycling facilities. An UltraBattery commercialization and distribution agreement with Japan's Furukawa Battery Company and United States manufacturer, East Penn, was signed in 2007 by CSIRO. This UltraBattery has been used in HEVs (medium HEV and micro HEV) and the performances have been reported in a series of papers [30, 31], showing the excellent performances of the design compared to standard VRLA batteries (Figure 8.6).

8.2.3

Activated Carbon/ $\text{Ni}(\text{OH})_2$ Hybrid Devices

Hybrid devices based on AC and nickel oxide/hydroxide as negative and positive electrodes, respectively, in the presence of an alkaline electrolyte has been initially disclosed by Russian groups at the end of the 1990s [8, 32]. These devices comprised

the common capacitive carbon electrode and a faradic Ni-oxide-based electrode similar to those used in Ni-Cd or nickel metal hydride battery. Interestingly, these systems are commercially available and more information can be found on the web site of ESMA [33]. More specifically, performance (operating voltage range, capacitance, energy stored, and internal ohmic resistance) is provided for capacitor cells. A typical cell voltage for these charged devices is 1.5 V, whereas the capacitance of a cell varied from 3 to 80 kF. A wide variety of capacitor modules made of these individual single cells are commercially available.

The use of a nickel hydroxide electrode has been shown to improve the performance (larger cell voltage and specific energy) in comparison with a symmetrical cell where both electrodes are made of carbon. Some information about the characteristics and performance of these systems can be found in a review on ECs [34]. It should be noted that these devices, similar to the AC/PbO₂ device behave more like a battery than a classical electrical double-layer capacitor. In fact, in the charge–discharge curves of such a hybrid device, the potential of the AC negative electrode cycled linearly over a wide potential range, while that of the nickel oxide positive electrode only slightly varied during charging and discharging. This is illustrated in Figure 8.7 for devices made of an AC (negative electrode) and Ni foam/nickel oxide (positive electrode).

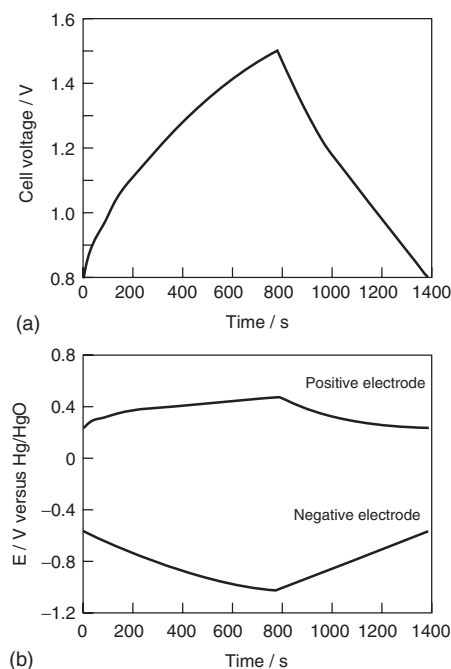


Figure 8.7 Variation in the cell voltage and the individual positive and negative electrodes during constant current charge/discharge of the hybrid capacitor. Reprinted from Refs. [35].

The commercialization of the ESMA cell and the interest in the EC have apparently stimulated more academic work on this system in the past decade [35–38]. These recent studies mostly focused on preparing nickel oxide by various methods and using various substrates onto which the metal oxide is deposited. For example, nickel oxide/hydroxide electrode was prepared by chemical bath deposition on a Ni foam substrate from a nickel sulfate solution [35]. Alternatively, hierarchical nickel oxide characterized by flower-like macroporous morphology was synthesized by a template-directed method based on commercially available block copolymer [38].

One disadvantage of the hybrid device relative to the symmetrical capacitor is its lower specific power densities. In one of the earliest studies on the AC/nickel oxide capacitor, the nickel oxide was mixed with AC in order to enhance the power density of the device [36]. With this new composite material (AC + nickel oxide), the rate capability of the hybrid capacitor was slightly improved in comparison with a system using only nickel oxide as the positive electrode.

Attempts have also been made to improve the energy and power densities of AC/Ni(OH)₂ device by increasing the capacity of the nickel-based electrodes. The resulting devices still operate in KOH or LiOH but nickel in the positive electrode is substituted by cobalt, manganese, or zinc, leading to the following electrode compositions: (Ni_{1/3}Co_{1/3}Mn_{1/3})(OH)₂ [39] or (Ni,Zn,Co)Co₂O₄ [40]. Alternatively, the nickel electrode can be completely replaced by nanostructured cobalt hydroxide [41, 42].

8.2.4

Aqueous-Based Hybrid Devices Based on Activated Carbon and Conducting Polymers

Electronically conducting polymers have been the subject of several studies since their discovery more than 30 years ago [43]. Some of these studies, a relatively small number in comparison to the body of literature on conducting polymers, have dealt with the use of these materials as active electrode materials in ECs. These studies have been reviewed in the past and the properties and performance of the various electrode materials will not be discussed here. Rather, this section specifically focuses on application of conducting polymers in hybrid devices that make use of an AC as the negative electrode and limited to those based on aqueous electrolytes. Hybrid systems based on a conducting polymer and electrode materials other than carbons (e.g., MnO₂) are discussed subsequently (Section 8.3.2).

Electronically conducting polymers generated some interest in the 1990s and their application as active electrode materials in ECs was envisioned because of the fast faradic redox reactions that occur not only at the polymer/electrolyte interface but also within the bulk. Consequently, these materials will be characterized by specific capacitance values higher than that of a capacitive material such as carbon for which charge storage occurs only at the interface. Thus, these materials have the potential for high specific energy and power densities. Most of these studies focused on the study of a single electrode and measurements with complete cells built with conducting polymers as electrode are limited. Furthermore, in the majority of these

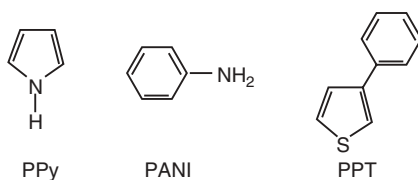


Figure 8.8 Pyrrole, aniline, and phenylthiophene monomers that are the precursors of the corresponding polymers, polypyrrole (PPy), polyaniline (PANI), and poly(3-phenylthiophene) (PPT), respectively.

studies, organic-based electrolytes were used. Electronically conducting polymers used in ECs consisted mainly of three different materials (Figure 8.8), namely, polypyrrole, polythiophene, and polyaniline derivatives but not limited to them [44]. When conducting polymers were used as both the positive and negative electrode, a major concern was their stability, especially for polythiophene derivatives that are prone to degradation when used as negative electrode [45].

It is important to point out that the initial AC/conducting polymer hybrid ECs were based on organic electrolytes [46–49]. This concept has been proposed to solve the problem associated with the instability of the negative conducting polymer electrode.

In the case of aqueous electrolytes, an AC/polyaniline device was developed using polyaniline as a positive electrode and AC as a negative electrode [50]. Polyaniline was produced by oxidative chemical polymerization. The hybrid capacitor can develop a cell voltage of 1.6 V in 6 M KOH electrolyte and can be cycled between 1 and 1.6 V (Figure 8.9), which is the potential range for which polyaniline is in its p-doped state and conducting form. The energy and power densities of the device, by taking into account only the weight of the electrode material, were 18 Wh kg⁻¹ and 1.25 kW kg⁻¹, respectively, and improved compared to those of symmetrical devices.

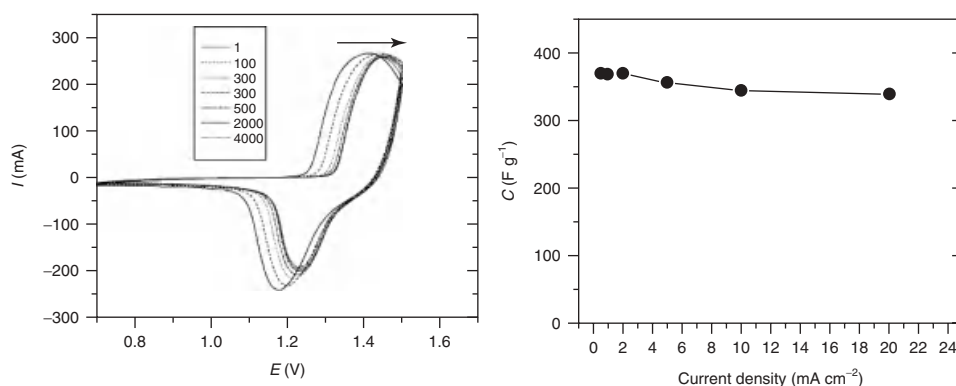


Figure 8.9 Cyclic voltammograms for PANI-AC hybrid EC capacitor as function of cycle number and specific capacitances of PANI-AC hybrid EC capacitor as function of charge-discharge current density. Reproduced from Ref. [50].

Table 8.2 Performance of various symmetrical and hybrid electrochemical capacitors.

Electrode materials		Supercapacitor characteristics			
Positive	Negative	U_{\max} (V)	E (Wh kg ⁻¹)	ESR (Ω cm ²)	P_{\max} (kW kg ⁻¹)
PANI	PANI	0.5	3.13	0.36	10.9
PPy	Ppy	0.6	2.38	0.32	19.7
PEDOT	PEDOT	0.6	1.13	0.27	23.8
Carbon Maxsorb	Carbon Maxsorb	0.7	3.74	0.44	22.4
PANI	Carbon Maxsorb	1.0	11.46	0.39	45.6
PPy	Carbon Maxsorb	1.0	7.64	0.37	48.3
PEDOT	Carbon Maxsorb	1.0	3.82	0.33	54.1

Reproduced from Ref. [14].

Béguin and coworkers [14] have reported the improved performance for the hybrid AC/conducting polymer configuration relative to the symmetrical conducting polymers or AC ECs. In their study, polyaniline, polypyrrole, and PEDOT were deposited on carbon nanotubes by chemical polymerization of the corresponding monomers and the performance of the various devices based on these materials and AC as electrodes can be found in Table 8.2. For these studies, the electrolyte was either 1 M H₂SO₄ or 2 M KNO₃. It can be seen that the energy and power densities of the hybrid devices are about twice larger than those of the symmetrical ones. This is due to the larger cell voltage of the hybrid devices, which can reach values of 1 V.

Alternatively, molecular hybrid electrodes (PAni + Polyoxometalates) were synthesized in order to improve the capacitance of the positive electrode in HClO₄-based electrolyte [51].

To the best of our knowledge, aqueous-based hybrid EC using conducting polymers are not commercially available. Theoretical calculations are provided in order to design optimized devices [52]. Snook *et al.* found that the electrode mass ratios have a significant impact on the swing voltages across the positive and negative electrodes. Operating a cell at E_{\max} will deliver the maximum specific energy but involves a trade-off in cycle life. The carbon-based electrode is well designed for achieving long-term cycling ability, but oversizing this electrode will lead to a less-than-optimum specific energy of the device. By limiting the swing on the positive conducting polymer electrode, cycle life is extended as the active material associated with this electrode is prone to early failure because of volume expansion and/or degradation during the redox process [52]. Thus, more work and new ideas are required to enable the development of commercial devices.

Despite interesting energy densities, the power density of aqueous hybrid devices is still limited by the rate capacity of the battery-type electrode as recently pointed out by theoretical calculations [53]. For a hybrid battery/capacitor-type device, its capacity matching ratio and power density increase, while specific capacitance and

energy density decline when the charge/discharge current density increases. This is one of the reasons why other asymmetric devices have been investigated, using EDLC or/and pseudocapacitive electrodes in order to improve the power capability.

8.3

Aqueous Asymmetric Electrochemical Capacitors

The report on the pseudocapacitive behavior of MnO_2 -based electrodes has given rise to a tremendous amount of work focused toward the investigation of the charge storage mechanism, capacitance improvement, cycling ability enhancement, structural/capacitance relationship, influence of the porosity, and so on, in more than 200 papers since 1999. However, only a few authors have pointed out the limited electrochemical window of MnO_2 in mild aqueous electrolytes such as K_2SO_4 or KCl . Subsequently, only a few symmetrical $\text{MnO}_2/\text{MnO}_2$ devices have been fabricated and characterized [13, 54]. The interest in low-cost and environmentally friendly electrodes and electrolytes, together with no-stress manufacturing processes, is lost when energy and power densities are measured on MnO_2 -based symmetrical ECs. A solution to this problem is to use a complementary negative electrode, thus designing an asymmetric EC with MnO_2 as positive electrode. The use of an AC negative electrode enables designing an asymmetric EC, which looks like a symmetrical carbon-based EC. The fact that MnO_2 behaves as a pseudocapacitive electrode, and not a faradic one as described in the previous section, leads to an intrinsically better long-term cycling ability and power capability [55].

8.3.1

Principles, Requirements, and Limitations

The principle of asymmetric ECs relies on the use of two capacitive or pseudocapacitive electrodes with complementary electrochemical windows (Figure 8.10). As for hybrid devices, which use a faradic electrode with a capacitive one, the main goal is to widen the maximum cell operating voltage compared to a symmetrical cell (Figure 8.10). In a symmetrical cell operating with MnO_2 electrodes, for example, the maximum operating cell voltage is ≈ 1.0 V. Each MnO_2 electrode operates in a limited electrochemical window of ≈ 0.5 V (Figure 8.10, dashed area), which means that the resulting capacitance (F g^{-1}) of the symmetrical device is only one fourth that of a single MnO_2 electrode. The use of a negative electrode with about the same capacitance as the positive electrode and complementary electrochemical window (also close to 1 V in the example shown in Figure 8.10) will result in an increase in the energy density by a factor of 4 without much loss in the power capability neither in the long-term cycling ability thanks to the capacitive or/and pseudocapacitive behavior of each electrodes.

Two examples of such asymmetric EC (based on a MnO_2 positive electrode) are depicted in Figure 8.11 and are compared to a symmetrical device using two MnO_2 electrodes [54]. Both the energy and power densities are improved compared to the

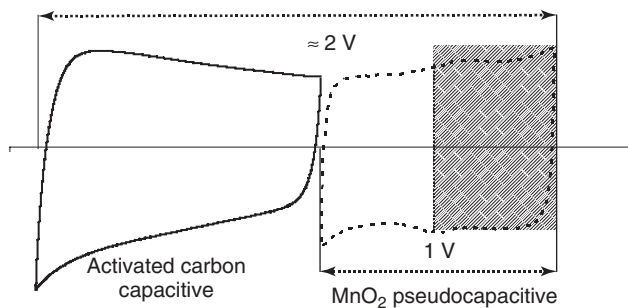


Figure 8.10 Schematic drawing of the cyclic voltammograms of an asymmetric EC electrodes in aqueous electrolyte (K_2SO_4 , etc.) operating with a negative activated carbon electrode and a positive pseudocapacitive electrode (MnO_2). The gain in operating cell voltage is depicted.

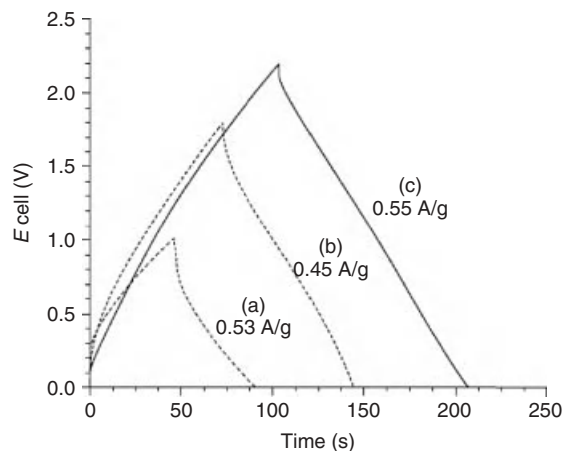


Figure 8.11 Galvanostatic charge/discharge cycles of the different electrochemical capacitors in K_2SO_4 : (a) MnO_2/MnO_2 , (b) Fe_3O_4/MnO_2 , and (c) activated carbon/ MnO_2 . From Ref. [54].

symmetrical device. Note that the shape of the asymmetric EC is similar to that of a carbon-based symmetrical EC.

The main requirements for positive and negative electrodes of the asymmetric EC are as follows:

- 1) Complementary electrochemical operating windows, that is, at least the cell operating voltage must be enhanced by $\approx 30\%$ to see some effect on the energy density.
- 2) Similar capacitance values for the positive and negative electrodes, which will help balance the electrode weight ratio. A negative effect of disproportional capacitance values on one of the electrodes is the difficulty in maintaining each electrode in its own electrochemical stability window upon long term cycling experiments.

- 3) Long-term cycling ability of each electrode that will result in the long-term cycling ability of the asymmetric EC.
- 4) Similar power capability of both electrodes in order to achieve high power density on the resulting device.

Usually, the two last requirements are the most difficult to fulfill. Many compounds have been proposed as potential pseudocapacitive electrodes for ECs but practically they hardly demonstrated more than a few hundred or few thousand cycles. Only RuO₂ [56], MnO₂ [55, 57], and to a less extent Fe₃O₄ [15, 58] have proved their good cycling ability, that is, more than 10 000 charge/discharge cycles.

The power capability is less difficult to achieve compared to a faradic battery electrode but there is often a factor of 2–10 on the time constant of a pseudocapacitive electrode compared to an AC-based electrode, which means that the resulting asymmetric EC cannot be operated below 5–10 s at constant current charge or discharge.

8.3.2

Activated Carbon/MnO₂ Devices

As previously stated, the assembly of AC/MnO₂ asymmetric devices was proposed as a pertinent strategy to overcome the limited voltage window of symmetrical MnO₂ EC. Since the first reports by Hong *et al.* [11] and Brousse *et al.* [12], the concept has been widely validated by different teams so that the feasibility of such a device is now recognized. Table 8.3 summarizes some of the most interesting MnO₂-based asymmetric devices.

From Table 8.3, it can be seen that combining most of the AC/MnO₂ asymmetric devices are operating at ≈ 2.0 V or even higher (2.2 V). Because of the enhanced operating voltage, the AC(–)/MnO₂(+) combination provides energy densities up to 28.8 Wh kg^{–1} (normalized to the total active material mass), nearly 1 order of magnitude higher than that for symmetrical MnO₂ devices, and comparable to conventional symmetric carbon/carbon ECs that utilize nonaqueous electrolytes.

The long-term cycling stability of the AC/MnO₂ asymmetric device has also been demonstrated by different authors [12, 55, 59, 61–63] and up to 190 000 cycles are reported with less than 20% capacity loss (Figure 8.12). Different parameters seem to influence the cycle life of the manganese dioxide electrode, for example, a steady mechanical failure of the MnO₂ electrode on cycling caused by cyclic volumetric variations of the oxide particles depending on the pristine MnO₂ polymorph [64]. Oxygen evolution reaction is also suspected to affect the electrode/current collector interface and promote corrosion problems [55], ultimately increasing the equivalent series resistance (ESR) of the cell.

Another drastic problem is related to manganese dissolution, which leads to a progressive loss of active material and a subsequent capacitance fade on cycling [65–67]. This is the reason why, for practical cells, it is important to carefully balance the mass and capacitance of the positive and negative electrodes in order to ensure that MnO₂ does not exceed its stable electrochemical window when cycled in the complete asymmetrical cell. For the so-called amorphous MnO₂-powder-based

Table 8.3 Performance of the different asymmetric EC devices which all show extended cell voltage (1.2–2.2 V).

Negative electrode	Positive electrode	Current collector	Electrolyte salt	Cell voltage ^a (V)	C ^a (F g ⁻¹)	ESR ^a (Ohm cm ²)	Energy density ^a (Wh kg ⁻¹)	Power density ^a (kW kg ⁻¹)	Number of cycles	References
AC	MnO ₂	Titanium	KCl	2.0	52	—	28.8	0.5	100	[11]
MnO ₂	MnO ₂	SS	K ₂ SO ₄	1.0	36	—	3.3	3.08	—	[54]
Fe ₃ O ₄	MnO ₂	SS	K ₂ SO ₄	1.8	21.5	—	8.1	10.2	5000	[54]
AC	MnO ₂	SS	K ₂ SO ₄	2.2	31	—	17.3	19	10 000	[54]
AC	MnO ₂	Titanium	K ₂ SO ₄	1.5	—	—	7.0	10	23 000	[12]
MnO ₂	MnO ₂	Gold	KNO ₃	0.6	160	1.56	1.9	3.8	—	[13]
AC	MnO ₂	Gold	KNO ₃	2.0	140	0.54	21	123	1000	[13]
PANI	MnO ₂	Gold	KNO ₃	1.2	—	0.57	5.86	42.1	500	[14]
Ppy	MnO ₂	Gold	H ₂ SO ₄	1.4	—	0.52	7.37	62.8	500	[14]
PEDOT	MnO ₂	Gold	KNO ₃	1.8	—	0.48	13.5	120.1	500	[14]
AC	MnO ₂	Ni foam	LiOH	1.5	62.4	—	19.5	—	1500	[59]
AC	LiMn ₂ O ₄	Ni grid	Li ₂ SO ₄	1.8	56	3.3	10.0	2	20 000	[60]
AC	MnO ₂	SS	K ₂ SO ₄	2.0	21	1.3	11.7	—	195 000	[55]
AC	MnO ₂	Gold	Na ₂ SO ₄	2.0	25	—	13.9	—	10 000	[61]
AC	K _{0.27} MnO ₂	Nickel	K ₂ SO ₄	1.8	57.7	—	17.6	2.0	10 000	[62]
AC	NaMnO ₂	Nickel	Na ₂ SO ₄	1.9	21	—	13.2	1.0	10 000	[63]

^aCheck reference for calculation details. (Inspired from Ref. [10].)

Abbreviation: AC, activated carbon; PANI, polyaniline; Ppy, polypyrrole; PEDOT, poly(3,4-ethylenedioxythiophene); SS, stainless steel; C, capacitance; ESR, equivalent series resistance.

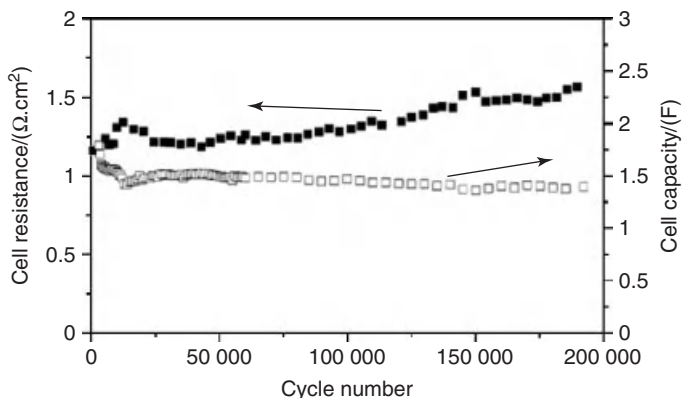


Figure 8.12 Capacitance (open squares) and resistance (black squares) of a hybrid AC–MnO₂ cell. Charge/discharge current 40 mA cm⁻² between 0 and 2 V, one charge/discharge cycle during 130 s at the beginning of the test. Ref. [55].

electrode, the potential must be maintained between 0 and 0.9 V vs Ag/AgCl on cycling in order to avoid Mn⁴⁺ reduction and the subsequent Mn³⁺ dismutation. An adjustment of electrode masses and maximum cell voltage is also a good way to achieve long-term cycling [61] but this remains strongly dependant on the individual performances of each electrode.

Recently, aqueous lithium-based electrolytes (Li₂SO₄, LiOH) have replaced Na⁺ or K⁺ salts [59, 60]. The intercalation of Li⁺ may be observed in MnO₂ or LiMn₂O₄-based electrode (Figure 8.13). Up to 20 000 cycles have been obtained with aqueous Li₂SO₄, with improved energy density up to 36 Wh kg⁻¹ [60]. However, the presence of an “intercalation” compound in the electrode combination obviously limits the

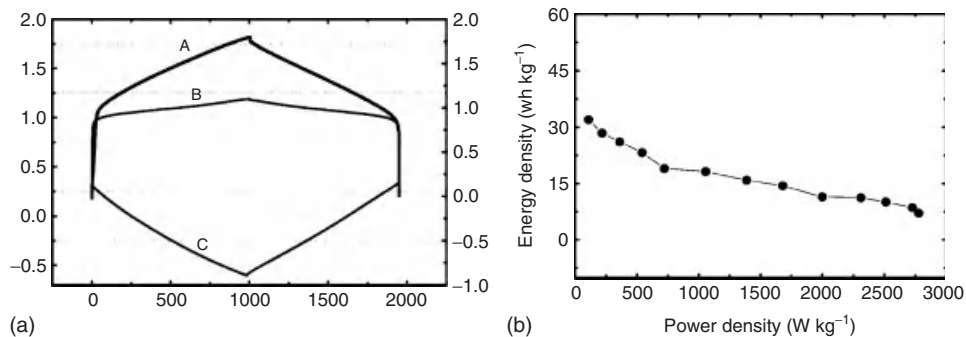


Figure 8.13 (a) Typical charge/discharge curves of the individual electrode (C) AC and (B) LiMn₂O₄ along with (A) a composite voltage profile of the hybrid aqueous AC/LiMn₂O₄ a 1 : 1 mass load ratio of AC/LiMn₂O₄ at a current rate of 3 mA/cm²

in 1 M aqueous Li₂SO₄. (b) Ragone plots of the AC/LiMn₂O₄ hybrid cell with a mass ratio of 2 : 1 between 1.8 and 0.5 V. The energy densities and power densities are calculated using the total weight of the active electrode materials. From Ref. [60].

power capability (Table 8.3), with charge/discharge cycles obtained in a few minutes rather than a few seconds.

Electrolyte formulation has also been investigated in order to improve the operating temperature range, especially on the low-temperature side. Indeed, transportation applications required operating temperatures as low as $-30\text{ }^{\circ}\text{C}$, which are difficult to achieve with neutral aqueous electrolytes. Highly concentrated nitrate solutions help fulfill this requirement, as recently reported [68, 69].

For electrolyte formulation, not only alkaline cations can be used, as a recent study reported more than 5000 cycles for a 2 V AC/MnO₂ cell operated in alkaline earth nitrate aqueous electrolyte (Mg²⁺, Ca²⁺, and Ba²⁺) [70].

The incorporation of MnO₂ electrodes into asymmetric cell configurations opens the way for safe aqueous-based ECs that deliver technologically relevant power and energy densities. Aqueous-based ECs present several advantages for device manufacturing: low-cost and environmentally friendly materials and components, no need for special atmospheres during cell assembly, and the use of simple nontoxic salts (e.g., Na₂SO₄). High-capacitance AC (-)/MnO₂ (+) asymmetric capacitors (300–700 F) were recently assembled using this technology [55], even if commercial products are not available at the moment (Figure 8.14).

Owing to its proven long-term cycling ability, asymmetric AC/MnO₂ ECs are extensively investigated. The main challenges are the improvement of both AC and manganese dioxide electrodes and the use of alternative electrolytes and current collectors.

This concept has also opened the way for other asymmetric ECs, taking advantage of the MnO₂ positive electrode.

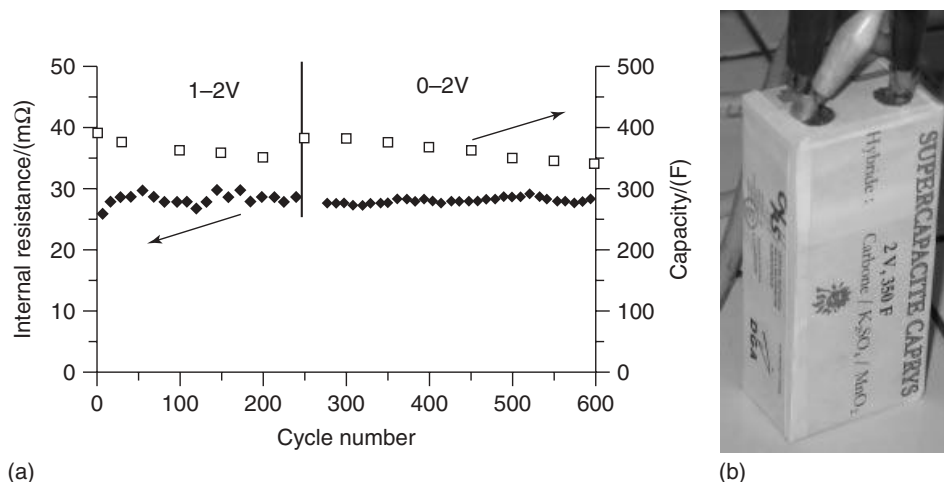


Figure 8.14 (a) Characterization of a 350-F hybrid supercapacitor demonstrator: (A) representative galvanostatic cycles (constant current = 2A) and (B) variation of capacity and resistance with cycle number. From Ref. [55]. (b) 350 F prototype of the AC/MnO₂ asymmetric electrochemical capacitor (5 cm × 4 cm × 10 cm). From Ref. [71].

8.3.3

Other MnO₂-Based Asymmetric or Hybrid Devices

Asymmetric MnO₂-based ECs can be operated with an alternative negative electrode, one with a useful electrochemical window complementary to that of MnO₂ (i.e., with a lower cutoff potential below 0 V vs Ag/AgCl). Apart from AC, materials that can satisfy this requirement in mild aqueous electrolytes include iron-based oxides (e.g., Fe₃O₄, FeOOH, or LiFeO₂) [15, 72, 73], titanium phosphates [74], and conducting polymers (e.g., polyaniline, poly(3,4-ethylenedioxythiophene) [14]. Some examples are given in Figure 8.15.

The main drawback of these devices is their low ability to fulfill long-term cycling operations, due to the alternative negative electrode. However, such an electrode can significantly improve the overall cell energy density if it demonstrates capacitance twice or greater compared to an AC electrode in a neutral aqueous electrolyte.

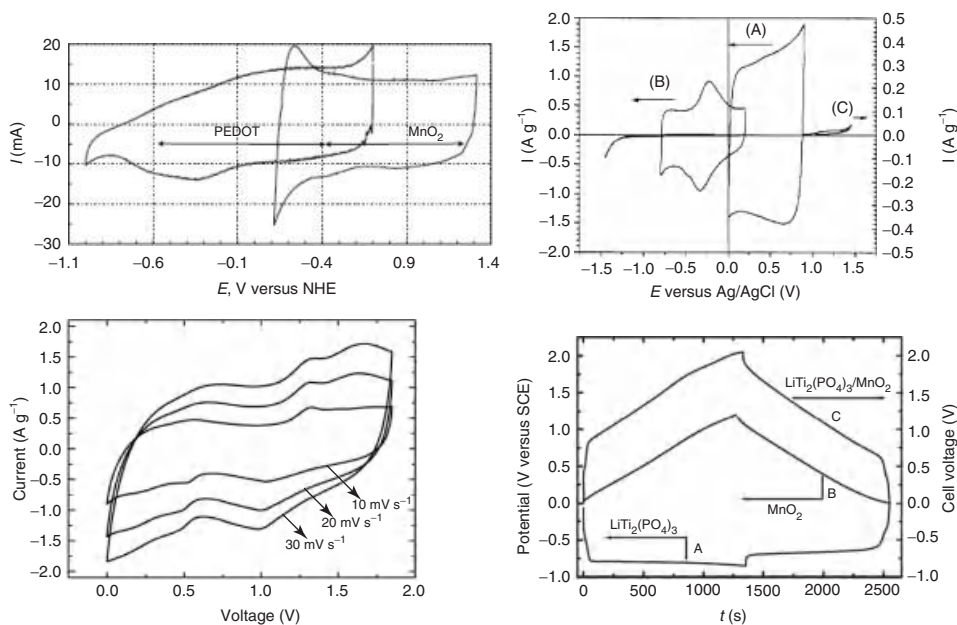


Figure 8.15 (a) Cyclic voltammograms in a three-electrode cell of manganese oxide (a-MnO₂/CNT (15 wt%) composite) and PEDOT (PEDOT/CNT(20 wt%) composite) at 10 mV s⁻¹ in 2 mol l⁻¹ KNO₃. From Ref. [14]. (b) Cyclic voltammogram of (A) the composite MnO₂ electrode (~70 wt% MnO₂), (B) the composite Fe₃O₄ (~65 wt% Fe₃O₄), and (C) stainless steel grid (current collector) at a scan rate of 10 mV s⁻¹ in 0.1 M K₂SO₄. From Ref. [15]. (c) CV

curves of MnO₂-FeOOH hybrid supercapacitor at different scan rates within voltage range of 0–1.85 V, varying from 10, 20, to 30 mV s⁻¹. from Ref. [72]. (d) Typical charge/discharge curves of individual electrode (A) carbon-coated LiTi₂(PO₄)₃ and (B) MnO₂ along with (C) a composite voltage profile of the LiTi₂(PO₄)₃/MnO₂ hybrid aqueous cell at a current rate of 2 mA cm⁻² in 1 M Li₂SO₄. From Ref. [74].

8.3.4

Carbon/Carbon Aqueous Asymmetric Devices

The concept of an asymmetric EC using two carbon electrodes has been reported in a series of papers using different designs [75–77]. Basically, the positive electrode is different from the negative electrode from the nature of the carbons (i.e., graphite as the negative and AC as the positive [75]) or from its pore size distribution [77]. However, it is only recently [78–81] that asymmetric carbon devices were proposed in aqueous media (Figure 8.16). In these devices, charging the electrical double layer is not the only mechanism, unlike what occurs with ACs in an organic electrolyte. An additional pseudo-faradic redox contribution involving oxygenated functionalities plays an important role in aqueous medium. The redox reactions are potential dependent and affect the performance of the positive and/or negative electrode in a different way, depending on the electrolyte. The equilibrium potential and the potential window of the electrodes are also controlled by oxygenated functionalities. These functionalities can be adjusted by the mean of controlled thermal treatments adapted to the carbon type.

Thus, it is possible to choose different optimized carbons as positive and negative electrodes to improve both the electrode capacitances and the cell voltage, which exceeds 1 V as usually observed for symmetric carbon/carbon EC in aqueous media [17]. As the positive and the negative electrodes have different electrochemical windows and different capacitances, their masses must be correctly balanced to optimize the asymmetric carbon device. Practically, the cell voltage can be increased up to 1.6 V by an appropriate design of carbons since the potentials of H_2 evolution and destructive oxidation of AC can be shifted to negative and positive potentials [79]. Energy density as high as 40 Wh kg^{-1} of carbon can be obtained (Figure 8.16). Excellent cycle life – up to more than 10000 cycles – have been demonstrated in 1 M H_2SO_4 electrolyte [78, 79].

Moreover, the acidic medium can be replaced by a neutral aqueous electrolyte such as 1 M Na_2SO_4 , keeping high energy density and excellent cycling ability [80, 81]. Hence, the carbon-based aqueous asymmetric EC presents improved

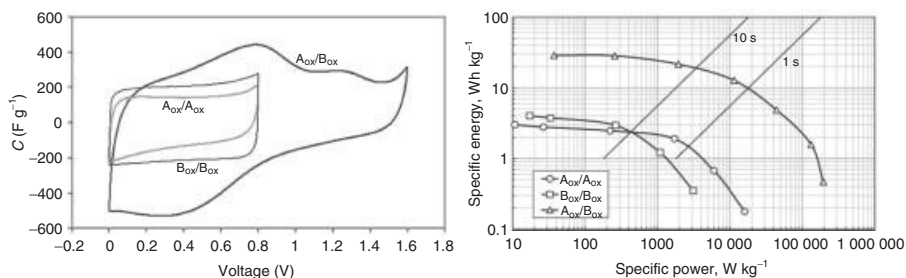


Figure 8.16 Cyclic voltammograms of an optimized asymmetric A_{ox}/B_{ox} capacitor and of symmetric A_{ox}/A_{ox} and B_{ox}/B_{ox} capacitors in $1 \text{ mol l}^{-1} H_2SO_4$. Scan rate of voltage 2 mV s^{-1} and Ragone plots for the

asymmetric A_{ox}/B_{ox} capacitor at a voltage of 1.6 V (triangles) and for the A_{ox}/A_{ox} (circles) and B_{ox}/B_{ox} (squares) symmetric capacitors at a voltage of 0.8 V. Electrolyte: $1 \text{ mol l}^{-1} H_2SO_4$. From Ref. [79].

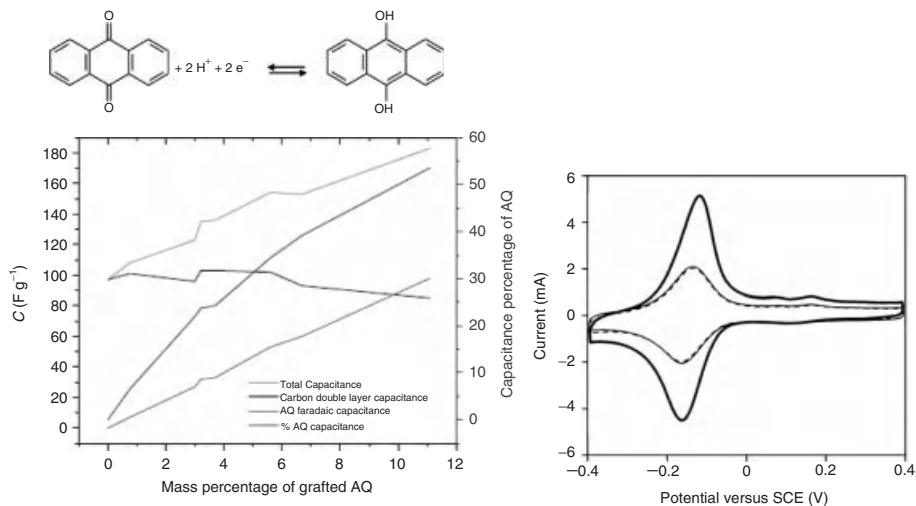


Figure 8.17 Redox process of anthraquinone in acidic conditions and evolution of capacitances of each element of the system with the amount of grafted AQ. From Ref. [87]. Cycling voltammograms at 100 mV s^{-1} of a Vulc-AQ electrode in $1.0 \text{ M H}_2\text{SO}_4$ (aqueous). The initial cyclic voltammogram is shown in bold, while the dashed curve was recorded following immersion in benzene for 15 min and the light solid curve was recorded following a second immersion in fresh benzene. From Ref. [90].

performances and can be fabricated in a safer environment and at a lower cost compared to EDLC in nonaqueous electrolytes.

Another interesting way to improve the capacitance of one of the carbon electrodes is to modify the carbon surface by chemical modification. More precisely, the covalent attachment of reversible redox moieties can add an extra faradic capacitance to the double-layer capacitance of ACs. The chemical grafting of organic radicals on carbon can be achieved by using standard diazonium chemistry [82–85] that was already reported and patented.

The usefulness of controlling carbon surface in aqueous-based ECs was demonstrated with sulfonated groups, which limit ionic depletion, and subsequently resistance increase, on charging/discharging the cell [86]. In aqueous electrolytes, anthraquinone (AQ) moieties were grafted (Figure 8.16) on different types of carbons: AC [87, 88], carbon fabric [89], or carbon black [90, 91]. The electrode capacitance can be nearly doubled [86] by superimposing the faradic contribution to double-layer capacitance as shown in Figure 8.17. The use of different surface functionalities for the positive [92] and negative electrodes leads to improved asymmetric ECs in aqueous electrolytes [93].

8.3.5

Carbon/RuO₂ Devices

It is not only MnO₂ that has been envisioned as the positive electrode in asymmetric aqueous-based devices. Taking advantage of the high capacitance of RuO₂

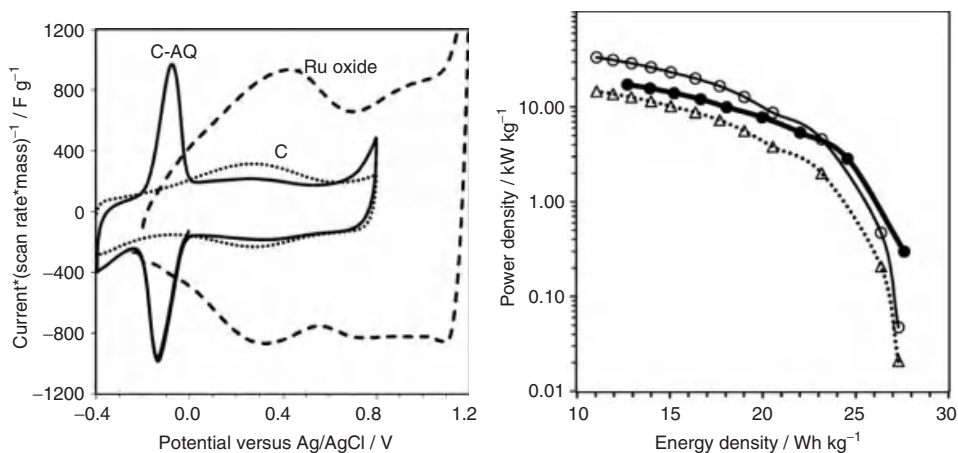


Figure 8.18 Cyclic voltammetry of an AQ-modified Spectracarb electrode (solid line; 14.8 mg; 2 mV s^{-1}), and unmodified Spectracarb electrode (dotted line; 14.3 mg; 20 mV s^{-1}) and a Ru oxide electrode (dashed line; 5.1 mg, 20 mV s^{-1}) in $1 \text{ M H}_2\text{SO}_4$ (aq) and Ragone plots for an AQ-C (15.1 mg)/Nafion 112/Ru oxide (8.5 mg) supercapacitor (solid

points; $V_{\text{initial}} = 1.3 \text{ V}$) and a Ru oxide (5 mg)/Nafion 112/Ru oxide (5 mg) supercapacitor (open circles; $V_{\text{initial}} = 1.0 \text{ V}$), both in $1 \text{ M H}_2\text{SO}_4$ (aqueous). The open triangles show the data for the symmetric Ru oxide device with the power values divided by a mass of 23.6 mg. All values were calculated for discharge to 0 V. From Ref. [94].

pseudocapacitive electrode, several authors have aimed at the design of asymmetric carbon/RuO₂ devices [94–96]. In order to compensate the high capacitance value of RuO₂ pseudocapacitive electrode, an AC electrode was doped by redox surface radicals [87, 89, 90] using diazonium chemistry. The resulting device is depicted in Figure 8.18. The lower potential limit of the composite negative electrode (AC + AQ) extends the cell voltage from 1.0 to 1.3 V and as a result improved energy densities are reached with the asymmetric EC.

A similar cell voltage increase is achieved with an asymmetric EC using a negative graphite electrode and a positive RuO₂ electrode in H₄SiW₁₂O₄₀ (SiWA) electrolyte. An increase in capacitance was also observed in that case and could be attributed to a pseudocapacitance from the reduction/oxidation of SiWA [95, 96].

On the basis of the same principle, a negative AC electrode combined with a positive pseudocapacitive electrode such as V₂O₅, several other devices have been proposed, exhibiting improved energy densities compared to symmetrical aqueous devices. However, their long-term cycling ability was not clearly established as only a few hundred cycles are usually shown in the related papers [97, 98].

As an alternative to aqueous hybrid cell and asymmetric ECs, a device was proposed some years ago, combining the technology of RuO₂-based ECs and tantalum electrolytic capacitors [16]. This device is depicted in the subsequent section.

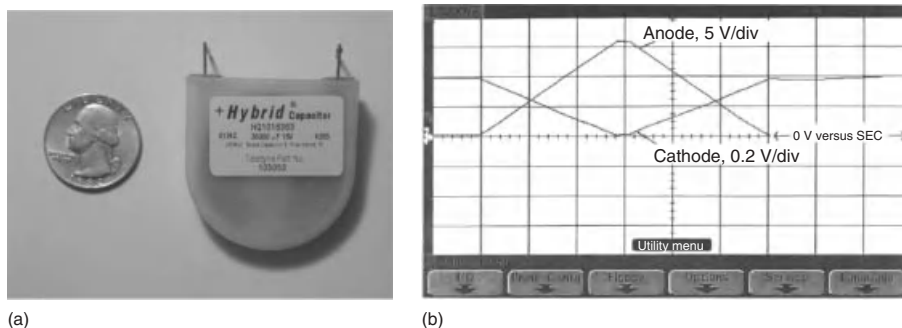


Figure 8.19 (a) The picture of a tantalum oxide–ruthenium oxide hybrid capacitor made by Evans Capacitor Company. The capacitor is rated as 36 mF and 16 V. (b) Potentials of cathode and anode electrodes during a DC current cycle at 10 mA at 300 K. The time scale is 20 s per division. From Ref. [16].

8.4

Tantalum Oxide–Ruthenium Oxide Hybrid Capacitors

The principle of the device proposed by Evans *et al.* [16] is a hybrid capacitor that is constructed with a pressed and sintered tantalum powder electrode as the anode and two RuO_2 films on Ta foil substrates as the cathode [99–101]. Concentrated (38 wt%) H_2SO_4 solution is used as the electrolyte. The resulting device combined the high capacitance of the RuO_2 electrode (with limited potential window) and the high-voltage operation of the dielectric tantalum-based capacitor (Figure 8.19). As a result, both energy and power densities are optimized. The device stores less energy than a standard AC EC, but fulfill the requirements of space or military electronic devices that need high rates operation, and can be operated from -50 up to 85°C or more.

Products are available from Evans Capacitor Company [102] with different rated voltage and capacitance, from 10 V up to 175 V.

8.5

Perspectives

Aqueous-based hybrid ECs are basically of two types: those using a battery-type electrode such as carbon/ PbO_2 (hybrid device) and those that take advantage of the combination of EDLC and pseudocapacitance such as carbon/ MnO_2 (asymmetric devices).

Hybrid devices are already commercially available. They combine high energy density compared to standard ECs with long-term cycling ability, which makes them pertinent for applications where repeated energy released is needed such as HEVs. However, they suffer from limited power capability, which limits their use in systems where charge/discharge must be performed within a few minutes but not a few seconds. Nanostructured materials can be helpful to promote the power

capability of the faradic electrode but the structural and microstructural changes occurring on cycling can cancel the effect of the nanostructuration depending on the electrolyte.

Improved power capability is achieved with aqueous asymmetric ECs, which use EDLC and/or pseudocapacitive electrodes. At the moment, there is no available commercial device to our knowledge. However, the performances of carbon/carbon or carbon/MnO₂-based systems will probably give rise to a new generation of cheap and environmentally friendly ECs. The main research directions are the increase in electrode capacitance coupled with a widening of the cell voltage by tuning gas evolution reactions.

In both cases, the use of aqueous electrolytes is a major advantage for manufacturing the devices as low-cost materials and processes can be used. In addition, the resulting hybrid or asymmetric capacitors can be operated more safely regarding their electrothermal behavior and the low environmental impact of electrolyte vapors in case of cell burst-out.

Despite these advantages, efforts have to be performed in order to optimize all the cell components including electrolyte formulation for low-temperature operations and current collectors resistant to oxidation in aqueous media.

References

1. Simon, P. and Burke, A. (2008) *The Electrochemical Society Interface*, Spring, pp. 38–43.
2. Kötz, R. and Carlen, M. (2000) Principles and applications of electrochemical capacitors. *Electrochim. Acta*, **45**, 2483–2498.
3. Zheng, J.P. (2003) The limitations of energy density of battery and double-layer capacitor asymmetric cells. *J. Electrochem. Soc.*, **150**, A484–A492.
4. Guillemet, P., Dugas, R., Scudeller, Y., and Brousse, T. (2005) Electro-Thermal Analysis of a Hybrid Activated Carbon/MnO₂ Aqueous Electrochemical Capacitor. 207th Meeting of the ElectroChemical Society Quebec City, Canada, May 15–20, 2005.
5. Zheng, J.P., Cygan, P.J., and Jow, T.R. (1995) Hydrous ruthenium oxide as an electrode material for electrochemical capacitors. *J. Electrochem. Soc.*, **142**, 2699.
6. Linden, D. and Reddy, T.B. (2002) *Handbook of Batteries*, 3rd edn, Mac Graw-Hill, New York.
7. Pell, W.G. and Conway, B.E. (2004) Peculiarities and requirements of asymmetric capacitor devices based on combination of capacitor and battery-type electrodes. *J. Power Sources*, **136**, 334–345.
8. Varakin, I.N., Klementov, A.D., Litvinenko, S.V., Starodubtsev, N.F., and Stepanov, A.B. (1998) New Ultracapacitors Developed by JSC ESMA for Various Applications. Proceedings of the 8th International Seminar on Double-Layer Capacitors and Similar Devices, Florida Educational Seminars Inc., Deerfield Beach, FL, December 1998.
9. Lipka, S.M., Reisner, D.E., Dai, J., and Cepulis, R. (2001) Proceedings of The 11th International Seminar on Double Layer Capacitors and Similar Energy Storage Devices, Florida Educational Seminars Inc., 2001.
10. Bélanger, D., Brousse, T., and Long, J.W. (2008) Manganese oxides: battery materials make the leap to electrochemical capacitors, *The Electrochemical Society Interface*, Spring.
11. Hong, M.S., Lee, S.H., and Kim, S.W. (2002) Use of KCl aqueous electrolyte for 2 V manganese oxide/activated

- carbon hybrid capacitor. *Electrochem. Solid-State Lett.*, **5**, A227.
12. Brousse, T., Toupin, M., and Bélanger, D. (2004) A hybrid activated carbon-manganese dioxide capacitor using a mild aqueous electrolyte. *J. Electrochem. Soc.*, **151**, A614.
 13. Khomenko, V., Raymundo-Piñero, E., and Bećguin, F. (2006) Optimisation of an asymmetric manganese oxide/activated carbon capacitor working at 2 V in aqueous medium. *J. Power Sources*, **153**, 183.
 14. Khomenko, V., Raymundo-Pinero, E., Frackowiak, E., and Bećguin, F. (2006) High-voltage asymmetric supercapacitors operating in aqueous electrolyte. *Appl. Phys. A Mater.*, **82**, 567.
 15. Brousse, T. and Bélanger, D. (2003) A hybrid Fe₃O₄-MnO₂ capacitor in mild aqueous electrolyte. *Electrochem. Solid-State Lett.*, **6**, A244.
 16. Chang, T.Y., Wang, X., Evans, D.A., Robinson, S.L., and Zheng, J.P. (2002) Tantalum oxide-ruthenium oxide hybrid[®] capacitors. *J. Power Sources*, **110**, 138–143.
 17. Toupin, M., Bélanger, D., Hill, I.R., and Quinn, D. (2005) Performance of experimental carbon blacks in aqueous supercapacitors. *J. Power Sources*, **140**, 203–210.
 18. Vol'fkovich, Y.M. and Shmatko, P.A. (1998) Proceeding of the 8th International Seminar on Double Layer Capacitors and Similar Energy Storage Devices, Deerfield Beach, FL, 1998, Special issue.
 19. Vol'fkovich, Y.M. and Serdyuk, T.M. (2002) Electrochemical capacitors. *Russ. J. Electrochem.*, **38**, 935.
 20. Conway, B.E. and Pell, W.G. (2003) Double-layer and pseudocapacitance types of electrochemical capacitors and their applications to the development of hybrid devices. *J. Solid State Electrochem.*, **7**, 637.
 21. Yu, N., Gao, L., Zhao, S., and Wang, Z. (2009) Electrodeposited PbO₂ thin film as positive electrode in PbO₂/AC hybrid capacitor. *Electrochim. Acta*, **54**, 3835.
 22. Yu, N. and Gao, L. (2009) Electrodeposited PbO₂ thin film on Ti electrode for application in hybrid supercapacitor. *Electrochem. Commun.*, **11**, 220–222.
 23. <http://www.axionpower.com/>.(accessed 7 November 2012).
 24. Perret, P., Brousse, T., Bélanger, D., and Guay, D. (2009) Electrochemical template synthesis of ordered lead dioxide nanowires. *J. Electrochem. Soc.*, **156**, A645.
 25. (a) Hazza, A., Pletcher, D., and Wills, R. (2004) A novel flow battery: a lead acid battery based on an electrolyte with soluble lead(II): part I. Preliminary studies. *Phys. Chem. Chem. Phys.*, **6**, 1773; (b) Hazza, A., Pletcher, D., and Wills, R. (2005) *J. Power Sources*, **149**, 103; (c) Li, X., Pletcher, D., and Walsh, F.C. (2009) *Electrochim. Acta*, **54**, 4688; (d) Pletcher, D. and Wills, R. (2004) *Phys. Chem. Chem. Phys.*, **6**, 1779; (e) Pletcher, D. and Wills, R. (2005) *J. Power Sources*, **149**, 96; (f) Pletcher, D., Zhou, H., Kear, G., Low, C.T.J., Walsh, F.C., and Wills, R.G.A. (2008) *J. Power Sources*, **180**, 621; (g) Pletcher, D., Zhou, H., Kear, G., Low, C.T.J., Walsh, F.C., and Wills, R.G.A. (2008) *J. Power Sources*, **180**, 630.
 26. Perret, P., Khani, Z., Brousse, T., Bélanger, B., and Guay, D. (2011) Carbon/PbO₂ asymmetric supercapacitor based on methanesulfonic acid electrolyte, *Electrochimica Acta*, **56**, 8122–8128.
 27. Petersson, E.A. (2000) Oxidation of electrodeposited lead–tin alloys in 5 M H₂SO₄. *J. Power Sources*, **91**, 143–149.
 28. Lam, L.T. and Louey, R. (2006) Development of ultra-battery for hybrid-electric vehicle applications. *J. Power Sources*, **158**, 1140–1148.
 29. Lam, L.T., Louey, R., Haigh, N.P., Lim, O.V., Vella, D.G., Phyland, C.G., Vu, L.H., Furukawa, J., Takada, T., Monma, D., and Kano, T. (2007) VRLA ultrabattery for high-rate partial-state-of-charge operation. *J. Power Sources*, **174**, 16–29.
 30. Cooper, A., Furakawa, J., Lam, L., and Kellaway, M. (2009) The UltraBattery—a new battery design for a new beginning in hybrid electric

- vehicle energy storage. *J. Power Sources*, **188**, 642–649.
31. Furukawa, J., Takada, T., Monma, D., and Lam, L.T. (2010) Further demonstration of the VRLA-type UltraBattery under medium-HEV duty and development of the flooded-type UltraBattery for micro-HEV applications. *J. Power Sources*, **195**, 1241–1245.
 32. Beliakov, A.L. and Brintsev, A.M. (1997) Development and Application of Combined Capacitors: Double Electric Layer—Pseudocapacity. Proceedings of the 7th International Seminar on Double-Layer Capacitors and Similar Energy Storage Devices, Deerfield Beach, FL, December 1997.
 33. N3 <http://www.elton-cap.com/products/> (accessed 7 November 2012).
 34. Burke, A. (2000) Ultracapacitors: why, how, and where is the technology. *J. Power Sources*, **91**, 37.
 35. Namba, Y. and Higuchi, E. (2010) Preparation and characterization of Ni-based positive electrodes for use in aqueous electrochemical capacitors, N5 H. Inoue. *J. Power Sources*, **195**, 6239.
 36. Park, J.H., Park, O.O., Shin, K.H., Jin, C.S., and Kim, J.H. (2002) An electrochemical capacitor based on a Ni(OH)₂/activated carbon composite electrode. *Electrochem. Solid-State Lett.*, **5**, H7.
 37. Nohara, S., Asahina, T., Wada, H., Furukawa, N., Inoue, H., Sugoh, N., Iwasaki, H., and Iwakura, C. (2006) Hybrid capacitor with activated carbon electrode, Ni(OH)₂ electrode and polymer hydrogel electrolyte. *J. Power Sources*, **157**, 605.
 38. Wang, D.-W., Li, F., and Cheng, H.-M. (2008) Hierarchical porous nickel oxide and carbon as electrode materials for asymmetric supercapacitor. *J. Power Sources*, **185**, 1563.
 39. Zhao, Y., Lai, Q.Y., Hao, Y.J., and Ji, X.Y. (2009) Study of electrochemical performance for AC/(Ni_{1/3}Co_{1/3}Mn_{1/3})(OH)₂. *J. Alloys Compd.*, **471**, 466–469.
 40. Wang, H., Gao, Q., and Hu, J. (2010) Asymmetric capacitor based on superior porous Ni–Zn–Co oxide/hydroxide and carbon electrodes. *J. Power Sources*, **195**, 3017–3024.
 41. Liang, Y.-Y., Li, H.-L., and Zhang, X.-G. (2008) A novel asymmetric capacitor based on Co(OH)₂/USY composite and activated carbon electrodes. *Mater. Sci. Eng., A*, **473**, 317–322.
 42. Kong, L.-B., Liu, M., Lang, J.-W., Luo, Y.-C., and Kang, L. (2009) Asymmetric supercapacitor based on loose-packed cobalt hydroxide nanoflake materials and activated carbon. *J. Electrochem. Soc.*, **156** (12), A1000–A1004.
 43. Skotheim, T.A. and Reynolds, J.R. (eds) (2007) *Handbook of Conducting Polymers*, 3rd edn, CRC Press.
 44. Naoi, K. and Morita, M. (2008) *The Electrochemical Society Interface*, Spring, p. 44.
 45. Bélanger, D. (2009) *Handbook of Thiophene-Based Materials: Applications in Organic Electronics and Photonics*, Properties and Applications, Wiley, Vol. 2, Chapter 15, pp. 577–594.
 46. Laforgue, A., Simon, P., Fauvarque, J.F., Sarrau, J.F., and Lallier, P. (2001) Hybrid supercapacitors based on activated carbons and conducting polymers. *J. Electrochem. Soc.*, **148**, A1130.
 47. Di Fabio, A., Giorgi, A., Mastragostino, M., and Soavi, F. (2001) Carbon-poly(3-methylthiophene) hybrid supercapacitors. *J. Electrochem. Soc.*, **148**, A845.
 48. Villers, D., Jobin, D., Soucy, C., Cossement, D., Chahine, R., Breau, L., and Bélanger, D. (2003) The influence of the range of electroactivity and capacitance of conducting polymers on the performance of carbon/conducting polymer hybrid supercapacitor. *J. Electrochem. Soc.*, **150**, A747–A752.
 49. Laforgue, A., Simon, P., Fauvarque, J.F., Mastragostino, M., Soavi, F., Sarrau, J.F., Lallier, P., Conte, M., Rossi, E., and Saguatti, S. (2003) Activated carbon/conducting polymer hybrid supercapacitors. *J. Electrochem. Soc.*, **150**, A645.
 50. Park, J.H. and Park, O.O. (2002) Hybrid electrochemical capacitors based on polyaniline and activated carbon electrodes. *J. Power Sources*, **111**, 185.

51. Cuentas-Gallegos, A.K., Lira Cantu, M., Casan Pastor, N., and Gomez-Romero, P. (2005) Nanocomposite hybrid molecular materials for applications in solid state electrochemical capacitors. *Adv. Funct. Mater.*, **15**, 1125–1133.
52. Snook, G.A., Wilson, G.J., and Pandolfo, A.G. (2009) Mathematical functions for optimisation of conducting polymer/activated carbon asymmetric supercapacitors. *J. Power Sources*, **186**, 216–223.
53. Li, J. and Gao, F. (2009) Analysis of electrodes matching for asymmetric electrochemical capacitor. *J. Power Sources*, **194**, 1184–1193.
54. Cottineau, T., Toupin, M., Delahaye, T., Brousse, T., and Bélanger, D. (2006) Nanostructured transition metal oxides for aqueous hybrid electrochemical supercapacitors. *Appl. Phys. A*, **82**, 599.
55. Brousse, T., Taberna, P.L., Crosnier, O., Dugas, R., Guillemet, P., Scudeller, Y., Zhou, Y., Favier, F., Bélanger, D., and Simon, P. (2007) Long-term cycling behavior of asymmetric activated carbon/MnO₂ aqueous electrochemical supercapacitor. *J. Power Sources*, **173**, 633.
56. Conway, B.E. (1999) *Electrochemical Supercapacitors Scientific Fundamentals and Technological Applications*, Kluwer Academic/Plenum Press, New York.
57. Lee, H.Y. and Goodenough, J.B. (1999) Supercapacitor behavior with KCl electrolyte. *J. Solid State Chem.*, **144**, 220.
58. Wu, N.-L., Wang, S.-Y., Han, C.-Y., Wu, D.-S., and Shiue, L.-R. (2003) Electrochemical capacitor of magnetite in aqueous electrolytes. *J. Power Sources*, **113**, 173.
59. Yuan, A. and Zhang, Q. (2006) A novel hybrid manganese dioxide/activated carbon supercapacitor using lithium hydroxide electrolyte. *Electrochem. Commun.*, **8**, 1173.
60. Wang, Y.-G. and Xia, Y.-Y. (2006) Hybrid aqueous energy storage cells using activated carbon and lithium-intercalated compounds. I. The C/LiMn₂O₄ system. *J. Electrochem. Soc.*, **153** (2), A450–A454.
61. Demarconnay, L., Raymundo-Pinero, E., and Béguin, F. (2010) Adjustment of electrodes potential window in an asymmetric carbon/MnO₂ supercapacitor. *J. PowerSources*. doi: 10.1016/j.jpowsour.2010.06.013
62. Qu, Q., Li, L., Tian, S., Guo, W., Wu, Y., and Holze, R. (2010) A cheap asymmetric supercapacitor with high energy at high power: activated carbon//K_{0.27}MnO₂·0.6H₂O. *J. Power Sources*, **195**, 2789–2794.
63. Qu, Q.T., Shi, Y., Tian, S., Chen, Y.H., Wu, Y.P., and Holze, R. (2009) A new cheap asymmetric aqueous supercapacitor: activated carbon//NaMnO₂. *J. Power Sources*, **194**, 1222–1225.
64. Hsieh, Y.C., Lee, K.T., Lin, Y.P., Wu, N.L., and Donne, S.W. (2008) Investigation on capacity fading of aqueous MnO₂·nH₂O electrochemical capacitor. *J. Power Sources*, **177**, 660.
65. Nam, K.W., Kim, M.G., and Kim, K.B. (2007) In situ Mn K-edge X-ray absorption spectroscopy studies of electrodeposited manganese oxide films for electrochemical capacitors. *J. Phys. Chem. C*, **111**, 749.
66. Wei, W., Cui, X., Chen, W., and Ivey, D.G. (2009) Electrochemical cyclability mechanism for MnO₂ electrodes utilized as electrochemical supercapacitors. *J. Power Sources*, **186**, 543.
67. Chang, J.K., Huang, C.H., Lee, M.T., Tsai, W.T., Deng, M.J., and Sun, I.W. (2009) Physicochemical factors that affect the pseudocapacitance and cyclic stability of Mn oxide electrodes. *Electrochim. Acta*, **54** (12), 3278–3284.
68. Mosqueda, H.A., Crosnier, O., Athouël, L., Dandeville, Y., Scudeller, Y., Guillemet, P., and Brousse, T., (2010) Electrolytes for hybrid carbon-MnO₂ electrochemical capacitors, *Electrochim. Acta*, **55**, 7479–7483.
69. Brousse, T. (2010) Toward a New Generation of Hybrid Carbon/MnO₂ Supercapacitors. 2010 International Conference on Advanced Capacitors (ICAC2010), Kyoto, Japan, May 31–June 2, 2010, Meeting abstract pp.
70. Xu, C., Du, H., Li, B., Kang, F., and Zeng, Y. (2009) Asymmetric activated carbon-manganese dioxide capacitors

- in mild aqueous electrolytes containing alkaline-earth cations. *J. Electrochem. Soc.*, **156** (6), A435–A441.
71. Brousse, T., Guillemet, P., Scudeller, Y., Crosnier, O., Dugas, R., Favier, F., Zhou, Y.K., Taberna, P.-L., Simon, P., Toupin, M., and Bélanger, D. (2007) Des Supercondensateurs Recyclables et Sécurisés, La lettre des techniques de l'ingénieur, énergies, n° 7 (juin 2007) pp. 2–3.
 72. Jin, W.H., Cao, G.T., and Sun, J.Y. (2008) Hybrid supercapacitor based on MnO₂ and columned FeOOH using Li₂SO₄ electrolyte solution. *J. Power Sources*, **175**, 686.
 73. Santos-Pena, J., Crosnier, O., and Brousse, T. (2010) Nanosized alpha-LiFeO₂ as electrochemical supercapacitor electrode in neutral sulfate electrolytes. *Electrochim. Acta*, **55**, 7511–7515.
 74. Luo, J.Y., Liu, J.L., He, P., and Xia, Y.Y. (2008) A novel LiTi₂(PO₄)₃/MnO₂ hybrid supercapacitor in lithium sulfate aqueous electrolyte. *Electrochim. Acta*, **53**, 8128.
 75. Khomenko, V., Raymundo-Piñero, E., and Béguin, F. (2008) High-energy density graphite/AC capacitor in organic electrolyte. *J. Power Sources*, **177** (2), 643–651.
 76. Aida, T., Murayama, I., Yamada, K., and Morita, M. (2007) High-energy-density hybrid electrochemical capacitor using graphitizable carbon activated with KOH for positive electrode. *J. Power Sources*, **166**, 462–470.
 77. Wang, L., Morishita, T., Toyoda, M., and Inagaki, M. (2007) Asymmetric electric double layer capacitors using carbon electrodes with different pore size distributions. *Electrochim. Acta*, **53**, 882.
 78. Ruiz, V., Blanco, C., Granda, M., and Santamaría, R. (2008) Enhanced life-cycle supercapacitors by thermal treatment of mesophase-derived activated carbons. *Electrochim. Acta*, **54**, 305–310.
 79. Khomenko, V., Raymundo-Pinero, E., and Béguin, F. (2010) A new type of high energy asymmetric capacitor with nanoporous carbon electrodes in aqueous electrolyte. *J. Power Sources*, **195**, 4234–4241.
 80. Béguin, F. (2010) High Voltage C/C Capacitor in Aqueous Electrolyte, 2010 International Conference on Advanced Capacitors (ICAC2010), Kyoto, Japan, May 31–June 2, 2010, Meeting abstract pp.
 81. Zheng, C., Qi, L., Yoshio, M., and Wang, H. (2010) Cooperation of micro- and meso-porous carbon electrode materials in electric double-layer capacitors. *J. Power Sources*, **195**, 4406–4409.
 82. Toupin, M. and Bélanger, D. (2007) Thermal stability study of aryl modified carbon black by in situ generated diazonium salt. *J. Phys. Chem. C*, **111** (14), 5394.
 83. Adenier, A., Cabet-Deliry, E., Chaussé, A., Griveau, S., Mercier, F., Pinson, J., and Vautrin-UI, C. (2005) Grafting of nitrophenyl groups on carbon and metallic surfaces without electrochemical induction. *Chem. Mater.*, **17**, 491.
 84. Bahr, J.L. and Tour, J.M. (2001) Highly functionalized carbon nanotubes using in situ generated diazonium compounds. *Chem. Mater.*, **13**, 3832.
 85. (a) Belmont, J.A. (1996) US Patent 5,554,739, Sep. 10 1996 (Cabot Corporation); (b) Belmont, J.A. (1998) US Patent 5,851,280, Dec. 22, 1998 (Cabot Corporation); (c) Belmont, J.A. and Adams, C.E. (1999) US Patent 5,895,522, Apr. 20, 1999 (Cabot Corporation); (d) Johnson, J.E. and Belmont, J.A. (1998) US Patent 5,803,959, Sep. 8, 1998 (Cabot Corporation).
 86. Pech, D., Guay, D., Brousse, T., and Bélanger, D. (2008) Concept for charge storage in electrochemical capacitors with functionalized carbon electrodes. *Electrochem. Solid-State Lett.*, **11** (11), A202–A205.
 87. Pognon, G., Brousse, T., and Bélanger, D. (2008) A New Concept for Charge Storage in Electrochemical Capacitors with Functionalized Carbon Electrodes. 214th Meeting of the Electrochemical Society, Honolulu, Hawaii, 12–17 October, 2008, abstract #.

88. Bélanger, D. (2010) Chemical Modification of Carbon by Using the Diazonium Chemistry for Application in Electrochemical Capacitors. 2010 International Conference on Advanced Capacitors (ICAC2010), Kyoto, Japan, May 31–June 2, 2010, Meeting abstract pp.
89. Kalinathan, K., DesRoches, D.P., Liu, X., and Pickup, P.G. (2008) Anthraquinone modified carbon fabric supercapacitors with improved energy and power densities. *J. Power Sources*, **181**, 182–185.
90. Smith, R.D.L. and Pickup, P.G. (2009) Voltammetric quantification of the spontaneous chemical modification of carbon black by diazonium coupling. *Electrochim. Acta*, **54**, 2305–2311.
91. Smith, R.D.L. and Pickup, P.G. (2009) Novel electroactive surface functionality from the coupling of an aryl diamine to carbon black. *Electrochem. Commun.*, **11**, 10.
92. Pognon, G., Cougnon, C., Mayilukila, D. and Bélanger, D., (2012) Catechol-modified activated carbon prepared by the diazonium chemistry for application as active electrode material in electrochemical capacitor *ACS Applied Materials and Interfaces*, **4**, 3788–3796.
93. Pognon, G., Cougnon, C., Brousse, T., and Bélanger, D., Anthraquinone/catechol modified activated carbon electrodes for asymmetric supercapacitor, in preparation. (7 November 2012)
94. Algharaibeh, Z., Liu, X., and Pickup, P.G. (2009) An asymmetric anthraquinone-modified carbon/ruthenium oxide supercapacitor. *J. Power Sources*, **187**, 640–643.
95. Tian, Q. and Lian, K. (2010) Solid asymmetric electrochemical capacitors using proton-conducting polymer electrolytes. *Electrochem. Commun.*, **12**, 517–519.
96. Tian, Q. and Lian, K. (2010) In situ characterization of heteropolyacid based electrochemical capacitors. *Electrochem. Solid-State Lett.*, **13** (1), A4–A6.
97. Qu, Q.T., Shi, Y., Li, L.L., Guo, W.L., Wu, Y.P., Zhang, H.P., Guan, S.Y., and Holze, R. (2009) $V_2O_5 \cdot 0.6H_2O$ Nanoribbons as cathode material for asymmetric supercapacitor in K_2SO_4 solution. *Electrochem. Commun.*, **11**, 1325–1328.
98. Chen, L.-M., Lai, Q.-Y., Hao, Y.-J., Zhao, Y., and Ji, X.-Y. (2009) Investigations on capacitive properties of the AC/ V_2O_5 hybrid supercapacitor in various aqueous electrolytes. *J. Alloys Compd.*, **467**, 465–471.
99. Evans, D.A. (1999) Proceedings of The 9th International Seminar on Double Layer Capacitors and Similar Energy Storage Devices, Florida Educational Seminars Inc., 1999.
100. Burke, A., Miller, M., and Chevallier, F. (2001) Proceedings of The 11th International Seminar on Double Layer Capacitors and Similar Energy Storage Devices, Florida Educational Seminars Inc., 2001.
101. Evans, D.A., Zheng, J.P., and Roberson, S.L. (2000) *The Battery Man*, Vol. 32.
102. <http://www.evanscap.com/index.htm>. (accessed 7 November 2012).

9

EDLCs Based on Solvent-Free Ionic Liquids

Mariachiara Lazzari, Catia Arbizzani, Francesca Soavi, and Marina Mastragostino

9.1

Introduction

EDLCs are supercapacitors featuring two high-surface-area porous carbon electrodes and an electrolyte are electrochemical energy storage systems that are electrostatically charged by separation of charge at both the electrode/electrolyte interfaces. They store charge in the double layers without chemical reactions and physical changes in the electrode material bulk and, hence, the charge/discharge process is highly reversible and fast. This implies the advantage of high power and long cycle life (at least 300 000 cycles). The maximum energy (E_{\max}) of supercapacitors, delivered between V_{\max} and $V_{\max}/2$, is calculated according to Eq. (9.1),

$$E_{\max} = \frac{3}{8} C_{\text{SC}} V_{\max}^2 \quad (9.1)$$

where C_{SC} is the supercapacitor capacitance expressed in F and V_{\max} the maximum cell voltage in V. The maximum power (P_{\max}) is given by Eq. (9.2),

$$P_{\max} = \frac{V_{\max}^2}{4\text{ESR}} \quad (9.2)$$

where ESR is the equivalent series resistance in Ω [1, 2].

Since the first patents on supercapacitors appeared, EDLCs have been largely used in consumer electronic products and in uninterruptible power supply (UPS) systems. Worldwide demand for “clean” energy in the past few years has fostered the interest in supercapacitors for applications in grid-connected renewable energy plants, so as to enhance grid reliability by buffering the small and rapid (\leq minute) fluctuations, and in sustainable transportation. EDLCs are also being increasingly exploited in hybrid diesel-electric seaport cranes, where they enable size reduction of the diesel engine and capture energy otherwise wasted as heat in the down movement of heavy containers [2–4].

In transportation, supercapacitors can store energy from regenerative braking and provide and/or assist power train in heavy electric vehicles (EVs) and hybrid-electric vehicles (HEVs) of limited driving range with frequent stop-and-go, such

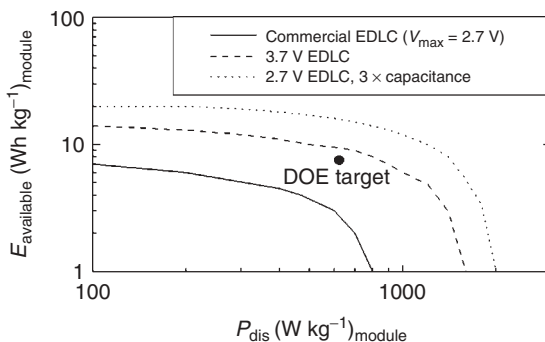


Figure 9.1 Simulated performance of a commercial 2.7 V-EDLC under USABC-DOE tests for a power-assist HEV and expected performance with V_{\max} rise to 3.7 V and a threefold increase in capacitance; the DOE target is also reported [6].

as in city transit buses and trash and delivery trucks [2–5]. Much effort is currently being devoted to the development of electrochemical energy storage systems for power-assisted HEVs. The requirements stated by the United States Advanced Battery Consortium and Department of Energy (USABC, DOE) for electrochemical systems in power-assisted HEVs are discharge pulse power of at least 625 W kg^{-1} for 10 s with a total available energy of 7.5 Wh kg^{-1} , energy efficiency $>90\%$, operating temperature range $-30/52^\circ\text{C}$ and safety, which is the primary target. EDLCs intrinsically meet such requisites with the exception of the energy target. Indeed, the best performing commercially available EDLCs, which operate in organic electrolytes with V_{\max} of 2.7 V, feature a maximum specific energy of 5 Wh kg^{-1} . In effect, an increase in EDLC energy would give them a competitive edge over the lithium-ion batteries for HEVs because of the additional advantages of higher safety and longevity the former should provide [6, 7].

Figure 9.1 reports the energy available for 10 s discharge pulses at different power ratings and shows that EDLCs on the market currently do not meet the USABC-DOE energy requisites for power-assisted HEVs, requisites that could be met by a threefold increase in capacitance or by an increase in V_{\max} up to 3.7 V [6].

Given the energy increases with V_{\max} and C_{SC} , the electrolyte electrochemical stability window (ESW) and carbon morphology play crucial roles. Much effort has been focused over the past decade on developing new electrolytes that exhibit higher thermal stability and greater electrochemical stability than those of conventional organic electrolytes. Research has also devoted much time to designing high-performing carbon materials by several synthetic methods that yielded a wide variety of carbons in terms of porosity and surface chemistry.

The most promising approach to increasing V_{\max} in EDLCs is the use of ionic liquids (ILs) as electrolytes. ILs, which are room-temperature (RT) molten salts, feature a wide ESW together with good conductivity and negligible vapor pressure [8–10]. Solvent-free ILs are viable electrolytes for increasing V_{\max} as high as 4 V and for developing high-energy EDLCs capable of working above RT in safe operating regimes. Furthermore, in order to achieve high capacitance response, the

carbon electrodes have to be properly designed to operate in ILs, and, hence, their characteristics must be tailored to proper porosity and surface chemistry [10–12].

9.2

Carbon Electrode/Ionic Liquid Interface

The carbon/IL interface in solvent-free ILs is not mediated by any solvent, and, hence, the structure of the double layer is different from that in conventional electrolytes, where solvent molecules separate electrode surface charges and electrolyte counterions, with the solvent properties strongly affecting the double-layer characteristics [13–16].

Given that carbon is a semiconductor, when the carbon electrode is polarized, the charge distribution extends into the bulk (space-charge region) and a double layer in the solid part of the electrode (C_c) is formed. Thus, the total electrode capacitance is given by Eq. (9.3)

$$\frac{1}{C} = \frac{1}{C_c} + \frac{1}{C_{\text{IL}}} \quad (9.3)$$

where C_{IL} is the capacitance in the liquid part of the electrified carbon electrode/IL interface [1, 16, 17].

The carbon electrode/IL interface is far from being well known, and studies have mainly been conducted on the metal/IL interface. However, assuming that the IL structure in the vicinity of the electrified electrode is not much affected by the nature of the latter, the results of the metal/IL interface studies can be extrapolated to the carbon/IL interface. Several studies suggest that at low electrode polarization this interface may be described by a simple Helmholtz model, which considers that the electrode charge is completely counterbalanced by a monolayer of ions located at the closest distance from the surface (compact layer). Capacitance (C_{H}) depends on IL chemistry and is given by Eq. (9.4)

$$C_{\text{H}} = \frac{k_0 \varepsilon A}{\delta_{\text{dl}}} \quad (9.4)$$

where k_0 is the vacuum permittivity ($8.85 \times 10^{-12} \text{ F m}^{-1}$), A the surface area of the carbon electrode involved in the double-layer, ε the IL dielectric constant, and δ_{dl} the double-layer thickness, which in turn is affected by size, orientation under electric field and polarizability of the IL ions. This model was proposed on the basis of sum frequency generation vibrational spectroscopy and electrochemical impedance spectroscopy results, which showed that the arrangement of ions at a Pt/BMIMBF₄ interface involve only one ion layer [18, 19]. Here, the orientation of the IL ions under the applied electric field and their stereochemistry are important in determining the double-layer thickness. Indeed, conformational studies by Fourier transform infrared (FT-IR) spectroscopy prove that in imidazolium-based ILs the plane of the imidazolium ring is normal to the surface at positive electrode polarization and becomes aligned more parallel to the surface plane at negative electrode polarization

[20]. However, at high electrode polarization the high surface charge density can be compensated by a multilayer arrangement of alternating charges [18, 19].

In certain cases, it is the intrinsic nature of the IL that determines a sort of “self-arrangement” in multilayers of alternating ions even at low electrode polarizations, as in the case of Pt/BMIM DCA [21]. Even recent computational studies suggest complex multilayer models for the double layer in the metal/IL interface. At wide electrode potential excursion, a model with a second layer of ions of the same sign, eventually with further layers for full compensation of the high surface charge density, is suggested [22].

The effect of the IL chemistry and temperature on the structure of the double layer has been investigated at glassy carbon (GC) electrodes and the results also show the role of ion association on electrode capacitance [15]. The fact that the double layer is affected by the nature of the IL has even been proved by studies of the capacitance response of negatively charged, high-surface-area, mesoporous carbons tested in the EMITFSI and $\text{PYR}_{14}\text{TFSI}$ ILs [14, 23]. All the carbons displayed pore-size distributions centered at values wider than 2 nm. Figure 9.2 shows that at 60 °C each carbon electrode displays a significantly higher specific capacitance in EMITFSI than in $\text{PYR}_{14}\text{TFSI}$. This cannot be explained by a different accessible surface area of the carbons for the double-layer formation in the two ILs because the maximum size of the EMI^+ and PYR_{14}^+ counterions involved in the double layer is not very different, that is, less than 1 nm and smaller than the main pore size of the carbon electrodes. The different capacitance in the two ILs is thus related to the different dielectric constant and thickness of the double layer, which are in turn related to the different properties of EMITFSI and $\text{PYR}_{14}\text{TFSI}$ at the interface. While unambiguous values of the dielectric constant at the interface are not available, EMI^+ can delocalize the positive electric charge in the imidazolium ring and its dipole moment is presumably higher than that of the PYR_{14}^+ , which features the electric charge in the sp^3 nitrogen atom. Consequently, the former should provide a higher dielectric constant in the double layer than the latter, with a positive effect on the electrode capacitance. The reorientation of the PYR_{14}^+ under the electric field is also hindered with respect to EMI^+ 's, both because of the strong interaction of the cation with the TFSI^- anion and of the steric hindrance of its alkyl groups [24]. The double-layer thickness δ_{dl} should thus be wider in $\text{PYR}_{14}\text{TFSI}$ than in EMITFSI and electrode-specific capacitance lower in the former than in the latter.

9.3

Ionic Liquids

ILs are generally characterized by low melting points, large liquid range extending even below RT, and very low vapor pressures; they are nonflammable and feature decomposition temperatures higher than 400 °C. ILs also display wide ESWs and good conductivities over RT, thereby giving a chance to develop safe, “green,” high-voltage EDLCs free of toxic and/or flammable organic solvents and able to operate

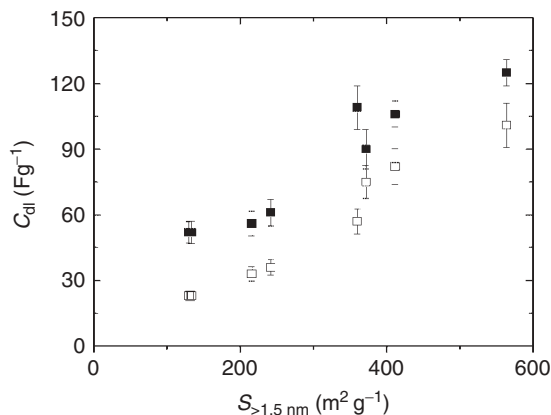


Figure 9.2 Specific capacitance (C_{dl}) of carbon electrodes versus specific surface area from pores >1.5 nm ($S_{>1.5 \text{ nm}}$). C_{dl} is evaluated from cyclic voltammetry at 60°C and 20 mV s^{-1} in the potential domain $-2.1/-0.2 \text{ V}$ versus Fc/Fc^+ in EMITFSI (solid square) and $\text{PYR}_{14}\text{TFSI}$ (open square) [23].

even at high temperature regimes ($60\text{--}80^\circ\text{C}$) that are not feasible for the EDLCs on the market, which operate with acetonitrile- and propylene-carbonate-based electrolytes [8–10].

ILs are generally composed of large unsymmetrical ions, the nature of which determines their chemical/electrochemical and physical properties. Table 9.1 summarizes the values of key properties for IL selection in EDLC applications, including molecular weight, melting/freezing point (evinced IL aptitude for supercooling), conductivity and ESW evaluated at smooth GC or Pt electrodes. The chemical formula of ions yielding ILs are shown in Figure 9.3.

Small anions such as BF_4^- yield ILs with large cations such as imidazolium, pyridinium, and piperidinium, while larger anions such as TFSI^- provide ILs with many more cations. IL density values are generally in the range of $1.2\text{--}1.5 \text{ g ml}^{-1}$, excluding ILs based on DCA^- anion, which show values lower than 1 g ml^{-1} ; the viscosity values of ILs are significantly higher than those of aqueous solutions. ILs at RT feature conductivities of $0.1\text{--}14 \text{ mS cm}^{-1}$, which can even be two orders of magnitude lower than those of aqueous electrolytes ($400\text{--}700 \text{ mS cm}^{-1}$), but of the same order as those of organic electrolytes such as tetralkylammonium salts in propylene carbonate, which feature 11 mS cm^{-1} . However, IL conductivities at $60\text{--}80^\circ\text{C}$ exhibit values of $20\text{--}30 \text{ mS cm}^{-1}$, an increase related to temperature dependence on IL viscosity and the ionic diffusion coefficient, which affect the conductivity after the Vogel–Tammann–Fulcher exponential equation [9].

The “free space model” is the best way of describing IL conductivity. This model is based on the observation of large volume variations ($20\text{--}30 \text{ vol}\%$) upon the melting of these salts. It assumes that there are empty spaces in the molten salts and suggests that conduction occurs via redistribution of the ions through free volumes that are constantly fluctuating in size because of the thermal motions, which increase with temperature. Conductivity is also influenced by the chemistry

Table 9.1 Ionic liquids for EDLCs: molar weight (MW), melting/freezing point, conductivity (σ), and electrochemical stability window (ESW) evaluated at glassy carbon electrodes at RT, except where otherwise indicated.

Cation	Ionic liquids	Anion	MW (g mol ⁻¹)	Melting/ freezing point (°C)	σ (mS cm ⁻¹)	ESW (V)	References
Ammonium	Me ₃ PrN ⁺	TFSI ⁻	382	22	3.3	5.7	[9]
	Me ₃ (CH ₂ OCH ₂)N ⁺		384	45	4.7	5.2	[8]
Sulfonium	Et ₂ Me(CH ₂ OC ₂ H ₅)N ⁺	BF ₄ ⁻	233	9/-35	4.8	6.0 ^a	[25]
	Et ₃ S ⁺	TFSI ⁻	399	-35	7.1	4.7	[9]
	Bu ₃ S ⁺		483	-7.5	1.4	4.8	
Phosphonium	P _{6,6,6,(103)} ⁺	TFSI ⁻	640	—	0.51	—	[26]
	P _{6,6,6,14} ⁺		764	-76 ^b	0.08	—	[27]
Imidazolium	EMI ⁺	FSI ⁻	291	-13	15.5	4.5	[28, 29]
	EMI ⁺	TFSI ⁻	391	-15/-50	8.4-9.2	4.1 ^a	[9]
	PrMeMeIm ⁺		419	-81/-130	3.0	4.2	
	BMIM ⁺		419	-4	3.9	4.6	
Pyrrolidinium	BMIM ⁺	BF ₄ ⁻	225	—	1.73-3.5	4.6 ^a	
	BMIM ⁺	PF ₆ ⁻	284	-8	1.4-1.8	4.4 ^a	
	PYR ₁₃ ⁺	FSI ⁻	308	-17	8.2	5.2	[28, 29]
	PYR ₁₄ ⁺	TFSI ⁻	422	-3	2.2	5.5	[9]
	PYR ₁₍₂₀₁₎ ⁺		424	-90	3.8	5.0 ^c	[30, 31]
	PYR ₁₄ ⁺	Tf ⁻	291	+3	2.0	6.0 ^c	[12]
Piperidinium	MePrPp ⁺	TFSI ⁻	422	8.7	1.51	5.6	[9]

^a Evaluated at Pt electrode.^b Glass transition temperature.^c 60 °C.

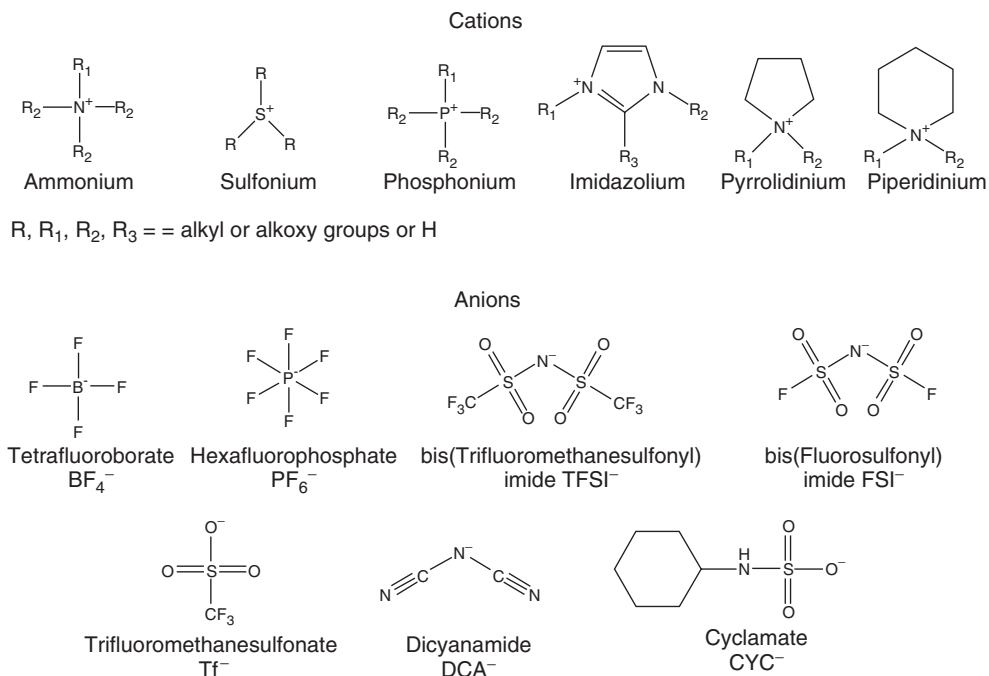


Figure 9.3 Chemical formula of ions yielding ILs.

of the IL ions and their interaction. If sufficiently long-lived, ion pairs appear neutral in the electric field and cannot contribute to conductivity [9–32]. The question of “how ionic an IL is” is thus of great importance. A qualitative approach based on the Walden rule ($\Lambda\eta = \kappa$, where Λ is the molar conductivity, η the viscosity, and k a constant) has been pursued and logarithmic Walden plots of several ILs built and compared with a reference plot of a 0.01 M KCl aqueous solution. The $\log \Lambda$ vs $\log \eta$ linear plots show two IL limit behaviors: one, exemplified by $\text{PYR}_{12}\text{DCA}$, lies quite close to the 0.01 M KCl plot and suggests that the IL is made up of almost independently mobile ions; the other, exemplified by $\text{P}_{6,6,6,14}\text{CYC}$, lies significantly lower than the reference line and corresponds to an ionicity of about 4%, a very low rate indicating that $\text{P}_{6,6,6,14}\text{CYC}$ is intermediate between a true IL and a true molecular liquid [33].

Several ILs are very stable with regard to electrochemical reduction and oxidation and show ESWs higher than 5 V. ESW values are determined by the ions composing the IL, with the cations mainly influencing the negative potential limit and the anions the positive one. In order to guarantee long cycle life of IL-based supercapacitors, a very important role is played by the hydrophobicity of these salts, which primarily depends on the chemistry of the anions and then of the cations. As anions change, hydrophobicity increases in the order CF_3CO_2^- , CH_3CO_2^- (hydrophilic) < Tf, BF_4^- < PF_6^- , TFSI (hydrophobic), while the cation effect is

modulated by the alkyl chain length of the substituent groups and hydrophobicity increases with the chain length [34]. Although ILs based on imidazolium and pyrrolidinium cations with BF_4^- , TF^- , TFSI^- , FSI^- , and PF_6^- anions are the most investigated for EDLC applications, some studies have been also performed on ILs based on asymmetric quaternary ammonium, phosphonium, and sulfonium cations [25, 26, 35].

Several studies have investigated the use of ILs as salts in organic solvents such as acetonitrile, propylene carbonate, and γ -butyrolactone. The replacement of conventional solid ammonium salts with ILs makes possible highly concentrated electrolyte solutions with wider ESW than those of conventional electrolytes. The presence of organic solvents yields better conductivity than neat ILs. As this chapter is devoted to EDLCs based on solvent-free ILs, for supercapacitors with mixed IL/organic solvent electrolytes see [36–41].

Note that the use of high-surface-area carbon electrodes narrows ESW values estimated on smooth electrodes. For example, the PYR14TFSI ESW of 5.5 V is reduced to 4.2 V when high-surface-area carbons are used [12]. ESW is not the only parameter guiding the choice of IL for EDLC applications, and conductivity and melting point are also important. As shown in Table 9.1, even if the asymmetric quaternary-ammonium-based ILs display notably wide ESWs, they generally feature melting temperatures higher than those of other ILs, which limits their use at high temperatures. Indeed, the melting process reflects on IL conductivity, which marks the temperature limit for its application in EDLCs. Imidazolium-based ILs are among those with the highest conductivities: EMITFSI, for example, features about a 10 mS cm^{-1} conductivity at RT. However, the ESWs of imidazolium-based ILs are not very wide compared to other ILs because the acidic proton of the imidazolium ring limits the cathodic stability potential, which is the main obstacle to the practical use of imidazolium-based ILs in high-voltage EDLCs. Wide ESWs are displayed by pyrrolidinium-based-ILs such as PYR13FSI, which matches a wide ESW to good conductivity at RT, although it melts at -17°C and its use in EDLC applications is limited at temperatures over 0°C [28, 29]. The most promising strategy for decreasing the melting temperature of pyrrolidinium-based-ILs is the introduction of methoxyethyl substituent in the pyrrolidinium ring as in PYR1(2O1)TFSI that remains liquid down to -90°C [30, 31].

The use of ILs for large-size EDLCs involves attention to specific weight and the cost of these electrolytes. Generally speaking, ILs feature high molecular weight, especially the TFSI-based ILs, although they are also the most hydrophobic. A key issue in the design of carbon electrode porosity is thus to avoid excess IL in the system. The challenge is to design ILs that feature a wide ESW together with high conductivity in a wide temperature range and as low a molecular weight as possible by tailoring the chemistry of the ions. In the past few years, many companies have moved to IL production and marketing, and several ILs can be purchased at a high purity level, although the prices are still high.

9.4 Carbon Electrodes

The use of hydrophobic ILs implies tailored morphologies of the carbon electrodes in terms of porosity and surface chemistry. For electrode capacitance responses $>100 \text{ F g}^{-1}$, the carbons should display a high surface area easily accessible to the ILs. If an average value of $20 \mu\text{F cm}^{-2}$ is assumed for the carbon in ILs, electrodes with accessible surface area $>500 \text{ m}^2 \text{ g}^{-1}$ should thus be used [42].

The down-limit size of the accessible carbon pores has been investigated by testing a series of carbide-derived carbons of comparable Brunauer, Emmett, Teller (BET) surface area ($1100\text{--}1600 \text{ m}^2 \text{ g}^{-1}$) but with different average pore widths in the range $0.65\text{--}1.10 \text{ nm}$ [43]. The tests were performed in EMITFSI, whose cations and anions in their widest sizes are 0.76 and 0.79 nm , respectively. The maximum capacitance response of 160 F g^{-1} was found for the carbon electrode featuring an average pore width of 0.7 nm , a value close to the size of the IL ions. Therefore, carbon pore size perfectly adapted to ion size was suggested as the most efficient way to maximize capacitance. The behavior of ions in the confined space of nanopores and the effect on the performance of EDLCs was further investigated by using both pore-controlled carbons with narrow distribution of pore size and ILs of increasing size [44]. This latter study demonstrated that under the effect of the electric field a distortion of the ions may occur owing to electrode polarization in relation to their flexibility, and therefore electrode pore size slightly lower than that of the ions may be effective for the double-layer charge process.

It is worth noting that compared to the high current density involved in the EDLC applications, these results were obtained at relatively low current regimes (5 mA cm^{-2} in the case of the galvanostatic tests in Ref. [43] corresponding to 0.3 A g^{-1}) and scan rates (1 mV s^{-1} in the case of voltammetry tests in Ref. [44]). In practice, it should thus not be of great advantage to design carbon electrodes with pores of the same size as cations or anions because carbons with not easily accessible surface area should display high charge resistance and poor charge/discharge rate capability. For a fast counterbalance of the electrode charge, the carbons should display the ions already present in the pores, and the best carbon design for exploiting all the feasible charge on the carbon surface in ILs should imply pore size higher than $2\text{--}3 \text{ nm}$ to coat the pore walls with at least an IL monolayer. Such pore size should prevent charge limitation by the electrolyte side at wide electrode polarizations, which implies a multilayer arrangement of ions. However, pore size should not exceed $8\text{--}10 \text{ nm}$ to avoid high pore volume ($>1 \text{ cm}^3 \text{ g}^{-1}$), which is detrimental to such intrinsic carbon properties as conductivity and charge storage capability because it reduces pore wall thickness. Furthermore, high pore volume lowers the volumetric capacitance of the carbon electrodes and involves excess electrolyte, which negatively affects the EDLC weight [10, 17, 45–47].

High capacitance response requires good wettability of the carbon electrodes by ILs and, hence, carbon surface chemistry plays a crucial role. As hydrophobic ILs are required for long-cycling stability of EDLCs, the hydrophilic groups usually found in high-surface-area activated carbons should be removed. Indeed, it has

been demonstrated that the double-layer capacitance of an activated carbon in the hydrophobic EMITFSI and $\text{PYR}_{14}\text{TFSI}$ significantly increased after heat treatment at about 1000°C in Ar atmosphere that removed the functional groups [14].

It is known that oxygen- and nitrogen-rich functional groups can yield reversible faradic reactions in conventional protic electrolytes, thereby producing pseudocapacitive effects that increase the carbon capacitance responses [1, 48, 49]. Indeed, an enhancement in the capacitance of activated carbons was recently observed after their oxidative treatment by HNO_3 even in protic ILs such as pyrrolidinium nitrate and pyrrolidinium formate [50]. However, the main concerns about these pseudocapacitive functional groups still remain the electrode stability over several thousand cycles.

Materials such as activated carbons, cryo/xerogel carbons, carbon fibers, template carbons, and carbon nanotubes (CNTs) have been investigated in different ILs [11, 12, 23, 35, 51–57]. While the capacitance values of high-surface-area, microporous activated carbons are all significantly higher than 100 F g^{-1} , the data are not of straightforward comparison because they are referred to different operational conditions. Mesoporous cryo/xerogel carbons featuring tunable pore-size distribution by chemical synthesis display relatively high specific surface areas and hydrophobic surfaces as well as specific capacitance values $>100\text{ F g}^{-1}$ in EMITFSI and $\text{PYR}_{14}\text{TFSI}$ even at a sweep rate as high as 20 mV s^{-1} [11]. Template synthesis of mesoporous carbons enables very good control of carbon porosity. Carbons prepared from ordered silica template [48, 49, 58] exhibit highly ordered structures and have the advantage of regularly interconnected micro- and mesopores. However, synthesis is not easy and is relatively expensive, a fact that may limit the use of these carbons. Disordered template carbons prepared from an MgO template mainly feature the same promising properties as the ordered ones, with the advantage of a relatively fast and low-cost synthesis [59]. CNTs, very appealing materials for the electronic properties enabling very high power capability, usually feature lower specific surface area than more conventional carbons and, hence, lower capacitance values. A surprisingly high capacitance value in EMITFSI is reported for a very thin electrode composed of activated vertically aligned CNTs [56]. The cost of CNTs is currently high and this limits their use in EDLCs.

9.5 Supercapacitors

IL-based electrolytes represent a promising strategy for increasing operating cell voltage, and, hence, specific EDLC energy without sacrificing power. And, given that ILs are not volatile and nonflammable electrolytes, they can also increase operating temperature range above RT and safety. Unlike IL-based supercapacitors, the EDLCs on the market with acetonitrile or propylene-carbonate-based electrolytes have shown a capacitance loss and resistance increase during accelerating aging tests under extreme conditions (elevated cell voltage up to 3.5 V or temperature above 70°C) due to formation of electrolyte degradation products in the porosity of

the electrodes. Can opening at the predesigned safety valve was also observed owing to the increase in internal pressure [60, 61]. The successful use of wide ESW ILs in EDLCs was demonstrated by a supercapacitor assembled with $\text{PYR}_{14}\text{TFSI}$ and a commercial activated carbon of capacitance $< 100 \text{ F g}^{-1}$ [51]. This $\text{PYR}_{14}\text{TFSI}$ -based-EDLC featured high cycling stability over several thousand galvanostatic charge–discharge cycles at cell voltages above 3 V and at 60°C . According to Eqs. (9.1) and (9.2), the E_{max} and P_{max} values at V_{max} of 3.2 V were 20 Wh kg^{-1} and 7 kW kg^{-1} (considering the electrode materials only), and coulombic efficiency was 100% at more than 10 000 cycles. A further increase of V_{max} to 3.5 V decreased coulombic efficiency to 95%, a value too low to guarantee the long cycle life required by EDLCs. This shows that the symmetric cell configuration of the $\text{PYR}_{14}\text{TFSI}$ -based-EDLC, which has the same carbon loading at both electrodes, does not make it possible to exploit the whole ESW of $\text{PYR}_{14}\text{TFSI}$ IL.

Figure 9.4 shows the potential excursions of EMITFSI, $\text{PYR}_{14}\text{TFSI}$, PYR_{14}Tf and $\text{PYR}_{1(201)}\text{TFSI}$ that are exploitable for IL-based carbon supercapacitors as evaluated by cyclic voltammetry (CV) at 60°C and 20 mV s^{-1} with high-surface-area carbon electrodes. The potential limit versus Fc/Fc^+ for the positive electrode is 1.6 V, and that for the negative electrode is -2.1 V for EMITFSI, -2.6 V for $\text{PYR}_{14}\text{TFSI}$ and PYR_{14}Tf and -2.4 V for $\text{PYR}_{1(201)}\text{TFSI}$. ESWs that are exploitable for high-voltage supercapacitors with such ILs are thus 3.7 V for EMITFSI, 4.2 V for $\text{PYR}_{14}\text{TFSI}$ and PYR_{14}Tf and 4.0 V for $\text{PYR}_{1(201)}\text{TFSI}$. Given that the typical potential of the discharged carbon electrodes is about -0.1 V versus Fc/Fc^+ , the maximum potential excursion of the positive electrode (ΔV_+) upon charge is 1.7 V. This value is narrower than that feasible with the negative electrode (ΔV_-), which is 2.0 V in EMITFSI, 2.5 V in $\text{PYR}_{14}\text{TFSI}$ and PYR_{14}Tf and 2.3 V in $\text{PYR}_{1(201)}\text{TFSI}$ [11, 12]. Thus, if we assume the same specific capacitance for the positive and negative electrodes in a symmetric configuration of EDLC, where the two electrodes have the same carbon loading, the maximum potential excursion for the negative electrode with these ILs would be limited by that of the positive, as is shown by Eq. (9.5)

$$\Delta V_- = \frac{C_+ w_+ \Delta V_+}{C_- w_-} \quad (9.5)$$

where C_+ , w_+ and C_- , w_- are the specific capacitance and carbon loading of the positive and negative electrode, respectively. In other words, symmetric EDLCs would operate up to 3.4 V with these ILs and, in the case of $\text{PYR}_{14}\text{TFSI}$, do not take full advantage of the electrolyte's wide ESW. A good strategy to exploit the IL's wide ESW is to assemble the supercapacitor with different loadings of the same carbon at the two electrodes, an asymmetric EDLC configuration labeled AEDLC hereinafter. Indeed, AEDLCs make it possible to charge each electrode up to the limit potential defined by IL stability and, hence, to reach maximum cell voltages significantly higher than those achievable with symmetric EDLC configurations.

AEDLCs featuring different carbon electrodes and ILs were tested. $\text{PYR}_{14}\text{TFSI}$ -based AEDLCs with xerogel carbon electrodes featuring capacitance responses of $110\text{--}120 \text{ F g}^{-1}$ were cycled at 60°C over more than 13 000 galvanostatic charge–discharge cycles with $V_{\text{max}} \geq 3 \text{ V}$ and up to 3.9 V with low capacitance

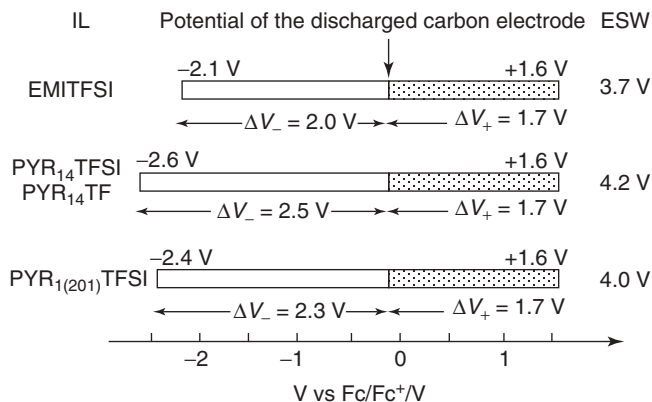


Figure 9.4 Electrochemical stability of EMITFSI, PYR₁₄TFSI, PYR₁₄Tf, and PYR₁₍₂₀₁₎TFSI ILs evaluated with high surface area mesoporous carbons at 60 °C by CV at 20 mV s⁻¹ with coulombic efficiency >95%. ESW width, IL reduction and oxidation limits, potential of the discharged carbon electrode and maximum feasible potential excursion for the negative (ΔV_-) and positive electrodes (ΔV_+) are indicated [11, 12].

fade and exhibited maximum specific energy and power of 30 Wh kg⁻¹ and 11 kW kg⁻¹ at 3.7 V [11]. PYR₁₄TFSI- and PYR₁₄Tf-based AEDLCs assembled with activated carbon electrodes featuring about 100 F g⁻¹ reached V_{\max} up to 4.0 V with a maximum specific energy and power of about 40 and 9 kW g⁻¹ and good cycling stability for over 20 000 galvanostatic charge–discharge cycles. The best cycling stability was achieved with an AEDLC assembled with high purity PYR₁₍₂₀₁₎TFSI (≤ 20 ppm of water); this supercapacitor was charged–discharged for 27 000 times with V_{\max} up to 3.8 V and a capacitance fade of only 2% [12]. These results show that IL-based AEDLC energy can significantly exceed that of the best performing EDLCs on the market. However, the former’s specific power is not as high as expected on the basis of the high V_{\max} of 4 V and this is due to high ESR values. In IL-based AEDLCs, the electrode charging resistance is generally the main contribution to ESR; it depends on IL conductivity in carbon pores and is also modulated by pore length. Hence, pore geometry is a key parameter that can differently amplify the effect of IL conductivity on the specific power of the supercapacitor [23, 46].

The PYR₁₍₂₀₁₎TFSI IL has the big advantage of a -90 °C freezing point. This makes it possible to span a wide operating AEDLC temperature range. Figure 9.5 shows the Ragone plot of AEDLCs based on PYR₁₍₂₀₁₎TFSI and activated carbon electrodes. In the figure, specific energy (E) and power (P) were evaluated from the galvanostatic discharges at different current densities (i) and temperatures between V_{\max} of 3.7 V and $0.55 V_{\max}$, that is, 2.035 V as in Eqs. (9.6) and (9.7)

$$E = i \int_{t_{V_{\max}}}^{t_{0.55V_{\max}}} \frac{V dt}{w_{\text{c.m.}}} \quad (9.6)$$

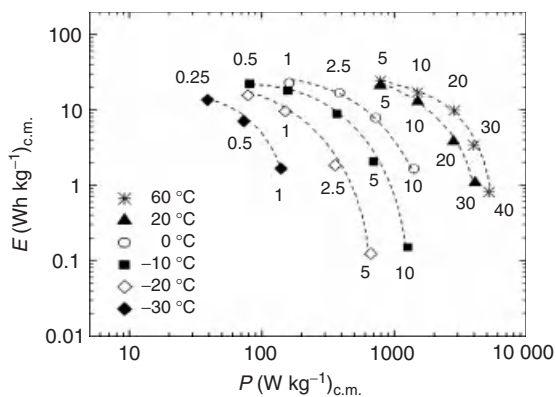


Figure 9.5 Traditional Ragone plot of the $\text{PYR}_{1(2\text{O}1)}$ TFSI-based AEDLC supercapacitor at different temperatures with specific energy (E) and power (P) values evaluated from galvanostatic discharges at different currents

with $V_{\text{max}} = 3.7 \text{ V}$ and $V_{\text{min}} = 2.035 \text{ V}$; the labels indicate the current densities in mA cm^{-2} . Reproduced with permission from *J. Electrochem. Soc.*, **156**, A661 (2009). Copyright 2009, The Electrochemical Society [62].

$$P = \frac{E}{t_{0.55V_{\text{max}}} - t_{V_{\text{max}}}} \quad (9.7)$$

where $t_{V_{\text{max}}}$ and $t_{0.55V_{\text{max}}}$ are the times at which the cells exhibit 3.7 and 2.035 V potentials and $w_{\text{c.m.}}$ is the total carbon-binder composite weight of the two electrodes. The figure shows that the $\text{PYR}_{1(2\text{O}1)}$ TFSI-based AEDLC can operate in the -30 and $+60$ °C temperature range.

While the Ragone plots are useful for comparison of the inherent energy and power of electrochemical energy storage systems for conventional applications, they are not suitable to evaluate the performance of the systems for power-assist HEVs and specific benchmark tests such as those of USABC-DOE protocols are required [6, 63, 64]. These tests include the evaluation of the total available energy of the supercapacitor at various depths of discharge (DODs) and of the power capabilities at different DODs by galvanostatic pulses of 10 s at 75% of the highest current feasible for the device (high-HPPC tests). Figure 9.6 shows the energy available in DOD ranges where a given pulse power is delivered and shows the performance of the $\text{PYR}_{1(2\text{O}1)}$ TFSI-based AEDLC, the DOE target for power-assist HEV and the expected performance of a commercial EDLC working with conventional organic electrolyte and V_{max} of 2.7 V at 30 °C. The $\text{PYR}_{1(2\text{O}1)}$ TFSI-based AEDLC with V_{max} of 3.7 V at $T \geq 30$ °C meets the challenging energy and power targets of 7.5 Wh kg^{-1} and 625 W kg^{-1} , targets that are far from being reached by a conventional EDLC [6, 62].

The figure data refer to the total weight of the complete supercapacitor (module), which is set as double the total composite electrode material loading, a very demanding condition. Module performance is greatly affected by weight component distribution and, particularly, by electrolyte-to-electrode-materials weight ratio. In IL-based supercapacitors, module design should take into account the amount of

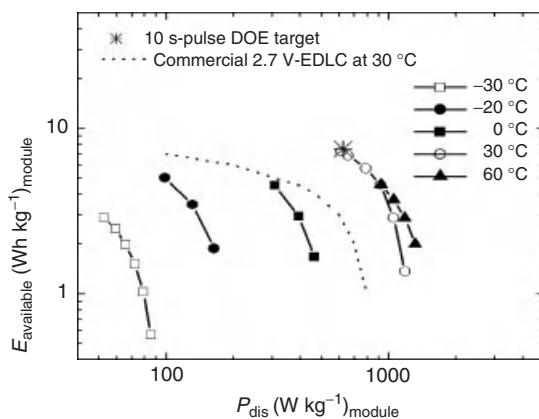


Figure 9.6 Available energy ($E_{\text{available}}$) versus discharge pulse power capability (P_{dis}) with $\Delta t_{\text{pulse}} = 10$ s of the $\text{PYR}_{1(201)}$ TFSI-based AEDLC from high-HPPC tests at different temperatures (*10 s-pulse DOE target;

dotted line: commercial EDLCs operating at 30 °C with $V_{\text{max}} = 2.7$ from Ref. [6]). Reproduced with permission from *J. Electrochem. Soc.*, **156**, A661 (2009). Copyright 2009, The Electrochemical Society [62].

IL that serves to deeply charge the system and to fill carbon pores. This balance is affected by electrode porosity and carbons of high specific capacitance, and moderate pore volume would prevent excess electrolyte in the electrodes [10, 46, 47]. This is the case of a 140 F g^{-1} disordered template carbon used to assemble a PYR_{14} TFSI-based AEDLC featuring a maximum specific energy 25–35% higher than that achieved with activated and xerogel carbons with the same IL. The moderate mesopore volume of the carbon (about $0.7 \text{ cm}^3 \text{ g}^{-1}$) makes it possible to achieve a composite electrode-to-electrolyte loading ratio of about 1, ratio that should yield a complete supercapacitor module weighing 2.5 times the electrode loading, while preventing charge storage limitation from the electrolyte side [23].

9.6

Concluding Remarks

High-performance IL-based supercapacitors require ILs of high purity, wide ESW, high conductivity and low freezing point. IL selection also has to take into account that the ion chemistry of these salts notably affects the double-layer structure at the electrode/IL interface and, hence, supercapacitor capacitance. The absence of a solvent implies the intimate contact of the IL with the carbon electrode, which has to be designed in relation to the IL. Carbon porosity is a crucial parameter affecting capacitance, module weight distribution, and power. Indeed, the main contribution to ESR is the electrode charging resistance that is modulated by pore size. The use of proper ILs and carbons in tailored AEDLC configurations is a successful

strategy for increasing the specific energy of supercapacitors and widening the safe temperature operating range of the systems without sacrificing power and cycle life.

Ionic Liquid Codes

BMIM BF ₄	1-butyl-3-methylimidazolium tetrafluoroborate
BMIM DCA	1-butyl-3-methylimidazolium dicyanamide
BMIM PF ₆	1-butyl-3-methylimidazolium hexafluorophosphate
BMIM TFSI	1-butyl-3-methylimidazolium bis(trifluoromethanesulfonyl)imide
Bu ₃ S TFSI	tributylsulfonium bis(trifluoromethanesulfonyl)imide
EMI FSI	1-ethyl-3-methylimidazolium bis(fluorosulfonyl)imide
EMI TFSI	1-ethyl-3-methylimidazolium bis(trifluoromethanesulfonyl)imide
Et ₂ Me(CH ₃ OC ₂ H ₅)N BF ₄	diethyl-methyl-methoxyethyl ammonium tetrafluoroborate
Et ₃ S TFSI	triethylsulfonium bis(trifluoromethanesulfonyl)imide
Me ₃ (CH ₃ OCH ₂)N TFSI	trimethyl-methoxymethyl ammonium bis(trifluoromethanesulfonyl)imide
Me ₃ PrN TFSI	trimethyl-propylammonium bis(trifluoromethanesulfonyl)imide
MePrPp TFSI	methyl-propyl-piperidinium bis(trifluoromethanesulfonyl)imide
P _{6,6,6,(103)} TFSI	tri-hexyl-methoxypropyl-phosphonium bis(trifluoromethanesulfonyl)imide
P _{6,6,6,14} CYC	tri-hexyl-tetradecyl-phosphonium cyclamate
P _{6,6,6,14} TFSI	tri-hexyl-tetradecyl-phosphonium bis(trifluoromethanesulfonyl)imide
PrMeMeIm TFSI	1-propyl-2-methyl-3-methylimidazolium bis(trifluoromethanesulfonyl)imide
PYR ₁₍₂₀₁₎ TFSI	methoxyethyl- methylpyrrolidinium bis(trifluoromethanesulfonyl)imide
PYR ₁₂ DCA	ethyl-methyl-pyrrolidinium dicyanamide
PYR ₁₃ FSI	propyl-methyl-pyrrolidinium bis(fluorosulfonyl)imide
PYR ₁₄ Tf	butyl-methyl-pyrrolidinium trifluoromethanesulfonate
PYR ₁₄ TFSI	butyl-methyl-pyrrolidinium bis(trifluoromethanesulfonyl)imide

Glossary

AEDLC	Asymmetric electric double-layer capacitor
σ	Conductivity
δ_{dl}	Double-layer thickness
ΔV_+	Maximum feasible potential excursion of the positive electrode
ΔV_-	Maximum feasible potential excursion of the negative electrode
BET	Specific area evaluated by the Brunauer, Emmett, Teller method
C_-	Double-layer specific capacitance of the negative electrode
C_+	Double-layer specific capacitance of the positive electrode
C_c	Capacitance in the solid part of the electrode
C_{dl}	Double-layer specific capacitance of carbon electrode
C_H	Helmholtz capacitance
C_{IL}	Capacitance in the liquid part of the electrified carbon electrode/IL interface
CNT	Carbon nanotube
C_{SC}	Supercapacitor capacitance
CV	Cyclic voltammetry
DOD	Depth of discharge
DOE	U.S. Department of Energy
E	Specific energy evaluated between V_{max} and $0.55 V_{max}$
EDLC	Electric double-layer capacitor
E_{max}	Maximum energy of supercapacitor
ESR	Equivalent series resistance
ESW	Electrochemical stability window
EV	Electric vehicle
FT-IR	Spectroscopy Fourier transform infrared spectroscopy
GC	Glassy carbon
HEV	Hybrid-electric vehicle
HPPC	Hybrid pulse-power characterization
i	Current density
IL	Ionic liquid
k_0	Vacuum permittivity
MW	Molar weight
P	Specific power evaluated between V_{max} and $0.55 V_{max}$
P_{max}	Maximum power of supercapacitor
RT	Room temperature
$S_{> 1.5 \text{ nm}}$	Specific surface area from pores $> 1.5 \text{ nm}$
$t_{0.55 V_{max}}$	Time at which the cell exhibits $0.55 V_{max}$ voltage
$t_{V_{max}}$	Time at which the cell exhibits V_{max} voltage
UPS	Uninterruptible power supply
USABC	United States Advanced Battery Consortium
V_{max}	Maximum cell voltage
w_+	Carbon loading of the positive electrode
w_-	Carbon loading of the negative electrode

$w_{c,m}$	Total carbon-binder composite weight of positive and negative electrodes
ϵ	Dielectric constant
Λ	Molar conductivity
η	Viscosity

References

- Conway, B.E. (1999) *Electrochemical Supercapacitors*, Kluwer Academic, Plenum Publishers, New York.
- Kotz, R. and Carlen, M. (2000) *Electrochim. Acta*, **45**, 2483–2498.
- Miller, J. and Burke, A.F. (2008) *Interface*, **17**, 53–57.
- Pickard, W.F., Shen, A.Q., and Hansing, N.J. (2009) *Renew. Sust. Energy Rev.*, **13**, 1934–1945.
- Karden, E., Ploumen, S., Fricke, B., Miller, T., and Snyder, K. (2007) *J. Power. Sources*, **168**, 2–11.
- Stewart, S.G., Srinivasan, V., and Newman, J. (2008) *J. Electrochem. Soc.*, **155**, A664–A671.
- Burke, A. (2007) *Electrochim. Acta*, **53**, 1083–1091.
- Zhang, S., Sun, N., He, X., Lu, X., and Zhang, X. (2006) *J. Phys. Chem. Ref. Data*, **35**, 1475–1517.
- Galiński, M., Lewandowski, A., and Stepniak, I. (2006) *Electrochim. Acta*, **51**, 5567–5580.
- Mastragostino, M. and Soavi, F. (2009) in *Encyclopedia of Electrochemical Power Sources*, Vol. 1 (eds J. Garche, C. Dyer, P. Moseley, Z. Ogumi, D. Rand, and B. Scrosati), Elsevier, Amsterdam, pp. 649–657.
- Lazzari, M., Soavi, F., and Mastragostino, M. (2008) *J. Power. Sources*, **178**, 490–496.
- Arbizzani, C., Biso, M., Cericola, D., Lazzari, M., Soavi, F., and Mastragostino, M. (2008) *J. Power. Sources*, **185**, 1575–1579.
- Bockris, J.O'M., Reddy, A.K.N., and Gamboa-Aldeco, M. (2000) *Modern Electrochemistry 2A Fundamentals of Electrode Processes*, Kluwer Academic, Plenum Publishers, New York.
- Lazzari, M., Mastragostino, M., and Soavi, F. (2007) *Electrochem. Commun.*, **9**, 1567–1572.
- Lockett, V., Sedev, R., Ralston, J., Horne, M., and Rodopoulos, T. (2008) *J. Phys. Chem. C*, **112**, 7486–7495.
- Islam, M.M., Alam, M.T., Okajima, T., and Ohsaka, T. (2009) *J. Phys. Chem. C*, **113**, 3386–3389.
- Hahn, M., Baertschi, M., Barbieri, O., Sauter, J.-C., Kötzer, R., and Gally, R. (2004) *Electrochem. Solid-State Lett.*, **7**, A33–A36.
- Baldelli, S. (2005) *J. Phys. Chem. B*, **109**, 13049–13051.
- Baldelli, S. (2008) *Acc. Chem. Res.*, **41**, 421–431.
- Nanbu, N., Sasaki, Y., and Kitamura, F. (2003) *Electrochem. Commun.*, **5**, 383–387.
- Aliaga, C. and Baldelli, S. (2006) *J. Phys. Chem. B*, **110**, 18481–18491.
- Federov, M.V. and Kornyshev, A.A. (2008) *Electrochim. Acta*, **53**, 6835–6840.
- Lazzari, M., Soavi, F., and Mastragostino, M. (2010) *Fuel Cells*, **10**, 840–847.
- Fujimori, T., Fuji, K., Kanzaki, R., Chiba, K., Yamamoto, H., Umebayashi, Y., and Ishiguro, S. (2007) *J. Mol. Liq.*, **131–132**, 216–224.
- Sato, T., Masuda, G., and Takagi, K. (2004) *Electrochim. Acta*, **49**, 3603–3611.
- Ania, C.O., Pernak, J., Stefaniak, F., Raymundo-Piñero, E., and Béguin, F. (2006) *Carbon*, **44**, 3126–3130.
- Fraser, K.J., Izgorodina, E.I., Forsyth, M., Scott, J.L., and MacFarlane, D.R. (2007) *Chem. Commun.*, **37**, 3817–3819.
- Matsumoto, H., Sakaebe, H., Tatsumi, K., Kikuta, M., Ishiko, E., and Kono, M. (2006) *J. Power. Sources*, **160**, 1308–1313.

29. Ishikawa, M., Sugimoto, T., Kikuta, M., Ishiko, E., and Kono, M. (2006) *J. Power Sources*, **162**, 658–662.
30. Zhou, Z.-B., Matsumoto, H., and Tatsumi, K. (2006) *Chem.—Eur. J.*, **12**, 2196–2212.
31. Passerini, S. and Appetecchi, G.B. (2007) Internal Report, FP6-EU Project “Ionic Liquid-based Hybrid Power Supercapacitors”, Contract No. TST4-CT-2005-518307.
32. Abbott, A.P. (2005) *ChemPhysChem*, **6**, 2502–2505.
33. MacFarlane, D.R., Forsyth, M., Izgorodina, E.I., Abbott, A.P., Annat, G., and Fraser, K. (2009) *Phys. Chem. Chem. Phys.*, **11**, 4962–4967.
34. Seddon, K.R., Stark, A., and Torres, M.-J. (2000) *Pure Appl. Chem.*, **72**, 2275–2287.
35. Wei, D. and Ng, T.W. (2009) *Electrochem. Commun.*, **11**, 1996–1999.
36. Lewandowski, A. and Olejniczak, A. (2007) *J. Power Sources*, **172**, 487–492.
37. Devarajan, T., Higashiya, S., Dangler, C., Rane-Fondacaro, M., Snyder, J., and Haldar, P. (2009) *Electrochem. Commun.*, **11**, 680–683.
38. Frackowiak, E., Lota, G., and Pernak, J. (2005) *Appl. Phys. Lett.*, **86**, 164104.
39. Frackowiak, E. (2006) *J. Braz. Chem. Soc.*, **17**, 1074–1082.
40. Zhu, Q., Song, Y., Zhu, X., and Wang, X. (2007) *J. Electroanal. Chem.*, **601**, 229–236.
41. Lewandowski, A., Olejniczak, A., Galinski, M., and Stepniak, I. (2010) *J. Power Sources*, **195**, 5814–5819.
42. Arbizzani, C., Beninati, S., Lazzari, M., Soavi, F., and Mastragostino, M. (2007) *J. Power Sources*, **174**, 648–652.
43. Largeot, C., Portet, C., Chmiola, J., Taberna, P.-L., Gogotsi, Y., and Simon, P. (2008) *J. Am. Chem. Soc.*, **130**, 2730–2731.
44. Ania, C.O., Pernak, J., Stefaniak, F., Raymundo-Piñero, E., and Béguin, F. (2009) *Carbon*, **47**, 3158–3166.
45. Barbieri, O., Hahn, M., Herzog, A., and Kötz, R. (2005) *Carbon*, **43**, 1303–1310.
46. Lewandowski, A. and Galinski, M. (2007) *J. Power Sources*, **173**, 822–828.
47. Robinson, D.B. (2010) *J. Power Sources*, **195**, 3748–3756.
48. Pandolfo, A.G. and Hollenkamp, A.F. (2006) *J. Power Sources*, **157**, 11–27.
49. Frackowiak, E. (2007) *Phys. Chem. Chem. Phys.*, **9**, 1774–1785.
50. Mysyk, R., Raymundo-Piñero, E., Anouti, M., Lemordant, D., and Béguin, F. (2010) *Electrochem. Commun.*, **12**, 414–417.
51. Balducci, A., Dugas, R., Taberna, P.L., Simon, P., Plée, D., Mastragostino, M., and Passerini, S. (2007) *J. Power Sources*, **165**, 922–927.
52. Lewandowski, A. and Galinski, M. (2004) *J. Phys. Chem. Solids*, **65**, 281–286.
53. Liu, H. and Zhu, G. (2007) *J. Power Sources*, **171**, 1054–1061.
54. Xu, B., Wu, F., Chen, R., Cao, G., Chen, S., and Yang, Y. (2010) *J. Power Sources*, **195**, 2118–2124.
55. Lu, W., Qu, L., Henry, K., and Dai, L. (2009) *J. Power Sources*, **189**, 1270–1277.
56. Zhang, H., Cao, G., Yang, Y., and Gu, Z. (2008) *Carbon*, **46**, 30–34.
57. Handa, N., Sugimoto, T., Yamagata, M., Kikuta, M., Kono, M., and Ishikawa, M. (2008) *J. Power Sources*, **185**, 1585–1588.
58. Ryoo, R., Joo, S.H., Kruk, M., and Jaroniec, M. (2001) *Adv. Mater.*, **13**, 677–681.
59. Morishita, T., Ishihara, K., Kato, M., and Inagaki, M. (2007) *Carbon*, **45**, 209–211.
60. Kötz, R., Ruch, P.W., and Cericola, D. (2010) *J. Power Sources*, **195**, 923–928.
61. Ruch, P.W., Cericola, D., Foelske, A., Kötz, R., and Wokaun, A. (2010) *Electrochim. Acta*, **55**, 2352–2357.
62. Lazzari, M., Soavi, F., and Mastragostino, M. (2009) *J. Electrochem. Soc.*, **156**, A661–A666.
63. INEEL (2003) FreedomCAR Battery Test Manual For Power-Assist Hybrid Electric Vehicles, Prepared for the U.S. Department of Energy.
64. INEEL (2004) FreedomCAR Ultracapacitor Test Manual, Prepared for the U.S. Department of Energy.

10

Manufacturing of Industrial Supercapacitors

Philippe Azaïs

10.1

Introduction

The storage of electrical charge in the interface between a metal and an electrolytic solution has been studied by chemists since the nineteenth century, but the practical use of double-layer capacitors only began in 1957, when a patent was placed by General Electric for an electrolytic capacitor using porous carbon electrodes [1]. It was noted that the capacitor exhibited an “exceptionally high capacitance.” In 1966, the Standard Oil Company, Cleveland, Ohio (SOHIO) patented a device that stored energy in the double-layer interface [2]. At this time, SOHIO acknowledged that “the double layer at the interface behaves like a capacitor of relatively high specific capacity.” SOHIO went on to patent a disk-shaped capacitor in 1970 utilizing a carbon paste soaked in an electrolyte. By 1971, however, a subsequent lack of sales led SOHIO to abandon further development and license the technology to Nippon Electric Corporation (NEC). NEC went on to produce the first commercially successful double-layer capacitors under the name “supercapacitor.” These low-voltage devices had a high internal resistance and were thus primarily designed for memory backup applications, finding their way into various consumer appliances. Since then, a number of companies started producing electrochemical capacitors. Panasonic developed the “Gold Capacitor” in 1978. Similar to those produced by NEC, these devices were also intended for use in memory backup applications. By 1987, Elna had begun producing their double-layer capacitor under the name “Dynacap.” News of these devices triggered a study by the US Department of Energy in the context of hybrid electric vehicles, and by 1992 its “Ultracapacitor Development Program” was under way at Maxwell Laboratories. For two decades, industrial research has proposed numerous solutions to manufacture supercapacitors with improved reliability and limited aging [3].

As shown in Figure 10.1, the number of patents has strongly increased after the end of the 1980s, demonstrating the growing interest in this technology.

Carbon/carbon supercapacitors working in organic medium are the most popular and developed supercapacitor types in the world. However, cell and module designs are strongly linked to targeted markets: small-size cells for backup and electronics,

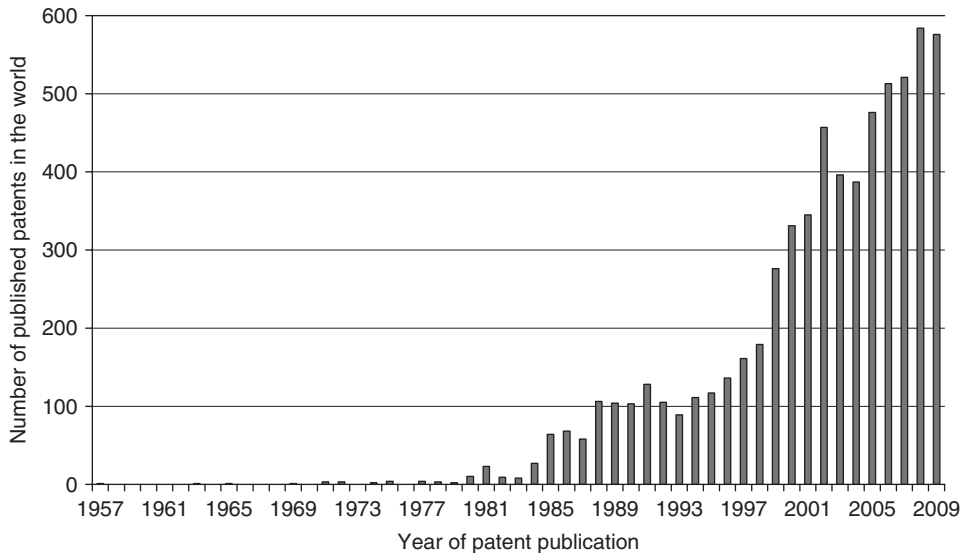


Figure 10.1 Number of published patents every year in the world since 1957.

medium-size cells for voltage network stabilization and large cells and modules for transportation and stationary applications.

Generally, supercapacitors are based on two electrodes separated by a dielectric porous film, called a separator, impregnated by an electrolyte. This electrolyte, which contains a large amount of ions, can be based on organic or aqueous solvents. This assembly is placed in a tight casing to avoid gas and/or liquid leakage.

To manufacture a supercapacitor, it is necessary to distinguish different steps:

- 1) Manufacturing of the electrode
- 2) Separator positioning (by winding or stacking)
- 3) Electrode assembly (current collection between electrode and external connection) by various processes
- 4) Electrolyte impregnation
- 5) Closing of the system.

During the 50 years, many industrial actors have tried to improve the performance of supercapacitors through three distinguished and complementary axes to enable the merger of this energy storage system: increase energy density, increase power density (i.e., decrease equivalent series resistance (ESR)) and increase the lifetime of components. To these three main technical axes, it is necessary to add two other critical points that are needed for viability of such energy storage systems: low price and robustness. Indeed, only products combining low cost and accurate performance have a hope of market penetration. Product robustness is a key parameter related to the market volume of components and thus to market development

and maturity. Cost reduction targets materials used in the supercapacitor and manufacturing processes for its implementation.

From an industrial point of view, two main classes of components can be distinguished:

- 1) High-capacitance supercapacitors that have a capacitance value higher than 350 F. These components are especially dedicated to urban transport market, uninterruptible power supply (UPS), automotive hybridizations, lifts, and so on. For all these markets, supercapacitors are assembled in modules and/or energy storage systems generally assisted by an electronic balancing.
- 2) Low-capacitance supercapacitors are essentially dedicated to low-cost electronic applications, such as backup applications, consumers, and so on. In these cases, components are generally directly welded on electronic cards.

This last market can be considered as quite mature. Component dimensions are directly inspired from electronic standards, such as electrolytic capacitor and dielectric capacitor or coin battery cells. Performance improvements of these components seem to be less crucial: cost and robustness are the key factors.

On the contrary, the high-capacitance component market fully emerges: component formats are not definitively set and module designs (voltage, capacitance, dimensions) are directly linked to the dedicated applications.

In the first part, the heart of the technology is detailed (electrode, separator, and electrolyte). The second part is dedicated to existing products and processes in the manufacture of supercapacitors. In the third part, modules are described.

10.2 Cell Components

10.2.1 Electrode Design and Its Components

The most important component of the supercapacitor is the electrode. Existing electrode designs are commented on hereinafter.

The electrode is the most important component in the heart of the technology. Generally, electrodes are made of a current collector, an active-material-based paste, a conductive additive, and a binder. In some cases, additives have been developed to increase lifetime.

10.2.1.1 Current Collector

To achieve low resistance, many solutions have been proposed. One of the most popular solutions is to deposit the active material on a metallic current collector, because of its very low ESR impact. Few former electrode designs have been developed without a current collector. This technology is called *self-supported* electrodes. Two ways were developed: in the first case, the electrode contained a high binder rate (ESR was extremely high); in the second case, activated carbon was

self-supported, such as carbon cloth. This last technology was extremely expensive and the energy density was low because of low material density. In both cases, ESR was high and these technologies were not efficient enough to reach high power density. All these self-supported technologies were quickly abandoned in favor of the metallic current collector technology.

In the present electrode technology, the current collector is the main physical link between the electrode and the supercapacitor external junction.

Microscopic active material decohesion from the current collector is assumed to be one of the main reasons for the ESR increase during lifetime. Many more or less cost-efficient solutions have been patented in order to optimize mechanical or chemical adhesion of the activated carbon on the current collector:

- Coating of a slurry or extrusion of a paste based on activated carbon on the current collector using aqueous or organic solvents: these processes are the most cost efficient and widely industrialized.
- To laminate carbon particles directly on the current collector without any binder (Honda [4], NEC [5]). This method is not efficient enough for thick electrodes to reach a low ESR value.
- To use surface groups of activated carbon as potential polymeric bridges using an isocyanate-based polymer in order to improve the mechanical properties of coated layer on aluminum [6]. However, it is assumed that surface groups of activated carbons are strongly involved in the aging phenomenon of supercapacitors.
- Activated carbon cloth bonded by plasma on an aluminum collector [7] (old supercapacitor design of Maxwell).

The choice of current collector is highly discriminated by its

- 1) electrochemical and chemical stability versus electrolyte
- 2) cost (purity and availability on market)
- 3) density
- 4) processability.

However, it is important to differentiate collectors stable in aqueous medium (acidic or basic medium) and those stable in organic medium.

Current Collector Working in Organic Electrolyte The most useful material for current collectors is aluminum: price and density are low and electrochemical stability is quite high versus standard electrolytes (propylene carbonate (PC) and acetonitrile (ACN)) [8]. Major industrially used current collectors have a special surface state in order to increase the mechanical adhesion between the coated layer (i.e., active material) and current collector. This surface state can be very different:

- It can be electrochemically corroded. In this case, the current collector is the same as the electrolytic capacitor anode. This special surface state is called *etched* aluminum [9, 10]. The thickness of such current collectors is between 15 and 40 μm . The manufacture of such current collectors is already advanced. Its price is also quite low. Figure 10.2 shows an example of an etched aluminum current collector.

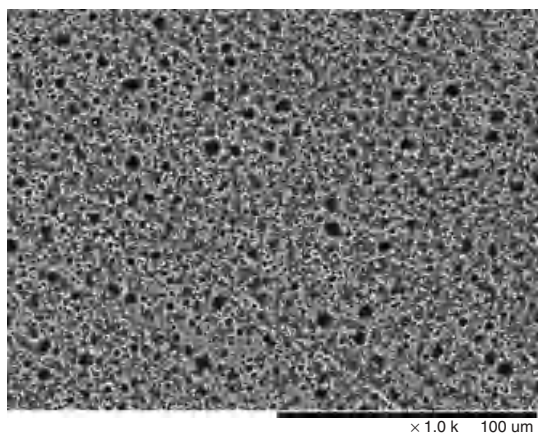


Figure 10.2 Example of etched current collector SEM picture ($\times 1000$). Courtesy of Batscap.

- One very thin underlayer (between hundreds of nanometers and few micrometers) can be placed between the current collector (with or without etching layer) and the active material layer. This thin layer, generally based on carbon black, carbon nanofiber [11], carbon nanotubes (CNTs), or graphite [12], has to be highly conductive compared to the electrode and contains a binder [13]. The main drawback of this underlayer is its cost because these collectors are especially developed for supercapacitors and batteries. Moreover, the thickness of such a layer cannot be negligible versus the thickness of the active material layer (Figure 10.3).
- Standard aluminum foil (i.e., not etched, Figure 10.4) can be used as current collectors [14]. The main advantage of such collectors is its cost. However, it is difficult to maintain electrode paste on such collectors using conventional binders such as polyvinylidene fluoride (PVDF) or polytetrafluoroethylene (PTFE). Generally, interface ESR is high but it can be low enough for energy-type supercapacitors. That is the reason Gore has developed an acetamide-based binder for such applications.
- In order to improve the adhesion between the electrode and collector, current collectors in various shapes have been patented:
 - Plurality of voids extending through a thickness of the collector in order to improve impregnation and shorten the ion travel distance to prevent or reduce localized electrolyte starvation within the electric double-layer capacitor (EDLC) [15]
 - Current collector with an underlayer containing perforations [16]
 - Aluminum grid. Such a collector is difficult to weld with external components (cover, casing).

Current Collector Working in Aqueous Medium The first supercapacitors worked in aqueous medium. Generally, aqueous electrolytes are based on strong acids (e.g., sulfuric acid) or strong bases (e.g., KOH) [17].

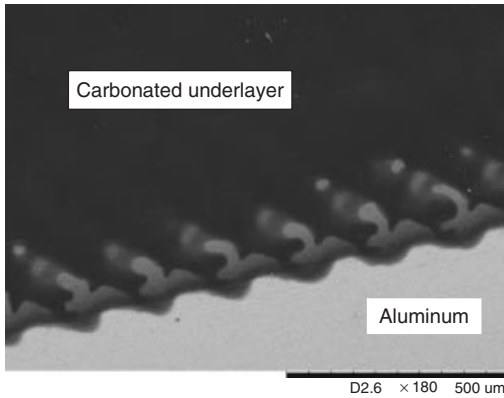


Figure 10.3 Nonetched collector with carbonated underlayer SEM picture ($\times 180$). Courtesy of Batscap.

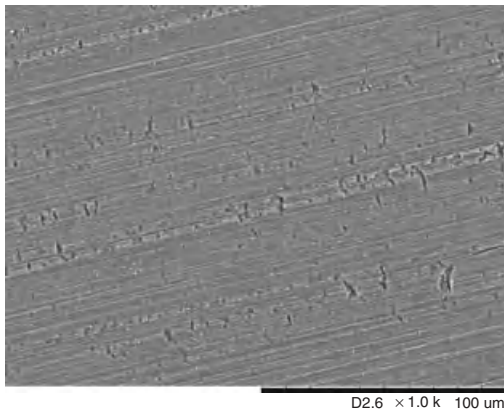


Figure 10.4 Nonetched aluminum collector. SEM picture ($\times 1000$). Courtesy of Batscap. White spots are mineral-inclusion-linked purity of aluminum series.

Because of such electrolytes, it is not possible to use an aluminum current collector. The materials most used are nickel and stainless steel [18]. However, such collectors are more expensive and heavier than aluminum collectors. Moreover, it is difficult to limit the interface ESR because these collectors are not etched. However, it is possible to decrease the ESR by increasing the roughness of the plain foil using a specific mill roll.

Other technologies have been developed to reduce ESR, such as grids and underlayer. These collectors are already used in Ni–MH, Ni–Cd, and lead-acid batteries that also work in aqueous medium.

10.2.1.2 Activated Carbons for Supercapacitors

Activated carbon is the solid active material (host site) of supercapacitors. In 1957, the first supercapacitor was based on a low porous carbon. Very soon, researchers

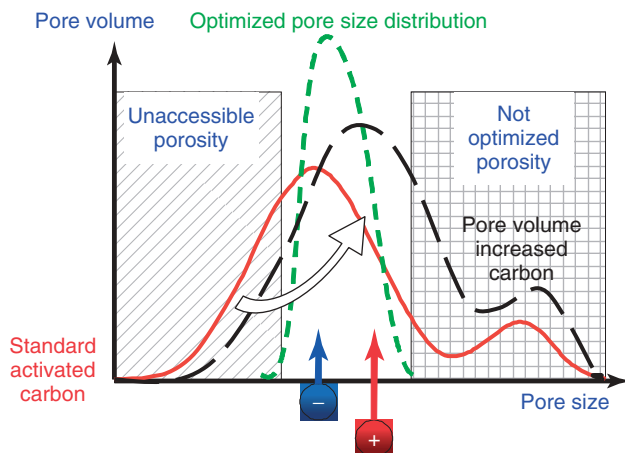


Figure 10.5 Standard activated carbon pore size distribution (PSD) and impact of pore volume increase (designated by arrow) via standard activation process on PSD. Comparison with theoretical optimized PSD.

understood that it was needed to increase the accessible surface to ions in order to increase capacity.

The first commercial activated carbons that were industrially available for supercapacitors were manufactured for filtration and sugar purification. Thus, these carbons were not developed for energy storage and posed many problems: low purity, high surface group content, and untuned particle size distribution. The lifetime of these supercapacitors was low. During the past 15 years, the main actors in the supercapacitor field have tried to increase gravimetric and volumetric capacities, especially in using superactivated carbon (e.g., Maxsorb activated carbon). More recently, a few researchers have understood that such superactivated carbons are in contradiction to high lifetime, low internal resistance, and low-cost design. Then, new carbons were developed or modified especially for supercapacitor applications.

It is generally accepted that only 20–30% of porosity is truly accessible to the ions, allowing the storage of energy [19–21]. In order to increase accessible porosity to ions, many studies have focused on developing porosity [22–27]. However, most of the developed processes increase porosity, increasing at the same time the surface area and enlarging the pore size distribution, as shown in Figure 10.5.

Carbon Availability Carbons can be distinguished in two main classes, taking into account activation modes (physical or chemical activation) and precursors (synthetic and natural) [28]. However, carbons developed at the laboratory scale are generally different from industrially available carbons [29]. Nevertheless, it is important to mention the most important works published during the past two decades.

Laboratory-Scale Carbonaceous Active Materials Numerous types of carbons that have been tried as electrodes in EDLCs can be summarized as halloysite templated

porous carbon [30], multibranched porous carbon nanofibers [31], nanostructured graphite [32], bamboo-based activated carbon [33], woven carbon cloth [34], CNTs [35], nanostructured mesoporous carbon [36], CNT/felt composite electrode [37], cresolformaldehyde-based carbon aerogel [38], mesoporous carbon composite (carbon nanofibers/porous carbon) [39], porous carbon from thermoplastic and MgO precursors [40], sodium-oleate-modified activated carbon aerogel [41, 42], carbon aerogel [43–46], activated carbonized methylcellulose [47], carbide-derived carbons (CDC) [48–51] silica MCM-48-templated mesoporous carbon [52], zeolite-templated carbon [53], electrospun activated carbon nanofibers [54], silica MCM-48- and SBA-15-templated mesoporous carbon [55], carbon nanofibers [56], carbon blacks, vegetable/wood-based activated carbons, activated novoloid fibers [57], activated needle coke from coal tar pitch [58], fullerene-soot [59], Nomex-derived activated carbon fibers [60], activated CNTs [61, 62], mesoporous carbon spheres [63], pyrolyzed carbons from graphite oxides [64], Ketjenblack/CNTs [65], multiwalled [66–69] and single-walled CNTs [70], exfoliated carbon fibers [71], CNTs/activated carbon composite [72], CNT array [73] and double-walled CNT/activated carbon [74], ex-polyvinylidene chloride (PVDC) activated carbon [75], or ex-PVDF activated carbon [76]. Among all these materials, a few comments are needed, especially for CNTs, and aerogels.

- CNTs have not shown superior electrochemical performance compared to conventional activated carbons. The price of such materials is still high and not competitive compared to industrialized purified activated carbons. Although the catalyst amount after synthesis has been decreased year after year, the toxicity is still questionable for industrial applications. However, studies have shown that such materials can be successfully used as conductive additive in electrodes [77, 78]. This could be the case if the price is competitive with low-cost carbon black.
- Many studies have been performed on carbon aerogels. Gravimetric and volumetric capacitance in organic medium is quite low, taking into account the fact that it is generally a mesoporous material. Such materials could be used as-produced (i.e., monolithic shape) avoiding binder and particle–particle electronic resistance. However, most such materials have a high surface group content and it is quite difficult to thermal treat (at high temperature) such materials without any volume modification. Then, the aging performance is poor. Owing to the large amount of mesoporosity, self-discharge (linked to ion diffusion) is an issue. Moreover, the price is extremely high. However, PowerStor commercializes EDLC (up to 50 F) with carbon aerogel electrodes working in organic electrolyte (quaternary ammonium salt/PC and/or acetonitrile).
- CDC materials have been developed recently in different laboratories. They have a distribution of pore sizes sufficiently tightened and were developed for this application. They are not from the activation of a precursor but are the residue of a chlorination reaction of a transition metal (e.g., titanium). The mass yield is quite low and the final product must then be carefully restated to remove traces of chlorine that is particularly harmful in aging. The price of this material is quite high. However, it is a great “model material” for supercapacitors.

Industrially Available Active Materials Many activated carbon manufacturers have recently been investigating supercapacitor applications. As a result, most companies have understood that the cost and performance are the two basic parameters of a successful carbon in this area.

The commercially available carbons are as follows:

- Wood-based activated carbons. These carbons are fairly low-volume capacity but also very low priced. The performances in aging, just as with all carbons, are linked to their purity, the surface groups, and so on. The activation of such activated carbon is performed with water vapor [79–81].
- Coconut-based activated carbons. This is by far the most common carbon in the field. They are a good compromise between pore volume, ESR, purity, and price because they are generally activated with water vapor [82].
- Petroleum-residue-based activated carbon (coke, coal tar, etc.) [83]. They are generally more capacitive than carbon from natural precursors (wood and coconut). They are also very expensive and the surface groups are generally numerous, thus increasing the aging of the supercapacitor [84]. Some manufacturers have found ways of improving performance in aging, but these products are still expensive because of the type of activation (usually potash) [85, 86].
- Carbohydrate-based activated carbons [87]. These carbons are relatively unusual but can be considered as a good compromise between coconut-based activated carbons and petroleum-residue-activated carbons. Such carbons are particularly clean but volumetric capacitance is still limited [88].
- Ex-resin-activated carbons (e.g., phenolic resin). They are by far the most pure carbons. They have an attractive performance in terms of aging, resistance, and capacity but are extremely expensive. They are pretty generally laid aside by the manufacturers of supercapacitors because of the economic equation they generate. One of the most popular carbons is the RP series from Kuraray Chemicals (RP15 and RP20), which are cited in a few publications [89].

Pore Size Distribution Optimization of Activated Carbons

Dissymmetrization and Its Effects Although cations and anions do not have the same size and volume, the use of symmetric carbon-based electrodes ends in a dissymmetrization of potentials in a standard component. A supercapacitor electrode made from the same positive and negative characteristics (thickness, type of carbon, binder rate, etc.), so geometrically and chemically identical, is necessarily asymmetrical in terms of potential. This fact is clearly identified using a reference electrode to determine cathodic and anionic potentials as demonstrated [90–93].

This dissymmetrization has a strong impact on electrolyte degradation in aging phenomena, especially for positive potential. To force this dissymmetrization is quite an old idea: this principle was clearly described in a Japanese patent dated 1986 [94]. This principle can be used in order to improve ESR, capacitance, and/or aging, and is summarized in Figure 10.6. One of the best ways is to fit pore size distribution of activated carbon to ion sizes [95].

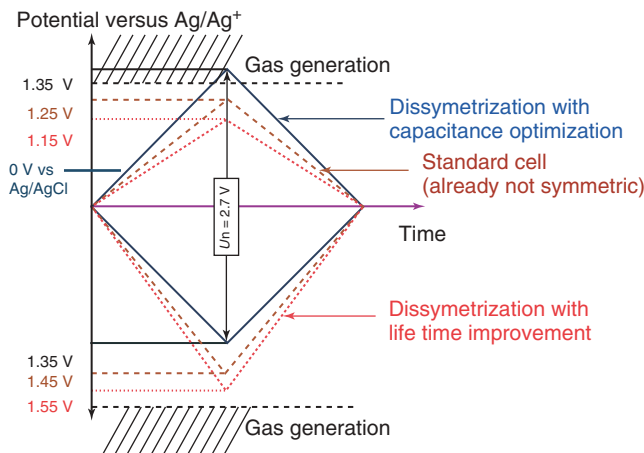


Figure 10.6 Dissymmetrization principle with alternative propositions.

Table 10.1 Dissymmetrization effect on aging and performance loss.

	Electrode thickness ratio (+ vs -)	Initial performance		Performance after 1000 h at 3.0 V/70 °C	
		ESR (Ω)	Capacitance (F)	ESR (Ω)	Capacitance loss (%)
Supercapacitor 1	1/0.6	6.5	1.00	7.4	-5
Supercapacitor 2	1/1	5.2	1.20	8.9	-30

Many ways have been investigated to improve performances:

- 1) Balancing weights and/or volumes of the two electrodes using the same activated carbon in order to improve aging.
- 2) Using different activated carbons in order to fit each pore size distribution of each carbon to one of the two ions in order to maximize capacitance and decrease ESR.
- 3) Adjusting each potential of each electrode in order to minimize aging.
- 4) Combining the three previous solutions.

In the patent dated 1986, the goal was to adjust the electrode potential of each electrode in order to minimize aging for the supercapacitor working in TEABF₄/PC electrolyte. The main advantage of such dissymmetrization is clearly demonstrated in Table 10.1.

One interesting solution in order to optimize performance consists of choosing two carbons with different pore size distributions adjusted to each ion size. The standard ionic salt used in electrolytes is TEABF₄. Unsolvated (C₂H₅)₄N⁺ size is considered to be between 0.348 [96] and 0.40 nm [97] and BF₄⁻ size is between 0.22 [20] and 0.245 nm [98]. Table 10.2 shows that capacitance value is increased and

Table 10.2 Pore size effect on volumetric capacitance and ESR. Electrode B has the smallest PSD.

	Negative electrode	Positive electrode	Volumetric capacitance (F cm ⁻³)	ESR (mΩ)
Supercapacitor 1	A	B	26.6	24
Supercapacitor 2	A	A	20.8	23
Supercapacitor 3	B	B	27.5	257
Supercapacitor 4	B	A	18.8	243

ESR is lowered when pore size distribution is lower for the positive electrode than for the negative electrode [99]. Reversing the electrodes demonstrates capacitance decrease and ESR increase. These facts prove that a compromise has to be found between ion size and pore size distribution of activated carbons [100].

Many other patents have been published on this dissymmetrization principle (EPCOS [101], Maxwell [102], Nisshinbo [92, 103], CapXX [104], Ultratec [105], etc.). All these patents are alternative solutions of the 1986 patent.

Although dissymmetrization seems very attractive, it is industrially more difficult to manage such productions of two different electrodes. In such cases, “poka-yoke” are needed.

10.2.1.3 Industrial Activated Carbons for Industrial Supercapacitors

For several years, it has been considered that gravimetric or volumetric capacity (related to the size of ions and the pore size of carbon) is proportional to the Brunauer-Emmet-Teller (BET) surface area (number related to the molecular size of nitrogen and the available pore volume for the same nitrogen molecules). As some authors have demonstrated (Béguin and Simon groups), it makes no sense: sizes of ions used (solvated or not) in supercapacitors are always greater than the nitrogen molecule. Figures 10.7 and 10.8 show that there is no proportionality between BET surface area measured by nitrogen and gravimetric capacity, either in aqueous or organic media.

As described previously, most industrial electrodes are produced from powders. Indeed, tissue carbons, very expensive and very low density, pose some problems for large size supercapacitor production: connection of such self-supported material to an external terminal is complex and the contact resistance generated is high.

Many recommendations regarding activated carbons for supercapacitors working in organic medium have been mentioned. One of the main recurrent recommendations concerns pore size distribution and pore volume of the electrode, for example:

- Asahi Glass Co. recommended in one patent to limit macropore volume to less than 10% of the pore volume and almost 50% of pore volume must be microporous (pore size lower than 2 nm) [107]. Specific surface area must be

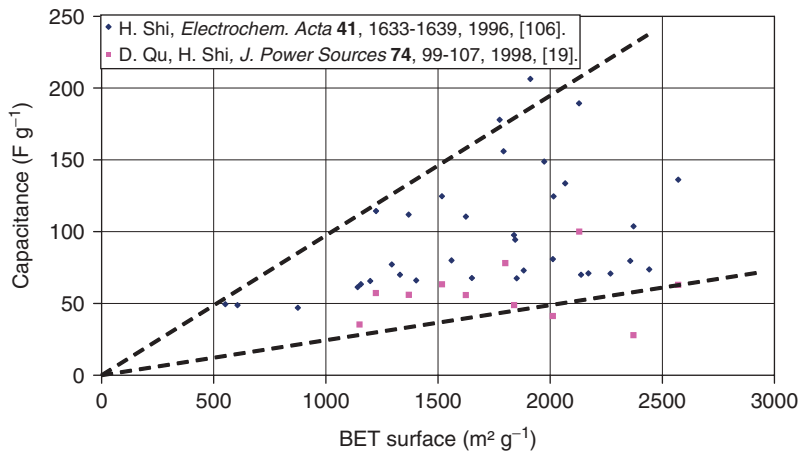


Figure 10.7 Gravimetric capacitance in aqueous electrolyte (KOH 30%) for numerous activated carbons versus BET surface area measured at 77 K with nitrogen.

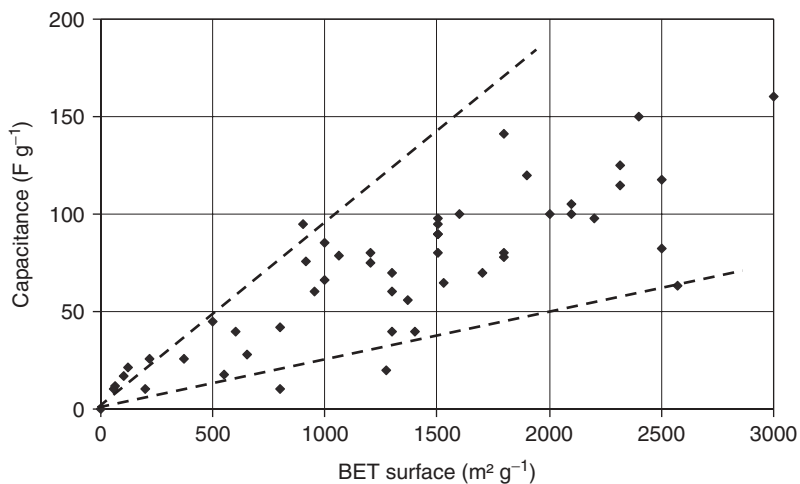


Figure 10.8 Gravimetric capacitance in organic electrolyte based on Et_4NBF_4 salt (solvent: PC or acetonitrile) for numerous activated carbons versus BET surface area measured at 77 K with nitrogen. Values are extracted from numerous academic publications and patents.

limited between 1000 and 1500 $\text{m}^2 \text{g}^{-1}$ and not between 2000 and 2500 $\text{m}^2 \text{g}^{-1}$ as mentioned by Morimoto *et al.* [108] a few years before.

- Kureha confirmed such limitation between 800 and 2000 $\text{m}^2 \text{g}^{-1}$ and preferentially between 1050 and 1800 $\text{m}^2 \text{g}^{-1}$ [109]. Many of Matsushita's patents confirm such values: BET surface area of activated carbons for supercapacitor application should be limited at around 1500 $\text{m}^2 \text{g}^{-1}$ and not at 2500 $\text{m}^2 \text{g}^{-1}$. Such carbons can be obtained by low temperature activation by alkali hydroxides (750–850 °C) [110].

- Endo *et al.* [111] have obtained good results with activated carbons having surface area lower than $1500 \text{ m}^2 \text{ g}^{-1}$. The best result is obtained by an alkali activated-carbon-based on Polyvinylchloride (PVC) precursor. The surface area is around $700 \text{ m}^2 \text{ g}^{-1}$. Gravimetric and volumetric capacitances are 168 F g^{-1} and 148 F cm^{-3} , respectively. Such results are comparable to superactivated carbon with $2500 \text{ m}^2 \text{ g}^{-1}$ BET surface (180 F g^{-1} and 80 F cm^{-3}). However, volumetric capacitance is higher because of material density.
- JEOL has demonstrated quite the same tendencies with low-surface-area activated carbons ($300\text{--}400 \text{ m}^2 \text{ g}^{-1}$) activated by KOH [112].

All these results confirm that there is no proportionality between capacitance values in organic media and BET surface area: a compromise has to be found between pore size distribution of carbons and ion sizes of electrolytes. Many recent publications have reached similar conclusions [50, 113, 114, 115, 116]. However, it is important that such capacitance optimizations do not reduce cyclability of supercapacitors and do not increase ESR.

Activated Carbon Precursor Impact on Performance Another solution patented to optimize the active material is to mix different activated carbons having different physicochemical characteristics [117]. The originality of such a concept is the simultaneous use of one graphitizable carbon and a second non-graphitizable carbon. Authors have demonstrated that the obtained results of each carbon measured separately are not as good as the mixture of these carbons. Structural reasons could essentially explain such a result: non-graphitizable carbon has good mechanical strength and has a low volume change in the phenomena charge–discharge, while the graphitizable carbon has a good capacitance density but a major expansion coefficient. The swelling suggests an insertion phenomenon, as claimed by Takeuchi *et al.* [118] and as confirmed by Hahn *et al.* [119, 120]. Then, a mix of these two carbons allows to limit swelling and to obtain quite a high volumetric capacitance. However, this expansion is particularly noticeable in the case of an electrolyte containing PC and is less likely in the case of an ACN-based electrolyte. Indeed, the phenomenon of intercalation of PC has been known for many years in the field of Li-ion batteries, which severely limits the use of PC in the electrolyte for such batteries. Another fact that may come into play in the electrochemical phenomena is the purity of the materials. Kuraray mentions a crucial problem linked to the presence of heavy metals [121]: such metals could favor short circuits or generate self-discharge if the total content is higher than 50 ppm. It means that it would be unreasonable to use natural-based activated carbons for supercapacitor applications without any special cleaning treatment. Alkalis are important impurities for supercapacitors [122]. Sulfur [123], iron, and magnesium [124] are also considered to be important impurities. Asahi Glass recommends strongly limiting chromium, iron, nickel sodium, potassium, and chloride contents to keep a stable activity over a long period of time by using a polarizable electrode made of activated charcoal. In the same time, the ash content must be limited to 0.5% [125].

Table 10.3 Impact of particle size on electrode density and volumetric capacitance.

EDLC	Average particle size (μm)	Electrode density	Electrostatic capacity density (F cm^{-3})
Example 1	2.36	0.924	33.6
Example 2	8.64	0.987	36.0
Example 3	9.8	0.983	35.7
Example 4	13.23	0.956	34.8
Example 5	26.28	0.913	33.0

10.2.1.4 Particle Size Distribution of Activated Carbons and Its Optimization

Although interparticle space creates some macroporosity, particle size distribution is an important parameter that has a strong impact on performance (e.g., volumetric and gravimetric capacitance).

One good example of such an impact is shown in Table 10.3 [126].

Kuraray [127] recommends that medium particle size (D50) be limited between 4 and 8 μm to provide a polarizable electrode for an EDLC, exhibiting good moldability and capable of realizing a high-density or high-capacity electrode. At the same time, almost 10% of particles (in cumulative volume) must be smaller than 2 μm [128].

A mixture of two activated carbons having two very different particle size distributions in order to increase electrode density has been tested and gives interesting results [129], although it is quite difficult to implement such a solution in the electrode manufacturing process.

Surface Group Impact on Performance and Solutions The capacitance decrease and resistance increase during the operation, and the self-discharge, are the key technical factors limiting market accessibility of organic electrolyte supercapacitors. Publications related to aging are limited because of the confidentiality of such information in the industrial environment. For this reason, it is important to undertake a literature review both in scientific journals and in patents. The research on supercapacitors based on activated carbon in organic media is essentially done in the industry in collaboration with academic laboratories and typically leads to the filing of patents, for 45 years.

The positive or negative impact of surface groups on the performance of supercapacitors is controversial: the presence of these groups seems to be desirable in aqueous medium for additional reversible pseudocapacitance for the contribution they make to the total capacitance (redox reactions of surface groups) [106, 130, 131]. This contribution was originally anticipated by Delahay [132, 133], and then generalized for both aqueous media [134] and organic media [135] by Schultze and Koppitz in the 1970s.

However, Sullivan *et al.* [136] showed that an excess of oxygen increases the resistance of the material, as confirmed both in aqueous and in organic media by Momma *et al.* [137] and Qiao *et al.* [138], respectively. The Kötzt group has also shown that glassy carbon, which is oxidized and then reduced in a second step, shows higher capacitance and lower resistance as the only oxidized glassy carbon [139].

In aqueous media, the acid groups are harmful [140] for the following reasons:

- They cause the release of gases at low potential (as confirmed by Mayer *et al.* [141]).
- They significantly reduce the supercapacitor lifetime [142].

For supercapacitors working in organic medium, Morimoto *et al.* [108] have shown that the reduction of capacitance during the operation is linked to oxygen. The more the activated carbon is rich in oxygen, the greater the amount of gas emitted is high (essentially hydrogen from electrolysis of water). Jow *et al.* [143] have shown that the surface group content of activated carbon has a strong impact on usable voltage window of supercapacitors. Therefore, in organic media, the choice must be worn on an oxygen-poor carbon and more specifically with few carboxyl groups in order to limit electrolyte decomposition.

According to Yoshida *et al.* [144], leakage current, that is to say a part of the self-discharge of a supercapacitor, is related to the amount of surface carboxylic acid groups.

Self-discharge According to theoretical studies by Conway *et al.* [145], three kinds of self-discharge mechanism can operate:

- 1) If the capacitor (or battery cell) has been overcharged beyond the respective decomposition potential limit of the electrolyte, then the self-discharge corresponds to the spontaneous decline of the overvoltage, h , owing to the overcharging current and arises on account of continuing discharge across the double-layer until h tends to 0. The leakage process corresponds to a faradic charge-transfer reaction having a potential-dependent faradic resistance, RF , operating in parallel across the double-layer capacitance, its value increasing with declining potential.
- 2) If the capacitor material and/or its electrolyte contain impurities are oxidizable or reducible within the potential range corresponding to the potential difference across the capacitor on charge, the capacitor becomes, to some extent, nonpolarizable. If only low concentrations of impurities are present, then the self-discharge redox process(es) is (are) diffusion controlled.
- 3) If the energy storage device has internal ohmic leakage pathways, for example, due to incomplete sealing of bipolar electrodes or interelectrode contacts, self-discharge will take place through a “Galvanic couple” effect.

Ricketts and Ton-That have linked the self-discharge of a supercapacitor operating in organic medium to diffusion of ions from regions where they are accumulated during the capacitor charge [146].

The oxidation of carbon can increase the capacitance but greatly accelerates the aging of the supercapacitor. As we have seen previously, the functionality of the carbon surface acts differently depending on whether the electrolyte is aqueous or organic.

Many treatments have been developed for surface modification of carbon for electrochemical applications: acid treatment [147, 148], oxidizing [149–151], electrochemical [152], thermal [153], by laser [154], by plasma [155, 156], by polishing [157], or by washing in a solvent [158], hydrogenation followed by a sulfonation [159], a first halogenation step by chlorine or bromine and a second step consisting in a dehalogenation under hydrogen [160] and so on.

Hirahara *et al.* [161] showed that lithium doping of activated carbon in an electrochemical way reduces the loss of capacitance (in floating and in galvanostatic charge–discharge) and increases the operating window of the electrolyte. However, no reasons have been mentioned to explain such facts. Meanwhile, Honda said that surface groups tend to lead to a loss of capacitance and proposed reducing under hydrogen or under nitrogen, but noted that hydrogen seems more efficient than nitrogen (the oxygen-containing groups are reformed within hours of pyrolysis under nitrogen, while hydrogen reduced) [162]. Such results have been confirmed by other studies [163, 164]: for Mitsubishi, surface functional groups' content must be limited to 0.5 meq g⁻¹ [165]. For Nippon Oil, alkali-activated carbon for supercapacitors must be thermal treated in an inert gas atmosphere of an oxygen concentration of 2000 ppm in volume or less to obtain an active carbon having a total amount of acid groups per unit weight of 0.2–1.2 [166]. Matsushita is consistent with such value of acidic groups (limited to 0.37 meq g⁻¹ of carbon) [167].

As a conclusion regarding surface groups, activated carbon manufacturers have strongly limited such amounts, especially acidic groups, in order to improve aging of supercapacitors, although pseudocapacitance phenomena are still not well understood in organic medium.

10.2.1.5 Binders

Adhesion and Cohesion: Key Parameters A binder must combine two functions: to make a strong cohesion between particles and enable adhesion of such an electrode on the collector.

In 1972, the authors of one of the first EDLC patents mentioned that one of the main problems to be solved was to obtain a good adhesion between coated paste and collector in order to limit ESR increase and capacitance decrease [168].

Binder content in the electrode must be low for the following reasons:

- 1) A maximum of particle–particle contacts and particle–current collector contacts must be ensured.
- 2) The electrolyte must impregnate the particles: intergranular volumes must not be clogged by the binder.
- 3) Most binders are insulating polymers: a high binder content in the electrode could increase the ESR of the component.

- 4) Binders are nonactive material and decrease volumetric and gravimetric capacitance values.

Electrode–Current Collector Interface and Existing Solutions The coating technology remains the easiest solution to implement. In 1988, Morimoto *et al.* [169] proposed to coat the current collector with an aqueous PTFE-activated carbon mixture to manufacture an EDLC working in organic medium (TEABF₄/ACN or sulfolane). This patent can be considered as the “parent patent” for most of the coating technology for supercapacitors.

The main advantage of the coating is to control the thickness of the electrodes and achieves a good volume density of power and energy. Later, most supercapacitor manufacturers chose this technology: Matsushita, Maxwell [170], SAFT [171], CEAC [172], Kureha [173], and so on. However, this technology has two main drawbacks:

- 1) The price of the electrochemical stable binder (available in aqueous or organic suspension).
- 2) Implementation process needs to produce an “ink” containing a large amount of solvent. This solvent must be removed by evaporation or by vacuum removal. An alternative method developed by Maxwell claims implementation with little or no solvent [174].

The most popular binder in the supercapacitor technology is PTFE because of its high electrochemical inertia and ability to keep a process in aqueous media [175]. Electrodes contain generally between 3 and 5% of PTFE. This polymer is not extrudable and it is easily detected in scanning electron microscopy (SEM) because it is generally fibrillated.

An alternative solution using the coating is to use a vinyl or cellulosic binder soluble in water such as PVA (polyvinyl alcohol) or CMC (carboxymethylcellulose) [176]. However, these binders are inconsistent with an operating voltage of about 2.7 or 2.8 V, which is to say to a potential of about +1.3 V/standard hydrogen electrode (SHE). Studies clearly show, for example, that the CMC is degraded at such voltage [177]. Generally, the CMC is not used alone but in combination with Styrene butadiene rubber (SBR) [178].

Polyimide is an interesting alternative to achieve electrode supercapacitors, which must operate at high temperatures (e.g., by coupling with ionic liquids). However, this polymer is not easily implemented (usually in the form of resins with organic solvent) and is extremely expensive. Moreover, the process requires evaporation and specific reprocessing of organic solvents. This latter type of binder has the advantage of having very good heat resistance, very good chemical inertness, and therefore a degassing at higher temperatures (400 °C) than other binders.

Table 10.4 compares the aging of different binders. The electrolyte is Et₄NBF₄ 1 M in PC and the separator is in polypropylene. The 1 A galvanostatic charge/discharges are performed between 0 and 2.8 V. As shown in Table 10.4, the drying binders accepting a higher temperature (polyimide) enable stabilization of resistance and capacitance over the operating time.

Table 10.4 Binder impact on aging performance (Varnish and Rickocoat are polyimide-type binders) [179].

Binder	Thermal treatment (temperature under low pression) (°C)	Initial properties		Properties after 3000 cycles at 2.8 V	
		Capacitance (F)	Internal resistance (Ω)	Capacitance (F)	Internal resistance (Ω)
U-Varnish A from Ube Industries	400	15.3	0.52	14.5	0.59
Rikacoat SN20E from Shin-Nihon Rika	350	15.4	0.51	14.7	0.56
Varnish, N7525 from TOYOBO	330	15.2	0.50	14.6	0.52
Cellulose	120	14.3	0.65	9.3	1.12
Polyvinyl alcohol	120	14.4	0.66	8.4	1.34

In the case of cellulose, there is a significant increase in resistance and a decrease in capacitance. The PVA gives the worst performance. It seems that formulation of the binder plays a key role in the evolution of the electrochemical performance of supercapacitors. However, current use of the CMC, owing to its low cost and the availability of a coating process, in aqueous media avoids waste management coatings. In addition, many CMC types have been developed for various applications. However, one of the major problems associated with the use of this product is the need to maintain a certain pH range (generally between 5 and 7) so as to maintain a good mechanical stability. This pH value therefore prohibited, in theory, the carbons containing many acidic groups [180]. However, the chemical modification of the CMC, for example, by grafting an ammonium salt instead of sodium, can change the pH range and for a better interaction between the carbon and binder. For example, Hitachi has showed that a mixture of PTFE and hydroxyalkylcellulose is more stable in the electrolyte than CMC and polyvinylpyrrolidone [181]. Recently, new aqueous based binders have been developed by Zeon Corporation (SBR-type with improved adhesion) and by JSR-Micro (new polyacrylamid-based binder for Li-ion batteries and supercapacitors).

However, Qu [182] has shown that capacitance is related to the wettability of carbon by an aqueous electrolyte, which necessarily depends on the type of surface groups present. The wettability particularly contributes to the increase in the adhesion between the carbon and the binder used to manufacture electrodes [138].

An alternative method to the coating is extrusion. The advantage of this method using a pressurized implementation of a paste is to limit sharply the use of solvent (organic or aqueous). These polymers, except PTFE and polyimide, are extrudable alone or in the process solvent. The charge rate is generally quite high (at least 80% activated carbon) and can achieve very high thicknesses easily [183–185].

As a conclusion regarding binders, PVDF [186] (use of organic solvent such as N-Methyl-2-pyrrolidone (NMP), Dimethyl sulfoxide (DMSO), (THF

(tetrahydrofuran), etc.) and PTFE (aqueous or ethanolic-suspension-based process) are very good alternative candidates to CMC or PVA binders.

10.2.1.6 Conductive Additives

As mentioned in the beginning of this chapter, active materials such as activated carbons are not very conductive materials. In 1972, Zykov *et al.* [187] proposed to add carbon black to activated carbon in a polymeric paste in order to improve conductivity of EDLC electrode: this patent is the basis of all present patents using coating and extrusion technologies.

It is generally necessary to add a suitable material capable of conferring electrical conductivity to the activated-carbon-based electrode in order to reduce its ESR. Many conductive additives have been developed – carbon black [188], mesoporous carbon black (Ketjenblack), acetylene black, carbon whiskers, carbon fibers, CNTs, natural or artificial graphite, metallic fibers such as aluminum or nickel fibers, metallic particles, and so on. It is particularly advantageous for the conductive material to have an average particle size, which is from 1/5000 to 1/2, and preferably from 1/1000 to 1/10, as large as the average particle size of the activated carbon [189].

Ketjenblack and acetylene black, both of which are types of carbon black, are generally preferred, although including these two kinds of carbon black can be slightly different [190]. Certain carbon blacks made via a gasification process, where carbon black is a by-product of the reaction (e.g., Ketjen EC600, Ketjen EC300, or Printex XE-2) have significant mesoporosity [191]. A comprehensive taxonomy of graphites and carbons has been reviewed by Wissler in 2006 [192].

Carbon black is electrically conductive and is widely applied for conductivity improvement in polymer engineering and the electrochemical industry. It is composed of more or less spherical particles (primary particles) with diameters in the size range of 10–75 nm, which form aggregates (fused primary particles) of 50–400 nm size. When homogeneously dispersed and mixed with the matrix, the aggregates form a compact one-, two-, or three-dimensional network of the conducting phase. Carbon black is usually very pure (about 97–99% C) and is considered to be “amorphous.” However, the microstructure is similar to graphite.

Generally, requirements for conductive additives are

- good electrical conductivity
- acceptable corrosion resistance
- availability in high purity
- low cost
- high thermal conductivity
- dimensional and mechanical stability
- light in weight and easy to handle
- availability in a variety of physical structures
- ease of fabrication into composite structures.

Up to now, only carbon blacks have been chosen by supercapacitor manufacturers because such carbons are a good compromise taking into account all

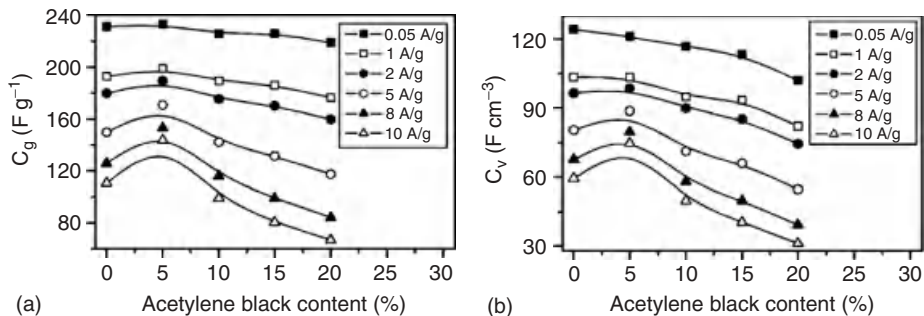


Figure 10.9 Variations of (a) gravimetric capacitance C_g and (b) volumetric capacitance C_v of activated-carbon-based electrodes with acetylene black content and with various galvanostatic rate.

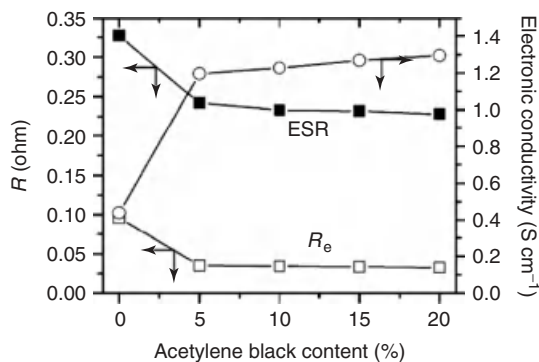


Figure 10.10 Variations of ESR (equivalent serial resistance), R_e (electronic resistance), and electronic conductivity of electrode with acetylene black content. R_e and electronic conductivity were measured by a four-point method.

their requirements. However, CNTs and carbon nanofibers could be interesting materials provided that their price decreases and purity increases.

An example of carbon black impact on volumetric and gravimetric capacitances and on ESR is presented in Figures 10.9 and 10.10, respectively [193]. However, it is important to notice that electrode thickness has a strong impact on ESR whatever the conductive additive content. Taking this fact into account, most of the manufactured electrode thicknesses for power application are in the range of 100 μm (from 50 to 120 μm).

10.2.2

Electrolyte

Various electrolytes exist in the market. Aging analysis is strongly linked to solvents and/or salts. Toxicity, conductivity, and thermal stability are other important key parameters.

10.2.2.1 Electrolyte Impact on Performance

The energy stored in supercapacitors is proportional to the square of the applied voltage. This voltage is generally limited by the electrochemical stability window of the system. For a solid–liquid system, this parameter is limited either by the electrochemical stability of the salt, solvent, or by the degradation of the electrode.

Electrolytes have a strong impact on the performance of supercapacitors because of their role in the energy storage principle. Electrolytes modify ESR, and capacitance values generate gases during aging [194]. In order to understand electrolyte impact, it is necessary to keep in mind that the electrolyte is an ionic thermodynamic system having limitation. Generally, the electrolyte is the greatest limitation of the supercapacitor if the electrodes are stable.

Key parameters of electrolytes are conductivity, electrochemical stability (i.e., aging), thermal stability, and security (i.e., toxicity).

Conductivity The conductivity of an electrolyte is linked to ion concentration, ion mobility, solvent or solvent mixtures, and to temperature.

Ions and Concentration Limits The first criterion for the choice of a salt is to obtain an electrolyte having good electrical conductivity. Thus, in supercapacitors, cations are often tetraalkylammonium ions, which have good solubility and good conductivity in solvents with high dielectric constant. These cations are preferable to alkaline cations because they avoid the possible occurrence of alkali metal at the cathode at a fortuitous overload, leading to a passivation of the electrode. In addition, the reduction potential of this cation is very low compared to Li/Li⁺, which provides a wide range of stability. Peter *et al.* [195] indicate the use of glassy carbon as the working electrode, which would achieve a stable cathodic tetraethylammonium in dimethylformamide (DMF) of about -3 V versus saturated calomel electrode at 25 °C (-2.96 V/Ag/AgCl, -2.78 V/ENH, 0.26 V/Li/Li⁺). Many investigations have been conducted on the reduction of tetraalkylammonium ions on various electrodes [196–202]. Whatever be the nature of the alkyl group, the cation RN₄⁺ is often reduced to alkanes, alkenes, and corresponding trialkylamines. The anions most often cited in the literature are BF₄[−], ClO₄[−], PF₆[−], SO₃CF₃[−]. These species are characterized by their relatively large size (except for BF₄[−]), and their anodic stability evolves in the following order: PF₆[−] ≥ BF₄[−] > SO₃CF₃[−] ≥ ClO₄[−].

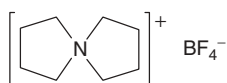
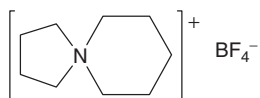
The most popular ions are Et₄NBF₄ (tetraethylammonium tetrafluoroborate or TEABF₄) and Et₃MeNBF₄ (triethylmethylammonium tetrafluoroborate or TEMABF₄). Asahi Glass [203] has studied different salts and proposed the use of Et₃MeNBF₄ instead of Et₄NBF₄ as the dielectric constant is higher for the first. Table 10.5 summarizes the conductivities of ions in four different solvents (PC, DMF, γ -butyrolactone, and ACN).

Given the high values of conductivity of solutions in ACN (55–58 mS cm^{−1} for 1 M TEABF₄) [205] compared to other solvents, the use of Et₄NBF₄ in ACN as electrolyte has been rapidly generalized. Only the Japanese industry prefers to replace ACN, because of its toxicity, by PC. Currently, the life of supercapacitors

Table 10.5 Conductivity of organic electrolytes (1 M, at 25 °C) in mS cm⁻¹ [204].

Electrolyte	Propylene carbonate (PC)	γ -Butyrolactone (GBL)	Dimethylformamide (DMF)	Acetonitrile (AC)
LiBF ₄	3.4	7.5	22	18
Me ₄ NBF ₄	2.7	2.9	7.0	10
Et ₄ NBF ₄	13	18	26	56
Pr ₄ NBF ₄	9.8	12	20	43
Bu ₄ NBF ₄	7.4	9.4	14	32
LiPF ₆	5.8	11	21	50
Me ₄ NPF ₆	2.2	3.7	11	12
Et ₄ NPF ₆	12	16	25	55
Pr ₄ NPF ₆	6.4	11	19	42
Bu ₄ NPF ₆	6.1	8.6	13	31
LiClO ₄	5.6	11	20	32
Me ₄ NClO ₄	2.9	3.9	7.8	7.7
Et ₄ NClO ₄	11	16	24	50
Pr ₄ NClO ₄	6.3	11	17	35
Bu ₄ NClO ₄	6.0	8.1	12	27
LiCF ₃ SO ₃	1.7	4.3	16	9.7
Me ₄ NCF ₃ SO ₃	9.0	14	24	46
Et ₄ NCF ₃ SO ₃	11	15	21	42
Pr ₄ NCF ₃ SO ₃	7.8	11	15	31
Bu ₄ NCF ₃ SO ₃	5.7	7.4	11	23
Et ₃ MeNBF ₄	15	—	—	60

Bold values are the three most common EDLC electrolytes.

**Figure 10.11** Examples of spiro salts.

based on PC electrolytes is lower than supercapacitor-based ACN, which shows the influence of the solvent on the lifetime of components [206].

Recently, “spiro-” type salts (Figure 10.11) have been developed by Japan Carlit [207] in order to provide higher concentration and higher electrochemical stability than Et₄NBF₄. However, such electrolytes are expensive in comparison with standard TEABF₄ 1 M in ACN, although performances are higher (Table 10.6).

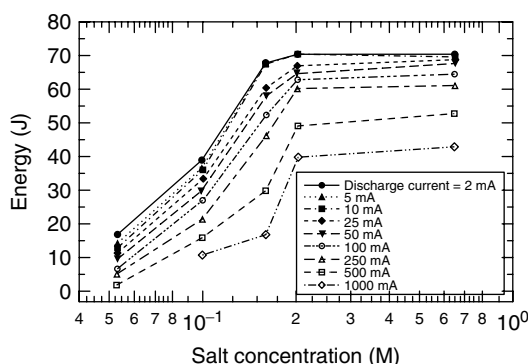
Regarding salt concentration, Zheng and Jow [208] showed that the operating voltage of supercapacitors is proportional to the concentration of salt in the electrolyte. On the other hand, a minimum concentration is required to obtain a maximum specific energy in the system (Figure 10.12).

Maxwell confirms such results: from 103 F g⁻¹ with 0.1 M Et₄NBF₄ in ACN, 166 F g⁻¹ is raised with 1.4 M with the same electrolyte [209].

Table 10.6 Performance improvements using “spiro”- type salts compared to standard PC-based electrolytes.

Electrolytic solution	Salt	Solvent	Electrolyte concentration (mol l ⁻¹)	Electrical conductivity (mS cm ⁻¹)		Long-term reliability		
				At 30 °C	At -40 °C	Initial capacitance at 20 °C (F)	Capacitance after 3000 h (F)	Capacitance decrease (%)
1	SBP-BF ₄	PC	2.50	20.41	1.53	1.55	1.41	9.0
3	PSP-BF ₄	PC	2.50	19.11	1.45	1.55	1.44	7.1
5	TEA-BF ₄	PC	0.69	11.21	1.31	1.57	1.34	14.8
6	TEMA-BF ₄	PC	1.80	16.15	1.45	1.55	1.30	16.2
7	TMI-BF ₄	PC	2.50	20.27	1.08	1.58	0.68	57.1

SBP-BF₄: spiro-(1,1)-bipyrrolidinium tetrafluoroborate PSP-BF₄: piperidine-1-spiro-1'-pyrrolidinium tetrafluoroborate TMI-BF₄: 1,2,3,4-tetramethylimidazolium tetrafluoroborate.

**Figure 10.12** Energy stored versus salt concentration and versus discharge current rate (from 2 to 1000 mA).

Most of the data given in publications are at room temperature. However, for most applications, it is important to remember that the temperature range of supercapacitor use is from -30 to 70 °C. For wide temperature range applications, -40 – 80 °C is required.

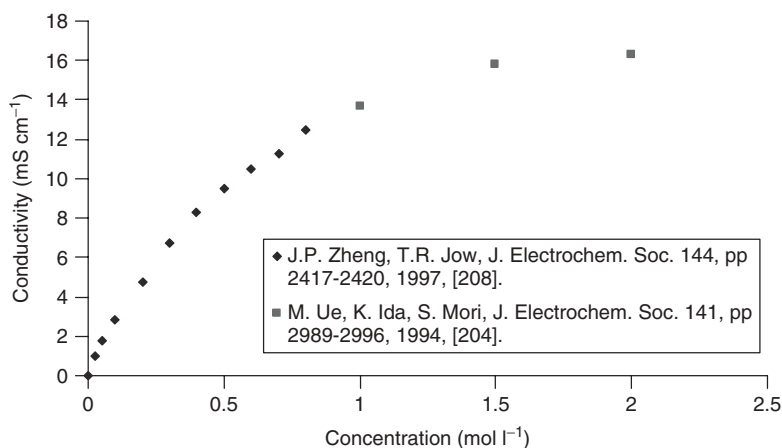
Although the concentration limit is strongly linked to temperature, it is important during application to not crystallize the salt of the electrolyte in supercapacitors in such temperature ranges.

Table 10.7 presents a few salts at two temperatures (room temperature and -40 °C). As a result, although the concentration limit of TEABF₄ in ACN is high (more than 1.5 M) at room temperature, precipitation of salt just begins at -40 °C if the salt concentration is 1 M [210].

Table 10.7 Precipitation at -40°C for various salt concentrations and conductivity values for various concentrations at 25°C .

Criteria	Precipitation at -40°C for various salt concentrations				Conductivity at 25°C (mS cm^{-1}) for various salt concentrations			
	0.9	1.0	1.5	2	0.9	1.0	1.5	2
Salt/solvent (M)	0.9	1.0	1.5	2	0.9	1.0	1.5	2
TEABF ₄ /acetonitrile	No	Yes	Yes	Frozen	54	57	64	Not fully dissolved
EtMe ₃ NBF ₄ /acetonitrile	No	No	No	Frozen	49	50.9	59.7	63.8
EtMePNBF ₄ /acetonitrile	<i>Not measured</i>	No	No	No	<i>Not measured</i>	55.5	64.5	67.8
TEABF ₄ /PC	Yes	Yes	Frozen	Frozen	13.6	14.0	Not fully dissolved	Not fully dissolved
EtMe ₃ NBF ₄ /GBL	No	No	No	No	<i>Not determined</i>	<i>Not determined</i>	20.8	22.5

Bold values in Table 10.7 demonstrate standard electrolyte issues in various test conditions.

**Figure 10.13** Conductivity of PC/TEABF₄ electrolyte for various concentrations at 25°C .

Such a study shows that an asymmetrical salt can provide a wider temperature range and increase the concentration limit. Of course, crystallization is strongly linked to interaction between solvent and salt.

For standard electrolytes, a difference between 1 and 1.5 M is not very significant (Figure 10.13 combined from [204, 208]).

Because supercapacitors are power devices, ESR performance is one of the important parameters. However, the resistance of the entire component is not related only to the conductivity of the electrolyte. As Table 10.8 shows, only a part of the resistance is related to the conductivity of the electrolyte.

Moreover, the electrolyte, and especially the salt, is one of the major parts of the supercapacitor cost.

Table 10.8 Conductivity impact on gravimetric power and energy at 25 °C.

Electrolyte	Capacitance (Ref: 100/ ACN)	Volumetric power at 25 °C (Ref: 100/ACN)	Volumetric energy at 25 °C (Ref: 100/ACN)	Gravimetric power at 25 °C (Ref: 100/ACN)	Gravimetric energy at 25 °C (Ref: 100/ACN)	Conductivity at 25 °C (mS cm ⁻¹) (Ref: 100/ACN)
PC/ TEABF ₄ 1 M	100	81	100	81	84	27
ACN/ TEABF ₄ 1 M	100	100	100	100	100	100

Taking into account all these reasons, most of the industrial companies limit electrolyte concentration of TEABF₄ to 1 M in ACN (or in PC).

Solvents Indeed, the criterion for the choice of solvent depends on the following points:

- Its responsiveness to the electroactive species and/or material of the electrode.
- Its dielectric constant (permittivity ϵ of the solvent) and its polarizability. The polarizability of an atom or group of atoms is the fact that under the action of a magnetic field, the atom or group of atoms has their travel expenses depending on the magnetic field. This concept is related to the charge density. The higher the load is concentrated on one point, the less polarizable it is, as opposed to a diffuse charge.
- Its electrochemical window stability [211]. This parameter depends on the chosen salt and impurities that may exist or develop in the system. Thus, traces of oxygen and water are very harmful in many systems. In this case, a reduction parasite phenomenon may interfere with the purely electrochemical behavior of the system, and thus limit the range of stability of the solvent–salt system [212].

Given these concerns, the solvents used for supercapacitors mainly belong to three classes:

- The dipolar aprotic solvents with a high dielectric constant (close to that of water $\epsilon_r = 78$) such as organic carbonates, ethylene carbonate (EC, $\epsilon_r = 89.1$), and PC (PC, $\epsilon_r = 69$).
- Solvents with low dielectric constant but with a strong donor character such as ethers, dimethoxyethane (DME, $\epsilon_r = 7.20$), and THF (THF, $\epsilon_r = 7.58$).
- Aprotic solvents with intermediate dielectric constant such as ACN (ACN, $\epsilon_r = 36.5$), DMF (DMF, $\epsilon_r = 37$).

Electrochemical Stability and Aging One of the important parameters for electrolyte use is the salt and the solvent electrochemical stability.

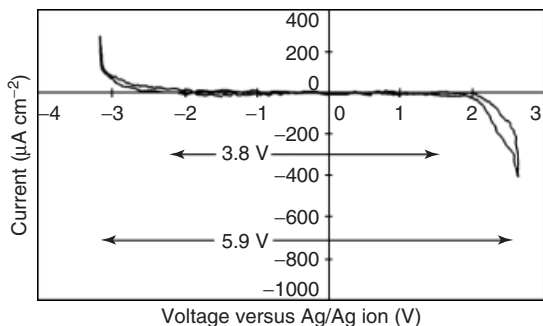


Figure 10.14 Electrochemical stability (3.8 V) of TEABF₄ 1 M containing 14 ppm of water. Theoretical stability of pure acetonitrile is 5.9 V.

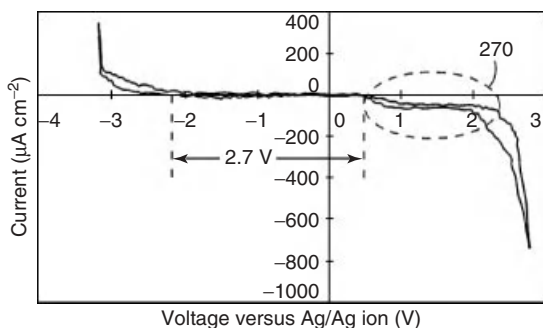


Figure 10.15 Electrochemical stability (2.7 V) of TEABF₄ 1 M containing only 40 ppm of water.

As demonstrated in many studies [213–215], open circuit voltage (OCV) is close to 3–3.2 V versus Li/Li⁺ depending on the working electrode: activated carbons do not have same OCV depending on surface group content and types.

Electrochemical Stability of Ions and Solvents The electrochemical stability of a solvent is strongly linked to impurities and to cathodic or anodic potential of this solvent [216]. As an example, oxygen and water traces are very harmful for many organic electrochemical systems. In this case, a parasitic reduction phenomenon can interfere with the purely electrochemical system and limit the electrochemical stability of the solvent–salt system [217].

To be used as a solvent, its electrochemical potentials must be wider than the potential excursions of the supercapacitor, and impurity contents must be controlled. Such an impact is demonstrated in Figures 10.14 and 10.15: the water content in TEABF₄ 1 M in ACN can dramatically impact the electrochemical stability of this electrolyte [146, 218].

A few common solvents are represented in Figure 10.16 [219].

Ions have electrochemical stability too. This parameter is very important, and has to be taken into account in order to limit electrolyte degradation.

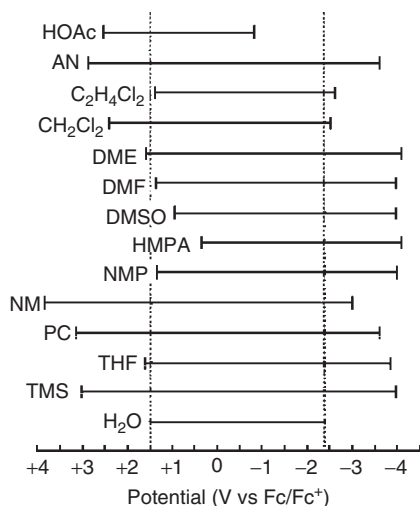


Figure 10.16 Potential windows in various solvents based on a common potential scale (vs Fc^+/Fc) obtained by voltammetry at a smooth Pt electrode at $10 \mu\text{A mm}^{-2}$. For redox potentials measured versus other reference electrodes, refer to [220].

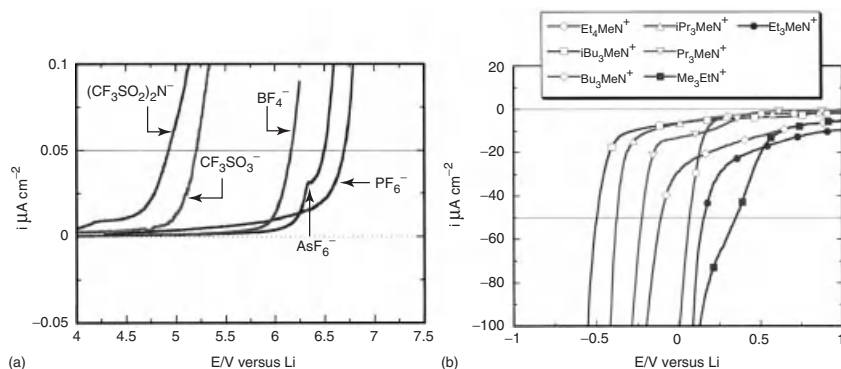


Figure 10.17 Anodic (a) and cathodic (b) limiting potentials for nonaqueous electrolytes comprising of the onium salts in EC/DMC (1 : 1), obtained by using GC (glassy carbon) as working electrode and

choosing $50 \mu\text{A cm}^{-2}$ cutoff current density. The cation of the salts used in (a) is Et_3MeN^+ 1 M, and anion in b is PF_6^- 1 M. Scan rate is 5 mV s^{-1} . Reference electrode: Li. Counter electrode: Pt.

Jow *et al.* [221] have published a complete study demonstrating such important parameters for many quaternary onium salts as nonaqueous electrolytes for supercapacitors in EC/DMC (dimethyl carbonate) (1 : 1) mixture (Figure 10.17).

Aging Causes due to Electrolyte If the electrolyte is pure and its stability is high, only interactions with other supercapacitor components can degrade this electrolyte. As discussed previously, one of the most important electrolyte degradations is

generated by adsorbed water and surface groups (especially acidic groups [222]) from activated carbon. Such interactions are exponentially generated if supercapacitor voltage is higher than 2.3 [223] to 2.5 V [224]. As a consequence of these interactions, gases are generated and ESR is increased via pore blocking of activated carbon and separator [225] and/or via electrode degradation [226]. A separator can provide other impurities [227]. The drying separator is one crucial step in order to reach high lifetime of the supercapacitor, higher capacitance, and lower resistance [228].

In the electrolyte, BF_4^- ions react with adsorbed water in the activated carbon on the positive electrode to produce high frequencies (HFs) through an electrolysis process. Then, protons behave as a catalyst for the decomposition reaction of PC.

Simultaneously, H_3O^+ ions migrate to the negative electrode and produce hydrogen gas, thereby increasing the leakage current. In this way, electrochemical reactions occur, favoring the gas generation.

Ufheil *et al.* [229] demonstrated that the PC could be decomposed into carbon dioxide and acetone, in particular when solvent is used in batteries. Kötzt *et al.* [230] analyzed the gases generated during the operation of a supercapacitor-based PC electrolyte (1 M TEABF₄/PC). These studies show the formation of propene, CO, CO₂, and hydrogen to an operating voltage of 2.6 V. These data were already mentioned in 2000 by Asahi Glass Co. [231]. This work was confirmed by Naoi *et al.* [232] who separately characterized gas and water generation from AC positive and negative electrodes working in a PC-based electrolyte as a function of applied cell voltage from 2.5 up to 4.0 V. The authors also detected these gases in the system and have shown through the development of an original process (Figure 10.18) that the gases generated by the two electrodes are different. Indeed, the positive electrode generates a significant percentage of propylene, ethylene, CO, and a small quantity of hydrogen, while the anode generates only CO₂ and CO emissions. The authors also observed a phenomenon of exfoliation of the surface layers of “graphene” layers in activated carbon for a 3 V operating voltage (Figure 10.19). This exfoliation is accompanied by hydrogen, CO, and CO₂ gas generation. The authors have suggested that CO and CO₂ are initiated by the decomposition of activated surface groups, while carbon dioxide is also generated by the oxidation of PC. Hydrogen is produced by electrolysis of the remaining water.

Kurzweil and Chwistek [233] propose several theories to explain degradation of ACN-based electrolyte:

- The authors suggest the presence of ACN gas, water steam, and ethene during the operation of the supercapacitor.
- The alkylammonium cation is degraded at high temperatures by elimination of ethene.
- The tetrafluoroborate anion is a source of fluoride, HF, and boric acid derivatives.
- Hydrogen is generated by the electrolysis of water and fluorination of carboxylic acids.

As described previously, gases are generated during the operation of the supercapacitor. The gas amount depends on the salt and the solvent [206]: H₂ is the

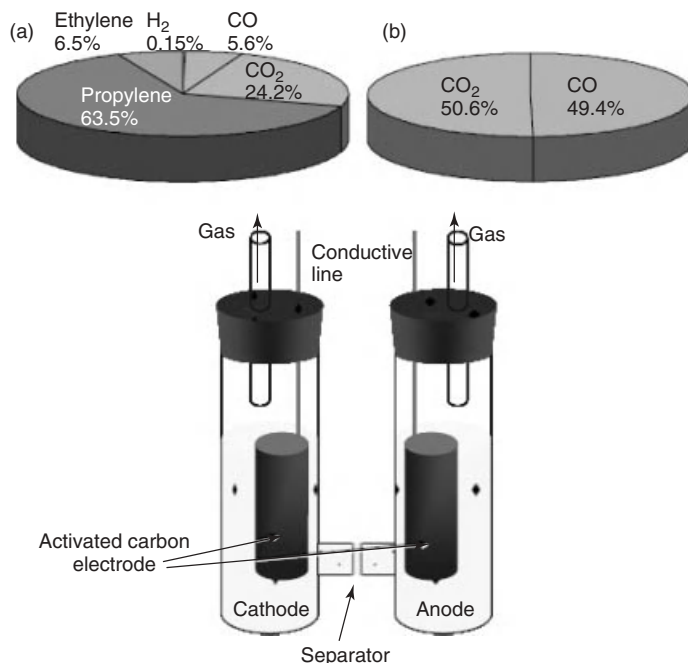


Figure 10.18 Components and ratio of the detected gaseous products in positive (a) and negative (b) compartments as a result of the floating test. The floating test was performed using an H-type cell at 4.0 V, 60 °C for 50 h.

main gas at the end of life for the ACN-based supercapacitor and results from an electrochemical reaction. H₂ increases continuously with floating operation. CO is present at the initial stage and increases continuously with floating time, but the CO content is low compared to H₂. PC-based supercapacitors have a three times shorter life span compared to ACN-based supercapacitor cells. CO is the main gas produced during operation of PC-based supercapacitors, as confirmed by the Naoi group. Although PC has a lower toxicity, PC-based cells have a more critical aging as they release CO.

As a conclusion, a supercapacitor working in organic medium must mechanically resist an increase of internal pressure in order to not leak. The main actors in the market have patented solutions in order to solve this technological problem. The solutions can be classified into five main categories:

- Solutions targeting gas evacuation from inside to outside of the component. Reversible valve [234], porous polymer membrane [235], and metallic or ceramic selective membranes [236] have been tested.
- Solutions in order to condense gas in the component using, for example, a getter material [237].
- Solutions in order to reinforce the component via extra thickness of cover(s) and/or of can.

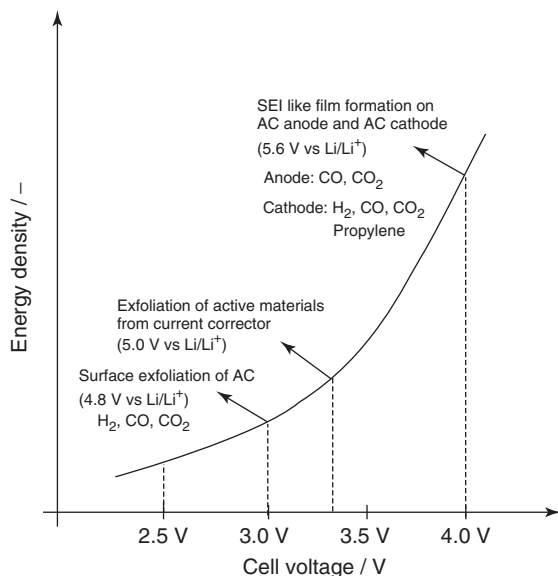


Figure 10.19 Speculations of crucial factors affecting the failure mode of PC-based electrolyte EDLCs in each cell–voltage range.

- Solution targeting a gas generation decrease using chemicals. This solution is developed hereafter.
- Solution targeting a control of component opening via an irreversible membrane or a venting [238]. This last solution has a main drawback: the cell can no more be used as an energy storage device and the electrolyte can leak.

Solutions have been proposed to reduce the decomposition of the electrolyte. Honda [239] has developed a PC-based electrolyte in 2007 containing a solid “antacid agent” such as silicate or carbonate. Such an agent is introduced in the positive electrode. The authors of this patent claim that it is possible to reduce the decomposition of PC by blocking H^+ , leading to the amount of generated gas being limited and thereby increasing the lifetime of the supercapacitor. Table 10.9 summarizes the impact of “antacid agent” on the initial and final performances of the supercapacitor.

These results show that the percentage of antacid agent is inversely proportional to the volume of gas generated. However, the loss of capacitance is not significant, but the initial capacity decreases sharply in the presence of an activating agent (from 5% for 1873 to 1380 F agent for 30% of antacid agent). Such data show that acid is a gas generator but capacitance decrease is not related to acid species. This data is rather restrictive for industrial application as the energy density is a critical factor. The antacid agent seems to have a positive effect on self-discharge, meaning that acid is generated by electrochemical reactions.

In 2008, the same authors proposed using sodium benzoate or potassium benzoate as ((antacid agent)) in order to limit electrolyte decomposition [240]. This

Table 10.9 Carbons used in these examples are alkali activated. Initial and final performances with and without addition of antacid agent in positive electrode.

	Amount of antacid agent (wt%)	Initial internal resistance (m Ω)	Initial capacitance (F)	Self-discharge (%)	Capacitance after 1000 h (F)	Capacitance maintaining ratio (%)	Amount of gas generated (ml)
Example 1	5	3	1873	92	1752	93.5	32
Example 2	10	3.1	1775	94	1668	94	18
Example 3	15	3.5	1676	95	1576	94	8
Example 4	30	4	1380	96	1300	94.2	2

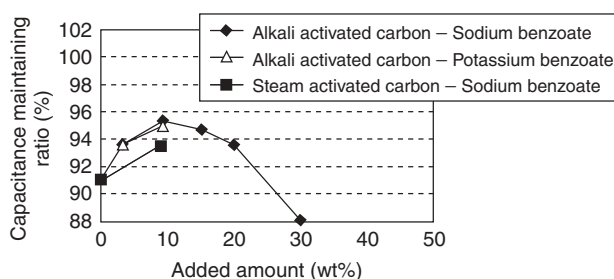


Figure 10.20 Impact of alkali benzoate amount on capacitance decrease.

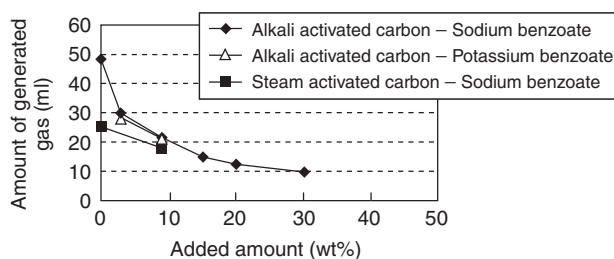


Figure 10.21 Impact of alkali benzoate on gas generation for a steam-activated carbon and an alkali-activated carbon.

effect is related to the appearance of a small amount of HF that would form NaF or KF and benzoic acid. The authors believe that the acid formed is adsorbed on activated carbon and is not active in the system. Figures 10.20 and 10.21 summarize the results reported in this patent.

On one hand, these data reveal that acids are generated during the operation of the supercapacitor. On the other hand, these chemical species are gas generators as the presence of an agent “antacid” reduces the volume of gas created. In conclusion, an interesting track is to avoid the acid formation during the operation of the cell.

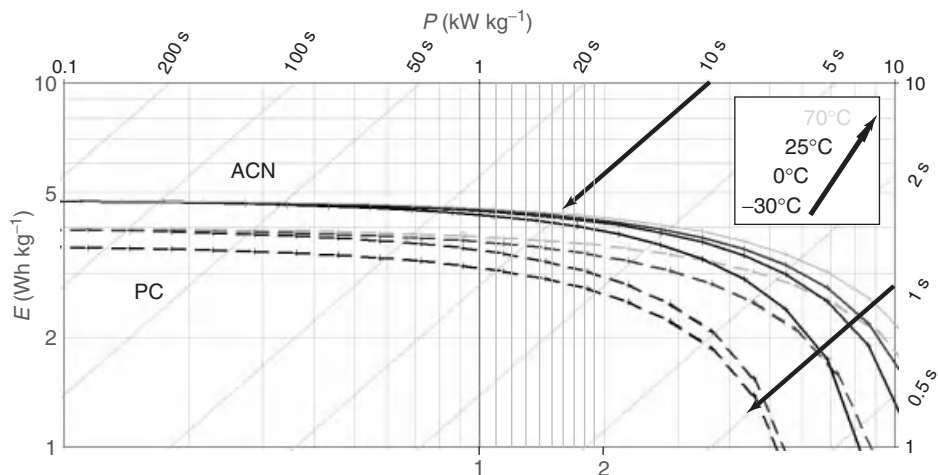


Figure 10.22 Ragone diagram for two same size supercapacitors at different temperatures and containing two different electrolytes (TEABF₄ 1 M in acetonitrile and TEMABF₄ 1.8 M in PC).

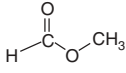
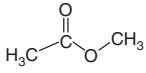
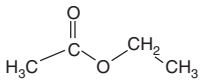
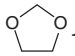
Thermal Stability and Performances As described previously, the electrolyte has an impact on performance (energy and power densities). Most of the data shown in publications are given at room temperature. For most applications, it is important to remember that the temperature range of supercapacitor use is from -30 to 70 °C. For wide temperature range applications, -40 to 80 °C is required.

Although the conductivity of the electrolyte increases with temperature, (20 °C; 70 °C) the range is generally not problematic. However, strong differences appear between electrolytes. As an example, the Ragone plot at different temperatures demonstrates such an impact (Figure 10.22).

The temperature range and conductivity of dimethylcarbonate/sulfolane or PC-based electrolyte can be improved by fluorobenzene addition [241] and use of EMPyrBF₄ (ethyl methyl pyrrolidinium tetrafluoroborate) salt.

Despite conditions that appear to favor a very low-temperature operation, -40 °C represents the typical rated lower operational limit for nonaqueous-based commercial cells [242]. Cells using aqueous-based electrolytes and rated for operation to -50 °C are available; however, they exhibit a lower energy density owing to the more limited maximum operating voltage. Thus, in order for currently available supercapacitors to find use in space avionics, they will require special thermal control apart from the rest of the electronic subsystems, as most space-rated electronics are expected to operate to at least the -55 °C limit [243]. Supercapacitor cells have been characterized extensively down to the -40 °C limit, mainly to study fundamental electrode processes and characterize leakage phenomena [244, 245]. These data indicate that cell performance is still acceptable at -40 °C, leaving open the possibility for even lower temperature operation [246]. There is a dearth of

Table 10.10 Potential solvent usable for low-temperature electrolytes.

Solvent	Freezing point (°C)	Boiling point (°C)	Dielectric constant (ϵ)	Viscosity (cP)
$\text{H}_3\text{C}-\text{C}\equiv\text{N}$ <u>Acetonitrile</u>	-45.7	81.60	37.5	0.345(25 °C)
 <u>Methyl formate</u>	-100	32	8.5	0.319(29 °C)
 <u>Methyl acetate</u>	-98	56.9	6.68	0.38(20 °C)
 <u>Ethyl acetate</u>	-83.6	77.1	6.0	0.426(25 °C)
 <u>1,3-Dioxolane</u>	-95	78	7.3	0.6(20 °C)

data for supercapacitors below this temperature limit, however, because of the relatively high freezing point of the solvents used in commercially available cells (PC or ACN). The most significant challenges in tailoring the electrolyte properties are to design electrolyte formulations with lower melting points while still maintaining adequate ionic conductivity, and to minimize the rise in ESR at lower temperatures caused by an increase in solvent viscosity. Few organic solvents have interesting physicochemical properties [247] (Table 10.10): methyl formate (MF), methyl acetate (MA), ethyl acetate (EA), and dioxolane (DX).

The conductivity of mixtures have been measured at various temperatures and compared to the standard ACN-based electrolyte. These mixtures show good results at very low temperatures until $-55\text{ }^\circ\text{C}$ (Figure 10.23). However, high temperatures and floating tests have not been measured for these electrolytes.

Other mixtures have been proposed in order to find a wider temperature range versus ACN (Figure 10.24) [248].

At high temperatures, conductivity is more favorable for high-power applications. Nevertheless, aging is generally accelerated because electrochemical reactions are activated by temperature.

ACN can be used at $80\text{ }^\circ\text{C}$ in peak applications. Above this temperature, PC-based electrolytes can be used but aging is highly impacted. Other solvents can be used as substituents such as sulfolane or EC, if applications are working only at high temperature.

For wider temperature ranges, ionic liquids can be a solution, as we describe hereafter.

Toxicity Although γ -butyrolactone is an interesting solvent for EDLC electrolyte, the toxicity of γ -butyrolactone (GBL) is questionable because it is potentially a Gamma hydrobutyric acid (GHB) initiator. In future, GBL could be a control substance [249].

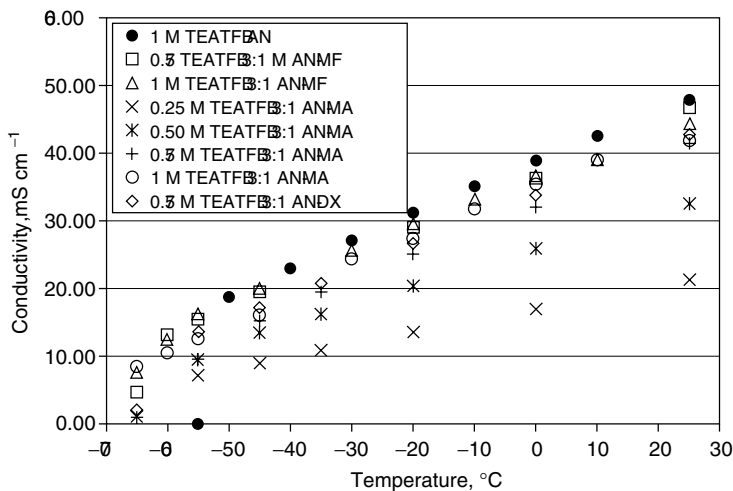


Figure 10.23 Electrolyte conductivity versus temperature for the electrolytes working at low temperatures compared to standard electrolyte TEABF_4 1 M in acetonitrile.

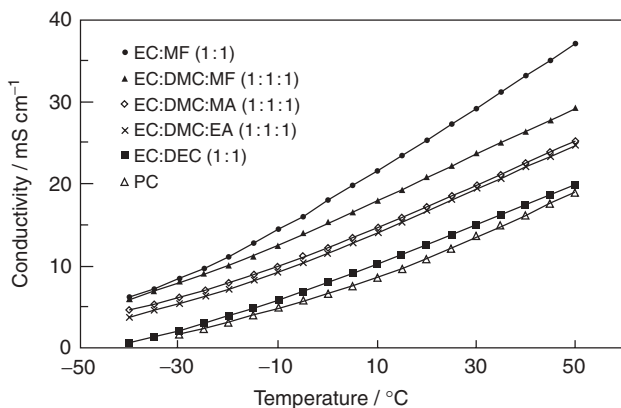


Figure 10.24 Specific conductivity versus temperature dependencies for different solvent systems (with addition of 1 M TEABF_4). EC: ethylene carbonate. DMC: dimethyl carbonate. DEC: diethyl carbonate.

A few very common solvents and their toxicity are mentioned in Table 10.11.

10.2.2.2 Liquid-State Electrolyte and Remaining Problems

As shown in previous table, the two main problems of ACN are its low flash point value and its toxicity. That is the reason most supercapacitor manufacturers have designed their cell in order to avoid electrolyte leakage during operation. Efforts are made by manufacturers to limit electrolyte quantity in cells to avoid liquid leakage if the cell is mechanically destroyed. Despite this technical improvement, ACN is still not accepted in Japan. Given the growing environmental constraints,

Table 10.11 Flammability, toxicity, and flash point for few usable solvents for EDLC electrolytes.

	Flash point (°C) FP	Boiling point (°C) BP	Toxicity
Acetonitrile (ACN)	5	81.6	Xn
3-methoxypropionitrile (MPN)	66	165	Xi
Propionitrile (PN)	6	97	T
Butyronitrile (BN)	16	116	T
Propylene carbonate (PC)	123	242	Xi
Ethylene carbonate (EC)	150	248	Xi
Dimethyl carbonate (DMC)	18	90	—
Diethyl carbonate (DEC)	25	126	—
Dimethylformamide (DMF)	57	153	T
2-Pentanone (2PN)	7	102	Xi
Methyl ethyl ketone (MEK)	−3	80	Xi
γ-Valerolactone (GVL)	96	207	Xi
γ-Butyrolactone (GBL)	104	206	Xn
Methyl propyl ketone (MPK)	7	102	Xi
Methyl formate (MF)	−19	32	Xn
Ethyl formate (EF)	−20	54	—
Ethyl acetate (EA)	−4	77.1	Xi
Methyl acetate (MA)	−10	56.9	Xi
Diethylsulfone (DES)	246	246	—
Dimethylsulfone (DMS)	143	238	—
Sulfolane (SL)	177	285	Xn
Dioxolane (DX)	−6	78	Xi

T, toxic; Xn, harmful; Xi, irritant; —, not dangerous. Flammability is directly related to FP and BP: extremely flammable, $FP < 0\text{ }^{\circ}\text{C}$ and $BP \leq 35\text{ }^{\circ}\text{C}$; highly flammable, $0\text{ }^{\circ}\text{C} \leq FP < 21$ and $35\text{ }^{\circ}\text{C} < BP$; flammable, $21\text{ }^{\circ}\text{C} \leq FP < 61$ and $35\text{ }^{\circ}\text{C} < BP$; combustible, $61\text{ }^{\circ}\text{C} < FP$.

studies (essentially in Japan) have been performed in order to replace ACN as electrolyte solvent and/or to improve PC-based supercapacitor performance, taking into account that many optimizations have already been done, such as “spiro” salts or TEMABF₄. As a result, no suitable alternative to ACN has been found, especially in terms of conductivity [169] and the thermal stability and electrochemical stability combination [250, 251]. It is important to note that mixtures of ACN have been tested and this can be interesting in terms of conductivity. However, they do not bypass a potential prohibition of ACN [243, 252]. As demonstrated previously, one of the major problems of a highly conductive liquid electrolyte is the low flash point value. In order to improve this value, flame retardants have been developed [253] but such a solution is still not industrialized.

10.2.2.3 Ionic Liquid Electrolyte

Pure ionic liquids (without any additional solvent) have been tested as electrolytes for supercapacitors [254]. Such electrolytes have the advantage of being solvent-free,

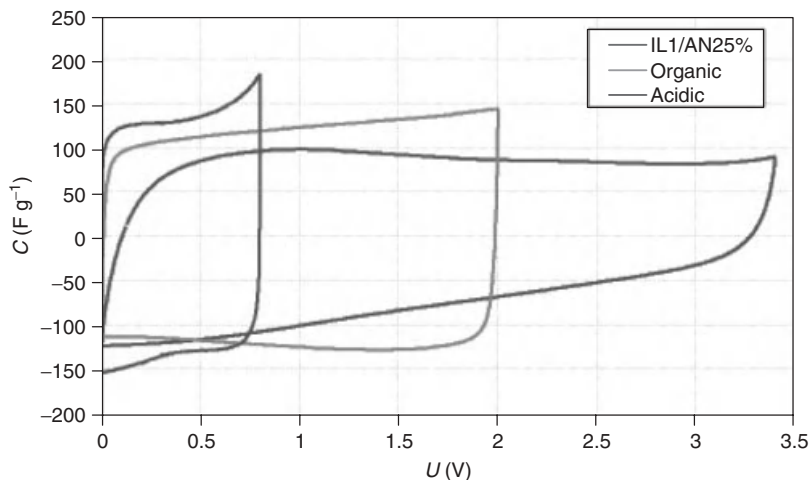


Figure 10.25 Voltammetry characteristics (5 mV s^{-1}) for activated-carbon-based supercapacitor with $[(\text{C}_6\text{H}_{13})_3\text{P}(\text{C}_{14}\text{H}_{29})] [\text{Tf}_2\text{N}]/\text{acetonitrile } 25\%$, organic and acidic electrolytic solutions.

stable over a wide temperature range, and not flammable. Unfortunately, conductivity is generally lower than that of electrolytes based on PC [255]. However, few ionic liquids such as alkylimidazolium tetrafluoroborate (except EMIBF₄ [256]) or *N*-butyl-*N*-methylpyrrolidinium-bis-(trifluoromethanesulfonyl) imide (PYR₁₄TFSI) [257] demonstrate high electrochemical stability [258–260]. In addition, these products are difficult to purify because they cannot be distilled [261, 262]. However, it is important to remember that the lifetime of supercapacitors is closely related to the purity of electrolytes [263]. This has resulted in increasing sharply the price of these products, making them potentially unsuitable for the industry. However, these new electrolytes can be good tracers to confirm the results of numerical simulations and, in particular, allow proving that the solvation of ions is not necessary to store energy [264]. In addition, they can be used at high temperatures [265].

As a result, ionic liquids are expensive compared to PC-based or ACN-based electrolytes. Such electrolytes could find applications in niche markets working at high temperatures or working at low power density but at high voltage (if purity is high). Ionic liquids have been tested as salts in organic electrolyte [266], as presented in Figure 10.25 [267]. Two very interesting studies have been dedicated to these mixtures and have demonstrated encouraging results in order to increase the conductivity of ACN-based electrolytes [268] and ACN-free electrolytes [269].

Products (cells and modules) are now available in Japan through an association between Nisshinbo and Japan Radio Co. [270, 271]. These products, using DEME-BF₄ (*N,N*-diethyl-*N*-methyl-*N*-(2 methoxyethyl)ammonium tetrafluoroborate), have demonstrated higher performance than standard PC-based electrolytes [272].

10.2.2.4 Solid-State Electrolyte

The main advantage of solid-state electrolytes is to concentrate, during the manufacturing process, the electrolyte and separator in the same material. Taking into account that electrolytes must not contain any electrochemical impurities, most solid-state electrolyte studies have been performed on alkaline systems working at low voltage to avoid aqueous degradations.

Supercapacitors are devices dedicated to power applications. Although interesting results have been found in aqueous medium with alkaline PVA electrolyte [273], organic-medium all-solid supercapacitors do not show attractive results, especially for conductivity reasons at low temperatures (as for ionic liquids) and for low impregnation of ions in electrodes. However, subvoltage micro-sized supercapacitors found application in digital electronics [274] because no power is needed and voltage management is easier than in a microbattery. Products working in solid-state electrolytes are commercially available from AVX (BestCap).

For these reasons, such electrolytes have not found success in large supercapacitor markets.

10.2.3

Separator

10.2.3.1 Separator Requirements

The requirements for separators are electrochemical stability (high purity and electrochemical stability of materials), high porosity, high thermal inertia, and chemical inertia versus electrolyte. In addition, because a separator is a nonactive material in a supercapacitor, the separator thickness should be as thin as possible and the cost must be low. Its minimum size nevertheless is limited by the following:

- 1) The electrical shortening failure risk due to free carbon particles, which may create a contact between the two electrodes (high self-discharge rate or short circuit) [275].
- 2) The mechanical strength in order to allow the winding process.

10.2.3.2 Cellulosic Separators and Polymeric Separators

Theoretically, supercapacitor electrodes can work without a separator if the distance between electrodes can be maintained [276]. Practically, it is quite impossible to maintain such devices without any short circuits. Numerous studies have been conducted to provide suitable separators for supercapacitor applications. Generally, these separators are very porous (more than 50%, up to 80%) in Li-ion separators (between 30% and 50%), in the order of 45–90%. However, when the porous separator is too high, it requires a greater quantity of electrolyte in the supercapacitor, and therefore the cost is higher. A compromise exists between separator cost, the electrolyte needed, and the resistance due to the separator. Paper separators consisting mainly of solvent-spun cellulose or recycled cellulose fibers are conventionally used as separators in supercapacitors. Figure 10.26 shows such a standard cellulosic separator made of cellulose fibers. These separators were developed initially for an aluminum electrolytic capacitor.

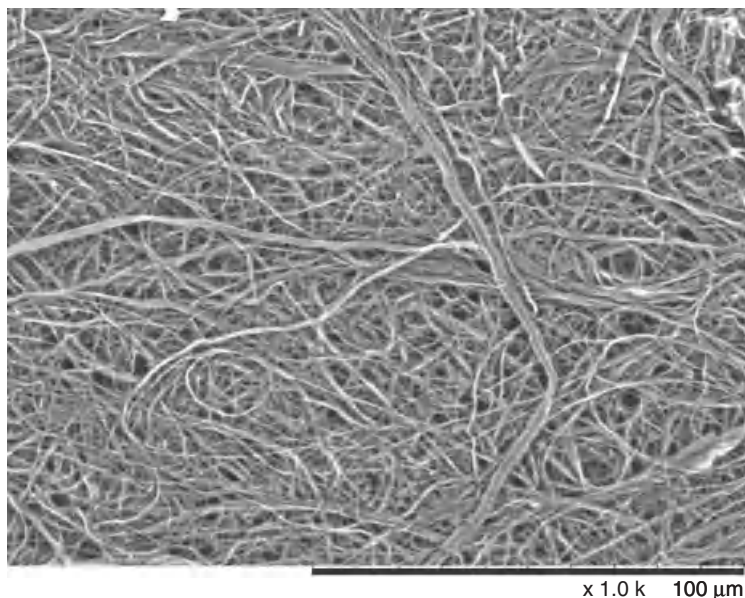


Figure 10.26 Standard cellulosic separator for EDLC ($\times 1000$, SEM picture). Courtesy of Batscap.

The thickness range is between 15 and 50 μm . The density of such materials is quite low (lower than 0.85). Owing to the large electronic market, the separator price is quite low and quality can be high (purity of cellulose). However, it is necessary to strongly dry such separators to avoid water contamination in supercapacitors [277–279]. The drying process can be performed by thermal outgassing or acetone washing [280]. As energy density and power density increase in proportion to the square of the voltage, there has been considerable activity in the improvement of electrode materials. As the upper limit voltage of conventional activated carbon electrodes is about 2.5–2.7 V, an electrode operating at an upper voltage limit has been developed. When paper separators are exposed to a high voltage of at least 3 V, oxidative deterioration occurs, resulting in a considerable decrease in strength possibly leading to tearing of the paper [281]. Thus, paper separators are unsuitable for use as separators in EDLCs operating at such high voltages.

That is the reason many polymeric-based separators have been developed and are now commercially available [282]:

- Cellulosic separators [283]. The separator is formed of a material that is soluble in the electrolyte. The material in the separator is dissolved in the electrolyte after the separator is impregnated with the electrolyte (Figure 10.27).
- Glass-fiber-based separators. Fiber size is generally in the range 1–4 μm with 70–90% of porosity. The thickness of such separators is higher than 30 μm , especially to avoid short circuits [284]. Thinner separators based on glass fibers

have been developed using a binder such as polyamide [285] to glue the fibers in between.

- Porous polypropylene films [286–288] (Figure 10.27). These separators have been developed for Li-ion applications. Most of these separators are not porous enough to maintain low ESR for EDLCs.
- Polyethylene separators with mineral charges [289] have been developed in order to increase heat resistance (Figure 10.27).
- Multilayer separator [290]. On one standard polymeric separator, a layer of ultrafine fibrous aggregate prepared by an electrostatic spinning process is deposited. Average fiber diameter of ultrafine fibers constituting the ultrafine fibrous aggregate layer is 1 μm or less. This process helps avoid short circuits between electrodes.
- A separator made of a thermoplastic resin and a pulp fiber [291]. This kind of separator has an excellent mechanical strength in addition to ion permeability, gas permeability, or liquid permeability. However, the price is quite high compared to a cellulosic separator.
- PTFE-based separators (Gore, Figure 10.27)
- Polyimide-based separators [292]. Owing to its very high heat resistance, polyimide can be used as separator for high-temperature applications. However, the price of such a separator is very high and can be only considered for niche markets.
- Polyamide-based porous film with TiO_2 for higher heat resistance [293] and aromatic polyamide fibers–cellulose fiber mixture [294].

An interesting work has been carried out on supercapacitor separators by T. L. Wade [295]. His conclusions are as follows:

- 1) The separator is a major contributor to the resistance of high-power supercapacitors (causing greater than 30% of the total resistance for four commercial separators investigated).
- 2) There is a reasonable linear relationship between supercapacitor resistance and separator thickness (demonstrated by varying the number of separator layers in a cell).
- 3) Supercapacitor resistance is a function of voltage.
- 4) The electrode bed may influence the resistance of the separators through electrolyte depletion and possibly other effects.

10.3

Cell Design

Numerous designs have been developed. Design is strongly linked to targeted market and cost efficiency. Assembly processes are hereinafter presented.

This part is dedicated to the description of cell design of various commercial supercapacitors. Analysis of components is described taking into account targeted markets.

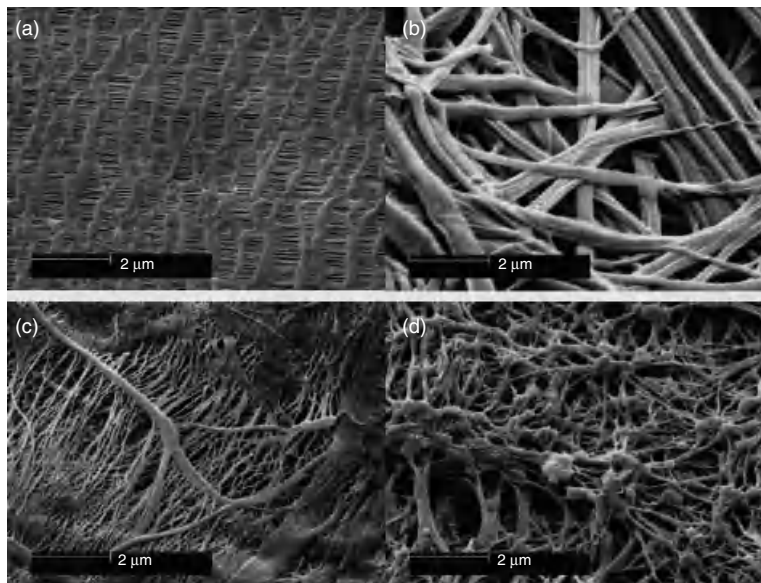


Figure 10.27 SEM images of commercial separators created using a variety of materials: Celgard 2500 (polypropylene) (a), Nippon kodoshi corporation (NKK) TF40 (cellulose) (b), Solupor 14P01A (ultrahigh molecular weight polyethylene) (c), Gore 11367985-3 (polytetrafluoroethylene) (d). All scale bars are 2 μm (T. L. Wade, PhD Thesis).

First of all, it is important to distinguish small components (coin type) and large components (capacitance higher than 300–500 F) because of their applications and their architecture.

Three main processes exist to package these cells:

- 1) By potting (aluminum electrolytic capacitor process). The stack or the wound is rolled up, fitted with pin connectors and placed in a cylindrical aluminum casing. The two most popular geometries are axial leads coming from the center of each circular face of the cylinder, or two radial leads or lugs on one of the circular faces. A butyl rubber gasket is placed on top of the header before the spinning operation, in which the case opening is folded over and pressed into the gasket, forming an effective seal of the system. The package is at the same potential as the electrolyte and one of the electrodes during capacitor operation, so when supercapacitors are connected in series, care must be taken to insulate the cases from one another. A safety vent can be provided in such supercapacitors so that the supercapacitor may relieve excessive pressure buildup in a controlled manner. This occurrence is known as *venting*, and is considered a failure mode. The vent may be installed as a rubber plug in the header or as a die-set slit impression in the can wall. The pressure at which the capacitor vents is predictable, and is usually designed to occur at about 7 atm pressure or even higher. The allowable pressure tends to be higher for small capacitors. After a capacitor vents, the electrolyte may evaporate out

until the capacitance diminishes. Generally, such supercapacitors have a high ESR and performances are not very high. This technology is well adapted for small supercapacitors dedicated to electronic applications. Such components are detailed hereafter.

- 2) Casing and cover are assembled by edge rolling, curling, or heading process with a gasket to ensure tightness and to avoid short circuit if electrodes are connected to casing and cover, respectively. Such a process has higher performances than the previous type. Tightness is high and well adapted to large supercapacitors. This technology has been accepted by Maxwell, Nesscap, LS Cable, and so on.
- 3) Casing and cover are assembled by glue and each part is connected to one electrode. In this case, the glue plays two roles: it helps ensure air and water tightness, and glue insulates the two parts. This design has been patented by Batscap.

10.3.1

Small-Size Components

Small components are quite exclusively dedicated to electronic applications as welded components on electronic cards: wireless communication for utility meters, energy storage for actuators, backup power for memory boards, and wireless base station power quality for telecommunications. Such components can also be found in after-market audio systems (5–15 F), laptop computer power management, as energy storage system for toys, as power system for LED flash of mobile handsets, and other portable applications (less than 1 F, thin cells). The main actors in these markets are Panasonic, NEC-Tokin, Elna, Seiko, Korship, Cooper Bussmann, Alumapro, CapXX, Shoen Electronics, Smart Thinker, Nichicon, Nippon Chemicon, Vina, Vishay, Rubycon, and so on.

The market increase of these components is still high, but technology can be considered as advanced. Energy and power densities are not key parameters except for new technology mobile applications explaining the thin cell developments.

These components can have two physical appearances:

- 1) *Coin cells*: The physical appearance is similar to a coin cell battery (Figure 10.28).
- 2) *Wound cells*: Generally, capacitance is higher than coin cell capacitance. Such components look like electrolytic and dielectric capacitors (Figure 10.29).

10.3.2

Large Cells

Large cell construction does not have standards for the moment (although standardization is in progress): each manufacturer designs its cells depending on internal developments and performance optimization.

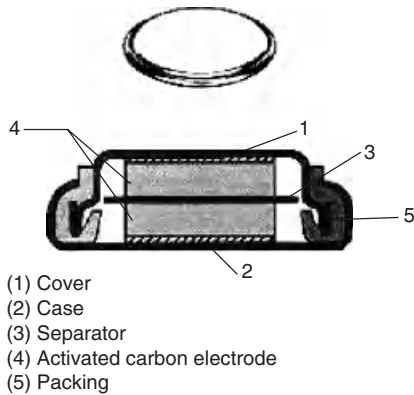


Figure 10.28 EN/EP Panasonic coin-type cell construction [296] (Gold capacitor).

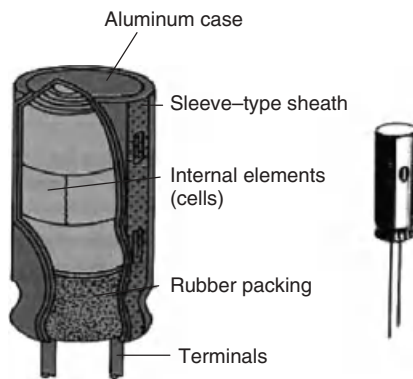


Figure 10.29 HW/HZ Panasonic wound-type cell construction [297] (Gold capacitor).

Two main types for such components can be distinguished:

- 1) High-power cells, dedicated to power application such as vehicle hybridization and urban transports
- 2) Energy cells for stationary applications such as uninterrupted power supply (UPS).

10.3.2.1 High-Power Cells

The main «high-power cell» manufacturers are Batscap (France), Maxwell Technologies (USA), Nesscap (South Korea), and LS Mtron (South Korea). Owing to targeted power applications, cell design is very simple in order to obtain the lowest ESR as possible.

One of the most important parameters is the time constant. This constant equals the capacitance value by ESR (total resistance or R_{sDC} “Direct Current” Resistance or ESR). For such cells, the time constant is lower than 1 s.



Figure 10.30 High-power cells. (a) Batscap (650–9000 F), cylindrical, (b) Maxwell Technologies (650–3000 F), cylindrical, (c) Nesscap (650–3000 F), cylindrical, and (d) LS Mtron (100–3000 F), prismatic and cylindrical.

In Figure 10.30, cells are presented. Generally, these cells have a limited number of components.

An advantage of the spiral wound cell of the double-layer capacitor is that large-surface-area electrodes can be rolled into a small case. The large electrodes greatly reduce the internal resistance of the capacitor and the case greatly simplifies the capacitor seal or the sealing required for the double-layer capacitor. In a bipolar design, each cell must be sealed around the perimeter of the electrode. However, in a wound design, only the outer can requires sealing. This design is not as efficient as a bipolar design when the cells are stacked in series, because the resistance of the lead wires will add to the ohmic losses.

As, for example, a direct laser welding between can (or cover) and current collector without any intermediate parts has been developed by Batscap to strongly limit the ESR (Figure 10.31). Maxwell Technologies and Nesscap have quite the same design using winding welded on an intermediate aluminum stamped part on the cover (or the can). Electrode thickness is generally thinner than 100 μm in order to limit ESR. All these cells are ACN based for conductivity and thermal stability reasons. These cells are 2.7 or 2.8 V rated.

Because of targeted application (automotive and urban transportation), extensive tests have been performed. As a conclusion, it is assumed that these cells have to resist overpressure (almost 5 bars) and must be totally sealed (electrolyte leakage is prohibited). Then, these cells must be water and airtight. The cover and can are aluminum based.



Figure 10.31 Batscap cell design with direct laser welding between cover and can.



Figure 10.32 Energy-type cells. (a) Nichicon evercap (600–4000 F) and (b) Nippon Chemicon DLSCAP™ (100–3000 F).

10.3.2.2 Energy Cells

The main <<energy cell>> manufacturers are Nippon Chemicon (Japan), Panasonic (Japan), Nichicon (Japan), Asahi Glass (Japan), and Meidensha (Japan). Most Japanese EDLC manufacturers are electrolytic capacitor manufacturers too and have extensive know-how in cell industrialization. The construction of these cells is more inspired by electrolytic capacitors (Figure 10.32). The ESR of this cell type is higher for three main reasons: these cells are PC-based electrolytes, the design is not optimized for power, and the thickness of the electrode is generally higher than power-type cells in order to increase the energy density value.

The use of a PC-based electrolyte and targeted application enable the energy cell manufacturer to use the same electrolytic capacitor parts in the design: plastic part, connection on the same side of the cell, rolling process, and so on.

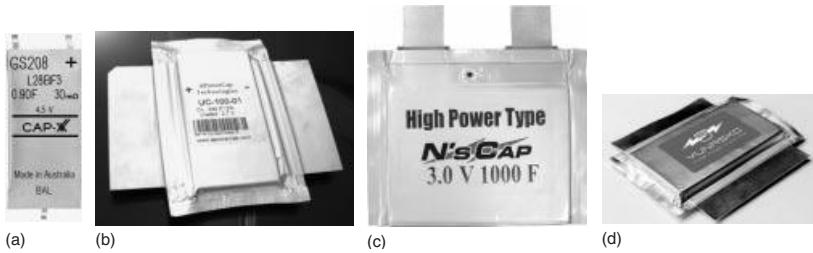


Figure 10.33 Pouch cells from CapXX ((a) 0.9 F, 4.5 V, size (mm max): $39 \times 17 \times 3.5$), APowerCap. ((b) 430 F, 2.7 V, 57 g, 45 ml), Nisshinbo. ((c) 1000 F, 3.0 V, size (mm): $135 \times 130 \times 9.2$, 202 g, 162 ml, with valve), and Yunasko ((d), 1500 F, $84 \times 240 \times 16$, 250 g).

These cells are generally rated to 2.3–2.5 V in order to limit the aging and because of the use of PC electrolyte.

10.3.2.3 Pouch Cell design

This kind of cell is generally manufactured for small and middle size EDLC (up to 1000 F). Such a design, directly inspired from the Li-ion cell phone design, enables maximizing the energy density (gravimetric and volumetric) and is convenient for flat integration in applications such as cell phones (CapXX, Figure 10.33a) and electronics. Large cells have been developed by APowerCap (Figure 10.33b), Nisshinbo (Figure 10.33c) and Yunasko (Figure 10.33d).

Because of the very light packing, these cells have higher power and energy densities. For small electronic devices, restrictive environment requirements are not needed. However, these cells have major inconveniences:

- It does not resist mechanical shocks.
- Thermal management efficiency is low compared to standard technologies.
- With gas generation, cell volume is strongly modified.
- Polymer-based sealed wraps are not water and airtight for long-term application.

10.3.2.4 Debate on Cell Design: Prismatic versus Cylindrical Cells

As mentioned previously, two main cell types coexist on the market.

For many applications, cell design is questionable. However, every cell design has found its market, linked to cell size (small and large). Taking into account these parameters, it is possible to summarize the present situation (Table 10.12).

As a result, large prismatic cells have a higher energy density, especially when they are assembled in modules for geometric aspects. However, these cells contain more parts than cylindrical and are more expensive to manufacture.

10.3.2.5 Aqueous Medium Cells

Aqueous-based electrolyte unit cells are not commercially available for reasons of low voltage: only modules are available and will be described in detail hereafter.

Table 10.12 Key parameters for prismatic and cylindrical cells.

Parameter	Prismatic	Cylindrical	Pouch
Up to 100 F	Very few design with metallic case (flat cells) <i>Manufacturer example:</i> NEC/Tokin, Cellergy, Maxwell Tech., OptiXtal, Kyocera-AVX, Tecate	Most acceptable design <i>Manufacturers:</i> Panasonic, Nippon Chemicon, NEC, Korchip, Maxwell Tech., Nichicon, Elna, and so on	Few design Very flat cells Manufacturers: CapXX
Advantages	Hermetic if sealed Convenient for cramped environment High volumetric energy density	More or less hermetic Low cost design	Very light Cheap Highest energy density
Inconveniences	High cost design	Not relevant for flat device	Poor lifetime in restrictive environment such as high temperature and/or humidity
Above 100 F	Nesscap LS Cable Nippon Chemicon Meidensha Ioxus	Most of manufacturers: Batscap, Maxwell, Nesscap, Nippon Chemicon, Panasonic, Elna, and so on	APowerCap Nisshinbo PowerSystem (unit cell of modules), Yunasko
Advantages	Higher energy density than cylindrical Hermetic	Cheaper to manufacture Generally better cycle or calendar life Low number of part High efficient thermal management	High energy density Cheap to manufacture Limiter number of part
Inconveniences	Higher ESR High cost design (high number of parts/cell) More expensive to manufacture Less efficient thermal management	Lowest energy density	Poor lifetime in restrictive environment such as high temperature and/or humidity Do not resist to chocks (potential electrolyte leakage) Very low efficient thermal management

Bold letters would be efficient to differentiate EDLC types (up to 100F, above 100F).

10.4 Module Design

Modules are designed for specific applications. High voltage and power efficiency are needed. Key parameters are commented on such as thermal management, cell assembly, connection, electronics, and balancing.

The use of supercapacitors in high-power applications can be done by combining several components in series, thereby achieving higher voltages. The main advantage of such voltage is the energy increase. At the same time, most applications require DC/DC converter: a very low voltage (such as 2.5 or 2.8 V) is not convenient for high-power applications (a converter would be expensive and efficiency would not be high).

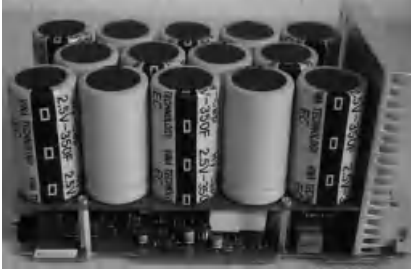


Figure 10.34 Example of small-size supercapacitor module based on welded components on an electronic card (Vina Technology).

Regarding small-size supercapacitor modules, these are generally assembled in series or in parallel directly on an electronic card (the example in Figure 10.34). Most applications (essentially memory backup) using such modules do not need any high current discharge, and thermal management is not a key parameter.

In the past, the lifetime of a module based on large cells was strongly decreased in comparison with unit cell lifetime.

For these reasons, many improvements have been performed by major manufacturers in the past five years.

Modules can be classified into two main families via their design:

- 1) Modules made of hard design unit cells (cylindrical or prismatic) connected in series or in parallel
- 2) Modules made of pouch unit cells.

10.4.1

Large Modules Based on Hard-Type Cells

These modules contain the following:

- 1) Unit cells
- 2) Metallic connections between cells
- 3) Two electric terminals
- 4) An electric insulator between cells and external envelope – can advantageously be a heat dissipator for the module
- 5) A balancing system
- 6) Other additional information via detectors
- 7) An enclosure (in plastic or in aluminum).

In a module, only unit cells contain active materials. For this reason, power and energy densities of the module are always lower than unit cell performances included in the module. Most manufacturers have designed their modules in order to minimize the passive materials versus the mass and volume of the cells, taking into account that safety, environment, and aging must not be degraded for the benefit of performance. In some cases, geometry can be very different from rectangular shape in order to be easily placed in the final application [298].

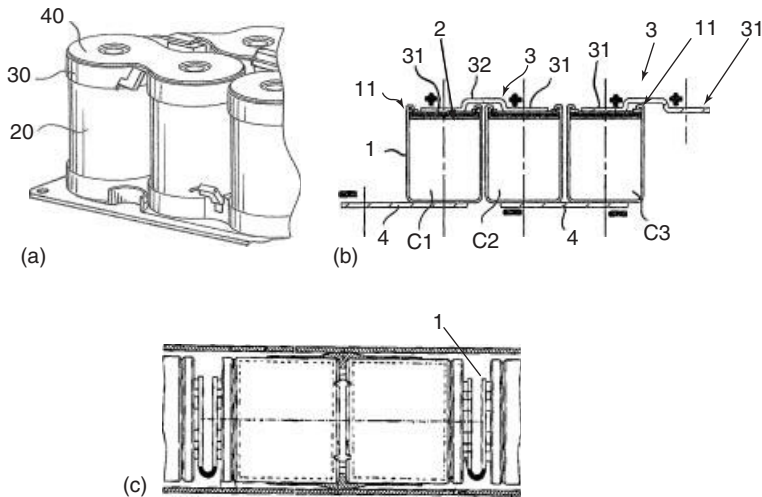


Figure 10.35 Various shapes of connecting strip. Flat ((a) Batscap, 40), with elevated edge ((b) EPCOS, 32), U-form for tubular design ((c) EPCOS, 1).

In the following paragraphs, a few solutions concerning passive components of this module type are detailed.

10.4.1.1 Metallic Connections Between Cells

To increase voltage (connections in series) or capacitance (connections in parallel), it is necessary to connect supercapacitor unit cells to each other. These connections are constrained by the geometry of cells and positioning of the terminals on the cells. For example, if cell terminals are flat, the connecting strip can be flat [299] too (Figure 10.35a). Strip geometry can be more complex if cells are rolled (Figure 10.35b) or if the module is tubular [300] (Figure 10.35c).

The mechanical connection between the components and connecting strip can be done, for example, by welding [301], by thermal difference between terminal and strip [302], brazed [303], screwed [304], and so on. Generally, connecting strips play the role of a thermal dissipater from the cell to the exterior of the module.

10.4.1.2 Electric Terminal for Module

Although high current load must be accepted by an electric terminal, the connection between terminals and the first and last cells, respectively, must demonstrate a very low resistance in order to strongly limit heat generation. This concept is strongly inspired by electrolytic capacitor technologies [305]. One common accepted way is to weld the module terminals directly on the first and the last cell of the module [306] (Figure 10.36).

10.4.1.3 Insulator for Module

It exists on the market as many insulating materials, based on polyolefins, polyesters, and so on.

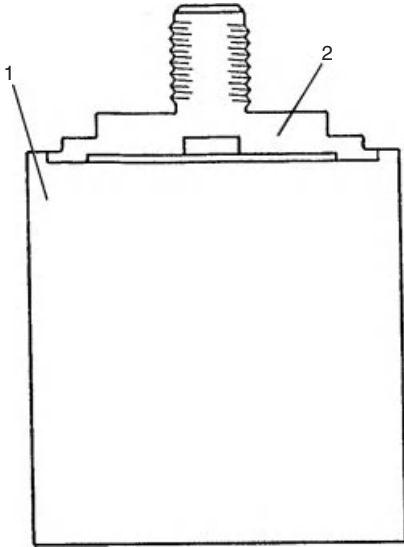


Figure 10.36 Terminal connection 1 on a cell 2 (first or last).

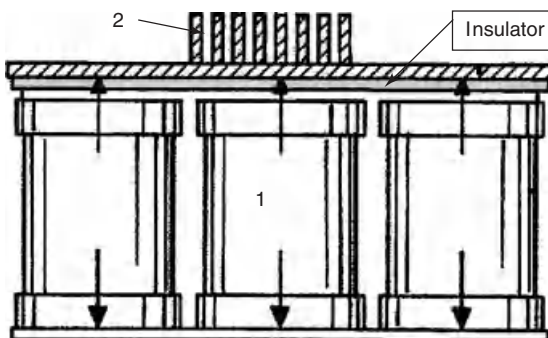


Figure 10.37 Insulator, heat dissipating wings (2) and cells (1). Arrows correspond to heat dissipation direction.

Polyimide and PTFE are convenient if thickness is small. A heat-conducting foil, which is plastically or elastically deformable under pressure, is provided between the terminals of the storage cells and the cooling plate. Such a heat-conducting foil preferably contains ceramic, silicone, wax, or a mixture of various thermally conductive substrates, and may have multilayer coatings [307].

One of the most useful materials used as an insulator is elastomeric based and filled with carbon black (Figure 10.37).

The layer of elastomer covers several functions simultaneously [308]. It allows the following:

- Electric insulation of the whole of storage with respect to case, thanks to a tension of breakdown higher than 1 kV

- Absorption of geometrical dispersions of the whole of storage because of the tolerances of manufacture, thanks to its aptitude for compression
- Improvement of heat exchange between the whole of storage and the outside of the module.

10.4.1.4 Cell Balancing and Other Information Detection

In order to ensure durability and safety of modules, thermal modeling of the supercapacitor cell can be a key factor in maintaining the operating temperature and the temperature uniformity of the supercapacitor module within a suitable range [309, 310].

Cell to cell voltage balancing is necessary to evenly distribute the total system end of charge voltage across a series of cells. Cell parameters (capacitance, series resistance, and self-discharge) are never fully equal because of process and aging variations [311]. Hence, if no balancing electronics is used, a risk of cell overvoltage exists and could result in excessive aging. Most common voltage balancing is achieved by driving a bypass current in or out of cells when the voltage goes above the nominal voltage. The most appropriate balancing voltage system consists in one balancing circuit per cell connected in series. Because a small part of the charge current is used, this electronics does not provide full protection against overvoltage. Its efficiency depends on the application cycle.



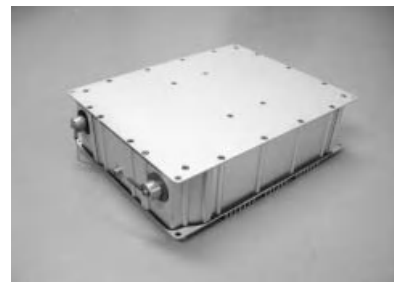
(a)



(b)



(c)



(d)

Figure 10.38 Module enclosure of (a) LS Cable (16.8 V/500 F), (b) Nesscap (111 F/48 V and 166 F/48 V), (c) Maxwell (165 F/48.6 V), and (d) Batscap (150 F/54 V).

In some high current applications and in extreme low-temperature applications, it is necessary to detect other additional information such as temperature cutoff system or electrolyte leakage or hydrogen detection to prevent accidents. Such detectors are expensive but can be convenient for niche markets.

10.4.1.5 Module Enclosure

Figure 10.38 illustrates an aluminum enclosure of various modules. Batscap 150 F 54 V module (Figure 10.38d), made of 3000 F unit cells, is dedicated to urban transport applications. For these applications, Batscap has made many efforts to meet the strongest requirements for advanced transportation systems (see Table 10.13 for more details). As, for example, this module is cooled by simple air ventilation (heat sink on one side) and conforms to fume and smoke standards (Table 10.14).

Although energy and power densities (3.4 Wh l^{-1} , 0.8 kW kg^{-1} at 10 s) are quite low compared to the cell's values (more than 6 Wh l^{-1} , 1.4 kW kg^{-1} at 10 s), such modules are very secure.

10.4.2

Large Modules Based on Pouch-Type Cells

As described previously, pouch cells are convenient to optimize energy and power densities because of passive component minimization.

Table 10.13 54 V 150 F Batscap module performances.

Parameter	Unit	value
Voltage	V	54
Capacitance (54 V, 20 °C)	F	150
ESR (DC, 54 V, 20 °C)	mΩ	5
ESR (1 kHz, 54 V, 20 °C)	mΩ	3
Time constant (54 V, 20 °C)	s	0.75
Rated RMS current	A	150
Maximum peak voltage	V	58
Stored energy(54 V, 20 °C)	Wh	61
Available power at 10 s (54 V, 20 °C, DODV 50%)	kW	13
Available power density at 10 s	kW kg ⁻¹	0.8
Volume	l	18
Weight	kg	17
IPrating IP	—	65
Temperature range	°C	40 to +65
Maximum peak temperature (low current)	°C	80
Insulation level, case to HV, 50 Hz 10 s	kV	2.8
Insulation level, LV to HV 50 Hz 10 s	kV	4.6
Number of cycles (54 V, 100 Amp RMS, 20 °C)	—	>5 million
Floating 50 V 20 °C	h	50 000

Table 10.14 Tests performed on 54 V 150 F Batscap module and its results.

Test	Standard reference or description	Result
Abuse storage	IEC 60068 −40 °C, 70 °C, 95% HR 45 °C	Passed
Salt spray	IEC 60068 96 h at 5%NaCl	Passed
Thermal shocks	IEC 60068 300 cycles (−40 °C/70 °C)	Passed
Vibrations and shocks	NF EN 61373 Catalyst 1 Class B	Passed
Crush	FreedomCar, two axes	Passed
Short circuit	Rshort circuit < 1 mΩ, 20 consecutive times Ishort circuit up to 17 kA	Passed
Nail test	FreedomCar	Passed
Overcharge	Standard reference or description result FreedomCar 200 and 400 A, no voltage limit	Passed
Thermal stability	FreedomCar	Passed
Open fire	Methanol fire, 45 min	Passed
Combined leakage and spark	ACN or H ₂ explosive concentrations	Simulated

To ensure high security of such an assembly, high mechanical strength of the enclosure is needed.

Power Systems has developed three different pouch-cell-based modules with interesting performance for numerous applications [312]:

- 216 V/15 F High power and high energy type (2.3 Wh l^{-1} , 2.9 Wh kg^{-1} , $RC = 1 \text{ s}$) based on a 54 V/60 F unit module. *Application*: container handling crane, electric power facility, copy machine, construction machine, AGV (automatic guided vehicle), stacker crane
- 216 V/5 F Ultrahigh power type based on 108 V/10 F unit module (1.2 Wh l^{-1} , 1.5 Wh kg^{-1} , $RC = 0.2 \text{ s}$). *Application*: injection press, electric welder.
- 405 V/0.9 F Compact size and ultrahigh power type based on two 202 V/1.8 F unit module (1 Wh l^{-1} , 1 Wh kg^{-1} , $RC = 0.18 \text{ s}$). *Application*: general-purpose machine tool, wwing-arm robot.

Other original modules have been developed by Meidensha (MeidenCap). These flat modules [313], based on stacking technology (Figure 10.39), have low capacitance values, high voltage, and interesting energy density performances [314] (Table 10.15). The main drawback is time constant ($RC \gg 1 \text{ s}$). For the moment, these modules are especially dedicated to the UPS market. In its construction, cells are laminated into a unified body (in stacks, as in aqueous medium). A single cell is composed of a pair of bipolar laminates, a pair of activated carbon electrodes (dipped in electrolyte), and separators, and provided with terminals. Both sides of the laminated stacks are sandwiched by end plates and tightened by bolts. The

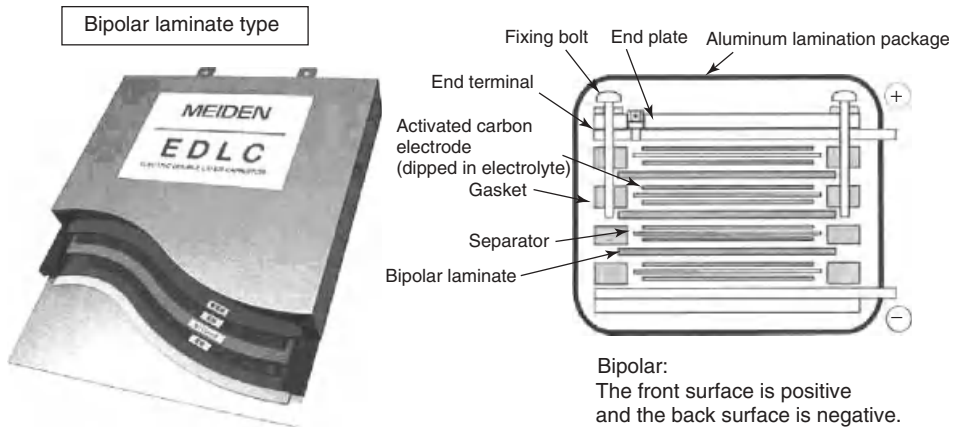


Figure 10.39 Meidensha module structure.

Table 10.15 Performances of Meidensha modules at 25 °C.

Type	600S1-70C	600L1-70C	150S1-38C	150S2-32C
Number of connected cells	70	70	38	32
External dimensions (W × H × l)	266 × 43 × 316 mm	266 × 43 × 316 mm	158 × 27 × 176 mm	158 × 30 × 176 mm
Mass (kg)	5.7	5.7	1.1	1.3
Rated voltage (V)	160	160	85	72
Maximum voltage during regeneration (V)	175	175	95	80
Capacitance (F)	4.5	3.7	2.0	4.0
ESR (Ω)	0.58	0.45	2.0	1.9
Gravimetric energy density (Wh kg ⁻¹)	2.8	2.3	1.8	2.2
Volumetric energy density (Wh l ⁻¹)	4.4	3.6	2.7	3.5
Time constant (s)	2.6	1.7	4.0	7.6

overall assembly is hermetically sealed in an aluminum lamination package. In these modules, it is not possible to provide a balancing system between cells.

10.4.3

Large Modules Working in Aqueous Electrolytes

No unit cells have been industrialized for the moment, owing to the poor performance of the aqueous medium. However, modules have been industrialized by



Figure 10.40 ESCap 90/300 Tavrma module (90 kJ/300 V) working in aqueous medium.

Tavrma Canada for a few years. The Tavrma design is based on large cylindrical stack (Figure 10.40). Energy densities are 0.7 Wh kg^{-1} and 1.1 Wh l^{-1} : these values are quite low compared to modules working in organic medium. The main advantage of these modules is the low ESR, providing a low time constant (0.6 s).

The main drawback of this technology is the temperature range of use: (-40°C ; $+55^\circ\text{C}$). $+55^\circ\text{C}$ is generally not high enough for the automotive market.

10.4.4

Other Modules Based on Asymmetric Technologies

As mentioned earlier in this chapter, the main drawback of the C/C supercapacitor is the low energy density.

For these reasons, other technologies based on two different technologies for each electrode have been developed.

We can distinguish the following types:

- 1) Activated carbon/ MnO_2 technology. Up to now, only cells were commercially available. These supercapacitors work in aqueous medium. For more details, refer to Chapter 8.
- 2) Lead/activated carbon working in aqueous medium. These cells and modules have been developed by CSIRO and are commercialized by Furukawa Battery.
- 3) NiOOH /activated carbon working in aqueous medium. This technology was developed in Russia for many years and is commercialized by ESMA and ELIT. Energy densities are increased compared to the standard C/C supercapacitor. However, cyclability is reduced and maximum temperature use is generally $50\text{--}55^\circ\text{C}$. The time constant is increased ($>3 \text{ s}$).
- 4) Graphite/activated carbon working in organic medium. Many Japanese manufacturers have developed this technology in the past four years. The energy density is strongly increased. The main drawback of this technology is the use

Table 10.16 Comparison between EDLC technologies and hybrid supercapacitor technologies.

Technology	EDLC	EDLC	EDLC	Hybrid	Hybrid	Hybrid	Hybrid
Description	EDLC ACN	EDLC PC	EDLC KOH (aq.)	C/MnO ₂ Aqueous	Pb/C	Pb/C	NiOOH/C
Working voltage	(0; 2.8 V)	(0; 2.8 V)	(0; 0.9 V)	(0; 2.0 V)	(1.2; 2.0 V)	(1.2; 2.0 V)	(0.9; 1.5 V)
E (Wh kg ⁻¹)	4–6	3–5	<1	3–4	>5	>5	2–8
E (Wh l ⁻¹)	5–10	5–10	<1	3–5	>10	>10	2–8
P (kW kg ⁻¹) (10 s)	1–2	0.5–1.5	<1	0.5–0.8	1.2	1.2	0.5–1
Thermal stability	Ok	Problem at –20 °C	Problem at high T	Problem at –20 °C	Problem at –20 °C	Problem at –20 °C	OK until 50 °C
T_{\max} (°C)	80	100	55	100	100	100	55
RC (time constant, s)	0.5–1.0	1.0–2.0	0.2	>1	?	?	>2
Self-discharge	<–20% U after one month	<–15% U after one month	?	?	–1% U after one month	–1% U after one month	<–20% U after one month
Cyclability	3	2	3?	2	1	1	1
Security/environment	2	2	3	3	2	2	3
Reverse polarity possible?	Yes	Yes	Yes	No	No	No	No
Efficiency at 10 s (%)	>98	>97	>98	>95	<60	<60	>92
Commercial cells?	Yes	Yes	No	Yes	No	No	Yes
Commercial modules?	Yes	Yes	Yes	No	Yes	Yes	Yes

ACN, acetonitrile-based electrolyte; PC, propylene carbonate-based electrolyte; RC, time constant, equivalent to $ESR \times \text{capacitance}$; E , energy density; P , power density; T_{\max} , maximum temperature for storage. Thermal stability: operating temperature range. Reverse polarity: consists to reverse the polarity of the energy storage.

of low temperature, limited to $-10-0^{\circ}\text{C}$. Demonstrated cyclability is 200 000 cycles at 25°C and should be improved in the coming years. This technology can be considered as an intermediate energy storage system between the C/C supercapacitor and power Li-ion battery.

All these technology performances are summarized in Table 10.16 and compared to standard C/C supercapacitors.

All these technologies have targeted to improve almost one supercapacitor drawback: environment (MnO_2/C) and energy density (C/graphite, NiOOH/C , Pb/C). However, power density and/or cyclability are degraded by these technologies.

10.5 Conclusions and Perspectives

It is important to differentiate small cells from large cells for targeted market reasons. Small cells have been commercially available for many years and performance improvements are small. Small cells have identified markets such as mobile applications, toys, backup, and so on.

Large supercapacitor cells are now commercially available. Markets grow year after year. The industrialization of supercapacitors is based on low-cost materials (aluminum, natural activated carbon, paper separator, etc.) to be competitive and for targeted market reasons. The cost of the supercapacitor may inhibit its use in some applications. Current costs of around $\$0.010-0.015 \text{ F}^{-1}$ need to be reduced to less than $\$0.005 \text{ F}^{-1}$ [315]. Users or potential users of supercapacitors have also pointed out that, apart from cost, a barrier to introduction is the lack of understanding of how to use them properly. Many improvements have been made in the past 10 years: millions of cycles can be reached and high power density has been proved. For some applications, for example, automotive, the energy density as well as the power density is important. This is particularly the case where the supercapacitor is in competition with a battery or is being considered for use in conjunction with a battery.

In a conventional symmetric supercapacitor, there is some scope to increase the energy density by increasing the operating voltage. Three main solutions have been tried: by making a slight change to the capacity ratio of the two electrodes, matching the ion size of the electrolyte to the carbon (complicate solution), or by matching the pore size distribution of activated carbon to the ions of the electrolyte, by electrolyte (solvent or ions) change.

Regarding electrolytes, ionic liquids are being considered, but the price targets are very high in comparison with conventional electrolytes and low-temperature conductivity is a main technical drawback. However, such electrolytes could find applications in niche markets.

Where supercapacitors are in direct competition with batteries in a specific application, the low specific energy (Wh kg^{-1}) is a disadvantage. Here, hybrid supercapacitors, which have a higher specific energy but degraded almost one parameter, may be the answer.

References

1. Becker, H.E. (1957) Patent US2800616 for General Electric.
2. Boos, D.I. (1970) Patent US3536963 for Standard Oil Co.
3. Miller, J.M. (2007) A Brief History of Supercapacitors. Batteries & Energy Storage Technology, Autum, pp. 61–78.
4. Okamura, M., Noguchi, M., Iwaida, M., Komazawa, E., and Mogami, A. (2001) Patent JP11121301 for Honda Motor and Jeol.
5. Saito, T. and Kibi, Y. (2001) Patent JP3341886 for NEC.
6. Richner, R. and Wokaun, A. (2001) Patent WO0145121 for Paul Scherrer Institut.
7. Farahmandi, C.J. and Dispennette, J.M. (2000) Patent US6059847 for Maxwell Technologies.
8. Hahn, M., Barbieri, O., Campana, M., Gallay, R., and Kötz, R. (2004) Charge-induced Dimensional Changes in Electrochemical Double Layer Capacitors. Florida Supercapacitor Seminar, pp. 40–48.
9. Gwinn, C.D. and Stephan, F.C. (1935) GB439479 for The Telegraph Condenser Co.
10. Claassen, A.F.P.J. and De Vries, J.D. (1940) DE695770 for Philips.
11. Portet, C., Taberna, P.-L., Simon, P., Flahaut, E., and Laberty-Robert, C. (2005) *Electrochim. Acta*, **50**, 4174–4181.
12. Kobayashi, K., Minihami, K., and Tachozono, S. (2005) EP1672652 for Hitachi Powder Metals and Japan Gore Tex.
13. Portet, C. (2005) Étude de supercondensateurs carbone/carbone à collecteur de courant en aluminium. PhD thesis, University of Toulouse, November 23 2005.
14. Kobayashi, K. (2009) WO2009139493 for Japan Gore Tex.
15. Zhong, L. and Xi, X. (2008) US20080089006 for Maxwell Technologies.
16. Hartmut, M., Scholtz, T., and Weber, C.J. (2004) US2004264110 for EPCOS.
17. Isley, R.E. (1972) US3656027 for Standard Oil Co.
18. Andrieu, X. (1984) FR2565400 for Compagnie Générale d'Electricité.
19. Qu, D. and Shi, H. (1998) *J. Power. Sources*, **74**, 99–107.
20. Pell, W.G., Conway, B.E., and Marincic, N. (2000) *J. Electroanal. Chem.*, **491**, 9–21.
21. Vix-Guterl, C., Frackowiak, E., Jurewicz, K., Friebe, M., Parmentier, J., and Béguin, F. (2005) *Carbon*, **43**, 1293–1302.
22. Okamura, M. (2000) US Patent 6064562 pour JEOL Ltd.
23. Murakami, K. *et al.* (2000) EP 1049116 pour Asahi Glass Co. Ltd.
24. Morimoto, T., Hiratsuka, K., Sanada, Y., and Kurihara, K. (1996) *J. Power. Sources*, **60**, 239–247.
25. Sonobe, N. *et al.* (2001) US Patent 6258337 pour Kureha Kagaku K. K. et Honda Giken K. K. K.
26. Nomoto, S. *et al.* (2001) EP1094478 pour Matsushita Electric Industrial Co. Ltd.
27. Endo, M. *et al.* (2002) EP1113468.
28. Bansal, R.C., Donnet, J.-B., and Stoeckli, F. (1988) *Active Carbon*, Marcel Decker, New York.
29. Obreja, V.V.N. (2008) *Physica E*, **40**, 2596–2605.
30. Liu, G., Kang, F., Li, B., Huang, Z., and Chuan, X. (2006) *J. Phys. Chem. Solids*, **67**, 1186–1189.
31. Tao, X.Y., Zhang, X.B., Zhang, L., Cheng, J.P., Liu, F., Luo, J.H., Luo, Z.Q., and Geise, H.J. (2006) *Carbon*, **44**, 1425–1428.
32. Gomibuchi, E., Ichikawa, T., Kimura, K., Isobe, S., Nabeta, K., and Fujii, H. (2006) *Carbon*, **44**, 983–988.
33. Kim, Y.J., Lee, B.J., Suezaki, H., Chino, T., Abe, Y., Yanagiura, T., Park, K.C., and Endo, M. (2006) *Carbon*, **44**, 1592–1595.
34. Niu, J., Pell, W.G., and Conway, B.E. (2006) *J. Power. Sources*, **156**, 725–740.
35. Kim, Y.T. and Mitani, T. (2006) *J. Power. Sources*, **158**, 1517–1522.
36. Prabakaran, S.R.S., Vimala, R., and Zainal, Z. (2006) *J. Power. Sources*, **161**, 730–736.

37. Rosolen, J.M., Matsubara, E.Y., Marchesin, M.S., Lala, S.M., Montoro, L.A., and Tronto, S. (2006) *J. Power. Sources*, **162**, 620–628.
38. Zhu, Y., Hu, H., Li, W.C., and Zhang, X. (2006) *J. Power. Sources*, **162**, 738–742.
39. Hsieh, C. and Lin, Y. (2006) *Micropor. Mesopor. Mater.*, **93**, 232–239.
40. Morishita, T., Soneda, Y., Tsumura, T., and Inagaki, M. (2006) *Carbon*, **44**, 2360–2367.
41. Wei, Y.-Z., Fang, B., Iwasa, S., and Kumagai, M. (2005) *J. Power. Sources*, **141**, 386–391.
42. Wei, Y.-Z., Fang, B., Iwasa, S., and Kumagai, M. (2006) *J. Power. Sources*, **155**, 487–491.
43. Lia, J., Wanga, X., Huang, Q., Gamboab, S., and Sebastian, P.J. (2006) *J. Power. Sources*, **158**, 784–788.
44. Kaschmitter, J.L., Mayer, S.T., and Pekala, R.W. (1998) US5789338 for D.O.E., Lawrence Livermore National Security LLC and University of California.
45. Pekala, R.W., Farmer, J.C., Alviso, C.T., Tran, T.D., Mayer, S.T., Miller, J.M., and Dunn, B. (1998) *J. Non-Cryst. Solids*, **225**, 74–80.
46. Pröbstle, H., Schmitt, C., and Fricke, J. (2002) *J. Power. Sources*, **105**, 189–194.
47. Firsich, D.W., Ingersoll, D., and Delnick, F.M. (1998) US5776384 for Sandia.
48. Arulepp, M., Leis, J., Lätt, M., Miller, F., Rumma, K., Lust, E., and Burke, A.F. (2006) *J. Power. Sources*, **162**, 1460–1466.
49. Fernández, J.A., Arulepp, M., Leis, J., Stoeckli, F., and Centeno, T.A. (2008) *Electrochim. Acta*, **53**, 7111–7116.
50. Chmiola, J., Yushin, G., Gogotsi, Y., Portet, C., Simon, P., and Taberna, P.-L. (2006) *Science*, **313**, 1760–1763.
51. Lätt, M., Käärik, M., Permann, L., Kuura, H., Arulepp, M., and Leis, J. (2010) *J. Solid State Electrochem.*, **14**, 543–548.
52. Vix-Guterl, C., Saadallah, S., Jurewicz, K., Frackowiak, E., Reda, M., Parmentier, J., Patarin, J., and Béguin, F. (2004) *Mater. Sci. Eng. B*, **108**, 148–155.
53. Portet, C., Yang, Z., Korenblit, Y., Gogotsi, Y., Mokaya, R., and Yushin, G. (2009) *J. Electrochem. Soc.*, **156**, A1–A6.
54. Kim, C. (2005) *J. Power. Sources*, **142**, 382–388.
55. Xing, W., Qiao, S.Z., Ding, R.G., Li, F., Lu, G.Q., Yan, Z.F., and Cheng, H.M. (2006) *Carbon*, **44**, 216–224.
56. Adhyapak, P.V., Maddanimath, T., Pethkar, S., Chandwadkar, A.J., Negi, Y.S., and Vijayamohan, K. (2002) *J. Power. Sources*, **109**, 105–110.
57. Barbieri, O., Hahn, M., Herzog, A., and Kötz, R. (2005) *Carbon*, **43**, 1303–1310.
58. Mitani, S., Lee, S.I., Saito, K., Yoon, S.-H., Korai, Y., and Mochida, I. (2005) *Carbon*, **43**, 2960–2967.
59. Egashira, M., Okada, S., Korai, Y., Yamaki, J.-I., and Mochida, I. (2005) *J. Power. Sources*, **148**, 116–120.
60. Leitner, K., Lerf, A., Winter, M., Besenhard, J.O., Viller-Rodil, S., Suárez-García, S., Martínez-Alonso, A., and Tascón, J.M.D. (2006) *J. Power. Sources*, **153**, 419–423.
61. Jiang, Q., Qu, M.Z., Zhou, G.M., Zhang, B.L., and Yu, Z.L. (2002) *Mater. Lett.*, **57**, 988–991.
62. Frackowiak, E., Delpeux, S., Jurewicz, K., Szostak, K., Cazorla-Amoros, D., and Béguin, F. (2002) *Chem. Phys. Lett.*, **361**, 35–41.
63. Li, W., Chen, D., Li, Z., Shi, Y., Wan, Y., Wang, G., Jiang, Z., and Zhao, D. (2007) *Carbon*, **45**, 1757–1763.
64. Kim, I., Yang, S., Jeon, M., Kim, H., Lee, Y., An, K., and Lee, Y. (2007) *J. Power. Sources*, **173**, 621–625.
65. Tashima, D., Kurosawatsu, K., Uota, M., Karashima, T., Otsubo, M., Honda, C., and Sung, Y.M. (2007) *Thin Solid Films*, **515**, 4234–4239.
66. Zhang, B., Liang, J., Xu, C.L., Wei, B.Q., Ruan, D.B., and Wu, D.H. (2001) *Mater. Lett.*, **51**, 539–542.
67. Niu, C., Sichel, E.K., Hoch, R., Moy, D., and Tennet, H. (1997) *Appl. Phys. Lett.*, **70**, 1480–1482.
68. Frackowiak, E., Jurewicz, K., Delpeux, S., and Béguin, F. (2001) *J. Power. Sources*, **97-98**, 822–825.

69. Ma, R.Z., Liang, J., Wie, B.Q., Zhang, B., Xu, C.L., and Wu, D.H. (1999) *J. Power. Sources*, **84**, 126–129.
70. An, K.H., Kim, W.S., Park, Y.S., Moon, J.-M., Bae, D.J., Lim, S.C., Lee, Y.S., and Lee, Y.H. (2001) *Adv. Funct. Mater.*, **11**, 387–392.
71. Soneda, Y., Toyoda, M., Hashiya, K., Yamashita, J., Kodama, M., Hatori, H., and Inagaki, M. (2003) *Carbon*, **41**, 2680–2682.
72. Emmenegger, C., Mauron, P., Sudan, P., Wenger, P., Hermann, V., Gally, R., and Züttel, A. (2003) *J. Power. Sources*, **124**, 321–329.
73. Chen, Q., Xue, K., Shen, W., Tao, F., Yin, S., and Xu, W. (2004) *Electrochim. Acta*, **49**, 4157–4161.
74. Portet, C., Taberna, P.L., Simon, P., and Flahaut, E. (2005) *J. Power. Sources*, **139**, 371–378.
75. Kim, Y.-J., Masuzawa, Y., Ozaki, S., Endo, M., and Dresselhaus, M.S. (2004) *J. Electrochem. Soc.*, **151**, E199–E205.
76. Tan, M.X. (1999) US5993969 for Sandia.
77. Plée, D. and Taberna, P.-L. (2005) WO2005088657 for Arkema.
78. Taberna, P.-L., Chevallier, G., Simon, P., Plée, D., and Aubert, T. (2006) *Mater. Res. Bull.*, **41**, 478–484.
79. Bansal, R.C., Donnet, J.B., and Stoeckli, F. (1988) *Active Carbon* Chapter 1, Marcel Dekker, New York, Basel, pp. 1–27.
80. Alford, J.A. (2007) US5926361 for Meadwestvaco Corp.
81. Lini, H. and Lini, C. (2002) WO20024308 for CECA S.A.
82. Ishida, S., Takenaka, H., Nishimura, S., Egawa, Y., and Otsuka, K. (2008) WO2008053919 for Kuraray Chemical.
83. Hijiriyama, M., Yasumaru, J., and Ishida, K. (1998) JP10199767 for Kansai Coke & Chemicals.
84. Hanioka, A., Matsuda, K., Yasumaru, J., and Asada, S. (2009) JP2009184850 for Kansai Coke & Chemicals.
85. Tokuyasu, A., Matsuda, K., Kasu, K., and Asada, M. (2010) JP2010105885 for Kansai Coke & Chemicals.
86. Abe, H. and Morohashi, K. (2006) JP2006024747 for Mitsubishi Gas Chemical.
87. Buiel, E.R. (2007) WO2007114849 for Meadwestvaco Corp.
88. Dietz, S. (2007) Production scale-up of activated carbons for ultracapacitors. DE-FG36-04GO1432, TDA Research.
89. Jänes, A., Kurig, H., and Lust, E. (2007) *Carbon*, **45**, 1226–1233.
90. Ruch, P.W., Hahn, M., Cericola, D., Menzel, A., Kötz, R., and Wokaun, A. (2010) *Carbon*, **48**, 1880–1888.
91. Carl, E., Landes, H., Michel, H., Schriker, B., Schwake, A., and Weber, C. (2004) WO2004038742 for EPCOS.
92. Nozu, R. and Nakamura, M. (2006) EP1724797 for Nisshinbo Industries.
93. Ruch, P.W., Cericola, D., Foelske, A., Kötz, R., and Wokaun, A. (2010) *Electrochim. Acta*, **55**, 2352–2357.
94. Fujiwara, M., Yoneda, H., and Okamoto, M. (1986) JP06065206B1 for Matsushita Electric Ind.
95. Wang, L., Morishita, T., Toyoda, M., and Inagaki, M. (2007) *Electrochim. Acta*, **53**, 882–886.
96. Conway, B.E., Verall, R.E., and Desnoyers, J.E. (1966) *Trans. Faraday Soc.*, **62**, 2738–2744.
97. Robinson, R.A. and Stokes, R.H. (1965) *Electrolyte Solutions*, 2nd edn, Butterworths, London.
98. Endo, M., Kim, Y.J., Ohta, H., Ishii, K., Inoue, T., Hayashi, T., Nishimura, Y., Maeda, T., and Dresselhaus, M.S. (2002) *Carbon*, **40**, 2613–2626.
99. Okamura, M. (2000) JP11067608 for Advanced Capacitor Tech., Jeol and Okamura Lab.
100. Maletin, Y., Strizhakova, N., Kozachkov, S., Mironova, A., Podmogilny, S., Danilin, V., Kolotilova, J., Izotov, V., Cederstrom, J., Konstantinovich, S.G., Aleksandrovna, J., Vasilevitj, V.S., Efimovitj, A.K., Perkson, A., Arulepp, M., Leis, J., Wallace, C.L., and Zheng, J. (2002) US20020097549 for Frankenburg Oil Company, Karbid Aozt and Ultratec.
101. Carl, E., Landes, H., Michel, H., Schriker, B., Schwake, A., and Weber, C. (2006) US2006098388 for EPCOS.
102. Mitchell, P., Xi, X., Zhong, L., and Zou, B. (2008) US2008016664 for Maxwell Technologies.

103. Yoshida, H. and Yuyama, K. (2007) EP1783791 for Nisshinbo Industries.
104. Paul, G.L. and Pynenburg, R. (2006) EP1724796 for CapXX.
105. Maletin, Y. and Strizhakova, N. (2003) US2003064565 for Ultratec.
106. Shi, H. (1996) *Electrochim. Acta*, **41**, 1633–1639.
107. Murakami, K., Mogi, Y., Tabayashi, K., Shimoyama, T., Yamada, K., and Shinozaki, Y. (2000) EP1049116 for Asahi Glass Co, Adchemco Corp and JFE Chemical
108. Morimoto, T., Hiratsuka, K., Sanada, Y., and Kurihara, K. (1996) *J. Power. Sources*, **60**, 239–247.
109. Sonobe, N., Nagai, A., Aida Tomoyuki, T., Noguchi, M., Iwaida, M., and Komazawa, E. (2001) JP4117056 for Kureha Chemical and Honda Motor.
110. Nomoto, S., Yoshioka, K., and Hirose, E. (2001) JP2001118753 for Matsushita Electric Ind.
111. Endo, M., Noguchi, M., Oki, N., and Oyama, S. (2002) JP2001189244 for Honda Motor.
112. Okamura, M. and Takeuchi, M. (2001) US6310762, Advanced Capacitor Technologies, Jeol, Okamura Laboratory and Power System.
113. Largeot, C., Portet, C., Chmiola, J., Taberna, P.-L., Gogotsi, Y., and Simon, P. (2008) *J. Am. Chem. Soc.*, **130**, 2730–2731.
114. Ania, C.O., Pernak, J., Stefaniak, F., Raymundo-Pinero, E., and Béguin, F. (2006) *Carbon*, **44**, 3126–3130.
115. Lin, R., Taberna, P.-L., Chmiola, J., Guay, D., Gogotsi, Y., and Simon, P. (2009) *J. Electrochem. Soc.*, **156**, A7–A12.
116. Raymundo-Pinero, E., Kierzek, K., Machnikowski, J., and Béguin, F. (2006) *Carbon*, **44**, 2498–2507.
117. Shinozaki, Y., Hiratsuka, K., Nonaka, T., and Murakami, K. (2002) EP1168389 for Adchemco Corp., Asahi Glass Co. and JFE Chemical Corp.
118. Takeuchi, M., Koike, K., Maruyama, T., Mogami, A., and Okamura, M. (1998) *Denki Kagaku*, **66**, 1311–1317.
119. Ruch, P.W., Hahn, M., Rosciano, F., Holzapfel, M., Kaiser, H., Scheifele, W., Schmitt, B., Novak, P., Kötz, R., and Wokaun, A. (2007) *Electrochim. Acta*, **53**, 1074–1082.
120. Hahn, M., Barbieri, O., Campana, F.P., Kötz, R., and Gallay, R. (2006) *Appl. Phys. A*, **82**, 633–638.
121. Sugo, N., Iwasaki, H., and Uehara, G. (2002) EP1176617 for Honda Motor and Kuraray Co.
122. Iwasaki, H., Sugo, N., Hitomi, M., Nishimura, S., Fujino, T., Oyama, S., and Kawabuchi, Y. (2004) WO2004011371 for Kuraray Chemical and Honda.
123. Zhong, L., Xi, X., Mitchell, P. (2008) US20080201925 for Maxwell Technologies.
124. Zhong, L., Xi, X., and Mitchell, P. (2008) WO2008106533 for Maxwell Technologies.
125. Morimoto, T., Hiratsuka, K., Sanada, Y., and Ariga, H. (1989) JP01241811 for Asahi Glass Co. and Elna.
126. Fujino, T., Oyama, S., Oki, N., Noguchi, M., Sato, K., Nishimura, S., Maeda, T., Kawabuchi, Y., and Haga, T. (2001) WO200113390 for Honda, Kuraray Chemical Co., Petoca.
127. Koyama, S., Iwaida, M., and Murakami, K. (2004) JP2004193569 for Kuraray Chemical and Honda.
128. Koyama, S., Iwaida, M., Murakami, K., Ozaki, K., Tsutsui, M., and Otsuka, K. (2004) JP2004189586 for Daido Metal Co., Honda and kuraray Chemical.
129. Tsuchiya, Y., Kurabayashi, K., and Morohoshi, H. (1990) US5136473 for Isuzu Motors.
130. Sarangapani, S., Tilak, B.V., and Chen, C.P. (1996) *J. Electrochem. Soc.*, **143**, 3791–3799.
131. Hsieh, C.T. and Teng, H. (2002) *Carbon*, **40**, 667–674.
132. Delahay, P. (1966) *J. Phys. Chem.*, **70**, 2373–2379.
133. Delahay, P. and Holub, K. (1968) *J. Electroanal. Chem.*, **16**, 131–136.
134. Schultze, J.W. and Koppitz, F.D. (1976) *Electrochim. Acta*, **21**, 327–336.
135. Schultze, J.W. and Koppitz, F.D. (1976) *Electrochim. Acta*, **21**, 337–343.
136. Sullivan, M.G., Kötz, R., and Haas, O. (2000) *J. Electrochem. Soc.*, **147**, 308–317.

137. Momma, T., Liu, X., Osaka, T., Ushio, Y., and Sawada, Y. (1996) *J. Power. Sources*, **60**, 249–253.
138. Qiao, W., Korai, Y., Mochida, I., Hori, Y., and Maeda, T. (2002) *Carbon*, **40**, 351–358.
139. Sullivan, M.G., Schnyder, B., Bärtsch, B., Alliata, D., Barbero, C., Imhof, R., and Kötz, R. (2000) *J. Electrochem. Soc.*, **147**, 2636–2643.
140. Nakamura, M., Nakanishi, M., and Yamamoto, K. (1996) *J. Power. Sources*, **60**, 225–231.
141. Mayer, S.T., Pekala, R.W., Kaschmitter, J.L. et al. (1993) *J. Electrochem. Soc.*, **140**, 446–451.
142. Pillay, B. and Newman, J. (1996) *J. Electrochem. Soc.*, **143**, 1806–1814.
143. Xu, K., Ding, M.S., and Jow, T.R. (2001) *Electrochim. Acta*, **46**, 1823–1827.
144. Yoshida, A., Tanahashi, I., and Nishino, A. (1990) *Carbon*, **28**, 611–615.
145. Conway, B.E., Pell, W.G., and Liu, T.C. (1997) *J. Power. Sources*, **65**, 53–59.
146. Ricketts, B.W. and Ton-That, C. (2000) *J. Power. Sources*, **89**, 64–69.
147. Haye, G. (1965) *Carbon*, **2**, 413–419.
148. Matsumura, Y., Hagiwara, S., and Takahashi, H. (1976) *Carbon*, **14**, 163–167.
149. Hagiwara, S., Tsutsumi, K., and Takahashi, H. (1978) *Carbon*, **16**, 89–93.
150. Frysz, C.A. and Chung, D.D.L. (1997) *Carbon*, **35**, 1111–1127.
151. Noh, J.S. and Schwarz, J.A. (1990) *Carbon*, **28**, 675–682.
152. Horita, K., Nishibori, Y., and Oshima, T. (1996) *Carbon*, **34**, 217–222.
153. Frysz, C.A., Shui, X., and Chung, D.D.L. (1994) *Carbon*, **32**, 1499–1505.
154. Strein, T.G. and Ewing, A.G. (1991) *Anal. Chem.*, **63**, 194–198.
155. Ishikawa, M., Sakamoto, A., Morita, M., Matsuda, Y., and Ishida, K. (1996) *J. Power. Sources*, **60**, 233–238.
156. Takada, T., Nakahara, N., Kumagai, H., and Sanada, Y. (1996) *Carbon*, **34**, 1087–1091.
157. Wigtman, R.M., Deakin, M.R., Kovach, P.M., Kuhr, W.G., and Stutts, K.J. (1984) *J. Electrochem. Soc.*, **131**, 1578–1583.
158. Shui, X., Frysz, C.A., and Chung, D.D.L. (1995) *Carbon*, **33**, 1681–1698.
159. Firsich, D.W. (1999) US5993996 for Inorganic Specialists.
160. Ohsaki, T., Wakaizumi, A., Kigure, M., Nakamura, A., Marumo, S., Miyagawa, T., and Adachi, T. (1999) US5948329 for Nippon Sanso Corp.
161. Hirahara, S., Okuyama, K., Suzuki, M., and Matsuura, K. (1999) US6094338 for Mitsubishi Chemicals.
162. Oyana, S., Oki, N., and Noguchi, M. (1999) US5891822 for Honda Motor.
163. Azaïs, P. (2003) Recherche des causes du vieillissement de supercondensateurs carbone/carbone fonctionnant en milieu électrolyte organique. PhD thesis, University of Orléans, November 27 2003.
164. Takeuchi, M. (2002) EP1264797 for Advanced Capacitor Technologie and Jeol.
165. Watanabe, F., Oshida, T., Miki, Y., and Sugano, K. (2008) JP2008195559 for Mitsubishi Gas Chemical.
166. Igai, K., Ono, H., Fujii, M., Takeshita, K., Tano, T., and Oyama, T. (2007) JP2007302512 for Nippon Oil Corp.
167. Yamada, C., Hirose, E., Takamuku, Y., and Shimamoto, H. (2007) EP1918951 for Matsushita Electric Ind.
168. Hart, B.E. and Peekma, R.M. (1972) US3652902 for IBM.
169. Morimoto, T., Hiratsuka, K., Sanada, Y., and Aruga, H. (1988) US4725927 for Asahi Glass Co. and Elna Co.
170. Farahmandi, C.J. and Dispennette, J.M. (1997) US5621607 for Maxwell Technologies.
171. Andrieu, X. and Josset, L. (1996) WO9620504 for SAFT.
172. Bonnefoi, L., Laforgue, A., Simon, P., Fauvarque, J.F., Sarrazin, C., Lailler, P., and Sarrau, J.F. (1999) FR2793600 for Compagnie Européenne d'Accumulateurs.
173. Meguro, K., Sato, and H., Tada, Y. (2001) US6327136 for Kureha Chemical Ind.
174. Xi, X., Mitchell, P., Zhong, L., and Zou, B. (2007) US7295423 for Maxwell Technologies.
175. Ishikawa, T., Suhara, M., Kuroki, S., and Kanetoku, S. (2001) US6264707 for Asahi Glass Co.

176. Imoto, K. and Yoshida, A. (1991) US5150283 for Matsushita Electric Ind. Co.
177. Azaïs, P. (2003) Study of ageing mechanisms of organic electrolyte supercapacitors based on activated carbons, PhD thesis, University of Orléans.
178. Barusseau, S., Martin, F., and Simon, B. (1999) EP0907214 for SAFT.
179. Hiratsuka, K., Morimoto, T., Suhara, M., Kawasato, T., and Tsushima, M. (2000) US6402792 for Asahi Glass Co.
180. Nakao, K., Shimizu, K., and Yamaguchi, T. (2001) WO9858397 for Matsushita Electric Ind.
181. Takabayashi, S., Asada, S., Edamoto, T., and Sato, K. (2001) US6282081 for Hitachi Maxell.
182. Qu, D. (2002) *J. Power. Sources*, **109**, 403–411.
183. Penneau, J.F., Capitaine, F., and Le Goff, P. (1998) EP0960154 for Bolloré and Batscap.
184. Drevet, H., Rey, I., Le Gal, G., and Peillet, M. (2005) WO2005116122 for Batscap.
185. Drevet, H., Rey, I., Peillet, M., and Abribat, F. (2006) WO2006082172 for Batscap.
186. Nanjundiah, C., Braun, R.P., Christie, R.T.E., and Farahmandi, J.C. (2001) WO0188934 for Maxwell Tech.
187. Zykov, V.P., Panov, A.A., Prudnikov, P.A., Khlopin, M.I., and Shlyapnikov, A.D. (1972) US3675087.
188. Probst, N. (1993) in *Carbon Black: Science and Technology*, 2nd Chapter 8 edn (eds J.-B. Donnet, R.C. Bansal, and M.-J. Wang), Marcel Dekker, New York, pp. 271–285.
189. Yoshida, H., Sato, T., Masuda, G., Kotani, M., and Izuka, S. (2005) EP1715496 for Nisshinbo Industries.
190. Zhu, M., Weber, C.J., Yang, Y., Konuma, M., Starke, U., Kern, K., and Bittner, A.M. (2008) *Carbon*, **46**, 1829–1840.
191. Green, M.C., Taylor, R., Moeser, G.D., Kyrlidis, A., and Sawka, R.M. (2009) US20090208751 for Cabot Corp.
192. Wissler, M. (2006) *J. Power. Sources*, **156**, 142–150.
193. Zhang, H., Zhang, W., Cheng, J., Cao, G., and Yang, Y. (2008) *Solid State Ionics*, **179**, 1946–1950.
194. Lust, E., Janes, A., and Arulepp, M. (2004) *J. Electroanal. Chem.*, **562**, 33–42.
195. Dahm, C.E. and Peters, G.D. (1996) *J. Electroanal. Chem.*, **402**, 91–96.
196. Simonet, J., Astier, Y., and Dano, C. (1998) *J. Electroanal. Chem.*, **451**, 5–9.
197. Ross, S.D., Finkelstein, M., and Petersen, R.C. (1970) *J. Am. Chem. Soc.*, **92**, 6003–6006.
198. Ross, S.D., Finkelstein, M., and Petersen, R.C. (1960) *J. Am. Chem. Soc.*, **82**, 1582–1585.
199. Simonet, J. and Lund, H. (1977) *J. Electroanal. Chem.*, **75**, 719–730.
200. Bernard, G. and Simonet, J. (1979) *J. Electroanal. Chem.*, **96**, 249–253.
201. Finkelsteinn, M., Petersen, R.C., and Ross, S.D. (1959) *J. Am. Chem. Soc.*, **81**, 2361–2364.
202. Finkelstein, M., Petersen, R.C., and Ross, S.D. (1965) *Electrochim. Acta*, **19**, 465–469.
203. Kawasato, T., Suhara, M., Hiratsuka, K., and Tsushima, M. (1999) US5969936 for Asahi Glass Co.
204. Ue, M., Ida, K., and Mori, S. (1994) *J. Electrochem. Soc.*, **141**, 2989–2996.
205. Farahmandi, C.J., Dispennette, J.M., Blank, E., and Crawford, R.W. (2001) US6233135 for Maxwell Tech.
206. Azaïs, P., Tertrais, F., Caumont, O., Depond, J.-M., and Lejosne, J. (2009) Ageing Study of Advanced Carbon/Carbon Ultracapacitor Cells Working in Various Organic Electrolytes. ISEE'Cap '09, Nantes.
207. Chiba, K. (2005) WO2005022571 for Japan Carlit Co.
208. Zheng, J.P. and Jow, T.R. (1997) *J. Electrochem. Soc.*, **144**, 2417–2420.
209. Farahmandi, C.J. and Dispennette, J.M. (1998) WO9611486 for Maxwell Tech.
210. Degen, H.-G., Ebel, K., Tiefensee, K., Schwake, A. (2006) DE102004037601 for EPCOS.
211. Aurbach, D., Daroux, M., Faguy, P., and Yeager, E. (1991) *J. Electroanal. Chem.*, **297**, 225–240.

212. Aurbach, D., Youngman, O., and Dan, P. (1990) *Electrochim. Acta*, **35**, 639–655.
213. Bruglachner, H. (2004) Neue Elektrolyte für Doppelschichtkondensatoren. PhD thesis, University of Regensburg.
214. Xu, K., Ding, S.P., and Jow, T.R. (1999) *J. Electrochem. Soc.*, **146**, 4172–4178.
215. Xu, K., Ding, M.S., and Jow, T.R. (2001) *J. Electrochem. Soc.*, **148**, A267–A274.
216. Aurbach, D. (1999) *Nonaqueous Electrochemistry* Chapter 4, CRC Press.
217. Cotton, F.A. and Wilkinson, G. (1966) *Advanced Inorganic Chemistry*, John Wiley & Sons, Inc., New York, p. 240.
218. Farahmandi, C.J., Dispennette, J.M., Blank, E., and Kolb, A.C. (1998) WO9815962 for Maxwell Tech.
219. Izutsu, K. (2009) *Electrochemistry in Nonaqueous Solutions*, Wiley-VCH Verlag GmbH, p. 105.
220. Pavlishchuk, V.V. and Addison, A.W. (2000) *Inorg. Chim. Acta*, **298**, 97–102.
221. Kang, X., Ding, M.S., and Jow, T.R. (2001) *J. Electrochem. Soc.*, **148**, A267–A274.
222. Noguchi, M., Oki, N., Iwaida, M., Aida, T., Nagai, A., and Ichikawa, Y. (2002) JP2001237149.
223. Farahmandi, C.J., Dispennette, J.M., Blank, E., and Kolb, A.C. (2000) US6094788 for Maxwell Tech.
224. Takeuchi, M., Koike, K., Mogami, A., and Maruyama, T. (2002) JP2002025867 for Advanced Capacitor Technologies and Jeol.
225. Jerabek, E.C. and Mansfield, S.F. (2000) US6084766 for General Electric.
226. Day, J., Shapiro, A.P., and Jerabek, E.C. (2000) US6110321 for General Electric.
227. Kimura, K., Kimura, F., and Kobayashi, T. (2001) JP3717782 for Japan Vilene Co.
228. Kimura, F., Kimura, K., Kobayashi, T., and Shimizu, M. (2001) JP2001185455 for Japan Vilene Co. and Power Systems Co.
229. Ufheil, J., Wursig, A., Schneider, O.D., and Novak, P. (2005) *Electrochem. Commun.*, **7**, 1380–1384.
230. Hahn, M., Baertschi, M., Barbieri, O., Sauter, J.C., and Kötz, R. (2004) *Elektrochem. Materialforschung*, **29**, 120–129.
231. Suhara, M. and Hiratsuka, K. (2002) WO0016354 for Asahi Glass Co. and Honda Motor.
232. Ishimoto, S., Asakawa, Y., Shinya, M., and Naoi, K. (2009) *J. Electrochem. Soc.*, **156**, A563–A571.
233. Kurzweil, P. and Chwistek, M. (2008) *J. Power. Sources*, **176**, 555–567.
234. Kanbe, Y. and Oya, M. (2000) JP2000216068 for NEC.
235. Schwake, A., Erhardt, W., and Goemann, H. (2007) DE102005033476 for EPCOS.
236. Caumont, O., Depond, J.M., Jourden, A., and Azaïs, P. (2009) WO2009112718 for Batscap.
237. Petersen, R.O'D., Kullberg, R.C., Toia, L., Rondena, S., and Mio, B.J. (2008) WO2008033560 for SAES Getters.
238. Beatty, T.R. (1984) CA1209201 for Union Carbide Corp.
239. Fujino, T. (2007) US7224274 for Honda Motor.
240. Fujino, T. (2007) US7457101 for Honda Motor.
241. Kawasato, T., Ikeda, K., Yoshida, N., and Hiratsuka, K. (2006) US7173807 for Asahi Glass Co.
242. Conway, B.E. (1999) *Electrochemical Supercapacitors: Scientific Fundamentals and Technological Applications*, Kluwer Academic Publishers/Plenum Publishers, New York.
243. Brandon, E.J., West, W.C., Smart, M.C., Whitcanack, L.D., and Plett, G.A. (2007) *J. Power. Sources*, **170**, 225–232.
244. Gualous, H., Bouquain, D., Berthon, A., and Kauffmann, J.M. (2003) *J. Power. Sources*, **123**, 86–93.
245. Kötz, R., Hahn, M., and Gallay, R. (2006) *J. Power. Sources*, **154**, 550–555.
246. Brandon, E.J., West, W.C., and Smart, M.C. (2008) US20080304207 for California Institut of Technology.
247. *CRC Handbook of Chemistry and Physics* (2006) 87th Edition, David R. Lide (Editor).
248. Jänes, A. and Lust, E. (2006) *J. Electroanal. Chem.*, **588**, 285–295.
249. Leblanc, F., Blais, R., and Letarte, A. (2000) *Bull. Info. Toxicol.*, **16**, 5–6.

250. Arulepp, M., Permann, L., Leis, J., Perkson, A., Rumma, K., Jänes, A., and Lust, E. (2004) *J. Power. Sources*, **133**, 320–328.
251. Jow, T.R., Xu, K., and Ding, S.P. (1999) Work Performed Under Contract N° DE-AI07-96ID13451 by U.S. Army Research Laboratory for US Department of Energy, September 1999.
252. Ding, M.S., Xu, K., Zheng, J.P., and Jow, T.R. (2004) *J. Power. Sources*, **138**, 340–350.
253. Schwake, A. (2004) US20040218347 for EPCOS.
254. Suna, G.-H., Li, K.-X., and Sun, C.-G. (2006) *J. Power. Sources*, **162**, 1444–1450.
255. Nanbu, N., Ebina, T., Uno, H., Ishizawa, S., and Sasaki, Y. (2006) *Electrochim. Acta*, **52**, 1763–1770.
256. Morita, M., Murayama, I., Fukutake, T., Yoshimoto, N., Egashira, M., and Ishikawa, M. (2006) 210th ECS Meeting (Electrochemical Society Meeting), Abstract #136.
257. Mastragostino, M. and Soavi, F. (2007) *J. Power. Sources*, **174**, 89–93.
258. Suarez, P.A.Z., Selbach, V.M., Dullius, J.E.L., Einloft, S., Piatnicki, C.M.S., Azambuja, D.S., De Souza, R.F., and Depont, J. (1997) *Electrochim. Acta*, **42**, 2533–2535.
259. Balducci, A., Bardi, U., Caporali, S., Mastragostino, M., and Soavi, F. (2004) *Electrochem. Comm.*, **6**, 566–570.
260. Frackowiak, E., Lota, G., and Pernak, J. (2005) *Appl. Phys. Lett.*, **86**, 164104-1–164104-3.
261. François, Y. (2006) Utilisation de l'électrophorèse capillaire (EC) pour la caractérisation des liquides ioniques. (LI) et intérêt des LI comme nouveaux milieux de séparation en EC. PhD thesis, Université of Paris VI.
262. Zhou, Z.B., Takeda, M., and Ue, M. (2004) *J. Fluor. Chem.*, **125**, 471–476.
263. Muldoon, M.J., Gordon, C.M., and Dunkin, I.R. (2002) *J. Chem. Soc., Perkin Trans.*, **2**, 4339–4342.
264. Ania, C.O., Pernak, J., Raymundo-Pinero, E., and Béguin, F. (2006) *Carbon*, **44**, 3113–3148.
265. Balducci, A., Dugas, R., Taberna, P.-L., Simon, P., Plée, D., Mastragostino, M., and Passerini, S. (2007) *J. Power. Sources*, **165**, 922–927.
266. Kim, Y.-J., Matsuzawa, Y., Ozaki, S., Park, K.C., Kim, C., Endo, M., Yoshida, H., Masuda, G., Sato, T., and Dresselhaus, M.S. (2005) *J. Electrochem. Soc.*, **152**, A710–A715.
267. Frackowiak, E. (2006) *J. Braz. Chem. Soc.*, **17**, 1074–1082.
268. Herzig, T. (2007) Die Synthese und Charakterisierung neuer Elektrolyte für Tieftemperaturanwendungen in elektrochemischen Doppelschichtkondensatoren. PhD thesis, University of Regensburg.
269. Bruglachner, H. (2004) Neue elektrolyte für doppelschichtkondensatoren. PhD thesis, University of Regensburg.
270. www.nissinbo.co.jp/r_d/capacitor/index.html. (2012).
271. www.njrc.co.jp/. (2012).
272. Sato, T., Masuda, G., and Takagi, K. (2004) *Electrochim. Acta*, **49**, 3603–3611.
273. Yang, C.-C., Hsu, S.-T., and Chien, W.-C. (2005) *J. Power. Sources*, **152**, 303–310.
274. Despotuli, A. and Andreeva, A. (2007) *Mod. Electron.*, **7**, 24–29 (in Russian and in English).
275. Richner, R.P. (2001) Entwicklung neuartig gebundener Kohlenstoffmaterialien für elektrische Doppelschichtkondensatorelektroden. PhD thesis, Swiss Federal Institute of Technology Zürich, p. 176.
276. Kobayashi, S. and Shinohara, H. (1993) JP3160725 for Japan Radio Co.
277. Tanaka, Y., Ishii, N., Okuma, J., and Hara, R. (1999) JP10125560 for Honda Motor.
278. Suhara, M., Hiratsuka, K., and Kawasato, T. (2000) JP2000040641 for Asahi Glass Co.
279. Wei, C., Jerabek, E.C., and Leblanc O.H. Jr., (2001) WO0019464 for General Electric.
280. Tanaka, Y., Ishii, N., Okuma, J., and Hara, R. (2001) US6190501 for Honda Motor.
281. Tsukuda, T., Midorikawa, M., and Sato, T. (2007) WO2007061108, for Mitsubishi Paper Mills.
282. Inagawa, M. and Inoue, Y. (2000) JP11135369 for NEC.

283. Mizobuchi, T., Yanase, M., and Shinsenji, T. (2000) JP2000331663 for NKK.
284. Tsushima, M, Morimoto, T., Hiratsuka, K., Kawasato, T., and Suhara, M. (2000) US6072693 for Asahi Glass Co.
285. Kobayashi, T., and Kimura, N. (2003) JP2003229328 for Japan Vilene.
286. Ito, T., Tsuchiya, K., and Yabe, K. (1989) JP2569670 for Toray Industries.
287. Fisher, H.M. and Wensley, C.G. (1999) US6368742 for Celgard.
288. Cheon, S.D., Hwang, K.Y., Oh, H.J., and Park, S.E. (2000) KR20000051312 for SK Corp.
289. Imoto, H., Matsunami, T., and Matsunami, T. (2005) JP4425595 for Nippon Sheet Glass Co.
290. Kobayashi, T., Kawabe, M., Kimura, F., and Amagasa, M. (2007) US7616428 for Japan Vilene.
291. Kobayashi, T. and Kimura, N. (2006) JP2006144158 for Japan Vilene.
292. Oya, N., Asano, Y., and Yao, S. (2003) JP2003229329 for Ube Industries.
293. Tsukuda, T., and Midorikawa, M. (2003) JP2003309042 for Mitsubishi Paper Mills.
294. Tsukuda, T. (2007) JP2007150122 for Mitsubishi Paper Mills.
295. Wade, T.L. (2006) High Power Carbon – Based Supercapacitors, Chapters 3, 4, 5 and 6, University of Melbourne, March 2006, pp. 47–142.
296. EN and EP Series (2012) <http://industrial.panasonic.com/www-data/pdf/ABC0000/ABC0000TE3.pdf>, p. 11.
297. HW and HZ Series <http://industrial.panasonic.com/www-data/pdf/ABC0000/ABC0000TE3.pdf>, p. 13.
298. Thrap, G., Shelton, S., Schneuwly, A., Lauper, P., and Soliz, R. (2008) US2008013253 for Maxwell Technologies.
299. Caumont, O., Depond, J.-M., and Juventin, A.-C. EP2198472 for Batscap.
300. Goesmann, H. and Setz, M., DE102004039231 for EPCOS, 2006.
301. Caumont Olivier, O., Juventis-Mathes, A.-C., Le Bras, K., and Depond, J.-M. (2008) EP2145360 for Batscap.
302. Thrap, G., Borkenhagen, J.L., Wardas, M., and Maheronnaghsh, B. (2007) US2007054559 for Maxwell Technologies.
303. Caumont, O., Paillard, P., and Saindrenan, G. (2007) WO2007147978 for Batscap and Ecole Polytechnique de l'Université de Nantes.
304. Goesmann, H. (2005) DE102004030801 for EPCOS.
305. Ashino, K. JP3034505 for Nippon Chemicon, 1991.
306. Setz, M., Nowak, S., and Hoerger, A. (2006) WO2006005277 for EPCOS.
307. Goesmann, H., Vetter, J., Mayr, M., and Pint, S. (2009) US20090111009 for BMW.
308. Caumont, O., Juventin-Mathes, A.-C., Le Bras, K., and Depond, J.-M. (2008) WO2008141845 for Batscap.
309. Schiffer, J., Linzen, D., and Sauer, D.U. (2006) *J. Power. Sources*, **160**, 765–772.
310. Lee, D.H., Kim, U.S., Shin, C.B., Lee, B.H., Kim, B.W., and Kim, Y.-H. (2008) *J. Power. Sources*, **175**, 664–668.
311. Desprez, P., Barraillh, G., Rochard, D., Rael, S., Sharif, F., and Davat, B. (2002) EP1274105 for SAFT.
312. Okamura, M., Yamagishi, M., and Mogami, A. (2000) EP1033730 for Advanced Capacitor Technologies, Okamura Laboratory and Powersystems.
313. Horikoshi, R. and Asai, T. (2009) USD586749 for Meidensha Corp.
314. EDLC Brochure of Meidensha available on internet: EDLC Catalog-Enov1808.pdf, 2009.
315. Weighall, M.J. (2009) *The Future of Ultracapacitors – Strategic Markets and Forecasts to 2014*, Pira International Ed.

11

Supercapacitor Module Sizing and Heat Management under Electric, Thermal, and Aging Constraints

Hamid Gualous and Roland Gallay

11.1

Introduction

The module sizing methodology presented is valid for all electrochemical energy storage systems. The sizing parameters will be, of course, different from one energy storage type to the other, as they will be different from one manufacturer to the other.

Electrochemical energy storage may be classified into different categories: batteries, hybrids, and supercapacitors. All of them exhibit redox and double-layer capacitance. Batteries are composed of two redox electrodes with a very small double-layer contribution. Supercapacitors have only “parasitic” redox reactions. Hybrids are built with one supercapacitor electrode and one battery electrode that can either be set up at the cathode or at the anode. In each different category there are different technologies. In the case of supercapacitors, one may identify, for example, aqueous, acetonitrile (AN), and propylene carbonate (PC) electrolyte.

The first step in the sizing of an energy storage system is to choose the technology. For high-power, high-cycling, or/and maintenance-free applications, supercapacitors are the favorite. For high-energy applications, batteries are preferred. Hybrids have performances that are in between, accumulating both advantages and disadvantages.

The supercapacitor capacitance increases slightly with the temperature and in a more important proportion with the applied voltage. It decreases in the course of time when a solicitation, which may be either a continuous voltage or charge/discharge cycles, is applied. The series resistance decreases with the temperature and increases with the aging time. The capacitance and the series resistance will also decrease as a function of the charge/discharge current, in other words, as a function of the frequency or cycling speed.

The sizing of supercapacitor modules must be calculated for the worst specified conditions, which are, in principle, found at the end of life, at low temperature, and at low voltage. The minimum voltage is imposed by the technology in the case of batteries and hybrids. Operating these components below the specified voltage value will destroy them. In the case of supercapacitors, the polarization could even be reversed (nevertheless it is better to avoid this reversal for optimum

performances), but for practical reasons in power electronics, the component is operated between the nominal voltage and half of this value. The definition of the end of life of a supercapacitor differs from one manufacturer to the other. The limit is generally set to 80% of the nominal capacitance, the initial value being generally 10% above the nominal one. The loss of capacitance is a problem because both the available power and the energy content are proportional to the capacitance.

One of the main problems occurring during the sizing of an energy storage system is the heating of the module, which is induced by the power losses generated in the internal (series) resistance by the current. The heating is proportional to the square of the effective current and inversely proportional to the module volume. In power applications, the modules are generally sized to respect a maximum heating of 10–20 °C. On the market, different types of supercapacitors designed specifically for high-power applications are available. They are built with thinner electrodes, use low-viscous electrolytes, and are small or broad. Generally, the integration of a cooling system is necessary to manage big currents. In most of the cases, this is achieved by an air circulation obtained with fans. As thermal conductivity is of the same physical nature as electronic conductivity, it is important to cool the conductors.

At that point it is important to understand the type of power used. On one hand, there is the power received or delivered by the load, depending on whether it is acting as a generator or a motor. On the other hand, there is the total power at which the storage component is charging or discharging. For a given application, the important values are the available energy and power in the load. The remaining power, the difference between the total power and the load power, will dissipate the remaining energy, the difference between the total stored energy and the available energy, in the internal resistor of the storage component.

The critical parameter for the sizing of a storage device is the power density. The Ragone plot is a diagram that shows the amount of available energy for the load as a function of the power in the load. Finally, it is a *plot of the efficiency*, defined as the ratio between the available energy in the load and the total energy stored in the component. At low power the efficiency is optimum. At high power, there is a limit when the load resistance is as small as the internal resistance, where half of the energy is dissipated in the component itself. When the load resistance is smaller than the internal resistance, as is the case for a short, the current is limited by the internal resistance and all the power and the energy are spent in the latter, heating the component.

11.2

Electrical Characterization

11.2.1

C and ESR Measurement

11.2.1.1 Capacitance and Series Resistance Characterization in the Time Domain

There are different methods available for determining the capacitance and the series resistance in the time domain. The supercapacitor charging and discharging may be performed either with the condition of:

- 1) a constant current
- 2) a constant power or
- 3) a constant load.

The values obtained depend strongly on the measurement conditions. The temperature increases the capacitance and reduces the series resistance. The capacitance and the series resistance drop very fast with the charge/discharge speed, in other words, with the frequency. Higher values of capacitance are found at higher voltage. The capacitance drops and the series resistance increases with the solicitation time, especially at the beginning of the supercapacitor operation. The supercapacitor recovers a part of its capacitance when it is left at rest. The interpretation of the measurement results is also problematic. For example, self-discharge is often considered as the consequence of poor electrode insulation, but could be effectively due to electrode areas that have not been fully charged during the experimental measurement. It is therefore capital to define the polarization time and the measurement sequence.

11.2.1.2 Capacitance and Series Resistance Characterization in the Frequency Domain

Impedance spectroscopy has been extensively used to characterize carbon, electrode, and capacitor properties [1–3]. From the frequency impedance spectrum shape it is possible to understand the physical origins of the observed characteristics, especially the different factors contributing to the series resistance.

The capacitance behavior is strongly dependent on the contributing surface position in the electrode [4]. If the considered surface lies deep into carbon micropores, the access time for the ions to this area will be longer and more “resistive” than for external carbon surfaces. In other words, the deep internal areas are relatively inaccessible for short electric impulses or high-frequency currents. These deep surfaces contribute to the capacitance with a high RC time constant. As a result, the capacitance amplitude drops with increasing signal frequency.

The double-layer capacitor series resistance drops also with increasing frequency. At high frequency, the deep carbon surfaces are no more accessible because the ions moving in the electrolyte do not have the time to reach them. As a consequence, the ions will neither contribute to the current transport nor to the ohmic losses. The “de Levie” transmission-line model [5] is an equivalent electrical model for the double-layer capacitor, which gives a simple explanation for the observed frequency behavior. The parallel string at the end of the transmission line, corresponding to the deep carbon micropore surfaces, has a high resistance that limits the current intensity through these paths. Finally, as a rule of thumb, by comparing the datasheet values published by the double-layer capacitor manufacturers, it is possible to state that the DC series resistance is approximately equal to twice the high-frequency series resistance.

11.2.2

Supercapacitor Properties, Performances, and Characterization

From an electrical point of view, the double-layer capacitor is a complex system built with materials developed for both the battery domain (carbon, separator, current collector, can, lid, etc.) and the electrolytic capacitor domain (current collector, can, lid, electrolyte, etc.). It, nevertheless, has capacitor-like properties. Besides its mechanical function, the aluminum collector contributes only to the electronic conduction improvement of the system. The separator provides two functions: the electrolyte ionic conduction and the electronic insulation between the two electrodes. In the carbon electrodes, both the electronic conduction inside the carbon particle and the ionic conduction in the electrolyte around the carbon particles contribute to the electrical charge transport [6].

The characterization of double-layer capacitors is sensitive to the measurement method used. The standards organization, IEC (International Electrochemical Commission) has issued the IEC62391 series of directives [7–9] to settle a base for supercapacitor testing conditions. Supercapacitor conditioning before the measurement is an important parameter that may lead to great divergences in results. Double-layer capacitors need hours to reach an equilibrium state because some areas are very distant or are difficult to access for the ions. For example, after a long polarization time, the measured capacitance and equivalent series resistance (ESR) values will be different from those found in the absence of a previous polarization. Moreover, this measurement effect will be mixed with the capacitance fading caused by aging. Consequently, it is important to always precisely define the experimental conditions of the measurements.

11.2.2.1 Capacitance and ESR as a Function of the Voltage

In some double-layer capacitors, especially in the case of organic electrolyte and “natural” carbon, the capacitance increases with the applied voltage. In the literature, the causes of this behavior are explained with different theories:

- Reduction of the solvent layer thickness caused by the increasing coulombic forces on the ions when the electric field in the double layer is increasing.
- Increase of the solvent dielectric constant caused by the compression of the solvent layer, if the concept of dielectric constant has still a meaning with such thin layers. The “microscopic” Maxwell equations’ formalism would be more appropriate. (“Macroscopic” Maxwell equations are applied to *macroscopic averages* of the fields, which vary wildly on a microscopic scale close to individual atoms. It is only in this averaged sense that one can define quantities such as the permittivity and permeability of a material, as well as the polarization and induction field).
- Increase in the electronic state density in the carbon pore walls with the voltage. Hahn *et al.* [10] measured double-layer capacitance and electronic conductance of an activated carbon electrode in an aprotic electrolyte solution, 1 mol dm^{-3} $(\text{C}_2\text{H}_5)_4\text{NBF}_4$ in AN. Both quantities show a similar dependency on the electrode potential with distinct minima near the potential of zero charge (PZC).

This correlation suggests that capacitance, similar to conductance, is governed substantially by the electronic properties of the solid, rather than by the ionic properties of the solution in the interface of the double layer.

- Salitra *et al.* [11] attributed this finding to the potential dependency of the ion penetration in nanopores, which was assumed to be minimal at the PZC.

Figures 11.1 and 11.2 show the frequency spectra of a 2600 F, 0.5 m Ω BCAP0010 supercapacitor capacitance and series resistance for three different polarization

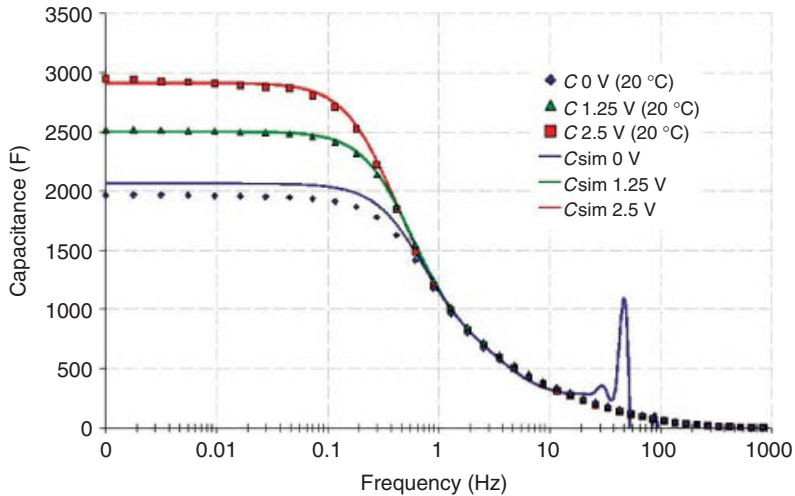


Figure 11.1 BCAP2600 capacitance for three different polarizations at room temperature.

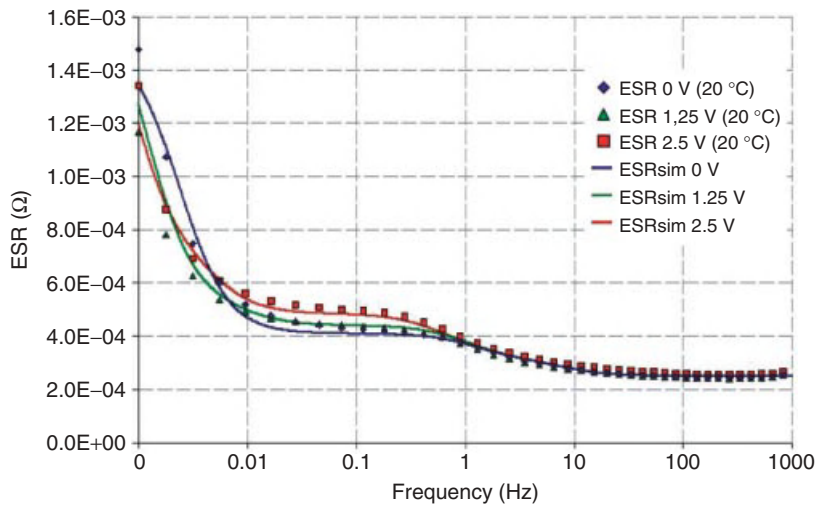


Figure 11.2 BCAP2600 ESR for three different polarizations at room temperature.

voltages. It is interesting to observe the lower capacitance value when there is no voltage polarization. This phenomenon should be studied as a function of the electrode thickness. If ionic depletion was the cause, a thick electrode should display a more pronounced effect.

The important ESR increase at low frequency is due to the charge redistribution within each electrode, which looks similar to the reduction of parallel resistance. In the case of self-discharge, the effect should be two times more important at 2.5 V than at 1.25 V, and should not be present with a bias of 0 V.

11.2.2.2 Capacitance and ESR as a Function of the Temperature

In the high-frequency range ($f > 10$ Hz), the series resistance variation with temperature can be neglected. In the low-frequency range, the ESR increases when the temperature decreases [12, 13]. This is caused by the electrolyte ionic resistance R_T , which is strongly influenced by the temperature. Above 0°C , R_T varies slowly with the temperature. Below 0°C , the temperature dependency is more important, especially for the series resistance. It is caused by the rapid increase in electrolyte viscosity in the low-temperature range [14].

In the case of $1 \text{ mol dm}^{-3} (\text{C}_2\text{H}_5)_4\text{NBF}_4$ in AN, a relationship between R_T and the temperature has been established from experimental results. It is given by the expression (11.1):

$$R_T = R_{20} \frac{\{1 + \exp[-k_T(T - T_{20})]\}}{2} \quad (11.1)$$

where R_{20} is the resistance at 20°C , T the surrounding temperature and k_T the temperature coefficient $k_T = 0.025^\circ\text{C}^{-1}$. At ultralow frequencies ($f < 0.1$ Hz), the capacitance is almost constant according to the temperature. It means that the ions penetrate deep into the electrode pores regardless of the temperature because they always have the time to reach the total surface. The capacitance is influenced by temperature mainly in the intermediate frequency range between 0.1 and 10 Hz. This corresponds to the actual domain of the supercapacitor working conditions. In that precise case, the ions do not have the time to reach and spread over the entire electrode surface.

Increasing the temperature will have the main effect of reducing the electrolyte viscosity and improving the accessibility of the surface for the ions. Thanks to their higher mobility in the warm solvent, the ions are able to reach the deeper carbon area in a shorter time. The increased accessible surface area results in a reduced double-layer capacitor series resistance and in an increased capacitance with the temperature. Figures 11.3 and 11.4 show the measured and simulated frequency spectra of the BCAP0010 double-layer capacitor capacitance and series resistance for different temperatures.

11.2.2.3 Self-Discharge and Leakage Current

Self-discharge is an important parameter for applications in which the supercapacitors are not connected to an electric network and therefore need to maintain their state of charge. In those applications, the device is supposed to be able to deliver power with a performance that does not deteriorate as a result of the rest time.

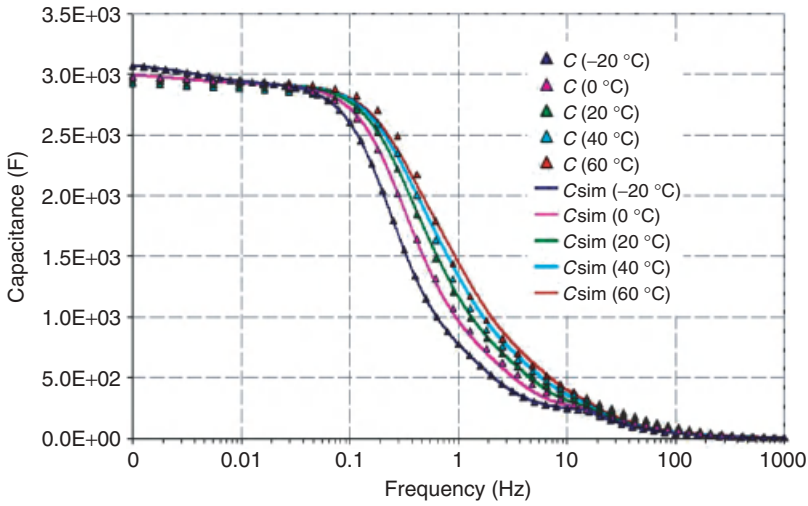


Figure 11.3 BCAP2600 capacitance for different temperatures measured with a polarization of 2.5 Vdc.

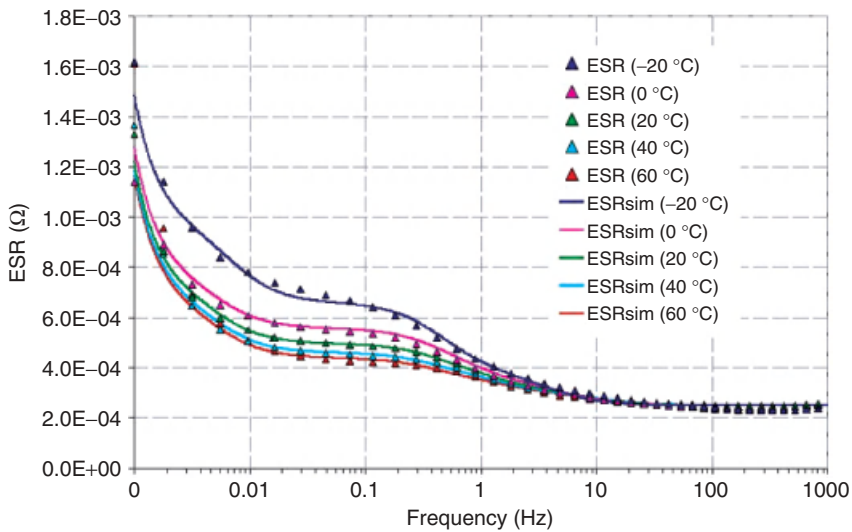


Figure 11.4 BCAP2600 ESR for different temperatures measured with a polarization of 2.5 Vdc.

A typical example is the starting of a car engine after a week spent at rest in an airport parking lot. In this case, it is necessary that the storage device maintains its voltage as high as possible because the available power and the stored energy decline with the square of this voltage.

The voltage drop of a charged capacitor in floating mode as a function of time may be caused by different discharging mechanisms, among which are leakage current and charge redistribution.

The charge redistribution corresponds to the displacement of charges from an easily accessible area of the electrode with a short access time, to a more difficult one, with a longer access time. The charge redistribution, in contrast to the self-discharge, may lead to a voltage increase measured at the capacitor terminal. After a fast capacitor discharge, the voltage may increase because of the arrival of charges previously stored in “slow” areas. The leakage current may be due to unwanted oxidation-reduction reactions, ionic charge diffusion or/and electronic partial discharge through the separator. The self-discharge rate is determined, either by measuring the current necessary to keep a constant voltage (in the microamperes range), or by recording the floating capacitor voltage as a function of time.

The self-discharge diagnostic can be performed according to the voltage time dependency. If the voltage drops with an unwanted logarithmic law, $U(t)$ versus $\log t$ (Figure 11.5), the mechanisms are controlled by faradic self-discharge from overcharge or from the oxidation-reduction reactions of the impurities. If the voltage drops following a square root function of the time, $U(t)$ versus $t^{1/2}$ (Figure 11.6), the mechanisms are controlled by diffusion processes.

These self-discharge behaviors have been demonstrated with different capacitor samples. BCAP0007 and BCAP0008 are Maxwell commercial products. They show only a diffusion-driven self-discharge mechanism. BCAPproto, which is a prototype with high impurity content, undergoes oxidation-reduction reactions.

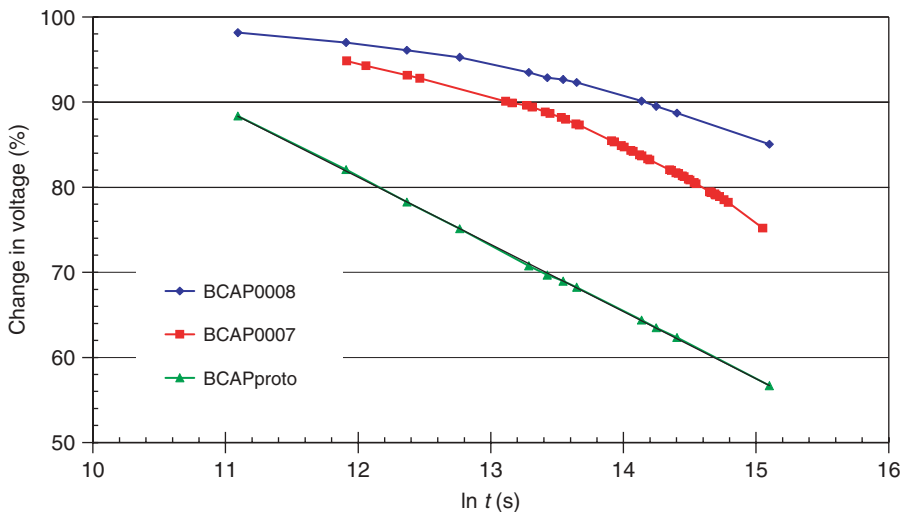


Figure 11.5 Supercapacitor self-discharges with different level of impurity concentrations in a logarithmic time scale.

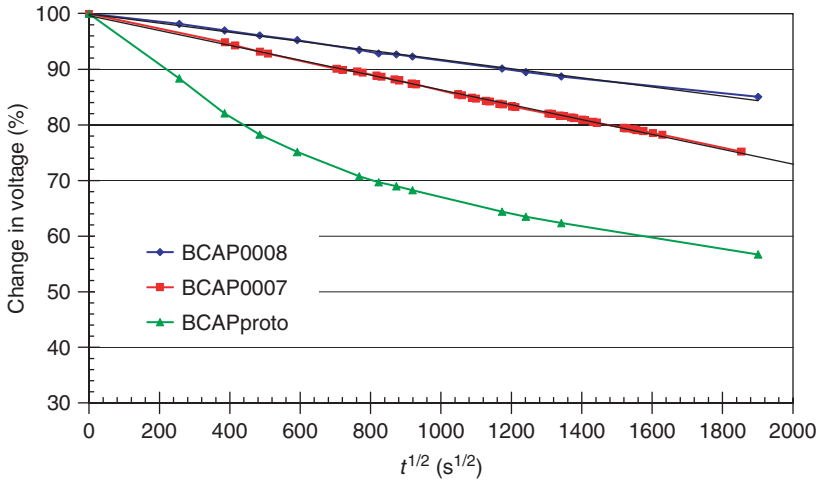


Figure 11.6 Supercapacitor self-discharges with different level of impurity concentrations in a square root time scale.

The two different plots show the respective linear drop in their respective time representation.

The double-layer capacitor's self-discharge performance is the result of a compromise with its power capability. The manufacturers could use a thicker separator to improve the voltage retention but this operation would increase in the same time as the series ionic resistance.

11.2.3

"Ragone Plot" Theory

The Ragone plot concept is based on the fact that the electrical current charging or discharging an electrical storage system has to flow through both its proper internal resistance and the load or generator resistance. The two resistances are connected in series as illustrated in Figure 11.7.

The resistance R_s is an equivalent resistance that is the result of a complex combination of series and parallel contributions owing to the geometric structure of the capacitor. The electrodes are very wide and the elementary areas do not all

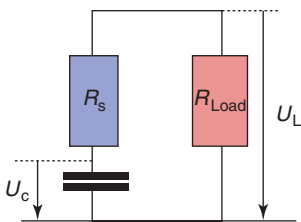


Figure 11.7 Supercapacitor electrical equivalent circuit.

contribute to the resistance in the same way. The length of the current paths is not the same for all parallel areas. Therefore, a parallel construction must be taken into account. For each of these surface areas, the electrical current flows first through the ohmic resistances of the electrode, the collector, and the connections and next through the ionic resistance of the electrolyte between the two capacitances. All these contributions are connected in series.

U_c is a theoretical value of the internal voltage on the capacitance, which is inaccessible for measurement. This value may be different as a function of the position on the surface electrode. U_L is the voltage at the physical terminals of the storage device. This simple model has the same validity for batteries, capacitors, and supercapacitors; only the amplitude of the internal resistance differs from one component type to the other. Batteries have a resistance that is about 10 times bigger than that of supercapacitors, which is again 10 times bigger than that of capacitors.

The series resistance is, in most power applications, the origin of sizing limitations of the storage device. On one hand, the heat generated by the ohmic losses increases the component temperature to unacceptable values; on the other hand, the voltage drop at the component terminals becomes too important.

The following development is elaborated with the intention of determining the efficiency of capacitive storage components. The first step is a calculation of the energies involved in the system. These values will then be expressed as a function of the maximum stored energy and the maximum available power and will be plotted in a Ragone plot.

With the assumptions that U_c is uniform on the electrode surface, that C and R_s are independent of the current, in other words, independent of the frequency, which is true only at very low frequency ($f \ll 1/\tau_0$), the following basic relations $U_L = R_L i$ and $U_L = u_c - R_s i$ may be combined to give

$$U_c = U_L \left(1 + \frac{R_s}{R_L} \right) \quad (11.2)$$

We need to distinguish different energy terms. In the case of a discharge, W_{\max} is the maximum energy stored in the electrical storage component.

$$W_{\max} = \frac{1}{2} C U_{c \max}^2 \quad (11.3)$$

W_L is the energy available for the supply of the electrical load that has a resistance R_L

$$W_L = R_L \int i^2 dt \quad (11.4)$$

W_s is the energy that is transformed in heat by the dissipation in the series resistance of the storage component.

$$W_s = R_s \int i^2 dt \quad (11.5)$$

It may be observed that both W_L and W_s depend on the current intensity, but that their sum does not.

$$W_{\max} = W_L + W_s = (R_L + R_s) \int i^2 dt \quad (11.6)$$

$$W_L = \frac{R_L}{R_L + R_s} W_{\max} \quad (11.7)$$

With the definition of a factor α ,

$$\alpha = \frac{R_L + R_s}{R_s}, \quad \alpha > 1 \quad (11.8)$$

the former relation may be written as

$$W_L = \frac{\alpha - 1}{\alpha} W_{\max} \quad (11.9)$$

- $\alpha \rightarrow 1$: $R_L \rightarrow 0$, maximum current, power remains in the capacitor
- $\alpha = 2$: match impedance
- $\alpha \gg 2$: low current, low power

11.2.3.1 Match Impedance

In the particular case of impedance matching when $R_s = R_L$, the power available for the application P_m and the power dissipated in the internal resistance P_s are equal.

$$P_m = P_s = P_L = U_L i = U_L \frac{U_L}{R_L} = \frac{U_L^2}{R_s} \quad (11.10)$$

The voltage on the “pure” capacitance, or at the capacitor terminal when the current is very low, is double that of the voltage at the capacitor terminal at match impedance.

$$U_c = \frac{U_L}{2} \quad (11.11)$$

The power available at match impedance is therefore equal to

$$P_m = \frac{U_E^2}{4R_s} \quad (11.12)$$

P_m is equal to a quarter of the maximum short power dissipated in the component when $R_L = 0$. Capacitor manufacturers often confuse between maximum and short power, and overestimate the power capability of their components.

At match impedance, the available energy is equal to half the maximum stored energy:

$$W_m = \frac{W_{\max}}{2} \quad (11.13)$$

Finally, it is possible to find a relation between the maximum available power and the maximum stored energy.

$$P_m = \frac{U_c^2}{4R_s} = \frac{W_{\max}}{2R_E C} = \frac{W_{\max}}{2\tau_0} \quad (11.14)$$

$T_0 = R_s C$ is the technology time constant or the time necessary to discharge the capacitor by a voltage factor “ e ” in a short. This time has a direct relation with the “cutoff frequency” observed on the capacitance curves as a function of the frequency (Figure 11.3).

11.2.3.2 Power Available for the Load, Ragone Equation

In the general case, in particular for the actual operation conditions,

$$\begin{aligned} P_L &= \frac{U_L^2}{R_L} = \frac{U_c^2}{R_L} \left(\frac{R_L}{R_L + R_s} \right)^2 = U_c^2 \frac{R_L}{(R_L + R_s)^2} = \frac{U_c^2}{4R_s} \frac{4R_s R_L}{(R_L + R_s)^2} \\ &= 4P_m \frac{\alpha - 1}{\alpha^2} \end{aligned} \quad (11.15)$$

With the introduction of the efficiency β defined as the ratio between the energy available for the load and the maximum stored energy in the component

$$\beta = \frac{W_L}{W_{\max}} = \frac{\alpha - 1}{\alpha^2} \quad (11.16)$$

The power available in the load is now given as a function of the maximum power available at match impedance P_m by

$$\frac{P_L}{P_m} = 4\beta(1 - \beta) \quad (11.17)$$

At match impedance, the efficiency β is equal to 0.5.

The resolution of this second-degree equation brings two solutions. The first “positive” one corresponds to the case where the load resistance is bigger than the internal resistance (Figure 11.8). This is the power regime in which the component is operated. W_L may be plotted as a function of the power available in the load P_L with the following relation:

$$W_L = \frac{W_{\max}}{2} \left(1 \pm \sqrt{1 - \frac{P_L}{P_m}} \right) \quad (11.18)$$

with

$$P_m = \frac{W_{\max}}{2\tau_0} \quad (11.19)$$

and

$$\tau_0 = R_s C \quad (11.20)$$

The stored energy can be transferred to the load with good efficiency only with small currents. In that condition, the Joule dissipation in the internal resistance of the component W_s is minimized.

At match impedance, exactly half of the energy is dissipated in the internal resistance.

The following charts are based on a typical carbon and organic electrolyte supercapacitor technology (300 F, 2 m Ω at 1 Hz). The typical time constant is $\tau_0 = 0.6$ s.

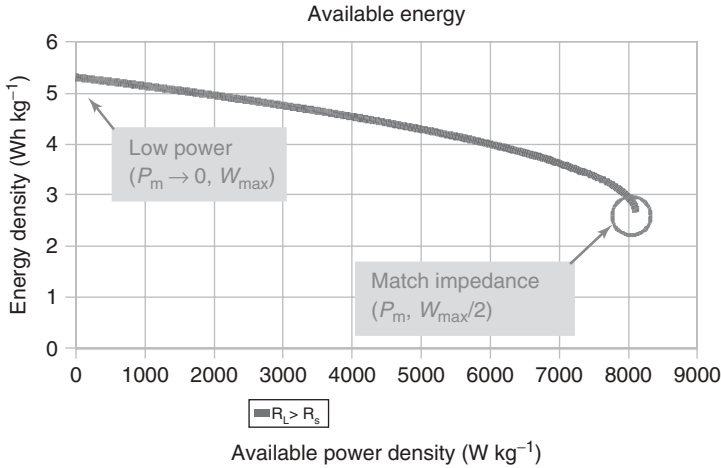


Figure 11.8 Ragone plot for $R_s < R_L$. At match impedance, the available energy is equal to half the maximum stored energy.

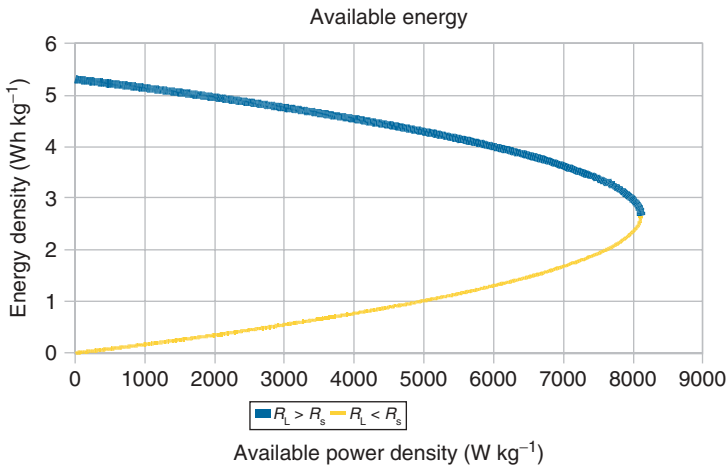


Figure 11.9 Ragone plot for $R_s < R_L$ (blue curve) and $R_s > R_L$ (yellow curve).

The second solution is available in the case of a load resistance smaller than the internal resistance (Figure 11.9). The relation giving the available energy W_L as a function of the power available in the load P_L differs from the former only by a minus sign before the square root. In this case, almost all the energy is burnt in the internal resistance of the storage component, with the consequence of fast heating. The extreme case is an electrical short of the component terminals.

Sizing a storage system requires some information: the available energy, the available power but also the power dissipated in the internal resistance of the

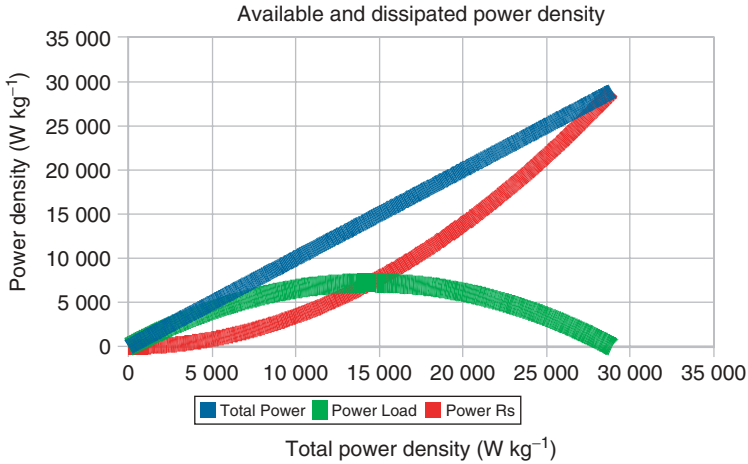


Figure 11.10 Plot of the load available power and the series resistance dissipated power as a function of the sum of the load available power and the series resistance dissipated power.

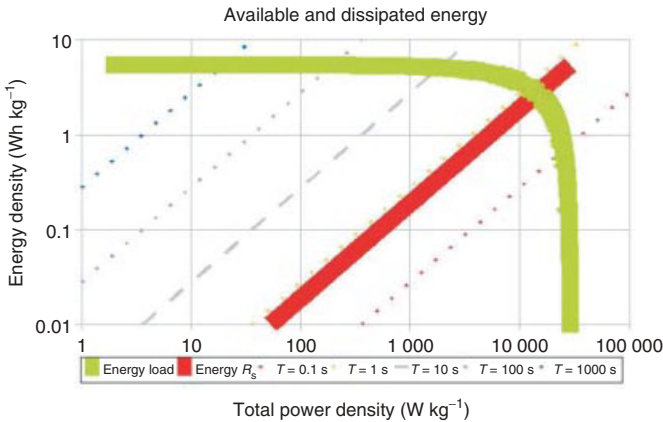


Figure 11.11 Ragone plot representing the load available energy and the series resistance dissipated energy as a function of the sum of the load available power and the series resistance dissipated power.

component. Both powers are related by the efficiency factor. The following chart represents these powers and the total power (Figure 11.10).

It is interesting to observe that the available power for the load reaches a maximum P_m at match impedance. It is therefore of no use to operate above this value (in the example, $P_{total} = 32 \text{ kW kg}^{-1}$ and $P_m = 16 \text{ kW kg}^{-1}$).

A classical chart is the log–log representation of the available energy as a function of the total power (Figures 11.11 and 11.12). This chart has the disadvantage of not informing about the actual available power.

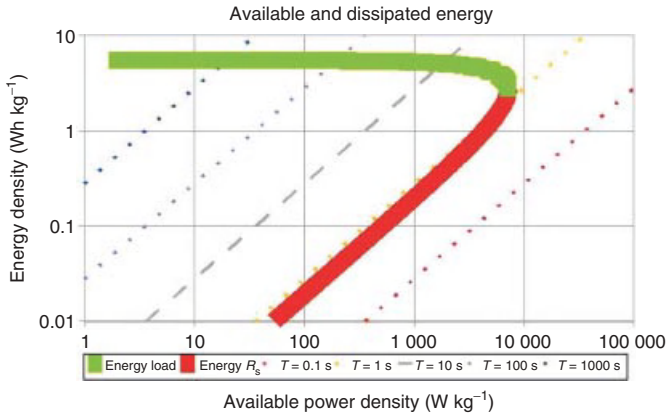


Figure 11.12 Ragone plot representing the load available energy and the series resistance dissipated energy as a function of the load available power.

The dotted lines represent the conditions where the storage system has the same time constant (energy/power). The intersection of the two energy curves corresponds to the match impedance. At that point, the time constant $\tau = 2\tau_0$ (in the example $\tau_0 = 0.6$ s). The dissipated energy curve shows that at \ll low \gg power, the efficiency is reversely proportional to the power.

In the second step, we have to consider that some part of the electrode area does not have the same accessibility as others. The current path may be longer in the electrolyte for different reasons. An important case may be that some part of one electrode is not well aligned with the counter electrode. A more general one is simply that the ion path is longer in reaching the part of the electrode area in the volume that is close to the collector surface.

This aspect may be simplified taking into account the frequency dependency of the series resistance and of the capacitance. Both are dropping with the frequency because the farther areas of the electrode are no more accessible. Only the small time constant areas are accessible, leading to an apparent smaller time constant. Consequently, it is to be expected that the Ragone plot also drops a bit faster with the power because the voltage decay is faster during a discharge at high power.

11.2.4

Energetic Performance and Discharging at Constant Current

The constant current charge/discharge (Figure 11.13) is the most widely used in laboratories because it is the easiest and the cheapest. Some derivatives of this method are used in production to control the quality of the supercapacitors. The measurement sequence starts at time t_0 by switching on a given current that is kept constant during the charge. The instantaneous voltage step observed, between U_0 and U_1 , is caused by the ohmic current flow in the capacitor series resistance. The current is switched off at time t_2 when the capacitor has reached the nominal voltage

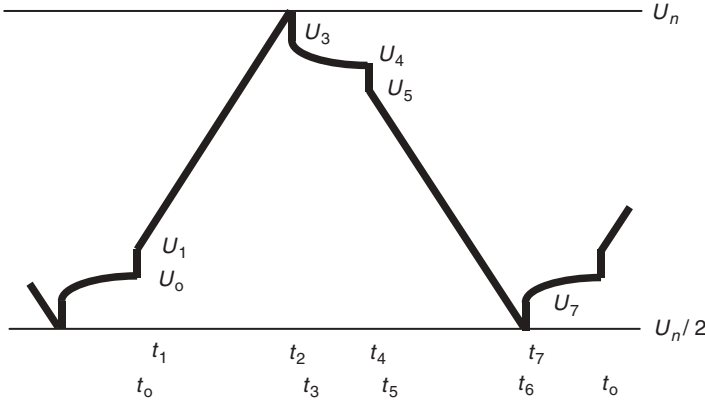


Figure 11.13 Voltage cycling sequence with a constant current.

U_n . The voltage drops instantaneously from U_n to U_3 because of the disappearance of the current. When the capacitor is left floating between time t_3 and t_4 , the voltage drops from U_3 to U_4 due to self-discharge and charge redistribution. The constant discharging current is switched on at time t_4 and switched off at time t_7 when the voltage has reached half the nominal value $U_n/2$ or even lower values to respect particular specifications. The value of the current intensity is defined in the IEC 62391 standards and depends on the type of double-layer capacitor (power, backup, etc.).

In the case of a capacitance that does not vary with the voltage, the mean capacitance C_n is determined from the time necessary to discharge the capacitor between two voltage limits with a constant current I with the relation (Eq. (11.21)).

$$C = I \frac{\Delta t}{\Delta U} \quad (11.21)$$

The IEC 62391 standard, which has been written to be adapted to high series resistance double-layer capacitor measurement, defines that the mean value should be calculated between 80 and 40% of the nominal voltage value.

In a more realistic model, the capacitance depends on the voltage. The capacitance is composed of a constant part, C_0 , and a linear-voltage-dependent one, $C_v = KU_c$, where K is a coefficient that depends on the technology. The total capacitance at the voltage U_c is given by $C = C_0 + C_v$.

That the relation between the current and the voltage must be derived from the relation between the current and the charge is always true. Substituting the expression for Q as a function of U_c and C and considering the indirect dependency of C with the time, it is easy to show that the current is given by Eq. (11.22).

$$i(t) = \frac{dQ}{dt} = \frac{d(CU_c)}{dt} = (C_0 + 2KU_c) \frac{dU_c}{dt} \quad (11.22)$$

Consequently, the time required for charging or discharging the supercapacitor with a constant current I_0 will be given by the following relation (Eq. (11.23)):

$$t_2 - t_1 = \left[\frac{C_0 U_c + K \times U_c^2}{I_0} \right]_1^2 \quad (11.23)$$

The series resistance is calculated from the voltage drop that occurs at the nominal voltage between t_2 and t_4 during the current interruption (Eq. (11.24)). The first part of the drop between t_2 and t_3 is really caused by the series resistance. The second part between t_3 and t_4 is driven by charge recombination and self-discharge. If t_4 was equal to t_3 , the drop would reflect exactly the value of the series resistance.

$$R_s = \frac{\Delta U_{23}}{I} \quad (11.24)$$

Of course, this value is difficult to obtain experimentally because of the band path width limitation of the measurement apparatus. The IEC 62391 standard defines the method to use to measure the series resistance. The self-discharge due either to the leakage current or to the charge redistribution adds a contribution to the voltage drop corresponding to R_p , the parallel resistance in the model.

In production, the method is adapted to the available time contingency. It is usual to charge the cell to a lower voltage to save time and electrical energy, and to calibrate the result with a coefficient factor resulting from a measured $U(t)$ curve for a given current.

11.2.5

Energetic Performance and Discharging at Constant Power

The charge and discharge at constant power P_L represent conditions closer to most parts of the applications. Special care must be brought to low-voltage conditions where the current is very large. In this situation, the Joule losses are proportionally bigger, which results in a much smaller efficiency.

To interpret the results, it is necessary to solve a more difficult differential equation for the voltage on the capacitor part $U_c(t)$ (the voltage at the supercapacitor terminal $U = U_L$ is equal to $U_c(t) + R_s i(t)$).

The capacitance of a supercapacitor increases with the voltage. If the capacitance is defined as $C = C_0 + KU_c$, the relation between the current and the voltage variation during a discharge is given by

$$i = -(C_0 + 2KU_c) U'_c(t) \quad (11.25)$$

The voltage as a function of time at constant power delivery $-P_L$ is given by the literal resolution of the following differential equation

$$R_s (C_0 + 2KU_c) U'_c(t)^2 + U_c U'_c(t) - \frac{P_L}{C_0 + 2KU_c} = 0 \quad (11.26)$$

The solution is obtained after a (U_c, t) variable separation and an integration and is given by

$$t_2 - t_1 = \frac{C_0}{4P_L} \left\{ \left[U_c \left(U_c + \sqrt{U_c^2 + 4R_s P_L} \right) + 4R_s P_L \ln \left(U_c + \sqrt{U_c^2 + 4R_s P_L} \right) \right] + \frac{K}{3P_L} \left[U_c^3 + (U_c^2 + 4R_s P_L)^{\frac{3}{2}} \right] \right\}_1^2 \quad (11.27)$$

For a typical supercapacitor specified 1 kg, $C = 6000$ F and $R_s = 0.1$ m Ω , the charging and discharging voltage curves at constant power $P_L = 2000$ W are shown in Figure 11.14. An acceleration of the discharge occurs when the voltage drops. The phenomenon is amplified by the capacitance drop.

On the Ragone plot, the discharge at constant power will be represented by a vertical line, starting on the Ragone curve corresponding to the initial voltage (nominal voltage is typically equal to 2.7 V) and ending on the Ragone curve for half the initial voltage.

To get a constant power during the discharge between U_n and $U_n/2$, the maximum power must be at least four times smaller than P_m . In the example shown in Figure 11.15, the maximum power could be only 1800 W kg⁻¹.

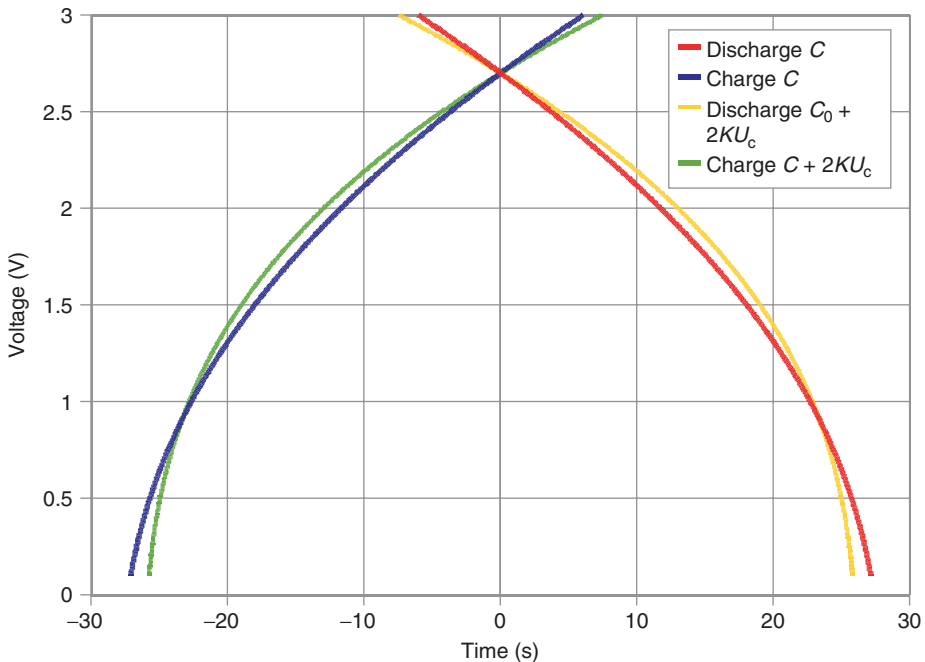


Figure 11.14 Two kilowatt constant power charge and discharge of a supercapacitor specified 1 kg, 6000 F, and 0.1 m Ω , with and without linear voltage dependency of the capacitance.

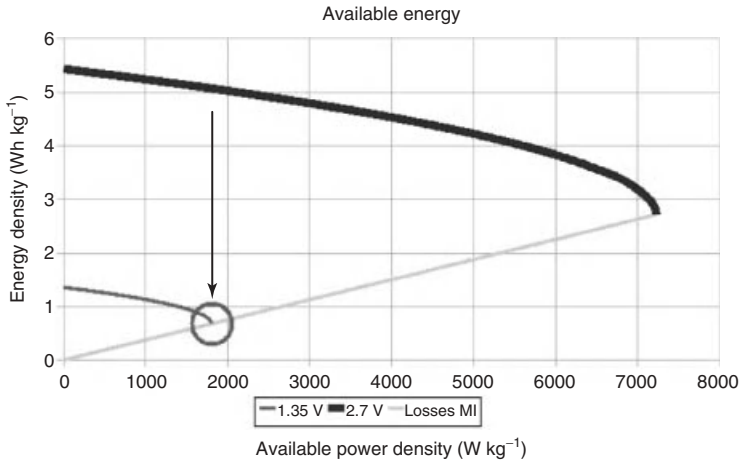


Figure 11.15 Linear drop in the maximum power P_m as a function of the voltage drop.

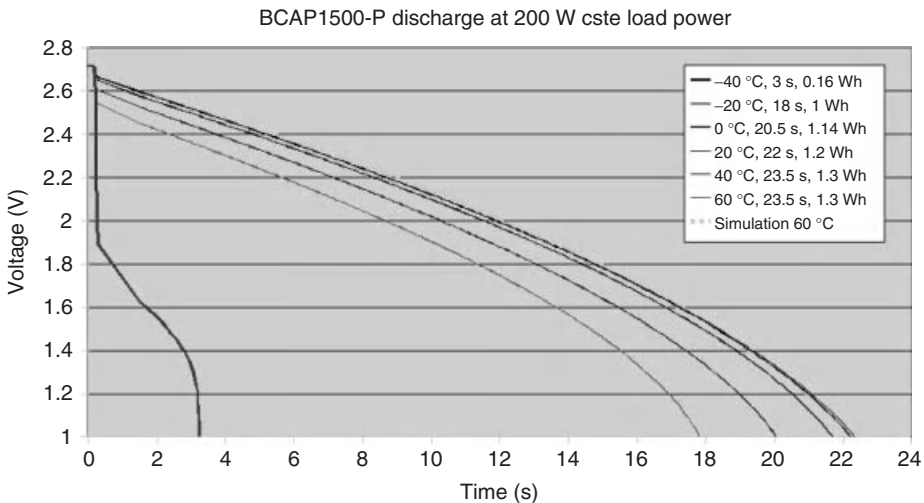


Figure 11.16 BCAP1500_P 200 W constant power discharge for different temperatures.

For a given available power, the losses increase when the voltage falls because the current increases to compensate the smaller voltage value to maintain the power. The efficiency decreases with the voltage during the discharge.

To get a constant current discharge between the two same voltage limits, it is necessary to limit the initial power to twice the final one: in this example 3600 W kg^{-1} .

A verification of the theory has been performed on BCAP1500_P and BCAP2600 supercapacitors, which have, respectively, a capacitance of 1500 and 2600 F (Figures 11.16 and 11.17). The BCAP1500_P is a power version with a thinner electrode in order to reduce the series resistance. These supercapacitors have

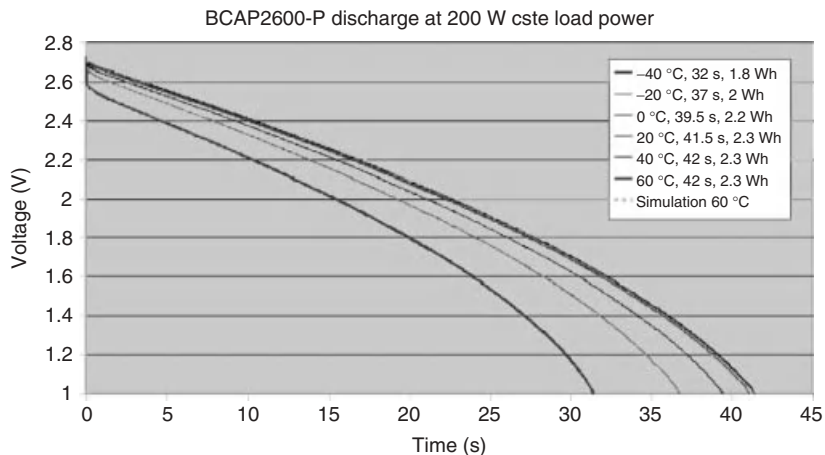


Figure 11.17 BCAP2600 200 W constant power discharge for different temperatures.

been manufactured by Maxwell Technologies. Thanks to the low solvent viscosity of the electrolyte, in this case AN, it is still possible to get some power at temperature as low as -40°C .

At the end of the discharge, the voltage drop is faster. This is due to the supercapacitor's smaller energy content at low voltage. The initial voltage step is due to the voltage drop in the series resistance when the current is turned on. The step is very important in the smaller supercapacitor at -40°C . This may be due either to internal problems as a result of the construction or the experimental setup. In any case, it is essential that the total series resistance remains as low as possible to get a good function of the supercapacitor.

The capacitance and the series resistance parameters have been determined with the relation developed theoretically (Eq. (11.27)) by fitting the experimental curves obtained when measuring the voltage evolution during a discharge at 200 W constant power (Table 11.1).

Table 11.1 BCAP1500 and BCAP2600 supercapacitor parameters used to fit the experimental 200 W discharge curves at different temperatures.

		-40°C	-20°C	0°C	$+20^{\circ}\text{C}$	$+40^{\circ}\text{C}$	$+60^{\circ}\text{C}$
2600 F	Co (F)	1010	1250	1430	1530	1530	1530
	K (F V^{-1})	280	280	275	275	275	275
	Co (F)	2144	2384	2544	2644	2644	2644
	Rs ($\text{m}\Omega$)	2	1	0.6	0.5	0.3	0.3
1500 F	Co (F)	500	650	750	820	850	850
	K (F V^{-1})	145	145	145	145	145	145
	C (F)	1087	1237	1337	1407	1437	1437
	Rs ($\text{m}\Omega$)	8	2	1.4	0.6	0.5	0.5

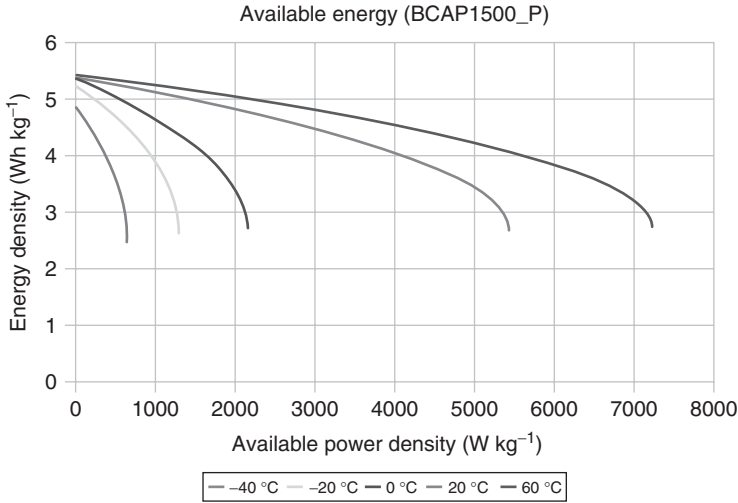


Figure 11.18 BCAP1500_P Ragone plot for different temperatures.

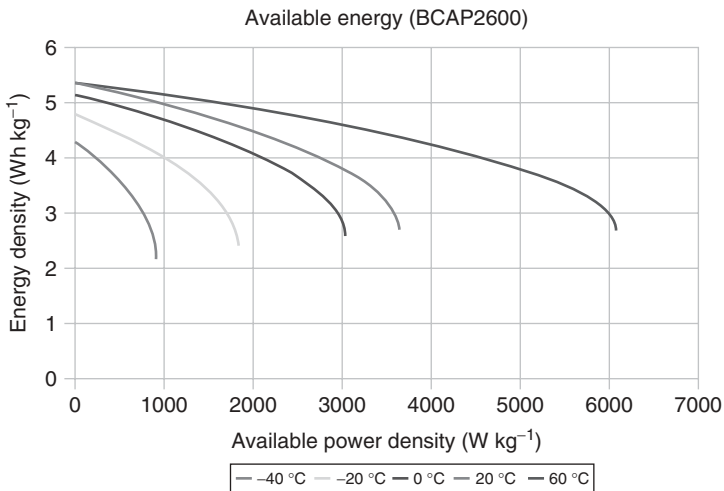


Figure 11.19 BCAP2600 Ragone plot for different temperatures.

The experimental measurements have been performed on both supercapacitors with the same 200 W constant power (Figures 11.18 and 11.19). In the 280 g BCAP1500_P, the power density of the discharge is higher than in the 500 g BCAP2600: 714 W kg^{-1} against 400 W kg^{-1} . At low temperatures, the match impedance is overcome in the small 1500 F supercapacitor. The Ragone plot curves have been obtained with Eq. (11.18), which depends only on R_s and C , parameters that are supposed to have been measured with low current, which is far from the truth, especially in the case of the 1500 F supercapacitor.

11.2.6

Energetic Performance and Discharging at Constant Load

The discharge in a constant load resistance is a method that does not require sophisticated material to perform the measurement. Recording the voltage on the terminals of the load gives direct information on the amplitude of the current and of the voltage on the capacitance.

11.2.7

Efficiency

The efficiency is calculated with the capacitance and series resistance parameters that are deduced from the discharge curve. The curves are interrupted when the voltage at the supercapacitor terminals reaches 1 V. The correlation of the time to discharge to 1 V with the experimental curves is good (Figures 11.20 and 11.21).

From the BCAP1500-P plot, it is obvious that this supercapacitor has a series resistance at -40°C , which is bigger than the load resistance. It is also straightforward that as the voltage drops during the discharge the efficiency drops too. This is of course due to the increase in the current, which compensates the voltage drop in order to maintain a constant power in the load. The consequence is that the power remains constant when the losses increase with the square of the current.

By integration of the losses over the discharge time, it is possible to obtain the resulting efficiency over a period t of the component. The total work in the load is equal to the product of the power by the time. The following plots represent the resulting efficiency at time t of the BCAP2600 for different temperatures (Figures 11.22 and 11.23).

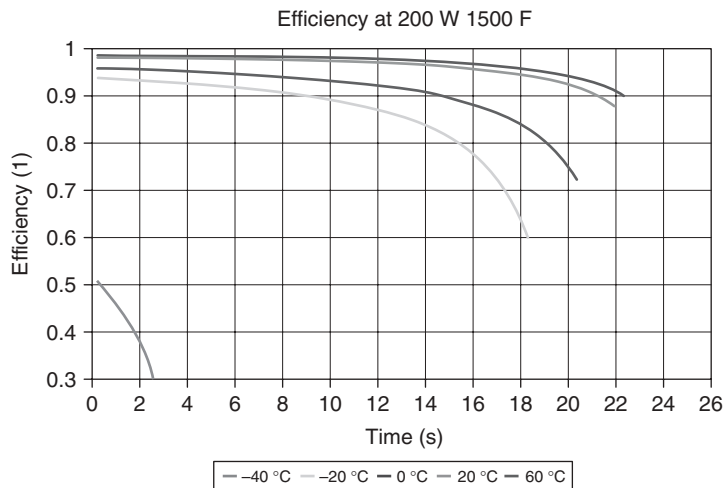


Figure 11.20 BCAP1500_P instantaneous efficiency as a function of time t for different temperatures.

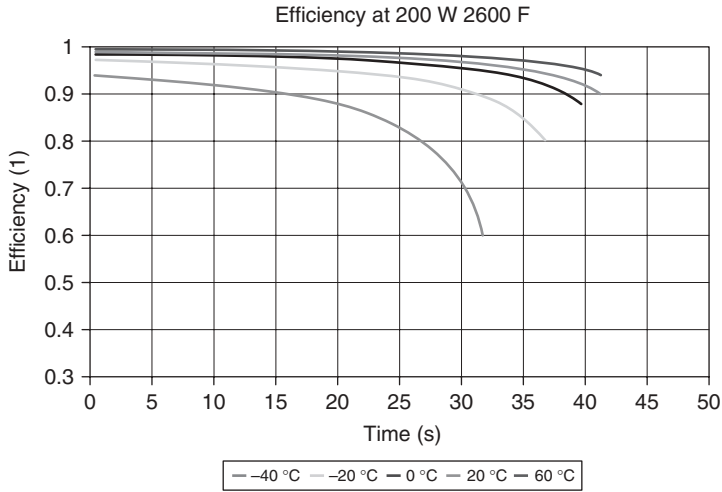


Figure 11.21 BCAP2600 instantaneous efficiency as a function of time t for different temperatures.

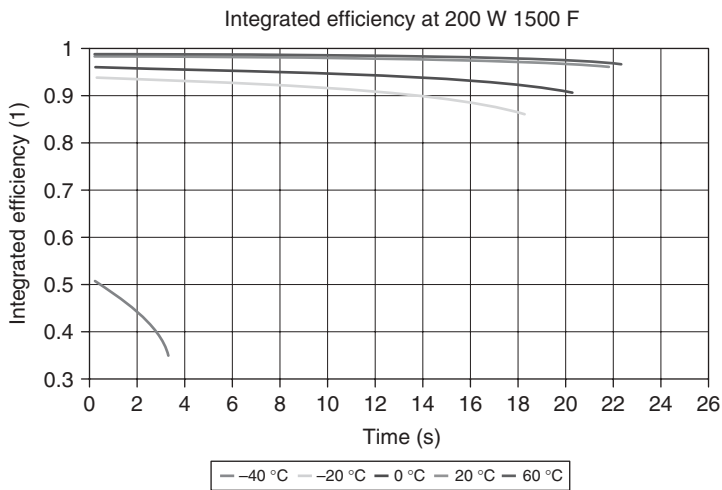


Figure 11.22 BCAP1500_P resulting efficiency over an integration period t for different temperatures.

11.3 Thermal Modeling

Heat production in supercapacitors is related exclusively to Joule losses. The supercapacitors support currents up to 400 A or more depending on cell capacitance and the technology used. The repetitive charge and discharge cycles of the supercapacitor cause a significant warming even though the ESR value is less than 0.4 m Ω

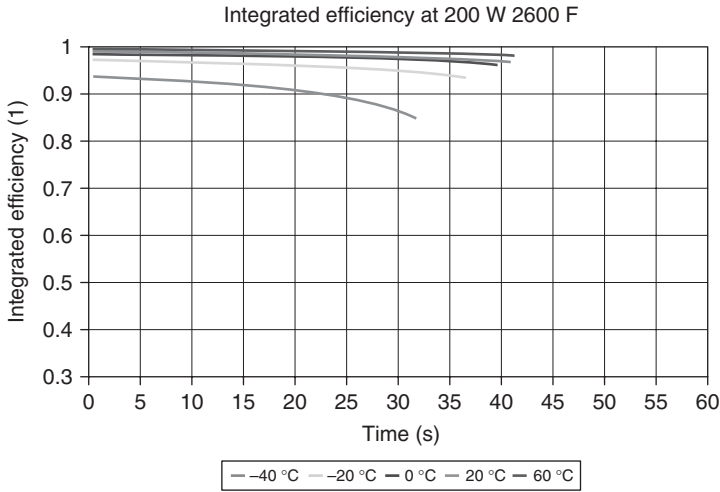


Figure 11.23 BCAP2600 resulting efficiency over an integration period t for different temperatures.

for a 2600 F. Several authors showed that the supercapacitor ESR varies according to the temperature [4]. In Ref. [16] the authors have studied the effect of the temperature and the voltage on the supercapacitor's aging. They have established a model that allows analyzing self-accelerating degradation effects caused by elevated voltages and temperatures. In Ref. [17], the authors have studied and modeled the temperature effect on the supercapacitor self-discharge.

This rise in temperature can have the following consequences:

- The deterioration of the supercapacitor characteristics, especially ESR, self-discharge, and lifetime, which affects its reliability and its electrical performance.
- The pressure inside the supercapacitor is increased.
- A premature aging of metal contacts; in fact, the repetitive heating and significant temperatures can deteriorate rapidly the terminal connections of the supercapacitor.
- The evaporation of the electrolyte and hence the destruction of the supercapacitor if the temperature exceeds 81.6°C , the boiling point of the electrolyte.

Therefore, it is important to know and to understand the heat behavior of supercapacitor cells and modules. This leads to an estimation of the space–time evolution of the temperature.

This paragraph deals with the thermal modeling of supercapacitors and heat management in supercapacitor modules. The originality of this work is based on the integration of thermocouples located inside the supercapacitor during its manufacturing. Cooling systems were also studied for supercapacitor modules subjected to a driving cycle.

11.3.1

Thermal Modeling of Supercapacitors

From a physical point of view, the transfer of heat finds its origin in the variations in temperature. Thus, a transfer of energy in the form of heat is obtained each time a variation in temperature exists within a system or when two systems, at different temperatures, are put in contact. In solids, the thermal energy may be transported by two mechanisms: lattice vibration and free electrons. In general, for the electrical conductors, a large number of free electrons move and transport electric charges; therefore, they also carry thermal energy from a high-temperature region to a low-temperature region. The thermal diffusion is related to the internal geometry of the capacitor and the operating conditions.

The temperature at any point of the supercapacitor depends on the three modes of heat transfer: conduction, convection, and radiation.

11.3.2

Conduction Heat Transfer

Conduction heat transfer is defined as the energy transferred inside the solid from one high-temperature zone to another zone where the temperature is lower. This chapter investigates the transient temperature T distribution inside and at the surface of the supercapacitor using the heat conduction equation [18]:

$$\nabla^2 T + \frac{P}{\lambda} = \frac{\rho C_p}{\lambda} \frac{\partial T}{\partial t} \quad (11.28)$$

where ∇^2 is the Laplace operator, r the density of the supercapacitor, l the thermal conductivity of the supercapacitor, C_p the heat specific capacity, and P the local volumetric density. In this work, the heat inside the supercapacitor is assumed to be axis-symmetrical and the heat conduction equation is used in two coordinate directions, that is, in the radial and the axial directions. The physical model considers a cylinder of length L and diameter D . The cylinder has an equivalent thermal conductivity λ_z along the axial and λ_r along the radial direction (Figure 11.24). The physical model is given by Eq. (11.29):

$$\rho C_p \frac{\partial T(r, z, t)}{\partial t} = \lambda_r \frac{\partial^2 T(r, z, t)}{\partial r^2} + \frac{\lambda_r}{r} \frac{\partial T(r, z, t)}{\partial r} + \lambda_z \frac{\partial^2 T(r, z, t)}{\partial z^2} + P \quad (11.29)$$

where $r_i < r < r_o$, $0 \leq z \leq L$, $0 < t \leq t_f$, r is the radial coordinate, z the axial coordinate, and r_i and r_o are the internal and the external radius of the supercapacitor, respectively.

The conductivities λ_r and λ_z are determined using an element of the supercapacitor containing three layers: the activated carbon layer, the separator layer, and the aluminum layer as shown in Figure 11.25. Electrodes + and - are formed by an aluminum thin film that is placed between two activated carbon layers (Figure 11.25a).

Figure 11.24 Supercapacitor cylindrical structure.

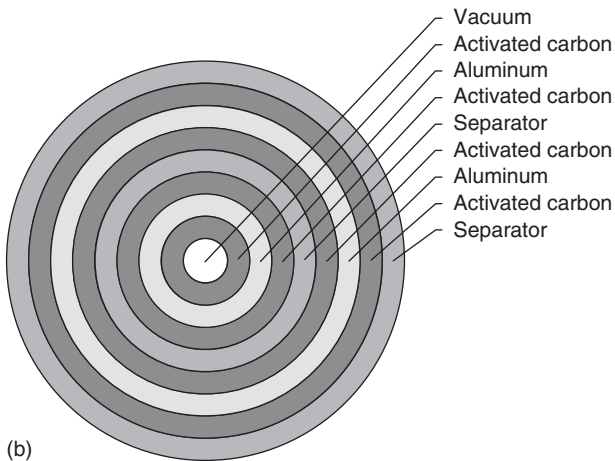
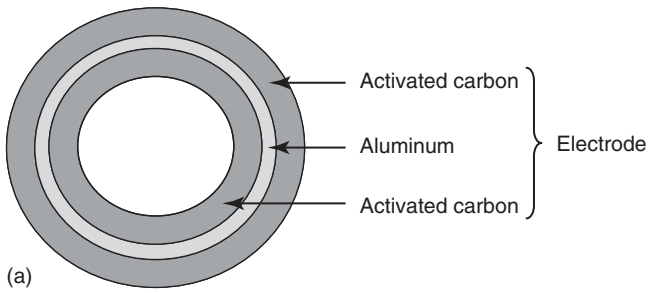
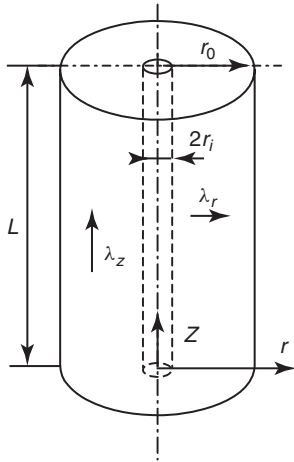


Figure 11.25 Simplified supercapacitor thermal model construction: (a) electrode structure and (b) cross section of supercapacitor first layer.

The thermal resistance of each layer is assumed to be equivalent to the thermal resistance of a long cylinder of inside radius r_i , outside radius r_o , and length L . For each layer, the length is very large compared to the radius. The thermal resistance can be written as

$$R_{th} = \frac{\ln(r_o/r_i)}{2\pi\lambda L} \quad (11.30)$$

The thermal resistance concept may be used for multiple cylindrical layers. For four layers (Figure 11.5), the equivalent thermal resistance along the radial direction can be written as follows:

$$R_{th} = \frac{1}{2\pi\lambda_c L} \ln\left(\frac{r_i + e_c}{r_i}\right) + \frac{1}{2\pi\lambda_s L} \ln\left(\frac{r_i + 2e_c + e_a + e_s}{r_i + 2e_c + e_a}\right) + \frac{l}{2\pi\lambda_c L} \ln\left(\frac{r_i + 2e_c + e_a}{r_i + e_c + e_a}\right) + \frac{1}{2\pi\lambda_a L} \ln\left(\frac{r_i + e_c + e_a}{r_i + e_c}\right) \quad (11.31)$$

where e_c is the activated carbon thickness, e_a is the aluminum thickness, and e_s is the separator thickness, λ_c is the activated carbon conductivity, λ_a is the aluminum conductivity, and λ_s is the separator conductivity. It is assumed that $e_a \ll e_c$ and $e_s \ll e_c$. Using these conditions, the equivalent thermal resistance becomes equal to the thermal resistance of the activated carbon. Therefore, the equivalent thermal conductivity along the radial direction is used equal to the activated carbon conductivity ($\lambda_r \approx \lambda_c$).

Along the axial direction, the thermal conductivity λ_z is assumed to be the same as the aluminum conductivity. This condition is deduced from the electrical analog used to represent the heat flow inside the supercapacitor by the parallel thermal resistances as follows:

$$\frac{1}{R_{th}} = \sum_{n=1}^N \frac{1}{R_{th,n}} \quad (11.32)$$

where $R_{th,n}$ is the thermal resistance of the layer number “ n ,” and N the total number of the layers (carbon, aluminum, separator). The thermal conductivity of aluminum is much higher than the thermal conductivity of the carbon and the separator. The thermal conductance of the carbon and the separator can be neglected compared to the thermal conductance of aluminum. Using this hypothesis, the equivalent thermal resistance along the axial direction may be written as

$$\frac{1}{R_{th}} = \frac{1}{R_{th,a}} \quad (11.33)$$

The axial thermal conductivity can be assumed to be equal to the aluminum conductivity ($\lambda_z \approx \lambda_a$).

11.3.3

Thermal Boundary Conditions

The thermal conduction equation is solved using the thermal boundary conditions, which are defined as follows:

- Before starting the experiments (at $t = 0$), the temperature in the supercapacitor is assumed to be uniform and equal to the measured value at the heat exchange surface.

$$T(r, z, 0) = T_0 \text{ for } r_i \leq r \leq r_o \text{ and } 0 \leq z \leq L$$

- On the inside surface of the supercapacitor, the plastic cylinder of radius r_i which is characterized with a very low thermal conductivity, is used as the isolated support. The heat flux is defined from the Fourier's law. It is expressed as a function of the temperature gradient in the radial direction. The radial thermal conductivity may be written as follows:

$$\lambda_r \frac{\partial T}{\partial r}(0, z, t) = 0, \text{ where } 0 < t \leq t_f \text{ and } 0 \leq z \leq L$$

- On the outside surface of the supercapacitor, the thermal energy is transferred by convection in the airflow and by radiation at the ambient temperature T_{amb} . The thermal energy can be transferred because of the electromagnetic radiation, which is propagated as a result of the temperature difference between a surface and its environment. The thermal radiation is proportional to the fourth power of the absolute temperature and the heat exchange surface of the supercapacitor. The heat flux transferred per unit of the surface is expressed as

$$q_{\text{rad}} = \varepsilon \sigma (T^4 - T_{\text{amb}}^4) \quad (11.34)$$

where ε is the surface emissivity that relates the radiation of the gray surface to that of an ideal black surface. σ is the Stefan–Boltzmann constant ($\sigma = 5.669 \times 10^{-8} \text{ W m}^{-2} \text{ K}^{-4}$). T and T_{amb} are the surface and the ambient temperatures, respectively. In this work, the radiation heat flux is written in the form of the following relation:

$$q_{\text{rad}} = h_{\text{rad}} (T - T_{\text{amb}}) \quad (11.35)$$

where the radiation heat transfer coefficient is expressed as

$$h_{\text{rad}} = \varepsilon \sigma (T - T_{\text{amb}}) (T^2 + T_{\text{amb}}^2) \quad (11.36)$$

Beside the radiation heat transfer, convection heat transfer is also considered at the external surface of the supercapacitor. In the air surrounding the supercapacitor, the heat transfer rate is related to the overall temperature difference between the external surface and the ambient room air. Newton's law of cooling is used to express the overall effect of convection on the heat exchange surface as follows:

$$q_{\text{conv}} = h_{\text{conv}} (T - T_{\text{amb}}) \quad (11.37)$$

where T is the surface temperature, T_{amb} the ambient room air temperature, h_{conv} the convection heat transfer coefficient, and q_{conv} is the heat flux transferred per unit of the heated surface.

In this work, the thermal boundary conditions are defined by taking into account the radiation and the convection heat transfer coefficients on the entire external surface. The local heat flux transferred by conduction at the interface between the air and the heat exchange surface is assumed to be equal to the heat flux received

by the air layer around the supercapacitor. The heat flux dissipated by conduction is defined using Fourier's law and the minus sign is inserted so that the second principle of thermodynamics will be satisfied. Thus, at the external radius ($r = r_o$):

$$-\lambda_r \frac{\partial T}{\partial r} (r_o, z, t) = h_t [T(r_o, z, t) - T_{\text{amb}}] \quad (11.38)$$

where $0 < t \leq t_f$, $0 \leq z \leq L$.

At the supercapacitor extremities ($z = 0$ and L), the temperatures are defined from the heat balance in the axial direction, which is defined by the following equations:

$$-\lambda_z \frac{\partial T}{\partial z} (r, L, t) = h_t [T(r, L, t) - T_{\text{amb}}] \quad (11.39)$$

where $0 < t \leq t_f$, $r_i \leq r \leq r_o$, $z = L$

$$-\lambda_z \frac{\partial T}{\partial z} (r, 0, t) = h_t [T(r, 0, t) - T_{\text{amb}}] \quad (11.40)$$

where $0 < t \leq t_f$, $r_i \leq r \leq r_o$, and $z = 0$.

The heat transfer coefficient h_t is defined as the sum of the convection and the radiation heat transfer coefficients.

$$h_t = h_{\text{rad}} + h_{\text{conv}}$$

11.3.4

Convection Heat Transfer Coefficient

In general, when the heated surface is exposed to the ambient room air without any imposed external motion of air, the ambient air will be in movement because of the temperature differences that are induced by the air density difference in the proximity of the heat exchange surface. In this case, the thermal energy is transferred in the ambient air by natural convection. The latter is the simplest method of cooling electronic components because the use of fans could introduce dust and contaminants in the system, and requires additional power.

The *heat transfer coefficient* for natural convection will have a dependency on the density, viscosity, velocity, and on the thermal properties, such as the conductivity and the specific heat capacity, of the fluid. The velocity profile of the fluid is greatly influenced by the fluid viscosity and the heat exchange surface geometry. The heat transfer coefficient is deduced from the Nusselt number, which is defined as follows:

$$Nu = \frac{h_{\text{conv}} D}{\lambda_{\text{air}}} \quad (11.41)$$

where D is the capacitor outside diameter and λ_{air} is the thermal conductivity of the ambient room air.

For natural convection, the dimensionless Nusselt number is expressed as a function of the dimensionless Rayleigh number (Ra).

$$Nu = ARa^m \quad (11.42)$$

where the dimensionless constant A and the exponent m are adjusted from experimental data.

The Rayleigh number is determined as the product of the Prandtl and the Grashof dimensionless numbers. The Prandtl number (Pr) depends on the properties of the fluid (air) and the Grashof number (Gr) depends on the geometry of the heat exchange surface. Thus,

$$Ra = Gr \times Pr \quad (11.43)$$

where

$$Pr = \frac{\mu_{\text{air}} C_{p,\text{air}}}{\lambda_{\text{air}}} \quad (11.44)$$

where μ_{air} is the dynamic viscosity of the air, λ_{air} the thermal conductivity of the air, and $C_{p,\text{air}}$ the specific heat capacity of the air.

$$Gr = \frac{\rho_{\text{air}}^2 g \beta (T - T_{\text{amb}}) D^3}{\mu_{\text{air}}^2} \quad (11.45)$$

where g is the gravitational acceleration, T the surface temperature, and β is the volume coefficient of expansion, which may be determined from tables of properties. For ideal gases, it may be calculated from the following expression:

$$\beta = \frac{1}{T_{\text{amb}}} \quad (11.46)$$

where T_{amb} is the absolute temperature of the air.

For laminar and turbulent natural convection around the horizontal cylinder, the Nusselt number is expressed subsequently.

In the case of a laminar convection ($10^3 \leq Ra \leq 10^9$):

$$Nu = 0.53Ra^{1/4}$$

In the case of a turbulent convection ($10^9 \leq Ra \leq 10^{13}$):

$$Nu = 0.10Ra^{1/3}$$

11.3.5

Solution Procedure

The discretization of the equations system is made by means of an implicit alternating direction method. For a three-dimensional space, the implicit alternating method was applied by using two intermediate values T^* and T^{**} . At each time $t + \Delta t$, the temperature T is computed from the temperature $T(t)$ using the following equations [19]:

$$\frac{T^* - T(r, z, \phi, t)}{\Delta t/2} = \frac{\partial^2 T^*}{\partial r^2} + \frac{1}{r} \frac{\partial T^*}{\partial r} + \frac{1}{r^2} \frac{\partial^2 T(r, z, \phi, t)}{\partial \phi^2} + \frac{\partial^2 T(r, z, \phi, t)}{\partial z^2} \quad (11.46)$$

$$\frac{T^{**} - T(r, z, \phi, t)}{\Delta t/2} = \frac{\partial^2 T^*}{\partial r^2} + \frac{1}{r} \frac{\partial T^*}{\partial r} + \frac{1}{r^2} \frac{\partial^2 T^{**}(r, z, \phi, t)}{\partial \phi^2} + \frac{\partial^2 T(r, z, \phi, t)}{\partial z^2} \quad (11.47)$$

$$\begin{aligned} \frac{T(r, z, \phi, t + \Delta t) - T(r, z, \phi, t)}{\Delta t/2} &= \frac{\partial^2 T^*}{\partial r^2} + \frac{1}{r} \frac{\partial T^*}{\partial r} + \frac{1}{r^2} \frac{\partial^2 T^{**}(r, z, \phi, t)}{\partial \phi^2} \\ &+ \frac{\partial^2 T(r, z, \phi, t + \Delta t)}{\partial z^2} \end{aligned} \quad (11.48)$$

Equation (11.46) is implicit only in the radial direction, Eq. (11.47) is implicit only in the angular direction, and Eq. (11.48) is implicit only in the axial direction. There is one unknown parameter per equation (T) and the Gaussian elimination method is used for each tridiagonal system that defined each equation. Equation (11.46) is solved for the first intermediate values T^* , which is used in the second equation (Eq. (11.47)). This equation is solved in order to determine the second intermediate temperature values T^{**} , which are used in the third equation (Eq. (11.48)), thus leading to the solution at the end of the whole time interval Δt .

The system of equations is solved by means of an implicit finite-difference scheme. The integration domain in each direction is divided into cells of dimensions Δr , Δz , and $\Delta \phi$ in the radial, axial, and angular directions. Each computing plane is indexed by “ i ” in the radial direction, “ j ” in the angular direction, and “ k ” in the axial direction. The solving method requires the temperature values for all the grid points on the cylinder extremities and the external surface, while respecting the thermal boundaries conditions. The derivative temperature functions in the longitudinal direction are approximated by backward differences. The derivative temperature terms are evaluated by the central difference in the radial and the angular directions.

$$\left. \frac{\partial T}{\partial r} \right|_{i,j,k} = \frac{T_{i+1,j,k} - T_{i-1,j,k}}{(r_{i+1,j,k} - r_{i-1,j,k})} \quad (11.49)$$

$$\left. \frac{\partial T}{\partial \phi} \right|_{i,j} = \frac{T_{i,j+1,k} - T_{i,j-1,k}}{(\phi_{i,j+1,k} - \phi_{i,j-1,k})} \quad (11.50)$$

$$\left. \frac{\partial T}{\partial z} \right|_{i,j,k} = \frac{-3T_{i,j,k} + 4T_{i,j,k-1} - T_{i,j,k-2}}{2\Delta z} \quad (11.51)$$

The system of the finite-difference equations forms the tridiagonal matrix that can be solved using the Thomas algorithm. For example, the system of linear equations in the radial direction is written in the following form:

$$A_{i,j,k} T_{i-1,j,k} + B_{i,j,k} T_{i,j,k} + C_{i,j,k} T_{i+1,j,k} = D_{i,j,k} \quad (11.52)$$

where T is a general vector containing j values. The coefficients of the matrix form $A_{i,j,k}$, $B_{i,j,k}$, $C_{i,j,k}$, and $D_{i,j,k}$ are defined as a function of the thermophysical properties and the temperatures in the others nodes.

11.3.6

BCAP0350 Experimental Results

A Maxwell BACP0350 supercapacitor, which has a capacitance of 350 F and a rated voltage of 2.5 V, is tested as shown in Figure 11.26. The supercapacitor is charged with different constant currents by using a DC/DC converter. The regulation of the current is performed by hysteretic control. The discharge is regulated at constant current using an active load. Figure 11.27 presents the supercapacitor current and voltage versus time during the charge and the discharge. The supercapacitor voltage is swept between its rated voltage (2.5 V) and half of this voltage (1.25 V). Generally, supercapacitors are operated between these two voltages because in this condition they can store and provide approximately 75% of its maximum energy, without generating big electronic design problems.

The studied supercapacitors have a 33 mm outside diameter, and a 61.5 mm length. The dissipated power inside the supercapacitor is assumed to be uniform. It is equal to 2.88 W for 30 A of charge/discharge current. For this experiment, the environmental temperature $T_a = 20^\circ\text{C}$ was constant over time. The supercapacitor is cooled with only a slowly moving air flow under the effect of the natural convection. The computations are conducted for a heat transfer coefficient of $12\text{ W m}^{-2}\text{ K}$. The radial thermal conductivity is equal to $0.5\text{ W m}^{-1}\text{ K}^{-1}$ and the axial thermal conductivity to $210\text{ W m}^{-1}\text{ K}^{-1}$. The thermal resistance in the axial direction is very low compared to that in the radial direction. Figure 11.28 shows the comparison between the experimental and the numerical results. Initially, the temperature of the supercapacitor is assumed to be uniform and equal to 20°C . The supercapacitor temperature increases exponentially over time. The experimental

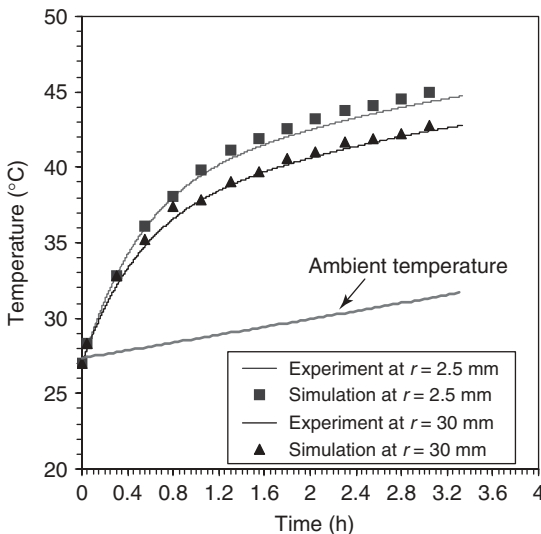


Figure 11.26 BCAP010 temperatures: comparison between simulation and experimental results.

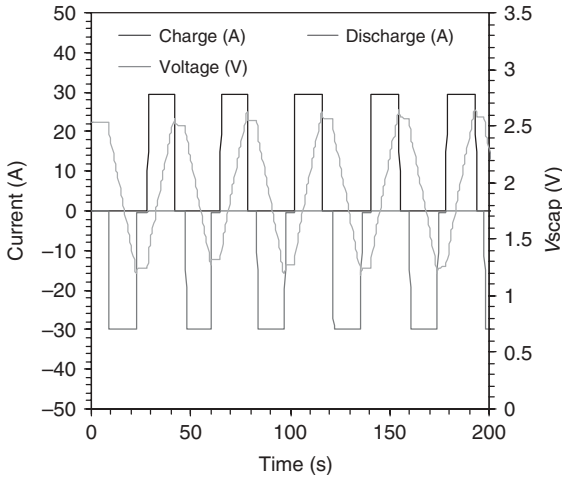


Figure 11.27 BCAP0350 current and voltage versus time.

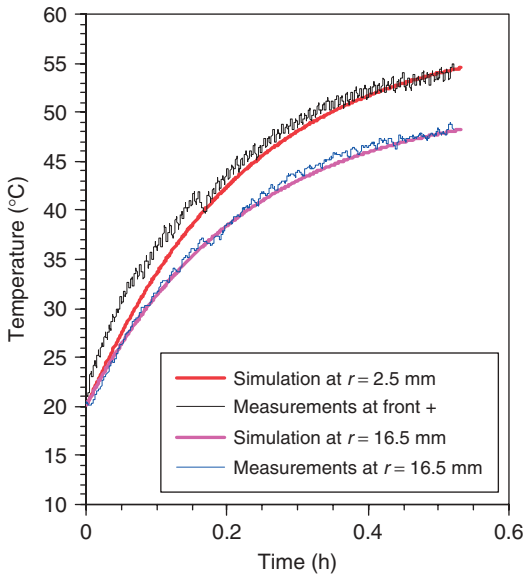


Figure 11.28 BCAP0350 temperature comparison between the model results and the experimental data for a charge/discharge current of 30 A.

and the predicted values are in very good agreement. The small difference between the measurements and the predicted values at $r = 2.5$ mm is due to the fact that the measured temperature at the supercapacitor positive pole is assumed to be equal to the temperature inside the supercapacitor at $r = 2.5$ mm. This hypothesis is confirmed by the experimental data obtained by Maxwell Technologies and the Paul Scherrer Institut in the case of the BCAP0010 supercapacitor. Figure 11.29

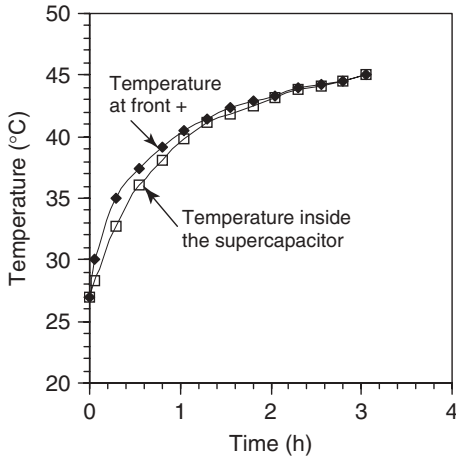


Figure 11.29 Comparison between the measured temperatures inside and on the positive pole of a BCAP0010 supercapacitor.

presents an example of the temperature profiles measured in transient and steady state using BCAP0010. The experiment is performed measuring the temperature inside and at the positive front of the supercapacitor. It is shown that the maximum difference between the two measured values is smaller than 2°C . This is due to the fact that the axial thermal resistance is very low.

The supercapacitor thermal resistance is determined using the developed thermal model. It has been estimated to be equal to 10.66 K W^{-1} for the BACP0350.

Under the same conditions, Figure 11.30 shows the time evolution of the temperature profiles along the radial direction for the BCAP0350 supercapacitor. These results show that the radial temperature decreases along the radius because of the dissipated convective heat flux on the external surface of the supercapacitor. The temperature difference between the inside of the supercapacitor and the external surface increases over time. This temperature increase over time is due to the fact that the supercapacitor accumulates heat during the charge and the discharge. The temperature distribution is due to the fact that the radial thermal resistance is higher than the axial one. It reaches 5°C after $t = 3200\text{ s}$ compared to 2°C after $t = 400\text{ s}$. This temperature difference can be neglected compared with the temperature between the initial state and the steady state. It can be seen (Figure 11.30) that steady-state temperature is equal to 56°C when the initial temperature is 20°C . For hybrid vehicle applications, the ambient temperature is higher and it is necessary to dimension a cooling system for the supercapacitor module.

Figure 11.31 shows the time evolution of the heat losses at the external surface of the supercapacitor. The heat flux through the outside radius is generated by convection. It is calculated using the Newton law that is defined by the following equation:

$$Q_w = hS(T_{r=r_o} - T_a) \quad (11.53)$$

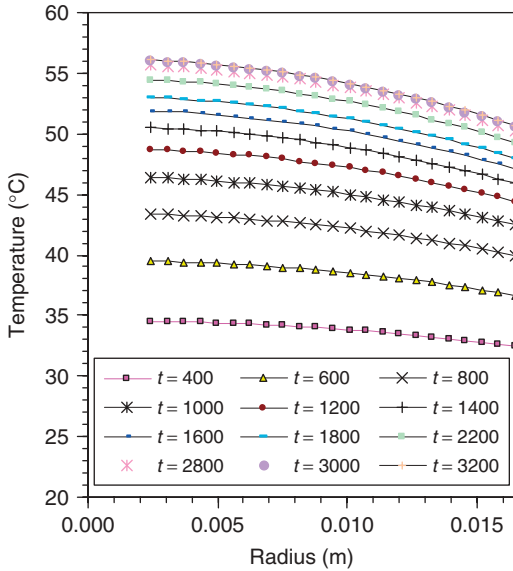


Figure 11.30 BCAP0350 temperature distribution as a function of supercapacitor radius for different time values.

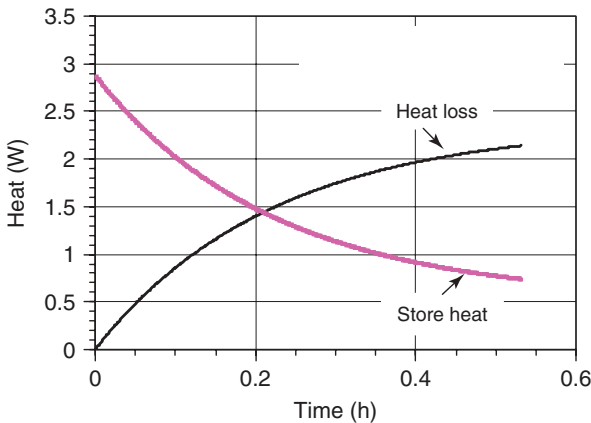


Figure 11.31 Heat exchange energies for BCAP0350 supercapacitor.

where the heat exchange surface is determined as

$$S = 2\pi r_0 L \quad (11.54)$$

D is the supercapacitor outside diameter and L is its length.

During time, the heat flux dissipated by the electrical current flowing inside the supercapacitor (Joule effect) is equal to the sum of the heat flux generated by convection at the external surface of the supercapacitor and the accumulated heat

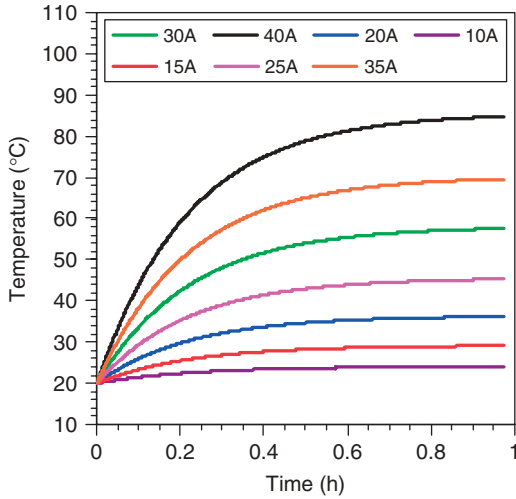


Figure 11.32 BCAP0350 internal temperatures for different charge and discharge currents.

energy inside the supercapacitor. Figure 11.31 shows that for each instant, the accumulated heat energy decreases when the convective heat losses increase on the external surface. During the experiment, the supercapacitor temperature increases until it attains the steady state. In this case, the difference between the surface temperature and the ambient temperature increases and it tends to increase the heat losses to the air ambient by natural convection. The thermal energy accumulated by the supercapacitor decreases during time because it results from the heat capacity of the supercapacitor that is necessary to raise the temperature of the mass. Higher heat capacity means a greater thermal energy that may be accumulated by the solid.

The temporal evolution of the supercapacitor temperature as a function of the electrical power accumulated or provided by the device has been studied. Figures 11.32 and 11.33 show, respectively, the temperature variations inside the supercapacitor according to the time (at $r = r_1$) and the variation in the heat loss on the supercapacitor's external surface. The initial temperature is fixed at 20 °C. The supercapacitor capacitance is 350 F. It is charged and discharged at constant current between its nominal voltage (2.5 V) and half of this voltage. For each current of charge and discharge, only the natural heat convection is considered. These results show that, in the steady-state case, for 35 and 40 A, the supercapacitor temperature exceeds its maximal operating value. This latter is recommended by the manufactures to be less than 65 °C.

For example, when the supercapacitor is charged and discharged with a 40 A constant current, the inside temperature becomes higher than 60 °C after 12 min. This necessitates a cooling system in order to maintain the temperature below the operating value.

Using the developed model, thermal resistance of BCAP0350 F is calculated for different supercapacitor currents of charge and discharge. Table 11.2 gives the

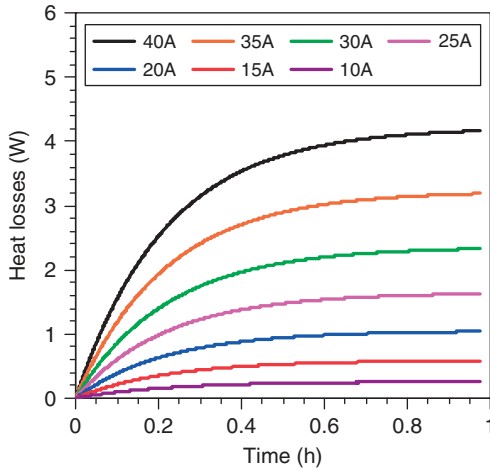


Figure 11.33 BCAP0350 heat losses for different charge and discharge current values.

Table 11.2 BCAP0350 thermal resistances.

I (A)	R_{th} ($K W^{-1}$)
10	10.670
15	10.734
20	10.755
25	10.764
30	10.665
35	10.775
40	10.777

supercapacitor thermal resistance when the device is charged and discharged with 10, 15, 20, 25, 30, 35, and 40 A for the BCAP0350. These results show that there is a very small difference between these values. The difference is less than 1%.

The supercapacitor cooling system can be realized using air forced convection. Figure 11.34 shows the evolution of the supercapacitor maximal temperature as a function of the convection heat transfer coefficient. The simulation conditions are that the current of charge and discharge is constant and its value is equal to 40 A. Two values of the ambient temperature, 20 and 35 °C, respectively, are considered.

These results show that the supercapacitor maximum temperature is higher than the maximum operating temperature when the convection heat transfer is less than 16 $W m^{-2} K$ for 20 °C and 26 $W m^{-2} K$ for 35 °C. In this case, it is obvious that it is necessary to install a cooling system in order to maintain the supercapacitor temperature at less than 60 °C. The supercapacitor should be equipped with the cooling system consisting of fans or air distribution channels. The choice of the cooling system depends on the level of the heat transfer coefficient and the higher operating

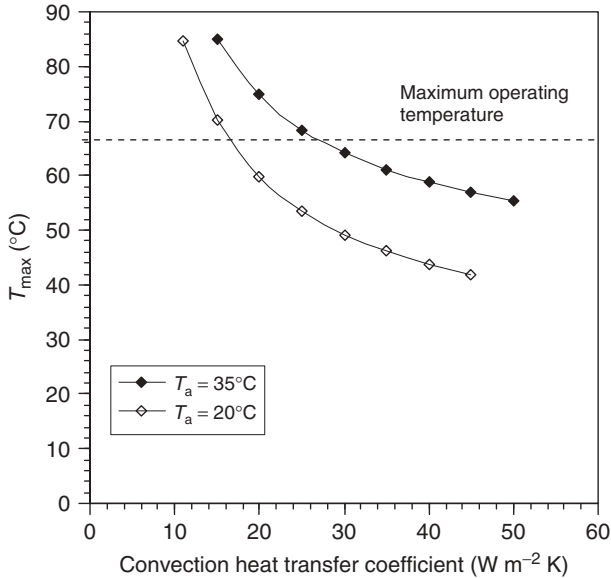


Figure 11.34 BCAP0350 maximum temperature as a function of the convection heat transfer coefficient for two different ambient temperatures.

temperature. The chosen cooling system should be sufficient to keep the supercapacitor temperature at a tolerable temperature level, which leads to a longer lifetime.

11.4 Supercapacitor Lifetime

The lifetime of an energy storage component is the time required to fail. *Failure* is defined as the lack of ability of a component to fulfill its specified function. One of its characteristics will be out of the specification. For example, the capacitance will be below its specified limit value, or the series resistance will be above its specified value, the component will be leaking, or will be open. The lifetime is a statistical value that gives the best estimate for the service life based on the Weibull theory. A detailed presentation of the Weibull failure statistic theory is available in Ref. [20].

The survivor function $F(t)$ is the number of elements of the statistical sample that have not failed or lost their function at time t and are still working.

$$F(t) = \exp^{-(\lambda_0 t)^p} \quad (11.55)$$

The failure rate is given in FIT (failure in time), which is the number of failures occurring during 10^9 h of working one object. $\lambda(t)$ and λ_0 must not be confused. The latter is a constant (independent of time, but dependent on the temperature and voltage) that corresponds to the inverse of the time necessary for 63% of the sample to fail. $\lambda(t)$ is the inverse of the mean time between failure (MTBF).

In the wear-out region, $\lambda(t)$ increases with time. The manufacturer specifications give the maximum value of $\lambda(t)$ within the announced lifetime: 50 FIT and 10 years of lifetime expectancy.

11.4.1

Failure Modes

The supercapacitors are concerned with typical failure modes:

- 1) “Early failures” and “wear-out failures” are reflected in the curve known as the *bathhtub* curve. At the beginning of the component usage, the failure rate rapidly decreases. The “youth” failures are screened by routine tests at the manufacturer or customer sites. They are due to design and process weaknesses which have not been detected by the design and process FMEA (Failure mode and effects analysis) performed during the development. They are more probably due to production process variations or to material quality changes. The process variations are due to tool wear, operator change, and lack of formation. This early failure mode is not taken into account by the Weibull model theory.
- 2) The cell container opens as a result of an internal overpressure [21, 22]. The voltage and the temperature generate a gas pressure inside the cell, which increases with the working time. When the pressure reaches a determined limit, a mechanical fuse, generally a groove on the can wall or a pressure relief on the lead, may open softly, avoiding an explosion of the device. The electrical functions of the supercapacitor are still working. The capacitance loss speed increases slightly. Some traces of the electrolyte salt are visible close to the aperture. Solvent vapors are released from the component. For this reason, it is required that supercapacitor modules should be ventilated. In case of opening, the component must be replaced.
- 3) With regard to leakage [23], the consequences are almost the same as in the previous case. The origin of the failure may be due to internal overpressure, bad seal position, weak welding, perforation of the wall during electrode contacting, and so on. Detection of the leakage is sometimes difficult. It may occur that some residual electrolyte is trapped in an area difficult to access, during component production, and becomes apparent in the application.
- 4) When the capacitance value is below 80% of the nominal one, the accessible carbon surface and the availability of ions are reduced during the electrochemical cycling.
- 5) When the series resistance value is twice the nominal one, the electrode adhesion on the collector weakens with time and temperature. The ion availability is reduced.

11.4.2

Temperature and Voltage as an Aging Acceleration Factor

For each failure mode, a statistical model must be developed. This is usually achieved by performing accelerated tests, increasing the temperature, or/and the

voltage, in steady-state or in accelerated cycling. The cycling experiments have the disadvantage of requiring a great deal of power, which consequently limits the number of samples that can be tested.

The given numerical values – 80% for the capacitance and 200% for the series resistance – may be adapted to particular application requirements that may be different. They change also from one manufacturer to another. This is an important point that must be kept in mind when comparing datasheets from different manufacturers.

To get an estimation of the time required to reach 20% of electrode capacitance loss, the coefficient λ_o and p must be determined for all the operating temperatures and for all the operating voltages. They are measured for a set of discrete values, and then, the coefficient λ_o and p for the other temperatures and voltages are calculated using the following solicitation ratio:

$$\frac{t_1}{t_2} = \left(\frac{V_2}{V_1}\right)^n \exp\left[\frac{E_a}{k}\left(\frac{1}{T_{1\text{abs}}} - \frac{1}{T_{2\text{abs}}}\right)\right] \quad (11.56)$$

In this relation, t_1 is the lifetime at the temperature T_1 and voltage V_1 , t_2 is the lifetime at the temperature T_2 and voltage V_2 , E_a is the activation energy determined by the experimental data, k is the Boltzmann constant, and n is a constant determined experimentally. An extensive study has been performed to demonstrate a general approach to assess electrochemical capacitor reliability as a function of operating conditions on commercial capacitor cells [24]. An Arrhenius law is used for the temperature dependency, while an inverse power law is used for the voltage dependency. Some electronic apparatus concepts are already available to estimate *in situ* the double-layer capacitor residual life by monitoring the temperature and voltage constraints of the application [25].

It is noteworthy that when the voltage is close to the electrochemical decomposition voltage, there is an acceleration of the degradation phenomena, especially in the higher temperature domain.

The challenge in most industrial applications is to size the storage system as small as possible, for both cost-saving and available volume reasons. To optimize the dimensions of the components and setting the reserve to a minimum value, all the available field data, which allow fitting precisely the actual application requirements, must be considered. Practically, the duration, temperature, and voltage solicitation stresses must be individually estimated. An equivalent stress weight is calculated for each contribution, based on the solicitation ratio in Eq. (11.56). The lifetime expectation is evaluated by summing all the estimated contributions.

The capacitance drop is not linear. The experimental work (Figure 11.18) shows that three phases may be distinguished on the capacitance drop curve.

- 1) A first phase that lasts between 1 and 12 h, depending on temperature and voltage, is in fact a measurement effect. It is caused by the charging of the electrode areas that have no counter electrode in their neighborhood. The ions need a long time to reach these distant areas. This leads to a discharge of the charges initially located on the paired electrode toward the unpaired electrode areas.

- 2) The second capacitance fading process is exponential. In the voltage and temperature conditions of Figure 11.17, the time constant is in the range of 2000 h. This part of the process may be attributed to a potential window shift combined with the aging due to the construction asymmetry.
- 3) The third one occurs after an approximate drop of the capacitance of 15–20%. It appears as linear, but may also be exponential with a long time constant. This is not possible to find out in the limited experimental time. The attribution of the second and third processes to a physical phenomenon is not well established. An attempt to correlate the exponential decay with leakage current measurement has been presented in the literature [21].

The increase in the ESR is linear with time. The values measured during the aging experiment at 50 °C and 2.5 V are aligned on a line the slope of which is equal to 7.5×10^{-4} [% h⁻¹].

11.4.3

Physical Origin of Aging

The physical origin of the aging is attributed to different phenomena such as the oxidation of the carbon surface, the closing of the pores access, or/and to the ionic depletion in the electrode due to electrolyte starving [26]. When a double-layer capacitor is opened, after an aging period under large stress, the oxidation of the separator may be observed. A brown coloration appears on the surface, especially on the side exposed to the positive electrode [27].

The electrolyte undergoes irreversible transformations that are accentuated by voltage and temperature. The electrochemical decomposition of the electrolyte generates a gas overpressure in the double-layer capacitor package (e.g., generation of H₂ in the case of AN and CO₂ in the case of polypropylene carbonate).

Hahn *et al.* [28] have shown for the first time the gas evolution in a double-layer capacitor cell employing activated carbon electrodes and an electrolyte solution of 1 M (C₂H₅)₄NBF₄ salt in a PC solvent. The gas has been monitored by means of online mass spectrometry differential electrochemical mass spectrometry (DEMS). During slow scan voltammetry, CO₂, propene, and H₂ were detected as the major gaseous decomposition products. Probably propene and H₂ are formed by solvent reduction at the negative electrode, while CO₂ is formed by solvent oxidation at the positive electrode. A small amount of propene has already been detected at cell voltage below 1 V. The onset of apparent faradic currents has already been found at a cell voltage of 1.6 V corresponding to half cell potentials of 2.1 and 3.7 V versus Li/Li⁺, respectively.

H₂ (*m/z* = 2) is first detected at a cell voltage of 3.4 V (*E*₋ = 1.1 V vs Li/Li⁺), well above the usual electric double-layer capacitor (EDLC) operation voltage limit of 2.7 V. The reduction of (trace) water is expected at potentials negative to 2 V versus Li/Li⁺. However, the water content of the electrolyte is very low (<20 ppm). Therefore, most of the H₂ may be regarded as a general reduction product of organic compounds (solvent and/or H-containing carbon surface groups). A smooth rise of the CO₂ signal (*m/z* = 44) is observed at a cell voltage of 2.7 V, again coinciding with the apparent faradic current rise. The corresponding positive electrode potential of

$E_+ = 4.3$ V versus Li/Li⁺ is in good agreement with most other values reported for the onset of oxidative PC decomposition [29].

Azaïs *et al.* [30] have studied the causes of supercapacitors aging in an organic electrolyte. The activated carbon electrodes have been characterized before and after prolonged floating (4000–7000 h) at an imposed voltage of 2.5 V. After aging, the positive and negative electrodes have been studied by XPS and NMR on the nuclear spin of ¹⁹F, ¹¹B, and ²³Na. Decomposition products have been found in the electrodes after aging. The amount of products depends on the kind of activated carbon and electrode polarity, suggesting electrolyte redox reactions with the active surface functionalities. Nitrogen adsorption measurements at 77 K on the used electrodes showed a decrease in accessible porosity owing to trapping of the decomposition products in the pores. The evolution of the supercapacitor performance with operation time, that is, the capacitance decrease and the resistance increase, are due to the decomposition of the organic electrolyte on the active surface of the carbon substrate, forming products that block a part of the porosity. The concentration of surface groups and their nature were found to have an important influence on the performance fading of supercapacitors.

Kötz *et al.* [31] have demonstrated that the gas evolution at capacitor voltages higher than 2.5 V depends significantly on the solvent used in supercapacitors, with identical high-surface-area carbon electrodes and the same salt for the electrolyte. Gas evolution and leakage current for the γ -butyrolactone (GBL)-based electrolyte is, at all voltages, drastically higher than for PC and AN. At a cell voltage of 3.25 V, gas evolution in PC is found to be a factor 10 higher than in AN⁻ despite the twofold higher leakage current in the AN-based electrolyte. The amount of leakage current is obviously not necessarily a good measure for the amount of gas evolved.

Kurzweil *et al.* [27] were able to gather the first insights into the thermal and electrochemical decomposition mechanisms of (C₂H₅)₄NBF₄ in AN. The experiments gave clear hints about the formation of volatile amines, intermediate amides, carboxylate anions of organic acids, and fluorinated compounds.

- 1) In the headspace of supercapacitors, excess AN, water vapor, carbon dioxide, and ethene, and fragments of metaboric acid and alkylboranes were detected.
- 2) The thermal decomposition of (C₂H₅)₄NBF₄ in AN requires the catalytical activity of the active carbon electrodes.
- 3) AN forms acetamide, acetic acid, and fluoroacetic acid, depending on the cell voltage and humidity of the electrolyte.
- 4) The alkylammonium cation is destroyed at elevated temperatures by the elimination of ethene. The trialkylamine by-product can be oxidized. Free ammonium ions were not detected.
- 5) Tetrafluoroborate is a source of fluoride, hydrogenfluoride, and boric acid derivatives.
- 6) The brownish salt residues at burst supercapacitors consist of acetamide, organic acids, fluoroacetic acid derivatives, and polymer products (polyamides?). A similar crystalline mass can be reproduced by electrolysis of the electrolyte at 4 V. The formation of fluorocarboxylic acids requires about 6 V. Acid gases escape.

- 7) In the liquid phase, heterocyclic compounds, such as pyrazines, are formed.
- 8) The active carbon electrodes lose cyclic siloxanes and aromatic contaminations even at room temperature, and are destroyed mainly at the anode.
- 9) The oxide layer on the etched aluminum support material under the active carbon layer is destroyed by fluorination.
- 10) Hydrogen is generated by electrolysis of water and by the fluorination of carboxylic acids. Water is generated by condensation of aminocarbonyl compounds.

Kötz *et al.* [21] have observed in a DC voltage test on BCAP0350 from Maxwell Technologies that the failure of all capacitors occurred via a can opening at the pre-designed safety valve as a consequence of increased internal pressure. Can opening was always preceded by the capacitor end-of-life in terms of 20% capacitance loss. The capacitors can be operated at 70 °C and nominal voltage for about 1600 h before the capacitance drops to 80% of the initial value. Capacitors aged at elevated voltages (3.3 V) exhibited a tilting of the low-frequency component in the Nyquist plots, which implies an increase in the heterogeneity of the electrode surface. This feature was not observed on aging at elevated temperatures (70 °C).

Charging and discharging creates mechanical stresses in the electrode. It has been shown that the application of a voltage induces a reversible expansion of the electrode [32, 33]. This mechanical motion, especially in the case of ionic insertion in the electrode, is known to be one of the origins of aging in the battery domain.

11.4.4

Testing

Supercapacitor reliability is estimated by means of different electrical tests that give complementary information. The manufacturers use two test types: “DC voltage test” and the “voltage cycling test.”

Calendar life testing is often mentioned in the literature [34]. This is a test that has its origin in the battery domain. The cells are prepared in different states of discharge (SOD) and stressed with different temperatures. The cell functionalities as the resistance and the capacitance are measured periodically with well-defined charge/discharge conditions. Between the measurements, the cells are floating: they are not connected to a power supply. In the case of supercapacitors, this type of measurement is disturbed by the self-discharge of the cells, which makes result interpretation difficult because of the voltage variation during the experiment.

11.4.5

DC Voltage Test

The measurements done to characterize aging are very sensitive to the polarization history. This remark is important, in particular, for the first measurement, used

as the initial reference value, because this is the only measurement starting from an initial nonpolarized state. In contrast, all the other subsequent values are obtained by starting the measurement from a polarization state corresponding to the nominal voltage.

At the beginning of the polarization stress, the electrode areas that are difficult to access for the ions, such as unpaired electrode area, are not charged because of the long distance the ions have to cover. In terms of electrical circuit, this corresponds to a long time constant owing to the high series resistance of the long ion path. During the capacitance measurement, the current flows from charged area toward the less charged area. The incidence on the measurement interpretation is a capacitance increase if the measurement is performed during the charge and a capacitance decrease if the measurement is performed during the discharge, as the standards require. After about 24–48 h, the supercapacitor may be considered in a steady state and the measured evolution starts to be monotone.

The capacitance and ESR of a BCAP0310_P, the powerful version of the Maxwell Technologies supercapacitor, have been measured periodically during a DC life test (Figure 11.35). The supercapacitor was placed in an oven at 65 °C with a continuous applied voltage of 2.7 V. The capacitor was polarized previously during the 24 h at 65 °C before starting the experiment. The measured initial capacitance was 322 F and the initial ESR was 2.1 mΩ. The capacitance and the ESR were then measured during a charge and a discharge once a week. The ESR was measured at the beginning of the charge at 1.35 V and at the beginning of the discharge at 2.7 Vdc. All the measurements were performed with a constant current of 10 A.

If the test is interrupted for a long time, an increase in capacitance is observed in the measurement. The increase amplitude is reversely exponential with the interruption time. When resuming the test, the capacitance decreases very fast to reach the value before the interruption.

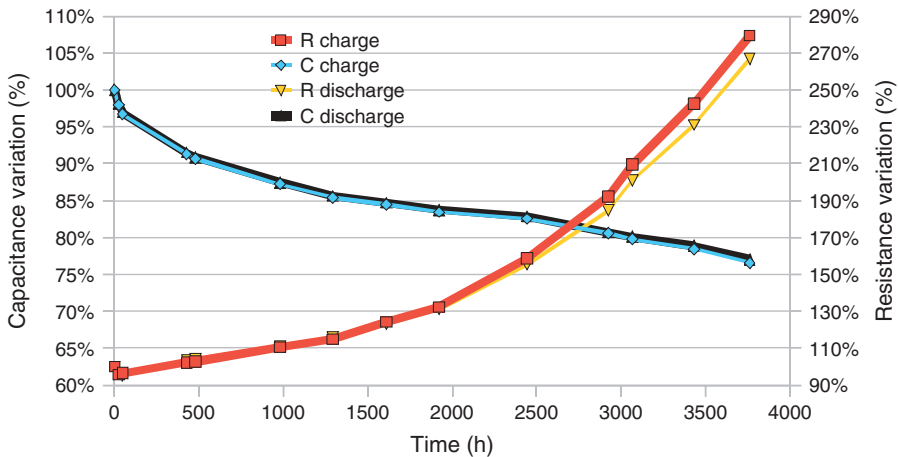


Figure 11.35 Capacitance and ESR during a DC life test on a BCAP0310_P at 2.7 Vdc and 65 °C.

11.4.6

Voltage Cycling Test

Voltage cycling requires more powerful and expensive equipment. This limits the number of samples that may be studied. This method presents the advantage that the capacitance and the ESR may be measured continuously during the experiment. A disadvantage is that it is difficult to have a control over the component temperature because it depends on both the current and the component thermal resistance.

For a small current, the aging during voltage cycling is equivalent to that during a DC voltage solicitation if:

- 1) the internal component temperatures are the same
- 2) the “mean” voltage obtained by pondering the voltage classes visited during the cycling with the power law presented above (Eq. (11.56)) are the same.

The voltage cycling sequence is performed as described in Figure 11.13. In this experiment type, it is necessary to take into account the component temperature increase due to the losses generated by the current in the resistances.

From a practical point of view, the intensity of the current increases both the number of cycles performed in a given time and the component internal temperature. The rest time period between the charge and discharge increases the time spent at high voltage and reduces the number of cycles performed in a given time.

The experimental data have been measured on a BCAP0310_P manufactured by Maxwell Technologies in Rossens, Switzerland, at room temperature between 20 and 22 °C (Figure 11.36). The supercapacitor has been cycled between 1.25 and 2.5 V without rest time with a current of 62 A. The current intensity has been chosen in order to get a component temperature of 65 °C. The 310 F nominal capacitance and the 1.7 mΩ nominal ESR are specified at room temperature and 1 Hz.

The capacitance and the ESR have been reported in Figure 11.36 as a function of the number of voltage cycles. They are measured with an impedance spectrometer

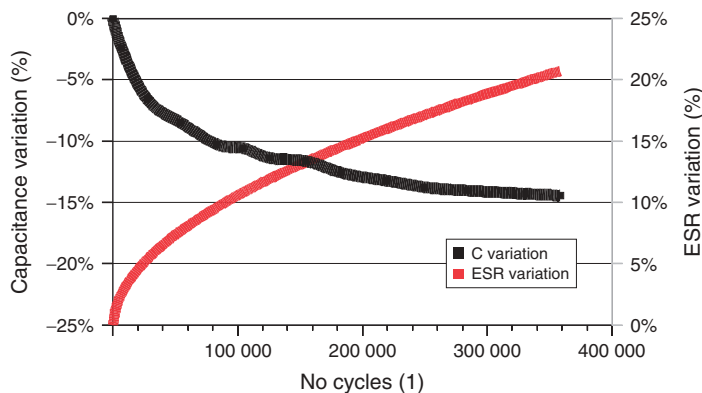


Figure 11.36 BCAP0310_P capacitance and ESR evolution when the supercapacitor is continuously charged and discharged with a current of 20 A.

at 10 mHz. The initial capacitance value was equal to 319 F, while the initial ESR value was 2.9 m Ω

During the experiment, the ESR increased by a factor of 20%. The capacitance decreased 15% of the initial value. With a cycle time of 25 s, the experiment lasted about 1000 h. A simple calculation shows that for cycling the voltage cell between 1.25 and 2.5 V without rest time, the equivalent continuous voltage would be 2.25 Vdc. With a large current of 62 A, the voltage drops due to the 2 m Ω series resistance will be equal to 0.120 V, so that the cell almost never sees the high voltage limit. An additional aging due to the current intensity is expected to explain the relative important aging found in the measurement.

11.5

Supercapacitor Module Sizing Methods

A supercapacitor module is sized according to specifications drawn up as per the required power and the time during which the module must provide this power.

The design methodology is illustrated in Figure 11.37. This method involves the following:

- Define the voltage and current ratings.
- Determine the total capacitance of the supercapacitor module.
- Determine the number of supercapacitor cells to put in series and in parallel.

We define the following parameters:

- P is the power set by the specifications.
- Δt is the duration of the power delivery by the supercapacitor module (discharge time).
- U_{\max} is the maximum voltage of the supercapacitor module.
- U_{\min} is the inimum voltage of the supercapacitor module.
- I is the average discharging current of supercapacitors.
- C_t is the total capacitance of the supercapacitor module.
- R is the total equivalent series resistance of the supercapacitor module.

Generally, $U_{\min} = U_{\max}/2$ because below this value the efficiency of the electronic converter drops very fast. When the supercapacitor module is discharged between U_{\max} and $U_{\max}/2$, 75% of the stored electrical power is consumed.

The total capacitance and the internal resistance R of the supercapacitor module are calculated on the basis of the number of cells in series or in parallel. These two parameters are given by

$$C_t = C \frac{N_{\text{parallel}}}{N_{\text{series}}} \quad (11.57)$$

$$R = \text{ESR} \frac{N_{\text{series}}}{N_{\text{parallel}}} \quad (11.58)$$

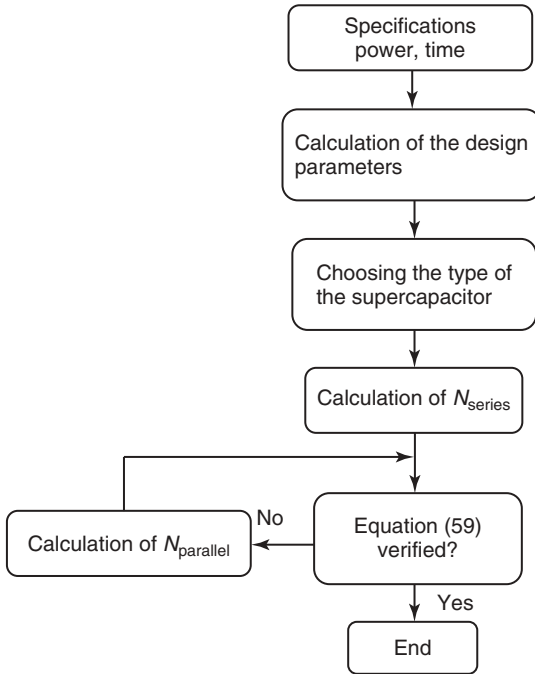


Figure 11.37 Algorithm describing the design of a supercapacitor module according to a given required power.

where C and ESR are the capacitance and the series resistance of the supercapacitor cells used to build the module, N_{series} is the number of cells connected in series, and N_{parallel} the number of cells connected in parallel.

N_{series} is calculated by the ratio of the supercapacitor module voltage (U_{max}) and the supercapacitor cell nominal voltage.

For given temperature and time profiles, the supercapacitor module voltage is expressed by

$$U_{\text{max}} - U_{\text{min}} = I \frac{\Delta t}{C} + RI \quad (11.59)$$

To determine the average current I , the following expressions are used:

$$I_{\text{max}} = \frac{P}{U_{\text{min}}}, I_{\text{min}} = \frac{P}{U_{\text{max}}}, I = \frac{(I_{\text{max}} + I_{\text{min}})}{2} \quad (11.60)$$

The supercapacitor datasheet specifies different voltage values. The main one, called *operating voltage*, which can be applied without degradation or damage during the lifetime of the supercapacitor that is typically 100 000 h. The second one, called *peak voltage*, is harmful to the components. It can be applied for a few hours. However, when a supercapacitor is subjected to a peak voltage, the organic electrolyte in the cell begins to decompose into a gaseous product. If this voltage

is applied continuously on the component, the pressure will increase until the opening of the component.

In practical application, the supercapacitors are solicited at different temperatures and different voltages during their operation. The lifetime is determined by a ponderated calculation based on the aging laws.

The analysis and the study conducted on the behavior of supercapacitors in their associations show the need for a balancing circuit to evenly distribute the voltage on each cell. Therefore, different manufacturers offer two types of balancing circuits, passive and active.

11.6 Applications

Power management for hybrid vehicles depends on the association of different energy sources as well as different types of motorization. Fuel cells (FCs) produce an electrical energy from an electrochemical reaction between a hydrogen-rich fuel gas and an oxidant (air or oxygen). The main by-products are water, carbon dioxide, and heat. FCs are electrically similar to batteries, since they both produce a DC voltage by using an electrochemical oxidoreduction process. Unlike batteries, however, FCs do not release stored energy; instead, they convert energy from hydrogen-rich fuel directly into electricity. FCs operate as long as they are supplied with fuel. Furthermore, they have a large time constant (several seconds) to respond to an increase or decrease in power output demand. The use of supercapacitors (SC) as a storage system in DC hybrid sources, in parallel with FC or batteries, permits to supply or cut off the transient power peaks and can compensate for the intrinsic limitations of the FC power thanks to their shorter time constant and higher power density. In addition, they are easily controlled by the power electronic system of conversion. The aim of power management is to increase the vehicle range, regulate the power, reduce the quantity of pollutant emissions (e.g., NO_x), minimize the quantity of fuel consumption, and also maintain the performance of the battery along its lifetime [35–41]. The power management uses the supercapacitors for starting the motor (peaks of load current) and for the energy recuperation during braking. The system management, often called BMS for “battery management system,” needs the definition of a strategy regarding the state of charge of the different components of the system [42–44]. The power and energy management problems in the hybrid vehicles are brought back to minimize a cost function, which generally represents the quantity of fuel (e.g., diesel or gasoline for the thermal engines, hydrogen for PEM (Proton Exchange Membrane) fuel cell, etc.). This optimization must be performed by taking into account the physical constraint on the energy sources (limited time constant, maximum temperature, maximum voltage, maximum current, aso). Several methods may be used to optimize the cost function: for example, predictive control [40, 42], optimal control [43, 44], and even fuzzy logic may be used for a complex control similar to the calculation of an optimal torque between the thermal engine and the electrical motor [39].

11.6.1

Power Management of Fuel Cell Vehicles**11.6.1.1 Problem Statement**

The fuel cell vehicle that is considered in this study has the same characteristics as the Volkswagen Bora HY Power [45] developed by the Paul Scherrer Institut. The electric system of the vehicle consists of two electric sources (fuel cell and supercapacitors) and of two DC/DC converters connected to a load via a DC link (Figure 11.38). The first converter is a simple boost; the second is a bidirectional converter which functions, in the boost mode when the supercapacitors provide electrical energy to the load, and in buck mode when DC link charges supercapacitors.

The fuel cell system has a power of 48 kW. It is built with two parallel blocks; each block contains three stacks connected in series. Each stack has a power of 8 kW delivered by 125 cells.

The supercapacitor pack must guarantee a maximum power of 50 kW during 15 s. The pack consists of two parallel blocks of supercapacitors; each block contains 141 supercapacitors of 1500 F assembled in series. The DC link voltage must be regulated at 400 V.

The objective of the power management in a fuel cell vehicle is to minimize the electrical energy provided by the fuel cell to the load during a driving cycle.

The fuel cell power P_{FC} is limited. The role of the supercapacitors is to provide the power difference ($P_{Scap} = P_{Load} - P_{FC}$). The supercapacitors take part during the load power peaks (acceleration of the vehicle) and in the recuperation of the energy coming from the load (braking). The state of charge of the supercapacitors must be brought back to a reference value at the end of each driving cycle. The optimal control was adopted for the study of the power management in the fuel cell vehicle.

11.6.1.2 Fuel Cell Modeling

The fuel cell voltage can be expressed by the Eq. (11.61):

$$U_{cell} = E - I_{cell}R_{cell} - A \ln(aI_{cell} + b) \quad (11.61)$$

where I_{cell} is the cell current and R_{cell} is the series resistance of the cell. $R_{cell}I_{cell}^2$ represents the ohmic losses. a and b are two constants. By considering the

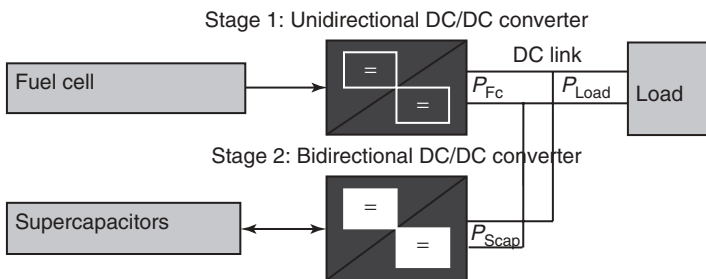


Figure 11.38 Vehicle electric system.

Table 11.3 Fuel cell parameters.

Constant	Value
E (V)	1.2
R_{cell} (Ω)	0.002
A (V)	0.06
a (A^{-1})	21.273
b	96.297

characteristic voltage-current of a proton exchange membrane fuel cell (PEMFC) [45], R_{cell} , a and b can be used to perform calculations (Table 11.3).

The total voltage provided by the PEMFC stacks is

$$U_{\text{FC}} = 375 U_{\text{cell}} = 375 \left[E - \frac{1}{2} I_{\text{FC}} R_{\text{cell}} - A \ln \left(\frac{1}{2} a I_{\text{FC}} + b \right) \right] \quad (11.62)$$

where I_{FC} is the stack current.

11.6.1.3 Supercapacitors Modeling

The supercapacitors are represented by a simple electric circuit (Figure 11.39)

where $C_{\text{Scap}} = 21.27$ F and $R_{\text{Scap}} = 92$ m Ω .

Let Q_{Scap} be the charge quantity of the supercapacitor pack

$$Q_{\text{Scap}} = C_{\text{Scap}} U_s \quad (11.63)$$

The supercapacitor pack current is given by

$$\frac{dQ_{\text{Scap}}}{dt} = -I_{\text{Scap}} \quad (11.64)$$

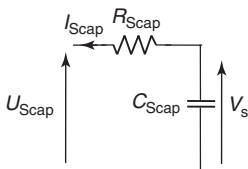
Its voltage is given by

$$U_{\text{Scap}} = U_s + R_{\text{Scap}} I_{\text{Scap}} \quad (11.65)$$

11.6.2

The Power Management of a Fuel Cell Vehicle by Optimal Control

The optimal control theory governs the control strategies to minimize a cost function while a dynamic system state moves. The optimal control is a static prolongation of optimization (e.g., to find the control parameters that define

**Figure 11.39** Equivalent circuit of the supercapacitor pack.

maximum or minimum ordinary of the algebraic functions). The general problem is to find control histories $u(t)$, which force the state variables of a system $x(t)$ to follow the optimal trajectory by minimizing a cost function [46].

11.6.2.1 Optimal Control without Constraint

The optimal control strategies for a dynamic system “ $\dot{x} = F(t, x, u)$ ” suppose that the initial state $x(t_0)$ is known with precision. The optimal control $u^*(t)$, $t_0 \leq t \leq t_f$ must minimize a cost function J . The cost function considered here consists of two parts, a scalar algebraic function q_f of the final state and final time, and a scalar integral function of the state and control.

$$J = \int_{t_0}^{t_f} l[s, x(s), u(s)] ds + q_f[t_f, x(t_f)] \quad (11.66)$$

11.6.2.2 The Hamilton–Jacobi–Bellman Equation

Consider the minimization of the cost function J during the interval “ $[t_0, t_f]$ ” where the control is unbounded. Having found the optimal control $u(t) = u^*(t)$, $t_0 \leq t \leq t_f$, the minimized function could be expressed as

$$U(t, x) = \min_{\substack{u(s) \\ t \leq s \leq t_f}} \int_{t_0}^{t_f} l[s, x(s), u(s)] ds + q_f[t_f, x(t_f)] \quad (11.67)$$

with the condition at final time $U[t_f, x(t_f)] = q_f[t_f, x(t_f)]$.

The equation of Hamilton–Jacobi–Bellman is given by Stengel [46] and Hisham [47]:

$$-\frac{\partial U(t, x)}{\partial t} = \min_u \left[l(t, x, u) + \frac{\partial U}{\partial x} F(t, x, u) \right] \quad (11.68)$$

For a problem affine-quadratic in u :

$$\begin{cases} \dot{x} = F(t, x, u) = f(t, x) + g(t, x) u \\ l(t, x, u) = L(t, x) + u^T R(t, x) u \end{cases}, \quad \text{with } R = R^T > 0$$

Using a stationary condition, the optimal control $u^*(t)$, $t_0 \leq t \leq t_f$ can be expressed as

$$\Delta_u \left\{ l(t, x, u^*) + \frac{\partial U}{\partial x} F(t, x, u^*) \right\} = 0 \quad (11.69)$$

This condition leads to the following explicit form:

$$u^*(t, x) = -\frac{1}{2} R(t, x)^{-1} g(t, x)^T \frac{\partial U(t, x)}{\partial x} \quad (11.70)$$

The Hamilton–Jacobi–Bellman equation can be written in the form:

$$\begin{aligned} -\frac{\partial U(t, x)}{\partial t} &= L(t, x) - \frac{1}{4} \frac{\partial U(t, x)}{\partial x} g(t, x) R(t, x)^{-1} g(t, x)^T \frac{\partial U(t, x)}{\partial x} \\ &+ \frac{\partial U(t, x)}{\partial x} f(t, x) \end{aligned} \quad (11.71)$$

With the condition at final time

$$U [t_f, x(t_f)] = q_f [t_f, x(t_f)]$$

To apply the optimal control to the system considered, it is written in the form:

$$\begin{cases} \dot{x} = F(t, x, u) = f(t, x) + g(t, x) u \\ l(t, x, u) = L(t, x) + u^T R(t, x) u \end{cases}, \quad \text{with } R = R^T > 0$$

with

$$P_{FC} = P_{Load} - P_{Scap} \quad (11.72)$$

The supercapacitor pack power is given by

$$P_{Scap} = U_{Scap} \times I_{Scap} = \frac{Q_{Scap}}{C_{Scap}} I_{Scap} - R_{Scap} I_{Scap}^2 \quad (11.73)$$

The fuel cell power is given by

$$P_{FC} = P_{Load} - \frac{Q_{Scap}}{C_{Scap}} I_{Scap} + R_{Scap} I_{Scap}^2 \quad (11.74)$$

The energy provided by the fuel cell pack during the time interval $[t_0, t_f]$:

$$\text{Energy}_{FC} = \int_{t_0}^{t_f} \left(P_{Load} - \frac{Q_{Scap}}{C_{Scap}} I_{Scap} + R_{Scap} I_{Scap}^2 \right) ds \quad (11.75)$$

It follows that

$$x = Q_{Scap}$$

$$x_{ref} = Q_{Scapref} = 21.27 * 360 = 8660 [C]$$

$$u = I_{Scap} - \frac{Q_{Scap}}{2R_{Scap} C_{Scap}}$$

$$l(x, u, t) = P_{FC}$$

and

$$q_f [t_f, x(t_f)] = [x(t_f) - x_{ref}]^2$$

The objective is to find the reference current trajectory of the supercapacitors, which will minimize the energy provided by the fuel cell required by the load.

$$\begin{cases} \dot{x} = -u - \frac{1}{2R_{Scap} C_{Scap}} x \\ l(t, u, x) = P_{Load} - \frac{1}{4R_{Scap} C_{Scap}^2} x^2 + R_{Scap} u^2, \quad \text{with } t_0 \leq t \leq t_f \\ q_f [t_f, x(t_f)] = [x(t_f) - x_{ref}]^2 \end{cases}$$

With P_{Load} considered as a known function of time, the Hamilton–Jacobi–Bellman equation can be written as

$$-\frac{\partial U(t, x)}{\partial t} = P_{\text{Load}} - \frac{1}{4R_{\text{Scap}}C_{\text{Scap}}^2}x^2 - \frac{1}{4R_{\text{Scap}}}\left(\frac{\partial U(t, x)}{\partial x}\right)^2 - \frac{x}{2R_{\text{Scap}}C_{\text{Scap}}}\frac{\partial U(t, x)}{\partial x} \quad (11.76)$$

At the final time,

$$U[t_f, x(t_f)] = [x(t_f) - x_{\text{ref}}]^2$$

The solution of the partial derivative equation (Eq. (11.76)) can be written as a polynomial function of x with coefficients depending on time as

$$U_a(t, x) = a_0(t) + a_1(t)x + a_2(t)x^2 \quad (11.77)$$

The first derivative of U_a with respect to time is

$$\frac{\partial U_a(t, x)}{\partial t} = \dot{a}_0(t) + \dot{a}_1(t)x + \dot{a}_2(t)x^2 \quad (11.78)$$

and of U_a with respect to x is

$$\frac{\partial U_a(t, x)}{\partial x} = a_1(t) + 2a_2(t)x \quad (11.79)$$

Then, the square derivative of U_a with respect to x becomes

$$\left[\frac{\partial U_a(t, x)}{\partial x}\right]^2 = a_1^2(t) + 4a_2^2(t)x^2 + 4a_2(t)x \quad (11.80)$$

Substituting Eqs. (11.77–11.79) in Eq. (11.76) and by identification, it results in

$$\begin{cases} \dot{a}_0(t) = -P_{\text{Load}} + \frac{1}{4R_{\text{Scap}}}a_1^2(t) & \text{(i)} \\ \dot{a}_1(t) = \frac{1}{2R_{\text{Scap}}C_{\text{Scap}}}a_1(t) + \frac{1}{R_{\text{Scap}}}a_2(t) & \text{(ii)} \\ \dot{a}_2(t) = \frac{1}{4R_{\text{Scap}}C_{\text{Scap}}^2} + \frac{1}{R_{\text{Scap}}C_{\text{Scap}}}a_2(t) + \frac{1}{R_{\text{Scap}}}a_2^2(t) & \text{(iii)} \end{cases} \quad (11.81)$$

To solve the system of differential equations (Eq. (11.81)), we first solve the equation given by Eq. (11.81(iii)), and to finish the solution is given by resolving Eq. (11.81(i)):

$$a_2(t) = \frac{R_{\text{Scap}}}{-t + K_2 R_{\text{Scap}}} - \frac{1}{2C_{\text{Scap}}} \quad (11.82)$$

$$a_1(t) = \frac{K_1}{-t + K_2 R_{\text{Scap}}} \quad (11.83)$$

$$a_0(t) = -\int_0^t P_{\text{Load}}(s) ds + \frac{K_1^2}{4R_{\text{Scap}}} \frac{1}{-t + K_2 R_{\text{Scap}}} + K_0 \quad (11.84)$$

where K_0 , K_1 , and K_3 are real constants to be determined.

However, we have

$$U_a [t_f, x(t_f)] = a_0(t_f) + a_1(t_f) x(t_f) + a_2(t_f) x(t_f)^2 = [x(t_f) - x_{\text{ref}}]^2 \quad (11.85)$$

By identification, we obtain

$$\begin{cases} a_2(t_f) = 1 \\ a_1(t_f) = -2x_{\text{ref}} \\ a_0(t_f) = x_{\text{ref}}^2 \end{cases}$$

The real K_0 , K_1 , and K_3 constants are expressed as

$$\begin{cases} K_2 = \frac{2C_{\text{Scap}}}{2C_{\text{Scap}}+1} + \frac{t_f}{R_{\text{Scap}}} \\ K_1 = -4 \frac{R_{\text{Scap}} C_{\text{Scap}}}{2C_{\text{Scap}}+1} x_{\text{ref}} \\ K_0 = \frac{1}{2C_{\text{Scap}}+1} x_{\text{ref}}^2 + \int_0^{t_f} P_{\text{Load}}(s) ds \end{cases}$$

As the optimal cost is given by

$$\begin{aligned} U_a(t, x) = & \int_t^{t_f} P_{\text{Load}}(s) ds + x_{\text{ref}}^2 \frac{(-t + t_f) + 2R_{\text{Scap}} C_{\text{Scap}}}{(-t + t_f)(2C_{\text{Scap}} + 1) + 2R_{\text{Scap}} C_{\text{Scap}}} \\ & - \frac{4R_{\text{Scap}} C_{\text{Scap}} x_{\text{ref}}}{2C_{\text{Scap}} R_{\text{Scap}} + (t_f - t)(2C_{\text{Scap}} + 1)} x \\ & + \left(\frac{R_{\text{Scap}} (2C_{\text{Scap}} + 1)}{2C_{\text{Scap}} R_{\text{Scap}} + (t_f - t)(2C_{\text{Scap}} + 1)} - \frac{1}{2C_{\text{Scap}}} \right) x^2 \end{aligned} \quad (11.86)$$

The optimal control is given by

$$u^*(t, x) = -\frac{1}{2R_{\text{Scap}}} \frac{\partial U_a(t, x)}{\partial x} \quad (11.87)$$

Then

$$u^*(t, x) = \frac{-2x_{\text{ref}} C_{\text{Scap}} + (2C_{\text{Scap}} + 1)x}{-(2C_{\text{Scap}} + 1)(t - t_f) + 2R_{\text{Scap}} C_{\text{Scap}}} - \frac{x}{2R_{\text{Scap}} C_{\text{Scap}}} \quad (11.88)$$

The reference current trajectory of the supercapacitors pack is given by

$$I_{\text{Scap}}^*(t, Q_{\text{Scap}}) = u^*(t, Q_{\text{Scap}}) + \frac{Q_{\text{Scap}}}{2R_{\text{Scap}} C_{\text{Scap}}} \quad (11.89)$$

A simple computation with $t \leq t_f$ leads to

$$I_{\text{Scap}}(t, Q_{\text{Scap}}) = I_{\text{Scap}}^*(t, Q_{\text{Scap}}) = \frac{-2Q_{\text{Scapref}} C_{\text{Scap}} + (2C_{\text{Scap}} + 1) Q_{\text{Scap}}}{-(2C_{\text{Scap}} + 1)(t - t_f) + 2R_{\text{Scap}} C_{\text{Scap}}} \quad (11.90)$$

11.6.3

Optimal Control with Inequality Constraints on the Fuel Cell Power and on the Fuel Cell Power Rate11.6.3.1 **Constraints on the Fuel Cell Power**

In practice, the state and control variables of all control problems are bounded by physical consideration. For fuel cell, the power is limited

$$P_{FC\min} \leq P_{FC} \leq P_{FC\max} \quad (11.91)$$

Substituting Eq. (11.74) in Eq. (11.91), it results in

$$P_{FC\min} \leq P_{Load} - \frac{1}{C_{Scap}} Q_{Scap} I_{Scap} + R_{Scap} I_{Scap}^2 \leq P_{e1\max} \quad (11.92)$$

Therefore, if the supercapacitor current, which is expressed by the Eq. (11.90), verifies the inequality (Eq. (11.92)), it will constitute an optimal supercapacitor pack current trajectory

$$I_{Scap} = I_{Scap\text{wc}}^* = \frac{-2Q_{Scap\text{pref}}C_{Scap} + (2C_{Scap} + 1)Q_{Scap}}{-\left(2C_{Scap} + 1\right)(t - t_f) + 2R_{Scap}C_{Scap}} \quad (11.93)$$

However, if $P_{Load} - \frac{1}{C_{Scap}}Q_{Scap}I_{Scap}^* + R_{Scap}I_{Scap}^{*2} \geq P_{FC\max}$, P_{FC} will be fixed to $P_{FC\max}$ and we compute the new I_{Scap}

$$I_{Scap} = I_{Scap\text{wc}}^* = \frac{\frac{Q_{Scap}}{C_{Scap}} - \sqrt{\left(\frac{Q_{Scap}}{C_{Scap}}\right)^2 - 4(P_{Load} - P_{FC\max})R_{Scap}}}{2R_{Scap}} \quad (11.94)$$

And, if $P_{Load} - \frac{1}{C_{Scap}}Q_{Scap}I_{Scap}^* + R_{Scap}I_{Scap}^{*2} \leq P_{FC\min}$, P_{FC} will be fixed to $P_{FC\min}$ and we compute the new I_{Scap}

$$I_{Scap} = I_{Scap\text{wc}}^* = \frac{\frac{Q_{Scap}}{C_{Scap}} - \sqrt{\left(\frac{Q_{Scap}}{C_{Scap}}\right)^2 - 4(P_{Load} - P_{FC\min})R_{Scap}}}{2R_{Scap}} \quad (11.95)$$

11.6.3.2 **Constraints on the Fuel Cell Power Rate**

The response time of the fuel cell is large compared to other energy sources. Consequently, it will not support important power (accelerations) during a long time. The PEMFC power variation is limited, as shown in Eq. (11.96).

$$\frac{dP_{FC}}{dt} \leq c_{wc} \quad (11.96)$$

Taking into account this inequality, the optimal supercapacitor pack current trajectory becomes

$$\begin{aligned}
 I_{Scap} &= I_{Scap_{wcf}}^* \\
 &= \begin{cases} \frac{\frac{Q_{Scap}}{C_{Scap}} - \sqrt{\left(\frac{Q_{Scap}}{C_{Scap}}\right)^2 - 4(P_{Load} - P_{FClim})R_{Scap}}}{2R_{Scap}} \\ I_{Scap_{wc}}^* \end{cases} \\
 &\quad \text{if } \frac{d\left(P_{Load} - \frac{1}{C_{Scap}}Q_{Scap} + R_{Scap}I_{Scap_{wcf}}^{*2}\right)}{dt} > c_{wc} \\
 &\quad \text{if } \frac{d\left(P_{Load} - \frac{1}{C_{Scap}}Q_{Scap} + R_{Scap}I_{Scap_{wc}}^{*2}\right)}{dt} \leq c_{wc}
 \end{aligned} \tag{11.97}$$

where P_{FClim} is computed from $\frac{dP_{FC}}{dt} = c_{wc}$.

Finally, the power management in the fuel cell vehicle by optimal control with constraints on the fuel cell power and on its rate can be expressed as

$$\begin{cases} \dot{Q}_{Scap} = -I_{Scap_f}^* \\ U_{Scap} = \frac{1}{C_{Scap}}Q_{Scap} - R_{Scap}I_{Scap_f}^* \\ P_{Scap} = U_{Scap}I_{Scap_f}^* \\ P_{FC} = P_{Load} - P_{Scap} \end{cases} \tag{11.98}$$

To simulate this system, the European speed cycle new european driving cycle (NEDC) is considered (Figure 11.40).

The load power profile P_{Load} is calculated from a mechanic characteristic of a fuel cell vehicle (Figure 11.41).

The simulation parameters are given by Table 11.4.

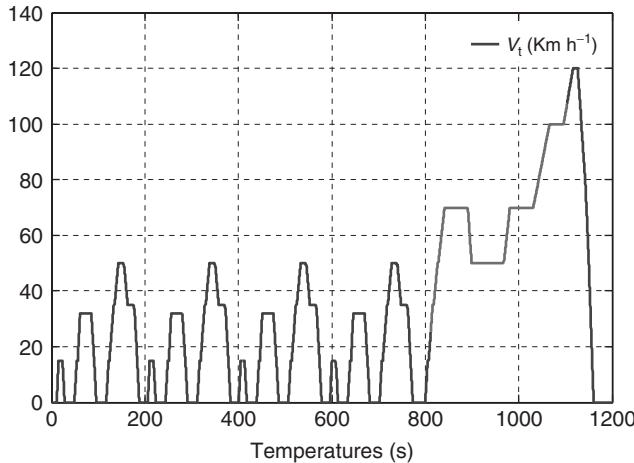


Figure 11.40 European speed cycle NEDC.

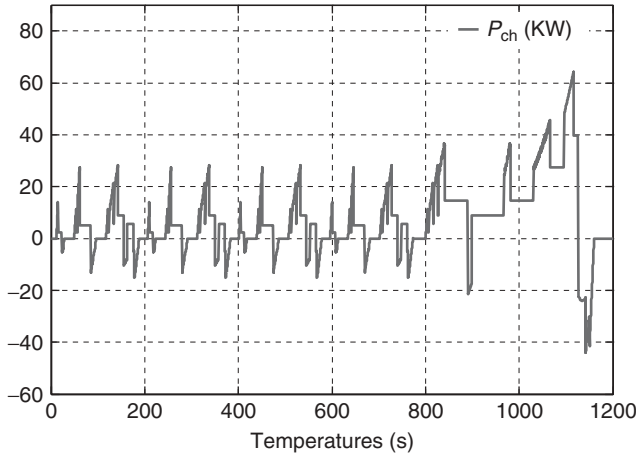


Figure 11.41 Power profile of fuel cell vehicle corresponding to the European speed cycle NEDC.

Table 11.4 Simulation parameters.

Constants	Value
$P_{FC_{min}}$ (kW)	1.2
$P_{FC_{max}}$ (kW)	40
t_f (s)	1200
c_{wc} ($W s^{-1}$)	500

The supercapacitor pack power, fuel cell power, and load power are mentioned in Figure 11.42.

We notice that the fuel cell power does not exceed the value $P_{FC_{max}}$ and its rate does not exceed the value c_{wc} .

The supercapacitor pack voltage is shown in Figure 11.43.

It can be seen that the supercapacitor pack voltage at ($t = 1200$ s) is stabilized at 355.5 V corresponding to the charge quantity reference.

11.6.4

Power Management of Fuel Cell Vehicle by Optimal Control Associated to Sliding Mode Control

The power management in a fuel cell vehicle discussed in the last section permits to calculate the reference supercapacitor pack current trajectory; this current is regulated by the bidirectional DC/DC converter. The DC link voltage is regulated by the unidirectional DC/DC converter (Figure 11.44)

In Figure 11.44, the control signals of the transistors T_1 , T_2 , and T_3 are respectively u_1 , u_2 , and u_3 . The regulation of the DC link voltage is realized by the

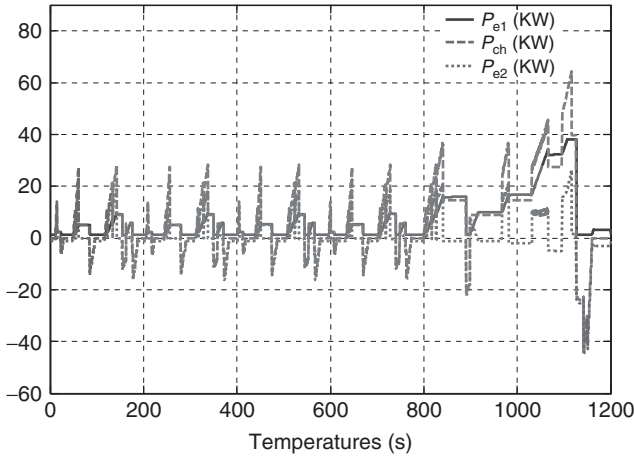


Figure 11.42 The supercapacitor pack power, fuel cell power, and load power.

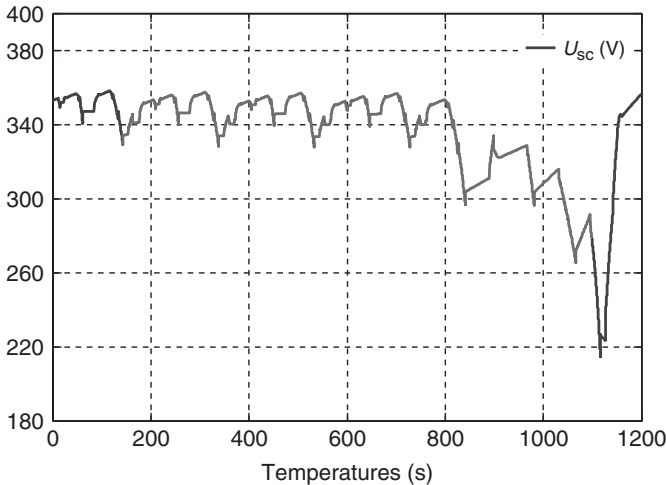


Figure 11.43 Variation of the supercapacitor pack voltage according to the time during the NEDC profile.

u_1 control signal. When the second converter (connected to the supercapacitors) functions in boost mode, the control signal u_2 is on and the control signal u_3 is off. When it functions in buck mode, the control signal u_2 is off and the control signal u_3 is on. These converters are nonlinear; it requires a robust control and rapid transient response. The control must be adapted to the variable structure systems and stable to the load current fluctuation. These advantages can be gathered in the control by sliding mode. Indeed, sliding mode control (see, for instance, [48]) makes it possible for state variables of the system to follow a desired trajectory. In this case, the control is performed using the sliding mode. This is expressed

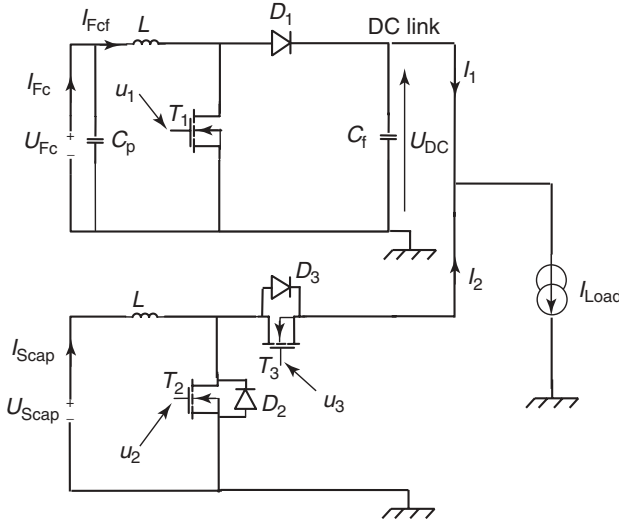


Figure 11.44 The fuel cell vehicle converter.

according to the state variables and their equilibrium values. According to the sign of the sliding surface σ , the control signal u_c commutates between two values $u_{c_{\max}}$ and $u_{c_{\min}}$.

$$u_c = \begin{cases} u_{c_{\max}} & \text{if } \sigma < 0 \\ u_{c_{\min}} & \text{if } \sigma > 0 \end{cases} \quad (11.99)$$

In order to use the sliding mode control, we first define the sliding surfaces for each converter. The first sliding surface is related to the boost converter connected to the fuel cell, is expressed as [49–51].

$$\sigma_1 = k_1 (\bar{U}_{DC_e} - U_{DC}) + k_2 (I_{FC_{fe}} - I_{FC_f}) + k_3 \int (\bar{U}_{DC_e} - U_{DC}) dt \quad (11.100)$$

k_1 , k_2 , and k_3 are constant and are determined to optimize the regulation of the DC link voltage. The current $I_{FC_{fe}}$ is given by

$$I_{FC_{fe}} = \frac{\left[I_{Load} \bar{U}_{DC_e} - \left(\frac{1}{C_{Scap}} Q_{Scap} - R_{Scap} I_{Scap_f}^* \right) I_{Scap_f}^* \right]}{U_{FC}} \quad (11.101)$$

The second sliding surface is related to the bidirectional converter when it functions in boost mode ($I_{Scap}^* \geq 0$). This sliding mode surface (σ_2) depends on the supercapacitor current. It is given by the following expression:

$$\sigma_2 = I_{Scap_f}^* - I_{Scap} \quad (11.102)$$

The third sliding surface is related to the bidirectional converter when it functions in buck mode ($I_{Scap}^* < 0$).

$$\sigma_3 = -I_{Scap_f}^* + I_{Scap} \quad (11.103)$$

For reasons of security of switches, the control signal's frequency is fixed to $f = 15$ kHz. The duty cycle of u_1 is given by

$$u_{1DC} = \begin{cases} 0.9 & \text{si } \sigma_1 < 0 \\ 0.1 & \text{si } \sigma_1 > 0 \end{cases} \quad (11.104)$$

The duty cycle of u_2 is given by

$$u_{2DC} = \begin{cases} 0.9 & \text{si } \sigma_2 < 0 \\ 0.1 & \text{si } \sigma_2 > 0 \end{cases} \quad (11.105)$$

The duty cycle of u_3 is given by

$$u_{3DC} = \begin{cases} 0.9 & \text{si } \sigma_3 < 0 \\ 0.1 & \text{si } \sigma_3 > 0 \end{cases} \quad (11.106)$$

This part consists in simulating the power management of the fuel cell vehicle by optimal control associated with sliding mode control in MATLAB/SIMULINK. The parameters of the studied converters are given in Table 11.5.

For this simulation, just a portion of the European speed cycle NEDC was considered (Figure 11.45).

The load current profile corresponding to the European speed cycle NEDC, the fuel cell current, and the supercapacitors pack current are given in Figure 11.46.

Table 11.5 Converter parameters.

Parameter	Intituled	Value	Unit
L	Inductance	3.3	mH
C_f	Capacitance	1.66	mF
C_p	Capacitance	1	mF

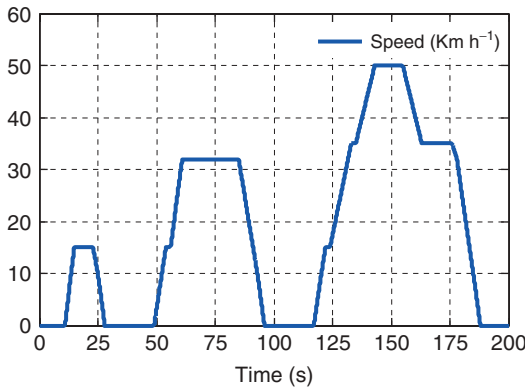


Figure 11.45 Portion of European speed cycle NEDC.

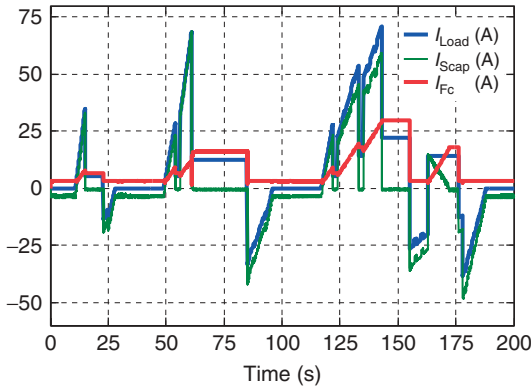


Figure 11.46 Load current profile, fuel cell current, and supercapacitor current.

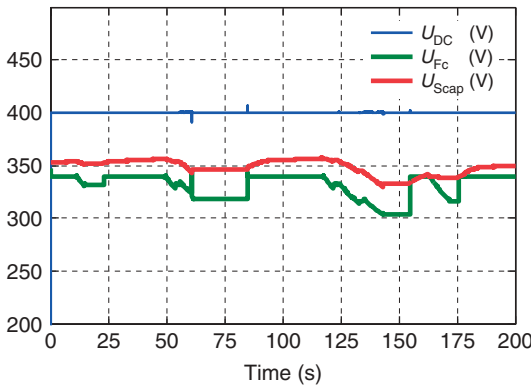


Figure 11.47 DC link voltage, fuel cell voltage, and supercapacitor pack voltage.

The regulated DC link voltage, fuel cell voltage, and supercapacitors pack voltage are given in Figure 11.47.

11.6.5

Conclusion

An optimal control of the power management in the fuel cell vehicle coupled to the sliding mode is established. The optimal control allows calculating the reference power of the supercapacitors, which minimizes the energy provided by the fuel cell, starting from the power demanded by the load (motorization and auxiliaries). The reference supercapacitor pack current trajectory is regulated by the sliding mode control via the bidirectional DC/DC converter. This control method takes into account the constraints imposed on the system. These constraints relate to the limitation of the power of the fuel cell and its dynamic response.

References

- Kötz, R. and Carlen, M. (2000) Principles and applications of electrochemical capacitors. *Electrochim. Acta*, **45**, 2483–2498.
- Taberna, P.L., Simon, P., and Fauvarque, J.F. (2003) Electrochemical characteristics and impedance spectroscopy studies of carbon-carbon supercapacitors. *J. Electrochem. Soc.*, **150** (3), A292–A300.
- Kurzweil, P. and Fischle, H.J. (2004) A new monitoring method for electrochemical aggregates by impedance spectroscopy. *J. Power. Sources*, **127**, 331–340.
- Rafik, F., Gualous, H., Gallay, R., Crausaz, A., and Berthon, A. (2007) Frequency, thermal and voltage supercapacitor characterization and modeling. *J. Power. Sources*, **165**, 928–934.
- de Levie R. (1967) *Advances in Electrochemistry and Electrochemical Engineering*, ed. P. Delahay and C.T. Tobias, Interscience, New York, Vol. 6, pp. 329–397.
- Verbrugge, M. and Liu, P. (2005) Microstructural analysis and mathematical modeling of electric double-layer supercapacitors. *J. Electrochem. Soc.*, **152** (5), D79–D87.
- IEC (2006) 62391-1. *Fixed Electric Double Layer Capacitors for use in Electronic Equipment – Part 1: Generic Specification*, Ed. 1.
- IEC (2006) 62391-2. *Fixed Electric Double Layer Capacitors for use in Electronic Equipment – Part 2: Sectional Specification – Electric Double Layer Capacitors for Power Application*, Ed. 1.
- IEC (2006) 62391-2-1. *Fixed Electric Double Layer Capacitors for use in Electronic Equipment – Part 2-1: Blank Detail Specification – Electric Double Layer Capacitors for Power Application – Assessment Level EZ*, Ed. 1.
- Hahn, M., Barbieri, O., Campana, P., Kötz, R., and Gallay, R. (2006) Carbon based double layer capacitors with aprotic electrolyte solutions: the possible role of intercalation/insertion processes. *Appl. Phys. A*, **82**, 633–638.
- Salitra, G., Soffer, A., Eliad, L., Cohen, Y., and Aurbach, D. (2000) Carbon electrodes for double-layer capacitors. *J. Electrochem. Soc.*, **147**, 2486–2493.
- Kötz, R., Hahn, M., and Gallay, R. (2006) Temperature behaviour and impedance fundamentals of supercapacitors. *J. Power. Sources*, **154**, 550–555.
- Alcicek, G., Gualous, H., Venet, P., Gallay, R., and Miraoui, A. (2007) Experimental Study of Temperature Effect on Ultracapacitor Ageing. European Conference on Power Electronics and Applications 2007, Vols 1–10, pp. 5123–5129.
- Gualous, H., Bouquain, D., Berthon, A., and Kauffmann, J.M. (2003) Experimental study of supercapacitor serial resistance and capacitance variations with temperature. *J. Power. Sources*, **123**, 86–93.
- Hermann, V., Schneuwly, A., and Gallay, R. (2001) High Power Double-Layer Capacitor Developments and Applications, ISE2001, San Francisco, CA.
- Schiffer, J., Linzen, D., and Sauer, D.U. (2006) Heat generation in double layer capacitors. *J. Power. Sources*, **160**, 765–772.
- Diab, Y., Venet, P., Gualous, H., and Rojat, G. (2009) Self-discharge characterization and modelling of supercapacitors used for power electronics applications. *IEEE Trans. Power Electron.*, **24** (2), 510–517.
- Bejan, A. (1984) *Convection Heat Transfer*, John Wiley & Sons, Inc., New York, p. 492148 illustrations, 387 references.
- Gualous, H., Louahlia-Gualous, H., and Gallay, R. (2009) Thermal modelling and experimental characterization of supercapacitor for hybrid vehicle applications. *IEEE Trans. Ind. Appl.*, **45** (3), 1035–1044.
- Gallay R. and Gualous H. in *Carbons for Electrochemical Energy Storage and Conversion Systems*, Chapter 11, ed. F. Béguin and E. Frackowiak, CRC Press (2009), pp. 430–468.
- Kötz, R., Ruch, P.W., and Cericola, D. (2010) Ageing and failure mode of

- electrochemical double layer capacitors during accelerated constant load tests. *J. Power. Sources*, **195**, 923–928.
22. Hahn, M., Kötz, R., Gallay, R., and Siggel, A. (2006) Pressure evolution in propylene carbonate based electrochemical double layer capacitors. *Electrochim. Acta*, **52**, 1709–1712.
 23. Miller, J.R., Klementov, A., and Butler, S. (2006) Electrochemical Capacitor Reliability in Heavy Hybrid Vehicles. Proceedings of the 16th International Seminar On Double Layer Capacitors and Similar Energy Storage Devices, Deerfield Beach, FL, p. 218.
 24. Goltser, I., Butler, S., and Miller, J.R. (2005) Reliability Assessment of Electrochemical Capacitors: Method Demonstration Using 1-F Commercial Components. Proceedings of the 15th International Seminar On Double Layer Capacitors and Similar Energy Storage Devices, Deerfield Beach, FL, p. 215.
 25. Yurgil, J. (2006) Ultracapacitor useful life prediction. US Patent /2006/012378, General Motors Corporation.
 26. Kurzweil, P. and Chwistek, M. (2008) Electrochemical stability of organic electrolyte in supercapacitors: spectroscopy and gas analysis of decomposition products. *J. Power. Sources*, **176**, 555–567.
 27. Kurzweil, P., Frenzel, B., and Gallay, R. (2005) Capacitance Characterization Methods and Ageing behavior of Supercapacitors. Proceedings of the 15th International Seminar On Double Layer Capacitors, Deerfield Beach, USA, p. 14.
 28. Hahn, M., Würsig, A., Gallay, R., Novák, P., and Kötz, R. (2005) Gas evolution in activated carbon/propylene carbonate based double-layer capacitors. *Electrochem. Commun.*, **7**, 925–930.
 29. Xu, K. (2004) Nonaqueous liquid electrolytes for lithium-based rechargeable batteries. *Chem. Rev.*, **104**, 4303–4417.
 30. Azaïs, P., Duclaux, L., Florian, P., Massiot, D., Lillo-Rodenas, M.A., Linares-Solano, A., Peres, J.P., Jehoulet, C., and Béguin, F. (2007) Causes of supercapacitors ageing in organic electrolyte. *J. Power. Sources*, **171**, 1046–1053.
 31. Kötz, R., Hahn, M., Ruch, P., and Gallay, R. (2008) Comparison of pressure evolution in supercapacitor devices using different aprotic solvents. *Electrochem. Commun.*, **10**, 359–362.
 32. Hardwick, L., Hahn, M., Ruch, P., Holzapfel, M., Scheifele, W., Buqa, H., Krumeich, F., Novák, P., and Kötz, R. (2006) An in situ Raman study of the intercalation of supercapacitor-type electrolyte into microcrystalline graphite. *Electrochim. Acta*, **52**, 675–680.
 33. Hahn, M., Barbieri, O., Gallay, R., and Kötz, R. (2006) A dilatometric study of the voltage limitation of carbonaceous electrodes in aprotic EDLC type electrolytes by charge-induced strain. *Carbon*, **44**, 2523–2533.
 34. Mizutani, A.Y., Okamoto, T., Taguchi, T., Nakajima, K., and Tanaka, K. (2003) Life Expectancy and Degradation behavior of Electric Double Layer Capacitor. Proceedings of the 7th International Conference on Properties and Applications of Dielectric Materials, Nagoya, June 2003.
 35. Lin, C.C., Peng, H., and Grizzle, J.W. (2002) Power Management Strategy for a Parallel Hybrid Electric Truck. Proceedings of the 2002 Mediterranean Control Conference, Lisbon, Portugal, July 2002.
 36. Lin, C.C., Filipi, Z., Wang, Y., Louca, L., Peng, H., Assanis, D., and Stein, J. Integrated, Feed-Forward Hybrid Electric Vehicle Simulation in Simulink and its Use for Power Management Studies, SAE 2001-01-1334.
 37. Assanis, D., Delagrammatikas, G., Fellini, R., Filipi, Z., Liedtke, J., Michelena, N., Papalambros, P., Reyes, D., Rosenbaum, D., Sales, A., and Sasena, M. (1999) An optimization approach to hybrid electric propulsion system design. *Mech. Struct. Mach.*, **27** (4), 393–421.
 38. Kalan, B.A., Lovatt, H.C., Brothers, M., and Buriak, V. (2002) System Design and Development of Hybrid Electric Vehicles. Power Electronics Specialists Conference 2002, pp. 768–772.
 39. Rajagopalan, A., Washington, G., Rizzoni, G., and Guezennec, Y. (2001) Development of Fuzzy Logic and Neural Network Control and Advanced

- Emissions Modeling for Parallel Hybrid Vehicles, Center for Automotive Research, Intelligent Structures and Systems Laboratory, The Ohio-State University, Columbus, OH, December 2001.
40. West, M.J., Bingham, C.M., and Schofield, N. (2003) Predictive Control for Energy Management in All/More Electric Vehicle with Multiple Energy Storage Units, EPE 2003-Toulouse.
 41. Scordia, J. (2004) Approche systématique de l'optimisation du dimensionnement et de l'élaboration de lois de gestion d'énergie de véhicules hybrides. Thèse à l'université Henri Poincaré à Nancy 1, 10 Novembre 2004.
 42. Vahidi A., Stefanopoulou A., Peng H. (2005) Recursive least squares with forgetting for online estimation of vehicle mass and road grade: theory and experiments, *Veh. Syst. Dyn.*, **43** (1), 31–55.
 43. Dixon, J., Ortuzar, M., and Moreno, J. (2003) DSP Based Ultracapacitor System for Hybrid Electric Vehicles. Proceedings of 20th Electric Vehicle, 2003.
 44. Moreno, J., Ortuzar, M., and Dixon, J. (2006) Energy management system for an electric vehicle, using ultracapacitors and neural networks. *IEEE Trans. Ind. Electron.*, **53**, 614–623.
 45. Dietrich, P., Büchi, F., Tsukada, A., Bärtschi, M., Kötzi, R., Scherer, G.G., Rodatz, P., Garcia, O., Ruge, M., Wollenberg, M., Lück, P., Wiartalla, A., Schönfelder, C., Schneuwly, A., and Barrade, P. (2003) Hy.Power—a technology platform combining a fuel cell system and a supercapacitor, in *Handbook of Fuel Cells – Fundamentals, Technology and Applications* ISBN, John Wiley & Sons, Ltd, Chichester. ISBN: 0-471-49926-9
 46. Stengel, R.F. (1994) *Optimal Control and Estimation*, Dover Publications, New York.
 47. Hisham, A.K. (2004) *La Commande Optimale des Systèmes Dynamiques*, Hermès Science Publication, Lavoisier.
 48. Utkin, V.I. (1992) *Sliding Mode Control Optimization*, Springer-Verlag, Berlin.
 49. Maker, H., Gualous, H., and Outbib, R. (2006) Sliding Mode Control with Integral of Boost Converter by Microcontroller. CCA Contributed, IEEE CCA/CACSD/ISIC, München, Germany, 2006.
 50. Maker H., (2008) Optimisation et gestion d'énergie pour un système hybride: association Pile à Combustible et Supercondensateurs. Thèse soutenue à Belfort le 4 Novembre 2008.
 51. Maker, H., Gualous, H., and Outbib, R. (2008) Power Management for an Electric Propulsion System Using Fuel Cells. Proceedings of the 9th WSEAS International Conference on AUTOMATION and INFORMATION (ICAI'08) Bucharest, Romania, June 24–26, 2008.

12

Testing of Electrochemical Capacitors

Andrew Burke

12.1

Introduction

This chapter is concerned with testing large prototype and commercial electrochemical capacitor devices intended for various industrial and vehicle applications. Testing of these devices is usually done using DC test procedures similar to those used to test batteries. Much of the testing of materials and small laboratory devices has involved the application of cyclic voltammetry and AC impedance test approaches. These approaches, in most cases, utilize small currents and limited voltage ranges and/or AC frequencies and are intended primarily to determine the electrochemical characteristics of the materials and electrodes used in the capacitors. The initial section of the chapter discusses in some detail the DC test procedures as they are applied to testing electrochemical capacitors. Later sections in turn consider the testing of carbon/carbon and hybrid (asymmetric) devices and the relationship between the AC impedance and DC testing. Typical data for the capacitance, resistance, energy density, power capability, and cycle life of various types of devices are presented. Uncertainties in the interpretation of the test results are discussed, especially in the comparison of the power capabilities of electrochemical capacitors and high-power lithium batteries.

12.2

Summaries of DC Test Procedures

There are similarities and differences in the test procedures for electrochemical capacitors and high-power batteries. It is customary to perform constant current and constant power tests of both types of devices. From the constant current tests, the charge capacity (capacitance (F) and Ah) and resistance of the devices are determined. From the constant power tests, the energy storage characteristics (Wh kg^{-1} vs W kg^{-1} – the Ragone curve) are determined. The currents and powers to be used in the testing are selected such that the charge and discharge times are compatible with the capabilities of the devices being tested. In the case of the

Table 12.1 Performance characteristics of electrochemical capacitors.

1	Energy density (Wh kg^{-1} vs W kg^{-1})
2	Cell voltage (V) and capacitance (F)
3	Series and parallel resistance (Ω and $\Omega \text{ cm}^{-2}$)
4	Power density (W kg^{-1}) for a charge/discharge at 95% efficiency
5	Temperature dependence of resistance and capacitance especially at low temperatures (-20°C and lower)
6	Cycle life for full discharge
7	Self-discharge at various voltages and temperatures
8	Calendar life (h) at fixed voltage and high temperature ($40\text{--}60^\circ\text{C}$)

Table 12.2 Testing of electrochemical capacitors.

1	Constant current charge/discharge Capacitance and resistance for discharge times of 60 to 5 s.
2	Pulse tests to determine resistance
3	Constant power charge/discharge Determine the Ragone curve for power densities between 100 and at least 1000 W kg^{-1} for the voltage between V_{rated} and $1/2 V_{\text{rated}}$. Test at increasing W kg^{-1} until discharge time is less than 5 s. The charging is often done at constant current with a charge time of at least 30 s.
4	Sequential charge/discharge step cycling Testing done using the PSFUDS (pulsed simple Federal Urban Driving Schedule) test cycle with the maximum power step being $500\text{--}1500 \text{ W kg}^{-1}$. From the data, the round-trip efficiency for charge/discharge is determined.
5	Tests modules with at least 15–20 cells in series

capacitors, the test discharge times are usually in the range of 5–60 s and for the batteries several minutes to a significant fraction of an hour even for high-power batteries. The differences in the recharge times for the devices are also large. For example, the capacitors can be fully charged in 5–10 s without difficulty, but the high-power batteries require a minimum of 10–20 min for a complete charge even when the initial charge current is set at a maximum value. In addition to the constant current and constant power tests, the capacitors and batteries are tested using charge/discharge pulses of 5–15 s. For these tests, the current and power levels for the capacitors and high-power batteries are comparable (on a normalized basis). Test cycles [1, 2] consisting of a sequence of charge and discharge pulses (power density for a specified time) meant to simulate how the devices would be used in particular applications are used to test both capacitors and batteries. The tests to be performed on capacitors and batteries are summarized in Tables 12.1 and 12.2.

These general test procedures have been applied in different ways by various groups around the world to meet their special needs. It is of interest to look at

these different testing approaches in some detail. In particular, the test procedures utilized by the USABC (United States Advanced Battery Consortium), IEC (International Electrochemical Commission), and UC Davis (University of California Davis) are discussed and data obtained by each group presented.

12.2.1

USABC Test Procedures

The USABC is a consortium of the Big Three US auto companies – Ford, Chrysler, and General Motors – that work in conjunction with the United States Department of Energy (DOE) to develop and test advanced batteries and ultracapacitors for vehicle applications. The DOE test procedures for ultracapacitors were first presented in 1994 in Ref. [1] and later issued as USABC/DOE test procedures in Ref. [2]. The initial test procedures were developed as a means of characterizing evolving ultracapacitor devices with little attention given to specific automotive applications. The later USABC test procedures were written with hybrid-electric vehicle applications in mind and thus were intended to show whether a particular ultracapacitor technology could meet the USABC design requirements for start-stop and power-assist hybrid vehicles. For this reason, the test procedures are not specified in terms easily interpreted for general characterization testing of devices, but, nevertheless, they do result in a body of data from which the complete characteristics of devices can be determined.

The USABC test manual [2] is a complete set of test procedures for all the types of tests listed in Table 12.2. The manual specifies a series of constant current and constant power tests to characterize the ultracapacitors, but the tests are specified in terms more appropriate for batteries than ultracapacitors. By that is meant that the discharge rates are given as nC -based on an effective Ah rating, where $Ah = C_{dev} (V_{max} - V_{min})/3600$. The rated capacitance C_{dev} is measured at the 5 C rate, which for a capacitor is a very low rate (12 min discharge). In general, the USABC constant current and constant power testing is concentrated at relatively low rates for capacitors and does not extend to the limits of device performance in terms of discharge times. However, capacitance and resistance values for devices can be calculated from the USABC test data. The USABC test procedures also specify in detail self-discharge and cycle life tests.

As noted previously, the USABC test procedures are intended to evaluate ultracapacitors for hybrid vehicle applications. For this reason, the test procedures specify a series of pulse test cycles that are quite demanding. The energy efficiency and life cycle tests are performed at 100 C currents with depths of discharge of 10% (UC10) and 50% (UC50) in discharge pulses of 4 and 8 s. The USABC also has a high rate pulse characterization test that systematically discharges the capacitor by a sequence of discharge/charge pulses. The intent of these tests is to determine the resistance of a device as a function of state of charge (SOC) and the round-trip efficiency for the charge/discharge cycles. Data taken at UC Davis using the USABC pulse characterization test procedures are shown in Figure 12.1.

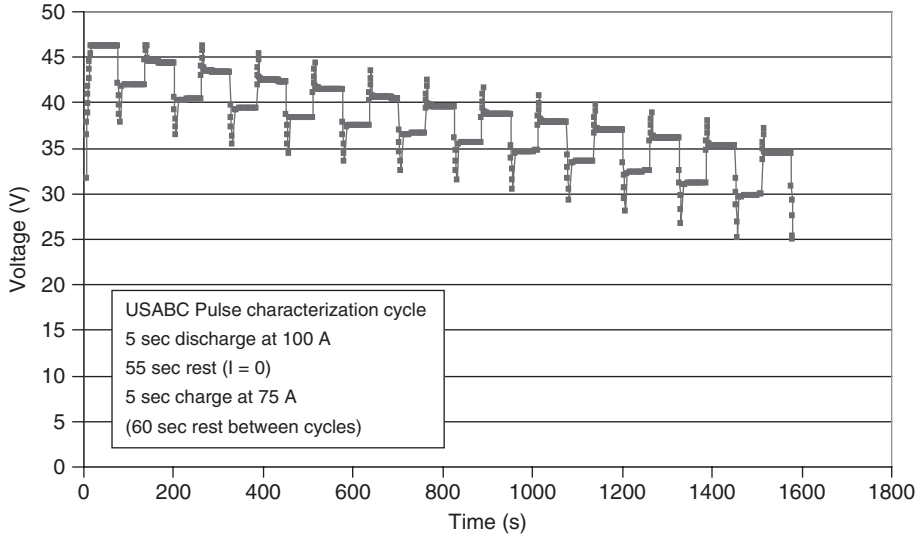


Figure 12.1 USABC pulse characterization test of a 46 V (14 cells in series) module.

12.2.2

IEC Test Procedures

The IEC has developed a test procedure [3, 4] for determining the capacitance C and resistance R of electrochemical capacitors. These procedures do seem to be applications oriented and are intended to yield the characteristics of specific devices. Recently, the IEC has tasked a committee with representatives from Europe, Asia, and the United States to update their test procedures to include vehicle applications. The objective of the IEC activity was quite limited in that it specified a single test intended to determine the performance of the capacitor at a single current – that at which the efficiency in charge and discharge was 95%. It was assumed that the capacitors to be tested behave as ideal double-layer capacitors with constant C and R . The resultant relationships for the test current are the following:

$$I_{\text{charge}} = \frac{V_0}{38R}, \quad I_{\text{discharge}} = \frac{V_0}{40R}, \quad V_0 = \text{rated voltage of the device}$$

The energy and power are to be calculated from the following idealized equations:

$$\text{Energy } E = \frac{1}{2} C V_0^2, \quad \text{Power } P = \frac{V_0^2}{4R}$$

The capacitance is calculated from the measured energy between specified voltage limits ($0.9 V_0$ and $0.7 V_0$) as follows:

$$C = 2E_{\text{meas.}} / [(0.9 V_0)^2 - (0.7 V_0)^2]$$

The resistance R is calculated from the voltage drop at the initiation of the discharge at $I_{\text{discharge}}$ assuming that the voltage versus time trace is linear with time. The IEC

Table 12.3 Application of the IEC test procedure to various ultracapacitor devices.

	Capacitance (F) IEC (1)	Capacitance (F) Full V (2)	Efficiency (3)(4)	Efficiency (3)(5)	R (mΩ) (4)	R (mΩ) meas (5)	Average current (A)
LS Cable	3045	3071	83.5/0.91	85/0.92	0.37	0.44	194
MaxWell	3202	3168	88.4/0.94	89.2/0.94	0.44	0.45	157
Ness	3254	3285	86.9/0.92	88.6/0.93	0.47	0.45	147
Ness-term conn	3253	3266	85/0.92	87/0.93	0.28	0.275	245
JSR	2070	1900	89.1/0.94	89.5/0.95	2.6	2.7	37

(1) Capacitance from $0.9 V_{\max}$ to $0.7 V_{\max}$ (2.43 to 1.89 V). For JSR from 3.48 to 2.84.

(2) Full V means discharge from V rated to 1.35 V.

(3) $x/y - x$ = round trip effic., y = charge or discharge effic. = sq root (round-trip effic.)

(4) Assumed resistance

(5) Measured resistance

procedure specifies the rest periods at the end of charge and discharge as 300 s. The charge and discharge are performed between V_0 and $V_0/2$. The energy efficiency for the charge/discharge cycle is calculated from the voltage and current data and compared with the requirement of 90% (95% for each of the charge/discharge steps).

The IEC test procedure is quite limited in scope, but as shown in Table 12.3, it appears to be a useful approach for characterizing devices if an accurate estimate of their resistance is known. Otherwise, an initial test is needed to measure the resistance.

12.2.3

UC Davis Test Procedures

Most of the data presented in this chapter have been obtained using test procedures utilized in the Hybrid Vehicle Power Systems Laboratory at UC Davis. These procedures are based primarily on those presented in Ref. [1] and are, therefore, well suited for the evaluation of the performance of devices of all sizes and states of development including commercial devices and those intended for use in hybrid-electric vehicles. The intent of the testing at UC Davis is summarized in Table 12.1 and the series of tests performed on the devices are summarized in Table 12.2.

The test conditions for a particular device are set on the basis of its capacitance, resistance, and weight. These values are provided initially by the developer/manufacturer of the devices to be tested. The general philosophy of the testing is to test the devices to their limit of performance in terms of currents (A) and power (W) consistent with the voltage and temperature limits set by the

Table 12.4 Summary of the performance characteristics of ultracapacitor devices.

Device	V rated	C (F)	R (mΩ)	RC (s)	Wh kg ^{-1a}	W kg ⁻¹ (95%) ^b	W kg ⁻¹ matched impedance	Weight (kg)	Volume (l)
Maxwell*	2.7	2885	0.375	1.08	4.2	994	8836	0.55	0.4
Maxwell	2.7	605	0.90	0.55	2.35	1139	9597	0.20	0.2
A PowerCap**	2.7	55	4	0.22	5.5	5695	50625	0.009	—
APower Cap**	2.7	450	1.4	0.58	5.89	2569	24595	0.057	0.045
Ness	2.7	1800	0.55	1.00	3.6	975	8674	0.38	0.277
Ness	2.7	3640	0.30	1.10	4.2	928	8010	0.65	0.514
Ness (cylindrical)	2.7	3160	0.4	1.26	4.4	982	8728	0.522	0.38
Carbon Tech Non-acetonitrile	2.85	1600	1.0	1.6	5.8	1026	9106	0.223	—
Asahi Glass (propylene carbonate)	2.7	1375	2.5	3.4	4.9	390	3471	0.210 (estimated)	0.151
Panasonic (propylene carbonate)	2.5	1200	1.0	1.2	2.3	514	4596	0.34	0.245
EPCOS	2.7	3400	.45	1.5	4.3	760	6750	0.60	0.48
LS Cable	2.8	3200	0.25	0.80	3.7	1400	12400	0.63	0.47
BatScap	2.7	2680	0.20	0.54	4.2	2050	18225	0.50	0.572
Power Systems (activated carbon, propylene carbonate)**	2.7	1350	1.5	2.0	4.9	650	5785	0.21	0.151
Power Systems (graphitic carbon, propylene carbonate)**	3.3	1800	3.0	5.4	8.0	486	4320	0.21	0.15
Fuji Heavy Industry-hybrid (AC/graphitic Carbon)**	3.3	1500	1.7	2.5	6.0	776	6903	0.23	0.15
JSR Micro (AC/graphitic carbon)**	3.8	1800	1.5	2.6	9.2	1025	10375	0.232	0.143
	3.8	1000	4	4	11.2	900	7987	0.113	0.073
	3.8	2000	1.9	3.8	12.1	1038	9223	0.206	0.132

^aEnergy density at 400 W kg⁻¹ constant power, v rated-1/2 V rated.

^bPower based on $P = 9/16 \times (1 - EF) \times V^2 / R$. EF = efficiency of discharge.

* Except where noted, all the devices use acetonitrile as the electrolyte.

** All device except those with ** are packaged in metal containers, these devices are in laminated pouches.

manufacturer. The testing includes constant current and constant power charge and discharge tests as well as pulse current and pulse cycle testing. A summary of recent test results [5–7] for various devices tested at UC Davis is given in Table 12.4.

12.3

Application of the Test Procedures to Carbon/Carbon Devices

In this section, the various test procedures discussed in the previous section are applied to carbon/carbon capacitors to determine their capacitance, resistance, energy density, and power capability. These devices use activated carbon in both electrodes and in nearly all cases, an organic electrolyte. The dominant energy storage mechanism in these devices is charge separation (double-layer capacitance).

12.3.1

Capacitance

The capacitance of a device can be determined directly from constant current discharge data. A typical V versus time trace for a carbon/carbon double-layer capacitor is shown in Figure 12.2. By definition,

$$C = \frac{I}{dV/dt} \quad \text{or} \quad C = I \left(\frac{t_2 - t_1}{V_1 - V_2} \right)$$

where subscripts 1 and 2 refer to two times during the discharge.

As the voltage trace is not exactly linear, the value of C calculated depends to some extent on the values of V_1 and V_2 used. As noted previously, the IEC procedure specifies that $V_1 = 0.9 V_0$ and $V_2 = 0.7 V_0$. Other choices for voltage range that have been used are V_0 to $V_0/2$ and V_0 to 0. When V_0 is used, it is important to include the IR drop in the determination of the effective V_1 value. As shown in Table 12.5, the differences in the calculated capacitance C are not large for the various selected voltage ranges. The results in Table 12.5 indicate that the determination of the capacitance of devices is relatively insensitive to the test procedure.

12.3.2

Resistance

The resistance of a capacitor or battery can be determined using one of the several methods.

- IR drop at the initiation of a constant current discharge
- Current pulses (5–30 s) at specified states of charge
- Voltage recovery at the interruption of a discharge or charge current
- Measurement of the AC impedance at 1 kHz.

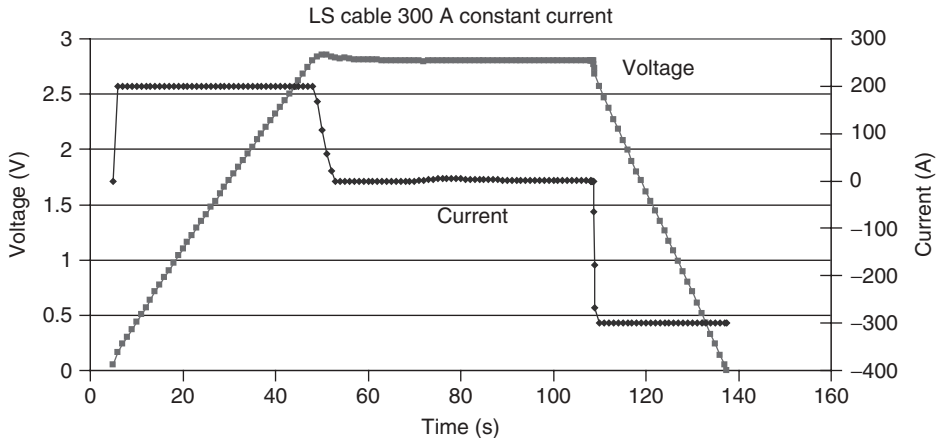


Figure 12.2 Voltage-time trace for a carbon/carbon ultracapacitor.

Table 12.5 Effect of voltage range and test current on the measured capacitance using the UC Davis and IEC test procedures.

	V_0 to 0 V				V_0 to $V_0/2$			
Device/developer								
3000 F/Maxwell	100 A	2880 F	200 A	2893 F	100 A	3160 F	200 A	3223 F
3000 F/Nesscap	50 A	3190 F	200 A	3149 F	50 A	3214 F	200 A	3238 F
450 F/APowerCap	20 A	450 F	40 A	453 F	20 A	466 F	40 A	469 F
		3.8 to 2.2 V		—		3.8 to 2.6 V		—
2000 F/JSR Micro	80 A	1897 F	200 A	1817 F	80 A	1941 F	200 A	1938 F

Device	Capacitance (F)	
	IEC 0.9 V_0 to 0.7 V_0	V_0 to 0
LS Cable	3045	3071
Maxwell	3202	3166
Ness	3254	3285
JSR	2070	1900 (3.8 to 2.2 V)

The method specified by both the IEC and the USABC test procedures as well as that used routinely at UC Davis involves analysis of the IR drop and voltage variation at the initiation of a constant current discharge. Determination of the resistance of the capacitor is complicated by the fact that the voltage decreases because of both the resistance and capacitance of the device. In addition, owing to the porous

Solution of the partial differential equations for the electron current in the solid carbon and the ion current in the electrolyte through the porous electrode. The voltage and currents are a function of x (position in electrode) and time. The solution for V is the following:

$$V = V_0 - I \times t / C_{\text{cell}} - I \times R_{\text{ss}} \left\{ 1 - (4/\pi^2) (2/3 + L_{\text{sep}} / L_{\text{electrode}}) \times A(t') \right\} *$$

$$\text{where } A(t') = \sum_{n=0}^{\infty} 1/n^2 e^{-n^2 t'}, \quad A(t' = \infty) = 0$$

$$t' = t/\tau, \quad \tau = 3/\pi^2 R_{\text{ss}} C_{\text{cell}}$$

* Assumes capacitance per unit volume and conductivities are constant.

$$R_{\text{ss}} = 2/3 \times L_{\text{electrode}} \times \text{effective resistivity of electrolyte} + \text{contact resistance}$$

$$R(t=0) = \text{contact resistance} + 2L_{\text{electrode}} / A_x (\sigma_{\text{carbon}} + \sigma_{\text{electrolyte}}) + L_{\text{sep}} / A_x \sigma_{\text{electrolyte}},$$

$$R_0 = 2L/A_x \sigma_{\text{carbon}}$$

Figure 12.3 Transient solution for the resistance of an ultracapacitor cell [8, 9].

character of the electrode, the resistance of the capacitor varies with time until the current distribution in the electrodes is fully established. This problem has been analyzed mathematically [8, 9]. The results of the analysis are shown in Figure 12.3, which indicates that the steady-state resistance R is not approached until several RC time constants into the discharge. The initial value of the resistance R_0 can be as low as $1/2$ the steady-state value.

As shown in Figure 12.4, the voltage–time trace does not become linear immediately at the initiation of the discharge, meaning that the use of the initial IR drop to calculate the cell resistance results in a value of R significantly less than the steady-state value, which is the desired quantity. A good estimate of the steady-state resistance can be obtained by extrapolating the linear portion of the voltage–time trace back to $t = 0$ and utilizing that IR drop value to calculate R .

For many applications of ultracapacitors, it is the steady-state resistance that is the resistance most relevant for the calculation of power capability/electrical losses/heating and not the R_0 value, which is smaller. It is important to define what resistance value is being reported. The dependence of resistance on discharge time at the initiation of a discharge is shown in Figure 12.5.

Another reliable method of determining the DC resistance of a capacitor is the current pulse method in which a short pulse (5–10 s) is applied to the device. In fact, for batteries, this is probably the only reliable method to determine the resistance using most battery testers. The pulse can be either a discharge or a charge pulse. The effective resistance ($R = \Delta V/I$) can vary with time through the pulse depending on the response time of the tester and/or mechanisms occurring in the device. It is, of course, greatly preferred if the former is negligible and only the latter is important. Unfortunately, this is often not the case. As shown in Figure 12.6, for a 1600 F device, the pulse tests show clearly the change in resistance from R_0 to R_{ss} .

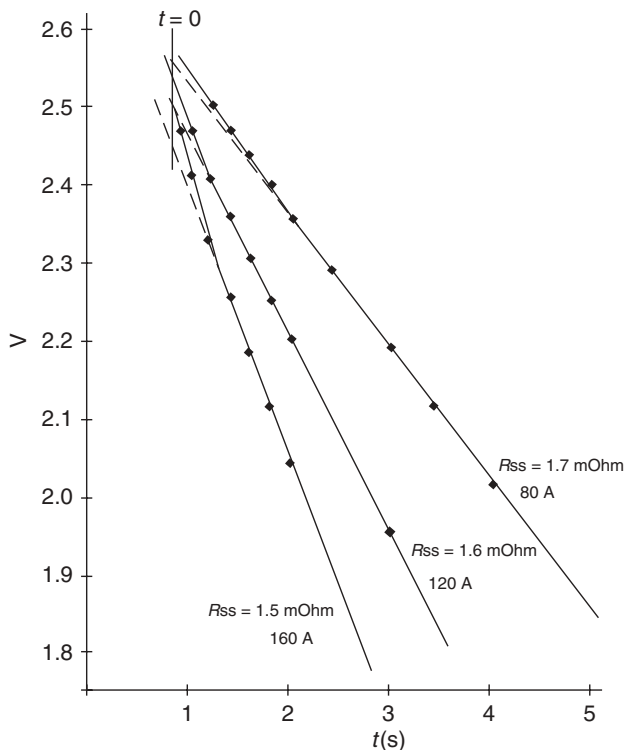


Figure 12.4 Method for determining the steady-state resistance by extrapolating the voltage trace to $t = 0$ (APowerCap 450 F cell).

The resistance of a capacitor or battery can also be inferred from the recovery of the voltage at the end of a current pulse when the current is removed ($I = 0$). Some researchers [10] prefer this method rather than that involving the initiation of the pulse because the current is zero and the effect of the capacitance of the device on the voltage is not present. However, there is the effect of the charge redistribution in the device with time at $I = 0$, and this effect on the voltage is both significant and not well understood. As a result, there is an uncertainty as to the time after the setting of $I = 0$ at which the voltage should be read and R calculated from $\Delta V/I$. This effect is illustrated in Figure 12.7. Comparing Figures 12.6 and 12.7 indicates that the current initiation and interruption methods yield the same value of resistance for the R_0 and R_{ss} . The voltage recovery time seems to be relatively short – being about equal to the RC time constant of the device tested. Additional comparisons of the steady-state resistances obtained using the two approaches are shown in Tables 12.6 and 12.7 for two capacitors. Clearly, either method can be used to measure the resistance of electrochemical capacitors, but the current interruption method is easier to implement in most cases.

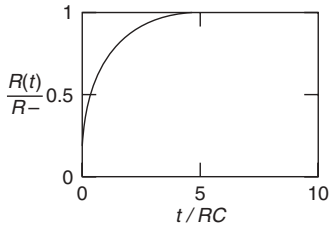


Figure 12.5 Change of resistance with time at the initiation of a discharge of an electrochemical capacitor [8].

The time required to achieve steady state resistance during constant current cycling. At one time constant τ , the resistance is at 70% of its steady state value.

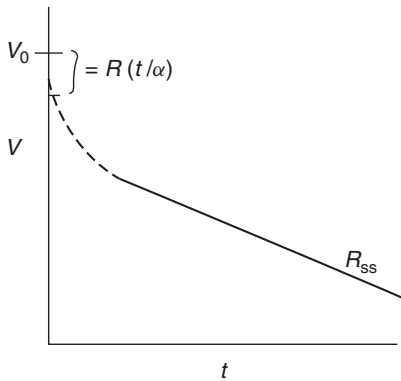


Table 12.6 Resistance of the 1600 F Skeleton Technologies capacitor using the current initiation and interrupt methods.

Current (A)	Voltage at interrupt	Resistance at current initiation at 2.7 V (m Ω)	Resistance at current interrupt (m Ω)
60	2.3	1.2	1.3
	1.3	—	1.3
100	2.3	1.35	1.4
	1.3	—	1.2
150	2.3	1.38	1.3
	1.3	—	1.2

For ultracapacitors, it is common for manufacturers to list the resistance measured with an AC impedance meter at 1 kHz. This value of resistance is always significantly lower than the DC value often by about a factor of 2. The power capability of devices should not be calculated using the AC impedance value of the resistance.

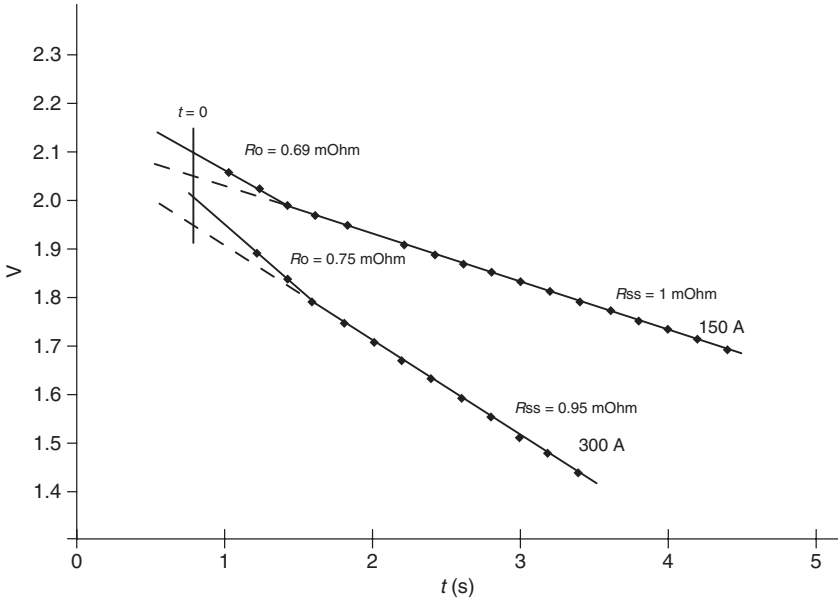


Figure 12.6 Voltage and resistance during a current pulse (Carbon Skeleton Tech 1600 F device).

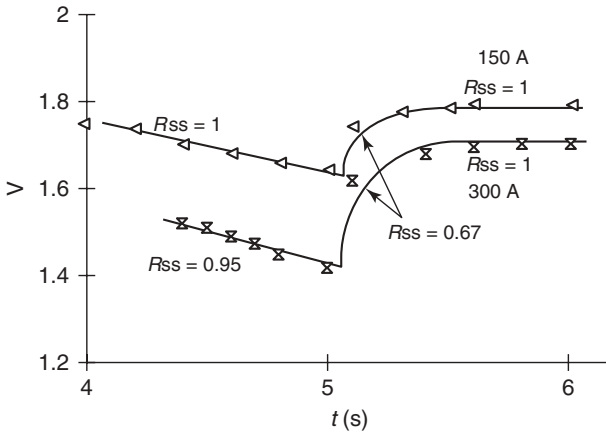


Figure 12.7 Resistance determination using voltage recovery after current interruption (Skeleton Tech 1600 F).

12.3.3 Energy Density

The total energy stored in a carbon/carbon capacitor can be calculated from the relationship $E = \frac{1}{2} CV_0^2$. If the voltage of the capacitor is restricted to the range V_0 to $V_0 / 2$, only 75% of the stored energy can be used. Hence, the usable energy

Table 12.7 Resistance of the Maxwell 2800 F capacitor using the current initiation and interrupt methods.

Current (A)	Voltage at interrupt	Resistance at current initiation at 2.7 V (mΩ)	Resistance at current interrupt (mΩ)
200	2.3	0.36	0.4
	1.3	—	0.4
300	2.3	0.37	0.37
	1.3	—	0.37
400	2.3	0.4	0.35
	1.3	—	0.375

density is given by

$$\text{Wh kg}^{-1} = \frac{3}{8} CV_0^2 / (\text{device weight})$$

This simple relationship is often used to calculate the energy density of ultracapacitors. The most reliable approach to determining the energy stored in a device, however, is to measure the Wh stored for a range of constant power densities W kg^{-1} . In general, tests should be made for power densities between 100 and 1000 W kg^{-1} or even higher for high-power devices. The plot of Wh kg^{-1} versus W kg^{-1} is called the *Ragone curve* for the device. Typical data for a commercially available 3000 F capacitor are shown in Table 12.8. Note that the energy density gradually decreases with W kg^{-1} . This is the case for all ultracapacitors. The value of energy density quoted by the device manufacturer is often calculated from the energy corresponding to $\frac{1}{2} CV_0^2$ using the rated voltage and specified capacitance. This value is too high as it is not the usable energy density and also it corresponds to a low power density of 100 W kg^{-1} or lower. As shown in Table 12.8, the effective capacitance C_{eff} of a device can decrease significantly with W kg^{-1} and often agrees with the value claimed by the manufacturer only for relatively low-power densities. Hence, combining the usable energy factor (0.75) and the effective capacitance reduction factor (0.9 from Table 12.8), the simple calculation of energy density from $\frac{1}{2} CV_0^2$ can overestimate the energy density of a device by at least 1/3. As shown in Table 12.9, for very high-power devices, the effective capacitance can remain constant for power densities almost to 2000 W kg^{-1} .

12.3.4

Power Capability

There is much confusion and unreliable information in the literature concerning the power capability of electrochemical capacitors and batteries [11]. This confusion stems to a large extent from the persistent use of the simple formula $P = V_0^2/4R$ to calculate the maximum power capability of electrochemical devices. This formula grossly overestimates the maximum power as it corresponds to the operation of

Table 12.8 Test data for the 3000 F Nesscap cylindrical device.

Constant current discharge data 2.7 V to 0.					
Current (A)	Time (s)	Capacitance	Resistance (mΩ)		
50	171	3190	—		
100	84.3	3181	0.44 (1)		
200	41.3	3157	0.42		
300	27	3140	0.37		
400	20	3150	0.40		
Constant power discharge data 2.7 to 1.35 V					
Power (W)	W kg ⁻¹ ^a	Time (s)	Wh	Wh kg ⁻¹	C _{eff}
100	192	84.8	2.36	4.52	3107
200	383	41.8	2.32	4.44	3055
300	575	27.1	2.26	4.33	2976
400	766	19.7	2.19	4.20	2884
500	958	15.4	2.14	4.1	2818
700	1341	10.9	2.12	4.06	2792

^aWeight of device 0.522 kg, dimensions of the device: 6 cm D , and 13.4 cm length $C_{\text{eff}} = 2(W \text{ s})/0.75 (2.7)^2$.

the device at the matched impedance point at which half of the discharge energy is electricity and half is in heat. The corresponding efficiency is 50%, which makes that operating condition unusable for nearly all applications. It is more reasonable to express the power capability of devices in terms of the pulse efficiency (EF). This can be done using the following relationships for ultracapacitors and batteries:

$$\text{Ultracapacitors : } P = \frac{9}{16}(1 - \text{EF}) \frac{V_0^2}{R}$$

$$\text{Batteries : } P = \text{EF} (1 - \text{EF}) \frac{V_{\text{oc}}^2}{R}$$

These relationships are derived in Ref. [11]. They are for pulse power and not constant power discharges. In the case of the ultracapacitor, the power pulse occurs at a voltage of $\frac{3}{4} V_0$ and is intended to remove only a relatively small fraction of the energy stored in the device. The battery relationship can be applied at any SOC by using the V_{oc} and R for that SOC. Note that the powers from both the matched impedance and efficiency EF relationships are proportional to V^2/R . The key parameters in determining the power capability are thus R and V_0 . High-power devices necessarily must have low resistance. Hence, once the resistance of a device is known, its power capability follows directly. It is unfortunate that device manufacturers often do not provide information concerning the resistance of their devices. This makes careful measurement of the resistance as discussed in the previous section very important.

Table 12.9 Test data for the Pouch packaged APowerCap device.

Constant current discharge data 2.7 V to 0.					
Current (A)		Time (s)	Capacitance (F)	Resistance (mΩ)	
10		120.5	450	Not calculate	
20		60.3	453	Not calculate	
40		30	453	Not calculate	
80		14.7	452	1.4	
120		9.6	455	1.4	
160		7.1	456	1.3	

Constant power discharges data 2.7 to 1.35 V					
Power (W)	W kg ⁻¹ ^a	Time (s)	Wh	Wh kg ⁻¹	C _{eff}
12.5	219	95.5	0.332	5.82	437
22	385	54.9	0.336	5.89	442
41.5	728	28.8	0.332	5.82	437
80.5	1412	14.6	0.326	5.72	429
120	2105	9.1	0.303	5.31	399

^aWeight of device –57 g as tested.

$$C_{\text{eff}} = 2 (W\text{-s})/0.75 (2.7)^2$$

For simple power pulses using capacitors, the ratio of the matched impedance to the efficiency power is $4/9/(1 - EF)$. In the case of batteries, the ratio is $1/4/[EF(1 - EF)]$. The ratios as functions of EF are given in Table 12.10. For ultracapacitors, the pulse efficiency specified by the USABC and IEC is 95%, which results in the usable maximum power being only about 1/10 the matched impedance power ($V^2/4R$). Hence for capacitors using the $V^2/4R$ formula to estimate the usable maximum power does not yield a realistic value for most applications, especially vehicle applications. Note that in Table 12.4 both the matched impedance and $EF = 95\%$ power densities are presented for the various devices.

The USABC has a procedure [2, 12] for calculating the power capability of ultracapacitors and batteries, which can be described as the min/max voltage approach. A pulse is envisioned initiated at a voltage $V_{\text{nom.OC}}$ and ending at V_{min} (discharge pulse) or V_{max} (charge pulse). The equations for calculating the power of the pulses are shown below.

- USABC method (batteries)

$$P_{\text{ABC}} = \frac{V_{\text{min}} (V_{\text{nom.OC}} - V_{\text{min}})}{R} \quad \text{discharge}$$

Table 12.10 Ratio of the efficiency and the matched impedance powers.

Efficiency (EF)	Ultracapacitor	Batteries
0.5	1.0	1.0
0.6	0.9	0.96
0.7	0.68	0.84
0.8	0.45	0.64
0.9	0.22	0.36
0.95	0.11	0.19

$$P_{ABC} = \frac{V_{\max} (V_{\max} - V_{\text{nom.OC}})}{R} \text{ charge}$$

$V_{\text{nom.OC}}$ is the open-circuit voltage at a mid-range SOC.

V_{\min} is the minimum voltage at which the battery is to be operated in discharge.

V_{\max} is the maximum voltage at which the battery is to be operated in charge (regen).

R is the effective pulse resistance of the battery measured from a 10 s pulse.

- **USABC method (ultracapacitors)**

$$P_{ABC} = \frac{V_{\min} (V_{\text{nom.OC}} - V_{\min})}{R} = \frac{1/8 V_{\text{rated}}^2}{R} \text{ discharge}$$

$$P_{ABC} = \frac{V_{\max} (V_{\max} - V_{\text{nom.OC}})}{R} = \frac{1/4 V_{\text{rated}}^2}{R} \text{ charge}$$

$V_{\text{nom.OC}}$ is the open-circuit voltage at a mid-range voltage ($3/4 V_R$).

V_{\min} is the minimum discharge voltage for the cap ($1/2 V_R$).

V_{\max} is the maximum regen voltage for the cap (V_R).

R is the pulse resistance of the ultracapacitor.

The USABC method is applied to capacitors and batteries in the following tables and the calculated maximum power compared with the value calculated using the pulse efficiency method as a function of pulse efficiency EF.

- **Ultracapacitor example**

$$V_{\text{rated}} = 2.7, \quad V_{\min} = 1.35, \quad V_{\max} = 2.7, \quad V_{\text{nom}} = 2.025$$

Efficiency EF	Discharge $P_{EF}/P_{\text{min/max}}$	Charge $P_{EF}/P_{\text{min/max}}$
0.95	0.225	0.11
0.90	0.45	0.23
0.85	0.675	0.34
0.80	0.9	0.45

- **Lithium-ion – iron phosphate example**

$$V_{\text{nom.OC}} = 3.2, V_{\text{min}} = 2, V_{\text{max}} = 4.0$$

Efficiency	EF (1 – EF)	Discharge $P_{\text{EF}}/P_{\text{min/max}}$	Charge $P_{\text{EF}}/P_{\text{min/max}}$
0.95	0.0475	0.20	0.15
0.90	0.09	0.38	0.29
0.85	0.1275	0.54	0.41
0.80	0.16	0.68	0.51
0.75	0.1875	0.80	0.60
0.70	0.21	0.90	0.67

- **Lithium-ion battery – nickel cobalt example**

$$V_{\text{nom.OC}} = 3.7, V_{\text{min}} = 2.5, V_{\text{max}} = 4.3$$

Efficiency	EF (1 – EF)	Discharge $P_{\text{EF}}/P_{\text{min/max}}$	Charge $P_{\text{EF}}/P_{\text{min/max}}$
0.95	0.0475	0.22	0.25
0.90	0.09	0.41	0.48
0.85	0.1275	0.58	0.68
0.80	0.16	0.73	0.85
0.75	0.1875	0.86	1.0
0.70	0.21	0.96	1.0

The results shown in the tables indicate that that the power capability is strongly dependent on efficiency EF and that the min/max voltage method yields power capabilities much higher than the pulse efficiency method until the pulse efficiency is 75–80%. The min/max values are only slightly lower than the simple matched impedance approach values. In comparing the power capability of various capacitors and batteries, it is important to know what resistance value and approaches/formulas were used.

12.3.5

Pulse Cycle Testing

As in many applications ultracapacitors experience highly transient operation, pulse cycle testing should be included in evaluating their performance

Table 12.11 Time power steps for the PSFUDS test cycle.

Step number	Time step duration (s)	Charge (C)/discharge (D)	$P/P_{\max} P_{\max} = 500 \text{ W kg}^{-1}$
1	8	D	0.20
2	12	D	0.40
3	12	D	0.10
4	50	C	0.10
5	12	D	0.20
6	12	D	1.0
7	8	D	0.40
8	50	C	0.30
9	12	D	0.20
10	12	D	0.40
11	18	D	0.10
12	50	C	0.20
13	8	D	0.20
14	12	D	1.0
15	12	D	0.10
16	50	C	0.30
17	8	D	0.20
18	12	D	1.0
19	38	C	0.25
20	12	D	0.40
21	12	D	0.40
22	> = 50	Charge to V_0	0.30

capabilities. Pulse cycles are a sequence of discharge and charge pulses of specified currents (A) or powers (W) of specified time duration (s). As discussed previously (Figure 12.1), the USABC has defined pulse cycle test procedures for hybrid-electric vehicle applications. Another pulse test cycle, the pulsed simple FUDS (PSFUDS), which was first defined in Ref. [1], has been used extensively at UC Davis to test ultracapacitors and high-power batteries. This test cycle, specified in terms of W kg^{-1} time steps, is given in Table 12.11. It can be utilized to test devices of all sizes and performance capabilities by adjusting the W kg^{-1} and time duration of the maximum power steps (6, 14, 18). The data of most interest in using the PSFUDS cycle is the round-trip efficiency, which is the ratio of the energy discharged to that charged during the cycle. Typical data using the PSFUDS cycle are shown in Tables 12.12 and 12.13. The round-trip efficiencies for the capacitors in most cases are greater than 95% even for peak power steps of 1000 W kg^{-1} .

Table 12.12 Round-trip efficiencies for the Ness 45V Module on the PSFUDS cycle [x].

Cycle ^a	Energy in (Wh)	Energy out (Wh)	Efficiency (%)
1	102.84	97.94	95.2
2	101.92	97.94	96.1
3	101.67	97.94	96.3

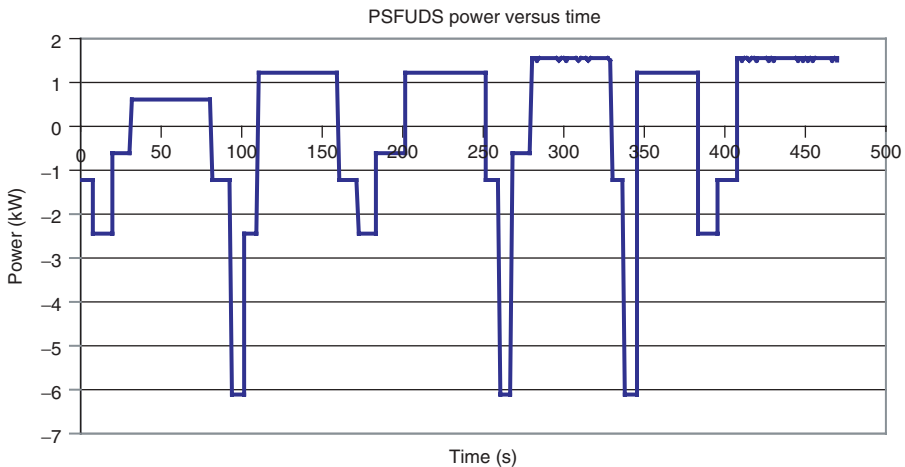
^aPSFUDS power profile based on maximum power of 500 W kg⁻¹ and the weight of the cells alone.

Table 12.13 Summary of the power capability of various ultracapacitors for constant and pulse power discharges.

Device/capacitance	RC (s)	Wh kg ⁻¹ ^a	Wh kg ⁻¹ 95%	(W kg ⁻¹) _{const.pw} (%) ^b	Round-trip efficiency PSFUDS 500, 1000 W kg ⁻¹
Batscap/2700 F	0.54	4.2	2050	1000, 90	0.98, 97
APowerCap/450F	0.63	5.8	2569	2105, 91	0.993, 0.989
Maxwell/2900 F	1.1	4.3	981	900, 89	0.97, 0.94
Nesscap/3150 F	1.3	4.5	982	1341/90	0.97, 0.94
JSR/1900 F	3.6	12	1037	971, 90	0.97, 0.94

^aUsable energy density at 200 W kg⁻¹ constant power.

^bW kg⁻¹ at constant power at which the energy is reduced to “%” of base energy density.



12.4

Testing of Hybrid, Pseudocapacitive Devices

Most of the electrochemical capacitors that have been available for testing are of the carbon/carbon type that use activated carbon in both electrodes and double-layer capacitance for energy storage. In this section, the testing of devices that use intercalation carbon or other battery-like (pseudocapacitive) materials in at least one electrode is considered. These devices are often referred to as *hybrid ultracapacitors*. Some testing of hybrid capacitors has been done and differences between testing carbon/carbon and hybrid capacitor devices are becoming apparent. These differences are discussed in this section with emphasis on how they affect test procedures and data interpretation. This will be done in a format similar to that followed for the carbon/carbon devices.

12.4.1

Capacitance

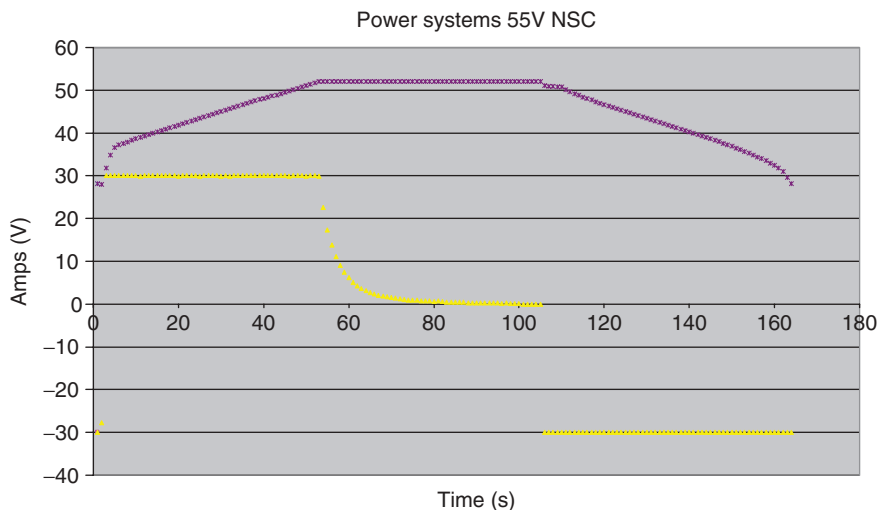
As is the case for carbon/carbon devices, the capacitance is determined from constant current discharge data. However, as shown in Figure 12.8, the character of voltage versus time traces for the hybrid capacitors is quite different from that of the carbon/carbon devices.

As seen in Figure 12.8, the key differences in the traces are the nonlinearity of the hybrid device traces, especially in charging, and the well-defined voltage below which the capacitance of the device is very small. Hybrid capacitors can also be assembled using various metal oxides in one or both electrodes. The character of the voltage versus time trace of those devices would be similar to those in Figure 12.8. As would be expected, the character of the V versus t trace must be considered in testing a particular hybrid capacitor device. In the case of the hybrid carbon device (12a), the voltage should be restricted to be between the rated voltage (3.8 V) and that of the shoulder (2.2 V). It is evident from Table 12.14 (test data for the JSR Micro device) that the selection of voltage limits makes a greater difference in the calculation of the capacitance for hybrid capacitors than for carbon/carbon devices. The best approach is to use the complete range between the rated and shoulder voltages to calculate the capacitance, but correct the initial voltage (V_1) for the IR drop as is done for the carbon/carbon devices. For hybrid capacitors, it is necessary to look closely at the V versus t trace before adapting a particular method for the calculation of capacitance. It seems unlikely that the simple IEC test procedure will be applicable to all types of hybrid capacitor devices without modification.

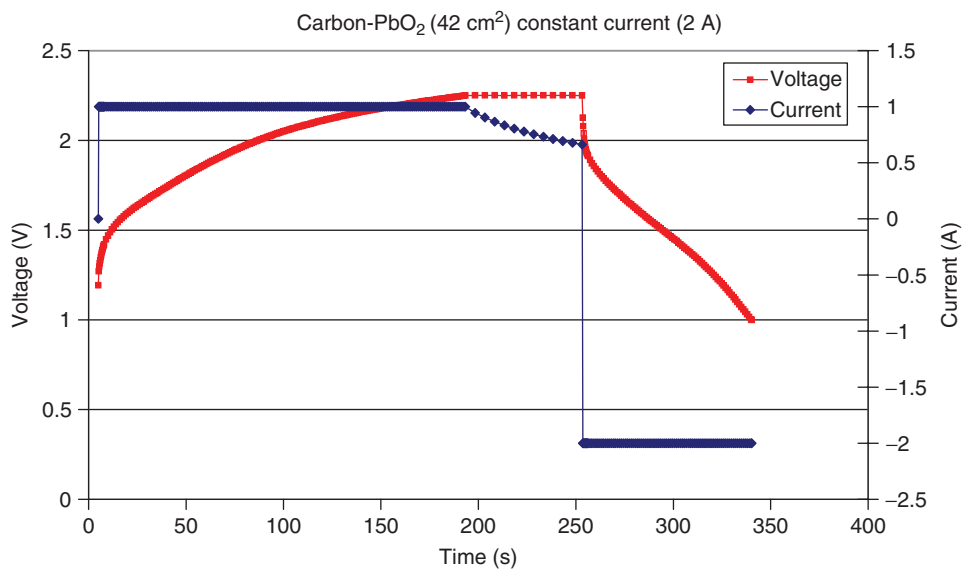
12.4.2

Resistance

The same method can be used for determining the steady-state resistance R_{ss} of the hybrid carbon capacitors as was used for the carbon/carbon devices. As shown



(a) Graphitic carbon/activated carbon device



(b) Carbon/PbO₂ device

Figure 12.8 Voltage versus time traces for the constant current discharges of hybrid capacitors.

Table 12.14 Characteristics of the JSR Micro 2000F cell.

Constant current discharge 3.8 to 2.2 V.						
Current (A)	Time (s)	C (F)	Resistance (mΩ) ^a			
30	102.2	2004	—			
50	58.1	1950	—			
80	34.1	1908	—			
130	19.1	1835	2.0			
200	11.1	1850	1.9			
250	8.2	1694	1.84			
Constant power discharges 3.8 to 2.2 V						
Power (W)	W kg ⁻¹	Time (s)	Wh	Wh kg ^{-1b}	C _{eff}	Wh l ^{-1b}
102	495	88.3	2.5	12.1	1698	18.9
151	733	56	2.35	11.4	1596	17.8
200	971	40	2.22	10.8	1508	16.9
300	1456	24.6	2.05	10.0	1392	15.7
400	1942	17	1.89	9.2	1283	14.4
500	2427	12.5	1.74	8.5	1181	13.3
Pulse test (5 s)		Resistance (mΩ)		RC (s)		
Current (A)						
100		2		3.8		
200		1.9		3.5		

^aResistance is steady-state value from linear V versus time discharge curve.

^bBased on the weight and volume of the active cell materials.

Cell weight 206 g, 132 cm³.

$C_{\text{eff}} = 2(W \text{ s}) / (3.8^2 \text{ to } 2.2^2)$.

Peak pulse power at 95% efficiency $R = 1.9 \text{ m}\Omega$.

$P = 9/16 \times 0.05 \times (3.8)^2 / 0.0019 = 214 \text{ W}, 1038 \text{ W kg}^{-1}$.

in Figure 12.9, the V versus t traces for constant current discharges of the hybrid carbon devices become linear within a couple of seconds and the IR drop can be determined by extrapolating back to $t = 0$. Hence $R_{\text{ss}} = (\Delta V)_{t=0} / I$. When testing any new hybrid device, one should check the linearity of V versus t trace near the initiation of discharge to determine whether the simple method of linear extrapolation is applicable. Pulse tests with the JSR Micro devices yield resistance values that are in good agreement with those obtained using the linear extrapolation

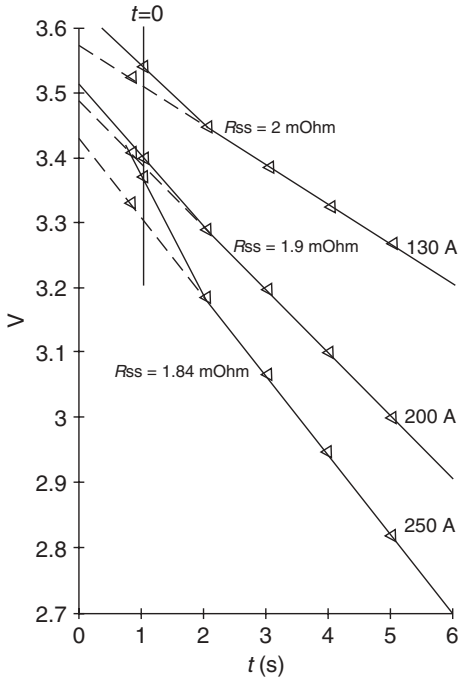


Figure 12.9 Determination of the steady-state resistance of a hybrid ultracapacitor (JSR Micro 2000 F cell).

method. The pulse method is the most universally applicable approach to determine the resistance of ultracapacitors and batteries. Test data for the JSR Micro 2000 F device are given in Table 12.14.

12.4.3

Energy Density

In simplest form, the energy stored in a hybrid capacitor can be expressed as

$$E_{\text{stored}} = \frac{1}{2} C_{\text{eff}} (V_{\text{rated}}^2 - V_{\text{min}}^2)$$

assuming that capacitance C_{eff} is a constant. In the case of the carbon/carbon devices, $V_{\text{min}} = 1/2 V_{\text{rated}}$. In the case of the hybrid capacitor, V_{min} is the minimum voltage at which the device stores significant charge. C_{eff} has been calculated from the test data for a carbon/carbon device in Tables 12.11 and 12.12 and for a hybrid capacitor in Table 12.14. It is clear from the comparison of the tables that the C_{eff} approximation and the simple $1/2CV^2$ relationship is valid to obtain the energy stored at low-power densities for the carbon/carbon devices, but not for the hybrid devices. Hence, the energy density of hybrid capacitors should be

obtained from testing them over a range of power densities. The simple $1/2CV^2$ relationship overestimates the energy stored in the hybrid capacitors. As is the case for carbon/carbon devices, energy density decreases with increasing power density owing to the effect of resistance on the operating voltage range of the device.

12.4.4

Power Capability and Pulse Cycle Tests

Pulse testing of hybrid capacitors to obtain the resistance and the round-trip efficiency on the PSFUDS is essentially the same as for carbon/carbon devices. The power capability of hybrid capacitors can be calculated using the same relationships used for carbon/carbon devices when V_{rated} and the pulse resistance R are known. As indicated in Table 12.13, the 95% efficient power capability of the JSR 2000 F device is 1038 W kg^{-1} , which is the same as in many of the carbon/carbon devices. Hence, the hybrid capacitor achieved the increase in energy density without a sacrifice in power capability.

As shown in Table 12.13, the JSR 2000 F device had round-trip efficiencies on the PSFUDS cycle of 97 and 94% for peak power steps of 500 and 1000 W kg^{-1} , respectively. These efficiencies are essentially the same as those measured for most of the carbon/carbon devices.

12.5

Relationships between AC Impedance and DC Testing

An electrochemical capacitor is assembled with porous electrodes consisting of a microporous material such as activated carbon. The capacitance and, therefore, the electrical energy storage take place in the double layers formed in the micropores of the carbon. It is convenient to model these complex processes in terms of equivalent electrical circuits as indicated in Figure 12.10. As shown in the figure, the circuit consists of multiple RC elements connected in a ladder, which accounts for the transport of the ions into the double layers along the length (depth) of the micropores.

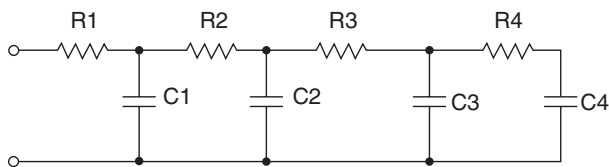


Figure 12.10 Equivalent circuit – multiple RC elements in series.

The simplest DC circuit for an electrochemical capacitor is a single RC element for which the charge and discharge response can be written as

$$\text{Charging: } \frac{V}{V_0} = 1 - \exp\left(\frac{-t}{RC}\right)$$

$$\text{Discharging: } \frac{V}{V_0} = \exp\left(\frac{-t}{RC}\right)$$

where V_0 is the rated voltage and RC is the time constant of the device.

For the simple RC circuit, the voltage changes by 36.8% of V_0 in time equal to one time constant and about 98% of the rated voltage in $t = 4RC$.

Experience [13, 14] has shown that for applications in which significant changes in power demand occur over a few time constants, the single RC element model predicts with reasonable accuracy the response of electrochemical devices. For other applications involving more rapid power changes, an equivalent circuit consisting of multiple RC elements is needed. The analysis of the response of this circuit involves the application of the concept of complex impedance from the AC circuit theory. The impedance $Z(\omega)$ is defined as

$$Z(\omega) = \frac{V(\omega)}{I(\omega)} = Z'(\omega) + jZ''(\omega), \quad |Z| = (Z'^2 + Z''^2)^{1/2}$$

where

$$V(\omega) = v'(\omega) + jv''(\omega), \quad i(\omega) = i'(\omega) + ji''(\omega) \quad j = \sqrt{-1}$$

The impedance can be treated similar to the resistance in DC circuits. For circuit elements in series,

$$Z = Z_1 + Z_2$$

For those in parallel,

$$\frac{1}{Z} = \frac{1}{Z_1} + \frac{1}{Z_2}$$

The circuit elements of interest in Figure 12.10 are capacitors C and resistors R . The corresponding impedance relationships are

$$Z_C = -\frac{j}{\omega C}$$

$$Z_R = R$$

The impedance of a capacitor and resistance in series is

$$Z_{RC} = R - \frac{j}{\omega C}, \quad \omega \gg \gg 1, \quad Z = R$$

and in parallel

$$\frac{1}{Z} = \frac{1}{R} + \frac{1}{-j/\omega C}$$

$$Z_p = \frac{R - jR^2 C \omega}{1 + R^2 C^2 \omega^2}$$

The impedance Z_{ladder} of the RC ladder circuit shown in Figure 12.10 can be expressed as a combination of terms of the form of Z_{RC} and Z_p . Hence,

$$Z_{\text{ladder}}(\omega) = F(\omega, R_1, R_2, \dots, C_1, C_2, \dots)$$

If the device is modeled by a simple RC circuit, the values for R and C can be determined from DC constant current tests. However, if the device is modeled using the ladder circuit, the multiple R and C values can be determined from AC impedance testing [15, 16] in which an AC voltage is applied to a device and its impedance is measured as a function of frequency ω . The test results are usually presented as Z'' versus Z' , C versus frequency, and R versus frequency. Typical AC impedance test data [17] for a carbon/carbon double-layer 100 F capacitor are shown in Figure 12.11. Software [18] is available to

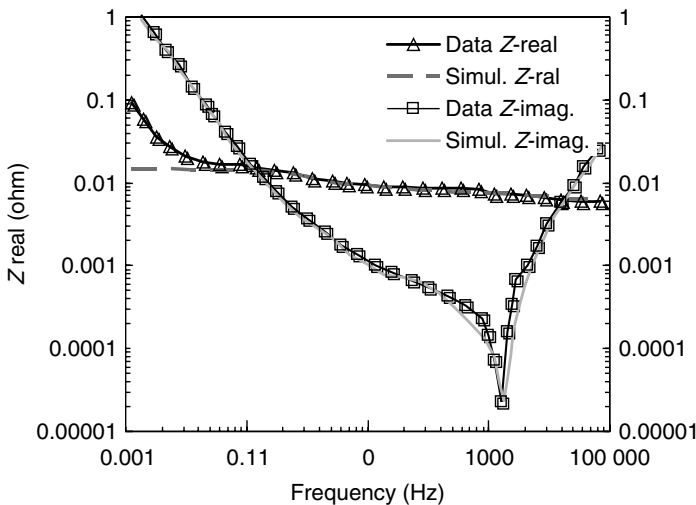


Figure 12.11 AC impedance data and equivalent circuit for a 100 F Maxwell capacitor. Taken from Ref. [17].

determine the R and C values in the ladder equivalent circuit directly from the AC impedance data. The equivalent circuit results in Figure 12.11 indicate that it is likely in most cases that a ladder consisting of two elements will be sufficient to match the AC characteristics of most electrochemical capacitor devices.

The next step is to relate the AC impedance results to the performance of the electrochemical/ultracapacitors in high-current applications, which are in many cases DC in character. One approach is to relate frequency f ($\omega = 2\pi f$) to the discharge time t_{disch} by the simple relationship t_{disch} (seconds) = $1/4f$, because each AC cycle consists of four (4) charge or discharge subcycles. $t_{\text{disch}} = 1$ s corresponds to $f = 0.25$ Hz and $t_{\text{disch}} = 30$ s corresponds to 0.0083 Hz; hence, for many applications, the AC frequencies of primary interest for electrochemical capacitors are between 0.01 and 1 Hz. The values for C and R for particular frequencies in the range of interest can be read from the Z'' versus Z' curve in Figure 12.11. These values can then be used to determine the corresponding energy and power capability of the device tested using the following equation for t_{disch} , which was derived in Ref. [19].

$$t_{\text{disch}} = \frac{1/2 CV_0^2}{P} \left[(1 - K_1)^2 - \left(\frac{V}{V_0} \right)^2 \right] + RC \ln \left[\frac{V/V_0}{(1 - K_1)} \right] \quad (12.1)$$

$$K_1 = \frac{PR}{V_0^2} = \frac{I_0 R}{V_0}, \frac{V}{V_0} = 0.5 \text{ for a typical discharge}$$

The energy stored is then $P t_{\text{disch}}$ and the corresponding energy and power densities are given as $P t_{\text{disch}}/w_d$ and P/w_d , respectively, where w_d is the weight of the device. For the 100 F Maxwell device, the product specifications by the manufacturer are $C = 100$ F, $R = 15$ m Ω , and $w_d = 25$ g. From Figure 12.11 at a frequency of 0.01 Hz, $t_{\text{disch}} = 25$ s, $C = 110$ F and $R = 17$ m Ω . For a discharge power of $P = 7.5$ W (300 W kg⁻¹), the calculated discharge time from Eq. (12.1) is 23 s, which is consistent with the frequency used in the calculations. Hence, it appears that it is possible to relate the AC impedance results with the DC characteristics of electrochemical capacitor devices. Further comparisons in this regard are given in Refs. [10, 20, 21].

The AC impedance testing method also permits an assessment of the time-dependent processes in the micropores of the carbon as the double layers are being formed. AC impedance data for a 10 F capacitor using a carbide-based carbon [22, 23] in the electrodes are shown in Figure 12.12. The processes in the pores depend on the diameter and depth of the pores. This problem is analyzed in Refs. [24, 25].

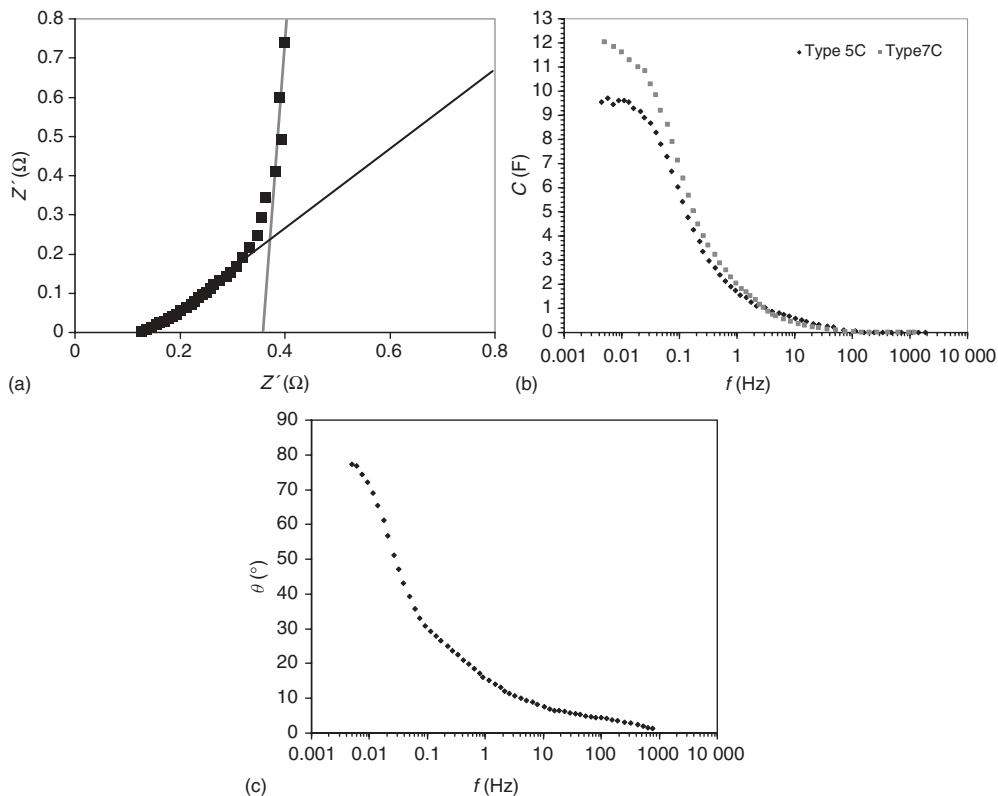


Figure 12.12 AC impedance data for a 10F capacitor using carbide-based carbon electrodes.

It was found that the impedance of the pore processes is

$$Z_p = \left[\frac{1-j}{2\Pi n(r_p^3 \kappa \omega C_{dl})^{1/2}} \right] \coth \left[l_p \left(\frac{\omega C_{dl}}{r_p \kappa} \right)^{1/2} (1+j) \right] \quad (12.2)$$

where n is the number of pores cm^{-3} , r_p is the pore radius and l_p is the pore length, C_{dl} is the pore capacitance cm^{-2} , κ is the electrolyte ionic conductivity, and ω is the frequency. Recall that $\coth x = (e^x + e^{-x})/(e^x - e^{-x})$, $x \gg 1$, $\coth x$ for large x tends to 1; $\coth x$ for small x tends to $1/x$. Hence, for these limiting frequencies, Eq. (12.2) becomes

$$\omega \gg 1 \text{ (high frequencies)} \quad Z_p = \frac{1-j}{2\Pi n(r_p^3 \kappa \omega C_{dl})^{1/2}}$$

$$\omega \ll 1 \text{ (low frequencies)} \quad Z_p = -\frac{j}{2\Pi n l_p r_p \omega C_{dl}} = \frac{-j}{\omega C_{total}}$$

$C_{\text{total}} = 2 \Pi n l_p r_p C_{\text{dl}}$ is the total capacitance of all the pores in the electrode.

At high frequencies, the Z'' versus Z' plot is a 45° line with respect to the Z' axis and at low frequencies, the plot is a straight line normal to the Z' axis. Note that the Z'' versus Z' plot in Figure 12.12 is of the form predicted by Eq. (12.2). This would seem to validate the pore charging model described in Ref. [24], which assumes uniform charging in the pores ($C_{\text{dl}} = \text{constant}$). However, it is likely that the processes are much more complex than this simple model.

As $Z' = R$, the intersection of the 45° line with the axis is the ohmic resistance of the device at very high frequency at which the pore resistance is zero. The pore resistance R_p is the difference between the Z' value at the intersection of the two lines and the minimum value R_0 . For the 10 F capacitor, R_0 0.12 Ω and the pore resistance R_p is 0.22 Ω . The frequency at the intersection point is given by $\omega = 1/Z''C$. Utilizing the C versus f curve in Figure 12.12, it is found that $C = 7.3$ F and $f = 0.1$ Hz.

The corresponding charge/discharge time is 2.5 s ($1/4f$). The RC time constant of the 10 F device is $7.3 \times 0.34 = 2.5$ s, indicating that the full resistance in the device, including the pore resistance, should be reached in about one time constant based on the AC impedance data. This is consistent with the DC test data previously discussed.

12.6 Uncertainties in Ultracapacitor Data Interpretation

Various aspects of testing carbon/carbon and hybrid ultracapacitors were discussed in the previous sections. The intent of the testing is to determine the performance of the devices to a high level of confidence and to provide data for a wide range of device operating conditions. On the basis of the present considerations of testing procedures, there are, however, a number of uncertainties that can arise in the interpretation of data available in the literature and/or on manufacturer's specification sheets for devices. These uncertainties are due to differences in test procedures and incomplete information on how the data were used to calculate device performance. The uncertainties in the following areas are discussed separately.

- 1) Charging algorithm
- 2) Capacitance
- 3) Resistance
- 4) Energy density
- 5) Power capability
- 6) Round-trip efficiency.

12.6.1

Charging Algorithm

Little has been discussed in the previous sections on the charging algorithm used in the testing. That is primarily because the energy stored in the capacitor is essentially independent of the charging current and the charging is terminated when the device reaches V_{rated} (no current taper as for batteries). It is common practice at UC Davis to hold the voltage about 60 s before the discharge test is initiated. This permits the charge in the capacitor to equalize and the current before initiation of discharge to be a small fraction of the discharge current. It would be advantageous if all capacitor test reports stated how the charge was terminated as the hold period can have a significant effect on the test data if it is too short.

12.6.2

Capacitance

The uncertainty in the capacitance is relatively small. It is only a few percent for carbon/carbon devices and up to 10% for hybrid devices. In nearly all cases, the capacitance is determined from the constant current discharge data. The largest source of uncertainty is the voltage range over which the capacitance ($C = \Delta Q / \Delta V$) is calculated. However, examination of the data (Tables 12.3 and 12.5) indicate that selecting different voltage ranges only has a minor effect on the capacitance calculated. The best approach is to calculate the capacitance based on the usable voltage operating range of the device. For carbon/carbon devices, the operating range is usually V_{rated} to $V_{\text{rated}}/2$. For hybrid devices, it seems appropriate to base the capacitance on the difference between the V_{rated} and the minimum operating voltage set by the shoulder of the voltage curve in charge or discharge. The capacitance depends only slightly on discharge current except for very low rates and very high rates. However, the IR voltage drop at the initiation of discharge should be included in the determination of ΔV when C is calculated. It is good practice to state the discharge current or time for which the capacitance value corresponds.

12.6.3

Resistance

Knowledge of the resistance of a device is important; unfortunately, the uncertainty in the resistance is relatively large. This is due both to the inherent difficulty in measuring the resistance of a low resistance ($<1 \text{ m}\Omega$) device and the variety of approaches that can be used to measure the resistance. Part of the difficulty is that the resistance at the initiation of a discharge or pulse varies during the period in which the current distribution is established in the electrodes. The resistance values reported by UC Davis correspond to the steady-state resistance after the current distribution has been established. This resistance value can be a factor of 2 higher than that measured at very short times after the discharge/pulse has

been initiated. Hence, the uncertainty in the resistance value can be as great as a factor of 2. It is important that when resistance values are given that the method and time for measuring the resistance be stated clearly. It is not uncommon for device manufacturers to give the resistance of their device measured by an AC impedance meter at 1 kHz. This value of resistance is about a factor 2 lower than the steady-state value.

12.6.4

Energy Density

The only reliable way to determine the energy stored and the energy density of an electrochemical capacitor is to test it over a range of power densities. This is especially true of hybrid capacitors. These measurements should be done over the usable operating voltage range of the device. The energy stored and discharged and the resultant energy density will decrease as the discharge rate (W kg^{-1}) increases. When energy and energy density values are reported, they should be usable values and indicate the discharge rate (W kg^{-1}) at which they were measured. Utilizing the $\frac{1}{2} CV^2$ relationship to calculate the energy density can overestimate the usable energy density by at least 1/3 for carbon/carbon devices and even greater for hybrid devices.

12.6.5

Power Capability

As discussed in previous sections, there is considerable confusion concerning the power capability of batteries and ultracapacitors and further concerning their relative power capabilities. That confusion is compounded as there is uncertainty in the measurement of the resistance of devices and the effect of the SOC on both the resistance and the open-circuit voltage of devices. Even if one states clearly the SOC at which the power capability is given, there is still the uncertainty in how the resistance of the devices was measured. In assessing the reliability of power capability claims for both ultracapacitors and batteries, it is important to know the resistance of the devices and how it was determined. Statements concerning power capability without information on the resistance are in most cases unreliable and often misleading.

The resistance value needed for the power calculation is the DC resistance of the device. Hence, measurement of the resistance at 1000 Hz will not yield the appropriate value of resistance. In fact, that resistance is consistently too low by about a factor of 2. The DC resistance can best be determined from pulse tests of the devices. The pulses can be either discharge or charge pulses. The duration of the pulses should be 5–10 s. The resistance calculated from the pulse tests will depend on the time at which the voltage drop or rise is read following the initiation of the pulse. If the voltage is read at times less than 1 s, the resistance calculated will be quite low. In general, the resistance inferred from the pulse test will be higher as the voltage is read at longer times after the pulse has been initiated.

Table 12.15 Comparisons of the projected power capabilities of various devices using the different methods for calculation.

Lithium batteries 60% SOC	Matched impedance	USABC min/max	Efficient pulse EF = 95%	Efficient pulse EF = 80%
Kokam NCM 30 Ah	2 893	2 502	550	979
Enerdel HEVNCM 15 Ah	5 491	4 750	1 044	1 858
Enerdel EV NCM 15 Ah	2 988	2 584	568	1 011
EIG NCM 20 Ah	2 688	2 325	511	909
EIG FePhosphate 15 Ah	2 141	2 035	407	725
Altairnano LiTiO 11 Ah	1 841	1 750	350	623
Altairnano LiTiO 3.8 Ah	4 613	4 385	877	1 561
Ultracapacitors $V_0 = 3/4V_{\text{rated}}$				
Maxwell 2890 F	8 836	4 413	994	—
Nesscap 3100 F	8 730	4 360	982	—
Batscap 2700 F	18 224	9 102	2 050	—
APowerCap 450 F	22 838	11 406	2 569	—
LS Cable 3200 F	12 446	4 609	1 038	—
JSR 2000 F	9 228	6 216	1 400	—

For lithium cells, the resistance inferred changes slowly after 2–3 s for the 10 s pulse. Another approach to determine the DC resistance is the current interruption method in which the current is set to zero during a constant current discharge or charge and the voltage is read during the recovery back to the open-circuit voltage. This method has been found to work well for both battery cells [19] and ultracapacitors (Tables 12.6 and 12.7). There is scatter of a few tenths of a megaohm in the resistance inferred, which seems to be unavoidable. The power capabilities calculated from the resistance determined in this manner can be considered to be reliable.

As discussed in Section 12.3 (Power capability), widely different power capability for batteries and ultracapacitors can be inferred even when the resistance and open-circuit voltage are accurately known. The three approaches most often applied to determine the power capability of devices are matched impedance power, the min/max method of the USABC, and the pulse energy efficiency approach used at UC Davis. As shown in Table 12.15 for a number of batteries and ultracapacitors, the usable maximum power values (W kg^{-1}) obtained using the three methods are very different. In general, the values obtained using the energy efficiency method for EF = 90–95% are much lower than the other two methods, which yield values corresponding to efficiencies of 70–75%. These values of power are achievable, but the devices will be operating near their minimum voltage with high rates of heat generation and resultant high stress. The higher powers calculated using the

min/max method can be provided occasionally, but should not be expected during normal operation of the vehicle.

12.6.6

Round-Trip Efficiency

The major uncertainty in interpreting round-trip efficiency concerns the test cycle for which the round-trip efficiency was measured. A key factor in the test cycle is the maximum power (Wkg^{-1}) and duration (seconds) of the maximum power step. In comparing round-trip efficiency values between capacitors and batteries, it is important to know the test cycles in each case. The peak power steps in capacitor tests are often significantly higher than those used to test batteries.

12.7

Summary

DC testing of electrochemical capacitors has been reviewed with emphasis on the test procedures used by the USABC, IEC, and UC Davis. Differences in the test procedures are identified and the effect of the differences on the inferred characteristics of various carbon/carbon and hybrid (pseudocapacitive) electrochemical devices evaluated from test data. The effect of the test procedures is greater for hybrid devices than carbon/carbon capacitors.

It was found that the differences in the test procedures have a minor effect on capacitance (less than 10%), but larger effects on resistance and energy density. The uncertainty in the resistance can be as high as a factor 2 depending on the pulse duration and the method used to infer it. The pulse power capability of devices can be calculated from the rated voltage of the device and its measured steady-state resistance. The calculated power values are highly dependent on the assumptions made concerning the efficiency EF of the pulse (fraction of energy into electricity). The inferred power capability of a device based on the matched impedance value ($V^2/4R$) is nearly a factor of 10 higher than that corresponding to an efficiency of 95% as required in the USABC and IEC test procedures.

References

1. (1994) Electric Vehicle Capacitor Test Procedures Manual. Report DOE/ID-10491, Idaho National Engineering Laboratory, October 1994.
2. (2004) FreedomCar Ultracapacitor Test Manual. Report DOE/NE-ID-11173, Idaho National Engineering Laboratory, September 21 2004.
3. IEC (2006) IEC 62391-1 *Fixed Electric Double-Layer Capacitors for Use in Electronic Equipment-Part 1: Generic Specification*.
4. IEC (2008) BS EN62576 :2010 *Electric Double-Layer Capacitors for Use in Hybrid Electric Vehicles-Test Methods for Electrical Characteristics, Finalized April 2008*.

5. Burke, A.F. and Miller, M. (2009) Electrochemical Capacitors as Energy Storage in Hybrid-Electric Vehicles: Present Status and Future Prospects. EVS-24, Stavanger, Norway, May 2009 (paper on the CD of the Meeting).
6. Burke, A.F. (2008) Considerations for Combinations of Batteries and Ultracapacitors for Vehicle Applications. Paper presented at the 18th International Seminar on Double-layer Capacitors and hybrid Energy Storage Devices, Deerfield Beach, Florida, December 2008.
7. Burke, A.F. (2009) Supercapacitors and Advanced Batteries: What is the Future of Supercapacitors as Battery Technology Continues to Advance? Paper presented at the Advanced Capacitor World Summit 2009, San Diego, California, March 2009.
8. Farahmandi, C.J. (1996) Analytical Solution to an Impedance Model for Electrochemical Capacitors. Advanced Capacitor World Summit 2007, San Diego, CA, June 2007, also Electrochemical Society Proceedings PV96-25.
9. Srinivasan, V. and Weidner, J.W. (1999) Mathematical modeling of electrochemical capacitors. *J. Electrochem. Soc.*, **146**, 1650–1658.
10. Chu, A. and Braatz, P. (2002) Comparison of commercial supercapacitors and high-power lithium-ion batteries for Power assist applications in hybrid electric vehicles: 1. Initial characterization. *J. Power. Sources*, **112**(1), 236–246.
11. Burke, A.F. (2010) The power capability of ultracapacitors and lithium batteries for electric and hybrid vehicle applications. *J. Power. Sources* **196**(1), 514–522, 2011 .
12. (2003) Freedom Car Battery Test Manual for Power-Assist Hybrid Electric Vehicles, DOE/ID-11069, October 2003.
13. Dougal, R.A., Gao, L., and Liu, S. (2004) Ultracapacitor model with automatic order selection and capacity scaling for dynamic system simulation. *J. Power. Sources*, **126** (1–2), 250–257.
14. Miller, J.M. *et al.* (2007) Carbon-Carbon Ultracapacitor Equivalent Circuit Model, Parameter Extraction, and Application. Ansoft First Pass Workshop, Maxwell Technologies Presentation, October 2007.
15. (2008) Basics of Electrochemical Impedance Spectroscopy (EIS), Applications Note AC-1, Princeton Applied Research.
16. Hammar, A. *et al.* (2006) Electrical Characterization and Modeling of Round Spiral Supercapacitors for High Power Applications (AC Impedance Testing). Paper presented at ESSCAP 2006, Lausanne, Switzerland.
17. Miller, J.R. and Butler, S.M. (2002) Development of Battery and Electrochemical Capacitor Equivalent Circuit Models for Power System Optimization. Paper presented at the 202nd Electrochemical Society Meeting, Salt Lake City, Utah, October 2002.
18. EIS300 Electrochemical Impedance Spectroscopy Software, Gamry Instruments, www.gamry.com.
19. Burke, A.F. (2010) Electrochemical capacitors, *Chapter in the Handbook of Batteries*, 4th edn, McGraw-Hill 2010.
20. Carlen, M., Christen, T., and Ohler, C. Energy-Power Relations for Supercaps from Impedance Spectroscopy Data. Proceedings of the 9th International Seminar on Double-Layer Capacitors and Similar Energy Storage Devices, Deerfield Beach, Florida, December 1999.
21. Arulepp, M. *et al.* (2006) The advanced carbide-derived carbon based supercapacitor. *J. Power. Sources*, **162** (2), 1460–1466.
22. Rafik, F., Gualous, H., Callay, R., Crausaz, A, and Berthon, A. (2006) Supercapacitors Characterization for Hybrid Vehicle Applications. Paper presented at ESSCAP 2006, Lausanne, Switzerland (available on web).
23. Gogotsi, Y. *et al.* (2003) Nanoporous carbide-derived carbon with tunable pore size. *Nat. Mater.*, **2**, 591–594.

24. DeLevie, R. (1967) Electrochemical response of porous and rough electrodes, in *Advances in Electrochemistry and Electrochemical Engineering*, Vol. 6 (ed. P. Delahay), Interscience Publishers.
25. Delnick, F.M., Jaeger, C.D., and Levy, S.C. (1985) AC impedance study of porous carbon collectors for Li/SO₂ primary batteries. *Chem. Eng. Commun.*, **35**, 23–28.

13

Reliability of Electrochemical Capacitors

John R. Miller

13.1

Introduction

Electrochemical capacitors (ECs) are being used currently in a variety of high-reliability applications, for example, as backup power sources for critical industrial processes. Some capacitor products are quantifiably more attractive for these sorts of applications than others. Certain system designs offer higher reliability. This chapter briefly reviews basic reliability concepts, relates these to EC technology, describes the methodology for quantitatively determining the reliability of a capacitor product, and presents straightforward engineering approaches to achieve the desired level of reliability from a capacitor system. It concludes with a practical example where a capacitor system is engineered to meet operating performance specifications concurrent with imposed reliability requirements.

13.2

Reliability Basics

Reliability has a very precise mathematical definition: *Reliability is the probability that an item will perform its intended function under stated conditions for some specified period of time.* It relates to the outcome expected from a large group of identical items all treated the same way. The reliability of an item is strongly influenced by its design, by how it is used, and by the environment in which it is used. Item quality can also significantly impact reliability.

Consider, for example, an automobile tire. Its reliability depends on the design: is it radial or bias ply; what type of vehicle it is mounted on – a small light car or a heavy utility vehicle; how will that vehicle be operated – in slow city traffic or at the race track; and the operating road surface – high-temperature asphalt or artic-temperature snow-pack. Precise details about tire design and how it will be used are necessary to make reliability statements.

Similar details are needed to make statements about EC reliability, calling for questions such as: Does the capacitor package have hermetic construction or

polymeric seals? Is the capacitor used by itself or as part of a system? Will it be charged or uncharged most of its life? Will its operating temperature be high or low, and constant or fluctuating? Will it be protected from overstress conditions? Many factors influence EC system reliability, and these are first examined at the cell level.

13.3 Cell Reliability

The reliability of an item is based on a mathematical representation of the cumulative life distribution curve. Various mathematical models are available to describe life, including exponential, normal, lognormal, and Weibull distributions. Although each is potentially useful for some component types, the life model almost universally used for capacitors is the Weibull life distribution [1]. Generally, this distribution well represents reality for capacitors – a Weibull will accurately fit life data at short, medium, and very long times.

With a Weibull distribution, the cumulative life distribution (fraction of the population failing after time t) is described by

$$F(t) = 1 - \exp[-(t/\alpha)^\beta] \quad (13.1)$$

The two parameters in this distribution are α , termed the characteristic life, and β , the shape factor.¹⁾ Figure 13.1 shows this equation (with $\beta = 4$) plotted versus normalized time, t/α . The Weibull cumulative life distribution $F(t)$ is an ever-increasing function of time, starting at 0 for $t = 0$ and rising to 1 at long times, after all of the population has failed.

The reliability function $R(t)$ is the fraction of the population that has *not* failed by time t . It is simply related to $F(t)$ by Eq. (13.2) and plotted in Figure 13.2 (with $\beta = 4$) versus normalized time.

$$R(t) = 1 - F(t) = \exp[-(t/\alpha)^\beta] \quad (13.2)$$

The reliability function has a value of 1 at very short times (100% reliable, no failures) and it decreases monotonically to 0 (the entire population failed) with increasing time. The probability density function $f(t)$ is the time derivative of the life distribution, $f(t) \equiv dF/dt$. It corresponds to the histogram of the lifetimes and is plotted for $\beta = 4$ in Figure 13.3. This curve is peaked near $t/\alpha = 1$. With this value of β , life essentially extends over the range $0.3 < t/\alpha < 1.5$, that is, few items have life shorter than 0.3α and few items have life longer than 1.5α .

The age τ_p at which the fraction P of a population has failed can be derived using Eq. (13.2) and is

$$\tau_p = \alpha[-\ln(1 - P)]^{1/\beta} \quad (13.3)$$

1) The general Weibull distribution equation has a third parameter associated with shifting

time, which is not important for the development in this chapter and is ignored.

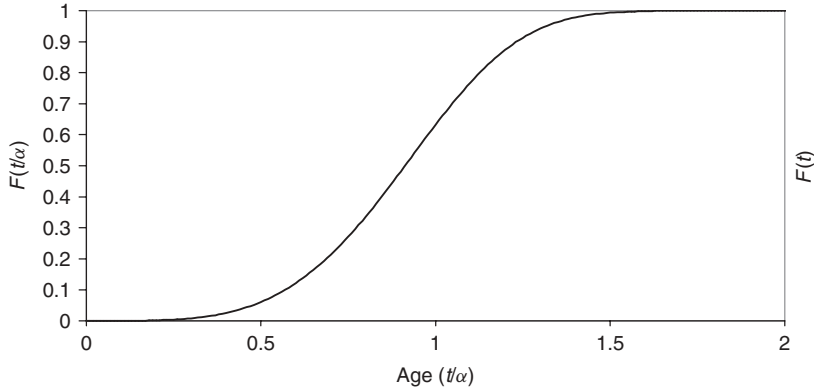


Figure 13.1 Weibull cumulative life distribution $F(t/\alpha)$ plotted against normalized time, t/α . The shape factor β equals 4 in this example.

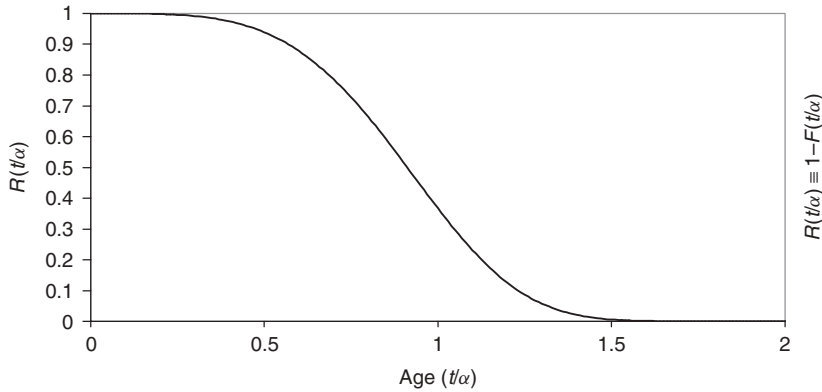


Figure 13.2 Weibull reliability function $R(t/\alpha)$ plotted against normalized time t/α with shape factor $\beta = 4$.

For $P = 1 - 1/e = 0.632$, $\tau_p = \alpha$ for all values of β . Thus, characteristic life for any Weibull distribution is the time at which 63.2% of the population has failed.

The Weibull life distribution is most often associated with Professor Walloidi Weibull (1887–1979) of the Royal Institute of Technology in Stockholm, Sweden. It first came to broad attention in the United States in connection with US Air Force studies on metal fatigue in aircraft during the early 1950s, although there are hints of similar methods as early as the 1920s. Because it can account for both increasing and decreasing failure rates, the Weibull distribution is able to describe the life of a wide variety of products. It allows simple graphical solutions, and before software became widely available for the purpose, distinctive Weibull paper made it possible to plot life data by hand and obtain directly both the characteristic life and the shape factor.

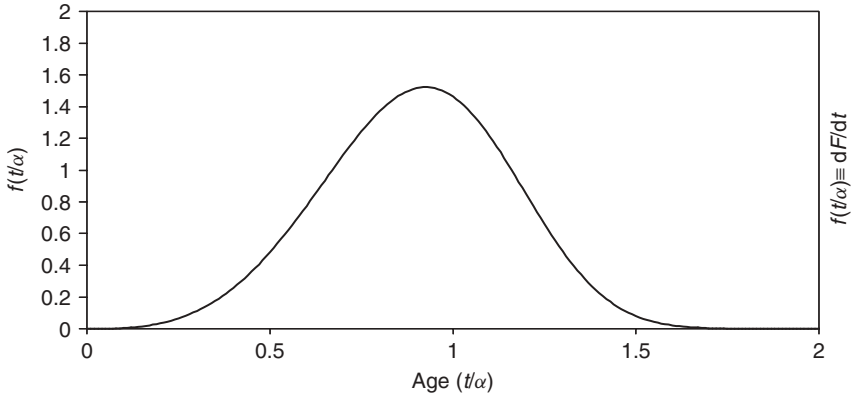


Figure 13.3 Probability density function $f(t/\alpha) = dF/dt$ plotted against normalized time t/α for a shape factor $\beta = 4$.

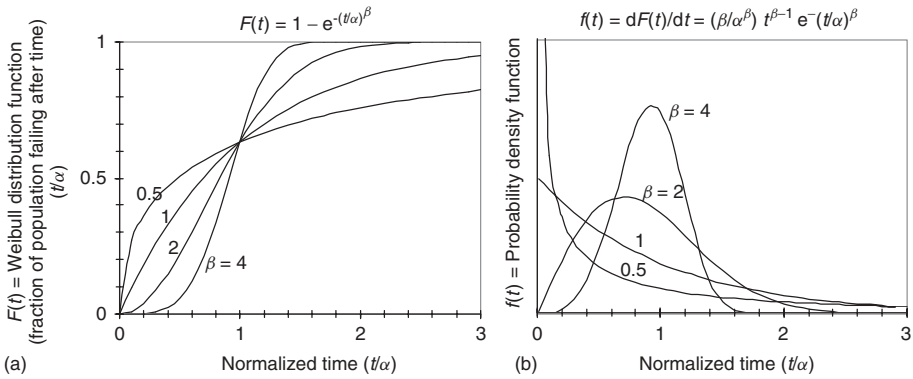


Figure 13.4 (a) Weibull cumulative life and (b) probability density distribution for four different values of the shape factor β . Time is normalized by the characteristic life α .

The Weibull distribution can represent increasing, constant, or decreasing failure rates by using different values for the shape factor β . When $\beta = 1$, the failure rate is constant (exponential distribution). If $\beta < 1$, failures are decreasing with time, the so-called infant mortality. If $\beta > 1$, failures are increasing with time. Weibull distributions for different values of the shape parameter, β , are shown in Figure 13.4 with the fraction of the population failing by normalized time t/α on (a) and the probability density functions on (b).

Note the common point where all lines intersect in (a), where $t/\alpha = 1$, when time is equal to the characteristic life. At this time, and independent of the value of the shape factor β , 63.2% of the population has failed.

Life distributions with different shape factors are often combined in what textbooks refer to as a *bathtub* curve, as shown in Figure 13.5. Infant mortality, due perhaps to errors in item assembly and characterized by a small β value, has

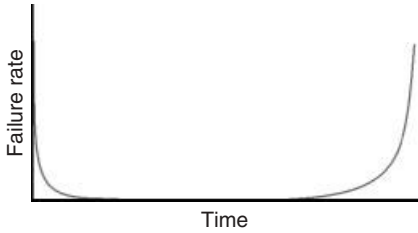


Figure 13.5 Typical failure rate for an item, showing higher rates at short times (infant mortality) and wear-out at long times. This so-called bathtub curve can be treated as the sum of two distributions, one with a decreasing failure rate and one with an increasing failure rate.

a downward slope from the start. At long times there is wear-out, characterized by a large β . The sum of these two distributions produces a bathtub curve. Having noted this, however, we will disregard it in favor of assuming the manufacturer has correctly manufactured and “burned in” the components or somehow dealt with factors that create early failures. The rest of the chapter assumes only wear-out failures, that is, an increasing failure rate characterized by a Weibull life distribution with a shape factor much greater than 1.

EC cells typically have β values in the range 5–15, depending on the product under consideration. Weibull life distributions with $\beta = 5, 10,$ and 15 are shown in Figure 13.6, assuming a characteristic life $\alpha = 1000$ h. Differences are clear: the distribution with smaller β is much wider than the one having a larger shape factor. In all cases, 63.2% of the population has failed by 1000 h. With $\beta = 15$, there are few failures before 700 h and the vast majority of the cells reach failure by about 1300 h. With $\beta = 5$, on the other hand, cell failures are easily observed as early as 400 h and as late as 1500 h. Using Eq. (13.3) with $\beta = 5$, 1% of the cells fail during the first 398 h, while with $\beta = 15$, it is not until 736 h that 1% of the cells reach failure.

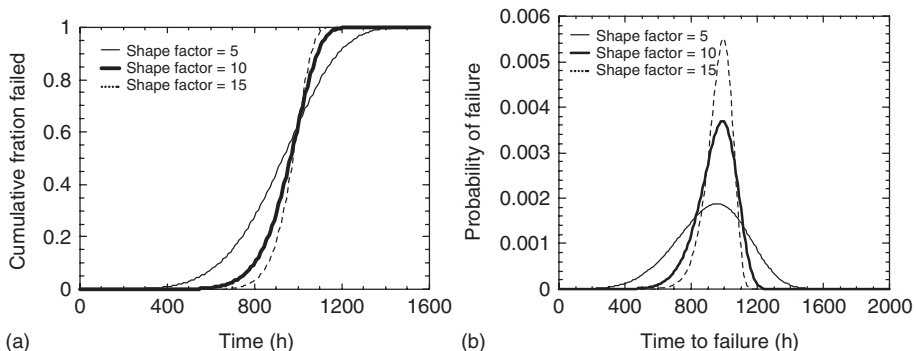


Figure 13.6 (a) Weibull cumulative life and (b) probability density distribution for three different values of the shape factor β , 5, 10, and 15.

13.4 System Reliability

The previous analysis considered the reliability of individual capacitor cells. Many applications operate at higher voltage, which means that more than one cell is used in a series string to meet voltage requirements. When cells are connected this way, however, the failure of a single cell will cause the entire string (system) to fail. This is analogous to a chain failing when only one of its links breaks. It is easy to recognize that the longer the chain and/or the more links it has in its length, then the lower its reliability, provided link failures are statistically independent.

Consider a capacitor system that is comprised of M identical cells, all connected in series, and that at each instant of time all cells are at the same voltage and temperature, that is, each and every cell is subjected to the same stress. (Later, a more realistic system with nonuniform temperature and voltage is considered.) If the cells are identical, all at the same temperature and charge state, and the failures are statistically independent, then the reliability function for the string of M cells R_M is the reliability function for a single cell, R_1 raised to the M power.

$$R_M(t) = [R_1(t)]^M \quad (13.4)$$

Stringing cells in series is analogous to the statistics associated with flipping a coin. The probability of heads with a “good” coin in a single flip is 50%. The probability of heads in a second flip is again 50%. The probability of getting two heads in a row is one quarter, the product of probability of the two independent and sequential steps. What then is the probability of getting 100 heads in a row? That probability is $1/2^{100}$, a very small number! The reliability function for a system of many cells is also particularly critical because of the large exponent associated with a long string of series-connected cells.

The Weibull life distribution for M series-connected cells can be derived in a straightforward manner by inserting Eq. (13.2) into (13.4), which is as follows:

$$R_M(t) = [R_1(t)]^M = \{\exp[-(t/a)^\beta]\}^M = \exp\left\{-\left(t/[a/M^{(1/\beta)}]\right)^\beta\right\} \quad (13.5)$$

Thus, the distribution for M series-connected cells is also a Weibull distribution, one having the same shape factor as the cells but with a characteristic life of

$$a_M = a/M^{(1/\beta)} \quad (13.6)$$

As the number of cells M is greater than 1 for a series-string, the characteristic life of the system will always be less than the characteristic life of its constituent cells.

It is interesting to examine, using a specific example, the impact on reliability of having systems composed of long strings of series-connected cells. Consider a system of 50 cells in series, the life of the cells being characterized by a Weibull life distribution with $\beta = 4$. Figure 13.7 shows the reliability function (a) and probability density function (b) for one cell and for the 50 cell series string. The average age of system failure is considerably less than the average age of cell failure. The peak in the population density is approximately $t = \alpha$ for a single cell failure

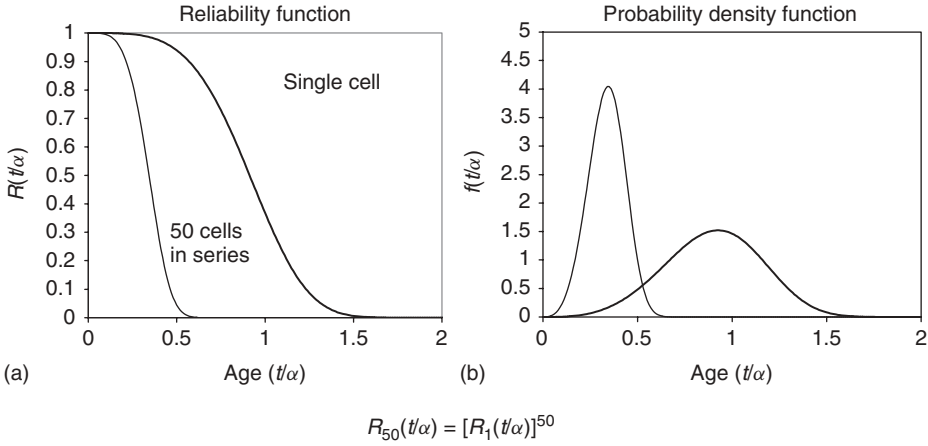


Figure 13.7 Reliability function and probability density function for a single cell ($\beta = 4$) and for systems comprising 50 of these cells connected in series. These functions are plotted against normalized age t/α .

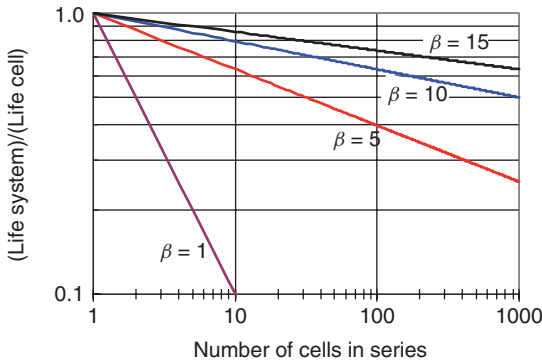


Figure 13.8 Plot of $\alpha_M/\alpha_1 = 1/M^{(1/\beta)}$, the ratio of the characteristic life of a string of M series-connected cells α_M to the characteristic life of single cells α_1 , versus the number cells in the string M . Cell failures are assumed to be statistically independent. As shown, the system comprising 10 series-connected cells will have $1/10$ the life of the constituent cells if they have a shape factor $\beta = 1$.

and approximately $t = \alpha/(50^{1/4}) \approx 0.4\alpha$ for system failure. Notice that the vast majority of 50 cell systems will fail before reaching an age of $t/\alpha = 0.5$.

The ratio of the characteristic life α_M of a string of M series-connected cells to the characteristic life α_1 of a single cell versus the number of cells in the string M (Eq. (13.6)) is shown graphically in Figure 13.8 for several shape factor values. Cell failures are assumed to be statistically independent, with *string failure* defined as having a single cell fail in the string of M cells. The shape factor $\beta = 1$ is shown, but values this small are not generally observed for ECs. This β value corresponds to the constant failure rate (an exponential life distribution), where a new cell is just as

likely to fail as an old cell. With this shape factor, a system of 10 series-connecting cells will have 10 times lower life, as can be determined graphically from the figure, than the single cell life. With $\beta = 15$, in contrast, the characteristic life of a 10 cell string will be 86% the characteristic life of a constituent cell.

Heavy-hybrid-vehicle energy storage systems typically operate at up to ~ 750 V. Using cells rated at 2.5 V, the storage system will need to have 300 or more cells in series. The characteristic life of a 300 cell string will only be $\sim 32\%$ that of the cell value for a shape factor $\beta = 5$, $\sim 56\%$ that of the cell value for $\beta = 10$, and $\sim 68\%$ that of the cell value for $\beta = 15$. The conclusion is clear – cells having a life distribution characterized by a large shape factor offer clear life advantages when assembling high-voltage systems. Large β implies a narrow probability density distribution, which means very strong wear-out behavior [2]. It is the left-side tail of the cell life distribution that most strongly affects the life of a series string of such cells because it takes but a single short-time failure to cause the entire system to fail.

A final example is used to illustrate the relationship between cell and system reliability. In this example, assume (i) systems are constructed with 200 cells in series, (ii) the cell life distribution is well characterized by a Weibull with a shape factor $\beta = 4$, and (iii) the cell manufacturer gives a strong assurance that his cells provide 10 years of life. What will be the life of such a 200 cell system?

First, the cell life distribution must be quantified. The manufacturer's statement that the cells provide 10 years of life is totally inadequate for this purpose – will only 0.1% of the cells fail in 10 years? Or does the manufacturer mean a different level of failure, $< 50\%$ failure for instance? Equation (13.3) can be used to derive the characteristic life using different assumptions on what the manufacturer means. With $\beta = 4$, 0.1% failures in 10 years means that the characteristic life will be $\alpha = 56.5$ years. With 1% failure in 10 years, then $\alpha = 31.6$ years. And if the manufacturer's statement relating to 10 years of life means that 90% of the cells operate for 10 years (that is 10% fail during 10 years of operation), then the characteristic life of these cells will be $\alpha = 17.6$ years.

The last step of this example is to examine system reliability (Eq. (13.6)) using the derived cell characteristic life, the shape factor $\beta = 4$, and the number of series cells $M = 200$. These results are listed in Table 13.1. Greater than 99% of the systems will operate for at least one year with each cell life interpretation. But differences do appear in year two. Cells having a characteristic life $\alpha = 17.6$ years (10% failure in 10 years) experience measurably higher system failures. And as time progresses, even greater differences are observed – a mere 27% of the systems with $\alpha = 17.6$ years continue to operate after five years. After 10 years, 82% of the systems constructed with “0.1% cell failure in 10 years” still operate, 13% made with the “1% cell failure in 10 years” still operate, and absolutely none of the systems made with the “10% cell failure in 10 years” still operate. Two messages are evident: (i) clear understanding is needed of a manufacturer's life statement and (ii) cells having a Weibull life distribution with a small shape factor may be unsuitable for use in high-voltage systems.

Table 13.1 Characteristic life α of cells that provide “10 year life,” assuming three different meanings of this statement, and 200 cell systems made using these constituent cells. If “10 year life” means 99.9% of the cells operate that long, then the characteristic life is $\alpha = 56.5$ years and 82% of the systems will be operating at 10 years. At the other extreme, if “10 year life” means 90% of the cells operate for 10 years then the characteristic life is $\alpha = 17.6$ years and absolutely none of the 200 cell systems will be operating after 10 years.

Percentage cell failures in 10 yr	Percentage of systems operating			
	1 yr	2 yr	5 yr	10 yr
0.1 ($\alpha = 56.5$ yr)	99.99	99.97	98.7	82
1.0 ($\alpha = 31.6$ yr)	99.98	99.7	88.2	13
10.0 ($\alpha = 17.6$ yr)	99.79	96.7	27.1	0

13.5

Assessment of Cell Reliability

EC reliability assessment has been reported in only a handful of studies. In 1992, Kobayashi [3] described accelerated aging of molded ECs at fixed voltage and several temperatures and derived Weibull life models. In 2005, Goltser *et al.* [4] discussed an efficient approach to gather EC reliability information over a range of temperatures and operating voltages and demonstrated this approach using commercial ECs. And in 2006, Miller *et al.* [5] presented reliability results from a study of 3000 F commercial capacitor cells. Two years later, Butler *et al.* [6] updated this long-term aging study. More recently, Kotz *et al.* [7] examined constant load aging of 350 F cells and identified failure modes. No historic field data has been published on ECs such as that found for other passive components in the US Military Electronic Components Handbook MIL-HDBK-217. And finally, EC capacitor manufacturers generally provide only limited reliability information about their products. Consequently, cell reliability assessments must often be performed by the technology user before a system of such cells can be deployed with confidence that the design will meet goals.

Despite its seeming triviality, the statement “life is unknown without death” is as true as it is critical for understanding reliability. Life can be measured only after failure has been observed. Thus, component testing must be continued to the very end of life for an accurate reliability determination. Field data was often collected and used in the past to develop life distributions of passive components. At present, it is more common to derive component life distributions using well-controlled laboratory testing rather than historic use information.

One general approach for reliability assessment is to age groups of identical capacitor cells at different stress levels, measuring the response of each individual cell to that stress over time. On the basis of some established definition of failure (component death) and on reaching that condition, the life of individual cells is

determined. This data can be used to develop a distribution of cell life for each group that can then be mathematically represented using various models, for instance, a Weibull life distribution.

Often, groups of cells are aged at stress levels well beyond what they would normally be exposed to in use (accelerated testing). The purpose here is to increase the failure rate so as to obtain life information at a quicker pace. Then, using the acceleration factor that was gained by analysis of life data from the reliability assessment, cell life predictions at field operating conditions can be made much earlier.

Returning to the tire example, reliability testing might involve subjecting groups of tires at various combinations of applied loads (different vehicle weights), imposed temperatures (operating environment), and rotation rates (driving speed). *Tire failure* might be defined as tire disassembly (blowout), deflation (flat tire), or cumulative tread wear. Tire life is the time (or an equivalent distance) needed to reach one of these failure conditions.

Larger test groups do improve statistics, of course, and thus can more accurately delineate the life distribution. But this usually requires greater effort, longer test time, and higher costs. A balance must be maintained between the size of the test groups and the budget available to complete the evaluation. The relationship between test group size and life model confidence levels can be readily established using standard statistical methods.

Capacitor failure (end of life) can take many forms. It could be complete and total loss of function, becoming, for instance, an open circuit or a dead short circuit. It could be an obvious problem such as package rupture with electrolyte leakage. Alternatively, failure could be “defined” by reaching some diminished level of performance, for example, reaching a discharge time that is 75% of its original value. A defined failure does not necessarily mean the device has stopped operating but rather that its performance or properties have changed by some quantifiable amount. The quantified value is then used to engineer the system to meet life requirements. For example, if *capacitor failure* is defined as a 30% loss in delivered energy, then the system would be engineered to provide proper function with up to 30% loss in delivered energy. Thus, system failure occurs at the exact moment that the capacitor reaches a defined failure.

EC specification sheets often include “endurance” statements with words such as “will operate continuously for 2000 h at rated voltage and maximum rated temperature with a capacitance decline less than 30% and an equivalent series resistance (ESR) increase less than 100%.” As previously discussed, such information will not permit capacitor system reliability engineering. However, a detailed knowledge of the life distribution of cells aged at the endurance condition does permit some rudimentary reliability engineering to be completed.

Assume that every cell in a group aged at an endurance condition of 70 °C and 2.5 V operates properly over the 2000 h endurance time. Further, assume that the cell with the minimum capacitance change showed an 11% decrease. Then, using 11% change as the definition of failure, every cell in the group reaches a defined failure in 2000 h of testing, where test group life data is totally complete. This data

can be fit to a life distribution, a Weibull distribution, for instance, which will be useful but have limited applicability.

Operating parameters that have the greatest influence on EC operating performance are voltage and temperature, although humidity can be important for some products. Unlike batteries, EC cycle life generally need not be measured, although very high-rate charge/discharge cycling may add stresses that should not be ignored. ECs follow the 10° rule approximately, that is, a 10°C decrease in temperature doubles the life of a cell. This rule has been shown to hold for most EC cells near their maximum rated voltage and temperature. The voltage rule that is approximately correct (for nonaqueous electrolyte symmetric EC cells near rated voltage) is that a 0.1 V decrease in voltage doubles the life of a cell. Therefore, a simple model equation relating cell life τ to operating temperature T and voltage V , in normalized form, can be written as

$$\tau(T, V) / \tau(T_0, V_0) = 2^{[(T_0 - T)/10]} \times 2^{[(V_0 - V)/0.1]} \quad (13.7)$$

where the life $\tau(T_0, V_0)$ is the characteristic life at a known T_0 and V_0 test condition, for example, the endurance test condition. This equation, in normalized form, is shown graphically in Figure 13.9.

Life distributions for a specific capacitor product will have the same Weibull shape factor under all normal operating conditions. Characteristic life will be longer under low-stress operation and shorter under high-stress operation, but the shape factor will remain the same. Operation at excessive stress conditions can change the shape factor owing to the introduction of one or more additional failure modes. Thus, Weibull shape factor comparisons can suggest when overly aggressive aging conditions have been used [3].

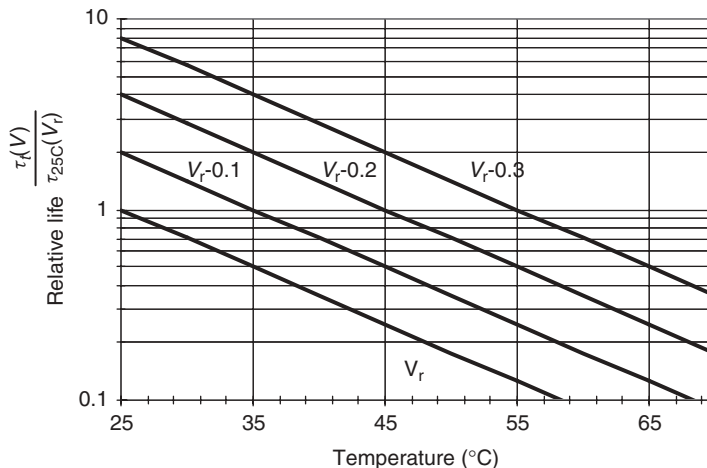


Figure 13.9 Electrochemical capacitor cell life relative to its value at 25°C and rated voltage V_r . Assumptions include life doubling with a 10°C temperature decrease or a 0.1 V per cell operating voltage decrease. This general behavior is typical for organic electrolyte electrochemical capacitor cells having a symmetric design.

Returning to the previous hypothetical example, where by definition every cell failed after 2000 h at 70 °C with 2.5 V applied (11% capacitance loss), life estimates can be made for operation at nearby voltage/temperature conditions. Assume that life data from the endurance group can be represented by a Weibull distribution with a characteristic life of 1800 h and a shape factor of 7.5. Cells of this type would then have two times longer life, 3600 h, if operated at 10 °C cooler temperature, at 60 °C and 2.5 V. The shape factor would remain unchanged at 7.5. And for operation at 2.3 V and 50 °C, characteristic life is predicted to be 16 times longer (4 times longer due to lower voltage and 4 times longer due to lower temperature). The shape factor is not changed. Thus, cells operated at 2.3 V and 50 °C are predicted to show an 11% capacitance loss after 28 800 h of aging.

The methodology of this example is limited to estimating life near the measured endurance condition. Life using definitions of failure other than 11% capacitance loss remains unknown. Aging could continue, of course, past 2000 h, for example, until every cell experienced 25% capacitance loss, and this would indeed provide additional life information. However, a different and more efficient approach can be used to obtain such information sooner. This involves simultaneously aging several groups of cells at different specified voltage/temperature conditions. These conditions should broadly span the range of intended use and be appropriately selected for statistical balance. Data from all of these groups is then combined to create a general life model that spans all examined temperature/voltage conditions. Such a model can then be used to provide credible predictions of future life performance. The following example is used to illustrate this general approach.

13.5.1

Experimental Approach Example

As considerable investment in time and money is expended in performing any reliability assessment, it is important that the highest quality information be obtained, which means that proper test samples are needed. Thus, the first step in any study is to examine the group of capacitors that will be used to determine their suitability as samples in an experimental design. They should be no better or no worse than capacitors that will be available later and used in assembled systems. Distributions of the important properties should be examined for normality. Physical properties such as mass and dimensions as well as electrical properties such as capacitance, equivalent series resistance, leakage current, and discharge energy should be measured and the statistics examined. Capacitors in the sample group with properties that clearly deviate from a normal distribution are suspect and should be excluded from the study. Scatter plots can be used to assist with assignment of samples to the different aging groups. The goal is to randomly populate each aging group with representative capacitors.

This approach is illustrated [8] using Panasonic AL-series electric double-layer capacitors, which are single-cell components with a tubular shape having a spiral-wound design. They are rated at 1.0 F with 2.5 V maximum operating voltage and 70 °C maximum operating temperature. Series resistance was measured at 1 kHz

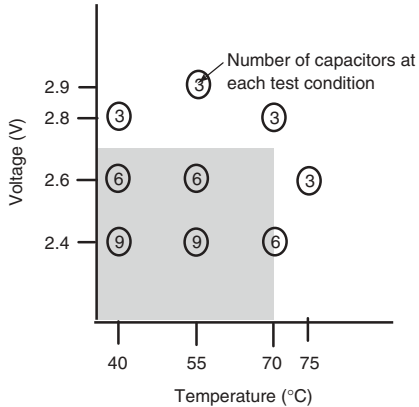


Figure 13.10 Experimental design used in the reliability study. Forty-eight capacitors were assigned to nine test groups. Aging was performed at constant temperature with constant applied voltage. The shaded region represents capacitor voltage and temperature ratings.

and capacitance was derived from the time needed to discharge with 0.5 A current. After verifying that the properties of the capacitor samples fit normal distributions, 48 were assigned to nine separate test groups (Figure 13.10), ensuring that each group contained samples with properties that spanned the range of each parameter. As shown, the highest stress groups contained three capacitors and the lowest stress groups nine capacitors. This uneven assignment anticipates expected failure rates at the different stress levels. Failures are needed to determine life, and therefore a larger number of samples are included at conditions having lower anticipated failure rates. Four of the nine groups were at operating conditions above the ratings of the capacitor (shaded region). Such conditions were included to increase stress levels and thereby accelerate capacitor aging. The pattern of the groups in Figure 13.10 (experimental design) was selected to permit the development of a second-order life model—one having temperature–voltage cross terms. Many other designs could have been used, some having fewer groups. An essential feature of any good design is that it broadly spans the parameter space in which the capacitors may be deployed. Additional details about the particular experimental design shown in Figure 13.10 are discussed by Goltser *et al.* [4].

Capacitor performance is measured periodically at room temperature and with enough frequency to show a smooth progression of performance changes, thus allowing the exact time of failure to be determined by interpolation. Figure 13.11 shows the capacitance and resistance of the two 70 °C aging groups. These parameters are normalized by the initial value of each capacitor. As shown, capacitance monotonically decreases with time, while equivalent series resistance monotonically increases with time. The six capacitors in the 2.4 V group have a smaller rate of change in capacitance and resistance than the three capacitors in the 2.8 V group, consistent with Eq. (13.7). Observed behavior is usual for ECs—this technology seldom shows discontinuous property changes in contrast with some other storage technologies, secondary batteries, for instance, that often show step

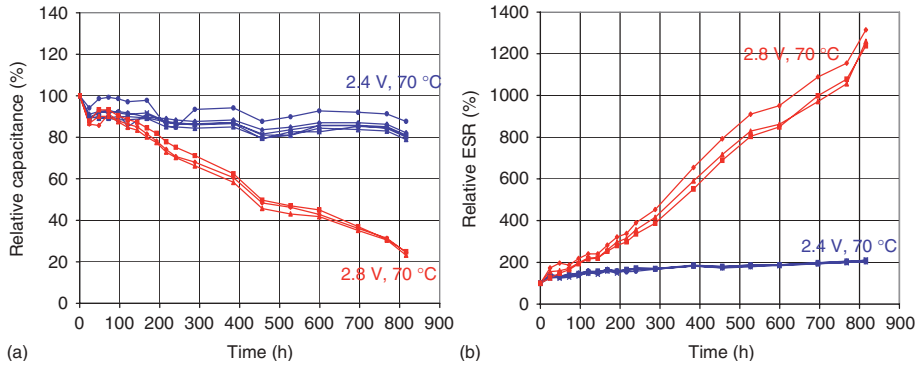


Figure 13.11 (a) Normalized capacitance and (b) normalized resistance for two groups during aging at 2.4V and 70°C and at 2.8V and 70°C. Notice the monotonic decrease in capacitance and increase in equivalent series resistance.

changes arising from catastrophic failures. Thus, almost any failure definition can be used with ECs. A popular end-of-life definition often listed on product specification sheets includes 30% capacitance loss and 100% series resistance increase.

Using this common failure definition, the life of each capacitor can be precisely determined through interpolation of the test data that brackets the failure time. Figure 13.12 shows continuous-line model fits derived for resistance data from each of the six capacitors aged at 2.6 V and 55 °C. Failure, here defined as reaching twice the initial resistance value, occurs over a narrow ~250 h range in time, from 1017 h to 1271 h. Failure times are used to derive Weibull life distribution models for each group, as shown graphically in Figure 13.13 for the 2.6 V, 55 °C group. Data points fall on a single straight line, meaning that the capacitor life in a group is well represented by a Weibull distribution. For the Figure 13.12 group, the characteristic

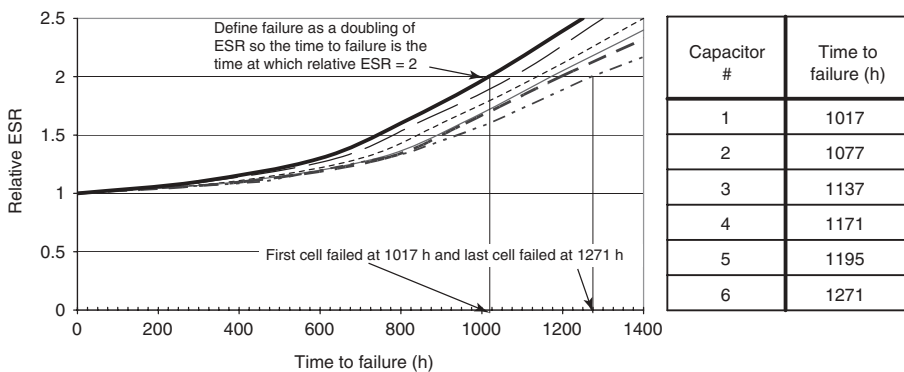


Figure 13.12 Continuous-line fits for the normalized resistance of the six capacitors aged at 2.6V and 55°C. Time to failure (a doubling of the series resistance) is obtained by interpolation. Values are listed in the table.

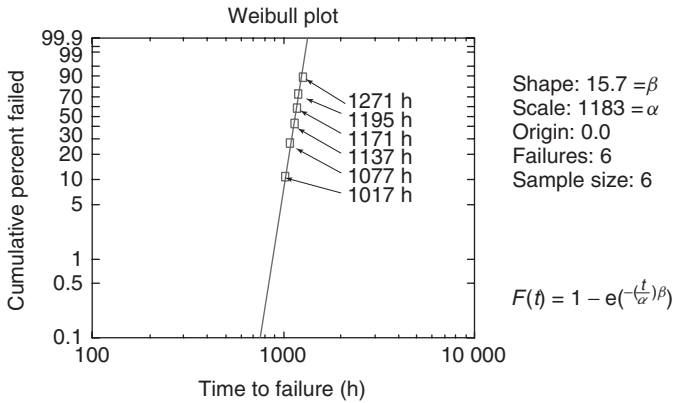


Figure 13.13 Weibull plot of life of the six Panasonic 1 F capacitors aged at 2.6 V and 55 °C, using series resistance doubling as the definition of failure. Note that failure times fit a straight line, indicating good fit to a Weibull life distribution.

Table 13.2 Test groups, number of capacitors assigned to each group, test time, number of capacitors that have failed after 6000 h of aging, and Weibull life distribution parameters.

Temperature (°C)	Voltage (V)	Number failed	Shape factor	Characteristic life (h)
70	2.8	3 of 3	8	100
70	2.4	6 of 6	25	760
55	2.9	3 of 3	11	150
55	2.6	6 of 6	16	1180
55	2.4	6 of 6	11	3970
40	2.8	3 of 3	10	900
40	2.6	6 of 6	9	3145
40	2.4	0 of 9	—	—
75	2.6	3 of 3	36	245

life is 1183 h and the shape factor is 15.7. Weibull parameters for all nine groups used in this aging experiment were derived and are listed in Table 13.2. Note that all capacitors reached defined failures during the study except those in the lowest stress group (2.4 V, 40 °C), where not a single failure was observed during 6000 h of aging.

Capacitors aged at different temperature/voltage conditions should still have the same Weibull shape factor, provided that life is limited by a common failure mechanism, for instance, irreversible chemistry, that is, an impurity reaction that generates gas. One such example is the conversion of the adsorbed oxygen on a carbon electrode to CO₂ gas. The conversion rate (chemical reaction rate) is, of course, strongly influenced by operating temperature and applied voltage and indirectly related to capacitor life.

Shape factors listed in Table 13.2 range from 8 to 36 and suggest that more than one mechanism may be operating. However, there is considerable uncertainty in the true values of the shape factors because only a small number of capacitors are used in some of the groups. At a 95% confidence level, the tolerance of the Weibull shape factor β is given by Abernethy *et al.* [1]:

$$\beta \exp\left(\frac{-0.78 \times 1.96}{\sqrt{n}}\right) \leq \beta \leq \beta \exp\left(\frac{0.78 \times 1.96}{\sqrt{n}}\right) \quad (13.8)$$

where n is the number of capacitors in a group. This means that there is a 95% chance that the “true” β will be positioned in the interval defined by Eq. (13.8). Small group size widens the interval. The value 15 falls within the shape factor tolerance of each group listed in Table 13.2, which implies that every group (experimental aging conditions used in the study) is likely to have the same dominant failure mechanism.

Taking the natural log of Eq. (13.7) yields the Arrhenius–Eyring life equation [9]

$$\ln(\tau) = A + B/T + CV \quad (13.9)$$

where τ is the characteristic life, T is absolute temperature in degrees Kelvin, V is voltage, and A , B , and C are constants. At constant voltage, this reduces to the common Arrhenius relationship, and at constant temperature, the equation reduces to the Eyring relationship between voltage and life. Figure 13.14 plots Table 13.2 characteristic life data versus aging voltage for the eight groups (the lowest stress group had no failures and thus an undefined characteristic life). As shown, life data for each temperature in this semi-log format does not fall on lines that are perfectly parallel as predicted by Eq. (13.9), suggesting temperature–voltage interactions. Figure 13.15 plots Table 13.2 characteristic life versus $1/T$, the reciprocal of the absolute temperature, again showing that the data at constant voltage does not

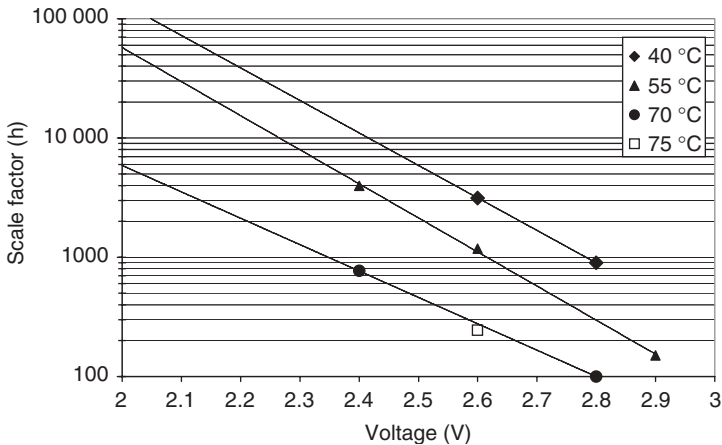


Figure 13.14 Table 13.2 characteristic life versus operating voltage for the Panasonic capacitor example using series resistance doublings as the definition of failure.

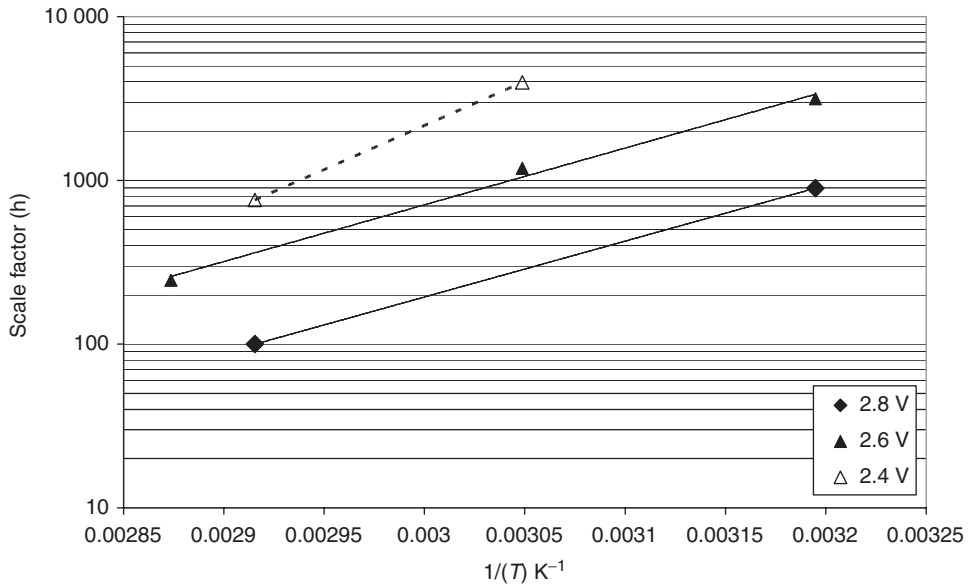


Figure 13.15 Arrhenius plot of the Panasonic capacitor characteristic life versus $1/T$, where T is the absolute temperature. The definition of failure is doubling of the series resistance. Lines should be parallel if there are no voltage–temperature interactions.

form parallel lines – voltage–temperature interaction terms are clearly needed to better represent observed behavior.

Equation (13.10) describes a quadratic life model with a temperature–voltage interaction term as well as second-order temperature and voltage terms.

$$\log(\tau) = A + B/T + D \times V + E/T^2 + F \times V^2 + G \times V/T \quad (13.10)$$

Here, A , B , D , E , F , and G are constants, τ is the characteristic life of the capacitor, T the absolute temperature, and V the applied voltage. The experimental design (Figure 13.10) in this example was devised specifically to allow for the development of a quadratic life response. Although one group has had no failures during the first 6000 h of aging, and thus has an indeterminate characteristic life, information from the other eight groups is sufficient to derive a quadratic life equation, Eq. (13.11). The T in this equation is in Kelvin, and characteristic life τ is in h.

$$\log(\tau) = -72.02 + 37080/T + 12.67V - 4482000/T^2 - 1.535V^2 - 2376V/T \quad (13.11)$$

Characteristic life data (Table 13.2) and the quadratic model predictions (Eq. (13.11)) are shown in Figure 13.16. The solid lines are predictions made using Eq. (13.11) and fit all data points quite well, better than the noninteraction model. Predictions made using the noninteraction model (Figure 13.14) differ greatly from those of the interaction model (Figure 13.16) at voltages below 2.4 V, which was an unmeasured region in this study. For example, the characteristic life at 2.0 V and 55 °C is

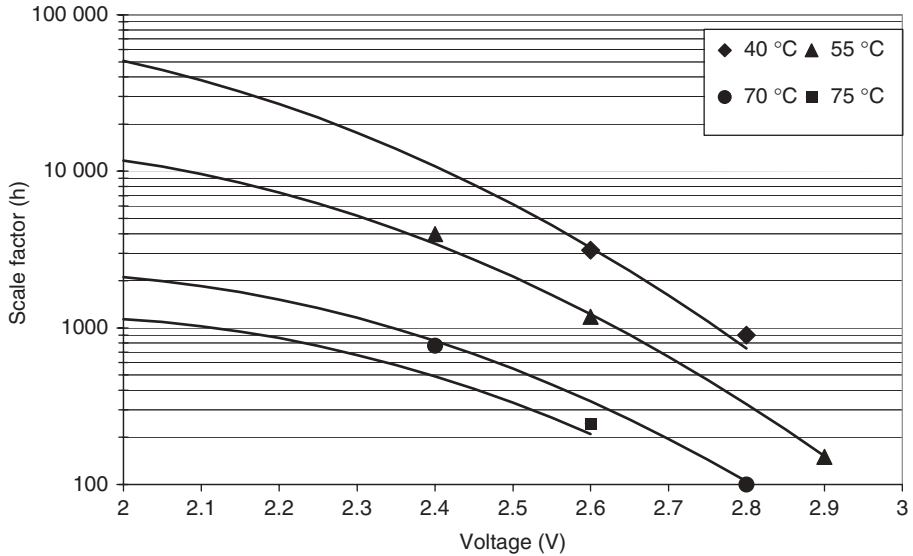


Figure 13.16 Interaction model predictions (lines) of the capacitor life at four measurement temperatures.

predicted to be $\sim 50\,000$ h using the noninteraction model and $\sim 12\,000$ h using the interaction model. Similarly, the 2.0 V, 70 °C characteristic life is predicted to be ~ 6000 h using the noninteraction model and ~ 2100 h using the interaction model.

The characteristic life interaction model (Eq. (13.11)) can be used to derive contours of constant characteristic life as a function of temperature and voltage, as shown in Figure 13.17. The right-most contour is for a 2000 h characteristic life. This means that if a large group of capacitors were aged at any T - V point on this curve, 63.2% of them will have series resistance values double that of their initial values after 2000 h. The next contour is for a 4000 h characteristic life. Again, a group of capacitors aged at any point on this curve will experience 63.2% failures (series resistance doubling) after 4000 h.

The projections shown in Figure 13.17 are made after only 6000 h of aging time. Thus, locations of the 2000 and 4000 h contours are quite accurately placed because groups of capacitors were aged at conditions on both sides of these curves. Confidence levels decrease as projections extend into the future. The 8000 h contour location is less certain, but certainly better than the more simplistic noninteraction model with its overly optimistic predictions. The 16 000 h contour is a projection that is made even farther into the future, ~ 2.7 times beyond the actual experimental aging time, so its exact location is even less certain. Nevertheless, the described interaction model combines life data from eight different test conditions to allow the best possible projections to be made. Confidence levels decrease at increased times. Projections in time of a factor of 3 or more are often made and used in engineering a system, depending on the application and the degree of risk assumed.

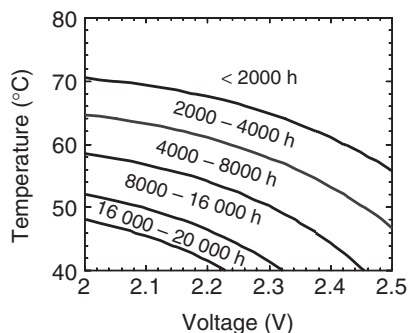


Figure 13.17 Contours of constant characteristic life (h) as a function of temperature and voltage.

13.6 Reliability of Practical Systems

Discussion to this point has assumed that cells in a series string were (i) all at the same voltage at all times and (ii) all at the same temperature at all times. This, however, is usually not found in practical systems, particularly those assembled from hundreds of cells that are located in several separate interconnected modules and operated dynamically in a changing environment, for example, a situation that might be found in the storage system of a hybrid-electric city transit bus.

Voltage nonuniformity among cells in a series string will always exist, even with active or passive cell voltage balance schemes, owing to the inherent variability present within any group of nominally identical items. And second, there will always be temperature nonuniformity among the cells that make up an energy storage system, even when active or passive thermal management approaches are used, again owing to inherent variability within any group.

With constant voltage applied to a string of series-connected cells, the leakage current of any cell establishes its voltage. Voltage balance schemes are most effective under these steady-state conditions. Here, the distribution of cell voltages will be directly controlled by the balance system, for instance, the distribution of resistance values when a passive resistor balance system is used. During transient operation, the ESR of a cell establishes its voltage. Thus, the voltage distribution of cells in a series string will be directly reflected by the distribution of cell ESR values. In either case, a common voltage distribution found for large groups of cells will be a normal (Gaussian) distribution.

Dynamic operation of any storage system generates heat. If the heat is not uniformly dissipated, then system temperature will not remain uniform. Cells in practical systems are often connected to heat sinks for thermal conditioning, but this nevertheless leaves at least some degree of temperature nonuniformity owing to the variability in the heat generated in each cell and the rate at which it is removed.

13.6.1

Cell Voltage Nonuniformity

The following example demonstrates the adverse effects that cell voltage nonuniformity can have on life. Consider a system comprising series-connected cells having a distribution of cell voltages described by a Gaussian distribution with an average value V_0 and a tolerance $\Delta V = \pm 0.1$ V. Further, assume that 99% of the cells meet this tolerance limit. Thus, only one cell out of every hundred will be outside the 0.2 V wide voltage band. The voltage probability density $G(V)$ for cells having this distribution can be mathematically represented by Eq. (13.12)

$$G(V) = A \times \exp[-1/2 [(V - V_0)/0.039]^2] \quad (13.12)$$

where V_0 is the average voltage and A is a constant. This equation is plotted in Figure 13.18a. For this example, also assume that a “0.1 V life doubling rule” is obeyed, that cell life doubles with a 0.1 V decrease in voltage or falls to half the value with a 0.1 V increase in voltage. Life dependence, normalized to the life of a cell held at V_0 , is shown in Figure 13.18b.

In this example, it is obvious that voltage nonuniformity changes the life distribution: cells operating at higher voltage will have shorter life and cells operating at lower voltage will have longer life. The mathematical approach to derive the probability density function of the sum of two random variables, in this

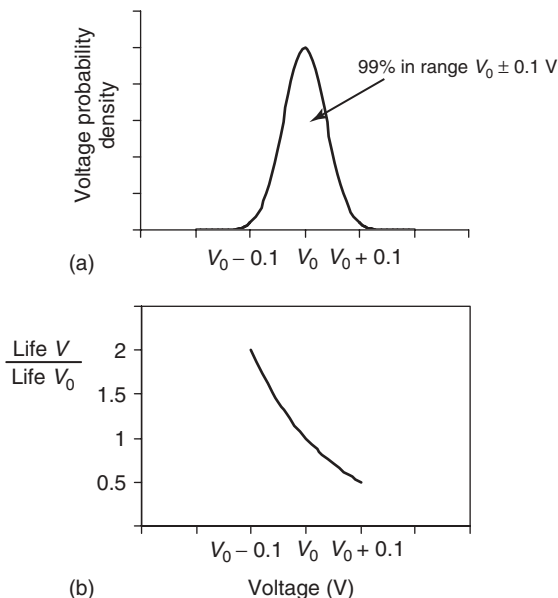


Figure 13.18 (a) Gaussian distribution of voltages about V_0 that is assumed to be the voltage variability in a group of cells. The tolerance is ± 0.1 V, and 99% of the population is contained within this tolerance. (b) The dependence of characteristic life on voltage using the “0.1 V life doubling rule.”

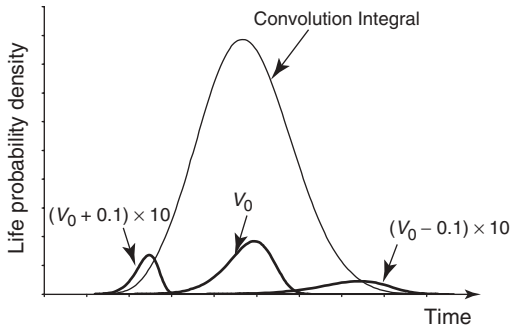


Figure 13.19 The Weibull life distribution with Gaussian variability of cell voltage included (convolution integral). Also shown is the Weibull contribution at V_0 and the two limiting contributions at the voltage extremes ($+0.1$ V and -0.1 V), which are magnified by 10 to better reveal their shapes.

case life and voltage, is to perform a convolution integral of the two distributions [10]. In effect, this new distribution can be thought of as the sum of many constant-voltage distributions, each with a characteristic life derived using the doubling rule and having a weight specified by the voltage distribution function. Figure 13.19 graphically shows three elements of the convolution integral – the life distribution for cells at V_0 , $V_0 + 0.1$ V, and $V_0 - 0.1$ V. (The heights of the curves at the two voltage tolerance limits in this figure have been multiplied by 10 to better reveal their shape.) As shown, the mean life of cells with voltage nonuniformity (the convolution integral) is only slightly changed, but life is more broadly distributed in time than the curve for cells held at constant V_0 .

With some distributions, convolution integrals can be performed analytically, but in practice it is often too complicated for such a solution and the integral is done numerically. The convolution integral of a Weibull distribution and a Gaussian distribution was performed numerically for the illustrated examples.

For concreteness, consider a 100 cell module consisting of cells characterized by a life that is well represented by a Weibull distribution with a shape factor $\beta = 10$ and a characteristic life $\alpha = 10\,000$ h when operated at voltage V_0 . Assuming these cells have a Gaussian voltage distribution with 99% of them falling within a 0.1 V band about V_0 , then taking the convolution integral (Figure 13.20) yields a life distribution that can again be represented by a Weibull distribution but with $\beta = 4.8$ instead of 10 and the same $\alpha = 10\,000$ h. The peak width at half height doubles from ~ 2500 h for the original distribution to ~ 5000 h in the resultant distribution.

These new Weibull parameters can be inserted in Eq. (13.6) to derive the life distribution of the 100 cell module with the specified voltage variability, $\alpha_{100} = 10\,000/100^{(1/4.8)} = 3831$ h. Thus, cells with a characteristic life of 10 000 h in use will have a characteristic life of 3831 h, or 38% of the original life when operated in a 100 cell module having a distribution of voltages characterized by a Gaussian with 99% of the cells within 0.1 V of the average voltage.

In this example, the shape factor β is reduced to about half its original value when only a very small degree of voltage variability is introduced, which significantly

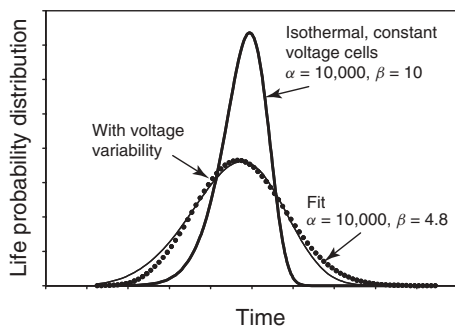


Figure 13.20 The original Weibull life distribution ($\alpha = 10\,000$ and $\beta = 10$) with fixed-voltage cells (tall solid line) and the Weibull life distribution with cells that have a Gaussian distribution of voltages (dotted line). The distribution with voltage variability is well represented by a Weibull life distribution with $\alpha = 10\,000$ and $\beta = 4.8$, as shown.

increases the number of cell failures at shorter times and adversely affects the life of systems comprising series-connected cells. The “bottom line” is that even a small degree of cell voltage nonuniformity in a system can significantly reduce its life.

13.6.2

Cell Temperature Nonuniformity

Irrespective of the sophistication used to establish temperature uniformity among cells in a large capacitor storage system, there will always be some distribution of temperatures, owing at least to cell manufacturing variability. The 10° rule (Eq. (13.7)) holds approximately for EC technology, that is, that a 10°C decrease in temperature will *double* the life of a cell, effectively shifting the distribution that represents cell life to values two times longer. This approximation provides a means of examining the influence of nonuniform temperature on the life of a group of cells comprising a module. Thus, a cell on the hot end of a module that is 10° higher in temperature than a cell on the cold end will have half the life of the cooler cell. As the cells are usually in a series string, this can represent a serious situation, because the hotter cell will, in fact, dictate the life of the entire system.

In an EC module, there may be many series-connected cells, and we assume that they all have the same voltage. In the real world, this assumption is almost always met because manufacturers of high-voltage modules usually include cell-voltage-balancing electronics, whether a simple parallel resistor string or an active voltage-equalizing circuit.

The module design may also contain thermal management features, especially in modules intended for use in continuous high-rate cycling applications. Such designs often attempt simply to prevent any one cell in the system from ever exceeding its maximum temperature rating – isothermal operation is usually not a design goal. Because heat generation is not uniform owing to cell property variability plus uneven heat removal rate from the cells, cell temperature nonuniformity is

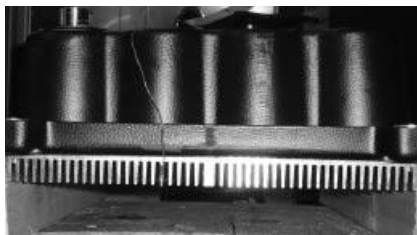


Figure 13.21 Photograph of an electrochemical capacitor module containing 20 cells anchored to heat fins to provide cooling. Air flow direction is into the page from this view.

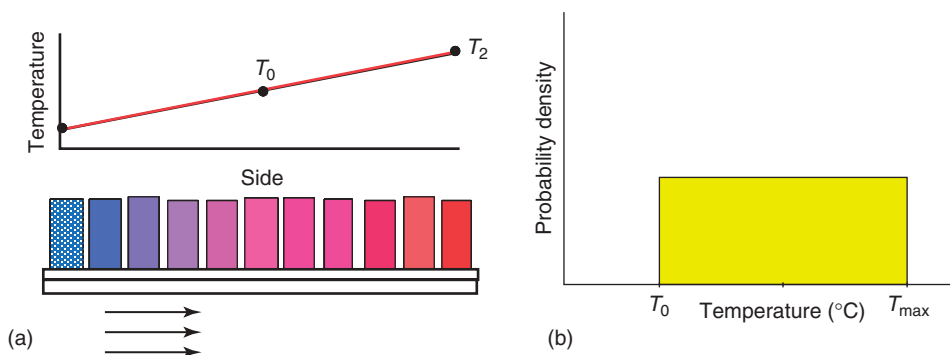


Figure 13.22 (a) Side view of a string of cells on a heat sink as shown in Figure 13.21 with cooled air flowing from the left. The resulting temperature profile is at the top. (b) The temperature probability density for this 1D example with cooling from one direction. The number of cells at each temperature in the range between T_0 and T_{max} is constant.

certain. This nonuniformity decreases system life, the magnitude dependent on the cell temperature probability density.

As a first example (1D), consider a module composed of a group of cells anchored to cooling fins as shown in the photograph in Figure 13.21 of an 18 cell module [11]. Air movement along these fins provides cooling. One end of the module will be cooler than the other, the one at the cooling air source. This design will have a temperature profile as shown in the schematic in Figure 13.22a – a monotonic temperature rise from air inlet to air outlet. This 1D example has cells evenly spaced in temperature between a maximum and a minimum value, thereby creating, except for cell granularity, a constant cell temperature probability density as shown in Figure 13.22b.

As a second example, this time with 2D heat flow, consider a group of cells mounted on a square heat sink, with cooling applied to the perimeter of the square such that this boundary is always maintained at a constant temperature [12]. Such boundary conditions can be realized using, for instance, liquid cooling. Thus, with uniform heat generation from each of the cells (again ignoring cell granularity), there will be a circular hot spot in the center of the square, nearly concentric

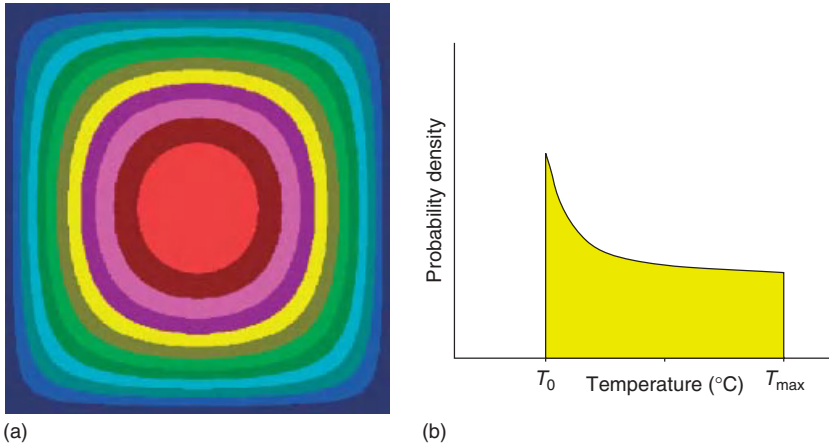


Figure 13.23 (a) Constant temperature contours for a square module with cooling on each edge of the square. Heat is generated and delivered uniformly over the area. The highest temperature is at the center (red circle) and (b) temperature probability density for the square module. The number of cells at the minimum temperature (at square edge) is greater than the number of cells at higher temperatures (near the center of the square).

isothermal circular rings around this hot spot at progressively lower temperatures, and then even lower temperature contours that morph from circular to square shape to satisfy the boundary condition. Figure 13.23a shows isotherms for this example. Note the symmetry. The temperature gradient is largest near the boundary of the square and highest at the center of each side. Temperature probability density for this 2D example is shown in Figure 13.23b. It is relatively flat for cells at high temperatures and increases for cells at low temperatures, that is, there are more cells at the minimum temperature than at the maximum temperature. From the relationship between temperature and life, the small decrease in the high-temperature end of the cell temperature probability density (being shifted to the low-temperature end) will enhance system life over that of the 1D example examined earlier. Thus, changing the thermal management design from 1D to 2D reduces the number of cells in the upper temperature range, decreasing system thermal stress.

And as a third example, consider a module in the shape of a cube with each face cooled to the same uniform temperature (Figure 13.24a). Again, liquid cooling is one means to achieve this boundary condition. Ignoring granularity from the discrete cells, heat will be generated uniformly throughout the cube volume, producing the maximum temperature at the cube center. Isothermal contours near the middle of the cube will be spherical and concentric. A cross-section slice through the center of this module that is parallel to a cube face would have temperature contours exactly as those shown in the 2D example. Note that the temperature gradient is steepest at the center of each cube face, indicating that maximum heat flux occurs at these six locations. This example with 3D cooling

Uniform heat generation in volume

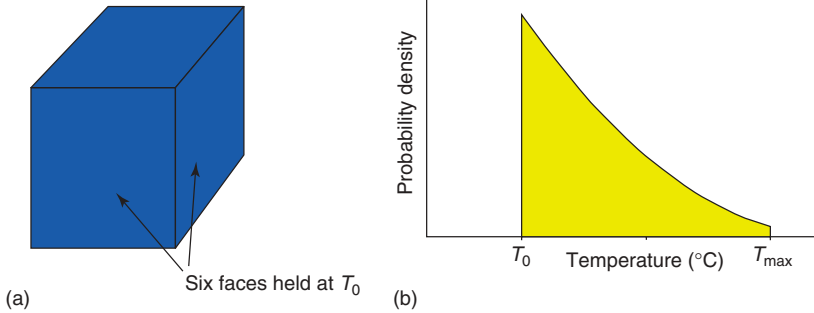


Figure 13.24 (a) Cubic module with cooling applied to all six faces – the boundary condition is each face is held at a fixed temperature. (b) Temperature probability density for a capacitor module in the shape of a cube with this boundary condition. There are few cells at the highest temperature and many more at the lowest temperatures.

produces a much different temperature probability density (Figure 13.24b) than the previous two examples.

As shown, cube geometry has fewer cells at high temperatures and more cells at low temperatures than the previous two examples. This is not surprising because distance from the maximum heat-extraction location (center of each cube face) to the hottest location (cube center) is less for a system with 3D cooling geometry than it is for an equivalent volume system employing either 1D or 2D cooling. The geometry of this third example positively impacts cell life – it has substantially fewer hot cells. Next examined is the impact on life that occurs from having such temperature probability densities in a module.

The life distribution of a module comprising many cells that are not uniform in temperature, including effects from having them connected in series, can be derived using a sequence of steps. This involves starting with the cell life distribution (at isothermal conditions), using the 10° rule that relates cell life to temperature, incorporating the cell temperature probability density determined by the module design, and finally deriving module life from the number of series-connected cells it contains.

This sequence is illustrated step-by-step using as an example a 100 cell module with a 1D thermal management design. Here, we assume (for simplicity) that cells are uniformly distributed in temperature over a 10°C range and that they can be accurately represented by a Weibull distribution having a characteristic life of 1000 h and a shape factor of 10.

Figure 13.25a shows the temperature probability density, and Figure 13.25b shows the life–temperature relationship. With temperature variability, the cell life distribution changes as discussed – lower temperature cells will have a longer characteristic life, and higher temperature cells will have a shorter characteristic life. Thus, the width of the life distribution having nonuniform temperature cells should increase. The life distribution modified by a temperature distribution is derived by performing a convolution integral, as previously discussed. Because the

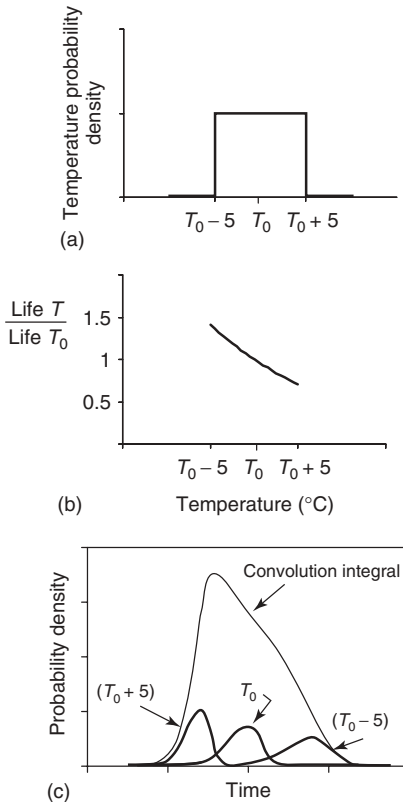


Figure 13.25 Reliability calculation for a module with cooling from one direction: (a) temperature probability distribution of cells assumed to span a 10°C range, (b) normalized life of cells per equation (13.7), and finally (c) life probability density (convolution

integral) for a group of cells with a 10°C span in temperature. Three elements of the integral are shown, life for the minimum and maximum temperatures and life for cells at the midpoint in temperature.

temperature probability density is uniform, the new distribution is equivalent to the sum of an infinite number of constant temperature distributions, each having equal weight and a relative life shown by Figure 13.25b. Figure 13.25c shows the life distribution (convolution integral) when cell temperatures are uniformly distributed over the range $\pm 5^\circ\text{C}$, the convolution constituent with no temperature variability (at T_0), and the convolution constituents at the two limits, $T_0 + 5^\circ\text{C}$ and $T_0 - 5^\circ\text{C}$.

The shape of the life distribution with $\pm 5^\circ\text{C}$ temperature variability (Figure 13.25c) is grossly distorted from the original constant temperature Weibull distribution. The peak of the new distribution is shifted to shorter times, to ~ 750 h from ~ 1000 h, with increased failures at short times. Such behavior was expected – cells having temperatures above T_0 will have characteristic life values shifted below the peak of the original isothermal life distribution curve.

The cell life distribution with the $\pm 5^\circ\text{C}$ temperature tolerance in this 1D example (Figure 13.26a) is poorly represented by a Weibull distribution. Thus, Eq. (13.6) cannot be used. Instead, the general definition of reliability of a string of cells where one cell failing means the entire string fails (Eq. (13.4)) can be used to numerically derive the life of a 100 cell module constructed using the cell life distribution with a 10°C span in temperature between the hottest and coldest cells. Steps include calculating cumulative failures (integral of curve), determining the surviving cells, which equals 1 minus the cumulative failures, raising this to the 100th power to derive surviving 100 cell strings, and differentiating 1 minus this function to determine system life distribution, shown graphically in Figure 13.26b. The life distribution of 100 cell modules with 1D thermal management is shown in Figure 13.26c. Note that the peak of the module life distribution curve occurs at ~ 650 h, well below the ~ 1000 h value of the original cell distribution under isothermal conditions. The “bottom line” is that the $\pm 5^\circ\text{C}$ cell temperature nonuniformity does indeed shift the life distribution to a significantly shorter time.

13.7

Increasing System Reliability

While cell durability is a fundamental limitation for many systems, it is system reliability that must be addressed. The reliability of any higher voltage system will always be lower than that of its constituent cells. In some applications, reliability is utterly critical, for example, in applications such as manned space flights. NASA uses redundancy (adding backup systems) to increase reliability. A second and perhaps even a third system is often included as backup in case of failure of a critical system. This is an expensive approach that generally cannot be afforded in size, mass, and cost in most applications. Other less costly approaches are available to increase capacitor system reliability. They include reducing stress applied to individual cells, performing component “burn-in,” using fewer series-connected cells (lower system operating voltage), using longer life cells, adding scheduled maintenance and, again, adding redundancy. Each of these approaches has advantages and disadvantages, which are discussed here.

13.7.1

Reduce Cell Stress

System reliability is strongly influenced by cell temperature, cell voltage, and uniformity of temperature and voltage among cells in a system. Thus, a most obvious approach for increasing reliability is to reduce the stress levels, which could include improving the thermal management system to lower the average cell temperature and/or increase the overall temperature uniformity. It also could include reducing the average voltage applied to each cell. Cells are routinely operated at reduced voltage in practical systems to help meet life requirements – maximum operating voltage on cells in a typical system is generally 10 to 15% below the rating.

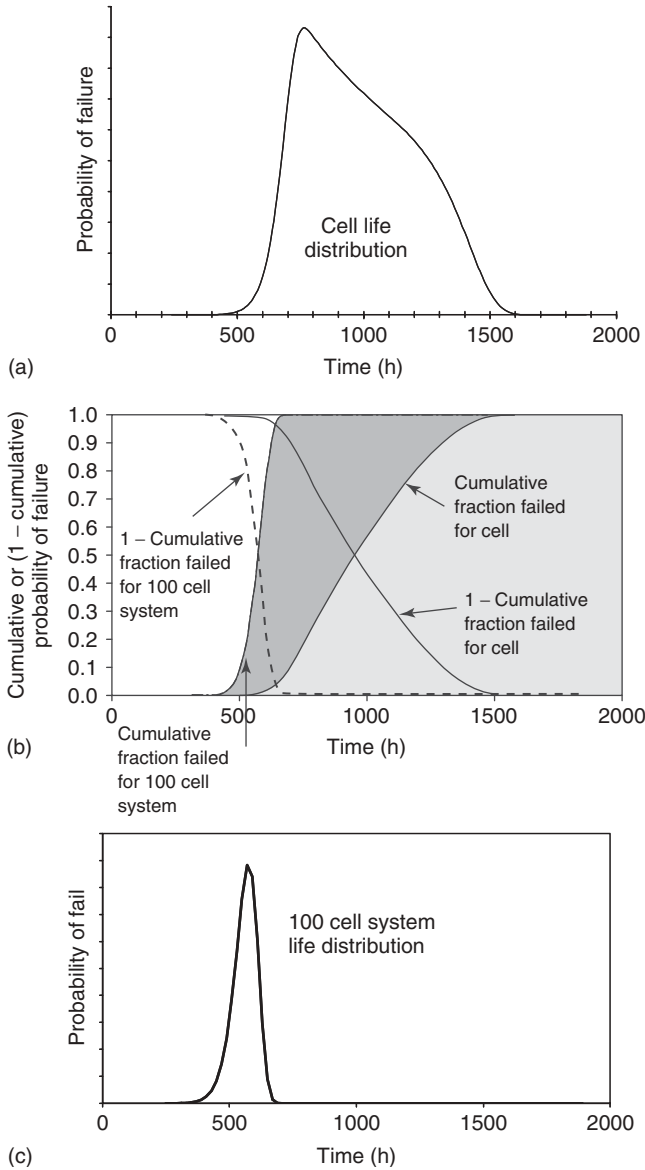


Figure 13.26 Derivation of the life distribution for 100 cell modules. (a) Cell life is assumed to be represented by a Weibull distribution having a characteristic life of 1000h, a shape parameter of 10, and a 10°C range of temperatures with equal number of cells at each temperature (Figure 13.25 result). (b) Sequence of calculations needed to derive the module life distribution. This includes calculating

cumulative failures (integral of curve); determining the surviving cells, which equals 1 minus the cumulative failures; raising this to the 100th power to derive surviving 100 cell strings; and differentiating 1 minus this function to determine system life distribution, shown in (c). Note that the peak of the system curve is at $\sim 650\text{h}$, well below the cell value of $\sim 1000\text{h}$.

This does, of course, increase the number of cells required in a series string to meet voltage requirements but this approach usually leads to a substantial increase in system life.

13.7.2

Burn-in of Cells

Except for temperature and voltage stress reduction, one of the simplest and often most effective approaches to increase system reliability is to “burn-in” the group of cells before use [13]. Burn-in generally consists of holding cells at some particular voltage and temperature for a specified time, often at rated voltage and maximum operating temperature, although slight overstress conditions are sometimes used. All cells exhibiting early failure (infant mortality) are thus eliminated from use right at the beginning. Burn-in also helps stabilize cell performance, and thus cell measurement information can be used to select those cells most suitable for use in a system, which would be those most uniform and totally free of any “strangeness.” Tighter cell property distributions can produce system-life distributions that approach the maximum possible value. After-burn-in cell property data is also useful for identifying manufacturing quality problems.

13.7.3

Use Fewer Cells in Series

Figure 13.8 demonstrates the impact that series-connected cells have on system life – shorter strings generally offer longer life. Thus, reconfiguring a system to have fewer cells in a string but with more strings in parallel can provide benefits. The total number of cells remains approximately the same, but system operating voltage will be lower. Care is needed when reducing system voltage, of course, so as not to create a temperature nonuniformity problem owing to additional heat generated from operation at higher currents. Systems comprising cells with strong wear-out behavior ($\beta \gg 1$) are least helped by reducing system operating voltage, while those having cells with a smaller shape factor ($\beta \sim 1$) will realize the most life-augmenting benefit.

13.7.4

Use “Long-Life” Cells

One strategy to increase system reliability is to construct it from cells with increased reliability. Most commercial ECs ultimately fail by gas generation within their package, that is, unwanted chemistry often associated with impurity reactions. Smaller cells tend to have relatively more “dead space” than larger cells and thereby provide relatively more volume for gas accumulation. Thus, the smallest cell in a capacitor product family often is the one providing the highest reliability.

Cell design strongly influences cell reliability. Another strategy to increase cell reliability is to redesign cells for long life at the expense of some other characteristics,

for instance, energy density or specific energy. As an example, cells that have life limitations related to water or other impurities passing through seal materials may benefit by using a different seal design or by adding a second seal. Or if impurity entry is by permeation through the package itself, then use of a thicker wall package may be helpful. The strategy is to reduce the significance of a dominant failure mode.

There are other design-related factors that impact system reliability. Generally, heat removal and thereby temperature uniformity is easier to maintain using smaller packages. Thus, a system comprising more number of smaller size cells may provide reliability advantages over fewer larger size cells in high-cycle-rate operation.

Vibration susceptibility is strongly design related. Smaller, lower mass cells generally are more robust to shock and vibration than large cells. Thus, pairs of parallel-connected half-size cells may provide reliability advantages over full-size cells in applications where vibration is a dominant stress factor.

In summary, care must be exercised to use cells that are well suited for the application. This requires intimate knowledge of both the application and the cell design.

13.7.5

Implement Maintenance

Scheduled maintenance is also a means to improve reliability. This is a common approach used by the military, for instance, where regular service and/or replacement is the policy, whether needed or not. The properties of an EC cell do establish its state of health, which can predict the need for maintenance if a regular schedule is not kept. And finally, visual inspections of cells and interconnects for signs of deterioration such as corrosion can be performed to prevent system failure. There are, of course, labor costs involved with this approach, but it is nevertheless a proven way for improving reliability.

13.7.6

Add Redundancy

Redundancy, although costly, is perhaps the ultimate solution to increase reliability and certainly justified in particular applications. NASA relies heavily on this approach. The mathematics of active redundancy is well established. With N identical systems in parallel and only one needed for operation, reliability is described by

$$R_p(t) = 1 - \prod_{i=1}^N [1 - R_i(t)] \quad (13.13)$$

where R_i is the reliability of a single system. If there are N identical systems in parallel and k are needed to operate, the reliability is described by

$$R_p(t) = \sum_{j=k}^N \binom{N}{j} [R(t)]^j [1 - R(t)]^{N-j} \quad (13.14)$$

where

$$\binom{N}{j} = \frac{N!}{(N-j)!j!} \quad (13.15)$$

Active redundancy usually does not provide much gain in terms of increased system life because only one system is needed, while the additional systems are present, operating, and all wearing out at the same time.

Better than active redundancy is a procedure where the backup system does not become active until the moment the first system stops functioning properly. This “standby” redundancy is more economical and provides more gain. If one system is required and an extra one is available, life is doubled. Two extra systems then provide three times the life, and so on.

In summary, the reliability of a capacitor system is generally lower than that of its constituent cells. While cell durability is the fundamental limitation for many applications, particularly at high voltage, it is the system reliability that matters. A detailed analysis is required to determine the optimum system configuration.

13.8 System Design Example

13.8.1

Problem Statement

A hybrid diesel-electric city transit bus is used as an example to demonstrate the sequence of steps that can be followed to design a capacitor energy storage system that meets both functional and reliability requirements. In this example, the power profile applied to the storage system is as shown in Figure 13.27, which is determined from the speed and mass of the bus. This profile has 90 kW peak discharge at the end of bus acceleration and 150 kW peak deceleration at the start of regenerative braking. The engine charges the storage system at 5 kW during constant speed driving (10–25 s) and during the time that the bus is stopped (30–45 s). Such triangular-shaped power ramps indicate that velocity changes are made at constant acceleration. The 45 s power profile is repeated continuously and models storage system performance requirements. In this example, the bus travels at an average speed of 15 mph (which may be high for some cities – average bus speed in Manhattan is reported to be only 7.6 mph).

For this example, assume bus design engineers have specified that energy storage system operation will be in the 300–600 V range and its operating temperature maintained at $45^\circ \pm 5^\circ\text{C}$. Thus, all capacitor cells in the system will operate in a 40–50°C temperature band. Financial considerations usually dictate the thermal management system’s temperature tolerance.

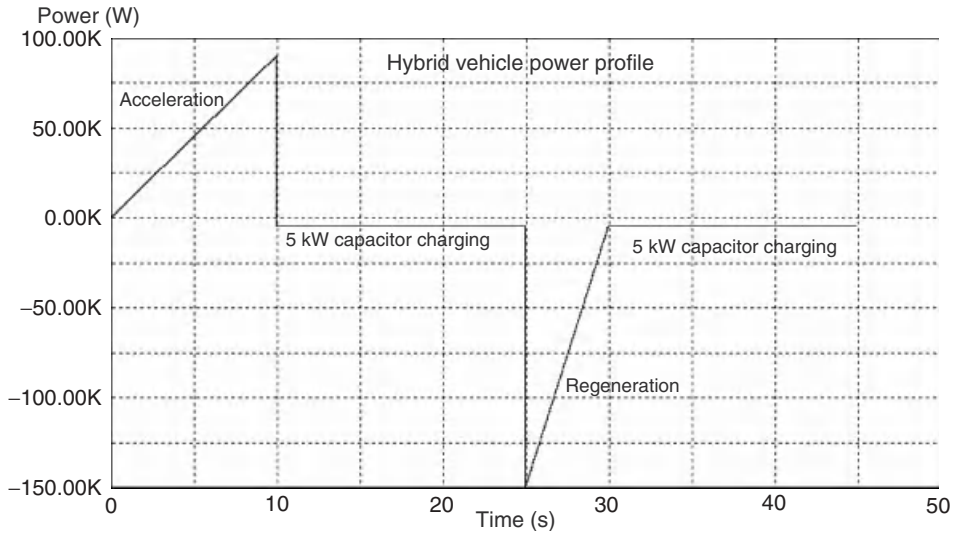


Figure 13.27 Power profile applied to the hybrid bus energy storage system. The bus accelerates at constant rate with peak power at 90 kW and stops at constant deceleration with peak power at -150 kW. The engine charges the storage system at 5 kW during constant speed driving (10–25 s) and while stopped (30–45 s). This 45 s power profile is repeated continuously and is used to model storage system power requirements.

Minimum bus reliability is specified as 98% for 50 000 miles and 80% for 200 000 miles (12 years' operation). This second longevity stipulation arises from regulations covering the expenditure of government transit funds. Thus, a city that buys 100 buses will need to have the capacitor storage systems on at least 98 buses provide 50 000 miles of service and on at least eighty buses provide 200 000 miles of service.

The manufacturer of the capacitor cells selected to use in the bus storage system specifies them as having less than 30% capacitance loss and 30% ESR increase during aging at 65°C and 2.5 V for 2000 h, with less than 1% of the cells failing. Cells, as determined by previous testing, can be modeled as a series-RC circuit with $RC = 1.3$ s. Furthermore, the cells are known to fit a Weibull life distribution having a shape factor $\beta = 10$. Capacitor life is assumed to follow standard rules – life is doubled for every 10°C decrease in operating temperature or 0.1 V decrease in operating voltage.

13.8.2

System Analysis

Step one is to size the storage system to meet performance requirements over the specified life. As the capacitor will have experienced a 30% increase in ESR and/or a 30% decline in capacitance at the end of its life (by definition), the storage system must be oversized by 30% so that application requirements are exactly met after

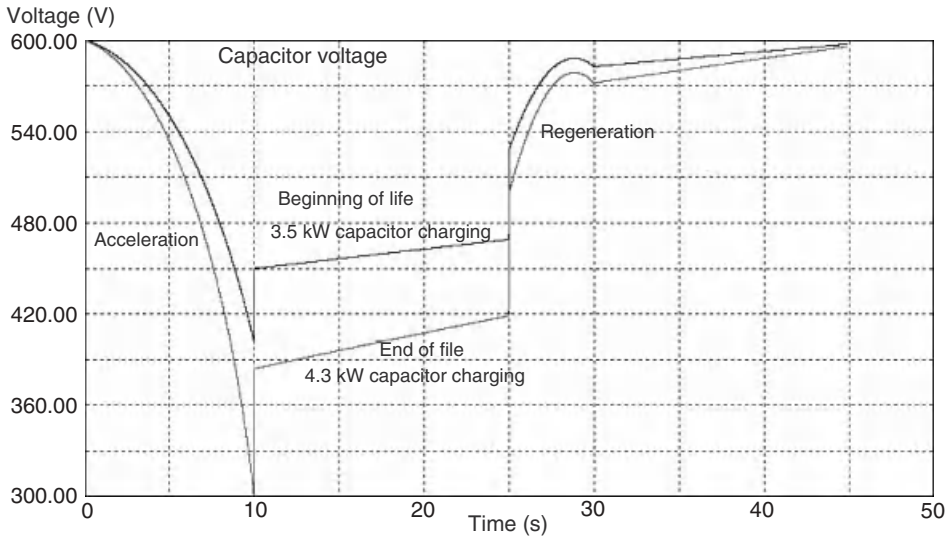


Figure 13.28 Voltage of two capacitors initially charged to 600 V and subjected to the Figure 13.27 power profile. The beginning of life capacitor is rated at 6 F with 0.21 Ω ESR. The end-of-life capacitor, which spans the entire 600–300 V operating voltage window, has 30% lower capacitance (4.6 F) and 30% larger ESR (0.28 Ω).

reaching this degree of performance fade. System ESR is treated the same way. An optimum capacitor storage system will span the entire voltage window each cycle, since energy is not delivered by or stored in a capacitor unless its voltage does change.

Figure 13.28 shows the response of a 4.6 F capacitor ($ESR = 1.3/4.6 = 0.28 \Omega$) initially charged to 600 V and then subjected to the Figure 13.27 power profile. While the power ramps from 0 to 90 kW, capacitor voltage declines from 600 to the minimum allowed value of 300 V. Then the capacitor is partially charged at 5 kW before regenerative charging begins at 25 s, followed by the constant 5 kW power recharge to the initial value. The beginning of life solution (where the capacitor is 30% larger and has 30% lower ESR: $C = 6.0$ F and $ESR = 0.21 \Omega$) is also shown in this figure. In this case, the minimum voltage reached is ~ 390 V, well above the minimum value due to its oversizing but necessary to compensate for normal performance fade. Common circuit analysis software can be employed, using an iterative procedure to size the capacitor system.

Note that according to Figure 13.28 capacitor voltage is at ~ 575 V for about half of the time, a condition that defines the stress on the system. Capacitor voltage at other times is substantially lower and applies negligible stress because of the 0.1 V doubling rule. This maximum stress level condition will later be used to determine the number of cells needed in a series string to meet reliability specifications.

The two specified reliability requirements can be recast remembering that the average bus speed is 15 mph, and that stress is applied during only half of this

time. Thus, 2% of the bus storage systems are allowed to fail in $\frac{1}{2} \times 50\,000/15 = 1667$ h and 20% of them are allowed to fail in $\frac{1}{2} \times 200\,000/15 = 6667$ h. Eq. (13.3) with $\beta = 10$ allows characteristic life values to be calculated, which for the 50 000 h requirement is $\alpha = 2463$ h at 575 V and is $\alpha = 7746$ h at 575 V for the 200 000 requirement. The first requirement ($\alpha = 2463$ h at 575 V) is automatically met when the second more stringent requirement is met. Then the storage system reliability requirement (with $\beta = 10$) can be distilled to: capacitor system characteristic life α_{system} must equal 7746 h minimum when held at 575 V and maintained at $45^\circ \pm 5^\circ\text{C}$.

The capacitor storage system will need to have about $600/2.4 = 250$ cells in series to meet system voltage requirements. Equation (13.6) relates the reliability of a string of cells to the reliability of the cells in the string. Thus, the characteristic life of a cell must be $\alpha_1 = \alpha_{250} \times (250)^{1/10} = 7746 \text{ h} \times 1.74 = 13\,500$ h. Note that the multiplier is quite insensitive to the exact number of cells in series because of the large shape factor – the multiplier is 1.70 for $M = 200$.

Although the cell temperature distribution is not specified in this example, only that all cells fall within a 10°C wide band, this level of nonuniformity will, as shown in an earlier section, decrease system life substantially, which is estimated to be a factor of 2 for this example. *Thus, cells used in this system must have a characteristic life $\alpha_{\text{cell}} = 27\,000$ h minimum.*

13.8.3

Cell Reliability

The capacitor cells used in this application experience less than 1% failure after aging at 65°C and 2.5 V for 2000 h. Here, the definition of failure is 30% capacitance loss and/or 30% ESR increase. The cells are known to fit a Weibull life distribution and have a shape factor $\beta = 10$. Capacitor life is assumed to follow standard rules – life is doubled for every 10°C decrease in operating temperature or 0.1 V decrease in operating voltage.

From Eq. (13.3), selected cells have a characteristic life $\alpha = 2000/[-\ln(0.99)]^{0.1} = 3168$ h. This is at 2.5 V and 65°C . The application needs $\alpha_{\text{cell}} = 27\,000$ h at 45°C . There is a 8.5-fold discrepancy between offered and needed life! Equation (13.6) and Figure 13.9 show how temperature and voltage reductions can increase life. First, dropping the temperature from 65 to 45°C increases life fourfold. Second, reducing the cell voltage from 2.5 to 2.29 V increases life 2.2-fold. Together, these operational changes provide the 8.5-fold increase in cell life needed to meet reliability specifications of this application.

Use of $600/2.29 = 262$ cells, each operating at 2.29 V or less in a $45^\circ \pm 5^\circ\text{C}$ environment, meets functional and reliability specifications of this application example. Finishing the design, the capacitor storage system at the beginning of life will be rated at 6.0 F with an ESR of 0.22Ω . Each cell will need to have at least a $262 \times 6 = 1572$ F capacitance rating with a $0.8 \text{ m}\Omega$ maximum ESR rating.

If the cells were to operate at their rated voltage of 2.5 V, the number required would be 240. By adding only 22 cells, about 10% of the total, the system can meet

the 12 year requirement of 80% reliability. The mismatch between the life of the cell and the life of the application was met by derating cell operating voltage from 2.5 to 2.29 V and reducing the average temperature to 45 °C. The resultant system will be heavier and more costly, but only by ~10%. At the end of 12 years, storage systems in 80 of 100 buses should still be in operation because the capacitor system has been designed to achieve this level of performance.

References

1. Abernethy, R.B., Breneman, J.E., Medlin, C.H., and Reinman, G.L. (1983) Weibull Analysis Handbook. Wright-Patterson AFB Report AFWAL-TR-83-2079, Aero Propulsion Laboratory, November 1983, p. 110.
2. Miller, J.R. and Butler, S.M. (2002) Reliability of High-Voltage Electrochemical Capacitors: Predictions for Statistically Independent Cells from a Single Distribution. Proceedings of the 12th International Seminar on Double Layer Capacitors and Similar Energy Storage Devices, Deerfield Beach, FL, December, 2002.
3. Kobayashi, Y. (1992) Acceleration Coefficient for the Molded-Type Electric Double Layer Capacitor (EDLC), NEC Corporation, May 19.
4. Goltser, I., Miller, J.R., and Butler, S.M. (2005) Reliability Assessment of Electrochemical Capacitors: Method Demonstration Using 1-F Commercial Components. Proceedings of the 15th International Seminar on Double Layer Capacitors and Similar Energy Storage Devices, Deerfield Beach, FL, December, 2005.
5. Miller, J.R., Klementov, A., and Butler, S.M. (2006) Electrochemical Capacitor Reliability in Heavy Hybrid Vehicles. Proceedings of the 16th International Seminar on Double Layer Capacitors and Similar Energy Storage Devices, Deerfield Beach, FL, December, 2006.
6. Butler, S., Klementov, A., and Miller, J.R. (2008) Electrochemical Capacitor Life Predictions Using Accelerated Test Methods. Proceedings ESSCAP 2008, Rome, November, 2008.
7. Kotz, R., Ruch, P.W., and Cericola, D. (2010) Aging and failure mode of electrochemical capacitor during accelerated constant load tests. *J. Power. Sources*, **195**, 923–926.
8. Miller, J.R., Butler, S.M., and Goltser, I. (2006) Electrochemical Capacitor Life Predictions Using Accelerated Test Methods. Proceedings of the 42nd Power Sources Conference, Paper 24.6, Philadelphia, PA, June 2006.
9. Nelson, W. (1990) *Accelerated testing: statistical models, test plans, and data analysis*, in Models for Life Tests with Constant Stress Chapter 2, John Wiley & Sons, Inc..
10. Davenport, W.B. Jr., (1970) *Probability and random processes*, in Functions of Random Variables Chapter 6, McGraw-Hill Book Company, New York.
11. Miller, J.R. and Butler, S.M. (2006) in *Recent Advances in Supercapacitors* (ed. V. Gupta) Chapter 1, Transworld Research Network, Kerala.
12. This two-dimensional problem is often used as an example and solved in introductory text books on conductive heat transfer. See, for example Arpaci, V.S. (1966) *Conductive Heat Transfer* Chapter 4, Addison-Wesley Publishing, Reading, MA.
13. Whole books have been written on this subject. See, for instance Jensen, F. and Petersen, N.E. (1983) *Burn-in: An engineering Approach to the Design and Analysis of Burn-in Procedures*, John Wiley & Sons, Inc.

14

Market and Applications of Electrochemical Capacitors

John R. Miller

14.1

Introduction: Principles and History

Electrochemical capacitors (ECs), often referred to as *supercapacitors* or *ultracapacitors*, store charge physically just as other types of capacitors do. But ECs differ in that they store tremendously greater amounts of charge, owing to the use of very high-surface-area electrodes with electric double-layer charge storage on that surface. The combination of a very small “plate” separation with a very large plate area yields devices with what, when they first appeared, were unheard-of capacitance values [1].

Physical charge storage does not rely on chemical reaction rates, as with batteries, which often limit power performance. Because of this, ECs, compared to other electrochemical devices such as batteries, enjoy essentially unlimited cycle life and have very high-power capability on both charge and discharge. They also deliver exceptionally low-temperature performance, even at -40°C . Last but not least, ECs age gracefully, seldom exhibiting catastrophic failure. Credible life predictions are thereby rendered unproblematically, a feature that makes ECs especially valued in applications requiring high reliability.

Capacitors based on double-layer charge storage were first patented by General Electric in 1957, but never commercialized. Subsequent double-layer capacitor designs patented by Standard Oil of Ohio (SOHIO) led to a commercial product introduced by the Nippon Electric Corporation (NEC) in 1978. Their Supercapacitor™ was rated at 5.5 V, with capacitance values up to 1.0 F. These $\sim 5\text{ cm}^3$ sized or smaller devices were used as battery substitutes to provide backup power for volatile CMOS (complementary metal oxide semiconductor) computer memory. Currently, these and other types of EC products are available from several dozen manufacturers around the world, and in sizes, easily held in one hand, of up to 9 kF or larger [2].

In the past, ECs and the market for them were something of a world apart from those of other capacitor types because EC properties and performance differed so greatly from conventional capacitors. EC capacitance per weight or volume is unmatched by any other technology, but compared with conventional capacitors

they have a very limited life at elevated temperatures. Further, ECs cannot charge or discharge quickly enough to be used for AC line filtering applications [3]. Despite this, however, they can still charge and discharge much more rapidly than can any battery technology, including the high-power lithium-ion batteries that are currently popular. As a result, electric double-layer capacitors are often used to complement batteries in applications with rapidly varying power requirements, electric and hybrid-electric vehicles being prominent cases in point. In some applications, they can even replace batteries.

14.2

Commercial Designs: DC Power Applications

14.2.1

Bipolar Designs

The general design of EC devices is shown in Figure 14.1, a cross section of an EC cell. There are two regions of active material, the two electrodes, generally of the same material and the same thickness, with a microporous separator between them, all bathed in an electrolyte. Sandwiching this at both top and bottom are current collectors for charge and discharge of the electric double layer located on the surface of the electrode material. Typical electrode thicknesses are ~ 100 μm for nonaqueous electrolytes and somewhat thicker with aqueous electrolytes. Separator thicknesses are typically 25 μm , with current collectors commonly ~ 50 μm thick.

The 1978 NEC SupercapacitorTM with H_2SO_4 as the electrolyte was marketed under license from SOHIO. Its primary use was, as mentioned earlier, CMOS memory backup, enabling applications to retain memory in the event of line power interruption. Figure 14.2 shows a product of this design, a 1 F capacitor rated at 5.5 V. At the left of the photograph is the stack of eight cells connected in series that enabled the device to operate at rated voltage. The cell stack is contained in a metal crimp package as shown on the right. As this 1 F capacitor used eight cells in series, each cell had to be 8 F. And owing to the fact that there are actually two capacitors in series within each cell, each electrode in each cell had to be about 16 F, yielding 256 F of capacitance in this 1 F device. This device stored ~ 15 J of energy in a ~ 10 cm^3 volume.

NEC has several different families of aqueous electrolyte EC products rated at 5.5 V, each optimized for a different performance, for example, low self-discharge rate or high-energy density or high-power density, and so on. Each of these early products was characterized by bipolar construction, that is, cells stacked one atop another, making external interconnects totally unnecessary. This is shown at the left in Figure 14.2, where current flows perpendicularly to each of the eight stacked cells. These ECs were used in applications where they were discharged over a period of many seconds, minutes, hours, days, and sometimes even months, their

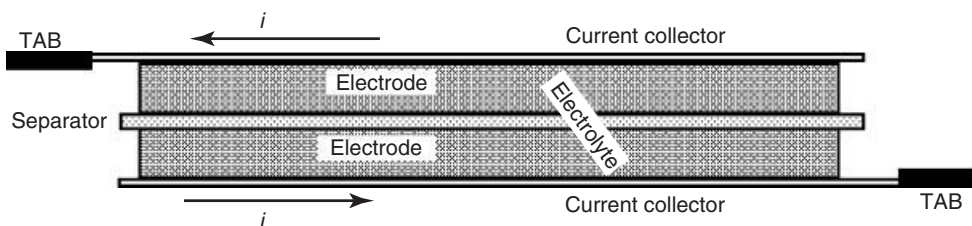


Figure 14.1 Cross section of an electrochemical capacitor cell.

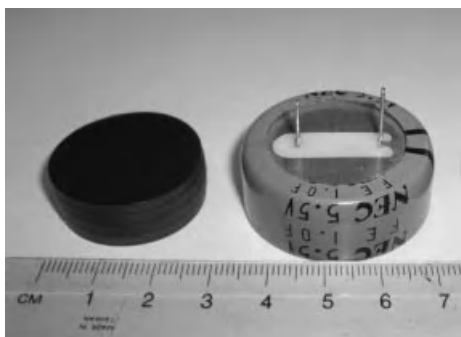


Figure 14.2 NEC Supercapacitor.

sole purpose being to provide DC power to keep volatile memory alive or to power clock chips. In such applications, ECs served as a direct substitute for button cell batteries.

Over the years since the NEC product introduction, this same bipolar design has been used by other EC manufacturers. Examples are shown in Figure 14.3, two aqueous electrolyte and one organic electrolyte EC. The ECOND (diameter 9 in.) and the ELIT (width 11 in.) capacitors, both produced in Russia, use KOH rather than H_2SO_4 as the electrolyte. They were optimized for high-power delivery at low temperatures and used, among other applications, for starting diesel locomotive and other heavy diesel engines, particularly under cold conditions where the demand for high cranking power is greatest.

The third EC of bipolar design in Figure 14.3 uses an organic electrolyte, which is an ammonium salt in propylene carbonate (PC) solvent. This EC was developed in Japan by the Meiden Corporation for a broad range of industrial applications, especially those connected with power quality. One attractive feature of the bipolar design is that it makes it easy to achieve high voltages in a small package. The ECOND capacitor is rated at 64 V and stores 60 kJ of energy. The ELIT capacitor is rated at 24 V and stores 50 kJ, and the Meiden EC (on the right) is rated at 160 V and stores 60 kJ. These products are all developed for high-rate-discharge applications and each uses a bipolar design.

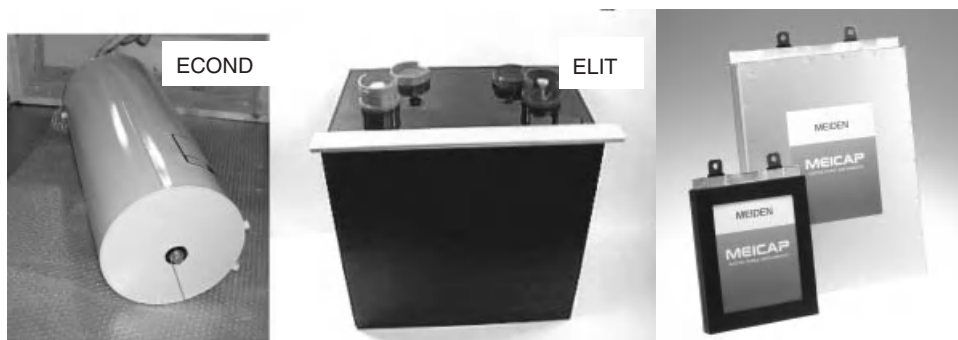


Figure 14.3 Electrochemical capacitors having bipolar designs. The ECOND capacitor is rated at 64 V, the ELIT at 24 V, and the Meiden capacitor at 160 V.

14.2.2

Cell Designs

The most popular design currently is a “cell” design using an organic electrolyte, that is, a single packaged cell with an organic electrolyte. Typical cells of larger size EC products are measured in kF, a common unit of measurement for ECs. Such cells can be externally connected in series to provide higher working voltage or in parallel to provide higher capacitance value. Figure 14.4 shows an assortment of products having this cell design. Maxwell Technologies (United States) has cells of the style shown, which are available in an assortment of different sizes from 650 F to 3 kF, all rated at 2.7 V. The Batscap (France) cell is rated at 2.7 V, 5 kF with other sizes available up to 9 kF. Manufacturers Nesscap (Korea), LS Mtron (Korea), and Ioxus (United States) offer cells of this general design, most commonly



Figure 14.4 Electrochemical capacitor cells, each using an organic electrolyte. Voltage ratings are 2.5 or 2.7 V, depending on the manufacturer. Cells are connected in series to provide higher working voltage.



1400 F/2.5 V 7,444 pcs/system

Figure 14.5 EC system designed to provide MW levels of power for several seconds.

using an organic electrolyte containing acetonitrile solvent. Nippon Chemi-Con and Nichicon, among other Japanese companies, offer cells with organic electrolyte containing PC solvent. Groups of these cells are connected externally in series to form modules. Depending on the application, modules can be interconnected to create systems that provide 300 or 700 V or even higher voltage levels to match application requirements.

Many applications use ECs to supply DC power. Figure 14.5 shows one such application, a large system that provides ~ 2 MW of power for several seconds [4]. As shown, this system comprises 7444 cells connected both in series and in parallel to achieve that level of performance. The motive for using ECs in such a situation is because they have extremely high reliability compared with alternative approaches, batteries, for instance. An EC's state of health and state of charge can be precisely known at any given moment. This application can provide short-term power backup for an entire factory that has high-value work in process, for example, a semiconductor foundry, where the loss of power for even a fraction of a second could be very costly. Short-term power from such a system can cover the majority of interruptions of the utility grid since these are generally less than a few seconds' duration. Longer term outages naturally require the use of chemical energy (liquid fuel with a backup generator) to provide power for a longer time. Capacitor systems, with their high cycle life and fast charge, cope easily and effectively with the general run of short-term power outages.

14.2.3

Asymmetric Designs

A significant advance in EC technology was made in the early 1990s by ESMA of Moscow, creator of the asymmetric EC design [5]. In this design, one of the electrodes relies on electric double-layer charge storage while the other relies on faradic charge storage as is found in a battery electrode. The capacity of the faradic electrode is generally many times greater than the capacity of the double-layer



Figure 14.6 All-electric bus powered by ESMA asymmetric electrochemical capacitors.

charge storage electrode, the source of the “asymmetric” name and the reason for such good cycle life and high-power performance. This design can greatly increase the energy density of an EC. It can also greatly reduce the self-discharge rate. The ESMA product uses NiOOH as the positive electrode and activated carbon as the negative electrode, with KOH as the electrolyte. Depending on the capacity ratio of the electrodes, this allows specific energy values from several Wh kg^{-1} up to $>10 \text{ Wh kg}^{-1}$. Of course, the higher the ratio of the battery electrode capacity to the capacitor electrode capacity, the higher the cycle life, but the specific energy and energy density will be lower. ESMA capacitors have been optimized in several different ways. One very interesting optimization is for the application shown in Figure 14.6, an all-electric bus [6]. This bus is powered only by a bank of asymmetric ECs, which stores $\sim 30 \text{ MJ}$ (8 kWh) of energy. The range of the bus is limited to $\sim 15 \text{ km}$. Operation is restricted to a shorter circular route in an exhibition park outside of Moscow, allowing it to be charged at the end of each circuit in less than 15 min. A genuine breakthrough in EC technology, this design continues to attract considerable attention currently.¹⁾

The year 2010 saw a similar transportation solution implemented in Shanghai, which has a fleet of capacitor-powered buses that are charged while passengers embark or disembark at bus stops. Figure 14.7 shows this bus with its charging arm extended vertically at a bus stop [7]. The charging time is about 20 s, after which the bus proceeds as a fully electric vehicle to the next bus stop, where charging once again takes place. The suspended catenary electric lines seen in conventional electric bus or trolley systems are absent, not only creating a visually more attractive solution to the delivery of bus power, but, in many cases, a less expensive one since electric power need be provided at only several fixed locations rather than being available all along the travel route. Route flexibility is increased as no catenary line is needed, making it possible for the bus to go from one charging station to several other different charging stations, depending on transportation demands. This fleet of Shanghai buses represents a signal advance over the original ESMA circular route configuration.

1) Asymmetric ECs using organic electrolytes with lithium salts (so called lithium ion capacitors or LICs) have experienced rapid development in recent years.



Figure 14.7 Capacitor-powered bus in Shanghai.

Over the years, ECs have been used in a great variety of other DC applications. One is in flashlights to power light-emitting diodes (LEDs). Figure 14.8 shows two examples of such EC-powered devices. The flashlight in (a) can be charged either by the solar cells located on the top of the flashlight body or by being plugged into the USB port of a computer [8]. Charging by the solar cells takes about 1 h in direct sunlight, while charging from the USB port takes only several minutes. The flashlight in (b) is an industrial grade product with three LED bulbs that can produce an intense beam of light for up to 2 h [9]. It can be recharged in a mere 90 s for another 2 h of operation. Perhaps the most impressive is the claim that it can operate in this manner for up to 50 000 cycles, making it essentially maintenance-free and thus producing extremely low life-cycle cost. Presently marketed to fire and police departments, it is much lighter than conventional primary battery-powered flashlights, with much higher reliability and the availability of up-to-the-moment information on its state of charge. Capacitor power in these flashlights also extends the range of low temperature operation.

Yet another interesting DC application is the Coleman portable screw gun shown in its charging stand in Figure 14.9, where ECs (no batteries) power an electric motor for driving screws [10]. The number of screws it can drive before recharging [10].

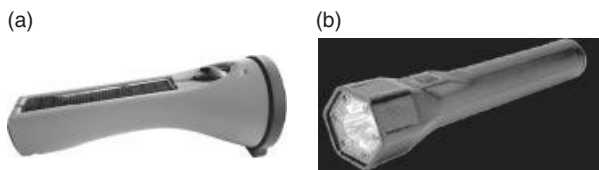


Figure 14.8 Capacitor-powered LED flashlights.

is limited to perhaps several dozen; however, since charging requires only about a minute, this presents no great problem. This tool is particularly popular with homeowners, since its capacitor power source has virtually unlimited shelf life with quick recharge possible right before each use, averting the usual complaints made by infrequent users of battery-powered screw guns.

These are some of the applications that have succeeded the original CMOS memory backup uses for which ECs were first brought to the market. All are DC power applications, of various sizes from city transit buses down to flashlights and handheld drills.

14.3 Energy Conservation and Energy Harvesting Applications

The next group of commercial applications to be discussed is those that require both charging and discharging of the storage element. Most prominent at present in the market are those applications that have to do with energy conservation – the capture and reuse of waste energy. In many of the present day industrial applications, significant quantities of energy are naturally available for such capture and reuse, provided that suitable storage media are available. EC technology is fast becoming the preferred medium for this purpose, owing to its rapid and efficient charging, its high cycle life, and very long operational life.

14.3.1 Motion and Energy

To get a clearer sense of the quantity of waste energy available for harvesting, consider the kinetic energy of moving masses at different speeds as shown in Figure 14.10. A 5 t mass moving at 30 mph has kinetic energy equal to ~ 500 kJ, and a 1 t mass moving at 60 mph has ~ 400 kJ. If we look, on the other hand, at the potential energy of a mass raised to various heights, as shown in Figure 14.11, we see that a 5 t mass lifted 10 m has ~ 500 kJ of potential energy. One metric ton



Figure 14.9 Coleman-capacitor-powered portable screw gun in charging stand.

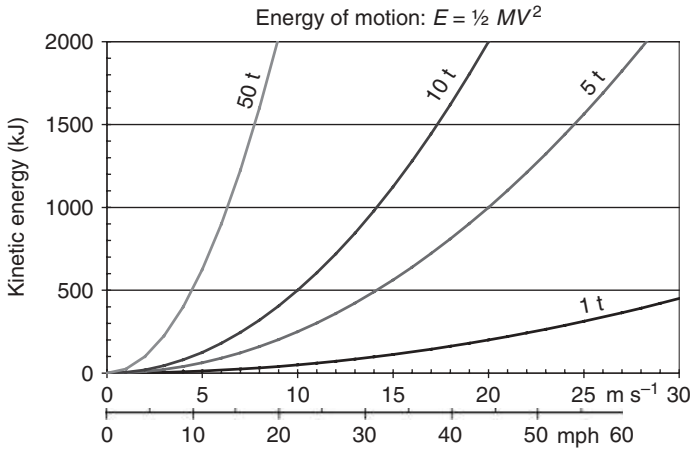


Figure 14.10 Kinetic energy of a moving object with the listed mass at different speeds.

lifted 30 m has ~ 300 kJ of potential energy. There is, clearly, much less energy involved in motion or in position than one might expect. Thus, the opportunity for energy harvesting need not, in many cases, require the use of a large-size storage system, but it does require that the system be capable of efficiently storing energy during the time when it becomes available, for instance, during a braking event of a heavy hybrid vehicle such as a city transit bus. Here, normal braking lasts from 5 to 10 s, which is the total span of time available for kinetic energy to be captured and stored.

The amount of energy captured and stored in a regenerative braking event by two state-of-the-art technologies, lithium-ion battery and EC, is shown in Figure 14.12 [11]. Here, the amount of energy captured by each of the two technologies during

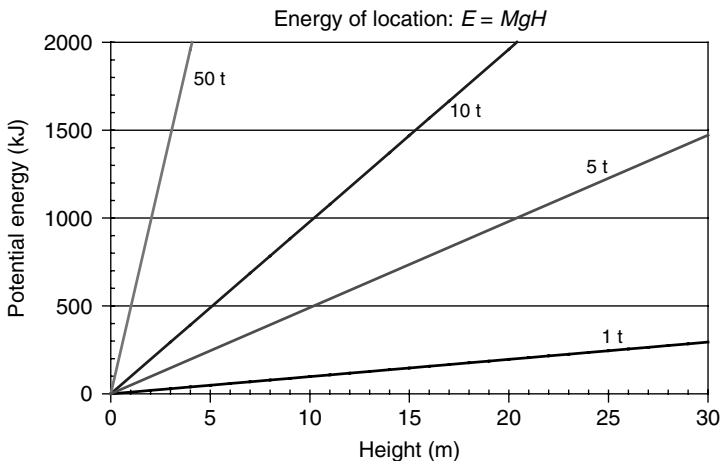


Figure 14.11 Potential energy of different raised masses.

constant-current charge and the amount of energy stored in the charging process are plotted versus charging time. Stored energy is captured energy that is available to perform subsequent work. In this comparison, charging was to the manufacturer-recommended upper voltage limits. The capacitor was initially at half its rated voltage and the battery at 10% state of charge. As shown, with charging times longer than ~ 10 min (600 s), the battery has a ~ 15 times specific energy advantage over the capacitor. However, at shorter charging times, the battery has less specific energy, while the capacitor value remains relatively constant. For example, during a 100 s charge, the battery captures about five times more energy than the capacitor on a weight basis. For a 10 s charge, specific energy capture is approximately the same for both technologies, but the capacitor can discharge $\sim 95\%$ of the amount captured, while the battery can only discharge $\sim 50\%$ of what it captures. Thus, the capacitor, in effect, has twice the specific energy of the battery during a 10 s regenerative energy capture event. Batteries, of course, cannot be repeatedly operated with such fast charging because of unacceptable temperature rise, high stress levels that can reduce operational life, and potential safety concerns. Batteries must be oversized to make them practical in such short-charging-time applications. Battery “super-sizing,” in effect, increases the charge time (shifts the operating point on the curve in Figure 14.12 to the right), making the specific energy of the two technologies surprisingly similar and disproving to a great degree the most common belief that batteries have higher specific energy than capacitors in typical hybrid vehicle applications.

14.3.2

Hybridization: Energy Capture and Reuse

Turning to examples, the first gas-electric heavy hybrid vehicle in the United States to use an EC storage system was a city transit bus demonstration project led by NASA in 1997 [12]. The bus stored 1.6 MJ (444 Wh) of energy in a

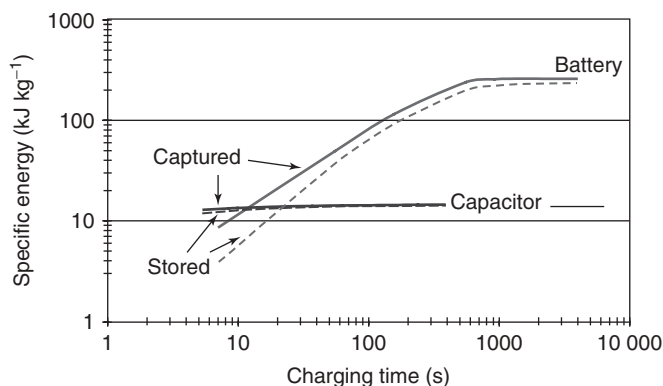


Figure 14.12 Comparison of the capture and storage of energy in an electrochemical capacitor and a lithium-ion battery.

20 F, 400 V aqueous electrolyte EC system. This project aimed to learn whether capacitor storage could overcome common problems found with earlier hybrid bus battery storage systems. These problems included inadequate operating life, limited current capability on charge and discharge, difficulty in accurately knowing the storage system's state of charge and, in some cases, problematic safety issues. The hybrid demonstration bus with EC storage met established performance goals, clearly showed that many battery-related problems could be overcome, and became the progenitor of a large number of city transit buses having EC energy storage systems. According to one source, more hybrid city transit buses use capacitor storage currently than do battery storage systems [13].

Over and above operating performance differences, there is an associated economically quite important maintenance difference between battery and capacitor systems [14]. In the case of New York City's maintenance requirements, battery hybrid buses need two maintenance workers to perform electrical system service work: one to watch while the other, fully suited in high-voltage protective gear, does the work. Capacitor hybrid buses, on the other hand, having had their storage system fully discharged before any maintenance work, present no unusual electrical hazards. Neither additional personnel nor any hampering voltage-protective gear are necessary.

Diesel-electric hybrid trash vehicles have also been constructed using EC storage, again an application with many start/stop cycles daily [15]. Energy savings result from efficient capture and storage of the braking energy generated with each stop. As with transit buses, there have been a number of very successful programs illustrating that energy conservation is readily achieved through the hybridizing of such large vehicles.

One remarkable energy conservation application is the Komatsu hybrid excavator shown schematically in Figure 14.13 [16]. The digging function remains hydraulic but turret rotation has been electrified and therefore hybridized. Normal operation includes repetitive $\sim 90^\circ$ bucket rotation, bucket dump, and bucket return to the original position, a wasteful start/stop operating cycle when performed at high rates. Electric turret rotation, in conjunction with a capacitor storage system, yields reported fuel savings of 30–40%, depending on the mode of operation. Needless to say, this is the first wave of a very popular approach for conserving energy that can only grow in the future.

Another application is shown in Figure 14.14, a light-rail electric train with an onboard EC storage system to store regenerated braking energy [17]. This diesel-electric vehicle has a limited amount of capacitor storage on its roof, as shown, but achieves substantial energy savings. These savings depend, of course, on the frequency of stopping, but for train stations separated by 4 km, $\sim 30\%$ energy savings are achieved. With 10 km station separation, $\sim 18\%$ energy savings are reported.

Figure 14.15 shows a rubber-tired gantry crane that moves shipping containers at seaports, including sorting, stacking, and loading them onto trains or truck beds after they have been unloaded from ships. This sort of vehicle moves considerable distances and so is not well suited for grid connection, as are the large stationary

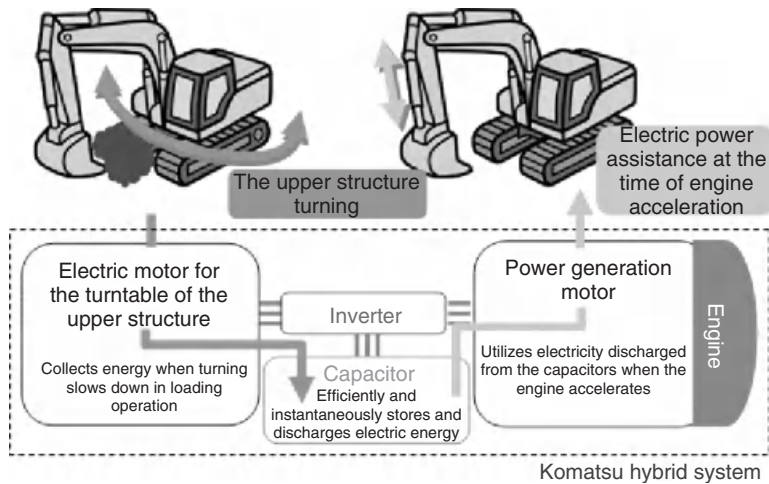


Figure 14.13 Hybrid electric Komatsu excavator with electrochemical capacitor energy storage.



Figure 14.14 Onboard electrochemical capacitor storage system for a light-rail system.

cranes used in the first instance for unloading the ships. In the gantry crane, a diesel engine is used to drive an electric generator that powers the motors for propulsion and container lifting/lowering. This is an ideal application for energy harvesting in that the load is first lifted and then this exact same load is dropped, approximately the same distance for each movement. This makes for a very predictable cycle, much more so than the operation of a city transit bus in traffic that generally accelerates and decelerates in a very nonperiodic manner. As shown in the figure, the capacitor storage system has been located on one of the uprights of the crane, a relatively small addition but one that still produces ~40% fuel savings and very significant emissions reductions [18]. Fuel savings come about for several reasons. First of all, the diesel engine that powers the generator does not need to be sized

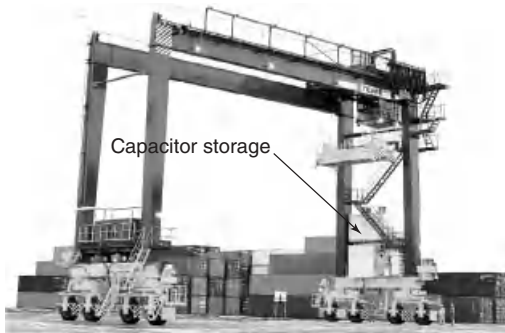


Figure 14.15 Rubber-tired gantry crane that has been hybridized using electrochemical capacitors.

for lifting the maximum load since some fraction of the power can be derived from stored energy, thus making possible the use of a smaller, less expensive, and more fuel efficient engine. Second, energy normally wasted as heat when the load is lowered back to the ground can be recovered, stored, and used for subsequent lifting operations. Gantry cranes such as this are seeing widespread use in seaports in the Far East and have proved themselves over and over again. The amount of energy storage needed is just not that great, and the capacitor system can be designed to be fully charged and fully discharged every cycle with no challenge to its cycle life.

14.3.3

Energy Conservation and Efficiency

In Figure 14.16, energy stored in an EC module can be used to rapidly heat the fusing roll of a copy machine [19]. The capacitor storage makes it possible for the machine to avoid idling continuously, with the associated energy waste such idling produces. Heating can thus be performed immediately before use, and at considerable energy savings. Owing to the limitations of the power that can be derived directly from a standard wall socket, the fusing roll can be heated much more quickly through use of the stored energy, generally much less than 1 min, which is in sharp contrast to the approximately 5 min normally required for normal heat up. Savings through this sort of application are widespread, with many similar examples to show how stored energy can help in reducing energy waste caused by equipment idling.

14.3.4

Engine Cranking

Another class of applications that exploits the high power of capacitors, particularly at low temperatures, is internal combustion engine starting. Historically, ECs were used in Russia specifically for cranking engines at low temperatures. ECOND's stated objective was to develop capacitors that could be used to effect reliable

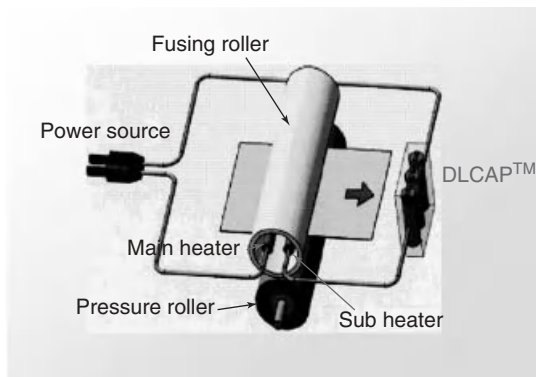


Figure 14.16 Ricoh copier schematic using an electrochemical capacitor-powered rapid heat up system.

starting of diesel locomotive engines in sizes up to 3000 HP. ELIT also developed ECs for engine cranking, and in the early 1990s reported successful development of a product optimized for this application [20]. Engine cranking is even more significant now owing to the need for the conservation of fuel and the reduction of emissions. There is some US legislation that greatly restricts engine idling, whether by over-the-road trucks or by school buses, to periods of very short duration. Again, this is a matter not only about energy conservation but also about air quality. In order to be assured that an engine will start after a stop, dependable and powerful cranking is utterly necessary. ECs have increasingly become that source of cranking power. Several papers, which discuss the various aspects of engine cranking using ECs, are available [21–26].

Saft America recently licensed the ESMA asymmetric EC technology to manufacture capacitors in the United States for engine cranking applications [27]. One of the most outstanding characteristics of this asymmetric capacitor for this application is that its self-discharge rate is among the lowest of all electrochemical storage technologies. ESMA-developed cranking capacitors have, in fact, a self-discharge rate that is much lower than lead acid batteries. They can be charged and still, months later, have sufficient charge remaining to crank a large diesel engine. This is an important characteristic for applications that may see infrequent use, as, for instance, in pleasure boats, private airplanes, and military vehicles. This is also important for use in safety applications that will hopefully only see infrequent use.

Engine cranking will become commercially more and more important with the start/stop vehicles that are now on the drawing boards and will appear soon on the road, initially in Europe. Here, the engine is fully stopped when the vehicle is not moving (absolutely no routine idling), with a restart when the gas pedal is depressed. There are various storage sources being considered for this start/stop application, ECs being among the most attractive owing to their high-power performance, quick recharge, and essentially unlimited cycle life. Engine cranking uses promise to become worldwide in practice, and ECs are anticipated by many to be the preferred storage source technology for this application.

14.4 Technology Combination Applications

14.4.1 Battery/Capacitor Combination Applications

Some applications derive great benefit from combining an EC with a battery. This can provide a more optimum solution for the application than could either technology alone, a solution that often will uniquely meet both energy and power requirements. Engine cranking is one example. In order to meet the high-power requirements of the crank cycle at low temperature, batteries on the vehicle must be greatly oversized. Although only a small fraction of the total energy available from a battery is actually used in a starting operation, oversizing is necessary in order to provide the power required for cranking. Combining a smaller battery with a capacitor creates a situation where a smaller and lighter system is better able to meet application requirements.

On a smaller scale, there have been many combinations of batteries and capacitors in portable electronics, ranging from digital cameras to laptop computers to wireless communication equipment. Such combinations divide power and energy functions, using the two components together so as to better meet the application requirements. One reported combination of a capacitor in parallel with a battery in a particular digital camera brought about an increase of some 50% in the number of pictures that could be taken, a very significant improvement in performance [28]. Similarly, in one wireless communication device, small capacitors that are added in combination with batteries provide a several-fold increase in operating time. It is the high-power performance and unlimited cycle life of ECs that make them so attractive to combine with high-energy batteries.

14.5 Electricity Grid Applications

14.5.1 Storage and the Utility Grid

Much emphasis is now being placed on improving the reliability of the electricity grid in the United States and elsewhere. One very promising way to do this is to add storage. This is particularly true with regard to generation sources that may not be completely dependable, for example, wind or solar power, which fluctuate according to weather conditions. Having stored energy to help ride through periods when there is little or no power generation can certainly make such sources more valuable.

Many studies have been conducted to determine what types of storage, given considerations of duration, size, and cost, would be best for electricity utility purposes. One particularly interesting US Department of Energy (DOE) report [29]

published in February of 2010 identified some 20 different applications for the electricity grid where storage would provide benefits. Durations considered were from seconds and minutes up to many hours. One area especially worthy of note is the load shifting associated with day/night bulk storage. Here, the storage system is filled at night, when there is excess generation but low demand, and then used the next day when demand would be highest. This involves a storage time of up to about 12 h.

The important metric in this application is storage cost per unit of energy. Most storage media are simply too expensive. Lead acid batteries, for instance, have an energy storage cost of $\sim \$0.30 \text{ kWh}^{-1}$ when used for this purpose, lithium-ion batteries even higher. At the other extreme of cost is pumped hydro storage, which involves lifting water uphill to a storage reservoir at night and allowing it to flow back down the next day to generate electricity. Storage costs for this approach are on the order of $\$0.01 \text{ kWh}^{-1}$ per cycle. The DOE recently solicited proposals to develop bulk storage technology [30] that would result in a storage cost of $\$0.025 \text{ kWh}^{-1}$.

ECs may offer a solution for bulk energy storage, particularly asymmetric ECs using aqueous electrolytes [31]. Such devices do not have the same manufacturing costs that symmetric organic electrolyte ECs have; for example, there is no need for carbon drying nor the requirement for hermetic metal packaging. Furthermore, asymmetric capacitors can be designed so that they will meet, but not exceed, the cycle requirements. Approximately 5000 cycles have been determined to be the appropriate number necessary for the day/night bulk storage application, given that only one cycle per day is involved. Two asymmetric EC systems have been discussed for this application. One has a lead oxide positive electrode with an activated carbon negative electrode and sulfuric acid electrolyte, a configuration that should offer 2 V operation and have a specific energy of $\sim 19 \text{ Wh kg}^{-1}$ [32]. The second asymmetric EC system has been described as having a sodium intercalation electrode and a double-layer charge storage electrode, with a neutral pH aqueous electrolyte [33]. Both these asymmetric ECs have the potential to provide storage and offer a cycle life for economic viability. The relatively low cycle life and various other limitations of the described technologies render them unsuitable for many nonstationary applications such as in hybrid vehicles, but for stationary applications where neither size nor mass are matters of real concern asymmetric EC technology holds great promise.

14.6

Conclusions

What becomes clear in a review such as this, covering applications in markets as diverse as consumer electronics, transportation, energy conservation, energy harvesting, power quality, and the utility grid, is that the role ECs play in shaping the quality of modern life and technological experience has grown greatly over the years and promises to grow still further. Technologies for energy storage differ

greatly, not only in principle and conception but also in the distinctive range of applications for which they are most suited. What ECs bring to the table across the panoply of the present day rapidly expanding market areas is their high-power performance, unlimited cycle life, and their near-invulnerable reliability.

References

1. Conway, B.E. (1999) *Electrochemical Supercapacitors: Scientific Fundamentals and Technological Applications*, Kluwer Academic/Plenum Publishers, New York.
2. Additional information in: Miller, J.R. (2007) A Brief History of Supercapacitors. *Battery + Energy Storage Technology* (Autumn issue 2007), pp. 61–78.
3. Miller, J.R. (2009) Electrochemical Capacitor Technology Basics for the Traditional Component Engineer. Proceedings 2009 CARTS USA, Jacksonville, FL, March 30–April 2, 2009.
4. Furukawa, T. (2006) DLCAP Energy Storage System Multiple Application. Proceedings Advanced Capacitor World Summit 2006, Hilton San Diego Resort, San Diego, CA, July 17–19, 2006.
5. Razoumov, S., Klementov, A., Litvinenko, S., and Beliakov, A. (2001) Asymmetric electrochemical capacitor and method of making. US Patent 6,222,723, Apr. 24, 2001.
6. Varakin, I.N., Klementov, A.D., Litvinenko, S.V., Starodubtsev, S.V., and Stepanov, A.B. (1997) Application of Ultracapacitors as Traction Energy Sources. Proceedings of the 7th International Seminar on Double Layer Capacitors and Similar Energy Storage Devices, Deerfield Beach, FL, December 8–10, 1997.
7. <http://www.sinautecus.com/>. (2012).
8. www.solareyinc.com/index.htm (2012).
9. www.511tactical.com/html511/static/LFLDemo.html (2011).
10. www.flashcellscrewdriver.com (2012).
11. Miller, J.R. and Klementov, A.D. (2007) Electrochemical Capacitor Performance Compared with the Performance of Advanced Lithium Ion Batteries. Proceedings of the 17th International Seminar on Double Layer Capacitors and Hybrid Energy Storage Devices, Deerfield Beach, Florida, December 10–12, 2007.
12. Viterna, L.A. (1997) Hybrid Electric Transit Bus. Proceedings SAE International Truck and Bus Meeting and Exposition, Paper 973202, Cleveland, OH, November 17–19, 1997.
13. Liedtke, M. (2010) New Markets for a Mature Product or Mature Markets for a New Product? Proceedings of the 10th International Advanced Battery and EC Capacitor Conference, Orlando, FL, May 19–21, 2010.
14. Hess, R. (2010) Application of Ultracapacitors for HEV Transit Buses. Proceedings of the 10th International Advanced Battery and EC Capacitor Conference, Orlando, FL, May 19–21, 2010.
15. Bolton, M. (2009) Energy Storage Systems for Severe Duty Truck Applications. Proceedings of the 9th International Advanced Automotive Battery and Ultracapacitor Conference and Symposia, Long Beach, CA, June 8–12, 2009.
16. www.komatsu.com/CompanyInfo/press/2008051315113604588.html (2012).
17. <http://www.bombardier.com/en/transportation/sustainability/technology/primove-catenary-free-operation> (2012).
18. Furukawa, T. (2006) DLCAP Energy Storage System Multiple Application. Proceedings of Advanced Capacitor World Summit 2006, Hilton San Diego Resort, San Diego, CA, July 17–19, 2006.
19. Uchi, H. (2005) Performance and Application—DLCAP. Proceedings of Advanced Capacitor World Summit 2005, Hilton San Diego Resort, San Diego, CA, July 11–13, 2005.

20. Beliakov, A.I. (1993) Russian Supercapacitors to Start Engines. Battery International (Apr. 1993), p. 102.
21. Beliakov, A.I. (1996) Investigation and Developing of Double Layer Capacitors for Start of Internal Combustion Engines and of Accelerating Systems of Hybrid Electric Drive. Proceedings of the 6th International Seminar on Double Layer Capacitors and Similar Energy Storage Devices, Deerfield Beach, FL, December 9–11, 1996.
22. Miller, J.R., Burgel, J., Catherino, H., Krestik, F., Monroe, J., and Stafford, J.R. (1998) Truck Starting Using Electrochemical Capacitors. International Truck and Bus Meeting and Exposition, Indianapolis, IN, November 16–18, 1998, SAE Technical Paper 982794.
23. Miller, J.R. (1999) Engineering Battery-Capacitor Combinations in High Power Applications: Diesel Engine Starting. Proceedings of the 9th International Seminar on Double Layer Capacitors and Similar Energy Storage Devices, Deerfield Beach, FL, December 6–8, 1999.
24. Ong, W. and Johnston, R. (2000) Electrochemical Capacitors and their Potential Application to Heavy Duty Vehicles. Truck and Bus Meeting and Exposition, Portland, OR, December 4–6, 2000, SAE Technical Paper 200-01-3495.
25. Miller, J.R. (2005) Standards for Engine-Starting Capacitors. Proceedings of the 15th International Seminar on Double Layer Capacitors and Hybrid Energy Storage Devices, Deerfield Beach, FL, December 5–7, 2005.
26. Furukawa, T. (2008) Proceedings of Advanced Capacitor World Summit 2008. Engine Cranking with Green Technology, Hilton San Diego Resort, San Diego, CA, July 14–16, 2008.
27. Hess, J. (2010) Saft – Domestic Production of Asymmetric Nickel Capacitors. Proceedings of the 10th International Advanced Battery and EC Capacitor Conference, Orlando, FL, May 19–21, 2010, www.safbatteries.com/SAFT/UploadedFiles/PressOffice/2009/CP_22-09_en.pdf (2012).
28. Saiki, Y. (2004) New Developments for Portable Consumer Applications after 25 Years in Business. Proceedings of Advanced Capacitor World Summit 2004, Washington, DC, July 14–16, 2004.
29. Eyer, J. and Corey, G. (2010) Energy Storage for the Electricity Grid: Benefits and Market Assessment Guide. SANDIA Report SAND2010-0815, Sandia National Laboratory, February 2010.
30. US Department of Energy ARPA-E Funding Opportunity (2010) Grid-Scale Rampable Intermittent Dispatchable Storage, DE-FOA-0000290, March 2, 2010.
31. Gyuk, I. (2004) Supercapacitors for Electricity Storage, Scope & Projects. Proceedings of Advanced Capacitor World Summit 2004, Washington, DC, July 14–16, 2004.
32. Kazaryan, S. (2007) Characteristics of the PbO₂|H₂SO₄|C ECs. Proceedings of Advanced Capacitor World Summit 2007, Hilton San Diego Resort, San Diego, CA, July 23–25, 2007.
33. <http://www.aquionenergy.com/> (2012).

Index

a

- accumulators 131
- acetonitrile (AN)-based electrolyte 82, 128–129, 169, 373
 - AN-based NHC 248
 - tetraethylammonium tetrafluoroborate (TEABF₄) in 220
- acetylene chemical vapor deposition in zeolite 141
- acidic electrolyte 220
 - capacitance vs current load 221
- activated-carbon-based electrical double-layer capacitor electrode 128, 167, 258, 312–317
 - and carbon availability 313–315
 - galvanostatic charge/discharge 228
 - impact of particle size on electrode density and volumetric capacitance 320–322
 - industrial 317–319
 - pore size distribution optimization of 315–317
 - positive or negative impact of surface groups on the performance 320–321
 - precursor impact on performance 319
 - self-discharge mechanism 321–322
 - voltammetry curve 227
- activated carbon fabrics 137
- activated carbon/MnO₂ device 274–277
 - long-term cycling stability 274
 - manganese dissolution 274
 - oxygen evolution reaction 274
 - performance of 275
- activated carbon powders 135–137
 - from coconut shell 135–136
 - graphene-type units 136
 - H₃PO₄ activation 135
 - HRTEM image 136
 - KOH activation 135
 - nanotextural and structural model of 137
 - physical activation process 135
 - pore texture of 136
- activated carbons (ACs) 73, 131. *see also* activated-carbon-based electrical double-layer capacitor electrode; activated carbon/MnO₂ device
 - AC/Ni(OH)₂ 259
 - AC/PbO₂ 259
- activity and activity coefficients 16–20, 24–25
 - activity, defined 17
 - activity of an electrolyte 18–19
 - dilute solutions of nonelectrolytes 16–17
 - fugacity 16
 - infinite dilution 18, 20
 - mean ion quantities 19
 - relation between f , γ , and γ , 19–20
 - solute activity, measurement of 18
 - solvent activity, measurement of 18
 - standard states 17
- aerogels 86
- 1-alkyl-3-methylimidazolium cations 157
- aluminum current collector 128
- anodic transfer coefficient 57
- antacid agent 336–337
- aqueous asymmetric electrochemical capacitors 272–281
 - activated carbon/MnO₂ device 274–277
 - cyclic voltammograms 273
 - examples 272
 - galvanostatic charge/discharge cycles 273
 - power capability 274
 - principles 272
 - requirements for positive and negative electrodes 273–274
 - use of a negative electrode 272

- aqueous-based devices
 - activated carbon/Ni(OH)₂ hybrid device 267–269
 - activated carbon/PbO₂ device 262–267
 - advantages 257
 - aqueous asymmetric electrochemical capacitors 272–281
 - aqueous lithium-based electrolytes 276
 - based on activated carbon and conducting polymers 269–272
 - energy density of 258
 - operating voltage 258
 - perspectives 282–283
 - principles, requirements, and limitations 259–262
- aqueous-based hybrid ECs 282
- aqueous capacitors (ACs) 78, 83–85
- aqueous electrolytes, advantages of 81
- asymmetric EC 259
 - designs 513–516
- asymmetric EDLC 93, 171
- b**
- Batscap (France) cell 512
- batteries, comparison with capacitor 72–73
 - of charge and discharge behavior 74
- battery-powered flashlights 515
- “battery-type” electrode 93
- battery-type energy storage devices 72
- Becker, H.I. 75
- binders 322–325
 - adhesion and cohesion parameters 322–323
 - advantage of coating 323
 - carbon black impact on volumetric and gravimetric capacitances 325–326
 - conductive additives 325–326
 - electrode–current collector interface and 323
 - impact on aging performance 324
 - PTFE 323–324
 - PVA (polyvinyl alcohol) or CMC (carboxymethylcellulose) coated 323
- bipolar designs of ECs 510–512
 - construction process 510
 - electrode thicknesses 510
 - separator thicknesses 510
 - using organic electrolyte 511
- bis(trifluoromethanesulfonyl)imide 82
- bituminous coal, KOH activation of 139
- Bjerrum treatment for ion pair formation 30
- Bode impedance plot 123
- Bode plots 122
- Boltzmann factor 30
- Born energy 13
- Born equation 9
 - testing 9
- Brunauer-Emmet-Teller (BET) surface areas 84, 138–139, 215, 297, 317
- bulk electrolyte resistance 116
- bulk solution 62
- Butler–Volmer equation 55, 121
 - multistep 57–58
- butylene carbonate 82
- 1-butyl-3-methylimidazolium hexafluorophosphate (BMIM-PF₆) electrolyte 97, 191
- 1-butyl-3-methylimidazolium nitrate (BMIM-NO₃)
 - BMIM⁺ ions on electrodes, contribution of 200
 - density near electrodes 198
- c**
- capacitance 70. *see also* pseudocapacitance
 - of acidic electrolyte 221
 - carbon black, impact of 325–326
 - carbon electrode/ionic liquid interface 291
 - carbon electrodes 298
 - C/C composite electrodes 218
 - characterization of 374–375
 - diffuse layer of electrolyte 174
 - double-layer 75, 78, 132
 - electric double-layer capacitor (EDLC) 138–141
 - endohedral capacitors 189
 - impact of particle size on electrode density 320–322
 - measurements in cyclic voltammetry 116–117
 - measurements of galvanostatic cycling 119
 - microporous template carbons 156–159
 - nitrogen-enriched carbons 217
 - normalized (capacitance per unit area) 79
 - normalized vs pore size 143
 - positive and negative, of CDC 145
 - space charge layer 175
 - testing of 443, 456
 - uncertainty testing of 465
 - volumetric 139–140
- capacitor-powered buses 515
- capacitors 69
 - classification 70
 - difference with battery 72–74
 - energy E (J) stored in 71
 - main factors of 70–71
 - maximum voltage during discharge 71

- parallel plate 70
- primary attributes of 71
- principles 70–71
- resistance of 71
- types of 69
- carbide-derived carbons (CDCs) 86, 142, 167
 - bare cation and solvated cation capacitance measurement 145
 - galvanostatic cycling of cell in ACN + 1 mol l⁻¹ Et₄NBF₄ electrolyte 146–147
 - as model materials for study of ion adsorption 142
 - normalized capacitance vs pore size 143
 - pore size distribution 142
 - porosity characteristics of 142
 - positive and negative electrode capacitance measurement 145
 - three-electrode cell CVs of 144–145
- carbon aerogels 138
- carbon-based EDLC 135–138
 - activated carbon fabrics 137
 - activated carbon powders 135–137
 - carbon aerogels 138
 - carbon nanotubes 138
- carbon-based electrochemical capacitors, classes 167
- carbon/carbon aqueous asymmetric devices 279–280
- carbon electrode/ionical liquid interface 291–292
 - capacitance 291
 - effect of IL chemistry and temperature on the structure 292
 - spectroscopy studies 291–292
- carbon electrodes 297–298
 - capacitance values 298
 - disordered template carbons 298
 - high capacitance response 297–298
- carbon/iodide electrochemical system 228
- carbon/iodide interface, electrochemical behavior of 226
 - during long-term cycling at a high current density 227
- carbonization, oxygen-rich precursor for 215
- carbonization products 219
- carbon nanotube array (CNTA) 213
- carbon nanotube forests (CNTFs) 197
- carbon nanotubes (CNTs) 83, 138, 208
 - capacitive behavior in EMI-BF₄ IL electrolyte 155
 - internal RTIL ions associated with 156–157
 - nonmonotonic change of 155
 - role in conduction paths 209
- carbon onions 167
- carbon/RuO₂ device 280–281
- carbons, porous texture of 151–153
- carboxylic groups (COOR) 215
- cathodic transfer coefficient 57
- cavity microelectrode (CME) 148–149
- C/C composite electrodes 217–218
 - capacitance vs current load for 218
- cell balancing system 80
- cell components of supercapacitors
 - activated carbon 312–317
 - binders 322–325
 - conductive additives 325–326
 - current collector 309–312
 - electrolytes 327–343
 - industrial activated carbons for industrial 317–319
 - particle size distribution of activated carbons and its optimization 319–322
 - separators 343–345
- cell design for supercapacitors
 - aqueous-based electrolyte unit cells 351
 - energy cells 349–351
 - high-power cells 348–349
 - large cells 347–348
 - main processes 346–347
 - pouch cell 351
 - prismatic vs cylindrical cells 351–352
 - small-size components 347
- cell potential 3
- charge on a good conductor 37
- charge storage mechanisms 93
- charge transfer at interface 49–57
 - act of charge transfer 53–55
 - Butler–Volmer equation 55
 - redox charge-transfer reactions 50–53
 - relation between k⁰ and I₀ 56–57
 - in terms of standard rate constant 56
 - transition state theory 49–50
- charge-transfer resistance 60
- charge-transfer step, rate of a 59
- chronopotentiometry 117
- CNT-based nanoarchitected electrodes 138
- CNT/MnO₂ 91
- Coleman portable screw gun 515
- complementary metal oxide semiconductor (CMOS) 509, 516
- concentrated electrolyte solutions 27–29
 - concentration correction 28
 - difference between the real and apparent concentrations 28
 - ion-hydration correction 28
 - Stokes–Robinson equation 27–29

- concentration correction 28
 - concentration dependence 59
 - conduction heat transfer 397–399
 - conductive additives for binders 325–326
 - conductive polymers 87
 - conductivity of an electrolyte 327–331
 - organic 328
 - π -conjugated polymer chains 208
 - constant phase element (CPE) 126
 - coordination number 16
 - Coulomb's law 37
 - counter electrode (CE) 111
 - current collector 309–312
 - cost-efficient solutions for 310
 - method to improve adhesion between electrode and 311
 - nonetched 312
 - nonetched aluminum 312
 - working in aqueous medium 311–312
 - working in organic electrolyte 310–311
 - C–V correlation on electrode potential 199–201
 - cyclability of supercapacitors 134
 - cyclic voltammetry 64, 115–117
 - accuracy of 115
 - of an activated-carbon-based supercapacitor 116
 - capacitance measurements 116–117
 - irreversible faradic reactions 116
 - i–V curve 116
 - of MnO₂ and RuO₂ 118
 - Q vs V, 116
 - two voltage boundaries 116
 - cyclic voltammetry on a nanoporous carbon cloth (ACC) 225
 - cyclic voltammograms (CVs) 141
- d**
- DC–DC converter 73
 - Debye–Huckel limiting law 25–26
 - approximations of 26–27
 - Debye–Huckel Model for calculating potential at surface 21–22
 - Debye–Huckel theory 23
 - Debye length 24
 - for monovalent electrolytes 174
 - de Levie analysis 126
 - density functional theory 139
 - dicyanamide 82
 - dielectric constants for organic electrolytes 173
 - diffuse layer of electrolyte 173–175
 - capacitance of 174
 - Debye length 174
 - effective thickness 175
 - GCS model 173, 175
 - in ILs 190–191
 - in series 173
 - diffusion coefficient 33
 - diffusion of solution 61–62
 - diffusion statistics 35–36
 - dilute solutions of nonelectrolytes 16–17
 - dimethyl carbonate (DMC) 134
 - dimethylimidazolium chloride (DMIM-Cl) 199
 - dissymmetrization principle 317
 - doping/undoping process 208
 - double-layer capacitance 75, 78, 132
 - double-layer capacitors 74–75, 124
 - capacitance 75
 - cell capacitance in series 78
 - compact layer 75
 - construction 77–86
 - diffuse layer 75
 - distribution of capacitance in porous electrodes 77
 - electrode–electrolyte interface 75, 78
 - equivalent circuit model 77
 - factors determining 75–76
 - heuristic model 76
 - movement of electrolyte ions within 76
 - porous materials model 75–77
 - practical use of 75
 - redistribution of ionic concentration profile 76
 - drift speed of ion 32
 - dual carbon lithium-ion capacitors (LICs) 99–100
 - Dubinin–Raduskevich micropore 139
 - Dynacap 307
 - dynamic electrochemistry
 - charge on a good conductor 37
 - electrically charged interface or double layer 32–36
 - electrochemical potential 39
 - force between charges 37
 - mass transport control 61–64
 - potential (ϕ) at a point 36–37
 - potential due to an assembly of charges 37–38
 - potential inside a good conductor 37
- e**
- ECOND capacitor 511
 - ECP–AC asymmetric hybrid devices 92
 - Einstein equation 33
 - Einstein–Smoluchowski equation 36
 - electrical characterization of supercapacitor

- capacitance and series resistance
 - characterization 374–375
- double-layer capacitors, characterization of 376
- efficiency 394–395
- energetic performance and discharging at constant current 387–389
- energetic performance and discharging at constant load 394
- energetic performance and discharging at constant power 389–393
- ESR characterization 376–378
- IEC62391 series of directives for testing 376
- Ragone concept 381–387
- self-discharge and leakage current 378–381
- supercapacitor conditioning 376
- electrically charged interface or double layer 39
- Bockris, Devanathan, and Muller Model 46–49
- charge transfer at 49–57
- charge-transfer resistance 60
- concentration dependence 59
- Gouy–Chapman or Diffuse Model 42–43
- Helmholtz model 40–42
- of ideally polarized electrode 40
- multistep processes 57–61
- rate-determining step 58–59
- Stern model 43–45
- electric charge on each electrode, ratio of 70
- electric double-layer capacitor (EDLC) 73
 - approach to increasing V_{\max} 290
 - in aqueous electrolytes 193–196
 - capacitance vs pore size 138–141
 - carbons used for 135–138, 170
 - cell voltage 81
 - charge storage in 170
 - classical theories for 172–176
 - co-ions, role in 199
 - dielectric constant of vacuum 132
 - “diffuse layer” 173–175
 - double-layer capacitance 132
 - electrical characteristics 133–134
 - electrode materials used 83–86
 - electrolytes used in 169
 - elements of 169–172
 - endohedral capacitors 171–172
 - evidence of desolvation of ions 141–148
 - exohedral capacitors 171
 - Helmholtz and Stern model 133
 - Helmholtz model 172
 - high surface area activated carbons 114
 - impedance of 114–115
 - industrial 131
 - internal resistance 80, 82
 - ionic liquid (IL) electrolytes in 169
 - low-temperature behavior 134
 - mesopores and micropores 197
 - in organic electrolytes 196–197
 - overall performance of 80
 - polarization at electrode/electrolyte interface 132
 - pore accessibility limitation 148–150
 - porosity saturation limitation 150–153
 - potential of zero charge (PZC) 170
 - relative dielectric constant of the electrolyte 132
 - representation of 79
 - in room temperature ILs 197–201
 - space charge layer 175–176
 - specific (gravimetric) capacitance of an electrode 78
 - specific surface area (SSA) of nanoporous carbons in 170
 - surface area variations, impact 133
 - theories 189–191
 - types of electrolytes in 80–83
 - van der Waals attractions 199
 - variation in radii, effect of 171
 - voltage limitation of 239–242
 - volumetric and gravimetric capacitance of electrode materials 79
- electricity grid applications 523–524
- electric wire-in-cylinder capacitor (EWCC) 76
- electrochemical capacitors (ECs), 69. *see* reliability concepts of ECs; testing of electrochemical capacitors
 - asymmetric EC designs 513–516
 - battery/capacitor combination applications 523
 - bipolar designs 510–512
 - cell designs 512–513
 - effective surface areas (SA) 71
 - electricity grid applications 523–524
 - electrode–electrolyte interface 71
 - energy conservation and energy harvesting applications 516–522
 - functional position of 72
 - mode of energy storage and construction 73–74
 - specific energy and power capabilities of 72
 - specific energy of 74
 - storage and utility grid 523–524

- electrochemical cell 111–114
 - electrochemical test configurations 112
 - electrode impedance 113
 - equivalent electrical circuit of 112
 - electrochemical energy storage 373
 - electrochemical impedance spectroscopy 119–123
 - electrochemical potential 39
 - electrochemical stability window (ESW) 290
 - of imidazolium-based ILs 296
 - PYR14TFSI 296
 - electrochemical workstation 111–112
 - electrode–electrolyte interface double layer 75, 78
 - electrolyte activity 18–19
 - electrolyte penetration 125
 - electrolytes of supercapacitors
 - choice of solvent 331
 - conductivity of 327–331
 - degradation of ACN-based electrolyte 334–335, 339
 - electrochemical stability and aging 331–338
 - impact on performance 327–340
 - improvement using “spiro”- type salts 329
 - ionic liquid 341–342
 - liquid-state 340–341
 - solid-state 343
 - thermal stability and performances 338–339
 - toxicity 339–340
 - electromotive force of the cell 3
 - electronically conducting polymers (ECPs) 87–92
 - asymmetric electrochemical capacitors 91–92
 - composites 91
 - ECP/CNT nanocomposites 208
 - electrochemical behavior of ECP/CNT composites 210
 - MWCNT/ECP composites 210
 - positive effect of nanotubes and/or graphenes in 209
 - pretreatment of the nanotubular material, need for 209
 - supercapacitor application of 208–212
 - electrosorption of hydrogen 222
 - electrostatic adsorption–desorption at electrode 93
 - ELIT capacitor 511
 - endohedral capacitors 171–172
 - models for 176–185
 - upper-bound capacitance of 189
 - energy conservation and energy harvesting applications of EC
 - in cranking engines 521–522
 - energy conservation and efficiency 521
 - hybridization 518–521
 - motion and energy 516–518
 - enthalpy of hydration of the anion 15
 - equilibrium electrochemistry
 - chemical reaction at equilibrium 5
 - Eh–pH diagram 6
 - Gibbs energy 1–3
 - maximum amount of electrical work of electrochemical cell 3
 - Nernst equation 5
 - relation between zero-current cell potential and 3–4
 - spontaneous chemical reactions 1
 - equivalent series resistance (ESR), 71
 - ethyl-methyl-imidazolium-trifluoro-methane-sulfonylimide (EMI-TFSI) IL 154, 157–158, 292, 297–300
 - Et₄NBF₄ electrolyte 146–147, 154, 161
 - Et₄NBF₄ (tetraethylammonium tetrafluoroborate or TEABF₄) 327–328
 - “exclusive solvation” phenomenon 155
 - exohedral capacitors 171
 - models for 187–189
 - positive curvature of 188
 - exohedral electric double-cylinder capacitor (xEDCC) 187–188
 - extent of reaction 1
- f**
- Faraday constant 4, 39, 122
 - faradic metal oxide electrode 93–94
 - faradic reactions of electrolytic solutions 226–231
 - faradic water decomposition 222
 - Fick’s first law 33–34, 62
 - Fick’s second law 33–34
 - (fluoromethanesulfonyl)imide 82
 - force between charges 37
 - formaldehyde 138
 - free energy of solution per mole of reference ions 21
 - calculation of 24
 - fuel cells (FCs) 420
 - power management 421–433
 - fuel cell vehicle converter 431
 - fugacity 16–17
 - Fuoss treatment for ion pair formation 30–31

g

- galvanic cell 5
- galvanostatic cycling 117–119
 - capacitance measurements 119
 - Q vs V , 118
 - resistance measurements 119
 - voltage variation, calculation of 118
- gamma-butyrolactone (GBL) 82
- generic chemical reaction 2
- Gibbs–Duhem equation 18
- Gibbs energy
 - chemical potential or molar 1
 - composition of the reaction mixture at equilibrium 2
 - defined 1
 - Eh–pH diagram 6
 - infinitesimal change at constant temperature and pressure 2
 - relation between zero-current cell potential and 3–4
 - standard 5–6
- glassy carbon (GC) electrodes 292
- gold capacitors 74, 307
- graphene materials 191
 - nitrogen plasma treatment of 222
- graphite electrode, formation cycles for preconditioning 245
- graphite-negative electrode 244

h

- halide-based systems 229
- heavy electric vehicles (EVs) 289
- Helmholtz layer 172–173
- Helmholtz model for parallel-plate capacitors 176
- Helmholtz plane 114
- Henry's law 16–17
- heteroatoms, pseudocapacitive effects of 214–215
- HF charge-transfer loop 126
- hierarchically porous carbon materials, models for 185–187
- high-capacitance supercapacitors 309
- high field approximations 58
- highly oxygenated carbon, method of preparing 216
- high-surface-area-active carbon electrodes 134
- hybrid capacitor systems 242. *see also* lithium-ion capacitor (LIC)
- hybrid diesel-electric seaport cranes 289
- hybrid-electric vehicles (HEVs) 289
 - lithium-ion batteries 290
 - power-assisted HEVs 290

- hybrid lead acid battery 96
- hydration number 16
- hydrogen
 - electrosorption on nanoporous carbon electrodes 226
 - galvanostatic charge/discharge curves 224
 - pseudocapacitance 222
 - temperature effects 224
 - TPD analysis of 224
- hydroquinone 231

i

- ice, structure of 10
- imidazolium 293
- impedance of a porous electrode 125
- industrial EDLC 131
- infinite dilution 18, 20
- iodide-based electrolyte 229
 - constant current charging/discharging curves for 229
- iodide ions
 - Pourbaix diagram of 226
 - striking effect of 227
- ion-buffering reservoirs 185
- ion cloud
 - radius of, at various concentrations of NaCl 26
 - thickness of. *see* Debye length
- ion dynamics 32–36
 - diffusion 33
 - drift speed of ion 32
 - Fick's second law 33–34
 - molar conductivity of the ion 32
 - net rate of change of concentration 34
 - rate of movement of charge 32
- ion-hydration correction 28
- ionic liquid codes 303
- ionic liquids (ILs) 292–296
 - application 296
 - based on imidazolium and pyrrolidinium cations 296
 - chemical/electrochemical and physical properties 293–294
 - chemical formula of ions 295
 - conductivity 293–295
 - electrochemical reduction and oxidation 295
 - hydrophobicity of 295, 297
 - imidazolium-based 296
 - for large-size EDLCs 296
 - $\text{PYR}_{1(201)}\text{TFSI}$ -based 300
 - pyrrolidinium-based 296
 - $\text{PYR}_{14}\text{TFSI}$ -based 300
 - as salts in organic solvents 296

- ionic liquids (ILs) (*contd.*)
 - solvent-free 296
 - TFSI-based 296
 - Walden plots 295
 - ionics
 - activity and activity coefficients 16–20
 - Born or simple continuum model 8–9
 - concentrated electrolyte solutions 27–29
 - electrostatic interaction 8
 - equations of single ionic species 9
 - heats of hydration for ions 15
 - ion dynamics 32–36
 - ion–ion interactions 20–27
 - ion pair formation 29–31
 - ions in solutions 6–7
 - ion–solvent interactions 7
 - reversible work to charge an ion 8
 - reversible work to discharge an ion 9
 - solvation number 16
 - structure of water 9–15
 - thermodynamics 8
 - ion–ion interactions 20–27
 - activity coefficient 24–25
 - in an explicit equation in f_{\pm} 25
 - approximating for ions of finite size 26–27
 - charge density 22–23
 - coulombic interactions between the ions 27
 - Debye–Huckel limiting law 25–27
 - Debye–Huckel Model for calculating potential at surface 21–22
 - Debye length 24
 - difference between real and ideal solutions 24
 - distance between their centers on collision 27
 - free energy of solution per mole of reference ions 21, 24
 - ionic strength in molar units 25
 - Poisson–Boltzmann equation 22–24
 - potential energy of reference ion 21
 - ion pair formation 29–31
 - Fuoss treatment 30–31
 - and square of the concentration 30
 - isocyanate-based polymer 310
- k**
- kinematic viscosity factor 64
 - knee frequency 125, 128
 - KOH activation of bituminous coal 139
 - Kornyshev’s model for EDL 190
- l**
- lead acid batteries 524
 - lead dioxide (PbO₂) 95–96
 - asymmetric capacitor technology using 95–96
 - Lennard–Jones beads 199
 - Leyden jars 69
 - lifetime of an energy storage
 - calendar life testing 415
 - DC voltage test 415–416
 - failure modes 411
 - failure rate 410
 - mean time between failure (MTBF) 410
 - physical origin of aging 413–415
 - temperature and voltage as an aging acceleration factor 411–413
 - voltage cycling test 417–418
 - Li-ion battery (LIB) 244
 - limiting current density 62, 64
 - LiMn₂O₄, mechanism of lithium removal from 212
 - lithium-ion capacitor (LIC)
 - cell configurations and mechanisms 243
 - drawbacks 244
 - limited charging rate 244
 - Li⁺ predoping for 245–246
 - low-temperature performance of 245
 - lithium-ion capacitor (LIC) 98–100
 - lithium manganese oxide (LiMn₂O₄) 99
 - lithium titanate (Li₄Ti₅O₁₂) 98–99
 - lithium-ion intercalation/deintercalation process 100
 - lithium titanate (Li₄Ti₅O₁₂) 247
 - advantages 248
 - carbon nanofibers (CNFs) (Li₄Ti₅O₁₂/CNF) 248
 - electrochemical and structural changes 248
 - Li₄Ti₅O₁₂/AC hybrid 247
 - nc-Li₄Ti₅O₁₂ negative electrode 249
 - as a redox material for hybrid capacitors 247
 - low-capacitance supercapacitors 309
 - low-temperature behavior of supercapacitors 134
- m**
- manganese dioxide (MnO₂) 97–98, 258
 - activated carbon/MnO₂ device 274–277
 - asymmetric MnO₂-based ECs 278
 - carbon/MnO₂ composites 213
 - conductivity of the positive carbon electrode 226

- cyclic voltammograms in a three-electrode cell of 278
 - energy density 258
 - incorporation into asymmetric cell configurations 277
 - intercalation of Li^+ 276
 - LiMn_2O_4 , mechanism of lithium removal from 212
 - $\alpha\text{-MnO}_2/\text{CNT}$ composite electrodes 213
 - porous hydrous 212
 - pseudocapacitive charge storage mechanism of 97–98
 - pure ($\lambda\text{-MnO}_2$) 212
 - redox exchange of protons and/or cations 213
 - symmetrical $\text{MnO}_2/\text{MnO}_2$ EC 258
 - maximum energy density 134
 - maximum power density 133–134
 - maximum theoretical charge 150–151
 - mean-field theory 174, 190
 - mean ion quantities 19
 - merit factor 129
 - mesoporous templated porous carbon materials 85
 - metal-oxide-based EC targets 93
 - metal oxide/carbon composites 212–214
 - porous hydrous MnO_2 212
 - pure manganese oxide ($\lambda\text{-MnO}_2$) 212
 - microporous activated carbon cloth (ACC) electrode 222
 - microporous template carbons 141
 - capacitance with ionic liquid in solutions 156–159
 - intercalation/insertion of ions 161–162
 - ions trapped in pores 159–161
 - in neat ionic liquid electrolyte 153–156
 - “microscopic” Maxwell equations’ formalism 376
 - migration of solution 61–62
 - MnO_2 – FeOOH hybrid supercapacitor 278
 - module design for supercapacitors
 - based on asymmetric technologies 360–362
 - based on hard-type cells 353–354
 - based on pouch-type cells 357–359
 - cell balancing and other information detection 356–357
 - electric terminal for 354
 - enclosures 357
 - insulator for 354–356
 - metallic connections between cells 354
 - working in aqueous electrolytes 359–360
 - molar conductivity of the ion 32
 - molecular dynamics (MD) simulations 168, 192–193
 - mole fraction positive ions 19
 - moles of ions 19
 - moles of positive ions 19
 - moles of solvent 19
 - monovalent electrolytes 174
 - movement of charge, rate of 32
 - multicelled asymmetrically supercapacitive lead-acid-carbon hybrid battery 96
 - multiwalled carbon nanotubes (MWCNTs) 138, 167, 209, 219
 - MWCNT/ECP composites 210
 - MWCNT/PANI composites 210
 - positive effect of 211–212
- n**
- Nafion[®] 230, 231
 - nanocomposite electrodes 213
 - nanohybrid capacitor (NHC) 247–248
 - comparison with LIC 249
 - internal resistance of 248
 - material design for 248–254
 - nanotextured carbons for EDLC applications 139
 - NaY zeolite 222
 - $\text{nc-Li}_4\text{Ti}_5\text{O}_{12}/\text{CNF}$ composites 249–250
 - charge-discharge measurements 254–255
 - electrochemical properties of 253
 - galvanostatic charge–discharge characteristics of 251–254
 - HR-TEM image 252
 - nanostructure and crystallinity of 250
 - nanostructure of 252
 - Ragone plots 255
 - thermogravimetric (TG) measurement 250
 - XRD patterns of 250–251
 - n-dopable polymers 87
 - n-doped ECPs 87
 - Nernst equation 5, 64
 - applications of 6
 - Eh–pH diagram 6
 - NEt_4^+ cations 150
 - Ni/AC asymmetric supercapacitor 97
 - nickel oxide (NiO) and nickel hydroxide ($\text{Ni}(\text{OH})_2$) 97
 - nickel-zinc secondary batteries 258
 - Nippon Electric Corporation (NEC) 307
 - nitrogen-enriched carbons 216–222
 - by ammoxidation of nanoporous carbons 216
 - beneficial effects 219
 - capacitance values vs nitrogen content of 217

- nitrogen-enriched carbons (*contd.*)
 - nitrogen adsorption/desorption isotherms 219
 - physicochemical and electrochemical characteristics of 220
- NMRO/AC asymmetric device 97
- nonaqueous electrolytes 82
- non-faradic carbon electrode 93–94
- nonpolarizable faradic electrode 93
- normalized capacitance (capacitance per unit area) 79
- Nyquist plots 122–124, 126–17
- o**
- Ohm's law 113
- Ohm's law potential difference 62
- one-dimensional (1D) end-capped CNTs 187
- open-circuit potential (OCP) 149
- operational amplifier (OA) circuit 113
- organic electrolytes 169
- oxygenated functional groups 215
- oxygen-enriched carbons 215–216
- p**
- PANI/Nafion composite 91
- parallel plate capacitor 38, 70
- PbC Ultracapacitor 96
- PbO₂/AC asymmetric capacitor 96
- p-dopable polymers 87, 208
- p-doped ECPs 87, 92
- permittivity
 - of the dielectric 70
 - of free space 70
- PFPT/AC asymmetric laboratory test cells 92
- piperidinium 293
- PMT/AC asymmetric device 92
- Poisson–Boltzmann (PB) equation 173–174
 - counterions 174
 - dielectric constant of solvent in diffuse layer 174
 - electrostatic ion–ion interactions 174
 - ion–ion correlations 174
 - limitations 174
- Poisson's equation 37
- polarizable faradic electrode 93
- polarography 64
- polyacrylonitrile (PAN) 216
 - CNT/PAN composites 217
- polyaniline (PANI) 86, 88–90, 208
 - MWCNT/PANI composites 210
- poly(3,4-ethylenedioxythiophene) (PEDOT) 90–91, 208
 - PEDOT/CNTs/MnO₂ 214
- poly(4-fluorophenyl-3-thiophene) (PFPT) 90
 - poly(3-methylthiophene) (PMTh) 90, 208
 - polypyrrole/MnO₂ 91
 - polypyrrole (PPy) 86, 90, 208
 - PPy/CNT-based symmetric capacitor 211
 - redox performance of 209
 - SWCNT/PPy nanocomposites 210
 - polythiophene (PTh) 86, 90–91, 208
 - pore accessibility limitation 148–150
 - pore size distribution
 - carbide-derived carbons (CDCs) 142
 - electric double-layer capacitor (EDLC) 138–141
 - optimization of 315–317
 - porosity characteristics for PC and VC 151–152
 - porosity saturation limitation 150–153
 - positive and negative electrode capacitance measurement 145
 - potassium hydroxide 81
 - potassium iodide (KI) 231
 - potential
 - difference between two phases in contact 38–39
 - due to an assembly of charges 37–38
 - electrochemical 39
 - inside a good conductor 37
 - at a point 36–37
 - at zero charge (PZC) 170, 192
 - potentiostat/galvanostat (PG) 111
 - schematic representation of 113
 - power-assisted HEVs 290
 - power cache 74
 - power capacitors 74
 - power management of fuel cells (FCs) 422–433
 - control by sliding mode 429–433
 - control in MATLAB/SIMULINK 432
 - DC link voltage 433
 - European speed cycle NEDC 432
 - Hamilton–Jacobi–Bellman Equation 423–426
 - with inequality constraints 427–429
 - optimal control strategies for a dynamic system 423
 - PEMFC power variation 427
 - sliding surfaces 431
 - PPy/vapor-grown carbon fiber/AC composite 208
 - primary solvation number 16
 - PRI Ultracapacitor 74
 - propylene carbonate (PC) 169
 - electrolyte 128, 373
 - solvent 82
 - pseudocapitance 207

- of metal oxide/carbon composites 212–214
 - with nanoporous carbons 222–226
 - of nitrogen-enriched carbons 216–222
 - of oxygen-enriched carbons 215–216
 - profits and disadvantages of 231–233
 - pseudocapacitive effects of heteroatoms 214–215
 - pseudocapacitors 73–74
 - electronically conducting polymers (ECPs) 87–92
 - equivalent electrical circuit of 115
 - lithium-ion capacitors 98–100
 - transition metal oxides 93–98
 - pseudo-faradic effects 226
 - Pt/BMIM DCA (dicyanamide) 292
 - pyridinium 293
 - PYR₁₍₂₀₁₎TFSI-based AEDLC 296, 301
 - Ragone plot 301
 - PYR₁₄TFSI-based AEDLC 296, 299, 302
- q**
- quantum capacitance of graphene materials 191–192
 - quasi-reference electrode 148
 - quinone/hydroquinone pair 215
- r**
- Ragone plots 131–132, 374, 449
 - case of impedance matching 383–384
 - nc-Li₄Ti₅O₁₂/CNF composites 255
 - PYR₁₍₂₀₁₎TFSI-based AEDLC 301
 - ratio between energy available and maximum stored energy 384–387
 - theory 381–387
 - for various electrochemical energy storage systems 132
 - Randles' electrical equivalent circuit 121
 - Randles–Sevcik equation 159
 - redox-active electrolytes 231
 - redox charge-transfer reactions 50–53
 - redox EC 73
 - redox pseudocapacitor 74
 - reference electrode (RE) 111
 - reference ion 21
 - reliability concepts of ECs
 - approach to assessment 481–484
 - basics 473–474
 - burn-in of cells 501
 - of cell 474–477
 - cell temperature nonuniformity 494–499
 - cell voltage nonuniformity 492–494
 - energy storage system, example 503–507
 - experimental approach example 484–490
 - of fewer cells in series 501
 - of long-life cells 501–502
 - maintenance aspects 502
 - method of increasing system 499
 - method of reducing cell stress 499–501
 - of practical systems 490
 - redundancy 502–503
 - of system 478–481
 - resorcinol 138
 - Rightmire, R. A. 75
 - room temperature ionic liquids (RTILs) 82, 153
 - rotating disk electrode 64
 - round-trip efficiency 469
 - ruthenium oxide (RuO₂) 94–95, 258
 - carbon/RuO₂ device 280–281
 - charge storage mechanism 95
 - in commercial devices 95
 - electrode in H₄SiW₁₂O₄₀ (SiWA) electrolyte 281
 - formation of composites 95
 - in H₂SO₄ electrolyte 259
 - hydrous forms of 95
 - ruthenium/tantalum oxide device 74
- s**
- saturation phenomenon 138
 - seaweed precursors 216
 - separators for supercapacitors 343–345
 - cellulosic 343–344
 - dryness of 344
 - polymeric-based 344–345
 - requirements for 343
 - SEM images of commercial 346
 - standard cellulosic 344
 - thickness range 344
 - Wade's work on 345
 - Shi's model for hierarchically porous carbon materials 186–187
 - signal waveform generator (SWG) 111
 - silver as electrode 148
 - simple chemical equilibrium 1
 - single-walled carbon nanotubes (SWCNTs) 138, 141, 167, 209
 - SWCNT/PPy nanocomposites 210
 - voltammogram of 141
 - sizing of supercapacitor modules
 - critical parameter for 374
 - problems with 374
 - sodium alginate 215

- sol-gel reaction 249–250
 - solid electrolyte interphase (SEI) 134
 - solid-state electrolytes of supercapacitors 343
 - solute activity, measurement of 18
 - solvation number 16
 - primary 16
 - solvent activity, measurement of 18
 - space charge capacitance theory 191–192
 - space charge layer 175–176
 - capacitance of 175
 - capacitance–potential curves 176
 - Debye screening length 175
 - spontaneous chemical reactions 1
 - stainless steel current collectors 227
 - standard cell potential 5
 - standard hydrogen electrode (SHE) 5
 - Standard Oil Company of Ohio (SOHIO) 75
 - standard states 17
 - stationary techniques for characterizing supercapacitors
 - electrochemical impedance spectroscopy 119–123
 - supercapacitor impedance 124–129
 - steady-state (time-independent) diffusion 62
 - Sterling's approximation 36
 - Stern layer 174
 - Stokes – Einstein equation 33
 - Stokes–Robinson equation
 - approximations 27
 - evaluation of 29
 - in terms of free energies 28
 - structure-broken region 11
 - sulfuric acid 81
 - supercapacitor impedance 124–129
 - supercapacitor module sizing methods
 - parameters 418–420
 - Supercapacitor™ 509
 - with H₂SO₄ 510
 - supercapacitor pack power 430
 - reference current trajectory of 426
 - supercapacitors 74, 114–115, 131, 298–302
 - approach to enhanced energy density of 243
 - average performances of 135
 - cyclability 134
 - equivalent circuit of 422
 - high-capacitance 309
 - industrial activated carbons for industrial 317–319
 - industrial point of view 309
 - low-capacitance 309
 - low-temperature behavior 134
 - maximum energy density 134
 - maximum energy (E_{\max}) of 289
 - maximum power density 133–134
 - modeling 422
 - product robustness 308–309
 - steps in manufacturing 308
 - surface functionalization of ACs 138
 - symmetrical AC/AC capacitors 226
 - symmetric EDLC 93, 171
 - symmetry factor 55
- t**
- Tafel equation 58
 - tantalum electrolytic capacitors 281
 - tantalum oxide–ruthenium oxide hybrid capacitors 282
 - TEA-BF₄/AN electrolyte 196–197
 - Teflon™ 142
 - temperature effects on galvanostatic charge/discharge characteristics 224–225
 - templated carbons 85, 167
 - template synthesis route 139
 - testing of electrochemical capacitors
 - capacitance of a device 443, 456
 - charging algorithm 466
 - comparisons of projected power capabilities 468
 - energy density 448–449, 459–460
 - of hybrid, pseudocapacitive devices 456
 - IEC test procedures 440–441
 - lithium-ion battery – nickel cobalt 453
 - lithium-ion – iron phosphate 453
 - power capability 449–453, 460
 - pulse cycle 454, 460
 - pulsed simple FUDS (PSFUDS) 453–454
 - relationships between AC impedance and DC testing 460–465
 - resistance of a capacitor 443–447, 456–459
 - round-trip efficiency 469
 - summaries of DC test procedures 437–439
 - UC Davis test procedures 441–443
 - ultracapacitors 452
 - uncertainties in ultracapacitor data interpretation 465
 - uncertainty 466–468
 - USABC method (batteries) 451
 - USABC method (ultracapacitors) 452
 - USABC test procedures 439–440
 - tetraalkylammonium 150, 152–153
 - tetraethylammonium tetrafluoroborate (TEA-BF₄) 82, 86, 116, 169
 - tetrafluoroborate 82

- tetralkylammonium salts 293
- thermal modeling of supercapacitors
- BACP0350 supercapacitor 404–410
 - conduction heat transfer 397–399
 - consequences of rise in temperature 396
 - heat transfer coefficient for natural convection 401–402
 - solution procedure 402–403
 - thermal boundary conditions 399–401
 - thermal diffusion 397
 - transfer of energy 397
- thermodynamic equilibrium constant 3
- thermoprogrammed desorption (TPD) analyses 223
- three-electrode cells 115, 148
- three-electrode measurement 78
- transient techniques for characterizing supercapacitors
- cyclic voltammetry 115–117
 - galvanostatic cycling 117–119
- transition metal oxides 93–98, 212–213
- conditions for 94
 - lead dioxide (PbO₂) 95–96
 - manganese dioxide (MnO₂) 97–98
 - nickel oxide (NiO) and nickel hydroxide (Ni(OH)₂) 97
 - ruthenium oxide (RuO₂) 94–95
- transition state theory 49–50
- transport number of an ion 32
- trimming capacitors 69
- two-electrode cells 115
- two-electrode measurement 78
- type I, II and III devices 87–88
- u**
- Ultracapacitor Development Program 307
- ultracapacitors 74
- ultra-centrifuging (UC) treatment 249–250
- ultramicropore 141
- uncertainty testing
- in capacitance 466
 - in energy density 467
 - in power capability 467–469
 - in resistance 466–467
 - in ultracapacitor data interpretation 465
- uninterruptible power supply (UPS) systems 289
- USABC-DOE protocols 301
- v**
- vacuum level 36
- vanadium-based aqueous electrolytes 229
- vanadyl sulfate (VOSO₄) solution 229, 231
- Vogel–Tammann–Fulcher exponential equation 293
- Volta, Alessandro 69
- voltage profiles for EDLC 244
- voltammetry cycling of a carbon electrode (AC) 223
- Volta's pile*, 69
- volumetric capacitance 139–140
- w**
- Walden rule 295
- Warburg element 121
- Warburg impedance 124
- water, structure of 9–15
- Born energy 13
 - breaking of H bond clusters 12
 - of bulk water 11
 - cavity formation 12
 - dipole moment 10
 - enthalpy of hydration of the anion 15
 - force between the ion and the dipole 14
 - in ice 10
 - induced dipole interaction 14–15
 - ion–dipole interactions 11–13
 - ion–quadrupole model 14
 - leftover water molecules 14
 - near an ion 11
 - O–H bonds 10
 - orientation of solvated ion 13–14
 - quadrupole moment of 14
 - sp³ hybrid orbitals 9
 - structure-broken region 11
 - theoretical and experimental ion–water interactions 10
- whole cell voltages 60–61
- working electrode (WE) 111
- impedance of 113
- x**
- xerogel carbon electrodes 299
- xerogels 86
- z**
- zero-current cell potential 3
- between electrodes of a galvanic cell 3
- zero-dimensional (0D) carbon onions 187